



HAL
open science

Collisional excitation of radicals of astrophysical interest

P Pirlot Jankowiak

► **To cite this version:**

P Pirlot Jankowiak. Collisional excitation of radicals of astrophysical interest. Physics [physics]. Université de Rennes, 2024. English. NNT: . tel-04842385

HAL Id: tel-04842385

<https://hal.science/tel-04842385v1>

Submitted on 17 Dec 2024

HAL is a multi-disciplinary open access archive for the deposit and dissemination of scientific research documents, whether they are published or not. The documents may come from teaching and research institutions in France or abroad, or from public or private research centers.

L'archive ouverte pluridisciplinaire **HAL**, est destinée au dépôt et à la diffusion de documents scientifiques de niveau recherche, publiés ou non, émanant des établissements d'enseignement et de recherche français ou étrangers, des laboratoires publics ou privés.



THÈSE DE DOCTORAT DE

L'UNIVERSITÉ DE RENNES

ÉCOLE DOCTORALE N° 638

Sciences de la Matière, des Molécules et Matériaux

Spécialité : *Physique*

Par

Paul PIRLOT JANKOWIAK

Collisional excitation of radicals of astrophysical interest

Thèse présentée et soutenue à Rennes, le 1er octobre 2024

Unité de recherche : Institut de Physique de Rennes

Rapporteurs avant soutenance :

Charlotte VASTEL Astronome, CNAP, Toulouse, France
Pascal LARREGARAY Directeur de recherche, CNRS, Bordeaux, France

Composition du Jury :

Président : Sébastien LE PICARD Professeur, Université de Rennes, France
Examineurs : Yohann SCRIBANO Maître de conférences, HDR, Université de Montpellier, France
 Jérôme LOREAU Professeur, KU Leuven, Belgique
 Nami SAKAI Directrice de recherche, RIKEN, Japon
Dir. de thèse : François LIQUE Professeur, Université de Rennes, France

Invité(s) :

Niyazi BULUT Professeur, Université Firat, Turquie

À Ethan

CONTENTS

1	Introduction	7
1.1	The interstellar medium	7
1.1.1	Composition and role of the interstellar medium	7
1.1.2	Phases of the ISM	8
1.1.3	Star formation	10
1.2	Astrochemistry	13
1.2.1	Importance of observations	13
1.2.2	Importance of experiments	14
1.2.3	Importance of modeling	15
1.3	Collisional excitation	17
1.3.1	General considerations about collisional processes	17
1.3.2	State of the art	18
1.4	Outline of the thesis	21
2	Theory and methodology	23
2.1	The time-independent Schrödinger equation	23
2.1.1	Molecular system	23
2.1.2	The Born-Oppenheimer approximation	24
2.2	Potential energy surface	27
2.2.1	<i>Ab initio</i> calculations	28
2.2.2	Analytical representation for potential energy surfaces	36
2.3	Notions of spectroscopy	38
2.3.1	Rotational structure	39
2.3.2	Fine structure	42
2.3.3	Hyperfine structure	44
2.4	Scattering theory	46
2.4.1	Collisional excitation of $^1\Sigma$ molecules induced by collisions with $^1\Sigma$ molecules	46
2.4.2	Approximations	51
2.4.3	Statistical Adiabatic Channel Model (SACM)	54
2.4.4	Validity of the methods	55
2.4.5	Scattering softwares	56

2.5	Radiative transfer	59
2.5.1	Radiative transfer equation	59
2.5.2	Statistical equilibrium equations	62
2.5.3	Line profile	64
2.5.4	Approximations	65
2.5.5	Quantities of interest	67
3	Collisional excitation in non-reactive systems	71
3.1	Molecules of interest	71
3.1.1	Objectives of this work	71
3.1.2	The C ₂ H molecule	72
3.1.3	The NH molecule	73
3.1.4	The interest for isotopologues	74
3.1.5	Rotational spectroscopy	75
3.2	Fine structure excitation of ^{2S+1} Σ molecules by ¹ Σ molecules	78
3.2.1	Close-Coupling approach	78
3.2.2	Results	81
3.3	Hyperfine structure excitation	90
3.3.1	Close-coupling approach	90
3.3.2	Recoupling approach	91
3.3.3	Infinite Order Sudden limit	93
3.3.4	Results	95
3.4	Astrophysical modeling	104
3.4.1	Critical density	104
3.4.2	Excitation of C ₂ H isotopologues in star-forming regions	106
3.4.3	Excitation of NH in the η Carinae binary star system	109
4	Collisional excitation in reactive systems	112
4.1	The OH ⁺ molecule as a test case	112
4.1.1	Objectives of this work	112
4.1.2	The OH ⁺ molecule	113
4.1.3	Spectroscopy of OH ⁺	115
4.2	Fine structure excitation of OH ⁺ by atomic hydrogen	117
4.2.1	Potential energy surface	117
4.2.2	Statistical Adiabatic Channel Model (SACM)	118
4.2.3	Results	119
4.3	Reactive collisions of OH ⁺ with H ₂	125
4.3.1	Potential energy surface	126

4.3.2	Dynamical calculations	129
4.3.3	Pure inelastic collisions	131
4.3.4	Inclusion of reactive processes	132
4.3.5	Rotational state-to-state rate coefficients of OH ⁺ induced by collisions with H ₂	134
5	Conclusions and outlooks	139
	Appendix	144
A	Notes on the V-matrix elements for $^{2S+1}\Sigma - ^1\Sigma$ interactions	144
B	Notes on Einstein coefficients for linear open-shell molecules	148
C	Peer-reviewed articles	150
C.1	Collisional excitation of NH by H ₂ : Potential energy surface and scattering calculations	151
C.2	Hyperfine excitation of ¹³ CCH and C ¹³ CH by collisions with <i>para</i> -H ₂ . . .	162
C.3	Collisional excitation of C ₂ H and C ₂ D by molecular hydrogen	172
C.4	BASECOL2023 scientific content	183
C.5	Hyperfine excitation of NH and ND by molecular hydrogen: Rate coefficients and astrophysical modeling	215
	Bibliography	229

INTRODUCTION

This chapter introduces the context and importance of the interstellar medium (ISM) in astrophysics in section 1.1, detailing its composition, phases, and role in star formation and galaxy evolution. It will then focus on the field of astrochemistry in section 1.2, emphasizing the significance of observations, laboratory experiments, and theoretical modeling in understanding the chemical processes within the ISM. Furthermore, section 1.3 discusses the state of the art of collisional excitation methodologies and the challenges of such theoretical calculations, from heavy molecules to reactive systems. Finally, the outline of the thesis is presented in section 1.4, highlighting its focus on investigating collisional excitation in reactive systems involving open-shell molecules in the ISM.

1.1 The interstellar medium

1.1.1 Composition and role of the interstellar medium

A galaxy can be approximately defined as a self-gravitating astrophysical object composed of a large number of stars. Its composition in mass is mostly made of dark matter while baryonic matter represents only about 10% of the total mass in galaxies like ours [1]. The interstellar medium (ISM) defines the baryonic matter present between stars of a galaxy and accounts for $\sim 1\%$ of its total mass. As the study of the Solar composition is an important key for understanding the formation and evolution of the Solar System, spectroscopic studies of stellar atmospheres like the Sun [2] or early B-type stars, interesting because they preserve their pristine abundances [3], enabled the determination of present-day atomic cosmic abundances in the Milky Way and consequently in the ISM. The most abundant atomic elements are hydrogen (H, 80%) and helium (He, $\sim 20\%$). Following these are oxygen (O), carbon (C), neon (Ne), iron (Fe) and nitrogen (N) that are about $10^3 - 10^4$ times less abundant than hydrogen. Heavier elements are present as traces. This composition is also distributed in the ISM as 99% of *gas* and about 1% of *dust*.

Even though the gas phase is the main state of matter in the ISM, dust remains an essential component for star formation and thermodynamic properties of the ISM [4].

Dust grains are formed at the end of a star's evolution through gas jets or stellar winds in the case of red giants [5]. Dust formation results in the *extinction* of starlight, first noted by Trumpler in 1930 [6]. Extinction usually involves a *reddening* of the light due to scattering when it interacts with grains. Observational spectra have shown that extinction varies with wavelength, revealing the chemical composition of the grains. Additionally, the larger attenuation of blue and shorter wavelengths constrains the size and distribution of the grains. Among the possible type of grains, the three main extinction peaks have been identified as (for a complete review, see *e.g.* Draine [4]):

- *Graphites*: These correspond to an absorption peak at 271.5 nm with a spherical shape [7]. *Polycyclic aromatic hydrocarbons* (PAH) smaller than 5 nm also contribute to such absorption.
- *Ices*: Usually present on grains as mantles, these are attributed to the 3.1 μm O-H stretching mode of H_2O , often observed in dense molecular clouds. Additional spectral features of CO , NH_3 or CH_3OH complicate the determination of their composition [5].
- *Silicates*: These amorphous grains show absorption peaks for 9.7 and 18 μm [8]. They are attributed to the Si-O and O-Si-O stretching modes, respectively.

Despite a small mass contribution to the galaxy, the ISM plays a crucial role in the evolution of galaxies and the universe. Interstellar matter can condense locally and, through gravitational collapse, lead to stars formation. During their existence, stars create heavier chemical elements through thermonuclear fusion in their cores, which are ejected into the ISM as stellar winds. At the end of their evolutionary cycle, stars disappear as supernovae, enriching the ISM with matter and causing significant energetic phenomena, making complex the dynamics of the ISM.

1.1.2 Phases of the ISM

Since the ISM is dynamic, the matter is found in a wide range of densities and temperatures, known as *phases* that coexist in a complex way. Early work like McKee & Ostriker proposed a three-phases model of the ISM in 1977 [9] including a hot, warm and cold medium. More recent works include a more detailed description of the composition of the phases of the ISM, where we summarize the main aspects (see Table 1.1), mostly referring to Draine [1] and Snow & McCall [10].

- *The Hot Ionized Medium* (HIM): Also referred as "coronal gas" due to its similar physical conditions as the corona of the Sun, this component is heated from temperatures up to 10^6 K and is collisionally ionized, notably containing O^{5+} absorption lines [11]. Coronal gas has typical dimensions of ~ 20 pc and is very tenuous, with

Phase	Density (cm^{-3})	Temperature (K)	Observations
Hot Ionized Medium (HIM)	$10^{-3} - 10^{-2}$	$> 10^6$	UV and X-rays
Warm Ionized Medium (WIM)	$0.3 - 10^4$	few 10^3	Optical
Warm Neutral Medium (WNM)	~ 0.6	few 10^3	21cm, Optical, UV
Cold Neutral Medium (CNM)	~ 100	10 – 100	21cm, Optical, UV
Molecular Clouds	$10^3 - 10^6$	< 50	IR, mm

Table 1.1 – Phases of the interstellar medium (from Draine [1]).

densities as $\sim 10^{-3} - 10^{-2} \text{ cm}^{-3}$.

- *The Warm Ionized Medium (WIM)*: This component results from the photoionization of atomic hydrogen by UV photons from stars, also referred as *HII regions* (or *planetary nebulae*, when photoionization is due to ejected gas from late stage evolution of stars of $\sim 1-8M_{\odot}$). This phase can reach temperatures about 5000 K and densities about $0.3-10^4 \text{ cm}^{-3}$, with about half of the ionized gas distributed within 500 pc of the galactic disk midplane.
- *The Warm Neutral Medium (WNM)*: Mostly composed of atomic gas, this phase fills $\sim 40\%$ of the galactic disk. The gas is heated by photoelectrons from dust up to ~ 5000 K and is very diluted, about 0.6 cm^{-3} .
- *The Cold Neutral Medium (CNM)*: Covering temperatures from 10 to 100 K, this phase consists of atomic and molecular clouds within the WNM. The external part of this phase is characterized by *diffuse atomic clouds* which are the most exposed to UV radiations and cosmic rays. These rays photodissociate most of molecules present in the gas. Diffuse atomic clouds are the warmest part of the CNM, with temperatures from 30 to 100 K and with low density conditions ($\sim 10-100 \text{ cm}^{-3}$). Then come *diffuse molecular clouds*, where external radiations are less energetic than the dissociation energy of H_2 , allowing their formation but still photodissociating molecules like CO. These gas usually reach densities of $100-500 \text{ cm}^{-3}$ and temperatures of $30-100$ K. When these gas are sufficiently shielded, molecules like CO can form, enabling more complex chemistry. However, these type of clouds still suffers of lack of comprehension due to disagreement between astrophysical models or lack of observations. Finally, *dense molecular clouds* are the coldest ($\sim 10-50$ K) and densest part of the local ISM (with densities larger than 10^4 cm^{-3}). They are characterized by a large extinction¹ ($A_V > 5-10$), with observations conducted in the infrared (IR) or millimeter wavelength range. Due to their opacity to external radiation field, molecular formation is facilitated, and

1. The extinction represents the quantity of radiation absorbed by interstellar gas and dust.

Type of cloud	Density (cm^{-3})	Temperature (K)	A_V (min)	Observations
Diffuse Atomic	10–100	30–100	0	UV, Optical, 21cm
Diffuse Molecular	100–500	30–100	~ 0.2	UV, Optical, IR, mm
Dense Molecular	$> 10^4$	10–50	~ 5 –10	IR, mm

Table 1.2 – Phases of the interstellar medium (from Snow & McCall [10]).

most of the atomic carbons turn into CO. Table 1.2 displays a summary of the composition of the CNM.

It should be noted that the description of the ISM is not strictly linear, as these phases coexist together and can only be locally separated. Of course these components of the ISM are also present in other galaxies and we can assume that the *intergalactic medium* is subject to the same processes as the ISM. It makes the ISM far from thermodynamic equilibrium, with permanent energy and mass exchange through strong radiations from supernovae or cosmic rays. It is clear that the ISM is a unique territory where completely different physical and chemical processes occur compared to Earth. Temperatures vary from ultra cold (less than 10 K) to ultra hot ($\sim 10^6$ K), and densities being at least 12 orders of magnitudes than typical terrestrial atmosphere.

1.1.3 Star formation

Stars are inherited from the collapse of a molecular cloud through its self-gravitation [12]. But all clouds are not yet star-forming regions, as *e.g.* the *Taurus Molecular Cloud 1* (TMC-1) [13]. The stability criterium of an astrophysical object is driven by the *virial theorem*:

$$\frac{1}{2}\ddot{I} = 2\mathcal{T} + \Omega \quad (1.1)$$

where \ddot{I} , \mathcal{T} and Ω are the second derivative of the total moment of inertia, the kinetic energy, and the gravitational potential energy of the system, respectively. The equilibrium condition is satisfied for $\ddot{I} = 0$, leading to:

$$2\mathcal{T} + \Omega = 0 \quad (1.2)$$

In a simple example, for a spherical and homogeneous perfect gas, isolated, isothermic and without any macroscopic motion, the thermic energy and the gravitational potential

energy can be written as:

$$\mathcal{T}_{th} = \frac{3}{2}Mk_B T; \quad \Omega = -\frac{3}{5}\frac{GM^2}{r} \quad (1.3)$$

where M is the total mass of the object, k_B is the Boltzmann constant, T is the temperature, G is the gravitational constant, and r is the radius of the object. Then, for these conditions, we can define that a cloud is unstable if its mass is larger than a critical mass M_{cr} (also referred as the Jean's mass):

$$M_{cr} = \left(\frac{5k_B T}{2G}\right)^{3/2} \left(\frac{4}{3}\pi n\right)^{-1/2} \quad (1.4)$$

where n is the density of the gas. Various factors, including magnetic, turbulence or thermal pressures, coupled to its geometry, density and velocity structures, play a role in the stability of a molecular cloud and complexify Eqs (1.3) and (1.4). A comprehensive review on this field of research is provided by McKee and Ostriker [14]. For instance, in presence of an external pressure p_{ext} and a magnetic field B , Eq. (1.2) is modified to:

$$3Mk_B T - 4\pi r^3 p_{ext} - \frac{1}{r} \left(\frac{3}{5}GM^2 - \frac{1}{3}r^4 B^2 \right) = 0 \quad (1.5)$$

Then, the critical mass M_{cr} becomes:

$$M_{cr} = \frac{c_1^3 5^{3/2}}{48\pi^2} \frac{B^3}{G^{3/2} n^2} \quad (1.6)$$

with c_1 is some factor taking in to account the structure of the object [15]. Early models proposed by Lizano & Shu [16] suggested that for magnetic clouds² possessing a mass $M < M_{cr}$, the gas compression is only possible through the distribution of the magnetic field by ambipolar diffusion, where ions are coupled with the magnetic field. This process involves ion-neutral collisions and is slow [15]. If magnetic pressure exceeds thermal pressure, the cloud may fragment and form low mass stars. Conversely, if $M > M_{cr}$, the magnetic field cannot prevent the condensation of the cloud by external pressure, leading to rapid collapse along the main component of the magnetic field and formation of massive stars.

2. A magnetic cloud designates here a molecular cloud subject to magnetic field effects contributing enough to its (un)stability.

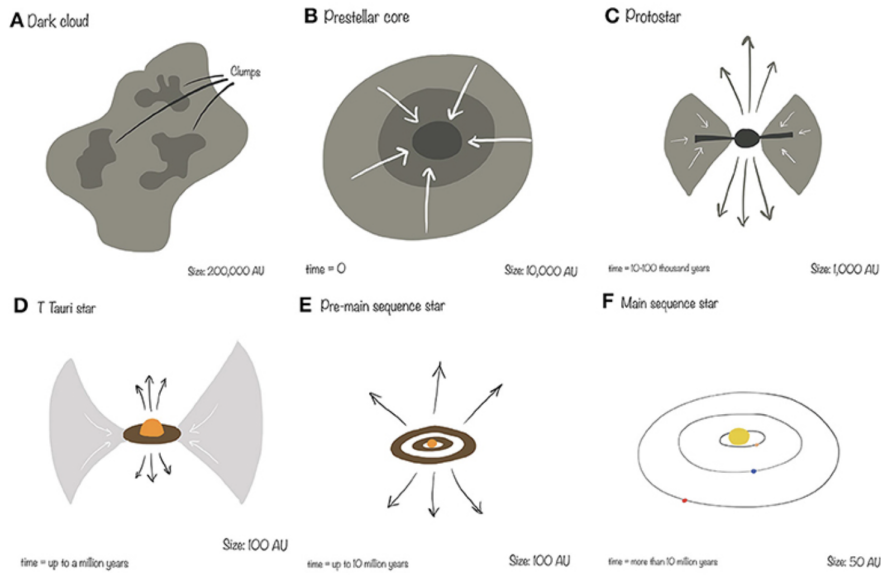


Figure 1.1 – Illustration of the stellar and planet formation in the ISM. Credit: Majken Brahe Ellegaard Christensen.

One way to classify the Sun-like star formation from an observational point of view is to identify the evolutionary stages of young stellar objects (YSOs), as they form from molecular clouds toward main-sequence stars. Such classification is based on the slope α of the spectral energy distribution (SED), defined as:

$$\alpha = \frac{d \log(\lambda S_\lambda)}{d \log(\lambda)} \quad (1.7)$$

with S_λ defined as the flux density at wavelength λ [17]. YSOs are considered as Class I sources for $\alpha \geq 0.3$, Class II for $-1.6 \leq \alpha < -0.3$, and Class III for $\alpha < -1.6$. An additional Class 0 source is added for YSOs that were not able to be detected in near-infrared [18]. Fig. 1.1 shows an illustration of the process of star and solar formation (and enumerated based on Caselli & Ceccarelli [19]), beginning with (A) a dense cloud where regions of gas and dust undergo gravitational collapse to form a dense structure as a *prestellar core* (B). This core is the precursor to a *protostar* (C), the early stage of a forming star. During the collapse, a *circumstellar disk* forms around the central protostar due to the conservation of angular momentum. Simultaneously, bipolar jets and outflows are launched along the poles. This is the Class 0 stage, where the protostar is deeply embedded in its envelope, and the bulk of its energy is emitted at submillimeter and far-infrared wavelengths [18]. This stage is approximately about 10^5 years. As the system evolves into the Class I stage, the envelope begins to dissipate, but the gas continues to accrete onto the disk and the protostar. When the surrounding envelope has dissipated significantly, the system

transitions into the *T Tauri star* stage (**D**), corresponding to the Class II stage, a typical age about few 10^6 years. The young star becomes optically visible, and is surrounded by a *protoplanetary disk*. Over several million years, the star evolves into a *pre-main sequence star* (**E**), which corresponds to the Class III stage. By this stage, most of the circumstellar material has dispersed. Planetary formation from the residual material is typically well underway, leading to a future solar system. Finally, the star transitions into a *main sequence star* (**F**), where nuclear fusion in the core maintains its luminosity.

1.2 Astrochemistry

This thesis work takes place in the context of astrochemistry. This is a research field focused on studying interstellar chemical processes to trace their origins and understand the chemical stages from star evolution to planet formation. Understanding the abundance of chemical elements in astrophysical environments helps to determine their characteristics, such as density, temperature, and dynamics. *In situ* measurements in the ISM are not possible and one can only rely on the interpretation of observational spectra. Analyzing these observations requires an accurate knowledge of molecular energy transfer mechanisms between a given molecule and its environment, as well as its intrinsic spectroscopic properties. This makes astrochemistry at the interface between astrophysics and physical chemistry.

1.2.1 Importance of observations

The first proof of the presence of chemical species in the ISM was attributed to Hartmann in 1904 who detected fixed Ca^{2+} absorption lines in the spectrum of the atmosphere of the double star δ Orionis, in which the lines change periodically their position [20]. In the 1940s, observations counted three molecules: CH, CH^+ [21], and CN [22], detected using UV absorption bands. This was a first surprising result, as the scientific community suggested that the low interstellar density and radiation fields coming from stars would proscribe the formation of molecules [23]. The emergence of radio astronomy in the 1960s, spanning wavelengths from centimeter to the infrared range, allowed detections of rotational transitions (or vibrational transitions for condensed molecules in ice mantles) [24] and permitted notably the first detection of OH [25] and the firsts detections of polyatomic molecules as NH_3 [26] and H_2O [27].

Thanks to technological advancements, the number of detected molecules drastically increased over the past decades (see Fig. 1.2). All ground-based telescopes and satellites developed and notably the *Herschel* satellite [28], the *Atacama Large Millimeter Array* (ALMA) interferometer [29], the Yebes 40 m radio telescope [30], the IRAM 30 m tele-

scope and the *James Webb Space Telescope* (JWST) [31] allowed to detect more than 300 molecules to date. Improvement of instruments induced unprecedented spectral resolution of the order of 1 kHz, depending on the frequency, resolving fine and hyperfine multiplets of rotational transitions [32]. The sensitivity achieved by the new instruments led to many detections of *complex organic molecules* (COMs) (≥ 6 atoms) like methanol (CH_3OH) [33], *long carbon-chains molecules* as HC_7N [34] and HC_9N [35], acetaldehyde (CH_3COOH), or propyne (CH_3CCH) [36], among all. A complete description of all detected interstellar species is reported for example in *The astrochymist* website. Databases such as CDMS [37] report many molecular detections through their rotational spectrum, spectroscopic data which are useful for line assignment or modeling.

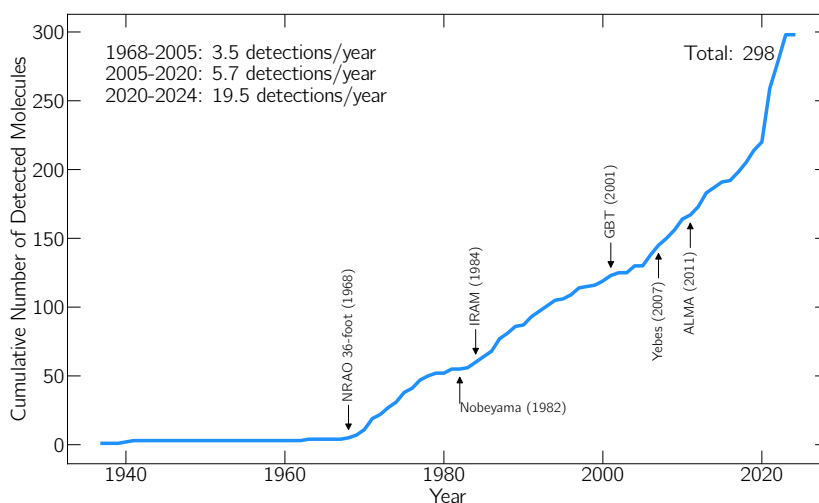


Figure 1.2 – Evolution of the number of cumulated detected molecules with years. This figure is generated using the `astromol` package from McGuire [24].

1.2.2 Importance of experiments

Low density conditions of the ISM allow exotic species like radicals to be maintained long enough to be detected. Their study is interesting as they react fastly in terrestrial conditions and are then hardly synthesized in laboratory. This leads to a complex and diverse chemistry in the ISM. Studying reaction processes occurring in the gas phase or at the grain surfaces is one of the aims of *laboratory astrophysics*. Particularly to the gas phase, molecular reactions can result in multiple products quantified by *branching ratios* for all possible channels. Such branching ratios are important to infer molecular formation pathways, for example to understand the formation of COMs at low temperatures [38]. Several challenges come naturally when studying reactions involving radicals, as one has to follow with precision the time evolution of concentration of unstables species. Low

temperature regime especially promotes quantum effects and then unpredictable behavior of the efficiency of the reaction, characterized by the *rate coefficient*, leads to large uncertainties in experimental measurements [39]. Among possible techniques to measure molecular reactions we can mention *crossed beam experiments*. Two molecular beams are crossing each other at a given angle and velocity in a way to follow single-collision conditions. Identification of products can be done through detection techniques as mass spectrometry or laser-based spectroscopic techniques (see Herman [40] for further reading). Also, mass spectrometry experiments have a broad range of applications, and some low temperature measurements have been done coupled to a CRESU³ apparatus [42]. Finally, reaction products can be analyzed by rotational spectroscopy techniques, requiring however a great sensitivity. In this context, the *Chirped Pulse Fourier-Transform MicroWave* (CPFTMW) has been developed for a large frequency range to cover multiple product formations [43].

Crossed beam experiments can also be applied for low collisional energy transfer processes. Among possible methods, Stark and Zeeman deceleration are powerful techniques for producing slow beams of cold molecules possessing electric and magnetic dipole moments, respectively. For example, it allows to study state-to-state inelastic scattering resonances with high accuracy, as shown in studies for the OH–He [44] or NH–He [45] collisional systems (see *e.g.* Hogan *et al.* [46] for more details).

1.2.3 Importance of modeling

The extreme physical conditions of the ISM make it difficult to replicate experiments on Earth. Consequently, understanding observed spectra relies on radiative transfer modeling, which aims to theoretically reproduce these spectra. This requires precise knowledge of the abundance of the studied molecules, specifically the distribution of their energy levels. Such distributions are driven by the energy transfer mechanisms between the molecule with its environment. One necessitates to understand the physicochemical processes involved. There are two main exchange mechanisms occurring in the gas phase of the ISM (see Fig. 1.3):

- Radiative processes: These involve the (de)excitation of an energy level by emission or absorption of a photon, universally described by *Einstein coefficients* A_{ul} , B_{ul} and B_{lu} .
- Collisional processes: These involve the (de)excitation of an energy level through kinetic or internal energy exchange with a collision partner. From a molecular

3. French acronym for Cinétique de Réaction en Écoulement Supersonique Uniforme. This was originally developed by Rowe and Marquette [41]. This is a remarkable technique, able to reproduce interstellar temperatures down to ~ 10 K.

scattering code, the collisional *rate coefficient*, which is the efficiency of a transition, can be deduced and characterizes the transition probability from one state to another.

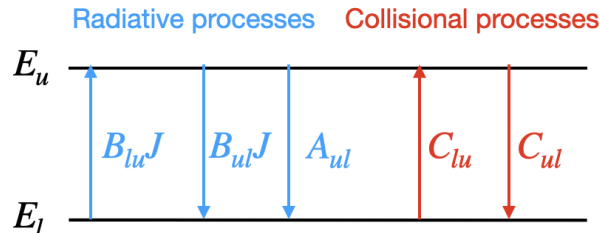


Figure 1.3 – Illustration of excitation processes participating in the population of two given energy levels E_u and E_l . Radiative coefficients are described by A_{ul} , B_{ul} and B_{lu} . Here J corresponds to the average profile of the radiation field. Collisional coefficients are characterized by C_{ul} and C_{lu} .

When collisions are dominant, the population of energy levels can be described by a Maxwell-Boltzmann distribution, and physical conditions are determined assuming Local Thermodynamic Equilibrium (LTE) conditions. However, low density conditions encountered in interstellar clouds are insufficient to reach equilibrium through collisions [47]. Consequently, a competition between radiative and collisional processes has to be explicitly taken into account in non-LTE modeling. Most of the time, non-LTE conditions result in subthermalization of the energy levels and physical conditions determined through LTE assumptions are, at best, an upper limit of the true parameters and, at worst, completely fail to reproduce observations (see *e.g.* Fig. 1.4).

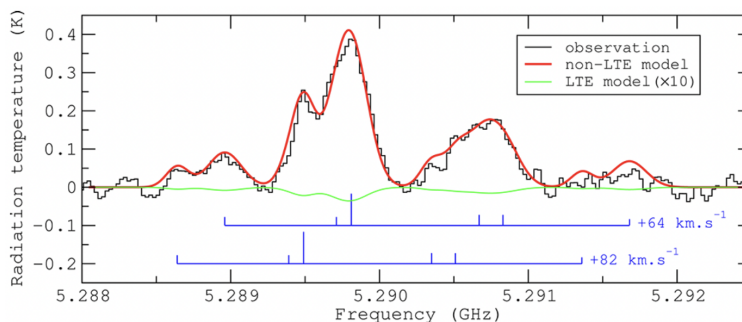


Figure 1.4 – Observational and model spectra of methanimine $1_{10} \rightarrow 1_{11}$ transition at 5.29 GHz toward Sgr B2(N) [48].

This is why quantifying excitation mechanisms as precisely as possible is primordial. On one hand, Einstein coefficients are computed through spectroscopic measurements of the transition frequencies of the molecule and its dipole moment. These are known for a wide range of molecules. In this thesis, we will use radiative data available on spectroscopic databases such as CDMS [37]. On the other hand, collisional rate coefficients are

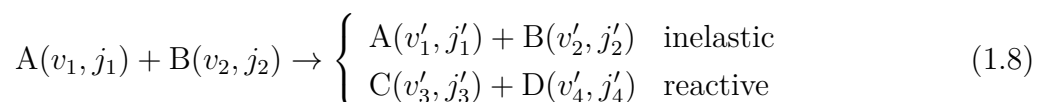
specific to each collisional system and their determination involves solving coupled differential equations for each state using quantum mechanics formalism. Such calculations are a true methodological and computational challenge, and collisional data are described only for ~ 70 collisional systems involving H, He and H_2 as main partners for the ISM. However, these data are sometimes incomplete due to limitations in temperature range, accuracy or the difficulty of including the structure of the collisional partner. Most of rate coefficients are available in the most active collisional databases as [LAMDA](#) [49], [EMAA](#) and [BASECOL](#) [50]. In this thesis, we will focus especially on the determination of state-to-state rate coefficients through theoretical calculations.

The determined abundance of a molecule can be compared to predictions made by chemical models. These rely on the initial composition, the temperature, the density of the gas, the cosmic-ray ionization of H_2 , elemental abundances and reaction rate coefficients. The abundance of molecules can then be simulated as function of time. The set of reaction rate coefficients considered is called a *chemical network* and each rate is determined through experiments and theoretical calculations. Efforts have been made to expand networks to include as many processes as necessary, such as incorporating grain surface processes into gas phase networks to explain the formation of molecular hydrogen [51]. Besides ion-molecule reactions at low temperatures, experiments including CRESU technique have shown the importance of neutral-neutral reactions involving one radical and one stable species (see *e.g.* [52]). Finally, the multiplication of detected molecules over the years requires more and more reactions to be included in astrochemical modeling. [KIDA](#) [53] and [UMIST](#) [54] are among the main databases compiling most of the known rate coefficients for application to the ISM. Chemical models are essential tools for understanding molecular formation, the importance of physical processes in play, and tracing the evolution of astrophysical environments (see Agundez & Wakelam [55] for more details).

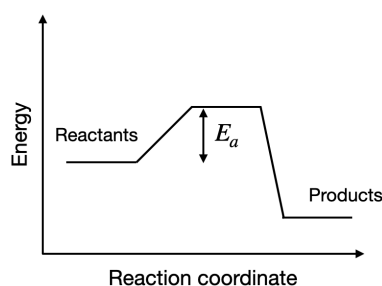
1.3 Collisional excitation

1.3.1 General considerations about collisional processes

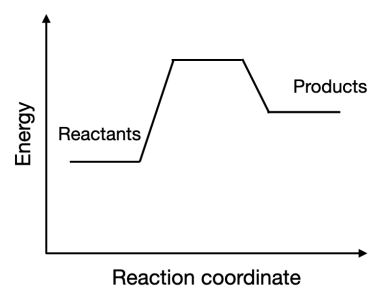
Several cases can occur during a collision between two molecules A and B in a given rovibrational state (v_1, j_1) and (v_2, j_2) , respectively:



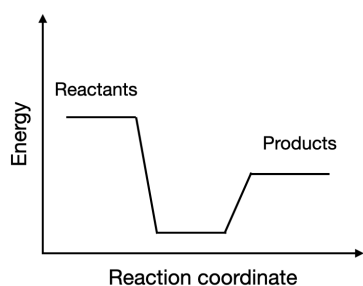
The first case involves an exchange of energy for A and B, known as an *inelastic collision* (see section 2.4 for more details). The second case leads to the destruction of the reactants to form new products C and D in rovibrational states (v'_3, j'_3) and (v'_4, j'_4) , respectively. This is known as a *reactive collision*. There are two types of reactions: *abstraction reaction* (or direct reaction) and *insertion reaction*, illustrated in Fig. 1.5. Direct reactions involve breaking the bond of one reactant to form products without forming an intermediate complex AB. These reactions exhibit a reaction barrier that requires activation energy E_a , making them less likely at low temperatures. Insertion reactions, on the other hand, proceed through the formation of an intermediate complex AB by creating bonds between reactants. Then the complex breaks down into products. Some of these reactions are barrierless and exothermic, meaning they do not require additional energy and can occur in cold interstellar environments. For such reactions, it is possible to form products also in rovibrationally excited levels.



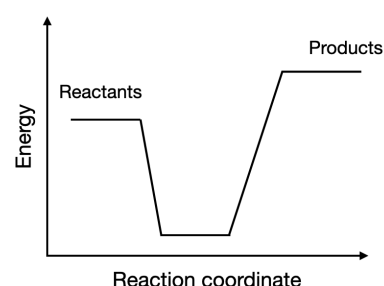
(a) Exothermic direct reaction



(b) Endothermic direct reaction



(c) Exothermic insertion reaction



(d) Endothermic insertion reaction

Figure 1.5 – Illustration of reactive processes.

1.3.2 State of the art

The most accurate way to describe the collisional excitation of a target molecule by a projectile at low temperatures is by solving the quantum *Time Independent Schrödinger equation* (TISE). However the exact solution stands only for the description of the hydrogen atom, *i.e.* for one proton and one electron. Over the past 60 years, scattering studies

have focused on overcoming this challenge to provide collisional data for astrophysical purpose. Arthurs & Dalgarno [56] were the first to develop the theory for the rotational excitation of a rigid diatomic molecule by a structureless particle using the *close-coupling* (CC) method. In such approach, the description of a molecular system relies on the interaction potential between the two colliders, expressed in internal coordinates in the *space-fixed frame* (SF). This approach is based on the Born-Oppenheimer approximation [57], considering nuclear and electronic motions separately. Quantum chemistry calculations are then performed to quantify the electronic interactions in a molecular system characterized by a *potential energy surface* (PES). The CC equations are finally solved for the nuclear motion based on this PES. This results in the extraction of the *S*-matrix from which state-to-state cross sections and consequently the rate coefficients can be determined. These aspects are given with more details in chapter 2.

Such approach is the most accurate to perform scattering calculations. However, it requires the inclusion of both open and closed channels (N_{chan} , see section 2.4), defined as the number of possible configurations satisfying the conservation of energy and angular momentum. As the computational time evolves as N_{chan}^3 , high temperature calculations or even low temperatures involving heavy systems can be significant. A collisional system is considered heavy when it involves too many energy levels to use the CC method in a reasonable time. To address this challenge, physical arguments can be used to reduce computational time. For inelastic collisions at low temperatures, one can assume that vibrational motions will have a negligible impact and focus only on collisional excitation through rotational motions. The molecule studied can be considered a *rigid rotor* with fixed internuclear distances at equilibrium. This approach has shown good agreement with experimental results, such as the state-to-state collisional cross sections of CO induced by H₂ measured by Chefdeville *et al.* [58].

Even using the rigid rotor approximation, a system is heavy when both colliders have an energetic structure, even when their rotational constant is high. This leads to a large number of energy levels and then a large number of transitions to converge accurately. Therefore, theoretical studies focused on the most abundant molecules in collision with the main partners in the ISM (H, He and H₂). These species have the advantage to be structureless or with a large space between energy levels. We can notably mention the works done from the 1970s to the 1990s on molecules like H₂ [59], [60], NH₃ [61], H₂O [62] or CO [63]. However, even calculations involving molecular hydrogen remained challenging, and it is customary to use He as a proxy for H₂. This is because *para*-H₂($j_2=0$) and He have both two valence electrons and a spherical shape. Then, cross sections are considered equal and rate coefficients only differ by the reduced mass μ of the collisional

system. Hence, one can quantify rate coefficients $k(T)$ for H_2 collisions by considering collisions with He as:

$$k_{X\text{-}para\text{-}\text{H}_2}(T) \sim \left(\frac{\mu_{X\text{-}\text{He}}}{\mu_{X\text{-}para\text{-}\text{H}_2}} \right)^{1/2} k_{X\text{-}\text{He}}(T) \quad (1.9)$$

where X is a given targeted species. This approach was found to be accurate within a factor of 2 for systems like HC_3N [64], moderate for H_2O [65], H_2CO [66], CO [67], CN [68], HCN or HNC [69] within a factor $\sim 1\text{--}3$, but completely fails for ions [70]–[73], where deviations between factors 2–100 have been observed. Of course this alternative is still used to provide data to cover astrophysical needs for very complex molecules like CH_3CN and CH_3NC [74].

In parallel, approximations like *coupled states* (CS), which neglects the centrifugal terms during a collision, or *infinite order sudden* (IOS), which ignores the rotational structure during a collision, can be used for heavy systems. These methods were employed in the 1970s for symmetric and asymmetric tops like NH_3 or H_2CO in collisions with atoms [75], [76]. More recent calculations have been performed for example for the SiS [77] or H_2O [78] molecules in collision with H_2 , employing more accurate PESs and for higher temperatures when the structure of H_2 cannot be ignored anymore. These approaches are usually accurate within $\sim 30\text{--}50\%$ with respect to CC. They are implemented in scattering codes such as MOLSCAT [79] and HIBRIDON [80].

When molecules possess a non vanishing electronic spin S and/or nonzero nuclear spins I , the presence of (hyper)fine structures introduces significant challenges, making CC calculations rarely feasible. Due to the weak coupling of the electronic spin to the rotation during a collision, Corey & McCourt [81] described interactions between $^{2S+1}\Sigma$ molecules and atoms using recoupling angular momentum algebra. This approach allows the computation of state-to-state fine structure cross sections based on accurate determination of the rotational *scattering matrices*. Alexander & Dagdigian extended this method for hyperfine calculations [82]. This method is implemented in the HIBRIDON suite of programs for both closed- and open-shell molecules in collision with a molecule. Faure & Lique [83] reported on the impact of recoupling, IOS and statistical methods compared to CC for hyperfine treatment. The recoupling approach is found to be the most reliable for low temperatures, although the computational cost is large.

Attention has been given also on studies of scattering collisions in reactive systems, for example the comprehension of the early universe chemistry [84], [85]. The complexity for such collisional processes is even harder to handle than for non-reactive collisions as the

description of reactive state-to-state transitions necessitates the inclusion of all degrees of freedom of the molecular system. Even if the description of H+H₂ reactions has been done with full-dimensional CC approach by Schatz & Kuppermann in 1976 [86], molecular reaction studies are still hardly achievable for systems with more than three atoms. Low temperature applications can be performed for example with the *ABC* code [87]. For collisions proceeding through abstraction reactions, cases occur where activation energy can be overcome and lead to a competition between inelastic and reactive processes. For endothermic reactions as the HD + H → D + H₂, results have shown that the impact of reactive and exchange channels in inelastic rate coefficients cannot be neglected over 300 K [88], [89]. For exothermic reaction like the HeH⁺ + H → He + H₂⁺, inelastic channels are found to be negligible at low temperatures, whereas competing with reactive channels for higher temperatures [90]. For higher temperature regimes, methods based on the solution of the *Time Dependent Schrödinger equation* (TDSE) are preferable. In these methods, collision processes are described *via* a wavepacket (WP) propagation over the PES [91]. Usually, WP methods are best suited for fast reactions but can also be performed for insertion reactions [92]. These methods have often shown good agreement with experiments and classical methods for very high temperature regimes as quantum effects have less and less importance [93].

1.4 Outline of the thesis

This thesis focuses on the excitation of open-shell molecules induced by collisions with molecular hydrogen in low temperature astrophysical environments. Interstellar hydrides (containing a single heavy atom and one or more hydrogen) and hydrocarbons are particularly interesting. They are important intermediate species to the formation of more complex and stable molecules like H₂O, NH₃ [32] or long carbon-chain molecules [13] and they are widely observed in various astrophysical sources like diffuse molecular clouds [10], strongly UV-irradiated gas like photodissociation (PDR) regions [94], shocks and turbulent regions [95] or cold dark clouds [19]. Studying such key species is fundamental to determine physical conditions of their detected sources. They can be used to probe the molecular hydrogen fraction or the cosmic-ray ionization rate (see *e.g.* Indriolo *et al.* [96]). Despite their simple chemical composition, light hydrides can be complex due to intrinsic properties like a non-vanishing electronic spin, leading to a fine structure and a larger amount of transitions in scattering calculations. Additionally, the presence of the H atom also involve a weak (however observed) coupling of its nuclear spin to the rotational motion, leading to a hyperfine splitting of the energy levels. The first aspect of this thesis

will focus on the collisional excitation of radical molecules. We will explore state of the art methods for treating the fine structure of these molecules. Then we will test the limits of these approaches and strategies to handle the hyperfine structure treatment to provide collisional data for astrophysical applications. The C_2H and NH radicals will be used as test cases. We will also explore the impact of the isotopic substitution on rate coefficients and simple radiative transfer applications.

Another complexity of light hydrides is their reactivity, as collisions with H_2 can result in exothermic and barrierless reactions. It means that reactive processes should dominate at low temperature and compete with inelastic processes for all temperature regimes. However, nowadays methods still hardly manage bimolecular reactions that account for both inelastic and reactive channels at low temperatures, resulting in limited collisional data for such collisional systems. The second aspect of this thesis aims to overcome this lack of data. We will base this work on recent implementation of a statistical method for non-reactive systems [97]. This method has been benchmarked with five collisional systems (OH^+-H , OH^+-He , CN^--H_2 , $CO-He$ and $CO-H_2$) against CC calculations including rotational excitation. This method have shown good agreement with the CC approach for strongly bound cases. This benchmark has been extended to rovibrational excitation and has been done for the H_2-H^+ , $HD-H^+$, SH^+-H and CH^+-H collisional systems [98]. We will specifically explore the impact of such approach on the fine structure treatment of open-shell molecules using the OH^+-H collisional system as a test case through non-reactive collisions and will be compared to pure CC calculations. Then we will propose a strategy to investigate the reactive behavior using this method and quantify the contributions of both reactive and non-reactive effects in rate coefficients. The exothermic $OH^+ + H_2 \rightarrow H_2O^+ + H$ reaction will be used as a case study.

This manuscript is organized as follow. In chapter 2, we will describe the theoretical framework of a molecular system. We will summarize the methods used to determine the interaction potential and will give a brief description of spectroscopic notions used over this manuscript. Then we will especially focus on the formalism for collision dynamics. Then notions about radiative transfer will be introduced for astrophysical applications. Chapter 3 will focus on results about both fine and hyperfine structure treatment for the studied non-reactive systems. The impact of these collisional data will be explored in simple radiative transfer modeling. Chapter 4 will present the strategies and results for reactive systems. Finally, conclusion and perspectives of this thesis will be drawn in chapter 5.

THEORY AND METHODOLOGY

This chapter provides an overview of the theoretical methods and numerical tools employed in this thesis. It begins in section 2.1 with a general introduction to molecular systems and the quantum mechanical formalism used to describe them, including the Born-Oppenheimer approximation and its implications for the study of collisional systems. Next, the principal techniques for studying potential energy surfaces are introduced in section 2.2. An overview of molecular spectroscopy is provided in section 2.3, focusing on the molecules of interest in this work. The chapter then moves into the details of dynamical calculations in section 2.4, which form the core of this thesis. Finally, the formalism of radiative transfer modeling is presented in section 2.5, highlighting its application to astrophysical scenarios.

2.1 The time-independent Schrödinger equation

2.1.1 Molecular system

A molecular system is composed of an ensemble of nuclei (protons and neutrons) and electrons, maintained together by electrostatic forces. An accurate treatment of the properties of a molecular system must be done using the quantum mechanics formalism. The observables defined by the energy and the wave function of the system can be determined by solving the time-independent Schrödinger equation:

$$\hat{H}(\mathbf{q}, \mathbf{Q})\Psi(\mathbf{q}, \mathbf{Q}) = E\Psi(\mathbf{q}, \mathbf{Q}) \quad (2.1)$$

with $\hat{H}(\mathbf{q}, \mathbf{Q})$ the hamiltonian operator of the system, E is the total energy of the system and $\Psi(\mathbf{q}, \mathbf{Q})$ is the molecular *wave function*. These functions depends on the internal coordinates (\mathbf{q}, \mathbf{Q}) of the electrons and nuclei respectively in the *laboratory frame*, where quantities in bold text are written in a vectorial notation.

Let us consider a molecular system of n electrons with coordinates $\mathbf{q} = (\mathbf{q}_1, \dots, \mathbf{q}_n)$ and N nuclei with coordinates $\mathbf{Q} = (\mathbf{Q}_1, \dots, \mathbf{Q}_N)$. The molecular hamiltonian operator

has the following form:

$$\hat{H}_{mol}(\mathbf{q}, \mathbf{Q}) = \hat{V}_{el-el}(\mathbf{q}) + \hat{V}_{nuc-nuc}(\mathbf{Q}) + \hat{V}_{el-nuc}(\mathbf{q}, \mathbf{Q}) + \hat{T}_{el}(\mathbf{q}) + \hat{T}_{nuc}(\mathbf{Q}) \quad (2.2)$$

where:

- $\hat{V}_{el-el}(\mathbf{q}) = \sum_{i' > i}^n \frac{e^2}{\|\mathbf{q}_i - \mathbf{q}_{i'}\|}$ is the electrostatic repulsion term between electrons
- $\hat{V}_{nuc-nuc}(\mathbf{Q}) = \sum_{j' > j}^N \frac{Z_j Z_{j'}}{\|\mathbf{Q}_j - \mathbf{Q}_{j'}\|}$ is the electrostatic repulsion term between nuclei
- $\hat{V}_{el-nuc}(\mathbf{q}, \mathbf{Q}) = - \sum_j^N \sum_i^n \frac{Z_j e^2}{\|\mathbf{Q}_j - \mathbf{q}_i\|}$ is the electrostatic attraction term between electrons and nuclei
- $\hat{T}_{el}(\mathbf{q}) = - \frac{\hbar^2}{2m} \sum_i^n \Delta_i$ is the kinetic term associated to electrons
- $\hat{T}_{nuc}(\mathbf{Q}) = - \sum_k^N \frac{\hbar^2}{2M_k} \Delta_k$ is the kinetic term associated to nuclei

$e^2 = \frac{q^2}{4\pi\epsilon_0}$, ϵ_0 is the vacuum permittivity, q is the elementary charge, Z_j is the atomic number of the j -th nucleus, $\hbar = \frac{h}{2\pi}$ is the reduced Planck constant, $\Delta = \frac{\partial^2}{\partial X^2}$ is the laplacian operator (and X being one of the coordinates of \mathbf{Q} or \mathbf{q}), m is the mass of the electron and M_k is the mass of the k -th nucleus. These are the most common terms appearing in the molecular hamiltonian.

The solution of Eq. (2.1) can be done exactly only for the case of the hydrogen atom, having only one nucleus and one electron. In general, this equation cannot be solved analytically for a system with $3(n + N)$ degrees of freedom. Then, it is necessary to employ approximations to extract the observables of the system.

2.1.2 The Born-Oppenheimer approximation

Both nuclei and electrons are subject to the same electrostatic interactions. Based on the conservation of the impulsion, electronic and nuclei impulsions are of the same order of magnitude

$$p_{el} \sim p_{nuc} \rightarrow v_{el} \sim \frac{M}{m} v_{nuc}$$

but since the mass of the nucleus is much larger than the mass of the electron ($\frac{M}{m} \sim 1836$), electrons move much faster than nuclei ($v_{el} \gg v_{nuc}$). We can consider in first approximation that nuclear motion can be neglected compared to the motion of electrons. It means that we can treat the electronic motion for fixed geometries of the nuclei. Born and Oppenheimer were the first to implement these ideas in order to separate nuclei and

electrons motions [57]. They expanded the molecular hamiltonian in terms of the ratio

$$x = \left(\frac{m}{M} \right)^{1/4}$$

where the exponent is here to keep the natural order of magnitude of energy contributions. We can write the nuclear kinetic term as a function of x :

$$\begin{aligned} \hat{T}_{nuc}(\mathbf{Q}) &= -x^4 \frac{\hbar^2}{2m} \sum_k^N \mu_k \Delta_k \\ &= x^4 \hat{H}_1(\mathbf{Q}) \end{aligned} \quad (2.3)$$

where $\mu_k = \frac{M}{M_k}$, and M is an average value of the M_k . One can rewrite the molecular hamiltonian such that:

$$\hat{H}(\mathbf{q}, \mathbf{Q}) = \hat{H}_0(\mathbf{q}; \mathbf{Q}) + x^4 \hat{H}_1(\mathbf{Q}) \quad (2.4)$$

where $\hat{H}_0(\mathbf{q}; \mathbf{Q}) \equiv \hat{H}_{el}(\mathbf{q}; \mathbf{Q}) = \hat{V}_{el-el}(\mathbf{q}) + \hat{V}_{nuc-nuc}(\mathbf{Q}) + \hat{V}_{el-nuc}(\mathbf{q}, \mathbf{Q}) + \hat{T}_{el}(\mathbf{q})$ is the electronic hamiltonian for a given coordinate \mathbf{Q} now considered as a parameter.

Then the Schrödinger equation becomes:

$$\left\{ \hat{H}_0(\mathbf{q}; \mathbf{Q}) + x^4 \hat{H}_1(\mathbf{Q}) - E \right\} \Psi(\mathbf{q}, \mathbf{Q}) = 0 \quad (2.5)$$

where E is an eigenvalue. To solve the Schrödinger equation we can expand the molecular wave function using nuclear functions $\varphi_i(\mathbf{Q})$ and electronic functions $\phi_i(\mathbf{q}; \mathbf{Q})$ as:

$$\Psi(\mathbf{q}, \mathbf{Q}) = \sum_i \varphi_i(\mathbf{Q}) \phi_i(\mathbf{q}; \mathbf{Q}) \quad (2.6)$$

This *adiabatic* basis set follows the orthonormal rules:

$$\langle \varphi_n(\mathbf{Q}) | \varphi_j(\mathbf{Q}) \rangle = \delta_{nj} \quad \langle \phi_m(\mathbf{q}; \mathbf{Q}) | \phi_i(\mathbf{q}; \mathbf{Q}) \rangle = \delta_{mi} \quad (2.7)$$

By setting $x = 0$ in Eq. (2.5), we obtain the Schrödinger of the 0^{th} order in x and we see that the nuclear contribution drops, the electronic hamiltonian remains so that only

$\phi_i(\mathbf{q};\mathbf{Q})$ are solutions of the equation:

$$\left\{ \hat{H}_{el}(\mathbf{q};\mathbf{Q}) - E_i(\mathbf{Q}) \right\} |\phi_i(\mathbf{q};\mathbf{Q})\rangle = 0 \quad (2.8)$$

where $E_i(\mathbf{Q})$ is defined as the *potential energy surface* (PES) for all coordinates \mathbf{Q} . When projecting Eq. (2.8) over electronic states $\langle \phi_m(\mathbf{q};\mathbf{Q}) |$, it is possible to use the *adiabatic approximation* to drop all potential couplings. It turns out:

$$\langle \phi_m(\mathbf{q};\mathbf{Q}) | \hat{H}_{el}(\mathbf{q};\mathbf{Q}) | \phi_i(\mathbf{q};\mathbf{Q}) \rangle = \delta_{mi} E_i(\mathbf{Q}) \quad (2.9)$$

Using (2.9), one can project Eq. (2.5) over electronic states:

$$\begin{aligned} \sum_i \langle \phi_j(\mathbf{q};\mathbf{Q}) | \left\{ \hat{H}_0(\mathbf{q};\mathbf{Q}) + x^4 \hat{H}_1(\mathbf{Q}) - E \right\} | \varphi_i(\mathbf{Q}) \rangle | \phi_i(\mathbf{q};\mathbf{Q}) \rangle &= 0 \\ \Rightarrow \sum_i \left\{ E_i(\mathbf{Q}) | \varphi_i(\mathbf{Q}) \rangle + x^4 \langle \phi_j(\mathbf{q};\mathbf{Q}) | \hat{H}_1(\mathbf{Q}) | \varphi_i(\mathbf{Q}) \rangle | \phi_i(\mathbf{q};\mathbf{Q}) \rangle - E | \varphi_i(\mathbf{Q}) \rangle \right\} &= 0 \end{aligned}$$

Here we can replace $\hat{H}_1(\mathbf{Q})$ by Eq. (2.3):

$$\begin{aligned} \sum_i \left\{ E_i(\mathbf{Q}) | \varphi_i(\mathbf{Q}) \rangle + x^4 \frac{\hbar^2}{2m} \sum_k^N \mu_k \langle \phi_j(\mathbf{q};\mathbf{Q}) | \Delta_k | \varphi_i(\mathbf{Q}) \rangle | \phi_i(\mathbf{q};\mathbf{Q}) \rangle \right. \\ \left. + x^4 \frac{\hbar^2}{2m} \sum_k^N \mu_k \langle \phi_j(\mathbf{q};\mathbf{Q}) | \nabla_k | \varphi_i(\mathbf{Q}) \rangle \nabla_k | \phi_i(\mathbf{q};\mathbf{Q}) \rangle \right. \\ \left. + x^4 \frac{\hbar^2}{2m} \sum_k^N \mu_k \langle \phi_j(\mathbf{q};\mathbf{Q}) | \Delta_k | \phi_i(\mathbf{q};\mathbf{Q}) \rangle | \varphi_i(\mathbf{Q}) \rangle - E | \varphi_i(\mathbf{Q}) \rangle \right\} = 0 \end{aligned}$$

Within the Born-Oppenheimer approximation, the non-adiabatic kinetic coupling terms drop and we can write:

$$\langle \phi_j(\mathbf{q};\mathbf{Q}) | \Delta_k | \phi_i(\mathbf{q};\mathbf{Q}) \rangle \sim 0 \quad ; \quad \langle \phi_j(\mathbf{q};\mathbf{Q}) | \nabla_k | \phi_i(\mathbf{q};\mathbf{Q}) \rangle \sim 0$$

The Schrödinger equation simplifies to

$$\left\{ x^4 \hat{H}_1(\mathbf{Q}) + E_i(\mathbf{Q}) - E \right\} | \varphi_i(\mathbf{Q}) \rangle = 0 \quad (2.10)$$

One can see that the PES $E_i(\mathbf{Q})$ in Eq. (2.10) can be regarded as a potential term

in the solution of the Schrödinger equation for the nuclei $|\varphi_i(\mathbf{Q})\rangle$. In a typical collisional system study, one has to proceed in two steps:

1. Use the Born-Oppenheimer approximation to uncouple electrons and nuclei motions. This leads to determine first the PES for electrons for each nuclear geometry. The solution of the Schrödinger equation for electrons can be undertaken through *ab initio*¹ methods since it only depends on fundamental constants and properties of the collisional system. These methods will be briefly presented in section 2.2.
2. Then, it is necessary to determine the analytical representation of the PES so that it can be used as a parameter to solve the Schrödinger equation for nuclei and determine its observables. The state of the art methods to treat molecular collisions will be introduced and discuss in section 2.4.

It should be noted that the Born-Oppenheimer approximation is valid only for distinct electronic states as it breakdown for close or degenerate electronic states.

2.2 Potential energy surface

The purpose of this chapter is to give a general introduction to the state of the art *ab initio* methods used to solve the Schrödinger equation (2.8). For the following discussions it is worth to introduce *atomic units* to simplify notations. This can be highlighted by expressing the Schrödinger equation for the hydrogen atom as dimensionless (where $\mathbf{q} \rightarrow \lambda \mathbf{q}'$ and $\lambda \in \mathbb{R}$) [99]:

$$\begin{aligned} & \left\{ -\frac{\hbar^2}{2m\lambda^2} \frac{\partial^2}{\partial \mathbf{q}'^2} - \frac{q'^2}{4\pi\epsilon_0\lambda\mathbf{q}'} \right\} \phi' = E\phi' \\ \Rightarrow & \frac{\hbar^2}{m\lambda^2} \left\{ -\frac{1}{2} \frac{\partial^2}{\partial \mathbf{q}'^2} - \frac{q'^2 m \lambda}{4\pi\epsilon_0 \hbar^2 \mathbf{q}'} \right\} \phi' = E\phi' \end{aligned} \quad (2.11)$$

The factor in front of the *zero-th* order term can be normalized if $\frac{mq^2\lambda}{4\pi\epsilon_0\hbar^2} = 1$. Then $\lambda = \frac{4\pi\epsilon_0\hbar^2}{mq^2} \equiv a_0$. This defines the *Bohr radius* and represents the most probable distance of the electron from the proton in a hydrogen atom. This was first introduced by Bohr and Rutherford in their description of the atom model in 1913. One can see in Eq. (2.11) that $\frac{\hbar^2}{m\lambda^2} = E \equiv E_h$ which defines the *hartree* unit of energy, and the Schrödinger equation can be written:

$$\left\{ -\frac{1}{2} \frac{\partial^2}{\partial \mathbf{q}'^2} - \frac{1}{\mathbf{q}'} \right\} \phi' = E' \phi'$$

1. *Ab initio* is a latin locution meaning "from the beginning".

with $E' = \frac{E}{E_n}$. For the following, the prime notation will be dropped, assuming all terms in atomic units.

In the case of a molecular system, the electronic hamiltonian turns to:

$$\hat{H}_{el}(\mathbf{q};\mathbf{Q}) = \sum_{i'>i}^n \frac{1}{\|\mathbf{q}_i - \mathbf{q}_{i'}\|} + \sum_{j'>j}^N \frac{Z_j Z_{j'}}{\|\mathbf{Q}_j - \mathbf{Q}_{j'}\|} - \sum_j^N \sum_i^n \frac{Z_j}{\|\mathbf{Q}_j - \mathbf{q}_i\|} - \frac{1}{2} \sum_i^n \Delta_i \quad (2.12)$$

2.2.1 *Ab initio* calculations

The orbital approximation

In the electronic hamiltonian (2.12), the electron-electron repulsive term takes into account the correlation between electrons. Then, the electronic wave function $\phi_i(\mathbf{q})$ (now assumed that the \mathbf{Q} coordinate is implicit) is multielectronic which means that it describes the probability of presence of one electron depending on the position of the others. This correlation makes the Schrödinger equation not easy to solve. One way to simplify the notation is to employ the *orbital approximation*, where $\phi_i(\mathbf{q})$ can be expanded as a *linear combination of atomic orbitals* (LCAO, see e.g. [100]) $\chi_j(\mathbf{q}_j)$ (or basis functions) such that:

$$\phi_i(\mathbf{q}) = \sum_j^{+\infty} c_{ij} \chi_j(\mathbf{q}_j) \quad (2.13)$$

where ϕ_i are called *molecular orbitals* and c_{ij} are their expansion coefficients. These functions should be able to describe electronic orbitals around the nucleus and can be classified as the known *s, p, d, f, g...* orbitals according to their angular momentum. Since electrons are treated as identical particles, they must respect the *Pauli exclusion principle* stating that fermions cannot occupy both the same state with the same spin. Then, molecular orbitals should be antisymmetric with respect to change of coordinate. The molecular orbital can be written as a *Slater determinant* [101], [102]:

$$\Phi = \sqrt{\frac{1}{n!}} \begin{vmatrix} \phi_1(\mathbf{q}_1) & \phi_2(\mathbf{q}_1) & \cdots & \phi_i(\mathbf{q}_1) \\ \vdots & \vdots & \ddots & \vdots \\ \phi_1(\mathbf{q}_n) & \phi_2(\mathbf{q}_n) & \cdots & \phi_i(\mathbf{q}_n) \end{vmatrix}$$

where $\sqrt{\frac{1}{n!}}$ is a normalization factor to avoid repetitions. The solution of the electronic Schrödinger equation using these defined molecular orbitals can be achieved by constraining the c_{ij} coefficients and the parameters related to the basis functions $\chi_j(\mathbf{q}_j)$ through the application of the *variational principle*, as done in the Hartree-Fock theory. Also a

wise choice of the basis functions must be done for the sake of simplicity of calculations.

Basis sets

Molecular orbitals defined by Eq. (2.13) are obtained from known functions $\chi_j(\mathbf{q}_j)$. To perform an exact calculation, an infinite number of functions should be used, which is not doable in practice. A restriction of the number M_{basis} of functions is imposed to the basis set since the computational cost scales as $t \propto M_{basis}^4$ [103]. In practice, any type of function can be used but there should have a balance between choosing the ones which best reproduce physical conditions for a quick convergence and choosing the ones to be mathematically easy to treat. There are two main types of functions used in the literature: *Slater Type Orbitals* (STO) and *Gaussian Type Orbitals* (GTO):

$$\begin{aligned} \text{STO} &\rightarrow \chi_{\zeta,n,l,m}(r, \theta, \varphi) = NY_{l,m}(\theta, \varphi)r^{n-1}e^{-\zeta r} \\ \text{GTO} &\rightarrow \chi_{\zeta,n,l,m}(r, \theta, \varphi) = NY_{l,m}(\theta, \varphi)r^{2n-2-l}e^{-\zeta r^2} \end{aligned}$$

where here N is a normalization factor, $Y_{l,m}(\theta, \varphi)$ is a *spherical harmonic* function, n, l, m are the quantum numbers for electrons, and ζ is a parameter optimized by the variational principle and expressed as a function of the size of the basis when it becomes large [104]. For this discussion, the j -th electron is represented in spherical coordinates $\mathbf{q}_j = (r_j, \theta_j, \varphi_j)$. STOs are *a priori* a better choice of functions to ensure a rapid convergence because they better reproduce the physical behavior of the wave function; and a calculation would require a lower number of functions than GTOs. However, STOs are very hard to integrate and an analytic integration become quickly inappropriate. On the other hand, the dependence of the exponential term of the GTOs is $\propto r^2$ whereas the STOs is $\propto r$. This makes that the description of the behavior of the electron close to the nucleus is poorer with GTOs, since these functions tend to zero quicker than STOs. The advantage of GTOs is that their mathematical treatment is easier and compensates this lack of accuracy and they are universally used in most computational programs for quantum calculations. It has been shown that a STO can be represented by a linear combination of GTOs (see Jensen [103]).

The purpose of these functions is to model the behavior of electronic orbitals around the nucleus for each atom in a molecular system. Orbitals can be interpreted as two sorts: *core* orbitals for the inner-shell electrons region of the wave function, and *valence* orbitals for the outer part of the wave function. On one hand, core orbitals are energetically important in the minimization of the wave function when applying the variational principle, while valence orbitals are considered as energetically unimportant since they represent

electrons far from the nucleus. On the other hand, chemical interactions depend much more on valence orbitals than core ones. Then, the number of functions and the way of minimizing the c_{ij} coefficients must be optimized as much as possible. For example, core orbitals participate in majority in the minimization of the electronic energy and an important number of functions N^{core} is required. However, the c_{ij} related to these functions do not change that much and are not necessary to be optimized. One can expand a contracted basis over *primitive* GTOs where core orbitals possess constant expansion coefficients a_i as:

$$\chi^{core} = \sum_i^k a_i \chi_i^{prim} \quad \text{with} \quad k < N^{core}$$

This decreases the accuracy of the energy but is compensated by the lower computing time. Also, there is a minimal number of functions to take into account to describe molecular orbitals but it is generally not enough to provide accurate result. It is customary to multiply the number of valence functions since it describes better the electrons distribution in different directions. These sizes of basis sets are denoted as VXZ for Valence X Zeta, where X \equiv Double (D), Triple (T), Quadruple (Q), ... and Zeta refers to the exponent parameter in GTOs. Dunning [105] introduced the notion of *correlation consistent* basis set for the recovery of the correlation of electrons. This is treated so that the minimization of the correlation energy is consistent with the size of the basis while reducing the number of primitive functions to use. It is also possible to introduce *polarization* functions to the basis set which are functions with high angular momentum to carry out correlated electrons far from each other. The basis can finally be *augmented* by adding diffuse functions, which are atomic orbitals with small exponents. For the PES used in this thesis and more generally in the literature, the basis sets employed will be labeled as aug-cc-pVXZ for *augmented-correlation-consistent-polarized Valence X Zeta*.

Finally, one important effect to take into account is the Basis Set Superposition Error (BSSE). This comes from the fact that the electronic density from one molecule can be described by orbitals of another molecule. It makes an artificial additional minimization of the energy which underestimates the true energy value. A way to compensate this error is the *counterpoise* (CP) method, first introduced by Boys and Bernardi [106] in 1970. For a molecular system in a given geometry $(AB)^*$ defined by two monomers A and B, one first has to make the difference between the energy of the whole molecular complex and energies of individual optimized molecules as:

$$\Delta E_{complex} = E(AB)_{ab}^* - E(A)_a - E(B)_b$$

where a and b represent the basis sets designed for calculating the energy of A and B, respectively. To determine the CP correction, one can calculate the energy of A with the ab basis separately from B and *vice versa*. Since this basis has a larger size than just a or b , these energies will be lower than the ones determined with their own designed basis set. It is then subtracted by the energy of A and B in the geometry of the complex:

$$\Delta E_{\text{CP}} = E(A)_{ab}^* + E(B)_{ab}^* - E(A)_a^* - E(B)_b^*$$

The electronic energy is then approximately corrected of the BSSE by applying $\Delta E_{\text{complex}} - \Delta E_{\text{CP}}$.

The Hartree-Fock approximation

The *Hartree-Fock* (HF) method, introduced by Hartree and Fock [107], [108] between 1928 and 1930, proposes a way to derive a solution to the electronic Schrödinger equation (2.8). This goes by the minimization of the HF electronic energy E_{HF} through the variational principle using a Slater determinant as a trial function $\tilde{\phi}$. The idea is to find the good function $\tilde{\phi}$ so that its variation by a infinitesimal amount $\delta\tilde{\phi}$ gives E_{HF} as a minimum. The presentation of the method is taken from the Szabo & Ostlund [99]. The variation of E_{HF} can be written as:

$$\begin{aligned} E_{\text{HF}} &= \langle \tilde{\phi} + \delta\tilde{\phi} | \hat{H}_{el} | \tilde{\phi} + \delta\tilde{\phi} \rangle \\ &= \langle \tilde{\phi} | \hat{H}_{el} | \tilde{\phi} \rangle + \delta E_{\text{HF}} + \dots \end{aligned} \quad (2.14)$$

where we look for the condition $\delta E_{\text{HF}} = 0$.

Taking the molecular wave functions (2.13) as a trial function $\tilde{\phi} \rightarrow \sum_i c_i \phi_i$, one can use the method of the *Lagrange multipliers* to minimize the following functional:

$$\begin{aligned} \mathcal{L} &= \langle \tilde{\phi} | \hat{H}_{el} | \tilde{\phi} \rangle - \lambda (\langle \tilde{\phi} | \tilde{\phi} \rangle - 1) \\ &= \langle \phi_j | \hat{H}_{el} | \phi_i \rangle - \sum_{ij} \lambda_{ij} (\langle \phi_j | \phi_i \rangle - \delta_{ij}) \end{aligned} \quad (2.15)$$

where λ_{ij} are the Lagrange multipliers. The first term of (2.15) contains the description of the correlations between electrons that we can explicit:

$$\langle \phi_j | \hat{H}_{el} | \phi_i \rangle = \sum_i \langle \phi_i | \hat{h}_i | \phi_i \rangle + \sum_{ij} (\hat{J}_{ij} - \hat{K}_{ij}) + \hat{V}_{nuc-nuc} \quad (2.16)$$

We defined the mono-electronic hamiltonian \hat{h}_i for the i^{th} electron, the Coulomb operator \hat{J}_{ij} representing the repulsion between the i^{th} and j^{th} electron, and the exchange operator \hat{K}_{ij} representing the anti-symmetry of the wave function with respect to the exchange between 2 electrons:

$$\begin{aligned}\hat{h}_i &= -\frac{1}{2}\Delta_i - \sum_k^N \frac{Z_k}{\|\mathbf{Q}_k - \mathbf{q}_i\|} \\ \hat{J}_{ij} &= \langle \phi_i(1)\phi_i(1) | \mathbf{q}_{12}^{-1} | \phi_j(2)\phi_j(2) \rangle \\ \hat{K}_{ij} &= \langle \phi_i(1)\phi_j(1) | \mathbf{q}_{12}^{-1} | \phi_j(2)\phi_i(2) \rangle\end{aligned}$$

where $\mathbf{q}_{12}^{-1} \equiv \frac{1}{\|\mathbf{q}_1 - \mathbf{q}_2\|}$ is written as this for simplicity. We can write the variation $\delta\mathcal{L} = 0$ using (2.16):

$$\begin{aligned}\delta\mathcal{L} &= \sum_i \left\{ \langle \delta\phi_i | \hat{h}_i | \phi_i \rangle + \langle \phi_i | \hat{h}_i | \delta\phi_i \rangle \right\} \\ &+ \sum_{ij} \left\{ \langle \delta\phi_i \phi_i | \mathbf{q}_{12}^{-1} | \phi_j \phi_j \rangle + \langle \phi_i \delta\phi_i | \mathbf{q}_{12}^{-1} | \phi_j \phi_j \rangle + \langle \phi_i \phi_i | \mathbf{q}_{12}^{-1} | \delta\phi_j \phi_j \rangle + \langle \phi_i \phi_i | \mathbf{q}_{12}^{-1} | \phi_j \delta\phi_j \rangle \right. \\ &- \langle \delta\phi_i \phi_j | \mathbf{q}_{12}^{-1} | \phi_j \phi_i \rangle - \langle \phi_i \delta\phi_j | \mathbf{q}_{12}^{-1} | \phi_j \phi_i \rangle - \langle \phi_i \phi_j | \mathbf{q}_{12}^{-1} | \delta\phi_j \phi_i \rangle - \langle \phi_i \phi_j | \mathbf{q}_{12}^{-1} | \phi_j \delta\phi_i \rangle \\ &\left. - \lambda_{ij} \left(\langle \delta\phi_i | \phi_j \rangle + \langle \phi_i | \delta\phi_j \rangle \right) \right\} = 0\end{aligned}\quad (2.17)$$

We can factorize $\delta\mathcal{L}$ by $\langle \delta\phi_i |$ to obtain

$$\delta\mathcal{L} = \sum_i \langle \delta\phi_i | \left\{ \hat{h}_i | \phi_i \rangle + \sum_j \left(\langle \phi_i | \mathbf{q}_{12}^{-1} | \phi_j \phi_j \rangle - \langle \phi_j | \mathbf{q}_{12}^{-1} | \phi_j \phi_i \rangle - \lambda_{ij} | \phi_j \rangle \right) \right\} + \dots = 0 \quad (2.18)$$

The factorization is to highlight that $\langle \delta\phi_i |$ is arbitrary so that the term in brackets should be zero for all i . By refining the Coulomb and exchange operators as

$$\begin{aligned}\hat{J}_j | \phi_i \rangle &= \langle \phi_j | \mathbf{q}_{12}^{-1} | \phi_j \phi_i \rangle \\ \hat{K}_j | \phi_i \rangle &= \langle \phi_i | \mathbf{q}_{12}^{-1} | \phi_j \phi_j \rangle\end{aligned}$$

we can rewrite the term in brackets of (2.18) to obtain the Hartree-Fock equation:

$$\left\{ \hat{h}_i + \sum_j \left(\hat{J}_j - \hat{K}_j \right) \right\} |\phi_i\rangle = \sum_j \lambda_{ij} |\phi_j\rangle \quad (2.19)$$

where the term on the left hand side is the Fock operator \hat{F} . However this equation is not diagonal. To consider this, we can apply an unitary transformation to the ϕ_i functions to obtain ϕ'_i as $\phi'_i = \sum_j U_{ji} \phi_j$ where \mathbf{U} is the unitary operator so that $\mathbf{U}\mathbf{U}^* = \mathbf{1}$. It is always possible to find an unitary transformation to get the canonical Hartree-Fock equation:

$$\hat{F}|\phi'_i\rangle = \lambda'_i |\phi'_i\rangle \quad (2.20)$$

This is the main starting point equation to compute the Hartree-Fock energy. There are two main known ways to solve this equation: the *restricted Hartree-Fock* (RHF) and *unrestricted Hartree-Fock* (UHF). The RHF procedure states that molecular orbitals possess the same spatial function for both spin orientation $\alpha(\omega)$ (spin up) and $\beta(\omega)$ (spin down) whereas orbitals in the UHF procedure possess their own spatial and spin functions:

$$\phi_i^{\text{RHF}} = \begin{cases} \chi_j(\mathbf{q})\alpha(\omega) \\ \chi_j(\mathbf{q})\beta(\omega) \end{cases} \quad \phi_i^{\text{UHF}} = \begin{cases} \chi_j^\alpha(\mathbf{q})\alpha(\omega) \\ \chi_j^\beta(\mathbf{q})\beta(\omega) \end{cases}$$

The solution of these equations allows to find the best trial wave function to recover 99% of the total electronic energy. However, since electronic interactions have been described in terms of mono-electronic orbitals, all correlations between electrons have been omitted which can be chemically important. In the following, we will introduce configuration interactions and coupled clusters methods that has been used to compute the PESs used in this thesis to take into account the electronic correlation energy. These were mainly taken from the Jensen [103].

Multi-Reference Configuration Interaction

The Hartree-Fock method is able to determine one single Slater determinant which recover 99% of the electronic energy. One way to improve the accuracy of this energy is to use a reference determinant Φ_{REF} (usually obtained through the HF procedure) as a starting point to construct a multi-determinant as a new trial function:

$$\Phi_{\text{CI}} = a_0\Phi_{\text{REF}} + \sum_i a_i\Phi_i \quad (2.21)$$

with Φ_i being the i^{th} excited HF determinant. Correlations methods focus on the quantification of the a_i coefficients through the variational principle, requiring that the energy is minimum, and the Φ_i functions represent the excited determinants. This procedure is known as *Configuration Interaction* (CI). By using the Lagrange multipliers method:

$$\mathcal{L} = \langle \Phi_{\text{CI}} | \hat{H}_{el} | \Phi_{\text{CI}} \rangle - \lambda \left(\langle \Phi_{\text{CI}} | \Phi_{\text{CI}} \rangle - 1 \right) \quad (2.22)$$

The variation $\delta\mathcal{L}$ leads to the solution of the following CI matrix equation

$$(\mathbf{H}_{el} - E\mathbf{I})\mathbf{a} = \mathbf{0} \quad (2.23)$$

where E are the CI energies which are the lowest values of the CI matrix, \mathbf{a} is the matrix containing a_i coefficients in front of excited determinants. The number of possible excited determinants is limited by the size of basis functions employed in a calculation. Ideally, the use of an infinite basis set (Full CI) would lead to the inclusion of all electronic correlation and then an almost exact solution of the Schrödinger, but time calculations would become prohibitive. Usually, the determinant of reference comes from a Hartree-Fock calculation and would require a lot of excited functions to recover the electronic correlation. In order to solve this issue, several methods have been employed to optimize the determinant of reference Φ_{REF} . A suitable linear combination of determinants is called *Configurational State Functions* (CSF) and can reduce the number of CI matrix elements in calculations. Then the combination of optimizing the a_i coefficients with the variational principle and the use of CSF functions is called the *Multi-Configuration Self-Consistent Field* (MCSCF) method. Finally, the *Multi-Reference Configuration Interaction* (MRCI) uses Φ_{REF} obtained with the MCSCF method and truncates the multi-determinant to singly (S) and doubly (D) excited basis functions. A use of larger number of excited functions is in practice computationally prohibited. The MRCI function Φ_{MRCI} is then written as:

$$\Phi_{\text{MRCI}} = a_0\Phi_{\text{REF}} + \sum_S a_S\Phi_{\text{REF}}^a + \sum_D a_D\Phi_{\text{REF}}^{ab} \quad (2.24)$$

and can be used to solve the CI matrix equation (2.23). Such method, while computationally expensive, can take into account up to 99% of the electronic correlation.

Coupled Clusters

Where CI methods are based on variational formalism, the *Coupled Clusters* (CC) method is an alternative approach, including corrections to the reference determinant up to infinite order, firstly proposed by Čížek [109]. These corrections are applied by defining an excitation operator \hat{T} as:

$$\hat{T} = \hat{T}_1 + \hat{T}_2 + \hat{T}_3 + \dots + \hat{T}_N \quad (2.25)$$

Such operator is applied to the reference HF determinant Φ_0 to generate the excited determinants:

$$\begin{aligned} \hat{T}_1 \Phi_0 &= \sum_i \sum_a t_i^a \Phi_i^a \\ \hat{T}_2 \Phi_0 &= \sum_{i < j} \sum_{a < b} t_{ij}^{ab} \Phi_{ij}^{ab} \end{aligned} \quad (2.26)$$

where t_i are the expansion coefficients of the excitation operator, similar as the a_i coefficients in CI methods. This operator is expressed in terms of Taylor's expansion as:

$$e^{\hat{T}} = 1 + \hat{T} + \frac{1}{2} \hat{T}^2 + \frac{1}{6} \hat{T}^3 + \dots = \sum_{k=0}^{\infty} \frac{1}{k!} \hat{T}^k \quad (2.27)$$

Finally, the wave function under the CC approach can be written as:

$$\begin{aligned} \Phi_{\text{CC}} &= e^{\hat{T}} \Phi_0 \\ &= \Phi_0 + \hat{T}_1 \Phi_0 + \left(\hat{T}_2 + \frac{1}{2} \hat{T}_1^2 \right) \Phi_0 + \left(\hat{T}_3 + \hat{T}_2 \hat{T}_1 + \frac{1}{6} \hat{T}_1^3 \right) \Phi_0 + \dots \end{aligned} \quad (2.28)$$

We can identify from Eq. (2.28) that the first term represents the reference function (0^{th} order), the second term generates singly excited states (1^{st} order). First and second parenthesis generate doubly and triply excited states (2^{nd} and 3^{rd} orders). A term like \hat{T}_2 can be interpreted as 2 electrons interacting with each other whereas a product like \hat{T}_1^2 corresponds to a non-interacting electron pair. The inclusion of all orders is equivalent of constructing the wave function with a CI procedure. In practice, one has to truncate at

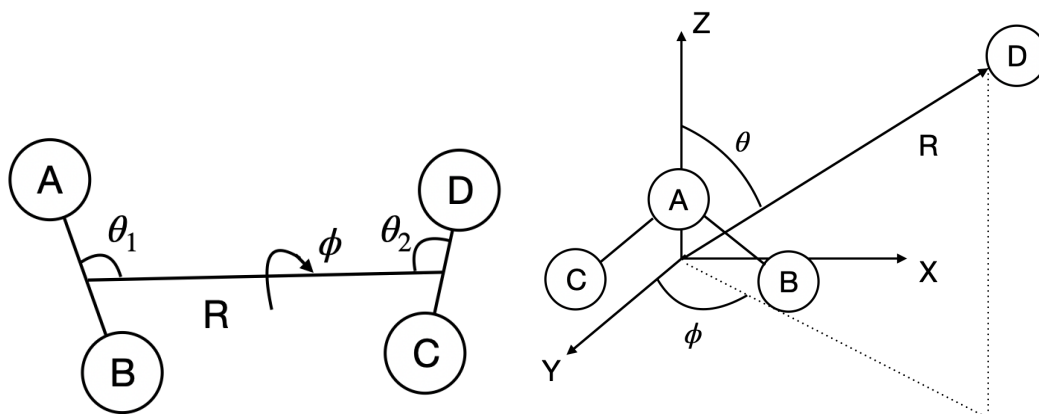


Figure 2.1 – Representation in Jacobi coordinates for two types of collisional systems. *Left*: linear-linear molecules, *Right*: asymmetric top-atom.

a certain order to keep balance between accuracy and computational time. It has been shown that the inclusion of the excitation operator up to the 3^{rd} order (CCSDT) is too much time consuming, however necessary to reproduce the correlation energy. Then, the 3^{rd} order is implemented perturbatively, showing reasonable computational time and can be applied for many molecular systems. Such method is often seen in the literature as CCSD(T) and was initially proposed by Pople et al. [110]. A further treatment is required for open-shell molecules, since their wave function employs unpaired orbitals which are not eigenfunction of the spin operator \hat{S}^2 anymore. This problem has been tackled by using of RHF functions as reference through the RCCSD(T) approach [111]. In general, Coupled Clusters methods are very time demanding as *e.g.* CCSD and CCSDT implying a computational effort scaling as M_{basis}^6 and M_{basis}^8 , respectively. Then, these are only applicable for systems with ~ 100 electrons. All presented *ab initio* methods are widely used for potential calculations in computational programs as MOLPRO [112].

2.2.2 Analytical representation for potential energy surfaces

There are many ways to extract the mathematical function fitting the PES for all geometries from *ab initio* points, *e.g.* reproducing kernel Hilbert space (RKHS) [113], interpolating moving least squares (IMLS) [114] or permutation invariant polynomial-neural network (PIP-NN) [115]. I will only focus on methods used in this thesis.

The description of motions of a collisional system must be done in an *ad-hoc* coordinate frame to be suitable for quantum dynamical calculations. The Jacobi coordinates are by far the best reference for time-independent calculations as illustrated in Fig. 2.1.

During this thesis, we focus on interactions between two linear molecules AB-CD and also between an asymmetric top ABC with an atom D. The restriction to the atom-molecule case, also studied here, will come directly from the simplification of the linear-

linear molecules interaction. Jacobi coordinates are described by the following variables:

- For linear-linear molecules interactions:
 - The vector \mathbf{R} characterizing the intermolecular distance between colliders. This usually joins the centers of mass the the two molecules.
 - θ_1 is the angle between the target AB and the intermolecular distance.
 - θ_2 is the angle between the projectile CD and the intermolecular distance.
 - ϕ is the dihedral angle between the (AB, \mathbf{R}) plane and the CD axis.
- For asymmetric top-atom interactions:
 - The vector \mathbf{R} characterizing the intermolecular distance between colliders.
 - θ is the rotation of the atom D around the molecule ABC in the xz plane of the laboratory frame.
 - ϕ is the rotation of the atom D around the molecule ABC in the xy plane of the laboratory frame.

Electronic interactions have to be described in the same coordinate system for numerical implementation reasons and optimized computational time. Usually, *ab initio* calculations are performed over a grid of points for several geometries. The number of angles chosen vary from $[0^\circ, 180^\circ]$ for a number of radial distances which cover the short, intermediate and long ranges of the PES. It is possible to take advantage of the symmetry properties of the system to avoid computing useless geometries, for example in the case of a homonuclear collider, orientations can be considered up to a rotation of 90° instead of 180° .

Scattering calculations require then an analytical representation of the PES for all geometries. It is customary to expand the angular dependence PES in terms of combinations of spherical harmonics, particularly adapted for scattering calculations, as these functions describe the best a non-reactive collision between two colliders. In the case of linear-linear molecules interactions the functional of the PES is written as:

$$\begin{aligned}
 V(R, \theta_1, \theta_2, \phi) &= \sum_{\lambda_1 \lambda_2 \lambda} v_{\lambda_1 \lambda_2 \lambda}(R) A(\theta_1, \theta_2, \phi) & (2.29) \\
 A(\theta_1, \theta_2, \phi) &= \sqrt{\frac{2\lambda + 1}{4\pi}} \left[\begin{pmatrix} \lambda_1 & \lambda_2 & \lambda \\ 0 & 0 & 0 \end{pmatrix} P_{\lambda_1 0}(\theta_1) P_{\lambda_2 0}(\theta_2) \right. \\
 &\quad \left. + 2 \sum_{m=1}^{\min(\lambda_1, \lambda_2)} \begin{pmatrix} \lambda_1 & \lambda_2 & \lambda \\ m & -m & 0 \end{pmatrix} P_{\lambda_1 m}(\theta_1) P_{\lambda_2 m}(\theta_2) \cos(m\phi) \right] & (2.30)
 \end{aligned}$$

Here $P_{\lambda m}$ denote associated Legendre polynomials, (\dots) represent 3j-Wigner symbols. λ_1, λ_2 and λ are chosen such that $|\lambda_1 - \lambda_2| < \lambda < \lambda_1 + \lambda_2$ and $v_{\lambda_1 \lambda_2 \lambda}(R)$ are the expansion coefficients of the potential. There are several ways to constrain these coefficients, usually

by spline interpolation methods. For the long range of the potential, a way to find expansion coefficients is to express them as a function of optimized coefficients $a_n(\lambda_1\lambda_2\lambda)$ as:

$$v_{\lambda_1\lambda_2\lambda}(R) = \sum_n a_n(\lambda_1\lambda_2\lambda)/R^n \quad (2.31)$$

where the coefficients $a_n(\lambda_1\lambda_2\lambda)$ are optimized using least-square fitting to *ab initio* points.

In the case of asymmetric top-atom interactions, the analytical representation of the potential is:

$$V(R, \theta, \phi) = \sum_{\lambda, \mu \geq 0} v_{\lambda\mu}(R)(1 + \delta_{\mu 0})^{-1}[Y_{\lambda}^{\mu}(\theta, \phi) + Y_{\lambda}^{-\mu}(\theta, \phi)] \quad (2.32)$$

where here the Y_{λ}^{μ} are spherical harmonics.

Ab initio calculations for the PESs considered in this thesis were not conducted by me. However, I contributed in the representation of the potentials to enable the treatment of isotopologues and reactive systems.

2.3 Notions of spectroscopy

Spectroscopy is an important field of physics that studies absorption or emission of electromagnetic radiation by matter in interaction with its environment. This allows to trace composition of matter. The signature of a molecule is represented by a molecular spectrum, which is a decomposition of its radiative flux (represented by peaks of intensity) into an energy range. Each peak corresponds to a transition between two energy levels. A molecule can be subject to several types of transitions:

- *Electronic transitions*: these are very energetic transitions (about a few eV) and occur in the optical and UV range. They could occur in very hot phases of the ISM ($T > 10^5$ K).
- *Vibrational transitions*: these are about 10^{-3} – 10^{-1} eV which is related to the infrared range, for typical temperatures about 100– 10^4 K. Some heavy and non-linear molecules can possess low frequency vibrational transitions due to their vibrational modes.
- *Rotational transitions*: these are weakly energetic transitions, about 10^{-4} eV. In this case it is customary to use the wavenumber unit (cm^{-1}) when referring to

such transitions. These occur in the cold phases of the ISM ($T \leq 100$ K), which corresponds to far-infrared and millimetric frequency ranges.

In this thesis, we focus on rotational transitions, adapted to cold astrophysical environments. We will briefly summary how rotational energy levels are defined for linear and asymmetric top molecules. Specific properties of open-shell molecules will be highlighted and how couplings coming from electronic and nuclear spin to the molecular rotation affect a rotational spectrum. Most of these information are taken from [116], [117].

2.3.1 Rotational structure

Linear molecules

The most simple case to present is the diatomic molecule, assumed to be a rigid rotor, with its internuclear distance set in the equilibrium geometry. In a classical analogy, it can be defined by the masses M_1 and M_2 of the two atoms, separated by their internuclear distance r_1 and r_2 according to the center of mass CM as in Fig. 2.2.

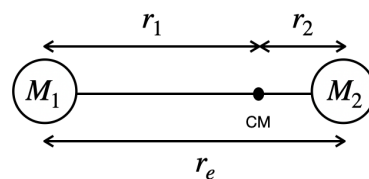


Figure 2.2 – Representation of a diatomic molecule in the rigid rotor model

The classical angular momentum of a rigid rotor is $\mathbf{J} = \mathbf{I}\omega$. Here ω is the angular velocity and I is the moment of inertia defined as

$$I = M_1 r_1^2 + M_2 r_2^2 \equiv \mu r_e^2 \quad (2.33)$$

Here in the right hand side of Eq. (2.33) we define a fictive particle of reduced mass $\mu = \frac{1}{M_1} + \frac{1}{M_2}$ moving at a distance r_e , similarly to the classical two-body problem. The rotational energy is then given by:

$$\begin{aligned} E_{rot} &= \frac{1}{2} I_a \omega_a^2 + \frac{1}{2} I_b \omega_b^2 + \frac{1}{2} I_c \omega_c^2 \\ &= \frac{J_a^2}{2I_a} + \frac{J_b^2}{2I_b} + \frac{J_c^2}{2I_c} \end{aligned} \quad (2.34)$$

The subscripts a, b, c in (2.34) refer to the principal axis of inertia of the molecule. In the case of a diatomic, we have $I_a = 0$ and $I_b = I_c \equiv I$. The quantum equivalent of the

rotational energy (2.34) is written as:

$$E_j = Bj(j + 1) \quad (2.35)$$

where $B = \frac{1}{2I}$ is defined as the *rotational constant* of the diatomic and j is the rotational quantum number, taking integer values as $j = 0, 1, 2, \dots$. This quantum number is the equivalent of the classical \mathbf{J} angular momentum, and the eigenvalues of \hat{j}^2 are $j(j + 1)$. This implies that quantum rotational energy levels are discrete and proportional to the rotational constants. They can be represented in the simplest way as in Fig. 2.3.

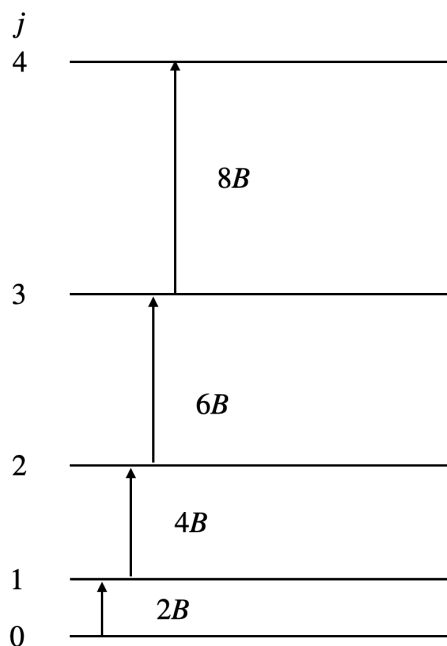


Figure 2.3 – Representation of a rotational energy levels diagram

The assumption of a fixed internuclear distance r_e is justified for low energies. The rigid rotor model becomes less and less true as contribution of centrifugal forces increases with energy levels. It is then necessary to take it into account as a correction to rotational energy levels. The expression for the centrifugal is given by the derivative of the nuclear kinetic energy [39]:

$$F_c = -\frac{d}{dr} \frac{j(j + 1)}{2\mu r^2} = \frac{j(j + 1)}{\mu r^3} = kr_e x; \quad x \equiv (r - r_e)/r_e \quad (2.36)$$

with k a constant of the force F_c . The contribution of F_c modifies the rotational energy (2.34):

$$E_{rot} = \frac{j(j+1)}{2\mu r^2} + \frac{1}{2}k(r-r_e)^2 = \frac{Bj(j+1)}{(1+x)^2} + \frac{1}{2}kr_e^2x^2 \quad (2.37)$$

where we can see that $(1+x)^2 = (r/r_e)^2$. From (2.36), we can see that for $r = r_e$:

$$x = \frac{j(j+1)}{k\mu r_e^4} = \frac{2B^2j(j+1)}{\omega^2} \quad (2.38)$$

where $\omega = \sqrt{k/\mu}$ is the classical vibrational frequency of the harmonic oscillator. x being small, we can use that

$$\frac{1}{1+x} \stackrel{x \rightarrow 0}{\approx} 1 - x + x^2 + \dots + (-1)^n x^n + o(x^n)$$

to write Eq. (2.37) in series of x truncated at the first order:

$$\begin{aligned} E_{rot} &\simeq Bj(j+1)(1-2x) = Bj(j+1)\left(1 - \frac{4B^2j(j+1)}{\omega^2}\right) \\ &= Bj(j+1) - Dj^2(j+1)^2 \end{aligned} \quad (2.39)$$

and $D \equiv 4B^3/\omega^2$ is the *centrifugal constant* of the molecule. We usually have $D \ll B$ so that this contribution is negligible for the lowest energy levels, and become more important for higher energies due to its dependence in j^2 .

Asymmetric top molecules

An asymmetric top is a molecule possessing three different moments of inertia ($I_a \neq I_b \neq I_c$, see Fig. 2.4) contrary to symmetric tops, having two identical moments of inertia ($I_a = I_b \neq I_c$ or $I_a \neq I_b = I_c$).

For such molecule, the quantification of its energy levels is not simple as for the diatomic case. The rotational hamiltonian is written as:

$$\hat{H}_{rot} = A\hat{j}_a^2 + B\hat{j}_b^2 + C\hat{j}_c^2 \quad (2.40)$$

with $A = \frac{1}{2I_a}$, $B = \frac{1}{2I_b}$ and $C = \frac{1}{2I_c}$ which define the rotational constants of an asymmetric top. The solution of the Schrödinger equation for the hamiltonian (2.40) is not easily solvable since the components j_a^2 , j_b^2 and j_c^2 do not present eigenvalues of angular functions. The strategy is to expand the asymmetric top wave function in

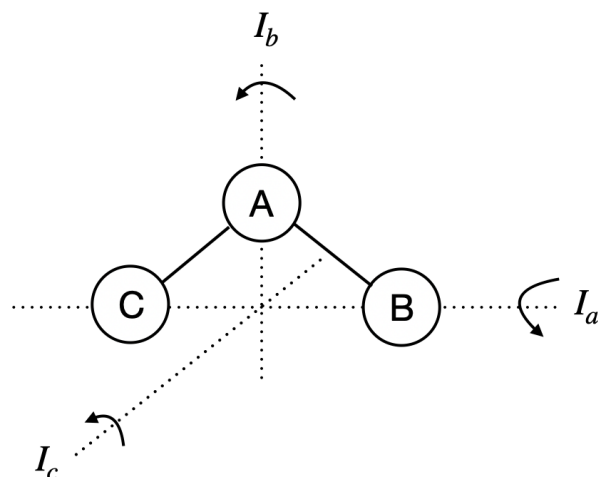


Figure 2.4 – Representation of the moments of inertia of an asymmetric top.

terms of symmetric top basis functions (the case with one moment of inertia lies along the molecular axis of symmetry) and solve the Schrödinger equation for the expansion coefficients and molecular energies.

In this thesis, we will just highlight the conventions used in the literature and that will be applied to collisional systems. Usually, moments of inertia are defined so that $I_a < I_b < I_c$, implying that $A > B > C$. From this, it is often seen to compare an asymmetric top according to the *oblate* or *prolate* symmetric top limit. If $I_b \rightarrow I_c$, the prolate symmetric top is approached (like a cigar). On the other hand, if $I_b \rightarrow I_a$, the oblate symmetric top is approached (like a lens). The position of the asymmetric top in one of these limits can be described by the κ parameter:

$$\kappa = \frac{2B - A - C}{A - C} \quad (2.41)$$

This parameter can vary from -1 to +1, corresponding to prolate and oblate limit, respectively. The case where $\kappa = 0$ is a "pure" asymmetric top. The rotational levels are labeled as $j_{k_a k_c}$ where k_a and k_c are the projections of the angular momentum according to the a and c axis. An energy levels diagram can be illustrated for the first quantum numbers j as in Fig. 2.5.

2.3.2 Fine structure

Open-shell molecules, by their denomination, possess unpaired electrons. These involve a nonzero electronic spin S which gives rise to a magnetic dipole moment

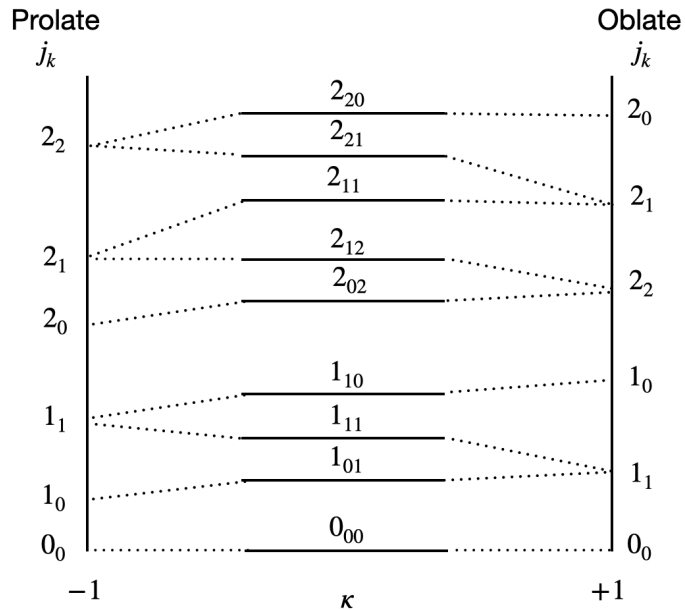


Figure 2.5 – Illustration of energy levels of an asymmetric top. The prolate and oblate limits are added with κ varying from -1 to +1.

$$\mu_S = -g_S \mu_B S \quad (2.42)$$

where g_S is the free electron g-factor and μ_B is the Bohr magneton. This will couple to the rotational motion and affect the molecular spectrum. The consequence of the fine structure is a splitting of rotational energy levels and will depend on the number of unpaired electrons and the strength of the coupling of S to the other angular momenta of the system. The classification of these different couplings are referred as Hund's coupling cases [118] which are idealized to understand interactions in play. In this thesis we focus on open-shell molecules described in their $2S+1\Sigma$ electronic state and can be understood in the Hund's case (b). In this description, the electronic spin will couple to the rotation through a weak magnetic field and result in the following coupling scheme:

$$\hat{j} = \hat{N} + \hat{S}$$

where \hat{N} is the electronic spin-free rotational quantum number (similar as j for the case of closed-shell molecules), and \hat{j} is the angular momentum including the electronic spin. This can be illustrated in Fig. 2.6.

For a molecule described in the Hund's case (b), a spin-rotation term will contribute to the molecular hamiltonian as:

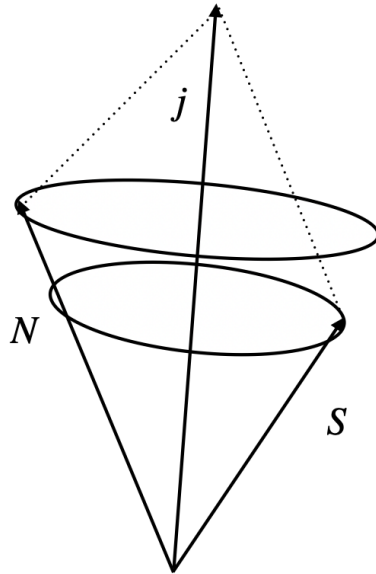


Figure 2.6 – Illustration of coupling vectors for molecules in Σ state described in the Hund's case (b).

$$\hat{H}_{\text{SN}} = \gamma(\hat{S} \cdot \hat{N}) \quad \text{:spin-rotation} \quad (2.43)$$

where γ is defined as the spin-rotation constant. For molecules having more than one unpaired electron, an additional spin-spin interaction term is involved in the hamiltonian as follow:

$$\hat{H}_{\text{SS}} = \frac{2}{3}\lambda(3\hat{S}_z^2 - \hat{S}^2) \quad \text{:spin-spin} \quad (2.44)$$

with λ being the spin-spin constant. Quantum numbers are varying for $N \in \mathbb{N}$, $|N - S| \leq j \leq N + S$ and the usual convention is to label fine structure energy levels as N_j .

2.3.3 Hyperfine structure

When the nucleus of a molecule possesses a non vanishing nuclear spin I , more complex interactions start to play a role in the molecular spectrum. We call hyperfine structure the splitting of rotational/fine structure energy levels by the coupling of the nuclear spin to the angular momentum j . First, from the presence of I arises a magnetic moment given by

$$\mu_I = -g_I \mu_N I \quad (2.45)$$

where g_I is the nuclear g-factor and μ_N is the nuclear magneton. For the case where there is only one nuclear spin, the coupling to the rotation will follow the coupling scheme:

$$\hat{F} = \hat{j} + \hat{I}$$

where $|j - I| \leq F \leq j + I$ is the rotational angular momentum including the nuclear spin, and a hyperfine energy level is labeled by N_{jF} . The coupling vector can be represented similarly as in Fig. 2.6. From the emergence of the hyperfine magnetic moment μ_I , several couplings are involved in the definition of the effective hyperfine hamiltonian from magnetic interactions: nuclear spin-rotation ($\hat{j} \cdot \hat{I}$), and the Fermi contact and dipole interactions ($\hat{I} \cdot \hat{S}$) for open-shell molecules:

$$\begin{aligned} \hat{H}_{jI} &= c(\hat{j} \cdot \hat{I}) \quad \text{:spin-rotation} \\ \hat{H}_F &= b_F(\hat{S} \cdot \hat{I}) \quad \text{:Fermi contact} \\ \hat{H}_{dip} &= \sqrt{6} g_S \mu_B g_N \mu_N \frac{\mu_0}{4\pi} \left\{ \frac{\hat{I} \cdot \hat{S}}{r^3} - \frac{3(\hat{I} \cdot \hat{r})(\hat{S} \cdot \hat{r})}{r^5} \right\} \quad \text{:dipole} \end{aligned} \quad (2.46)$$

Here c is the nuclear spin-rotation constant, b_F is the Fermi contact constant, μ_0 is the magnetic constant. As for the fine structure, a spin-spin interaction ($\hat{I}_1 \cdot \hat{I}_2$) should exist when there are more than one nonzero nuclear spin. However it is very small and is often neglected in gas phase studies.

One last type of interaction occurring in hyperfine structure phenomena is coming from the electric quadrupole moments of the nuclei. The nuclear quadrupole interaction stands only for nuclei possessing a nuclear spin $I \geq 1$. This is due to the asymmetry of distribution of the charge of the nuclear spin about the nucleus and arises an electric field gradient. This type of interaction can be represented by the term:

$$\hat{H}_Q = \frac{eQq}{2j(2j-1)I(2I-1)} \left\{ 3(\hat{I} \cdot \hat{j})^2 - \frac{3}{2}(\hat{I} \cdot \hat{j}) - \hat{I}^2 \hat{j}^2 \right\} \quad (2.47)$$

Overall, the molecular hamiltonian for an open-shell molecule including all its spectroscopic properties will be described as:

$$\hat{H}_{mol} = \hat{H}_{rot} + \hat{H}_{SN} + \hat{H}_{SS} + \hat{H}_{jI} + \hat{H}_F + \hat{H}_{dip} + \hat{H}_Q \quad (2.48)$$

showing a complex energetic structure. Especially, hyperfine couplings are about three orders of magnitude weaker than fine structure ones. The precision of spectroscopic instruments in laboratory or in telescopes are often sufficient to resolve spectra up to the MHz or kHz, which is able to describe hyperfine transitions.

2.4 Scattering theory

Within the Born-Oppenheimer approximation, we can use the PES as an input for quantum dynamical calculations. The typical case occurring during a collision between two molecules AB and CD is:



resulting in an energy transfer between internal states (j_1, j_2) of the colliders without breaking none of the molecules. We call this an *inelastic collision*. A change toward a higher internal energy level than the initial state is an *excitation* where the contrary is a *de-excitation*.

In this thesis, we focus on both reactive and non-reactive collisions for low temperature applications. In the following, we will introduce the treatment non-reactive collisions through quantum scattering approaches and some useful approximations when accurate methods become prohibitive in terms of computational time. Arthurs and Dalgarno were the first to propose a quantum scattering description of a rigid rotor by a structureless atom [56]. This formulation can be extended to the case of two linear molecules. The approach for two closed-shell molecules will be presented based on the work of Launay [119]. Details about collisions involving open-shell molecules will be given in section 3.2.

2.4.1 Collisional excitation of $^1\Sigma$ molecules induced by collisions with $^1\Sigma$ molecules

Wave function and S -matrix

The description of collision between two molecules has to be done in a suitable frame. In the literature, it is general that a collisional system is described in the *space-fixed* (SF) or the *body-fixed* (BF) frame. In the SF frame, the origin of the coordinate axis is chosen

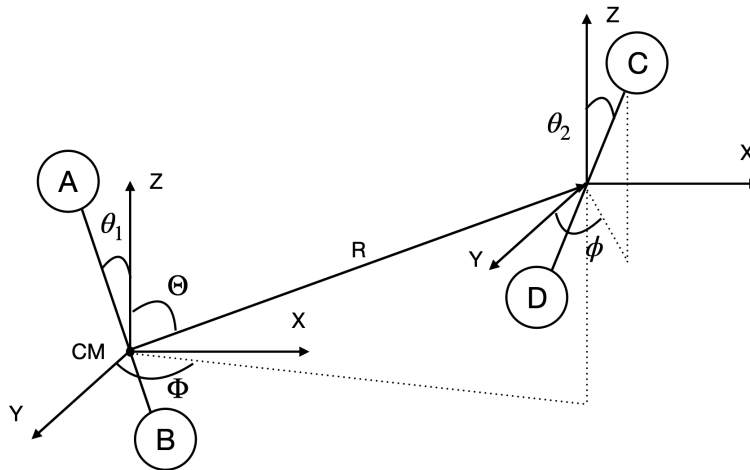


Figure 2.7 – Polar coordinates of two colliding diatomic molecules represented in the space-fixed frame. The xyz axis takes its origin in the center of mass (CM) of the target AB. The xyz represented on the projectile CD is to show the orientations of its coordinates for schematic view.

to coincide with the center of mass of the target. In the BF frame, the coordinate axis is chosen to coincide with the center of mass of the collisional complex and is rotating with the system by applying Euler angles. Even if these representations should be equivalent, the BF frame is not suitable for scattering calculations because the apparition of quantum numbers related to centrifugal forces are dominating at high distances which still couple equations. Then a transformation to the SF frame would be required to uncouple them. However, the representation of the coupled equations in the BF frame are in a simpler form when treating about approximations such as the *Coupled States* (CS) approach or the *Infinite Order Sudden* (IOS) limit. In the following, we will restrict the description of the equations in the SF frame. An schematic view of the SF can be seen in Fig. 2.7.

We are looking for the solution of the Schrödinger equation (2.1) for collisions between two linear molecules, where we drop now the electronic coordinates \mathbf{q} . The molecular hamiltonian has the form:

$$\hat{H}_{mol}(\mathbf{Q}) = -\frac{1}{2\mu R} \frac{\partial^2}{\partial R^2} R + \frac{\hat{L}^2}{2\mu R^2} + \frac{\hat{j}_1^2}{2I_1} + \frac{\hat{j}_2^2}{2I_2} + \hat{V}(\mathbf{Q}) \quad (2.50)$$

where now $\mathbf{Q} \equiv (R, \theta_1, \theta_2, \phi)$ the coordinates describe the nuclear motion of the molecular system (see Fig. 2.7), j_1, j_2 are the rotational angular momenta of the two molecules, L is the orbital angular momentum of the collisional system. These quantum numbers will couple with each other to form a new basis of angular momenta:

$$\hat{j}_{12} = \hat{j}_1 + \hat{j}_2; \quad \hat{J} = \hat{j}_{12} + \hat{L}$$

Usually, spherical harmonics $|jm\rangle \equiv Y_{jm}$ are eigenfunctions of the operators \hat{j}_1^2 , \hat{j}_2^2 and \hat{l}^2 but not for \hat{J}^2 . However, the use of the rules of addition of angular momenta can give the following eigenfunction:

$$|\alpha JLM\rangle = \sum_{(m)} C_{m_1 m_2 m}^{j_1 j_2 j} C_{m_1 m_L M}^{j_1 j_2 L J} |j_1 m_1\rangle |j_2 m_2\rangle |L m_L\rangle \quad (2.51)$$

where $\alpha \equiv j_1 j_2 j$ and the (m) mentions that the summation is done over all projections of the quantum numbers involved, and M is the projection of J . The C coefficients are *Clebsch-Gordan* coefficients defined as:

$$C_{def}^{abc} = (-1)^{a-b+f} [c]^{1/2} \begin{pmatrix} a & b & c \\ d & e & -f \end{pmatrix} \quad (2.52)$$

with $[x] \equiv (2x+1)$ and (\dots) is a $3j$ -Wigner symbol. These symbols contain the information about the coupling between quantum numbers. The angular functions (2.51) satisfy the orthogonality rules:

$$\langle \alpha' J L' M | \alpha J L M \rangle = \delta_{\alpha\alpha'} \delta_{LL'} \quad (2.53)$$

These form the basis set of angular functions in which we can expand the solutions of the Schrödinger equation, namely:

$$\Psi_{\alpha L}^J(\mathbf{Q}) = \sum_{\alpha' L'} \frac{F_{\alpha L, \alpha' L'}^J(R)}{R} |\alpha' J L' M\rangle \quad (2.54)$$

This wave function is decomposed for each total angular momentum J . The $F_{\alpha L, \alpha' L'}^J(R)$ function contains the radial dependence of the system. We can now implement the wave function (2.54) and the molecular hamiltonian (2.50) into the Schrödinger equation (2.1). Solutions of this equation for the radial part are obtained by doing an average over the angles, so by integrating over $\langle \alpha'' J L'' M |$ we obtain:

$$\begin{aligned}
 & \langle \alpha'' JL'' M | \left(-\frac{1}{2\mu R} \frac{\partial^2}{\partial R^2} R + \frac{\hat{L}^2}{2\mu R^2} + \frac{\hat{j}_1^2}{2I_1} + \frac{\hat{j}_2^2}{2I_2} + \hat{V}(\mathbf{Q}) \right) \Psi_{\alpha L}^J(\mathbf{Q}) = \langle \alpha'' JL'' M | E \Psi_{\alpha L}^J(\mathbf{Q}) \\
 \Rightarrow & \sum_{\alpha' L'} \left(-\frac{1}{2\mu R} \frac{\partial^2}{\partial R^2} R + \frac{L''(L''+1)}{2\mu R^2} + \frac{j_1''(j_1''+1)}{2I_1} + \frac{j_2''(j_2''+1)}{2I_2} \right) F_{\alpha L, \alpha' L'}^J(R) \\
 + & \sum_{\alpha' L'} \langle \alpha'' JL'' M | \hat{V}(\mathbf{Q}) | \alpha' JL' M \rangle F_{\alpha L, \alpha' L'}^J(R) = E F_{\alpha L, \alpha' L'}^J(R) \tag{2.55}
 \end{aligned}$$

Multiplying each side by 2μ and defining the *wave vector*:

$$k_{j_1'' j_2''}^2 = 2\mu \left(E - \frac{j_1''(j_1''+1)}{2I_1} - \frac{j_2''(j_2''+1)}{2I_2} \right) \tag{2.56}$$

we can rewrite the system of equations (2.55) as:

$$\begin{aligned}
 & \left(\frac{\partial^2}{\partial R^2} + k_{j_1'' j_2''}^2 - \frac{L''(L''+1)}{R^2} \right) F_{\alpha'' L'', \alpha L}^J(R) = \\
 & 2\mu \sum_{\alpha' L'} \langle \alpha'' JL'' M | \hat{V} | \alpha' JL' M \rangle F_{\alpha' L', \alpha L}^J(R) \tag{2.57}
 \end{aligned}$$

The set of coupled equations (2.57) are called the *close-coupling* (CC) equations. These depend on the potential V -matrix elements $\langle \alpha'' JL'' M | \hat{V} | \alpha' JL' M \rangle$. V -matrix elements are system dependent. For the case of two linear molecules, we use the potential interaction (2.29) and combined with angular functions (2.51), we obtain [59]:

$$\begin{aligned}
 \langle \alpha'' JL'' | \hat{V} | \alpha' JL' \rangle &= (4\pi)^{-3/2} \sum_{\lambda_1 \lambda_2 \lambda} v_{\lambda_1 \lambda_2 \lambda}(R) [\lambda] [\lambda_1 \lambda_2 j_1' j_1'' j_2' j_2'' j_{12}' j_{12}'' L' L'']^{1/2} \\
 &\times (-1)^{J+j_1'+j_2'+j_1''} \\
 &\times \begin{pmatrix} \lambda_1 & j_1'' & j_1' \\ 0 & 0 & 0 \end{pmatrix} \begin{pmatrix} \lambda_2 & j_2'' & j_2' \\ 0 & 0 & 0 \end{pmatrix} \begin{pmatrix} \lambda & L'' & L' \\ 0 & 0 & 0 \end{pmatrix} \\
 &\times \begin{Bmatrix} L'' & L' & \lambda \\ j_{12}' & j_{12}'' & J \end{Bmatrix} \begin{Bmatrix} j_{12}'' & j_2'' & j_1'' \\ j_{12}' & j_2' & j_1' \\ \lambda & \lambda_2 & \lambda_1 \end{Bmatrix} \tag{2.58}
 \end{aligned}$$

Knowing the asymptotic behavior of the radial function, one can extract the S -matrix as:

$$\begin{aligned}
 F_{\alpha'L',\alpha L}^J(R) &\underset{R \rightarrow \infty}{\sim} \delta_{\alpha\alpha'} \delta_{LL'} e^{-i(k_{j_1 j_2} R - \frac{L\pi}{2})} - \sqrt{\frac{k_{j_1 j_2}}{k_{j'_1 j'_2}}} S_{\alpha'L',\alpha L}^J e^{i(k_{j'_1 j'_2} R - \frac{L'\pi}{2})} \\
 F_{\alpha'L',\alpha L}^J(R) &\underset{R \rightarrow 0}{\sim} 0
 \end{aligned} \tag{2.59}$$

where $S_{\alpha'L',\alpha L}^J$ is a *scattering-matrix* element for a given total angular momentum J and a given channel². The S -matrix is linked to the *transition* matrix as $\mathbf{T} = \mathbf{1} - \mathbf{S}$.

Cross section and rate coefficient

The scattering and transition matrices define the *cross section* which is the observable of interest to extract from the CC equations. It characterizes the probability that a transition occurs from an initial state to a final one. The state-to-state cross section is resolved for each J as:

$$\sigma_{j_1 j_2 \rightarrow j'_1 j'_2}^J = \frac{\pi}{[j_1 j_2] k_{j_1 j_2}^2} [J] \sum_{j_{12} j'_{12} LL'} |\langle \alpha' L' | T^J | \alpha L \rangle|^2 \tag{2.60}$$

where $[x] \equiv (2x + 1)$. The total cross section for a given transition is the summation of all partial ones:

$$\sigma_{j_1 j_2 \rightarrow j'_1 j'_2} = \sum_J \sigma_{j_1 j_2 \rightarrow j'_1 j'_2}^J \tag{2.61}$$

In astrophysical environments, usually out of LTE, collisional processes are competing with radiative processes and we use the rate coefficients to quantify the efficiency of a transition, which means how fast a transition participates in the (de)population of a given energy level. The rate coefficient depends on the cross section and is determined for a given kinetic temperature T by integrating the cross section over a Maxwell-Boltzmann distribution:

$$k_{j_1 j_2 \rightarrow j'_1 j'_2}(T) = \left(\frac{8}{\pi \mu (k_B T)^3} \right)^{1/2} \int_0^\infty \sigma_{j_1 j_2 \rightarrow j'_1 j'_2}(E_c) E_c e^{-E_c/(k_B T)} dE_c \tag{2.62}$$

2. A channel is a combination of the angular momenta satisfying the conservation of the total angular momentum as *e.g.*

$$\alpha + L = J = \alpha' + L'$$

where μ is the reduced mass of the collisional system, E_c is the collisional energy and k_B is the Boltzmann constant. The rate coefficient (2.62) assumes that collision energies are in LTE.

Because the S -matrix is diagonal, the transition probabilities satisfy the *micro reversibility* which allows to write the equality:

$$[j'_1 j'_2] e^{-(E_{j'_1} + E_{j'_2})/(k_B T)} k_{j'_1 j'_2 \rightarrow j_1 j_2}(T) = [j_1 j_2] e^{-(E_{j_1} + E_{j_2})/(k_B T)} k_{j_1 j_2 \rightarrow j'_1 j'_2}(T) \quad (2.63)$$

This equation represents the *detailed balance*. One can re-write a de-excitation rate coefficient as a function of the excitation one:

$$k_{j'_1 j'_2 \rightarrow j_1 j_2}(T) = \frac{[j_1 j_2]}{[j'_1 j'_2]} e^{\Delta E/(k_B T)} k_{j_1 j_2 \rightarrow j'_1 j'_2}(T) \quad (2.64)$$

with $\Delta E = E_{j'_1} + E_{j'_2} - E_{j_1} - E_{j_2}$.

2.4.2 Approximations

The solution of the CC equations would imply to use an infinite number of channels to describe cross sections. In practice, cross sections can be converged for a reasonable truncation of the number of coupled equations to consider, even though the CC equations require the inclusion of closed states for a proper convergence. However, the computational time being proportional to the cubic of the number of channels ($t \propto M_{chan}^3$ [120]), the computation of the S matrices can become very intensive and prohibitive when the number of energy levels is large. There are some alternatives to compute cross sections.

A way to lighten the computational cost of the CC equations is to neglect couplings to some angular momenta. Such neglect is called a sudden approximation. In this thesis, we used the *Infinite Order Sudden* (IOS) limit, which consist in two sudden approximations:

1. The centrifugal sudden approximation. For systems dominated by short range interactions, one can replace the centrifugal terms by an average value $\bar{L}(\bar{L}+1)/R^2$. This reduces the dimensionality of the equations by block diagonalization of the V -matrix elements [81]. This approximation is also called *coupled states* (CS) and has been developed by Pack [121] and McGuire [122].
2. The energy sudden (ES) approximation. When the collisional energy is much larger than the space between energy levels, it is possible to ignore the rotational structure during a collision. It means that we assume a fast enough collision to state that the target is not rotating during the process. One can replace the wave

vector by an average value $\bar{k}^2 \sim 2\mu E$ in the CC equations. This was first employed by Secrest [123].

Overall, the CC equations within the IOS approximation are completely uncoupled and have the form:

$$\left(\frac{\partial^2}{\partial R^2} + \bar{k}^2 - \frac{\bar{L}(\bar{L} + 1)}{R^2} - 2\mu V(R, \bar{\theta}) \right) F^J(R, \bar{\theta}) = 0 \quad (2.65)$$

where $\bar{\theta}$ are averaged angles. Now the S matrices $S^{\bar{L}}(\bar{\theta})$ depend parametrically on the angles. The S -matrix can be expanded with the same angular dependence as the PES, so the S -matrix elements will have a similar form:

$$\begin{aligned} \langle \alpha' j'_{12} L' | S^{\bar{L}}(\bar{\theta}) | \alpha j_{12} L \rangle &= (4\pi)^{-3/2} \sum_{\lambda_1 \lambda_2 \lambda} [\lambda] [\lambda_1 \lambda_2 j_1 j'_1 j_2 j'_2 j_{12} j'_{12} L L']^{1/2} \\ &\times (-1)^{J+j_1+j_2+j_{12}} \\ &\times \begin{pmatrix} \lambda_1 & j'_1 & j_1 \\ 0 & 0 & 0 \end{pmatrix} \begin{pmatrix} \lambda_2 & j'_2 & j_2 \\ 0 & 0 & 0 \end{pmatrix} \begin{pmatrix} \lambda & L' & L \\ 0 & 0 & 0 \end{pmatrix} \\ &\times \begin{Bmatrix} L' & L & \lambda \\ j_{12} & j'_{12} & J \end{Bmatrix} \begin{Bmatrix} j'_{12} & j'_2 & j'_1 \\ j_{12} & j_2 & j_1 \\ \lambda & \lambda_2 & \lambda_1 \end{Bmatrix} S^{\bar{L}}_{\lambda_1 \lambda_2 \lambda} \end{aligned} \quad (2.66)$$

The rotational IOS cross section can be written as:

$$\begin{aligned} \sigma_{j_1 j_2 \rightarrow j'_1 j'_2}^{\text{IOS}} &= \frac{\pi}{k^2 [j_1 j_2]} \sum_{\substack{J j_{12} j'_{12} \\ L L'}} [J] |\langle \alpha' j'_{12} L' | T^J | \alpha j_{12} L \rangle|^2 \\ &= \frac{\pi}{k^2 [j_1 j_2]} \sum_{\substack{J j_{12} j'_{12} \\ L L'}} [J] (4\pi)^{-3} \sum_{\lambda_1 \lambda_2 \lambda} [\lambda]^2 [\lambda_1 \lambda_2 j_1 j'_1 j_2 j'_2 j_{12} j'_{12} L L'] \\ &\times \begin{pmatrix} \lambda_1 & j'_1 & j_1 \\ 0 & 0 & 0 \end{pmatrix}^2 \begin{pmatrix} \lambda_2 & j'_2 & j_2 \\ 0 & 0 & 0 \end{pmatrix}^2 \begin{pmatrix} \lambda & L' & L \\ 0 & 0 & 0 \end{pmatrix}^2 \\ &\times \begin{Bmatrix} L' & L & \lambda \\ j_{12} & j'_{12} & J \end{Bmatrix}^2 \begin{Bmatrix} j'_{12} & j'_2 & j'_1 \\ j_{12} & j_2 & j_1 \\ \lambda & \lambda_2 & \lambda_1 \end{Bmatrix}^2 |T^{\bar{L}}_{\lambda_1 \lambda_2 \lambda}|^2 \end{aligned} \quad (2.67)$$

Eq. (2.67) can be simplified by seeing that

$$\sum_J [J] \left\{ \begin{array}{ccc} L' & L & \lambda \\ j_{12} & j'_{12} & J \end{array} \right\}^2 = \frac{1}{[\lambda]} \quad \text{and} \quad \sum_{j_{12}j'_{12}} [j_{12}j'_{12}] \left\{ \begin{array}{ccc} j'_{12} & j'_2 & j'_1 \\ j_{12} & j_2 & j_1 \\ \lambda & \lambda_2 & \lambda_1 \end{array} \right\}^2 = \frac{1}{[\lambda_1\lambda_2]}$$

and the cross section can be written

$$\begin{aligned} \sigma_{j_1j_2 \rightarrow j'_1j'_2}^{\text{IOS}} &= [j'_1j'_2] \sum_{\lambda_1\lambda_2\lambda} \left(\begin{array}{ccc} \lambda_1 & j'_1 & j_1 \\ 0 & 0 & 0 \end{array} \right)^2 \left(\begin{array}{ccc} \lambda_2 & j'_2 & j_2 \\ 0 & 0 & 0 \end{array} \right)^2 \sigma_{\lambda_1\lambda_2\lambda} \\ \sigma_{\lambda_1\lambda_2\lambda} &= \frac{\pi}{k^2} \sum_{LL'} (4\pi)^{-3} [\lambda LL'] \left(\begin{array}{ccc} \lambda & L' & L \\ 0 & 0 & 0 \end{array} \right)^2 |T_{\lambda_1\lambda_2\lambda}^{\bar{L}}|^2 \end{aligned} \quad (2.68)$$

We want to express the IOS cross section in terms of transitions out of the fundamental level. If we set $j_1 = 0$ and $j_2 = 0$, we can see that the $3j$ symbols are nonzero only for $j_{1'} = \lambda_1$ and $j_{2'} = \lambda_2$. The relation (2.68) can be re-written:

$$\sigma_{00 \rightarrow \lambda_1\lambda_2}^{\text{IOS}} = [\lambda_1\lambda_2] \left(\begin{array}{ccc} \lambda_1 & \lambda_1 & 0 \\ 0 & 0 & 0 \end{array} \right)^2 \left(\begin{array}{ccc} \lambda_2 & \lambda_2 & 0 \\ 0 & 0 & 0 \end{array} \right)^2 \sigma_{\lambda_1\lambda_2\lambda} \quad (2.69)$$

We can see that:

$$[\lambda_1] \left(\begin{array}{ccc} \lambda_1 & \lambda_1 & 0 \\ 0 & 0 & 0 \end{array} \right)^2 = 1; \quad [\lambda_2] \left(\begin{array}{ccc} \lambda_2 & \lambda_2 & 0 \\ 0 & 0 & 0 \end{array} \right)^2 = 1$$

which simplifies $\sigma_{\lambda_1\lambda_2\lambda} = \sigma_{00 \rightarrow \lambda_1\lambda_2}^{\text{IOS}}$ that we can report in Eq. (2.68) to have:

$$\sigma_{j_1j_2 \rightarrow j'_1j'_2}^{\text{IOS}} = [j'_1j'_2] \sum_{\lambda_1\lambda_2} \left(\begin{array}{ccc} \lambda_1 & j'_1 & j_1 \\ 0 & 0 & 0 \end{array} \right)^2 \left(\begin{array}{ccc} \lambda_2 & j'_2 & j_2 \\ 0 & 0 & 0 \end{array} \right)^2 \sigma_{00 \rightarrow \lambda_1\lambda_2}^{\text{IOS}} \quad (2.70)$$

It should be noted that the transition out of the fundamental can be replaced by the ones obtained with the CC method. This formula stands also for rate coefficients and is similar that the one found in [124]. It is also possible to use the detailed balance to express the IOS cross section as a function of de-excitations:

$$\sigma_{00 \rightarrow \lambda_1\lambda_2}^{\text{IOS}} = [\lambda_1\lambda_2] \sigma_{\lambda_1\lambda_2 \rightarrow 00}^{\text{IOS}} \quad (2.71)$$

Here there is no exponential dependence since $\Delta E = 0$ within the IOS approach.

2.4.3 Statistical Adiabatic Channel Model (SACM)

The previous presented approximations are based on quantum approaches for non-reactive collisions. However, calculations involving a large number of atoms cannot be achieved with quantum methods mainly coming from the large number of degrees of freedom. In the past decades, statistical approaches have been developed to propose alternatives for dynamical calculations. The general idea of statistical methods is to assume that the well depth of a potential is sufficiently deep to not only form a intermediate complex but a long-lived one. The long meta-stability of the complex induces the assumption that no coupling exists between the initial (α) and final (α') state of the collisional system anymore. The system "forgets" its initial conditions and the probability to decay in a given channel of products is statistically distributed.

Such methods were developed in the 1950s for nuclear physics and adapted to molecular collisions in the 1960s [125]–[127]. In this thesis, we will use the *Statistical Adiabatic Channel Model* (SACM) [97] and we present here the general features. This method is based on the approach developed by Quack & Troe [128] in 1975. In this approach, the CC equations are solved excluding the kinetic term $\partial^2/\partial R^2$ of Eq. (2.57). Then, the molecular hamiltonian (2.50) is diagonalized for each total angular momentum and CC equations are simplified as:

$$\sum_{\alpha'} \left\langle \alpha' \left| \frac{\hat{j}_1^2}{2I_1} + \frac{\hat{j}_2^2}{2I_2} + \hat{V} + \frac{\hat{L}^2}{2\mu R^2} \right| \alpha \right\rangle F_{\alpha}^J(R) = 0 \quad (2.72)$$

This results in a set of adiabatic curves or *adiabats* as illustrated in Fig. 4.5.

Adiabats represent a given channel and the asymptotic value is associated to an internal energy level of the collisional system. The transition probability will depend on the number of open channels for a given total energy E and a total angular momentum J . In the SACM, a channel is considered as open if the long range of the adiabat, including the maximum value of the centrifugal barrier V_i^{max} , is below E ($V_i^{max} < E$, with i labelling a given adiabat) and is considered closed on the contrary ($V_i^{max} > E$). For example in Fig. 4.5, channels a and b are open whereas c and d are closed. Then, each S -matrix elements have an equal probability for each open channel and zero otherwise:

$$|\langle \alpha' | S^J(E) | \alpha \rangle|^2 = \begin{cases} \frac{1}{N_{tot}(E,J)} & \text{open channels} \\ 0 & \text{otherwise} \end{cases} \quad (2.73)$$

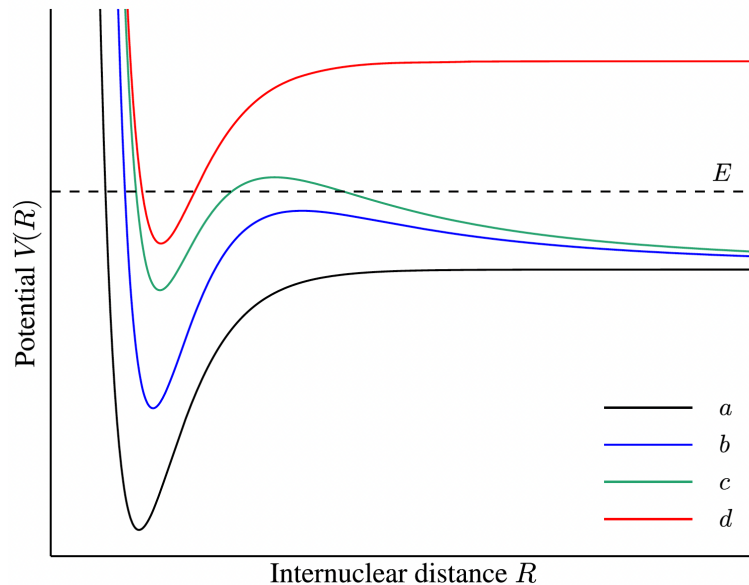


Figure 2.8 – Illustration of adiabats as a function of the distance. The total energy threshold is shown by the dashed line. Channels a and b are considered open whereas c and d are closed. This figure is taken from [97].

where $N_{tot}(E, J)$ is the total number of open channels for a given tuple (E, J) . The total collisional cross section is determined as:

$$\sigma_{\alpha \rightarrow \alpha'}^{\text{SACM}} = \frac{\pi}{k^2 [j_1 j_2]} \sum_{JLL'} [J] |\langle \alpha' | S^J(E) | \alpha \rangle|^2 \quad (2.74)$$

Summations over the orbital angular momenta L and L' give directly the number of channels for the reactants and the products, respectively, and allow to write the collisional cross section as:

$$\sigma_{\alpha \rightarrow \alpha'}^{\text{SACM}} = \frac{\pi}{k^2 [j_1 j_2]} \sum_J [J] \frac{N_\alpha(E, J) N_{\alpha'}(E, J)}{N_{tot}(E, J)} \quad (2.75)$$

2.4.4 Validity of the methods

The CC method is the most accurate quantum approach, only based on the Born-Oppenheimer approximation, which has never ceased to prove its efficiency for treating collisional excitation between two species. However, this method becomes prohibitive in term of computational time for heavy collisional systems. The interest of the presented approximations is to save computational resources but this degrades somehow the cross sections accuracy. Judging quantitatively the precision of an approximation is not easy,

especially when experimental data are missing. The most theoretical confident way is to compare it with CC calculations which is not always achievable. Based on physical arguments, one can estimate qualitatively the relevance of an approximation.

The IOS approximation assumes that the target do not rotate during the collision. It means that the rotational structure is neglected and the collision depends parametrically on the orientations of the system. The CC equations within the IOS approximation become uncoupled, saving a lot of computational time. This method has proven to reproduce quite well CC calculations for high collisional energy (or high temperatures). However, when the collisional energy is the same order of magnitude than the space between energy levels, this assumption become non relevant and cross sections at very low energy may not be reliable. A consequence is that this approximation might be efficient for heavy systems, which means systems with a high moment of inertia and then a small rotational constant, leading to a close space between energy levels.

The SACM consists in an identical statistical distribution of the transition probability over all channels during a collision based on a long-lived intermediate complex. This requires a deep well depth. A consequence is that this approximation can be reliable for low temperatures and not anymore at high temperatures since the collision is occurring too fast and the intermediate complex is not expected to live long enough. It should be noted that this method ignores quantum effects due to the couplings between initial and final states. Then, it may not be highly applicable for extremely low temperatures ($T \leq 10\text{K}$) since the number of channels involved is small, and the statistical distribution may be not reliable to reproduce these strong quantum effects at these temperatures.

2.4.5 Scattering softwares

The most known scattering programs used to perform non-reactive collisions are MOLSCAT [79] and HIBRIDON [80]. These softwares solve the CC equations using propagator algorithms that we will introduce. In this thesis, we computed fine structure inelastic cross sections in the CC level of theory for all collisional systems studied with the HIBRIDON code. We describe below the main steps to perform a typical collisional study.

Implementation of the PES

Independently of the type of collisional interaction (referred here as a *basis type*), HIBRIDON asks the radial coefficients $v_\lambda(R)$ of the PES expansion as an input file (where λ is a general notation but include any combination of indexes according to the collisional system). One must specify coefficients for each λ index and several radial points. The

program will determine the missing ones through 3rd degree polynomial interpolation. The values of the radial coefficients are used to determine the V -matrix elements. It should be noted that a careful attention must be taken when constructing the PES involving an asymmetric top molecule in order to properly match the axis of quantization with the quantum dynamical program. Here, we adapted the PES for the $\text{H}_2\text{O}^+-\text{H}$ complex where the a inertial axis is an axis of the C_2 symmetry (details of this implementation is done in section 4.3.1).

Scattering calculations

The HIBRIDON scattering package of programs got its name through the use of hybrid propagator algorithms: the log-derivative [129] and Airy [130] propagators. First we can re-write the CC equation under a matrix form:

$$\left[\mathbf{1} \frac{d^2}{dR^2} + \mathbf{W}(R)\mathbf{F}(R) \right] = 0 \quad (2.76)$$

where $\mathbf{1}$ is the identity matrix and $\mathbf{W}(R)$ is a matrix written as:

$$\mathbf{W}(R) = \mathbf{k}^2 - \mathbf{L}^2 - 2\mu\mathbf{V}(R) \quad (2.77)$$

Here, \mathbf{k} and \mathbf{L} are diagonal matrices representing the wave vector and the orbital angular momentum. To reach numerical stability [131], it is more suitable to propagate the logarithmic derivative of the solution matrix $\mathbf{F}(R)$ rather than the solution itself

$$\mathbf{Y}(R) = \mathbf{F}'(R)\mathbf{F}(R)^{-1} \quad (2.78)$$

The advantage of the Airy propagator is its ability to increase the propagator steps for the long range. Overall, the log-derivative matrix is propagated at a large enough R so that the potential becomes negligible compared to the wave vector. Finally, the propagated matrix $\mathbf{Y}(R_{end})$ must match with the same asymptotic conditions (2.59) as $\mathbf{F}(R)$:

$$\lim_{R \rightarrow \infty} \mathbf{F}(R) = \mathbf{h}^{(2)}(R) - \mathbf{S}\mathbf{h}^{(1)}(R) \quad (2.79)$$

where \mathbf{S} is the S -matrix, and with $\mathbf{h}^{(1)}(R)$ and $\mathbf{h}^{(2)}(R)$ being diagonal matrices defined

as:

$$h_i^{(1,2)} = k_i^{-1/2} \left(j_l(x) \pm iy_l(x) \right) \quad (2.80)$$

and j_l , y_l are spherical Bessel functions [132]. Then cross sections are computed as Eq. (2.60).

Numerical parameters

A scattering calculation relies on several parameters that must be constrained to reach convergence of cross sections. The presented parameters below are independent and have been constrained for all collisional systems to reach a convergence of $\sim 1\%$ of error on inelastic cross sections per parameter, the elastic ones being out of interest for astrophysical applications and hard to converge anyway. We introduce the numerical parameters asked in input by HIBRIDON.

- **N1MAX/J2MIN/J2MAX**: These represent the basis size of the two colliders and are related to the number of rotational levels to include. For a given total energy E , one must include additional closed channels to reach convergence. These parameters must be adapted for each energy range of calculation, since the increase in energy leads to additional open levels to consider.
- **JTOT1/JTOT2**: These parameters are associated to the total angular momentum. This parameter increase also with the total energy since it regulates the number of channels involved.
- **RSTART/RENDLD/RENDAI**: RSTART is the starting point of the propagation of the wave function. This depends on the definition of the radial part of the potential. Usually for neutral reactions, the propagation starts around $3.75 - 4a_0$. However, for ionic species, the minimum of the PES can be at very small distances and propagation must start at distances lower than $3a_0$. RENDLD is the ending point of the log-derivative propagator. Then it switches to the Airy propagator, ending with the value given by the RENDAI parameter.
- **SPAC**: This is the step of the grid used for the log-derivative propagator. This parameter usually do not affect the computational cost and can be safely put as a low value.

2.5 Radiative transfer

The determination of the physical and chemical conditions in the ISM relies on astronomical observations. These are based on the exploitation of molecular spectra. Knowing the distribution of its lines in the frequency range informs on the nature of the molecule, which is most of the time known through experimental measurements prior to observations. However, the intensity of the line is directly related to the influence of the physical conditions of the medium on the molecular distribution of energy levels. A precise knowledge of the molecular energy transfer mechanisms is required to interpret observations properly. On one hand, radiative processes are defined by the absorption or emission of a photon emitted by another molecule or through the irradiation of the continuum. The molecule can also spontaneously emit radiation. On the other hand, collisions of given species with the surrounding gas can contribute to change the number of molecules in a given state. We present below general idea about the formalism used to perform radiative transfer calculations and quantities related to the evolution of the molecular population of energy levels. Most of the information has been taken from Rutten [133] and Draine [1].

2.5.1 Radiative transfer equation

The main equation describing the change in energy dE_ν of a radiation interacting with the environment is the *radiative transfer equation*. The transported energy through a surface area dA , in a time interval dt , a frequency range $d\nu$ and over a solid angle $d\Omega$ is defined by:

$$dE_\nu \equiv I_\nu dA dt d\nu d\Omega \quad (2.81)$$

with I_ν being the *specific intensity* ($\text{W}/\text{m}^2/\text{Hz}/\text{ster}$). When interacting with matter, the absorption of a specific intensity element can be defined by the monochromatic *extinction coefficient* $\alpha_\nu(s)$ (m^{-1}):

$$dI_\nu(s) \equiv -\alpha_\nu(s) I_\nu(s) ds \quad (2.82)$$

At the opposite, photons emitted within a volume dV in the propagation direction of the radiation can be defined by the monochromatic *emissivity* $j_\nu(s)$ ($\text{W}/\text{m}^3/\text{Hz}/\text{ster}$):

$$dI_\nu(s) \equiv j_\nu(s)ds \quad (2.83)$$

In the case where there is only extinction over a distance D , the specific intensity is written as:

$$I_\nu(D) = I_\nu(0)e^{-\tau_\nu(D)} \quad (2.84)$$

which defines the *opacity* (or optical thickness) of the medium:

$$d\tau_\nu(s) \equiv \alpha_\nu(s)ds \quad (2.85)$$

This represents the fraction of the absorbed radiation through the medium. It means that photons have a probability $e^{-\tau_\nu}$ to travel over an optical path. The whole process of interaction of the radiation with the medium can be illustrated as in Fig. 2.9.

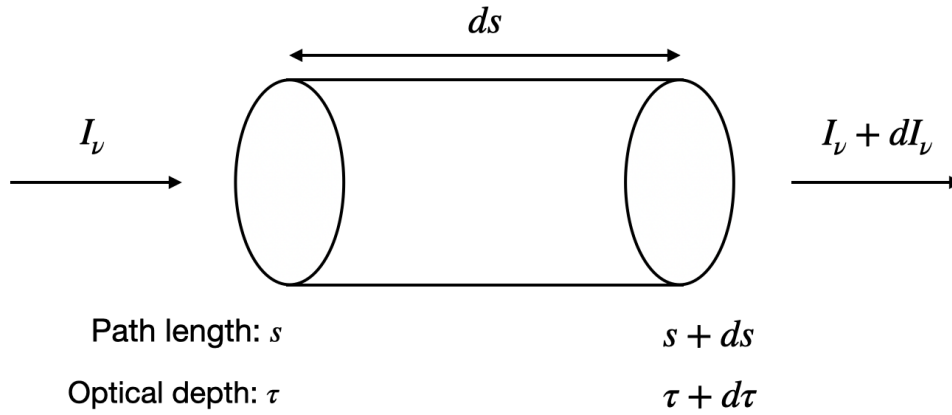


Figure 2.9 – Variation of the specific intensity I_ν along a path length element ds and opacity element $d\tau$.

Combining absorption (2.82) and emission (2.83) we obtain:

$$dI_\nu(s) = I_\nu(s + ds) - I_\nu(s) = j_\nu(s)ds - \alpha_\nu(s)I_\nu(s)ds \quad (2.86)$$

By introducing the *source function* $S_\nu \equiv j_\nu/\alpha_\nu$ and using the definition (2.85), we can rearrange the terms in Eq. (2.86) to obtain the general radiative transfer equation:

$$\frac{dI_\nu}{d\tau_\nu} = S_\nu - I_\nu \quad (2.87)$$

The general solution of Eq. (2.87) can be found by multiplying each side by e^{τ_ν} . We get:

$$e^{\tau_\nu} dI_\nu = (S_\nu - I_\nu)e^{\tau_\nu} d\tau_\nu \Rightarrow d(e^{\tau_\nu} I_\nu) = S_\nu e^{\tau_\nu} d\tau_\nu \quad (2.88)$$

Then, integrating each side gives:

$$I_\nu(\tau_\nu) = I_\nu(0)e^{-\tau_\nu} + \int_0^{\tau_\nu} S_\nu(x)e^{x-\tau_\nu} dx \quad (2.89)$$

where dx is an element of integration over the optical path. Eq. (2.89) is not easily solvable because of the spatial dependence of the function source to the structure of the medium and different opacity with the frequency. The simplest approximation is to assume a homogeneous medium, in which S_ν does not vary with space. For a propagation over a distance D , Eq. (2.89) simplifies to:

$$I_\nu(D) = I_\nu(0)e^{-\tau_\nu(D)} + S_\nu(1 - e^{-\tau_\nu(D)}) \quad (2.90)$$

The specific intensity is then described by the contribution of the continuum $I_\nu(0)$ and the source function S_ν . From Eq. (2.90), two extreme cases can be highlighted. The opacity can be used as an indicator of the thickness of a medium, being optically thick if $\tau_\nu \gg 1$ (no photon can escape from the medium):

$$I_\nu(D) \sim S_\nu \quad (2.91)$$

and optically thin if $\tau_\nu \ll 1$ (a photon can escape and be detected):

$$I_\nu(D) \sim I_\nu(0) + (S_\nu - I_\nu(0))\tau_\nu(D) \quad (2.92)$$

These cases can be summarized in Fig. 2.10. When $\tau_\nu \gg 1$, no photon can escape from the object and intensity is only given by the surface temperature of the gas which

is not exploitable from the observer point of view. When the object is optically thin, we can observe lines in emission or in absorption whether the continuum is weaker than the source function $I_\nu(0) < S_\nu$ or stronger than the source function $I_\nu(0) > S_\nu$. If the object is optically thick at the frequency of the line, the absorbed or emitted line can saturate to $I_\nu \sim S_\nu$.

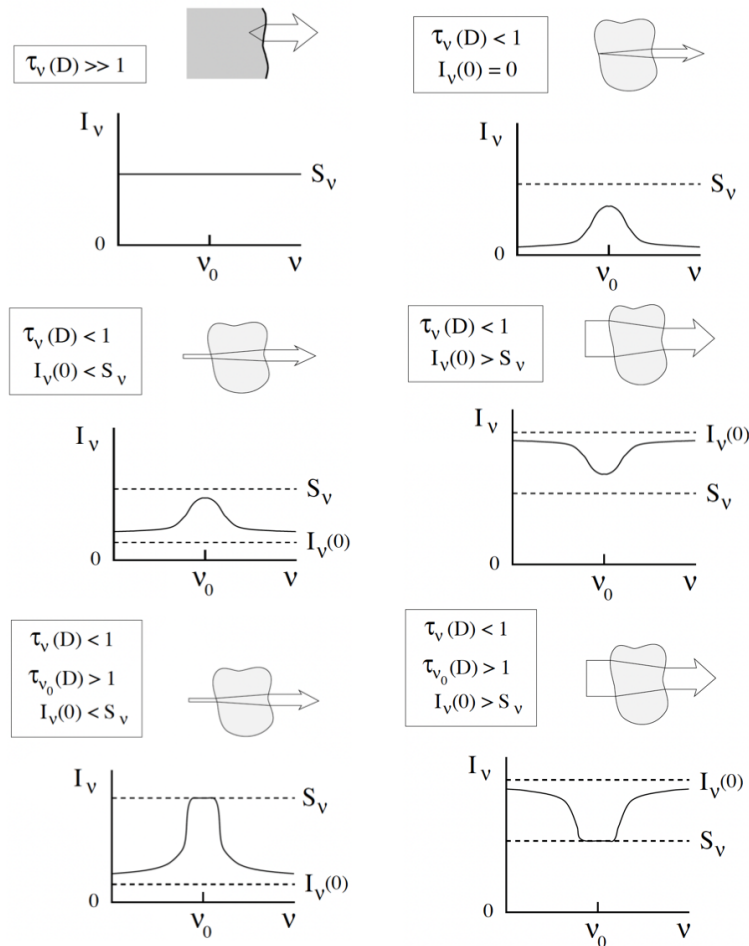


Figure 2.10 – Different cases of spectral intensities for a homogeneous medium. This figure is taken from Rutten [133].

2.5.2 Statistical equilibrium equations

The distribution of the number n_i of energy levels of a molecule by volumic units is driven by its interactions with radiation fields and by collisional processes with other partners. The balance of these interactions is summarized as the *statistical equilibrium equations*. This equilibrium implies that level populations are independent of time:

$$\frac{dn_i}{dt} = \sum_{j \neq i} n_j (R_{ji} + C_{ji}) - \sum_{j \neq i} n_i (R_{ij} + C_{ij}) = 0 \quad (2.93)$$

where R_{ij} and C_{ij} are the radiative and collisional rate, respectively. The radiative rate is determined by the balance between emission and absorption of a photon:

$$R_{ij} = A_{ij} + B_{ij} \bar{J}_{\nu_0}^x \quad \text{for } E_i > E_j \quad (2.94)$$

where $\bar{J}_{\nu_0}^x$ is the profile-weighted average of the radiation field. The Einstein coefficient A_{ij} (s^{-1}) is the transition probability for spontaneous de-excitation from a state i to a state j per second per particle. This quantity relies on intrinsic properties of the molecules, as radiative transitions occur through coupling of the electric dipole moment $\hat{\mu}$ with states $\mu_{ij}^2 = |\langle j | \hat{\mu} | i \rangle|^2$:

$$A_{ij} = \frac{64\pi^4}{3hc^3} \nu_{ij}^3 \mu_{ij}^2 \quad (2.95)$$

The Einstein coefficient B_{ij} is the number of induced radiative de-excitations from a state i to a state j per second per particle, and $C_{ij} \equiv n_{col} k_{ij}$ is the collision rate from a state i to a state j per second and depends on the density of the collider n_{col} and the rate coefficient k_{ij} defined by Eq. (2.62). Einstein coefficients can be coupled by the *Einstein relations*:

$$\frac{B_{ji}}{B_{ij}} = \frac{g_i}{g_j}, \quad \frac{A_{ij}}{B_{ij}} = \frac{2h\nu^3}{c^2} \quad (2.96)$$

where g is the degeneracy of a given energy level.

We can rewrite the extinction coefficient α_ν and the emissivity j_ν in terms of the Einstein coefficients:

$$\begin{aligned} \alpha_\nu &= \frac{h\nu}{4\pi} (n_j B_{ji} - n_i B_{ij}) \\ j_\nu &= \frac{h\nu}{4\pi} n_i A_{ij} \end{aligned} \quad (2.97)$$

We can report coefficients (2.97) into the source function, and using the relations (2.96):

$$\begin{aligned}
 S_\nu &= \frac{n_i A_{ij}}{n_j B_{ji} - n_i B_{ij}} = \frac{\frac{A_{ij}}{B_{ij}}}{\frac{n_j B_{ji}}{n_i B_{ij}} - 1} \\
 &= \frac{2h\nu^3}{c^2} \frac{1}{\frac{n_j g_i}{n_i g_j} - 1}
 \end{aligned} \tag{2.98}$$

Eq. (2.98) is the general expression for the line source function. What matters is how n_i and n_j are computed.

2.5.3 Line profile

A molecular line is not a single peak at the frequency rest of the transition and several processes participate in its broadening. The mathematical function characterizing such broadening is called a *line profile*. First, the line possess an intrinsic profile represented by a Lorentz function:

$$\phi_\nu^{intr.} = \frac{4\gamma_{ij}}{16\pi^2(\nu - \nu_{ij})^2 + \gamma_{ij}^2} \tag{2.99}$$

where $\nu_{ij} \equiv (E_i - E_j)/h$. This is called intrinsic because it does not depend on the thermodynamic properties of the object but only on the spectroscopic aspects of the molecule. Especially, this broadening is due to the Heisenberg's indeterminacy principle related to the lifetime of the energy levels i and j compared to the transitions of the others. The quantity γ_{ij} and the intrinsic full width at half maximum (FWHM) are defined as:

$$\gamma_{ij} \equiv \gamma_{ji} = \sum_{k<i} A_{ik} + \sum_{k<j} A_{jk}; \quad (\Delta\nu)_{FWHM}^{intr.} = \frac{\gamma_{ij}}{2\pi} \tag{2.100}$$

Another type of perturbation is the *Doppler broadening* related to the thermal motion of the molecules in the object. These can be described by their velocity distribution approximated by a gaussian function:

$$\chi_\nu^{therm} = \frac{1}{\sqrt{2\pi}} \frac{1}{\sigma_v} e^{-(\nu-\nu_0)^2/(2\sigma_v^2)}; \quad (\Delta\nu)_{FWHM}^{therm} = \sigma_v \sqrt{8\ln(2)} \tag{2.101}$$

and $\sigma_v \equiv \sqrt{k_B T/m}$ is a one dimensional velocity dispersion with m is the mass of the

molecule. For a precise spectroscopic study of transition lines, the natural and thermal broadening must be convolved to form a *Voigt line profile*. Also, *pressure broadening* (or collisional broadening) due to collisions between other particles in the medium can participate in the alteration of the line profile. Such effect is also described by a lorentzian, however rather negligible because of the low density conditions encountered in the ISM.

2.5.4 Approximations

The line intensity is described by fluctuations of the emitted photons by interactions with radiative fields, depending themselves on the molecular composition of the object and its spatial distribution. Then, the radiative transfer and statistical equilibrium equations (2.87) and (2.93) must be solved simultaneously. Several approaches are proposed to simplify the treatment of these equations.

Local Thermodynamic Equilibrium (LTE)

The simplest approach to consider is to assume that the object is in LTE. This means that the thermodynamic properties of the gas of the object (density, temperature, pressure, chemical composition) reached locally in their equilibrium value. In this approach, collisions between components of the gas occur frequently enough compared to radiative processes to follow a Maxwell-Boltzmann distribution of energy and population:

$$\frac{C_{ji}}{C_{ij}} = \frac{n_i}{n_j} = \frac{g_i}{g_j} e^{-(E_i - E_j)/(k_B T_{kin})} \quad (2.102)$$

where k_B is the Boltzmann constant. The thermal distribution (2.102) gives the population ratio of a transition at a given *kinetic temperature* T_{kin} , describing the random thermal motion of the degrees of freedom of molecules with an energy of $k_B T/2$ per degree of freedom.

Using (2.102), it is interesting to see that the source function (2.98) becomes similar to a black-body described by a Planck function:

$$\begin{aligned} [S_\nu]_{\text{LTE}} &= \frac{2h\nu^3}{c^2} \frac{1}{\left[\frac{n_j g_i}{n_i g_j} \right]_{\text{LTE}} - 1} \\ &= \frac{2h\nu^3}{c^2} \frac{1}{e^{h\nu/(k_B T_{kin})} - 1} \equiv B_\nu(T_{kin}) \end{aligned} \quad (2.103)$$

From the Planck function, we can define the *brightness temperature* T_B which is the

temperature of a black-body for the same measured line intensity. In the LTE assumption and for a homogeneous object, we can rewrite Eq. (2.90) in terms of temperatures:

$$B_\nu(T_B) = B_\nu(T_{bg})e^{-\tau_\nu} + B_\nu(T_{kin})(1 - e^{-\tau_\nu}) \quad (2.104)$$

where T_{bg} is the *background temperature*.

Rayleigh-Jeans approximation

The *Rayleigh-Jeans approximation* states that for a specific frequency regime $h\nu \ll k_B T$, we can expand $e^{h\nu/(k_B T)} \sim 1 + h\nu/(k_B T)$ and the Planck function can be simplified as:

$$B_\nu(T_B) \equiv I_\nu = \frac{2h\nu^3}{c^2} \frac{1}{e^{h\nu/(k_B T_B)} - 1} \sim \frac{2\nu^2}{c^2} k_B T_B \quad (2.105)$$

Then the brightness temperature can be re-written within the Rayleigh-Jeans approximation:

$$T_B = \frac{c^2}{2k_B \nu^2} I_\nu \quad (2.106)$$

This approximation is useful in the way that the brightness temperature is directly proportional to the specific intensity. It depends also on the temperature and is valid for $\nu \ll 200$ GHz in cold environments. We can rewrite Eq. (2.104) as:

$$T_B = T_{bg}e^{-\tau_\nu} + T_{kin}(1 - e^{-\tau_\nu}) \quad (2.107)$$

Escape probability

There are often situations where non-LTE effects appear in interstellar objects. One way to uncouple radiative transfer equation from the statistical equilibrium one through non-LTE calculation is to consider the *escape probability* approach, first introduced by Sobolev [134] in 1960. The principle is to introduce a probability β that a photon escapes from the object at a given position toward the observer. Such probability is defined for different types of geometry of the object:

$$\begin{aligned}
\beta &= \frac{(1 - e^{-\tau})}{\tau} \quad \text{for an expanding sphere} \\
\beta &= \frac{1 - e^{-3\tau}}{3\tau} \quad \text{for an homogeneous slab} \\
\beta &= \frac{1.5}{\tau} \left[1 - \frac{2}{\tau^2} + \left(\frac{2}{\tau} + \frac{2}{\tau^2} \right) e^{-\tau} \right] \quad \text{for a uniform sphere} \quad (2.108)
\end{aligned}$$

The escape probability applied for an expanded sphere is widely used in resolution methods of radiative transfer as the *Large Velocity Gradient* (LVG) method. The principle is to state that the velocity gradient of the medium is much larger than the thermal broadening of the spectral lines. This method assumes that the density of the object is uniform and that the gradient dv/dr is independent of the distance r for an expanding sphere.

2.5.5 Quantities of interest

Critical density

The critical density $n_{crit}^u(T)$ represents the gas density from which an upper state u can be (de)populated equally by collisions or by radiations, $\sum_{i<u} A_{ui} = \sum_{u\neq i} C_{ui}(T)$. This can be considered as an indicator of the departure from the LTE regime. For $n_{gas} \ll n_{crit}^u$, collisional processes are less efficient than radiative ones and the upper state is *sub-thermalized*. For $n_{gas} \gg n_{crit}^u$, we consider that the density of the collider is large enough for collisions to be dominant and the LTE is reached for this upper state. The critical density can be computed as follow for a multilevel system:

$$n_{crit}^u(T) = \frac{\sum_{i<u} A_{ui}}{\sum_{u\neq i} k_{ui}(T)} \quad (2.109)$$

The critical density strongly depends on the intrinsic properties of the molecule since the Einstein coefficient $A_{ij} \propto \nu^3 \mu^2$. On one hand, the dependence on μ^2 involves selection rules due to coupling of the angular momenta to the line strength. On the other hand, the dependence in ν^3 implies a sensitivity to the heaviness of the molecule. The value of the frequency is directly related to the moment of inertia of the molecule since it is inversely proportional to the rotational constant of the molecule and then how the energy levels are structured. Molecules with a low moment of inertia will show non-LTE effects in very high density objects ($n_{crit} \sim 10^6 - 10^8 \text{ cm}^{-3}$), whereas radiative and collisional processes of heavy molecules can compete at lower densities ($n_{crit} \sim 10^2 - 10^3 \text{ cm}^{-3}$).

It should be noted that rate coefficients can have a large impact on the values of the critical density since no strict selection rule govern collisional processes. All transitions participate to the (de)population of an upper level (an illustration of such example can be found in Fig. 2.11). Moreover, the dependence of rate coefficients to the temperature can change the critical density by orders of magnitude, especially when incorporating homonuclear molecules like H₂, showing a strong dependence to the *ortho-to-para*-H₂ with the temperature.

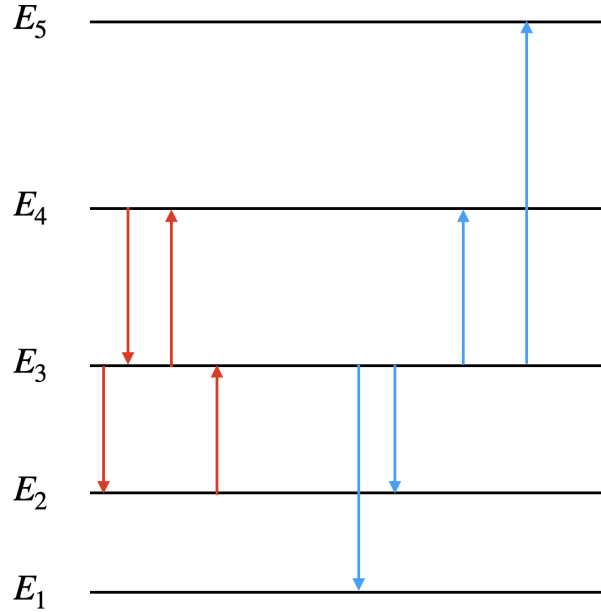


Figure 2.11 – Illustration of population and de-population of the 3rd level by radiative (red) and collisional (blue) processes for a system with five energy levels.

Excitation temperature

Eq. (2.102) supposes that all transitions are described by the same kinetic temperature T_{kin} in LTE. In a general case, each transition is represented by the *excitation temperature* T_{ex} (and we can replace $T_{kin} \rightarrow T_{ex}$ in Eq. (2.102)). Such quantity do not have a physical meaning but one can use it as an indicator of departure from LTE for a given transition. Restricting Eq. (2.93) for two levels $i > j$ for simplicity we have:

$$n_j(B_{ji}\bar{J} + C_{ji}) = n_i(A_{ij} + B_{ij}\bar{J} + C_{ij}) \quad (2.110)$$

with $\bar{J} \equiv \frac{8\pi h\nu^3}{c^3} \frac{1}{e^{h\nu/(k_B T_{bg})} - 1}$. By neglecting the background temperature ($h\nu \gg k_B T_{bg}$), we have $\bar{J} \sim 0$ and Eq. (2.110) can be simplified. We can write:

$$\frac{n_i g_j}{n_j g_i} = e^{-h\nu/(k_B T_{ex})} = e^{-h\nu/(k_B T_{kin})} \frac{1}{\frac{A_{ij}}{C_{ij}} + 1} \quad (2.111)$$

We can isolate T_{ex} by rearranging the terms to have finally:

$$T_{ex} = \frac{h\nu/k_B}{h\nu/(k_B T_{kin}) + \ln(1 + \frac{A_{ij}}{C_{ij}})} \quad (2.112)$$

We can see from Eq. (2.112) that for $C_{ij} \gg A_{ij}$, we have $T_{ex} \equiv T_{kin}$ and the transition is in LTE. If $T_{ex} < T_{kin}$, we say that a transition is *sub-thermalized*. On the contrary, if $T_{ex} > T_{kin}$, the transition is *supra-thermalized*. These regimes are specific for non-LTE effects.

Column density

The column density is a fundamental quantity representing the number of molecules along a line-of-sight toward the object. The expression for a given level is:

$$N_i = \int n_i ds \quad (2.113)$$

and we can express it as a function of the total column density N_{tot} :

$$\frac{N_i}{N_{tot}} = \frac{g_i}{Q(T_{ex})} e^{-E_i/(k_B T_{ex})}; \quad Q(T_{ex}) = \sum_i g_i e^{-E_i/(k_B T_{ex})} \quad (2.114)$$

with $Q(T_{ex})$ being the *partition function* which is the sum of all the micro-states. Within the optically thin assumption, we can express the column density as a function of the opacity. First, we can use Eqs. (2.85) and (2.97) to rewrite the opacity:

$$\begin{aligned} \tau_\nu &= \int \alpha_\nu(s) ds = \frac{h\nu}{4\pi} \int \left(n_j(s) B_{ji} - n_i(s) B_{ij} \right) ds = \frac{h\nu}{4\pi} \int n_i(s) B_{ij} \left(\frac{n_j(s) B_{ji}}{n_i(s) B_{ij}} - 1 \right) ds \\ &\stackrel{(2.96)}{=} \frac{h\nu}{4\pi} \int n_i(s) B_{ij} \left(\frac{n_j(s) g_i}{n_i(s) g_j} - 1 \right) ds \stackrel{(2.102)}{=} \frac{h\nu}{4\pi} B_{ij} \left(e^{-h\nu/(k_B T_{ex})} - 1 \right) \int n_i(s) ds \\ &\stackrel{(2.113)}{=} \frac{h\nu}{4\pi} B_{ij} \left(e^{-h\nu/(k_B T_{ex})} - 1 \right) N_i \end{aligned} \quad (2.115)$$

Then, by using relations (2.96) and (2.114), we can rearrange the terms to express

N_{tot} :

$$N_{tot} = \frac{8\pi\nu^2}{c^3} \frac{Q(T_{ex})}{g_i A_{ij}} \frac{e^{E_i/(k_B T_{ex})}}{e^{h\nu/(k_B T_{ex})} - 1} \tau_\nu \quad (2.116)$$

Then, information coming from one transition enable to derive the total column density (2.116) of the detected molecule.

The quantities introduced here will be used in section 3.4 to assess the reliability of the computed collisional data during this thesis.

COLLISIONAL EXCITATION IN NON-REACTIVE SYSTEMS

In this chapter, we present the results of the collisional excitation studies for the non-reactive systems explored in this thesis. Section 3.1 provides an overview of the radicals investigated in this work. Section 3.2 introduces the theoretical framework for collisional excitation including the treatment of fine structure, followed by the corresponding results. Section 3.3 focuses on the hyperfine structure treatment of these systems, emphasizing the applicability of the methods and the outcomes. Finally, Section 3.4 discusses the application of the newly computed collisional data in radiative transfer modeling.

3.1 Molecules of interest

3.1.1 Objectives of this work

Radical molecules are chemical species possessing one or more unpaired electron. These molecules are highly unstable, allowing possibility to react easily with other colliders. However, radicals are widely detected in the ISM [47] showing that they are maintained long enough before being destroyed but also they are subject to collisional excitation processes. Their unpaired electrons lead to the presence of a fine structure, complexifying its energetic structure and the description of collisional excitation mechanisms. Such description is enhanced by the possible presence of nuclear spins, also in the case of isotopologues, leading to a hyperfine structure in their energy levels. Such spectroscopic properties involve methodological and numerical challenges to provide accurate collisional data for these molecules. Especially when colliding with molecular hydrogen, the internal structure of the projectile has an impact on the collisional excitation of neutral radicals and it is important to take into account its structure in the scattering calculations. We will face these challenges using the C_2H and NH molecules as test cases. These are not only good candidates for testing (hyper)fine excitation by molecular hydrogen but also present high astrophysical interests. The objectives of this work are the following:

1. To investigate the fine structure excitation of C_2H and NH and their isotopologues

induced by collisions with H₂.

2. To explore the impact of approximations for quantifying the hyperfine excitation for these collisional systems when the most precise methods are not applicable.
3. To provide new state-to-state rate coefficients for the C₂H–H₂, C₂D–H₂, ¹³CCH–H₂, C¹³CH–H₂, NH–H₂ and ND–H₂ collisional systems.

3.1.2 The C₂H molecule

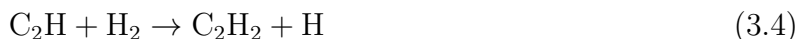
The ethynyl radical C₂H is one of the most abundant hydrocarbon in the ISM. It was one of the first radicals to be detected in space in the 1970s [135]. Then, many rotational lines have been widely detected over the past decades in cold environments [136]–[141], protoplanetary disks [142] or photodissociation regions (PDRs) [143]–[146]. C₂H is an important intermediate in the chemistry of carbon and in the formation pathway of long carbon-chains molecules [13]. Its formation mostly comes from electron recombination reactions [13], [137]:



or by neutral-neutral reaction [147]:



The destruction of C₂H by H₂ proceeds as:



which is an exothermic reaction with an activation barrier of ~ 1600 K [148], [149]. Then, we will assume it to be non-reactive for low temperature applications. Recent work on similar type of reactions have shown that inelastic collisions are dominant at low temperatures and reactive processes can be safely neglected [88], justifying our choice. The first (hyper)fine resolved rate coefficients for the C₂H radical was provided by Spielfiedel *et al.* [150] where collisions with He as a proxy for H₂ were considered. Later, Najjar *et al.* [151] determined fine structure resolved rate coefficients for C₂H–*para*-H₂ collisions up to 100 K, excluding the rotational structure of H₂. Based on the PES computed by these

authors, Dumouchel *et al.* [152] were able to extend calculations to take into account the hyperfine structure of C₂H, up to 80 K. More recently, Dagdigian [153] included the internal structure of H₂ to provide hyperfine resolved rate coefficients for C₂H in collision with both *ortho*- and *para*-H₂, up to 300 K, based on a new PES computed by Dagdigian [154].

3.1.3 The NH molecule

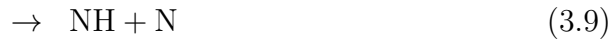
The NH radical belongs to the family of interstellar hydrides, possessing one heavy atom and one hydrogen and is an intermediate to the formation of important species such as ammonia NH₃ [32]. Nitrogen-bearing molecules are useful tracers of the physical conditions as for example the inversion lines of ammonia tracing the temperature of dense ISM [155]. Nitrogen is also present in many types of molecules, including COMs that are observed in star-forming regions [156]. Then a precise determination of the abundance of these molecules is important to understand the nitrogen chemistry and its reservoirs, still a topic of ongoing exploration [157].

NH is observationally challenging to detect, due to its low moment of inertia, leading to a large rotational constant and *a fortiori* high frequency transitions from the sub-millimeter to far-infrared range (~ 1 THz). This makes rotational transitions hardly detectable from ground-based instruments. Then, its first detections have been done in the UV range in absorption toward ζ Per and HD 27778 diffuse clouds [158]. Later development of instruments permitted infrared detections toward molecular clouds [159], [160], protostars [161], [162], star-forming regions [163], nebulae [164] and PDRs [165]. However, from the first detection of NH to now, large discrepancies between abundances from spectral interpretations and from chemical modeling were observed [166].

The NH molecule can be mainly formed in cold molecular clouds through the following electron recombination reactions [167]:



Dislaire *et al.* [168] suggested an additional path to the formation of NH by the electron recombination reaction of N₂H⁺ to explain the observed abundances:



This process has been corroborated through ion storage ring measurements [169], showing a branching ratio of 93% for products (3.8) and 7% for products (3.9). Recently, Goicoechea & Roncero [165] investigated the unfavorable reaction



by computing reactive rate coefficients through quantum wave packet and quasi-classical methods, showing enhancement of the column density of NH by a factor ~ 25 in diffuse clouds when considering the reaction of N with highly vibrationally excited H_2 .

Finally, the $\text{NH} + \text{H}_2 \rightarrow \text{NH}_2 + \text{H}$ abstraction reaction is highly endothermic by ~ 5700 K [170], so we can safely assume that inelastic collisions will be dominant in astrophysical media.

Up to now, a few studies about collisional excitation of NH have been done using He as a projectile. Toboła *et al.* [171] computed fine structure resolved rate coefficients up to 350 K based on the PES computed by Cybulski *et al.* [172]. These calculations were extended by Dumouchel *et al.* [173] to provide hyperfine resolved rate coefficients up to 150 K. More recently, fine structure rate coefficients based on a 3D PES for the NH–He collisional system including vibrational motion [174] has been used for studying differential and integral cross section measurements with crossed molecular beam apparatus combined to Zeeman decelerator [45].

3.1.4 The interest for isotopologues

Usually, the abundance of a molecule necessitates the determination of its column density. As this quantity scales linearly to the opacity for a given transition (see Eq. (2.116)), a molecule which is found to be highly abundant can have optically thick lines. Then, photons cannot escape from the medium and the intensity of the line is given by the temperature of the surface of the object, and the column density cannot be easily derived. Then, attention has been pushed to infer physical conditions of the ISM through the observation of isotopologues, being less abundant than the parent molecule, and then less affected by opacity effects. On one hand, they can be used to determine the abundance

of parent species [137]. On the other hand, they can be used as tracers of molecular formation of isotopic species.

For example, it has been observed that the abundance ratio between a deuterated molecule and the hydrogenated one can be significantly different from the elemental distribution $[D]/[H] \sim 2 \times 10^{-5}$ [175] in a given medium, showing high deuteration degree in the ISM [176]–[178]. This deuteration fractionation is a useful tool to trace the evolution stages of star-forming regions [139]. In this sense, the quantification of collisional excitation of C_2D and ND by H_2 is interesting to study the origin of the chemical diversity.

Similar attention is paid to ^{13}C isotopologues species. It is common to find deviations between the galactic elemental ratio $[^{12}C]/[^{13}C] \sim 60$ [179] and those derived by modeling for a given source. Also, abundance anomalies between the two ^{13}C carbon-bearing isotopologues ^{13}CCH and $C^{13}CH$ have been reported in many astrophysical environments varying as $[C^{13}CH]/[^{13}CCH] \sim 1.2$ – 2.2 [137], [140], [145], [180]–[182]. This may be due to different excitation mechanisms between the two species that can involve different line intensities, or by non-equivalent pathway formations [183]. This why it is interesting to provide accurate collisional data for these isotopologues in collision with molecular hydrogen to explore the impact of collisional processes to this abundance anomaly.

3.1.5 Rotational spectroscopy

C_2H and its isotopologues are linear molecules in their $^2\Sigma^+$ ground electronic state, and $^3\Sigma^-$ ground states for NH and ND . All systems being open-shell molecules, they possess nonzero electronic spin S , and its coupling to the rotational quantum number N is described in the Hund’s case (b) as

$$j_1 = N + S$$

This involves the emergence of a fine structure with a molecular hamiltonian described by formulae mentioned in section 2.3.2. In the case of C_2H and isotopologues, $S = 1/2$ and the fine structure hamiltonian is only characterized by a spin-rotation term given by Eq. (2.43). Each rotational level is splitted in two fine structure components.

In the case of NH and ND , $S = 1$ and an additional spin-spin term is added to the effective hamiltonian (see Eq. (2.44)). Then, each rotational level is splitted into three fine structure components and the wave function can be written in the intermediate coupling scheme [116]:

$$\begin{aligned}
|F_1 j_1 m_1\rangle &= \cos(\theta)|N = j_1 - S, j_1 m_1\rangle + \sin(\theta)|N = j_1 + S, j_1 m_1\rangle \\
|F_2 j_1 m_1\rangle &= |N = j_1, j_1 m_1\rangle \\
|F_3 j_1 m_1\rangle &= -\sin(\theta)|N = j_1 - S, j_1 m_1\rangle + \cos(\theta)|N = j_1 + S, j_1 m_1\rangle
\end{aligned}
\tag{3.11}$$

which can be compacted to the following form:

$$|F_i j_1 m_1\rangle = \sum_{N=j_1-S}^{N=j_1+S} c_{NF_i}^{j_1} |NS j_1 m_1\rangle
\tag{3.12}$$

with θ is a mixing angle coming from the diagonalization of the molecular hamiltonian (2.48). We will label energy levels by N_{j_1} used for a pure Hund's case (b) ($\theta \rightarrow 0$) with the simplification

$$\begin{aligned}
F_1 &\rightarrow j_1 = N + S \\
F_2 &\rightarrow j_1 = N \\
F_3 &\rightarrow j_1 = N - S
\end{aligned}
\tag{3.13}$$

where only the notation for F_1 and F_3 labels in (3.13) will stand for the energy levels of $^2\Sigma$ molecules. We present the first 25 fine structure energy levels of C_2H , C_2D , NH and ND in Tables 3.1 and 3.2, computed using the experimental spectroscopic parameters given in Tables 3.3 and 3.4.

These molecules possess also one or more nonzero nuclear spins due to the composition of their nucleus. For C_2H and C_2D , the presence of the nuclear spin of the hydrogen atom $I_1(H) = 1/2$ or the deuterium $I_1(D) = 1$ that will couple to the rotation and the electronic spin through interactions described in section 2.3.3, giving the following scheme

$$F = j_1 + I_1$$

leading to a splitting of each fine structure level into two and three hyperfine energy levels, respectively, that are labeled as $N_{j_1 F}$.

In the case of ^{13}CCH , $C^{13}CH$, NH and ND , the energetic structure is even more complicated due to the addition of the nuclear spin from the isotopic carbon $I_2(^{13}C) = 1/2$ or the nitrogen $I_2(N) = 1$. In the case of two nuclear spins, the coupling to the rotation will take the following scheme

Level	N	j_1	E (cm ⁻¹)	
			C ₂ H	C ₂ D
1	0	0.5	0.000	0.000
2	1	1.5	2.913	2.405
3	1	0.5	2.916	2.408
4	2	2.5	8.739	7.217
5	2	1.5	8.744	7.221
6	3	3.5	17.479	14.434
7	3	2.5	17.486	14.441
8	4	4.5	29.132	24.058
9	4	3.5	29.142	24.067
10	5	5.5	43.699	36.088
11	5	4.5	43.711	36.099
12	6	6.5	61.180	50.525
13	6	5.5	61.194	50.537
14	7	7.5	81.575	67.367
15	7	6.5	81.591	67.381
16	8	8.5	104.883	86.616
17	8	7.5	104.901	86.632
18	9	9.5	131.105	108.271
19	9	8.5	131.125	108.288
20	10	10.5	160.240	132.332
21	10	9.5	160.262	132.351
22	11	11.5	192.289	158.799
23	11	10.5	192.314	158.820
24	12	12.5	227.252	187.672
25	12	11.5	227.278	187.696

Table 3.1 – The first 25 fine structure energy levels of C₂H and C₂D.

$$F_1 = j_1 + I_1; \quad F = F_1 + I_2$$

Then, each hyperfine level will be labeled as $N_{j_1 F_1 F}$. Spectroscopic parameters for the structure of the molecules of interest are summarized in Tables 3.3 and 3.4.

We can see from spectroscopic constants in Tables 3.3 and 3.4 that the spacing between fine structure energy levels is about 10–100 times smaller compared to rotational levels for the first quantum numbers and by a factor of 1000–10 000 for hyperfine energy levels.

Level	N	j_1	E (cm ⁻¹)	
			NH	ND
1	0	1	0.0000	0.0000
2	1	0	31.5706	16.4114
3	1	2	32.5046	17.4163
4	1	1	33.3556	18.2195
5	2	1	97.5646	52.1941
6	2	3	97.7164	52.4632
7	2	2	98.6736	53.3458
8	3	4	195.5071	105.0954
9	3	2	195.6137	105.0304
10	3	3	196.5477	106.0353
11	4	5	325.7409	175.3010
12	4	3	326.0268	175.3625
13	4	4	326.8546	176.2879
14	5	6	488.2485	263.0751
15	5	4	488.6854	263.2354
16	5	5	489.4297	264.1037
17	6	7	682.8220	368.4156
18	6	5	683.3961	368.6614
19	6	6	684.0674	369.4826
20	7	8	909.2134	491.3213
21	7	6	909.9170	491.6451
22	7	7	910.5208	492.4247
23	8	9	1167.1341	631.7917
24	8	7	1167.9624	632.1888
25	8	8	1168.5020	632.9299

Table 3.2 – The first 25 fine structure energy levels of NH and ND.

3.2 Fine structure excitation of $^{2S+1}\Sigma$ molecules by $^1\Sigma$ molecules

3.2.1 Close-Coupling approach

The representation of a molecule in a $^{2S+1}\Sigma$ electronic state can be done in the Hund's case (b). The coupling of the electronic spin S to the rotational quantum number N gives the coupling scheme:

$$\hat{j}_1 = \hat{N} + \hat{S}$$

The set of angular functions describing the system in these scheme is given by:

Parameters (MHz)	C ₂ H [184]	C ₂ D [185]	¹³ CCH[186]	C ¹³ CH[186]
B_0	43674.542(6)	36036.035(14)	42077.462(1)	42631.383(1)
D_0	0.1076(8)	0.068(7)	0.09813(4)	0.10157(6)
γ_0	-62.647(4)	-55.84(3)	-60.080(6)	-61.073(8)
$b_F(\text{H})$	40.54(20)		44.42(3)	44.75(4)
$c(\text{H})$	12.26(26)		12.17(5)	12.64(5)
$b_F(\text{D})$		6.35(7)		
$c(\text{D})$		1.59(26)		
eQq(D)		0.21(9)		
$b_F(^{13}\text{C})$			900.7(6)	161.63(10)
$c(^{13}\text{C})$			142.87(3)	64.07(5)

Table 3.3 – Spectroscopic parameters for C₂H and its isotopologues. Parenthesis represent errors of last significant digits.

Parameters (MHz)	NH [187]	ND [188]
B_0	489959.0768(40)	263265.4735(45)
D_0	51.05111(33)	14.62876(74)
γ_0	-1644.4860(72)	-883.4853(70)
λ_0	27577.848(11)	27545.194(12)
$b_F(\text{H})$	-66.131(15)	
$c(\text{H})$	90.291(28)	
$b_F(\text{D})$		-10.0724(82)
$c(\text{D})$		13.986(37)
eQq(D)		0.295(47)
$b_F(\text{N})$	18.830(10)	18.9172(64)
$c(\text{N})$	-67.9224(96)	-67.873(23)
eQq(N)	-2.883(62)	-3.210(17)

Table 3.4 – Spectroscopic parameters for NH and ND. Parenthesis represent errors of last significant digits.

$$|NSj_1\rangle = \sum_{m_N m_S} C_{m_N m_S m_1}^{NSj_1} |Nm_N\rangle |Sm_S\rangle \quad (3.14)$$

where $C_{m_N m_S m_1}^{NSj_1}$ is a Clebsch-Gordan coefficient defined by Eq. (2.52), and m_N, m_S and m_1 are the projections of the N, S and j_1 quantum numbers. The projectile is characterized by its rotational quantum number j_2 and arise a new coupling scheme:

$$\hat{j}_{12} = \hat{j}_1 + \hat{j}_2; \quad \hat{J} = \hat{j}_{12} + \hat{L}$$

with J and L being the total angular momentum and the orbital angular momentum, respectively. The set of angular functions describing the collisional system is:

$$\begin{aligned}
 |\alpha j_2 j_{12}\rangle &= \sum_{m_1 m_2} C_{m_1 m_2 m_{12}}^{j_1 j_2 j_{12}} |NSj_1\rangle |j_2 m_2\rangle \\
 |\alpha j_2 j_{12} L J M\rangle &= \sum_{m_{12} m_L} C_{m_{12} m_L M}^{j_{12} L J} |\alpha j_2 j_{12}\rangle |L m_L\rangle
 \end{aligned} \tag{3.15}$$

Here (m) are the projections of their corresponding quantum numbers in the SF frame, and $\alpha \equiv NSj_1$. We can now define the total wave function in the same manner as in Eq. (2.54):

$$\Psi_{\alpha j_2 j_{12} L}^J(\mathbf{Q}) = \sum_{\alpha' j_2' j_{12}' L'} \frac{F_{\alpha j_2 j_{12} L, \alpha' j_2' j_{12}' L'}^J(R)}{R} |\alpha' j_2' j_{12}' L' J M\rangle \tag{3.16}$$

where $\mathbf{Q} \equiv (R, \theta_1, \theta_2, \phi)$ the coordinates of the collisional system, that will be detailed in section 3.2.2. Similarly to Eq. (2.57), we can write the CC equations for describing collisions between $^{2S+1}\Sigma$ molecules with $^1\Sigma$ molecules as:

$$\begin{aligned}
 &\left(\frac{\partial^2}{\partial R^2} + k_{\alpha''}^2 - \frac{L''(L'' + 1)}{R^2} \right) F_{\alpha'' j_2'' j_{12}'' L'', \alpha j_2 j_{12} L}^J(R) = \\
 &2\mu \sum_{\alpha' j_2' j_{12}' L'} \langle \alpha'' j_2'' j_{12}'' L'' J M | \hat{V} | \alpha' j_2' j_{12}' L' J M \rangle F_{\alpha' j_2' j_{12}' L', \alpha j_2 j_{12} L}^J(R)
 \end{aligned} \tag{3.17}$$

with $k_{\alpha''}^2 = 2\mu(E_{\text{tot}} - E_{Nj_1} - E_{j_2})$. As mentioned in section 2.3.2, Hund's cases are idealized couplings of the angular momenta and some of open-shell species like $^3\Sigma$ molecules must be described by an intermediate coupling, as given by Eq. (4.5) for NH and ND. In the following, we will restrict the presentation of the approaches only for a pure Hund's case (b) even though CC calculations have been done in the intermediate coupling for NH and ND.

The analytical representation of the potential describing the electronic interaction between two molecules is given by Eq. (2.29). The V -matrix elements $\langle \alpha'' j_2'' j_{12}'' L'' J M | \hat{V} | \alpha' j_2' j_{12}' L' J M \rangle$ are described for a given J . Also, the potential is independent of the electronic spin, which gives the simplification

$$\langle \alpha'' j_2'' j_{12}'' L'' J M | \hat{V} | \alpha' j_2' j_{12}' L' J M \rangle = \delta_{JJ'} \delta_{MM'} \delta_{SS'} \delta_{m_S m_S'} \langle \alpha'' j_2'' j_{12}'' L'' J | \hat{V} | \alpha' j_2' j_{12}' L' J \rangle \tag{3.18}$$

where we omitted now M . The V -matrix elements will have the form (see Ap-

pendix A):

$$\begin{aligned}
 \langle \alpha'' j_2'' j_{12}'' L'' J | \hat{V} | \alpha' j_2' j_{12}' L' J \rangle &= (4\pi)^{-3/2} \sum_{\lambda_1 \lambda_2 \lambda} v_{\lambda_1 \lambda_2 \lambda}(R) \frac{[\lambda]}{[S]} [\lambda_1 \lambda_2 N' N'' j_1' j_1'' j_2' j_2'' j_{12}' j_{12}'' L' L'']^{1/2} \\
 &\times (-1)^{N'+j_1'+S+L'+N''+j_1''+j_{12}''+L''+J} \\
 &\times \begin{pmatrix} N'' & \lambda_1 & N' \\ 0 & 0 & 0 \end{pmatrix} \begin{pmatrix} j_2'' & \lambda_2 & j_2' \\ 0 & 0 & 0 \end{pmatrix} \begin{pmatrix} L'' & \lambda & L' \\ 0 & 0 & 0 \end{pmatrix} \\
 &\times \left\{ \begin{matrix} j_1' & N' & S \\ N'' & j_1'' & \lambda_1 \end{matrix} \right\} \left\{ \begin{matrix} j_{12}'' & L'' & J \\ L' & j_{12}' & \lambda \end{matrix} \right\} \left\{ \begin{matrix} j_1' & j_1'' & \lambda_1 \\ j_2' & j_2'' & \lambda_2 \\ j_{12}' & j_{12}'' & \lambda \end{matrix} \right\} \quad (3.19)
 \end{aligned}$$

The functions $F_{\alpha' j_2' j_{12}' L', \alpha j_2 j_{12} L}^J(R)$ are following the same asymptotic conditions (2.59) which allows to extract the S -matrix elements $S_{\alpha' L', \alpha L}^J$ and compute the cross section similarly to Eq. (2.60).

3.2.2 Results

Potential energy surface

In this thesis, we used existing PESs to perform scattering calculations and adapted them for the treatment of isotopologues. We remind here the principal features of the NH–H₂ [189] and C₂H–H₂ [154] PESs.

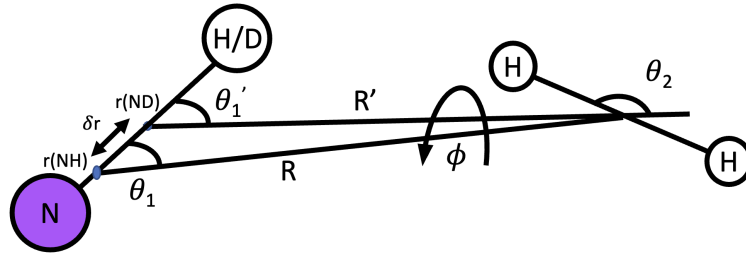


Figure 3.1 – Jacobi coordinates for the NH–H₂ (unprimed) and the ND–H₂ (primed) complexes.

The most suitable coordinates for inelastic scattering calculations for non-reactive systems are the Jacobi coordinates, as illustrated in Fig. 3.1. These are defined by an intermolecular vector \mathbf{R} lying in the centers of mass of NH and H₂, along the z-axis of the SF frame. The angle θ_1 is related to the orientation of NH with respect to the vector \mathbf{R} . The orientation of H₂ is defined by the angles (θ_2, ϕ) . The PES is then described by four degrees of freedom. Since the activation energy of the NH + H₂ reaction is $E_a \sim$

4000 cm⁻¹ [170], reactive processes can be neglected and we can consider both NH and H₂ as rigid rotors and fixing their internuclear distances in their ground vibrational state as $r_{\text{NH}} = 1.958a_0$ and $r_{\text{HH}} = 1.449a_0$ [190].

Ab initio calculations were performed considering NH and H₂ in their ground electronic state using the RCCSD(T)-F12/aVTZ method [111] with the MOLPRO software [112]. The BSSE correction was taken into account using the Boys and Bernardi counterpoise scheme [106], as presented in section 2.2.1. Calculations included 33 516 *ab initio* geometries. The analytical representation of the PES was done in terms of bispherical harmonics as in Eq. (2.29). Radial coefficients $v_{\lambda_1\lambda_2\lambda}(R)$ were chosen so that $\lambda_1^{\text{max}} = 10$, $\lambda_2^{\text{max}} = 4$ and $|\lambda_1 - \lambda_2| < \lambda < \lambda_1 + \lambda_2$, leading to 86 coefficients.

The global minimum of the PES was found for $R = 6.30a_0$ in a linear geometry $(\theta_1, \theta_2, \phi) = (180^\circ, 0^\circ, 0^\circ)$ and a well depth $D_e = 149.10$ cm⁻¹, where H₂ is pointing toward the nitrogen end. A local minimum was also found for $R = 7.9a_0$ for a *T*-shaped geometry $(\theta_1, \theta_2, \phi) = (0^\circ, 90^\circ, 0^\circ)$ and a well depth $D_e = 109.52$ cm⁻¹, where the hydrogen end is pointing toward the H₂ moiety. This PES has been validated through comparisons between bound states calculations and experimental measurements done by Fawzy *et al.* [191]. The procedure for this validation can be found in Pirlot Jankowiak *et al.* [189].

Since isotopologues possess the same electronic structure, it is possible to use the PES of the parent molecule to determine the one for the isotopic substituted species. The only difference will be in the placement of the center of mass. The two molecules have also the same bond length within the rigid rotor approximation. The change from NH to ND gives rise to a shift of the center of mass by $\delta r = r_{\text{ND}} - r_{\text{NH}} = -0.1149a_0$ toward the deuterium end. The transformation of coordinates from the NH–H₂ to the ND–H₂ PES $(R, \theta_1, \theta_2, \phi) \rightarrow (R', \theta'_1, \theta_2, \phi)$ is given by:

$$\begin{aligned} R' &= \sqrt{R^2 + \delta r^2 + 2R\delta r \cos(\theta_1)} \\ \theta'_1 &= \cos^{-1}\left(\frac{R \cos(\theta_1) - \delta r}{R'}\right) \end{aligned} \quad (3.20)$$

where we neglected the transformation over (θ_2, ϕ) as it did not have any impact on scattering calculations. The determination of the radial coefficients $v_{\lambda_1\lambda_2\lambda}(R)$ for the ND–H₂ PES have been extracted using a Gauss-Legendre quadrature for 588 geometries, using $\lambda_1^{\text{max}} = 10$, $\lambda_2^{\text{max}} = 4$.

Fig. 3.2 shows contours plots for the two PESs at the distance corresponding to the NH–H₂ global minimum $R = 6.30a_0$. We can see that both PESs are very anisotropic with respect to θ_1 and θ_2 orientations but show small relative differences. The most noticeable difference in the potentials is for the repulsive behavior for $\theta_1 = 0^\circ$ and for $\theta_2 = 90^\circ$. The

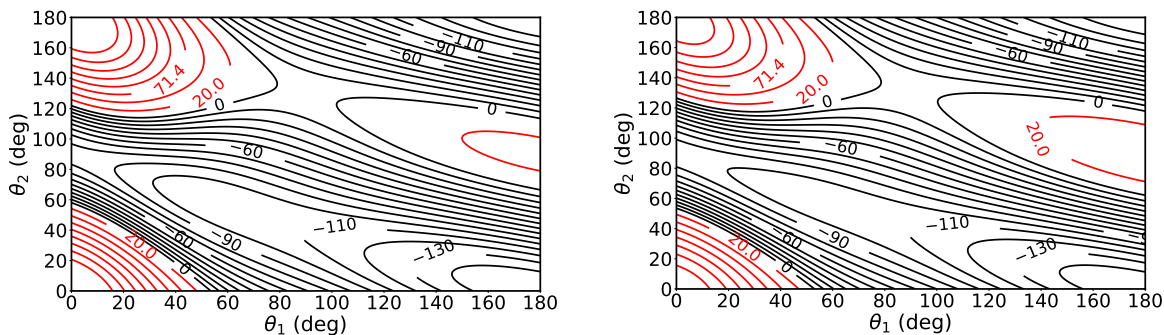


Figure 3.2 – Contour plots of the NH–H₂ (left) and ND–H₂ (right) PESs for an intermolecular distance $R = 6.30a_0$ and $\phi = 0^\circ$.

well depth of the potential being small, we do not expect that collisional cross sections and rate coefficients will be strongly impacted by the shift of the center of mass. However, the energetic structure of ND is about two times denser than the one of NH which will have influence on scattering calculations, as demonstrated by Dumouchel *et al.* [173].

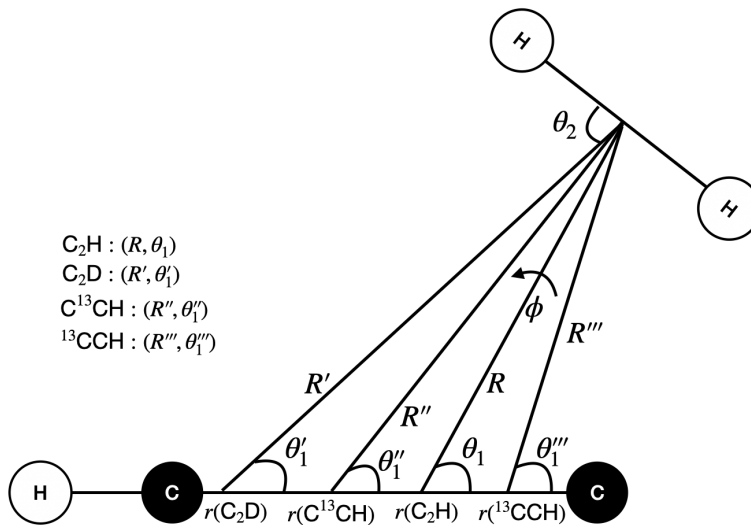


Figure 3.3 – Jacobi coordinates for the C₂H–H₂ complex and its isotopologues. The displacement of the center of mass is exaggerated for clarity.

The C₂H–H₂ PES is also described in Jacobi coordinates (see Fig. 3.3) in the rigid rotor approach, since its reaction with H₂ requires an activation energy of ~ 1600 K. Internuclear distances for H₂ was chosen as $r_{HH} = 1.449a_0$ [190] and for C₂H, $r_{CC} = 2.299a_0$ and $r_{CH} = 1.968a_0$ [192]. *Ab initio* calculations were performed considering the two partners in their ground electronic state. The RCCSD(T)/aVQZ method [111] was employed using the MOLPRO program [112] and applying a counterpoise correction [106]. Overall, the total number of geometries computed for the potential was 43 165.

The interaction potential was also fitted using Eq. (2.29) for $\lambda_1^{max} = 12$, $\lambda_2^{max} = 6$, leading to 174 expansion coefficients $v_{\lambda_1\lambda_2\lambda}(R)$. A global minimum was found for an intermolecular distance $R = 7.82a_0$, corresponding to a *T*-shaped geometry $(\theta_1, \theta_2, \phi) = (180^\circ, 90^\circ, 0^\circ)$, where the hydrogen end of the C_2H collider points toward the center of mass of H_2 . This results in a well depth of $D_e = 133.4 \text{ cm}^{-1}$.

The treatment of the isotopologues was done using the same procedure as for the $NH-H_2$ and $ND-H_2$ PESs. We used Eq. (3.20) to transform the C_2H-H_2 interaction potential into C_2D-H_2 ($\delta r = 0.1157a_0$), $^{13}CCH-H_2$ ($\delta r = -0.049a_0$) and $C^{13}CH-H_2$ ($\delta r = 0.039a_0$) PESs. We used a Gauss-Legendre quadrature over 686 geometries, with $\lambda_1^{max} = 12$, $\lambda_2^{max} = 6$ for the PES expansion.

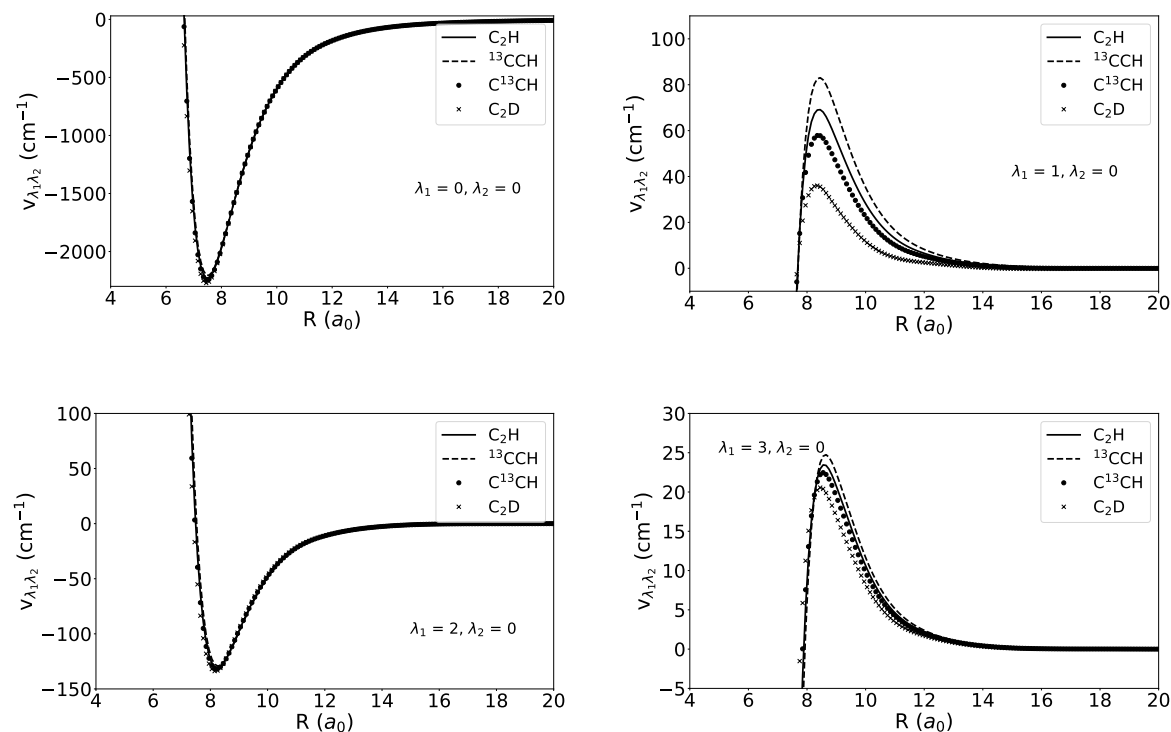


Figure 3.4 – Radial cuts of the firsts expansion coefficients for the C_2H-H_2 PES and its isotopologues. Solid lines correspond to C_2H , dashed lines for ^{13}CCH , dotted lines for $C^{13}CH$, and crossed lines for C_2D . Summation of the coefficients has been done over λ for clarity.

It is interesting to look at the differences between these PESs. Fig. 3.4 shows the radial dependence of several expansion coefficients for all C_2H isotopologues. We can see that the isotopic substitution has negligible effect on even λ_1 radial coefficients. The largest differences can be seen for odd anisotropies, especially for $\lambda_1 = 1$ where $v_{\lambda_1\lambda_2}^{^{13}CCH} > v_{\lambda_1\lambda_2}^{C_2H} > v_{\lambda_1\lambda_2}^{C^{13}CH} > v_{\lambda_1\lambda_2}^{C_2D}$. This trend can be understood by the shift of the center of mass toward the carbon end in the case of ^{13}CCH , leading to larger anisotropies than for the other isotopologues, where the displacement of the center of mass tends to be close to the

center of the molecule. Contrary to NH and ND, we expect that the principal differences in cross sections and rate coefficients will come from the changes in the PES, since their rotational structures are very similar, especially for the ^{13}C substitution.

Scattering calculations

The following results have been published in four peer-reviewed articles that can be found in appendix C. We summarize here the most important findings.

Fine structure transitions have been computed within the CC approach, using the `HI-BRIDON` suite of programs [80], where a summary of the propagation procedure can be found in section 2.4.5. We remind here that the total energy grid must be very dense for very low total energies in order to describe quantum effects (resonances) promoted in this energetic regime. The total energy step can increase more and more with the energy, as cross sections tend to have a monotonic behavior. All scattering parameters have been chosen to converge collisional cross sections within 1% of accuracy per parameter. Calculations included the first 25 energy levels of NH and ND for temperatures up to 300 K; and the first 41 levels of C_2H up to 500 K, the first 31 levels of C_2D up to 200 K and the first 25 levels of ^{13}CCH and C^{13}CH up to 100 K. Details about the optimized parameters can be found in appendix C for the $^{13}\text{CCH-H}_2$ and $\text{C}^{13}\text{CH-H}_2$ systems [193], the $\text{C}_2\text{H-H}_2$ and $\text{C}_2\text{D-H}_2$ systems [194]; and the NH-H_2 and ND-H_2 systems [195]. All scattering calculations have been performed including the *ortho*- $\text{H}_2(j_2=1)$ and *para*- $\text{H}_2(j_2=0)$ forms, except for the treatment of $^{13}\text{CCH-H}_2$ and $\text{C}^{13}\text{CH-H}_2$ where we restricted to collisions with *para*- $\text{H}_2(j_2=0)$ as it will be explained in section 3.3.4. Overall, calculations required up to ~ 2000 channels per energy point for the treatment of NH and ND and up to ~ 7000 channels for C_2H and its isotopologues which can be handled by nowadays facilities with the CC method. This required $\sim 100\,000$ CPU hours for NH-H_2 and ND-H_2 calculations and less than $300\,000$ CPU hours for $\text{C}_2\text{H-H}_2$ and isotopologues calculations using the cluster Physix of the IPR and the TGCC (Très Grand Cluster de Calcul) supercomputer.

Influence of the projectile

Fig. 3.5 presents several fine structure cross sections for NH excitation by *ortho*- and *para*- H_2 . We can first notice the presence of shape and Feshbach resonances, attributed to some peaks of intensity in cross sections at low collisional energies. These are related to the formation of an intermediate complex during a collision. When the collisional energy is matching with one of the bound states of the complex, the system is temporarily trapped to form one of these states before dissociating [196]. These are pure quantum effects that can be hardly described by approximate methods and are usually important in the determination of rate coefficients at low temperatures.

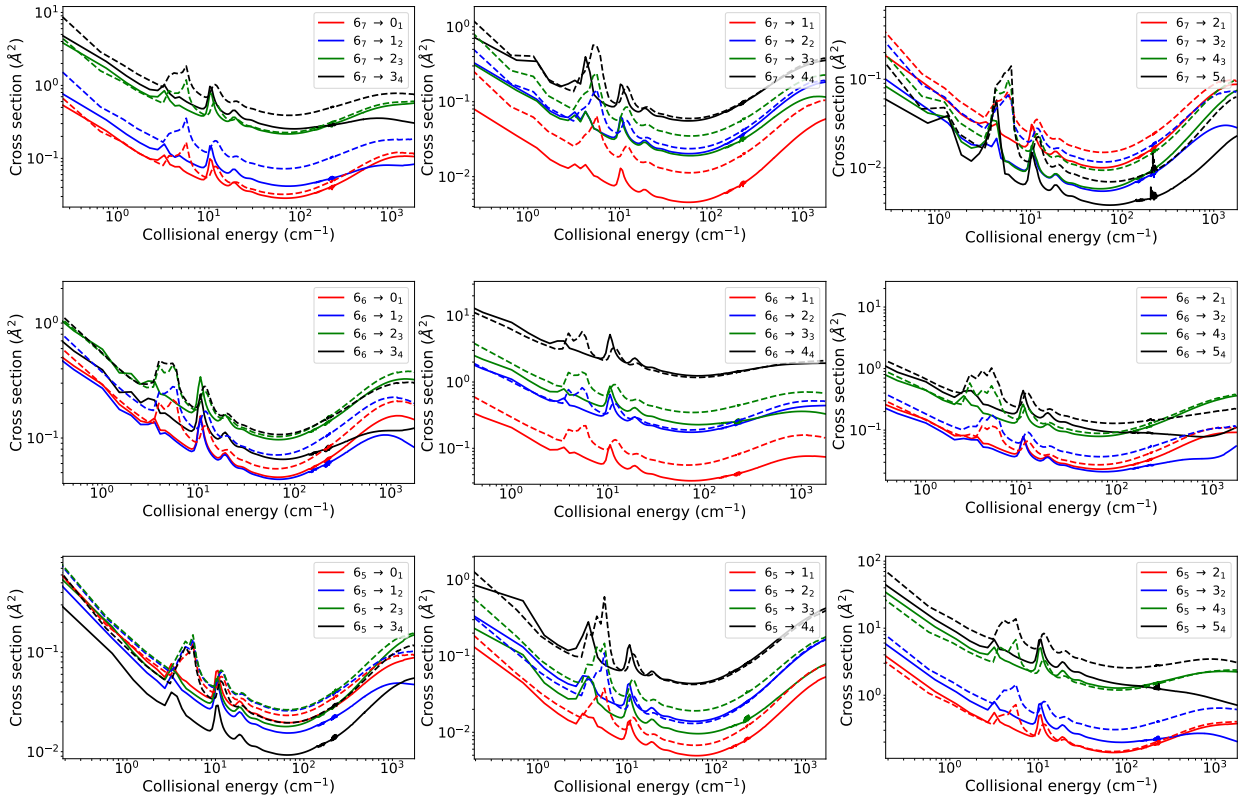


Figure 3.5 – Comparison between fine structure cross sections for NH in collision with *para*-H₂ (solid) and *ortho*-H₂ (dashed). For initial levels: 6₇ (top), 6₆ (middle) and 6₅ (bottom). For final levels: $N'_{N'+1}$ (left), $N'_{N'}$ (middle) and $N'_{N'-1}$ (right).

Secondly, we can see that the magnitude of cross sections depends on the initial and final energy level. We call that *propensity rules* and they are system specific. A general trend observed in the literature is that cross sections decrease with increasing ΔN . This can be explained by a tendency of the system to minimize the angular momentum transfer and the energy gap during a collision. In the case of open-shell molecules in a $^3\Sigma^-$ electronic state, we can see that transitions preserving the fine structure label ($\Delta N = \Delta j_1$) are larger than those changing the fine structure label ($\Delta N \neq \Delta j_1$). As pointed out by Alexander & Dagdigian [197] and Corey *et al.* [198], since the interaction potential is independent of the electronic spin S , a collision cannot affect directly the orientation of S . Then, a change in a fine structure label transition is only possible through a reorientation of the nuclear rotational quantum number N and a change of axis of quantization of S , indirectly affecting the rotational quantum number j_1 . Consequently, as shown in Fig. 3.5, the system tends to preserve the orientation of the angular momenta during a collision and the magnitude of transitions is described as $N_{N\pm 1} \leftrightarrow N'_{N'\pm 1} > N_N \leftrightarrow N'_{N\pm 1} > N_{N\pm 1} \leftrightarrow N'_{N'\mp 1}$.

Finally, it clearly appears that collisions are different whether *ortho*- or *para*-H₂ is in-

volved. Most of *ortho*-H₂ transitions are larger than those for *para*-H₂ by a factor 3-10. This is attributed to the exploration of more anisotropies in the potential for colliders with $j_2 > 0$, as it is the case for *ortho*-H₂. This is a general trend observed for neutral-neutral collisions [199], [200]. More specifically, we can see that collisions involving *ortho*-H₂ collider are larger than those for *para*-H₂ for odd ΔN transitions. All this discussion stands also for collisions with ND and rate coefficients follow the same trends.

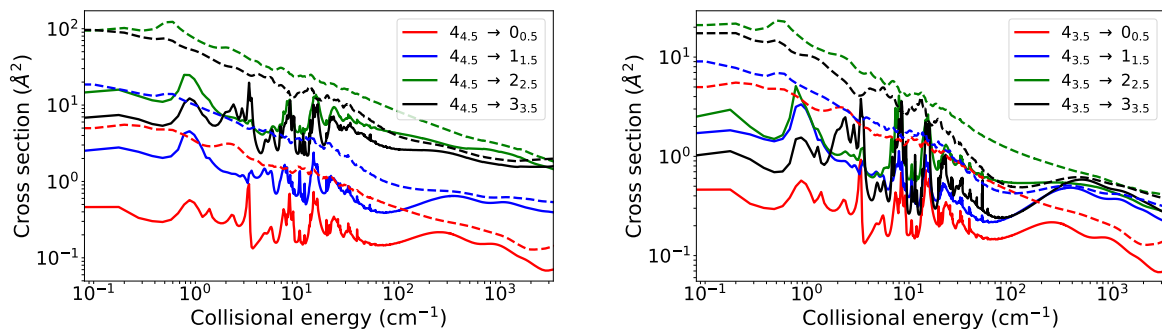


Figure 3.6 – Comparison between fine structure cross sections for C₂H in collision with *para*-H₂ (solid) and *ortho*-H₂ (dashed) for fine structure conserving transitions (left) and fine structure changing transitions (right).

Almost the same rules are applied for C₂H collisions, except that larger collisions are observed for even ΔN transitions when involving *ortho*-H₂ than for *para*-H₂, as shown in Fig. 3.6. This type of effect cannot be predicted easily and a strict calculation of the potential should be done to observe this. It is worth noting that C₂H–H₂ transitions show much more resonances than for NH–H₂ transitions. This is related to the presence of much more bound states in the C₂H–H₂ well depth than in the NH–H₂ one. It can be intuitively understand that the denser the rotational structures of the colliders are, the denser the energetic structure of the complex will be.

It is common to use He as a proxy for *para*-H₂ when collisional data involving molecular hydrogen are not available. Rate coefficients between the two colliders are assumed to be the same, only different by the ratio of the reduced mass of the collisional system and computed as:

$$k_{X-para-H_2}(T) \sim \left(\frac{\mu_{X-He}}{\mu_{X-para-H_2}} \right)^{1/2} k_{X-He}(T) \quad (3.21)$$

where X is a given target. We compare our sets of data for NH–H₂ and C₂H–H₂

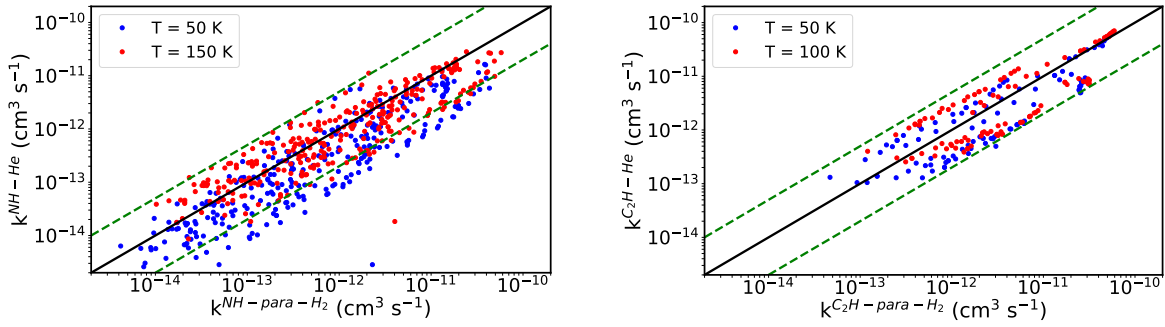


Figure 3.7 – Systematic comparison between fine structure rate coefficients for NH (left) and C₂H (right) in collision with He and *para*-H₂. Dashed lines represent deviations within a factor of 5.

with those provided by Dumouchel *et al.* [173] for NH–He and by Spielfiedel *et al.* [150] for C₂H–He. Such comparison can be seen in Fig. 3.7¹. Most of rate coefficients are different up to a factor of 5 for C₂H collisions and even up to an order of magnitude for NH collisions. In both cases, this is due to a large difference in the interaction potential with He and H₂. First, both interaction potential with He are two dimensional and then much less anisotropic than PESs involving H₂. The well depth of the C₂H–He PES is also smaller than the 4D PES for C₂H–H₂ by a factor of ~ 5 . As well, the depth for the NH–He PES computed by Cybulski *et al.* [172] is smaller than the 4D PES for NH–H₂ computed by Pirlot Jankowiak *et al.* [189] by a factor of ~ 7 . We show that caution must be taken when using He as a prototype collider for H₂.

Impact of the isotopic substitution

It is interesting to explore the impact of the isotopic substitution on rate coefficients. For the case of NH and ND, Fig. 3.8 shows large differences for both H₂ colliders, within a factor 3–5. We saw in section 3.2.2 that the shift of the center of mass between NH–H₂ and ND–H₂ frames is minor. Then, these discrepancies can be explained by the large difference between the rotational structures of the targets, with the rotational constant of ND being almost twice smaller than the one of NH as $B_0(\text{NH}) = 16.343 \text{ cm}^{-1}$ [187] and $B_0(\text{ND}) = 8.782 \text{ cm}^{-1}$ [188]. This results in lower space between energy levels for ND which can impact the magnitude of cross sections.

In the case of C₂H and C₂D, their rotational constants are similar and the main differences are coming from the displacement of the center of mass in the C₂H–H₂ interaction potential. However, differences are found to be less than a factor of 2 between the two targets. Even the largest rate coefficients almost match perfectly between each other. We

1. This has been already discussed by Dagdigian [153] for the case of C₂H.

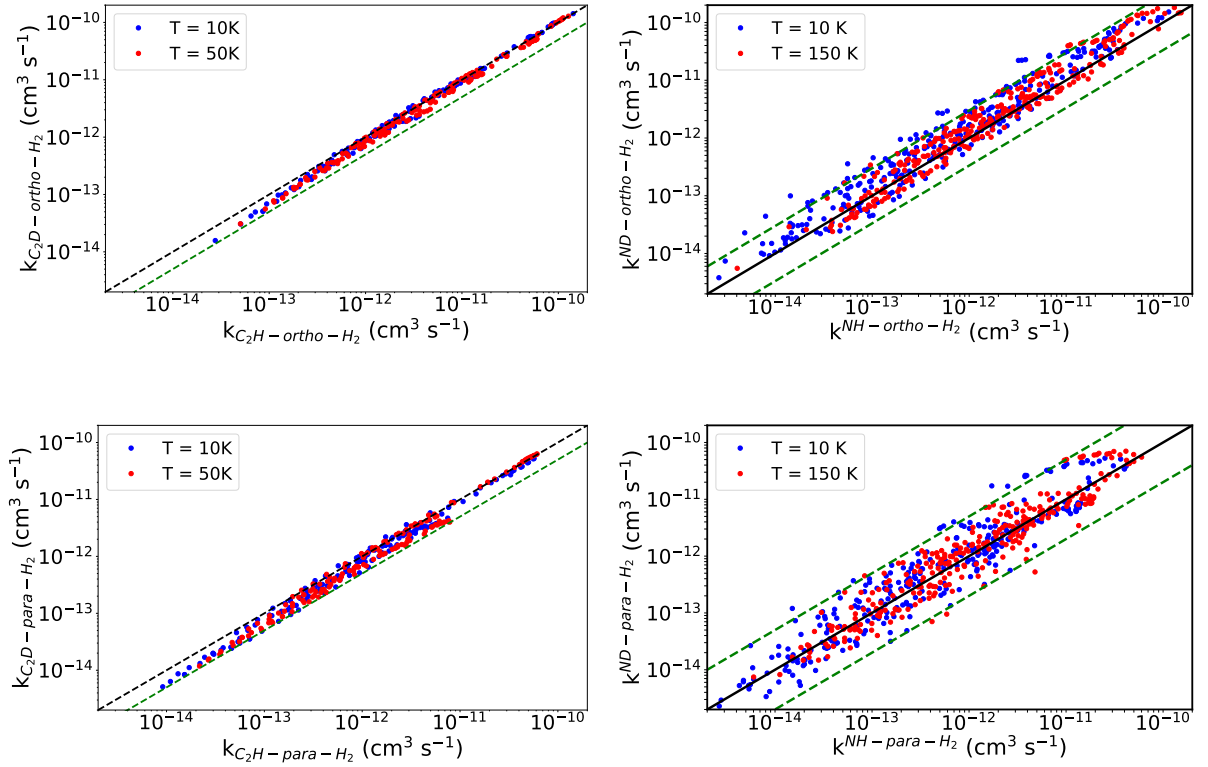


Figure 3.8 – Systematic comparison between fine structure rate coefficients for C₂H and C₂D collisions (left), NH and ND collisions (right) with *ortho*-H₂ (top) and *para*-H₂ (bottom).

can mention that C₂H rate coefficients are systematically larger than those with C₂D. This can be understood by a displacement of the center of mass toward the middle of the target, which reduces the anisotropies of the PES (see Fig. 3.4, where the $v_{10}(R)$ expansion coefficients is the lowest for the C₂D–H₂ PES).

This can be also visible by seeing the ¹³C substitution in Fig. 3.9. Differences between ¹³C isotopologues rate coefficients are not more than 30%, even less with respect to C₂H. Transitions involving ¹³CCH are however the largest among the targets due to the closest center of mass position to the edge of the molecule, leading to the largest anisotropies in the PES.

Finally, even if the deuterium is twice heavier than hydrogen, its isotopic substitution is found to be more significant on the rotational structure when the parent molecule is light than on the PES and when the parent molecule is heavy. The effect becomes more and more negligible when the isotopic substitution occurs with a heavier atom.

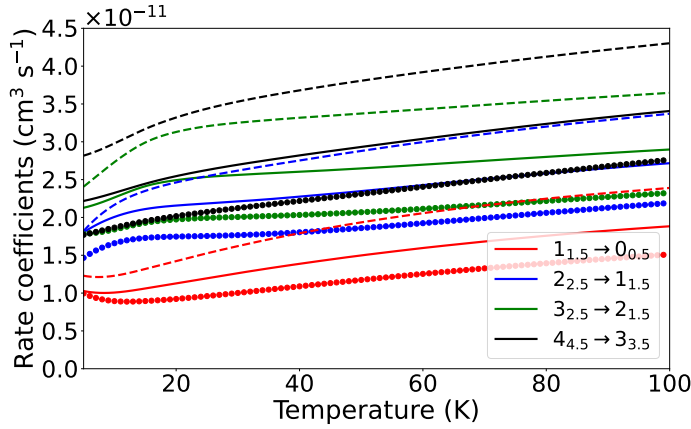


Figure 3.9 – Evolution of fine structure rate coefficients of C_2H -*sph*- H_2 (solid), ^{13}CCH -*sph*- H_2 (dashed) and $C^{13}CH$ -*sph*- H_2 (dotted) with the temperature.

3.3 Hyperfine structure excitation

3.3.1 Close-coupling approach

To solve the Schrödinger equation to describe collisions between a linear open-shell molecule presenting two non-zero nuclear spins I_1 and I_2 ; and a linear closed-shell molecule presenting a rotational structure j_2 , the coupling scheme for defining the angular functions used in the CC approach is given as:

$$\hat{N} + \hat{S} = \hat{j}_1; \quad \hat{j}_1 + \hat{j}_2 = \hat{j}_{12}; \quad \hat{j}_{12} + \hat{I}_1 = \hat{F}_1; \quad \hat{F}_1 + \hat{I}_2 = \hat{F}; \quad \hat{F} + \hat{L} = \hat{J}$$

where the F_1 and F labels correspond to the quantum numbers describing the coupling of I_1 and I_2 to the rotation, respectively. The corresponding basis set of angular functions is $|NSj_1j_2j_{12}I_1F_1I_2FL, J\rangle \equiv |\alpha\beta j_2j_{12}L, J\rangle$, with $\alpha = NSj_1$ and $\beta = I_1F_1I_2F$ regroup all quantum numbers related to the rotational/fine structure and hyperfine structure of the target, respectively. These functions depends on the angular functions (3.15) where we add the couplings of the nuclear spins:

$$|\alpha\beta j_2j_{12}L, J\rangle = \sum_{m_F m_L} C_{m_F m_L}^{FLJ} |\alpha\beta j_2j_{12}\rangle |Lm_L\rangle \quad (3.22)$$

$$|\alpha\beta j_2j_{12}\rangle = \sum_{\substack{m_{F_1} m_{I_2} \\ m_{12} m_{I_1}}} C_{m_{F_1} m_{I_2} m_F}^{F_1 I_2 F} C_{m_{12} m_{I_1} m_{F_1}}^{j_{12} I_1 F_1} |\alpha j_2j_{12}\rangle |I_1 m_{I_1}\rangle |I_2 m_{I_2}\rangle \quad (3.23)$$

$$|\alpha j_2j_{12}\rangle = \sum_{m_1 m_2} C_{m_1 m_2 m_{12}}^{j_1 j_2 j_{12}} |j_1 m_1\rangle |j_2 m_2\rangle \quad (3.24)$$

The total wave function can be defined with the new angular functions:

$$\Psi_{\alpha\beta j_2 j_1 L}^J(\mathbf{Q}) = \sum_{\alpha' \beta' j'_2 j'_1 L'} \frac{F_{\alpha\beta j_2 j_1 L, \alpha' \beta' j'_2 j'_1 L'}^J(R)}{R} |\alpha' \beta' j'_2 j'_1 L', J\rangle \quad (3.25)$$

The CC equations for the radial dependence will have the form:

$$\begin{aligned} & \left(\frac{\partial^2}{\partial R^2} + k^2 - \frac{L''(L'' + 1)}{R^2} \right) F_{\alpha'' \beta'' j''_2 j''_1 L'', \alpha' \beta' j'_2 j'_1 L'}^J(R) \\ &= 2\mu \sum_{\alpha' \beta' j'_2 j'_1 L'} \langle \alpha'' \beta'' j''_2 j''_1 L'' | \hat{V} | \alpha' \beta' j'_2 j'_1 L' \rangle F_{\alpha' \beta' j'_2 j'_1 L', \alpha\beta j_2 j_1 L}(R) \end{aligned} \quad (3.26)$$

with $k^2 = 2\mu(E_{\text{tot}} - E_{Nj_1 F_1 F} - E_{j_2})$. The CC equations must be solved according to the asymptotic conditions (2.59).

The problem is that the inclusion of the electronic spins and the two nuclear spins lead to a large number of energy levels to consider in the scattering calculations. The addition of the structure of the projectile, even light, involve too many coupled equations to be solved with nowadays computational resources. That is why we need to find alternative methodologies to compute hyperfine resolved rate coefficients for the C₂H–H₂ and the NH–H₂ collisional systems, including their isotopologues in order to provide accurate collisional data for astrophysical modeling.

3.3.2 Recoupling approach

Corey & McCourt [81] pointed out that the interaction potential is independent of the spins involved in collisions. Then, we can consider that I_1 and I_2 are spectators during a collision. In the case of hyperfine calculations, we mentioned in section 2.3.3 that the coupling of the nuclear spin with other angular momenta is very weak, resulting in a very small hyperfine splitting of energy levels. The order of magnitude of a hyperfine coupling constant is usually $\sim 10^{-6} - 10^{-4} \text{ cm}^{-1}$, much lower than couplings arising from the fine structure ($\sim 10^{-3} - 10^0 \text{ cm}^{-1}$). It can be safely assumed that collisional energies involved are much larger than the space between hyperfine energy levels and these can be considered as degenerated. Thus, it is possible to compute hyperfine resolved collisional cross sections using the S matrices determined with the CC approach for the fine structure. We follow the approach of Offer *et al.* [201], extended to two non-vanishing nuclear spins.

We change the coupling scheme of the angular momenta of the collisional system so that the nuclear spins are uncoupled from the rotational momenta:

$$\hat{N} + \hat{S} = \hat{j}_1; \quad \hat{j}_1 + \hat{j}_2 = \hat{j}_{12} \quad \hat{j}_{12} + \hat{L} = \hat{J} \quad \hat{J} + \hat{I}_1 = \tilde{F}_1 \quad \tilde{F}_1 + \hat{I}_2 = \hat{J}_T$$

with now J and J_T being the nuclear spin-free total angular momentum and the total angular momentum, respectively. This gives the set of angular functions $|\alpha j_{12} L J \tilde{F}_1, J_T\rangle$. We use the same procedure as Offer *et al.* [201] to simplify the coupling scheme by introducing a perturbing angular momentum j_R such that:

$$\hat{j}_2 + \hat{L} = \hat{j}_R; \quad \hat{N} + \hat{S} = \hat{j}_1; \quad \hat{j}_1 + \hat{I}_1 = \hat{F}_1; \quad \hat{F}_1 + \hat{I}_2 = \hat{F}; \quad \hat{F} + \hat{j}_R = \hat{J}_T$$

giving the basis $|\alpha j_R F_1 F, J_T\rangle$.

Now we can express the $|\alpha j_R F_1 F, J_T\rangle$ recoupling basis as a function of the $|\alpha j_{12} L J \tilde{F}_1, J_T\rangle$ basis by using an unitary transformation [202]:

$$|\alpha j_R F_1 F, J_T\rangle = \sum_{j_{12}} \langle j_{12} | j_R \rangle \sum_J \langle J | F_1 \rangle \sum_{\tilde{F}_1} \langle \tilde{F}_1 | F \rangle |\alpha j_{12} L J, J_T\rangle$$

The coefficients in brackets are given by [202]:

- $\langle j_{12} | j_R \rangle = (-1)^{j_1+j_2+l+J} [j_{12} j_R]^{1/2} \begin{Bmatrix} j_1 & j_2 & j_{12} \\ L & J & j_R \end{Bmatrix}$
- $\langle J | F_1 \rangle = (-1)^{j_R+j_1+I_1+\tilde{F}_1} [J F_1]^{1/2} \begin{Bmatrix} j_R & j_1 & J \\ I_1 & \tilde{F}_1 & F_1 \end{Bmatrix}$
- $\langle \tilde{F}_1 | F \rangle = (-1)^{j_R+F+I_2+J_T} [\tilde{F}_1 F]^{1/2} \begin{Bmatrix} j_R & F_1 & \tilde{F}_1 \\ I_2 & J_T & F \end{Bmatrix}$

Then the T -matrix elements can be written as:

$$\begin{aligned} \langle \alpha' j'_R F'_1 F', J_T | T^{J_T} | \alpha j_R F_1 F, J_T \rangle &= \sum_{J j'_{12} j_{12} \tilde{F}_1} [j_{12} j'_{12} j_R j'_R F F' F_1 F'_1]^{1/2} [\tilde{F}_1] [J] \\ &\times (-1)^{j_2+j'_2+L+L'+F+F'} \\ &\times \begin{Bmatrix} j_1 & j_2 & j_{12} \\ L & J & j_R \end{Bmatrix} \begin{Bmatrix} j_R & j_1 & J \\ I_1 & \tilde{F}_1 & F_1 \end{Bmatrix} \begin{Bmatrix} j_R & F_1 & \tilde{F}_1 \\ I_2 & J_T & F \end{Bmatrix} \\ &\times \begin{Bmatrix} j'_1 & j'_2 & j'_{12} \\ L' & J & j'_R \end{Bmatrix} \begin{Bmatrix} j'_R & j'_1 & J \\ I_1 & \tilde{F}_1 & F'_1 \end{Bmatrix} \begin{Bmatrix} j'_R & F'_1 & \tilde{F}_1 \\ I_2 & J_T & F' \end{Bmatrix} \\ &\times \langle \alpha' j'_R L' J, J_T | T^J | \alpha j_{12} L J, J_T \rangle \end{aligned}$$

where now the T -matrix elements are expressed as a function of nuclear spin-free matrices, and the nuclear spins dependences only appear in the $6j$ symbols. We get the hyperfine resolved cross section:

$$\begin{aligned}
 \sigma_{\alpha F_1 F, j_2 \rightarrow \alpha' F'_1 F', j'_2}^{\text{rec}} &= \frac{\pi}{k_{\alpha F_1 F}^2 [F j_2]} \sum_{J_T} [J_T] \sum_{LL' j_R j'_R} |\langle \alpha j'_R F'_1 F', J_T | T^{J_T} | \alpha j_R F_1 F, J_T \rangle|^2 \\
 &= \frac{\pi}{k_{\alpha F_1 F}^2 [F j_2]} \sum_{J_T} [J_T] \sum_{LL' j_R j'_R} \sum_{j_{12} j'_{12}} \sum_{JJ' \tilde{F}_1 \tilde{F}'_1} [j_{12} j'_{12} j_R j'_R F F' F_1 F'_1 \tilde{F}_1 \tilde{F}'_1 J J'] \\
 &\times \begin{Bmatrix} j_R & F_1 & \tilde{F}_1 \\ I_2 & J_T & F \end{Bmatrix} \begin{Bmatrix} j_R & F_1 & \tilde{F}'_1 \\ I_2 & J_T & F \end{Bmatrix} \begin{Bmatrix} j'_R & F'_1 & \tilde{F}_1 \\ I_2 & J_T & F' \end{Bmatrix} \begin{Bmatrix} j'_R & F'_1 & \tilde{F}'_1 \\ I_2 & J_T & F' \end{Bmatrix} \\
 &\times \begin{Bmatrix} j_R & j_1 & J \\ I_1 & \tilde{F}_1 & F_1 \end{Bmatrix} \begin{Bmatrix} j_R & j_1 & J' \\ I_1 & \tilde{F}'_1 & F_1 \end{Bmatrix} \begin{Bmatrix} j'_R & j'_1 & J \\ I_1 & \tilde{F}_1 & F'_1 \end{Bmatrix} \begin{Bmatrix} j'_R & j'_1 & J' \\ I_1 & \tilde{F}'_1 & F'_1 \end{Bmatrix} \\
 &\times \begin{Bmatrix} j_1 & j_2 & j_{12} \\ L & J & j_R \end{Bmatrix} \begin{Bmatrix} j_1 & j_2 & j_{12} \\ L & J' & j_R \end{Bmatrix} \begin{Bmatrix} j'_1 & j'_2 & j'_{12} \\ L' & J & j'_R \end{Bmatrix} \begin{Bmatrix} j'_1 & j'_2 & j'_{12} \\ L' & J' & j'_R \end{Bmatrix} \\
 &\times \langle \alpha' j'_{12} L' J, J_T | T^J | \alpha j_{12} L J, J_T \rangle \langle \alpha' j'_{12} L' J', J_T | T^{J'} | \alpha j_{12} L J', J_T \rangle^* \quad (3.27)
 \end{aligned}$$

3.3.3 Infinite Order Sudden limit

As mentioned in section 2.4.2, the Infinite Order Sudden approximation (IOS) relies both on an average of the centrifugal terms in the CC equations and ignoring the rotation of the system during a collision [203]. It is then expected to be accurate at high collisional energies. Following the discussion in section 2.4.2, the S matrices depend parametrically on the angles and can be expanded with the same angular dependence as the PES. In the case of collisions between a linear open-shell molecule in a $^{2S+1}\Sigma$ state and a closed-shell molecule in a $^1\Sigma$ state, it would give:

$$\begin{aligned}
 \langle \alpha' j'_2 j'_{12} L' | S^{\bar{L}}(\bar{\theta}) | \alpha j_2 j_{12} L \rangle &= (4\pi)^{-3/2} \sum_{\lambda_1 \lambda_2 \lambda} \frac{[\lambda]}{[S]} [\lambda_1 \lambda_2 N N' j_1 j'_1 j_2 j'_2 j_{12} j'_{12} L L']^{1/2} \\
 &\times (-1)^{N'+j'_1+S+L'+N''+j''_1+j''_{12}+L''+J} \\
 &\times \begin{pmatrix} N' & \lambda_1 & N \\ 0 & 0 & 0 \end{pmatrix} \begin{pmatrix} j'_2 & \lambda_2 & j_2 \\ 0 & 0 & 0 \end{pmatrix} \begin{pmatrix} L' & \lambda & L \\ 0 & 0 & 0 \end{pmatrix} \quad (3.28) \\
 &\times \begin{Bmatrix} j_1 & N & S \\ N' & j'_1 & \lambda_1 \end{Bmatrix} \begin{Bmatrix} j'_{12} & L' & J \\ L & j_{12} & \lambda \end{Bmatrix} \begin{Bmatrix} j_1 & j'_1 & \lambda_1 \\ j_2 & j'_2 & \lambda_2 \\ j_{12} & j'_{12} & \lambda \end{Bmatrix} S^{\bar{L}}_{\lambda_1 \lambda_2 \lambda}
 \end{aligned}$$

The fine structure IOS cross section can be written as:

$$\begin{aligned}
 \sigma_{Nj_1j_2 \rightarrow N'j'_1j'_2}^{\text{IOS}} &= \frac{\pi}{k^2[j_1j_2]} \sum_{\substack{j_{12}j'_{12} \\ LL'}} [J] |\langle \alpha' j'_2 j'_{12} L' | T^J | \alpha j_2 j_{12} L \rangle|^2 \\
 &= \frac{\pi}{k^2[j_1j_2]} \sum_{\substack{j_{12}j'_{12} \\ LL'}} [J] (4\pi)^{-3} \sum_{\lambda_1 \lambda_2 \lambda} \left(\frac{[\lambda]}{[S]} \right)^2 [\lambda_1 \lambda_2 N N' j_1 j'_1 j_2 j'_2 j_{12} j'_{12} L L'] \\
 &\quad \times \begin{pmatrix} N' & \lambda_1 & N \\ 0 & 0 & 0 \end{pmatrix}^2 \begin{pmatrix} j'_2 & \lambda_2 & j_2 \\ 0 & 0 & 0 \end{pmatrix}^2 \begin{pmatrix} L' & \lambda & L \\ 0 & 0 & 0 \end{pmatrix}^2 \\
 &\quad \times \left\{ \begin{matrix} j_1 & j'_1 & \lambda_1 \\ j_2 & j'_2 & \lambda_2 \\ j_{12} & j'_{12} & \lambda \end{matrix} \right\}^2 \left\{ \begin{matrix} j'_{12} & L' & J \\ L & j_{12} & \lambda \end{matrix} \right\}^2 \left\{ \begin{matrix} j_1 & N & S \\ N' & j'_1 & \lambda_1 \end{matrix} \right\}^2 |T_{\lambda_1 \lambda_2 \lambda}^{\bar{L}}|^2
 \end{aligned} \tag{3.29}$$

Eq. (3.29) can be simplified by seeing that

$$\sum_J [J] \left\{ \begin{matrix} j'_{12} & L' & J \\ L & j_{12} & \lambda \end{matrix} \right\}^2 = \frac{1}{[\lambda]} \quad \text{and} \quad \sum_{j_{12}j'_{12}} [j_{12}j'_{12}] \left\{ \begin{matrix} j_1 & j'_1 & \lambda_1 \\ j_2 & j'_2 & \lambda_2 \\ j_{12} & j'_{12} & \lambda \end{matrix} \right\}^2 = \frac{1}{[\lambda_1 \lambda_2]}$$

and the cross section can be written

$$\begin{aligned}
 \sigma_{Nj_1j_2 \rightarrow N'j'_1j'_2}^{\text{IOS}} &= \frac{[N N' j'_1 j'_2]}{[S]^2} \sum_{\lambda_1 \lambda_2 \lambda} \begin{pmatrix} N' & \lambda_1 & N \\ 0 & 0 & 0 \end{pmatrix}^2 \begin{pmatrix} j'_2 & \lambda_2 & j_2 \\ 0 & 0 & 0 \end{pmatrix}^2 \left\{ \begin{matrix} j_1 & N & S \\ N' & j'_1 & \lambda_1 \end{matrix} \right\}^2 \sigma_{\lambda_1 \lambda_2 \lambda} \\
 \sigma_{\lambda_1 \lambda_2 \lambda} &= \frac{\pi}{k^2} \sum_{LL'} (4\pi)^{-3} [\lambda LL'] \begin{pmatrix} L' & \lambda & L \\ 0 & 0 & 0 \end{pmatrix}^2 |T_{\lambda_1 \lambda_2 \lambda}^{\bar{L}}|^2
 \end{aligned} \tag{3.30}$$

From this point, the fine and hyperfine resolved cross section within the IOS approximation is system dependent and we will present the specific case for the treatment of NH and the ^{13}C isotopologues of C_2H separately.

3.3.4 Results

Selection of a suitable method for computing hyperfine resolved collisional data

$^{13}\text{CCH-H}_2$ and $\text{C}^{13}\text{CH-H}_2$

The recoupling method is currently the most accurate approach for hyperfine treatment. However, the inclusion of two nuclear spins leads to $\sim 4\text{--}6$ more times channels depending on the system, and the inclusion of the structure of the projectile even only for $j_2 = 1$ would imply ~ 3 times more channels to consider in scattering calculations, making this recoupling method not doable in terms of computational time and memory. Moreover, interference terms in Eq. (3.27) prevent to perform calculations for one given total angular momentum and the full grid must be included in the calculation of a given total energy. Then, we need to test several approaches to overcome this computational challenge. We decided to test two possibilities:

- Restrict the use of the recoupling approach to an interaction of a molecule with a structureless atom, *i.e.* neglecting the structure of H_2 .
- Use the IOS approximation including the two nuclear spins of the target and the structure of molecular hydrogen.

To estimate the accuracy of these tests, comparisons will be done with respect to the recoupling method including one nuclear spin and the structure of H_2 . The $\text{C}_2\text{H-H}_2$ collisional system will be our reference for testing these methods.

In the case of ^{13}CCH and C^{13}CH , we can take advantage that they are detected mostly in cold astrophysical environments (~ 10 K) so that eventually, only the *para*- $\text{H}_2(j_2=0)$ rotational state will be significantly populated compared to excited states. The reduction of the dimension of the system goes by restricting the degrees of freedom of the 4D PES to 2D (see Fig. 3.10).

To mimic a 2D PES from a 4D one, we start from the analytical representation given by Eq. (2.29) that we can re-write as:

$$V(R, \theta_1, \theta_2, \phi) = \sum_{\lambda_1 \lambda_2 \lambda} v_{\lambda_1 \lambda_2 \lambda}(R) \sum_{(m)} C_{m_{\lambda_1} m_{\lambda_2} m}^{\lambda_1 \lambda_2 \lambda} Y_{\lambda_1 m_{\lambda_1}}(\theta_1, 0) \times Y_{\lambda_2 m_{\lambda_2}}(\theta_2, \phi) Y_{\lambda m}^*(\Theta, \Phi) \quad (3.31)$$

where the $Y_{\alpha\beta}$ are spherical harmonics and (Θ, Φ) are the relative angles of the molecular complex (see Fig. 2.7). We set $j_2=0$ so that only terms with $\lambda_2 = 0$ will remain. Then, we will have $\lambda_1 \equiv \lambda$ and:

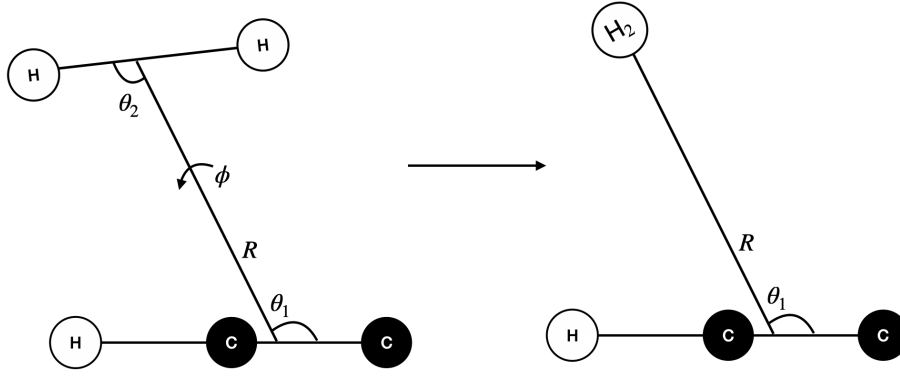


Figure 3.10 – Illustration of the dimensional reduction of the 4D PES for the C_2H-H_2 collisional system.

- $Y_{\lambda m}^*(\Theta, \Phi) \rightarrow Y_{\lambda m}^*(0, 0) = [(2\lambda + 1)/(4\pi)]^{1/2} \delta_{m0}$ (see Green [59])
- $C_{m_{\lambda_1} m_{\lambda_2} m}^{\lambda_1 \lambda_2 \lambda} \rightarrow C_{000}^{\lambda 0 \lambda} = 1$
- $Y_{\lambda_1 m_{\lambda_1}}(\theta_1, 0) \rightarrow Y_{\lambda 0}(\theta_1, 0) = [(2\lambda + 1)/(4\pi)]^{1/2} P_{\lambda}(\cos \theta_1)$
- $Y_{\lambda_2 m_{\lambda_2}}(\theta_2, \phi) \rightarrow Y_{00}(\theta_2, \phi) = 1/(4\pi)^{1/2}$

We can see that the dependence in (θ_2, ϕ) drops and the analytical formula for a 2D PES becomes:

$$\begin{aligned}
 V(R, \theta_1) &= \sum_{\lambda} v_{\lambda 0 \lambda}(R) \frac{(2\lambda + 1)}{(4\pi)^{3/2}} P_{\lambda}(\cos \theta_1) \\
 &\equiv \sum_{\lambda} v_{\lambda}^{sph}(R) P_{\lambda}(\cos \theta_1)
 \end{aligned} \tag{3.32}$$

Then, one has to multiply the expansion coefficients $v_{\lambda 0 \lambda}(R)$ from the 4D PES by $(2\lambda + 1)/(4\pi)^{3/2}$ to obtain the form of the 2D PES. In practice, it makes that only 13 out of the 174 expansion coefficients for the 4D PES of the C_2H-H_2 collisional system will be used in scattering calculations, reducing drastically the computational time. For dynamical calculations, one can substitute $I_2 = 0$ in section 3.3.2 to obtain hyperfine rate coefficients for the case with one nuclear spin with the 4D PES ($k_{N_{j_1} F}^{AD-rec}(T)$) (see also Offer *et al.* [201]) and also $j_2 = 0$ for the case of a molecule/atom interaction with the 2D PES ($k_{N_{j_1} F}^{2D-rec}(T)$) (see also Daniel *et al.* [204]).

In the case of the IOS approximation, we used the formula developed by Alexander [205] in the Hund's case (a) and generalized to hyperfine transitions by Faure & Lique [83]:

$$\begin{aligned}
 k_{Nj_1F \rightarrow N'j'_1F'}^{\text{IOS}}(T) &= [j_1][j'_1][F'] \sum_{\lambda} \frac{[\lambda]}{\lambda+1} \\
 &\times \left(\begin{array}{ccc} j'_1 & \lambda & j_1 \\ -\frac{1}{2} & 0 & \frac{1}{2} \end{array} \right)^2 \left\{ \begin{array}{ccc} j_1 & j'_1 & \lambda \\ F' & F & I(\text{H}) \end{array} \right\}^2 \\
 &\times \frac{1}{2} [1 + \epsilon(-1)^{j_1+j'_1+\lambda}] k_{0, \frac{1}{2} \rightarrow \lambda, \lambda + \frac{1}{2}}^{\text{CC}}(T)
 \end{aligned} \tag{3.33}$$

where ϵ is the parity index, $I(\text{H})$ is the nuclear spin of the hydrogen and $|j_1 - j'_1| < \lambda < j_1 + j'_1$. Here we replace IOS transitions by those of CC out of the fundamental level $N_{j_1} = 0_{1/2}$. To prevent too many deviations at low temperatures, we can apply a scaling relation proposed by Neufeld & Green [206] as:

$$k_{Nj_1F \rightarrow N'j'_1F'}^{\text{NG}}(T) = \frac{k_{Nj_1F \rightarrow N'j'_1F'}^{\text{IOS}}(T)}{k_{Nj_1 \rightarrow N'j'_1}^{\text{IOS}}(T)} k_{Nj_1 \rightarrow N'j'_1}^{\text{CC}}(T) \tag{3.34}$$

This scaling relation satisfies the following condition

$$\sum_{F'} k_{Nj_1F \rightarrow N'j'_1F'}^{\text{NG}}(T) = k_{Nj_1 \rightarrow N'j'_1}^{\text{CC}}(T) \tag{3.35}$$

It should be noted that Eq. (3.34) necessitates elastic rate coefficients (with $N = N'$ and $j_1 = j'_1$) to compute hyperfine *quasi-elastic* transitions (with $N = N'$, $j_1 = j'_1$ and $F \neq F'$). However, these are usually hard to converge and we will not provide them. Quasi-elastic transitions will be then computed through Eq. (3.33).

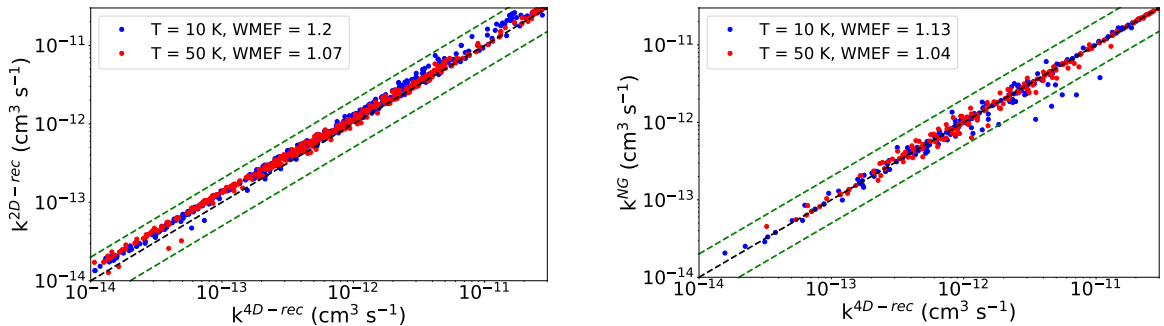


Figure 3.11 – Systematic comparison of hyperfine rate coefficients for the $\text{C}_2\text{H}-\text{H}_2$ collisional system between recoupling approach in reduced dimension of the PES (left) and IOS approximation (right) with respect to recoupling method including the 4D PES. Dashed lines represent deviations by a factor of 2.

Results of these tests appear in Fig. 3.11. We can see that both methods seem to be consistent with respect to the reference method. This can be highlighted by computing the *Weighted Mean Error Factor* (WMEF) [97] which quantifies deviations according to the magnitude of the rate coefficients. This is defined as:

$$\text{WMEF} = \frac{\sum_i k_i^{\text{4D-rec}} r_i}{\sum_i k_i^{\text{4D-rec}}} \quad (3.36)$$

where the index corresponds to the i^{th} transition. $r_i = \max(k_i^{\text{4D-rec}}/k_i^{\text{2D/NG}}, k_i^{\text{2D/NG}}/k_i^{\text{4D-rec}})$ so that $r_i \geq 1$. In both cases, the WMEF is of the same order of magnitude (deviations within 20% for most of transitions) and both methods could be applicable for data production for $^{13}\text{CCH-H}_2$ and $\text{C}^{13}\text{CH-H}_2$. In particular, IOS calculations perform very well even at low temperatures, probably due to the low space between energy levels and to the NG correction. It should be noted that some transitions deviate by more than a factor of 2. These are attributed to the quasi-elastic transitions, provided without the NG correction. Finally, we decided to choose the reduced dimension approach with the recoupling method for the treatment of the ^{13}C isotopologues. In fact, this is the method in which only one approximation was done, and also because differences are quasi systematically overestimating the 2D calculations. We do not retain the IOS approach here because of the inconsistency in the calculations between quasi-elastic transitions and others.

NH–H₂ and ND–H₂

Contrary to ^{13}CCH and C^{13}CH , the NH molecule is detected both in cold and warm environments ($T > 100$ K), and ignoring the structure of H_2 would probably involve significant errors in astrophysical modeling, since *ortho*- $\text{H}_2(j_2 = 1)$ is expected to be populated in these temperature regimes. Then, the IOS approach would probably remain a correct alternative. However, formalism describing hyperfine resolved transitions through the IOS approximation for a $^3\Sigma$ molecule in collision with a projectile with $j_2 \neq 0$ was not available in the literature. Then, we decided to propose a formulation for such type of systems. From Eq. (3.30), we will write the fine structure cross section $\sigma_{Nj_1j_2 \rightarrow N'j_1'j_2'}^{\text{IOS}}$ expressed as a function of the transition out of the initial level $N_{j_1} = 1_0$. Then, for the projectile we will distinguish two cases: *para*- H_2 by setting $j_2 = 0$ and in parallel *ortho*- H_2 with $j_2 = 1$.

Considering *para*- H_2 , we set $N = 1$, $j_1 = 0$, $S = 1$ and $j_2 = 0$ in Eq. (3.30) and we label the cross section for *para*- H_2 with the superscript IOS-p. It simplifies to:

$$\begin{aligned} \sigma_{100 \rightarrow N' j'_1 j'_2}^{\text{IOS-p}} &= \frac{[N' j'_1 j'_2]}{3} \sum_{\lambda_1 \lambda_2 \lambda} \begin{pmatrix} N' & \lambda_1 & 1 \\ 0 & 0 & 0 \end{pmatrix}^2 \begin{pmatrix} j'_2 & \lambda_2 & 0 \\ 0 & 0 & 0 \end{pmatrix}^2 \\ &\times \left\{ \begin{matrix} 0 & 1 & 1 \\ N' & j'_1 & \lambda_1 \end{matrix} \right\}^2 \sigma_{\lambda_1 \lambda_2 \lambda} \end{aligned} \quad (3.37)$$

The $3j$ and $6j$ symbols are together nonzero for $j'_1 = \lambda_1$, $N' = \lambda_1 + 1$ and $N' = \lambda_1 - 1$. For the next steps, we will only keep the case where $N' = \lambda_1 + 1$. For the collider, the non cancellation corresponds to $j'_2 = \lambda_2$. Eq. (3.37) gives

$$\begin{aligned} \sigma_{100 \rightarrow \lambda_1 + 1, \lambda_1 \lambda_2}^{\text{IOS-p}} &= \frac{[\lambda_1 + 1][\lambda_1 \lambda_2]}{3} \begin{pmatrix} \lambda_1 + 1 & \lambda_1 & 1 \\ 0 & 0 & 0 \end{pmatrix}^2 \begin{pmatrix} \lambda_2 & \lambda_2 & 0 \\ 0 & 0 & 0 \end{pmatrix}^2 \left\{ \begin{matrix} 0 & 1 & 1 \\ \lambda_1 + 1 & \lambda_1 & \lambda_1 \end{matrix} \right\}^2 \sigma_{\lambda_1 \lambda_2 \lambda} \\ \sigma_{\lambda_1 \lambda_2 \lambda} &= \frac{3 \times \sigma_{100 \rightarrow \lambda_1 + 1, \lambda_1 \lambda_2}^{\text{IOS-p}}}{[\lambda_1 + 1][\lambda_1 \lambda_2] \begin{pmatrix} \lambda_1 + 1 & \lambda_1 & 1 \\ 0 & 0 & 0 \end{pmatrix}^2 \begin{pmatrix} \lambda_2 & \lambda_2 & 0 \\ 0 & 0 & 0 \end{pmatrix}^2 \left\{ \begin{matrix} 0 & 1 & 1 \\ \lambda_1 + 1 & \lambda_1 & \lambda_1 \end{matrix} \right\}^2} \end{aligned} \quad (3.38)$$

It is possible to replace Eq. (3.38) into Eq. (3.30) such that

$$\begin{aligned} \sigma_{N j_1 j_2 \rightarrow N' j'_1 j'_2}^{\text{IOS-p}} &= \frac{[N N' j'_1 j'_2]}{[S]^2} \sum_{\lambda_1 \lambda_2 \lambda} \frac{\begin{pmatrix} N' & \lambda_1 & N \\ 0 & 0 & 0 \end{pmatrix}^2 \begin{pmatrix} j'_2 & \lambda_2 & j_2 \\ 0 & 0 & 0 \end{pmatrix}^2 \left\{ \begin{matrix} j_1 & N & S \\ N' & j'_1 & \lambda_1 \end{matrix} \right\}^2}{\begin{pmatrix} \lambda_1 + 1 & \lambda_1 & 1 \\ 0 & 0 & 0 \end{pmatrix}^2 \begin{pmatrix} \lambda_2 & \lambda_2 & 0 \\ 0 & 0 & 0 \end{pmatrix}^2 \left\{ \begin{matrix} 0 & 1 & 1 \\ \lambda_1 + 1 & \lambda_1 & \lambda_1 \end{matrix} \right\}^2} \\ &\times \frac{3 \times \sigma_{100 \rightarrow \lambda_1 + 1, \lambda_1 \lambda_2}^{\text{IOS-p}}}{[\lambda_1 + 1][\lambda_1 \lambda_2]} \end{aligned} \quad (3.39)$$

By analyzing the $3j$ and $6j$ symbols, it is possible to see that

•

$$\frac{1}{[S] \left\{ \begin{matrix} 0 & 1 & 1 \\ \lambda_1 + 1 & \lambda_1 & \lambda_1 \end{matrix} \right\}^2} \equiv [\lambda_1]$$

•

$$\frac{1}{[\lambda_1 + 1] \begin{pmatrix} \lambda_1 + 1 & \lambda_1 & 1 \\ 0 & 0 & 0 \end{pmatrix}^2} \equiv \frac{[\lambda_1]}{\lambda_1 + 1}$$

•

$$\frac{1}{[\lambda_2] \begin{pmatrix} \lambda_2 & \lambda_2 & 0 \\ 0 & 0 & 0 \end{pmatrix}^2} \equiv 1$$

Eq. (3.39) is greatly simplified to

$$\begin{aligned} \sigma_{Nj_1j_2 \rightarrow N'j'_1j'_2}^{\text{IOS-p}} &= [NN'j'_1] \sum_{\lambda_1\lambda_2} \frac{[\lambda_1]}{\lambda_1+1} \begin{pmatrix} N' & \lambda_1 & N \\ 0 & 0 & 0 \end{pmatrix}^2 \begin{pmatrix} j'_2 & \lambda_2 & j_2 \\ 0 & 0 & 0 \end{pmatrix}^2 \\ &\times \left\{ \begin{matrix} j_1 & N & S \\ N' & j'_1 & \lambda_1 \end{matrix} \right\}^2 \sigma_{100 \rightarrow \lambda_1+1, \lambda_1 \lambda_2}^{\text{IOS-p}} \end{aligned} \quad (3.40)$$

We can also express the fundamental cross section as a function of the de-excited cross section toward the fundamental level through the detailed balance

$$\sigma_{100 \rightarrow \lambda_1+1, \lambda_1 \lambda_2}^{\text{IOS-p}} = [\lambda_1 \lambda_2] \sigma_{\lambda_1+1, \lambda_1 \lambda_2 \rightarrow 100}^{\text{IOS-p}}$$

The extension to the hyperfine structure formula is given by multiplying the fine structure cross section by the proper statistical weights and $6j$ symbols [39] to obtain the final expression:

$$\begin{aligned} \sigma_{Nj_1F_1F_2 \rightarrow N'j'_1F'_1F'_2}^{\text{IOS-p}} &= [NN'j_1j'_1F_1F'_1F'_2] \sum_{\lambda_1\lambda_2} \frac{[\lambda_1]}{\lambda_1+1} \begin{pmatrix} N' & \lambda_1 & N \\ 0 & 0 & 0 \end{pmatrix}^2 \\ &\times \begin{pmatrix} j'_2 & \lambda_2 & j_2 \\ 0 & 0 & 0 \end{pmatrix}^2 \left\{ \begin{matrix} N' & N & \lambda_1 \\ j_1 & j'_1 & S \end{matrix} \right\}^2 \\ &\times \left\{ \begin{matrix} j_1 & j'_1 & \lambda_1 \\ F'_1 & F_1 & I_X \end{matrix} \right\}^2 \left\{ \begin{matrix} F_1 & F'_1 & \lambda_1 \\ F' & F & I_N \end{matrix} \right\}^2 \\ &\times \sigma_{100 \rightarrow \lambda_1+1, \lambda_1, \lambda_2}^{\text{IOS-p}} \end{aligned} \quad (3.41)$$

with $X \equiv \text{H or D}$.

Now, similarly to *para*-H₂, we still set $N = 1$, $j_1 = 0$, $S = 1$ but the fundamental level of *ortho*-H₂ will be $j_2 = 1$. We label the following equations by the superscript IOS-o. Reporting in Eq. (3.30) we have

$$\begin{aligned}\sigma_{101 \rightarrow N' j'_1 j'_2}^{\text{IOS-o}} &= \frac{[N' j'_1 j'_2]}{3} \sum_{\lambda_1 \lambda_2 \lambda} \begin{pmatrix} N' & \lambda_1 & 1 \\ 0 & 0 & 0 \end{pmatrix}^2 \begin{pmatrix} j'_2 & \lambda_2 & 1 \\ 0 & 0 & 0 \end{pmatrix}^2 \\ &\times \left\{ \begin{matrix} 0 & 1 & 1 \\ N' & j'_1 & \lambda_1 \end{matrix} \right\}^2 \sigma_{\lambda_1 \lambda_2 \lambda}\end{aligned}\quad (3.42)$$

As the same as earlier, the $3j$ and $6j$ symbols are together nonzero for $j'_1 = \lambda_1$, $\lambda_1 = N' + 1$ but this time it is also nonzero for $j'_2 = \lambda_2 + 1$. With only the non vanishing terms we simplify Eq. (3.42) to

$$\begin{aligned}\sigma_{101 \rightarrow \lambda_1+1, \lambda_1, \lambda_2+1}^{\text{IOS-o}} &= \frac{[\lambda_1 + 1][\lambda_1][\lambda_2 + 1]}{3} \begin{pmatrix} \lambda_1 + 1 & \lambda_1 & 1 \\ 0 & 0 & 0 \end{pmatrix}^2 \begin{pmatrix} \lambda_2 + 1 & \lambda_2 & 1 \\ 0 & 0 & 0 \end{pmatrix}^2 \\ &\times \left\{ \begin{matrix} 0 & 1 & 1 \\ \lambda_1 + 1 & \lambda_1 & \lambda_1 \end{matrix} \right\}^2 \sigma_{\lambda_1 \lambda_2 \lambda} \\ \sigma_{\lambda_1 \lambda_2 \lambda} &= \frac{1}{\begin{pmatrix} \lambda_1 + 1 & \lambda_1 & 1 \\ 0 & 0 & 0 \end{pmatrix}^2 \begin{pmatrix} \lambda_2 + 1 & \lambda_2 & 1 \\ 0 & 0 & 0 \end{pmatrix}^2 \left\{ \begin{matrix} 0 & 1 & 1 \\ \lambda_1 + 1 & \lambda_1 & \lambda_1 \end{matrix} \right\}^2} \\ &\times \frac{3 \times \sigma_{101 \rightarrow \lambda_1+1, \lambda_1, \lambda_2+1}^{\text{IOS-o}}}{[\lambda_1 + 1][\lambda_1][\lambda_2 + 1]}\end{aligned}\quad (3.43)$$

It is possible to simplify Eq. (3.30) with the same analysis than the previous case. Just here there is an additional term

$$\frac{1}{[\lambda_2 + 1] \begin{pmatrix} \lambda_2 + 1 & \lambda_2 & 1 \\ 0 & 0 & 0 \end{pmatrix}^2} \equiv \frac{[\lambda_2]}{\lambda_2 + 1}$$

and the fine structure cross section will be

$$\begin{aligned}\sigma_{N j_1 j_2 \rightarrow N' j'_1 j'_2}^{\text{IOS-o}} &= [N N' j'_1 j'_2] \sum_{\lambda_1 \lambda_2 \lambda} \begin{pmatrix} N' & \lambda_1 & N \\ 0 & 0 & 0 \end{pmatrix}^2 \begin{pmatrix} j'_2 & \lambda_2 & j_2 \\ 0 & 0 & 0 \end{pmatrix}^2 \left\{ \begin{matrix} j_1 & N & S \\ N' & j'_1 & \lambda_1 \end{matrix} \right\}^2 \\ &\times \frac{[\lambda_1]}{\lambda_1 + 1} \frac{[\lambda_2]}{\lambda_2 + 1} \sigma_{101 \rightarrow \lambda_1+1, \lambda_1, \lambda_2+1}^{\text{IOS-o}}\end{aligned}\quad (3.44)$$

with the detailed balance

$$\sigma_{101 \rightarrow \lambda_1+1, \lambda_1, \lambda_2+1}^{\text{IOS-o}} = \frac{[\lambda_1][\lambda_2+1]}{3} \sigma_{\lambda_1+1, \lambda_1, \lambda_2+1 \rightarrow 101}^{\text{IOS-o}}$$

Finally, hyperfine cross section through the IOS approximation with *ortho*-H₂ is

$$\begin{aligned} \sigma_{N j_1 F_1 j_2 \rightarrow N' j'_1 F'_1 j'_2}^{\text{IOS-o}} &= [N N' j_1 j'_1 F_1 F'_1 j_2 j'_2] \sum_{\lambda_1 \lambda_2} \frac{[\lambda_1]}{\lambda_1+1} \frac{[\lambda_2]}{\lambda_2+1} \\ &\times \begin{pmatrix} N' & \lambda_1 & N \\ 0 & 0 & 0 \end{pmatrix}^2 \begin{pmatrix} j'_2 & \lambda_2 & j_2 \\ 0 & 0 & 0 \end{pmatrix}^2 \left\{ \begin{matrix} N' & N & \lambda_1 \\ j_1 & j'_1 & S \end{matrix} \right\}^2 \\ &\times \left\{ \begin{matrix} j_1 & j'_1 & \lambda_1 \\ F'_1 & F_1 & I_X \end{matrix} \right\}^2 \left\{ \begin{matrix} F_1 & F'_1 & \lambda_1 \\ F' & F & I_N \end{matrix} \right\}^2 \\ &\times \sigma_{101 \rightarrow \lambda_1+1, \lambda_1, \lambda_2+1}^{\text{IOS-o}} \end{aligned} \quad (3.45)$$

Eqs. (3.41) and (3.45) can be used to describe the hyperfine excitation of a molecule in a ³Σ electronic state in collision with a linear closed-shell molecule. We tested this approach including only one nuclear spin *I*(H) or *I*(D) using the NG correction given by Eq. (3.34) and compared it with the recoupling approach for the NH–H₂ and ND–H₂ collisional systems.

Fig. 3.12 displays comparisons between these two methods. One can see that most of transitions are in agreement within a factor of 2 between IOS and recoupling. Especially, even cross sections with the largest magnitude match almost perfectly between the two approximations in the two sets of collisional energies. It was expected that IOS calculations improve the agreement at high energies. The WMEF shows almost a similar order of magnitude for all samples except for *ortho*-H₂ collisions, showing larger discrepancies than for *para*-H₂ collisions. This is due to some transitions at 50 cm⁻¹ that are deviating by more than a factor of 2 and correspond to quasi-elastic transitions. As mentioned earlier, these cannot be predicted with the NG correction and were computed only with Eqs. (3.41) and (3.45). Also, the energy of the fundamental level of *ortho*-H₂ which is not zero and then expected to be badly predicted by the IOS approximation. It should be noted that the derivation of this formulae has been done assuming a pure Hund's case (b) because the incorporation of the intermediate coupling was not easy to handle, even though we used fine structure cross sections presented in section 3.2.2, computed in the intermediate coupling. However, NH and ND being light molecules, we expect a weak intermediate coupling and that this approximation will have a minor impact on the results. Finally, we decided to use this approach for data production, as results are in agreement with the reference method between ~10–50% for most of the tested transitions. Since the coupling of the nuclear spin of the nitrogen is even weaker than the one of hydrogen or

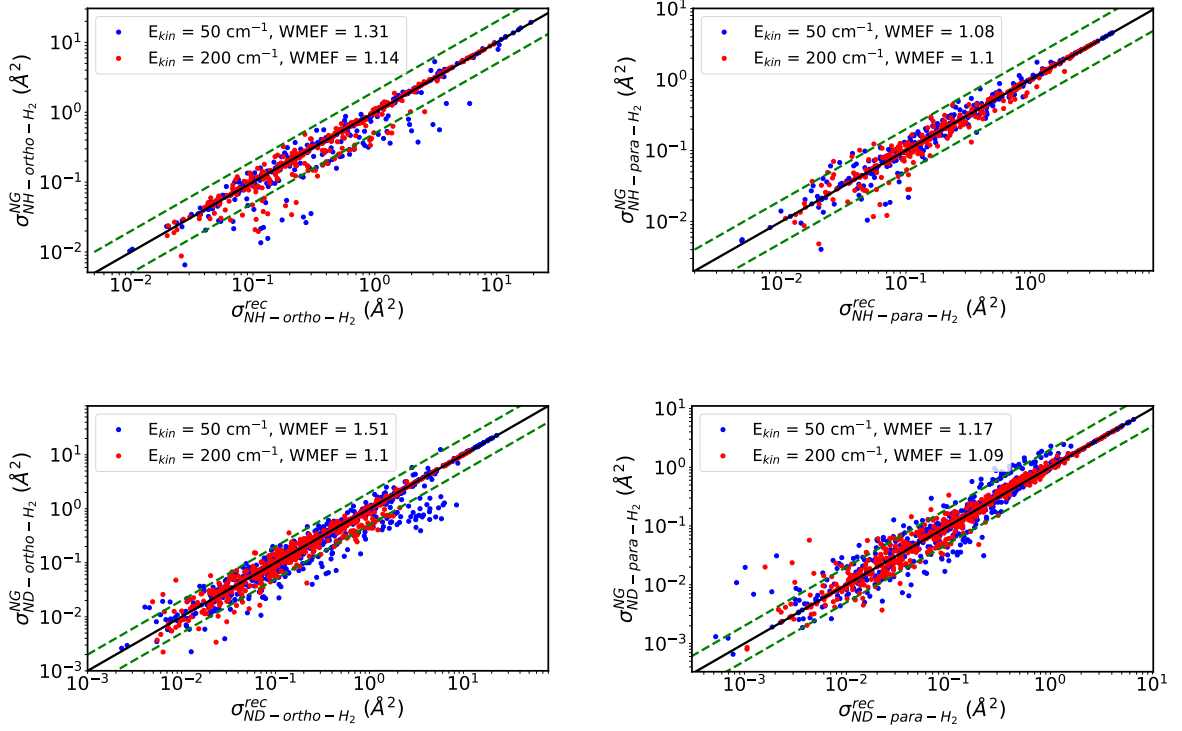


Figure 3.12 – Systematic comparison of two samples of cross sections for NH (top) and ND (bottom) collisions with both *ortho*-H₂ (left) and *para*-H₂ (right) between NG and recoupling calculations. Quasi-elastic transitions provided with the IOS approach are also incorporated. Dashed lines represent deviations by a factor of 2.

deuterium, we assume that its inclusion in scattering calculations will not involve large errors.

Scattering calculations

Scattering calculations have been done with the HIBRIDON software [80] for the treatment of C₂H and its isotopologues. Hyperfine excitation of C₂H and C₂D by molecular hydrogen was done using the recoupling approach without any more approximation. Scattering calculations have been performed including the 38 first hyperfine levels of C₂H and the first 55 levels of C₂D up to 100 K. We estimate that these calculations required less than 500 000 CPU hours for both systems using the TGCC supercomputer. On the other hand, calculations for ¹³CCH and C¹³CH in collision with *sph*-H₂ included the 98 first energy levels of the isotopologues up to 100 K. This was estimated to require \sim 500 000 CPU hours between the Physix cluster and the TGCC supercomputer. Finally, hyperfine calculations for the NH–H₂ and ND–H₂ collisional systems took less than five minutes on a laptop.

No anomaly were found in the propensity rules followed by hyperfine rate coefficients. All rules previously described in section 3.2.2 for the fine structure discussion stand also for hyperfine structure rate coefficients as they follow the same logic of preserving the orientation of the rotational angular momentum and tend to minimize the transfer of angular momentum during a collision. These rules are already discussed by Alexander & Dagdigan [82] and are well known for many systems as *e.g.* for the case with one nuclear spin [207], [208] or with two nuclear spins [173], [204].

3.4 Astrophysical modeling

Once fine and hyperfine resolved rate coefficients are computed, it is possible to test their impact in radiative transfer modeling under non-LTE conditions. We will present parts of applications that have been done for the NH, C₂D, ¹³CCH and C¹³CH molecules where details can be found in Pirlot Jankowiak *et al.* [193]–[195]. These modelings have been done using the RADEX public software [209]. Discussion about the excitation of C₂H in the ISM has been done by Dagdigan [153] and will not be treated here.

3.4.1 Critical density

Because of their different spectroscopic properties, all molecules do not behave the same to the competition between energy transfer mechanisms. This can have an impact on the critical density, which is a rough indicator of the gas density where a given energy level u is (de)populated equivalently between radiative and collisional processes, as explained in section 2.5.5. When the contribution of both *ortho*- and *para*-H₂ is included in rate coefficients, the critical density is computed as:

$$\begin{aligned} n_{\text{cr}}^u(T) &= \frac{\sum_{i<u} A_{ui}}{\sum_{u\neq i} k_{ui}(T)} \\ &= \frac{\sum_{i<u} A_{ui}}{\sum_{u\neq i} \left[\frac{\text{OPR}}{1+\text{OPR}} k_{ui}^{\text{ortho-H}_2}(T) + \frac{1}{1+\text{OPR}} k_{ui}^{\text{para-H}_2}(T) \right]} \end{aligned} \quad (3.46)$$

with OPR is the *ortho*-to-*para*-H₂ ratio assumed to follow a thermal distribution, A_{ui} and k_{ui} are the Einstein and rate coefficient for a transition $u \rightarrow i$, respectively. We applied the Einstein coefficients for hyperfine transitions from the CDMS [37].

Fig. 3.13 displays several critical densities for hyperfine energy levels of C₂H isotopologues and NH. While critical densities for some of the first hyperfine components of the $N = 1$ level are similar between C₂H isotopologues ($\sim 10^4 - 10^5 \text{ cm}^{-3}$), those of NH are

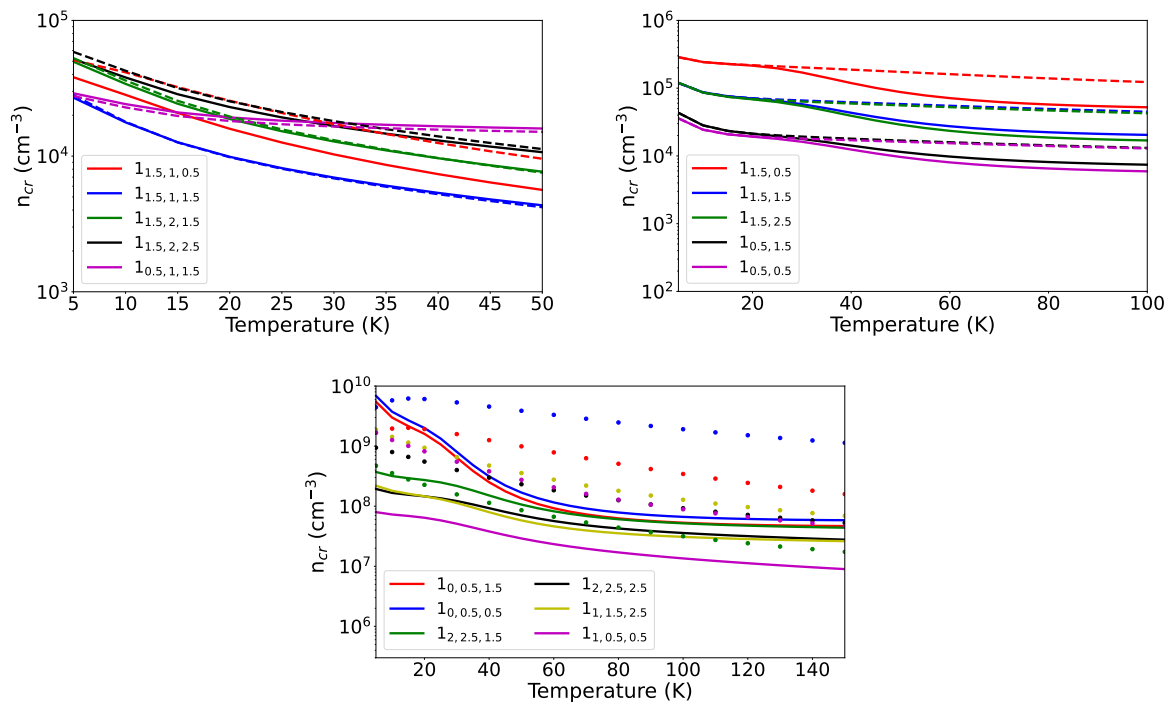


Figure 3.13 – Evolution of the critical density with the temperature for several hyperfine transitions. Left panel: C^{13}CH (solid) and ^{13}CCH (dashed). Right panel: C_2D including *ortho*- and *para*- H_2 collisions (solid), and only *para*- H_2 collisions (dashed). Bottom panel: NH including collisions with molecular hydrogen (solid) and with He (dotted).

much larger by several orders of magnitude ($\sim 10^7 - 10^{10} \text{ cm}^{-3}$). This is clearly due to their different moment of inertia, leading to differences in rotational constants and then to transitions between energy levels. As Einstein coefficients are proportional to the cubic of the frequency, the major difference will come from these quantities, as rate coefficients are approximately of the same order of magnitude for most of these systems. We can note more and more discrepancies between critical densities with the temperature when including collisions with *ortho*- H_2 . This is expected since the $j_2 = 1$ rotational state of H_2 is more and more populated with the temperature, as shown for example in the case of C_2D . Finally, since rate coefficients for He collisions are lower than those for H_2 collisions, we can mention strong discrepancies in the magnitude of the critical densities for hyperfine levels of NH , up to a factor of 10.

Of course, it is hard to estimate correctly the critical density when collisional data are not available, but then it can serve to predict possible non-LTE behavior of transitions that are not observed yet, and orient the interest for a given molecule.

3.4.2 Excitation of C₂H isotopologues in star-forming regions

We restrict radiative transfer modeling for cold environments in which the C₂H isotopologues are detected as *e.g.* in L1521B, L134N [181], TMC-1 [137], L1527 [140] L1544 or HH211 [182]. For all systems, we will assume a kinetic temperature $T_{kin} = 10$ K, a background temperature as the one of the Cosmic Microwave Background (CMB) $T_{bg} = 2.73$ K, a typical column density of $N = 10^{13}$ cm⁻² and a linewidth of 0.5 km s⁻¹ to make sure that all studied lines are optically thin. Einstein coefficients were taken from CDMS [37]. We adopted a uniform sphere geometry in the use of the escape probability from RADEX.

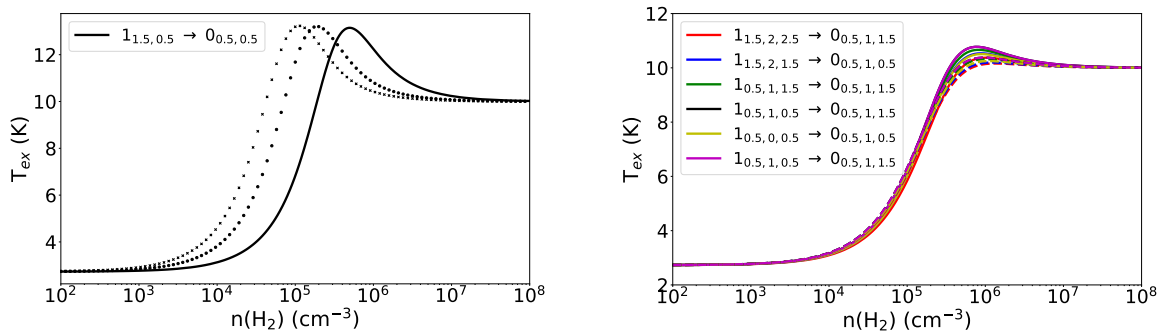


Figure 3.14 – Evolution of the excitation temperature with the molecular gas density $n(\text{H}_2)$ for $T_{kin} = 10$ K for hyperfine component of the $N = 1 \rightarrow 0$ rotational line. Left panel: For C₂D with 100% of *para*-H₂ (solid), 25% of *ortho*-H₂ (dotted) and 75% of *ortho*-H₂ (crossed). Right panel: For C¹³CH (solid) and ¹³CCH (dashed).

Fig. 3.14 presents excitation temperatures for some detected lines of ¹³CCH and C¹³CH, and for one line of C₂D. From these curves, we can distinguish three regimes. For low densities, values converge toward T_{bg} characterizing the radiative regime, when the excitation is dominated by radiations. Then, for intermediate densities, we observe $T_{bg} < T_{ex} < T_{kin}$ showing non-LTE behavior. Finally the excitation temperature converges to T_{kin} for large densities, where collisions are dominant satisfying the LTE regime.

We can see for C₂D the influence of the collider in excitation temperature. The LTE regime is reached for lower densities when incorporating more and more *ortho*-H₂ in the composition of the gas kinetics. This is due to the larger rate coefficients for *ortho*-H₂ collisions than those for *para*-H₂ collisions, making collisions more efficient for *ortho*-H₂ than *para*-H₂. Of course at 10 K, the presence of molecular hydrogen in $j_2 = 1$ state is negligible but this serves as an illustrative example.

On the other hand, all presented transitions for ¹³CCH and C¹³CH do not present significant differences. As their spectroscopic constants are very similar and rate coefficients

between these two molecules being different by $\sim 30\%$ at worst, we cannot conclude that each molecule has its own excitation, at least at very low temperature.

As pointed out by many authors, ^{13}CCH and C^{13}CH present an anomaly in their abundance ratio of $[\text{C}^{13}\text{CH}]/[^{13}\text{CCH}] \sim 1.2\text{--}2.2$ depending on the medium. This means either that these isotopologues present significant different formation pathways, or that they are not presenting the same excitation in the ISM. It is interesting to test the second possibility with our new collisional data.

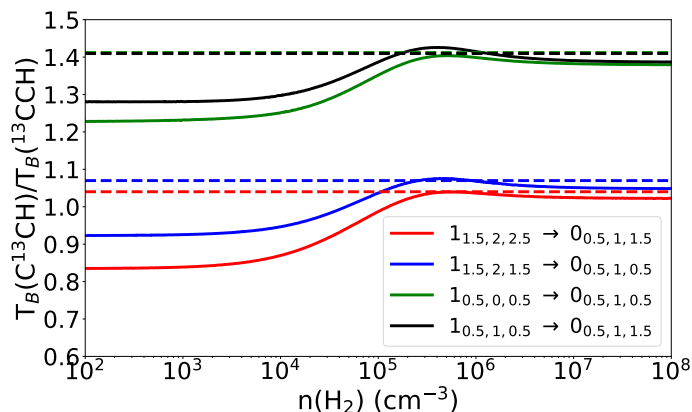


Figure 3.15 – Ratio of brightness temperatures between C^{13}CH and ^{13}CCH hyperfine lines. Dashed curves represent the ratio of the corresponding Einstein coefficients.

Fig. 3.15 displays the ratio of the brightness temperatures of the two isotopologues for a given hyperfine transition. This ratio remains in agreement with the ratio of the Einstein coefficient by $\sim 10\%$ over the range of molecular gas kinetics. This is not enough to assess that collisional excitation has a true impact on the brightness temperature of these molecules. We can just mention that since rate coefficients for $^{13}\text{CCH}\text{--}sph\text{--H}_2$ collisions are almost systematically larger than for $\text{C}^{13}\text{CH}\text{--}sph\text{--H}_2$ collisions, leading to a tendency to excite more ^{13}CCH than C^{13}CH . This would enhance the brightness temperatures for ^{13}CCH which decreases the isotopic ratio of T_B and would worsen this anomaly.

Moving to C_2D , we investigated the determination of the column density $N(\text{C}_2\text{D})$ and the gas kinetics $n(\text{H}_2)$ with our new set of rate coefficients and compared it with the one computed by Yoshida *et al.* [140] under the LTE assumption for observations of hyperfine lines of the $N = 1 \rightarrow 0$ (72 GHz) rotational line in L1527. To do so, we fixed $T_{kin} = 10$ K and run RADEX for $N(\text{C}_2\text{D}) = [10^{12}\text{--}10^{14}] \text{ cm}^{-2}$ and $n(\text{H}_2) = [5 \times 10^5 - 3 \times 10^6] \text{ cm}^{-3}$. For each tuple $(N(\text{C}_2\text{D}), n(\text{H}_2))$, we compared the computed integrated intensity for several hyperfine transitions to observations in order to minimize the χ^2 parameter:

$$\chi^2 = \sum_{i=1}^M \left(\frac{F_i^{obs} - F_i^{calc}}{\sigma_i} \right)^2 \quad (3.47)$$

where M is the number of transitions, F_i^{obs} and F_i^{calc} are the observed and computed integrated intensities, respectively. σ_i is the uncertainty of the i^{th} observation.

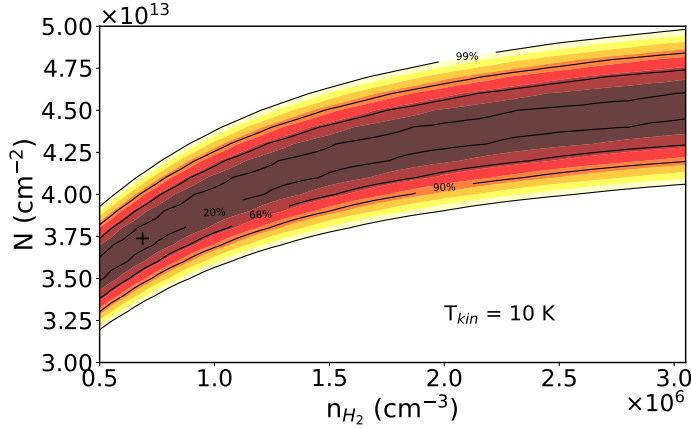


Figure 3.16 – Contour plots of the χ^2 parameter for a range of column densities (y axis) and density of the gas (x axis) for $T_{kin} = 10$ K. The crossed dot represents the minimum value χ_{min}^2 .

Fig. 3.16 presents values of the statistical test χ^2 for different column densities and gas densities. We can see that our procedure fails in constraining the density. The column density best reproducing observations is found to be within $N(\text{C}_2\text{D}) = (3.2\text{--}4.9) \times 10^{13} \text{ cm}^{-2}$ within a confidence of 99% [210]. The value corresponding to the best solution χ_{min}^2 is $N(\text{C}_2\text{D}) = 3.7 \times 10^{13} \text{ cm}^{-2}$. An illustration of the best solution can be seen in Fig. 3.17². These results are in agreement up to a factor ~ 1.5 with observations, where the LTE assumption gave $N(\text{C}_2\text{D}) = (4.7 \pm 0.3) \times 10^{13} \text{ cm}^{-2}$. This set of rate coefficients can be then useful for further observations in less dense regions, where non-LTE effects should be more visible.

2. Some lines are shifted between observations and our calculations. Yoshida *et al.* [140] reported differences between observed frequencies and those provided in the CDMS [37], that we used here.

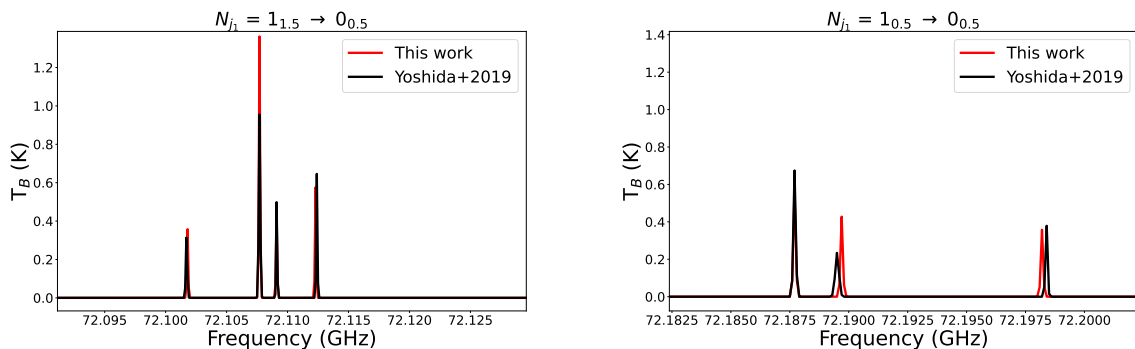


Figure 3.17 – Synthetic spectra of the observed (black) and computed (red) hyperfine components of the $N = 1 \rightarrow 0$ rotational line of C_2D corresponding to our best estimation (χ_{min}^2).

3.4.3 Excitation of NH in the η Carinae binary star system

Gull *et al.* [164] reported detection of the fine structure transitions of the $N = 1 \rightarrow 0$ rotational line of the NH molecule in emission toward the ejecta of the η Carinae binary star system. They estimated the column density of NH to be $N(NH) = 5 \times 10^{15} \text{ cm}^{-2}$ through non-LTE modeling based on estimation of rate coefficients when these were not available. It is interesting to test the sensitivity of our new data in the determination of the column density. Since the hyperfine structure of NH is not resolved in the survey, we will use the fine structure collisional rate coefficients. It should be noted that fine structure Einstein coefficients were not available on the CDMS so we decided to compute them by our-self following the procedure described in appendix B. We selected a linewidth of 188 km s^{-1} to ensure that the lines are optically thin. The kinetic temperature was set to $T_{kin} = 200 \text{ K}$, we used the same column density $N(NH) = 5 \times 10^{15} \text{ cm}^{-2}$ as the previous study and we set the escape probability model to be as an expansion sphere. However, the ejecta being located close to a stellar system, the intensities of the lines can be subject to a strong infrared continuum. So we can also compare excitation processes when applying the continuum used by Gull *et al.* [164] and the CMB where $T_{bg} = 2.73 \text{ K}$ and see the influence of the rate coefficients for NH– H_2 and NH–He [171] on the excitation temperature.

Fig. 3.18 displays different behaviors of the excitation temperature for models including NH– H_2 or NH–He rate coefficients. Since there was no anomaly in fine structure excitation temperatures, we did an average $\langle T_{ex} \rangle$ over these lines. We can see that radiative processes have much more impact on the excitation temperature when incorporating the modified continuum rather than the CMB. Especially for the strong continuum, transitions depart from the radiative regime for a gas density $\sim 10^7 \text{ cm}^{-3}$ where lines present already non-LTE behavior for $n(H_2) > 10^4 \text{ cm}^{-3}$ in the case of the CMB. For model-

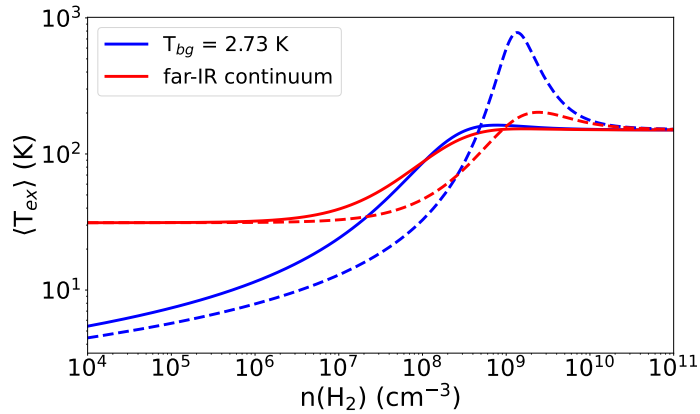


Figure 3.18 – Excitation temperature of fine structure components of the $N = 1 \rightarrow 0$ rotational line as a function of the density of the gas. Solid lines stand for the NH–H₂ rate coefficients. Dashed lines correspond to NH–He collisional data.

ing including H₂ collisions, the difference between the two continua becomes negligible for $n(\text{H}_2) > 10^8 \text{ cm}^{-3}$. For collisions involving He, the excitation temperature displays more variations especially including the CMB, showing supra-thermal effect. On the contrary, the excitation temperature departs from the radiative regime for $n(\text{H}_2) \sim 10^8 \text{ cm}^{-3}$. This can be anticipated regarding the discrepancies in the magnitude of rate coefficients between H₂ and He collisions. In that sense, a line will be more sensitive to radiative processes when including collisional data involving He.

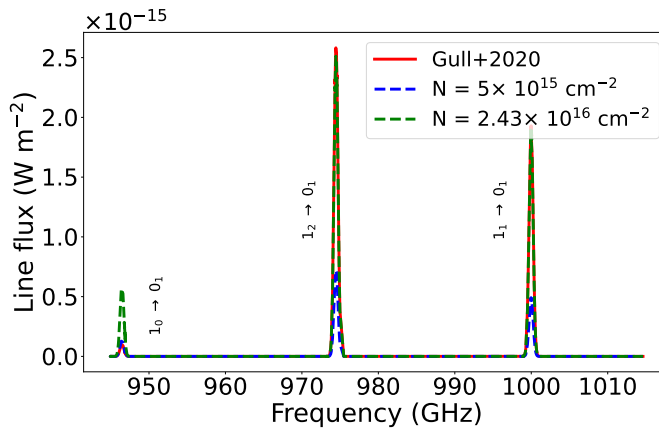


Figure 3.19 – Synthetic spectra of the $1_{j_1} \rightarrow 0_1$ fine structure transitions of NH for the observed (solid) and computed (dashed) line fluxes.

As illustration, we show in Fig. 3.19 a model of the line fluxes taken from observations [164] with those computed with RADEX with the previous determined column density $N(\text{NH}) = 5 \times 10^{15} \text{ cm}^{-2}$. This was not enough to reproduce the two most intense transitions. We re-estimated the column density that reproduces the best the three transitions

line fluxes by satisfying the statistical test χ^2 as in Eq. (3.47), fixing the density to $n(\text{H}_2) = 10^8 \text{ cm}^{-3}$. The best solution is displayed in Fig. 3.19 for $N(\text{NH}) = 2.43 \times 10^{16} \text{ cm}^{-2}$. This is increasing the precedent value by a factor of ~ 5 which is not negligible for astrophysical applications. It is hard to discuss the provenance of the main differences since the way of estimating the rate coefficients by Gull *et al.* [164] is not clear. Of course this is just an example of the sensitivity of our data into a simple approach, and precise radiative transfer modeling are required to model such a complex medium as the η Carinae system.

To conclude, we presented the impact of the new collisional data for the $\text{C}_2\text{D}-\text{H}_2$, $^{13}\text{CCH}-\text{H}_2$, $\text{C}^{13}\text{CH}-\text{H}_2$ and $\text{NH}-\text{H}_2$ collisional systems into simple radiative transfer modeling. We saw that the excitation of the observed lines display non-LTE effects for densities corresponding to the media they are detected, showing the importance of incorporating the competition between radiative and collisional processes in astrophysical applications. When both sets of collisional data for H_2 and for He were available, we saw that their strong differences have a major impact on the excitation temperature. Moreover, the isotopic substitution for very similar systems like ^{13}CCH and C^{13}CH did not show significant differences in their excitation temperatures and that collisional processes cannot explain isotopic anomalies. We would expect more differences between NH and ND modeling.

COLLISIONAL EXCITATION IN REACTIVE SYSTEMS

In this chapter, we focus on the collisional excitation in reactive systems which is the main part of this thesis. Section 4.1 will present the system of interest for this work. Then, theoretical approaches and procedures about the fine structure treatment will be detailed in section 4.2. Finally, a focus on the inclusion of the reactivity of the system is stressed out in section 4.3.

4.1 The OH^+ molecule as a test case

4.1.1 Objectives of this work

Theoretical studies about collisional excitation in reactive systems is still a topic of ongoing exploration. Especially for exothermic and barrier-less reactions, a competition between reactivity and collisional excitation can exist at low temperatures and the inclusion of inelastic and reactive channels must be considered in scattering calculations. In this context, it becomes necessary to develop new approaches to treat the competition between non-reactive and reactive processes to quantify state-to-state molecular collisions for low temperatures. We will use the OH^+ molecule as a test case to illustrate this work after explaining the astrophysical relevance of this molecule. We will use the SACM to overcome this challenge. However, prior to analyze the impact of the reactivity on the collisional excitation, we have to investigate the use of statistical approach for considering fine structure excitation. This chapter has then three main objectives:

1. To explore the impact of the SACM approach presented in section 2.4 on the fine structure treatment of reactive systems for low temperature applications, which is missing in the literature. We will perform the test on the OH^+-H collisional system.
2. To evaluate the use of the SACM when including both inelastic and reactive channels. This work will be performed on the $\text{OH}^+ + \text{H}_2 \rightarrow \text{H}_2\text{O}^+ + \text{H}$ reaction.

3. To provide new state-to-state rate coefficients for the $\text{OH}^+\text{-H}_2$ collisional system, taking into account the balance between inelastic and reactive processes.

4.1.2 The OH^+ molecule

OH^+ belongs to the family of interstellar hydrides, having one heavy atomic element with one hydrogen. Notably, OH^+ is one of the most simple oxygen-bearing molecules and represents a key ingredient for the formation of more complex molecules such as H_2O . In the gas phase, especially in diffuse clouds, the oxygen chemistry can be well understood in first approximation by thermochemistry parameters [32], [211]. First, the bond-dissociation energies D_0 of OH^+ , H_2O^+ and H_3O^+ are greater than those of H_2 ($D_0 > 4.48$ eV), then the following reactions



are exothermic, which means that the production of these ions is very efficient at low temperatures, requiring no activation energy. Then, the production of water can be done by dissociative recombination with the products of reaction (4.3). Reaction (4.1) is very efficient in cold diffuse gas but is very dependent on the fraction of H_2 . In dense gas, the following reaction



is privileged due to a high fraction of H_2 ionized by cosmic rays which will react with H_2 to form H_3^+ . The study of OH^+ or H_2O^+ is then useful for tracing the molecular hydrogen fraction and the cosmic-ray ionization rate ζ [96].

The low reduced mass of OH^+ lead to high rotational constant $B_0 = 492.346$ GHz [212]. This has two main consequences. First, rotational transitions are reported in the sub-millimeter frequency range which is hardly detectable by ground-based telescopes; even though the OH^+ cation has been first detected in the ISM through hyperfine components of the $N = 1 \rightarrow 0$ rotational line in absorption against the strong continuum source Sagittarius B2 [213] with the Atacama Pathfinder EXperiment (APEX) ground telescope [214]. Second, rotational transitions at high frequencies induce large spontaneous radiative decay rates. It means that transition lines are highly sub-thermalized and high gas

densities ($\sim 10^8 - 10^9 \text{ cm}^{-3}$) are needed to observe competition between radiative and collisional processes. With the development of the ground-based ALMA interferometer and the launch of the *Herschel Space Observatory* [28] over the last decade, OH^+ has been detected in absorption toward low redshift objects as infrared galaxy Mrk 231 [215] with the Spectral and Photometric Imaging REceiver (SPIRE) [216], the Galactic disk of the Milky Way [96] with the Heterodyne Instrument for the Far-Infrared (HIFI) [217], and toward the quasar PKS 1830-211 [218] with ALMA. It has been also detected in emission toward the Orion Bar PDR [219] with the HIFI instrument, planetary nebulae [220] with the Photodetector Array Camera and Spectrometer (PACS) [221]. Finally, OH^+ was detected in low redshift galaxy as NGC 7130 [222] with the SPIRE instrument, as well as high redshift objects like NGC 1068 [223], the quasar SDSS J231038.88+185519.7 [224] and Hot Dust-Obscured Galaxy (Hot DOG) W0410-0913 [225].

These observations have shown that various processes are participating in the production or excitation of OH^+ . Indeed, collisional excitation, chemical pumping and reactivity play a role in the population of OH^+ energy levels, as it is possible for a molecule to be formed in an excited rovibrational state. This encouraged theoretical and experimental studies to improve the reliability of the interpretation of observations. In the case of the study of the formation of OH^+ , experiments conducted for reaction (4.1) have been investigated at low temperatures (15–300 K) by Kovalenko *et al.* [226] using a cryogenic 22-pole RF ion trap (AB-22PT instrument) [227]. These measurements show a good agreement with the Langevin rate coefficient and do not follow the same behavior than the theoretical rate coefficient computed by Bulut *et al.* [228]. Reaction (4.4) was explored by merged-beams experiment and it was found a strong dependence of the rate coefficient with the temperature between 10 and 1000 K, revising the common branching ratio used in astrochemical models [229]. Gomez-Carrasco *et al.* [230] investigated reaction (4.1), computed state-to-state rate coefficients using a wave packet (WP) method excluding effects from the electronic spin, in good agreement with experimental measurements [231], [232].

Excitation of OH^+ has been also extensively studied for astrophysical application in media dominated by H, H_2 and He. Gomez-Carrasco *et al.* [230] explored the fine structure excitation of OH^+ by He (as a proxy for H_2). These results suffer of lack of experimental and theoretical data and cannot be validated. However, we can think that the reliability of these data is doubtful due to the nature of the $\text{OH}^+ + \text{H}_2$ exothermic and barrier-less reaction contrary to the $\text{OH}^+ + \text{He}$ one, and caution must be taken when including these data in radiative transfer. Overall, these data were included in a chemical model [233],

showing that chemical pumping has a minor effect on the excitation of OH^+ rotational levels, compared to inelastic collisions. More recently, Bulut *et al.* [228] computed rotational rate coefficients for $\text{OH}^+ + \text{H}$ collisions using WP methods. Stoecklin *et al.* [234] corroborated these calculations using CC and Quasi-Classical Trajectories (QCT) methods. The extension to hyperfine calculations was done later with the IOS approximation [235]. We detail several aspects of the $\text{OH}^+ + \text{H}$ study in section 4.2, being the starting point of this part of the thesis work.

Finally, several authors investigated the reactivity of OH^+ . Reactions (4.2) and (4.3) have been undertaken at low temperatures (15–300 K) by Tran *et al.* [236] using similar ion trap instruments as Kovalenko *et al.* [226]. They revealed that the total rate coefficients exhibit deviations from the common Langevin model for these reactions. Kumar *et al.* [237] performed similar measurements for temperatures up to 150 K. Finally, Song *et al.* [238] explored the $\text{OH}^+ + \text{H}_2 \rightarrow \text{H}_2\text{O}^+ + \text{H}$ reaction at high temperatures using WP method within the CS approach. We will refer to their results when we will treat the reactive aspects in section 4.3.

4.1.3 Spectroscopy of OH^+

OH^+ is a linear molecule in a $^3\Sigma^-$ electronic state. Having a vibrational frequency $\omega = 3113.4 \text{ cm}^{-1}$ [239] makes its first vibrational state open at $T \sim 4500 \text{ K}$. We can safely neglect its vibrational structure and describe it as a rigid rotor for low and intermediate temperature studies. The molecule possesses a nonzero electronic spin $S = 1$, which couples to the rotational quantum N number as

$$j = N + S$$

where each rotational level is splitted into three fine structure components and the wave function is expressed in the intermediate coupling scheme.

$$|F_i j m\rangle = \sum_{N=j-S}^{N=j+S} c_{NF_i}^j |NS j m\rangle \quad (4.5)$$

As for NH, we will label energy levels by N_j used for a pure Hund's case (b) with the simplification

$$\begin{aligned}
 F_1 &\rightarrow j = N + 1 \\
 F_2 &\rightarrow j = N \\
 F_3 &\rightarrow j = N - 1
 \end{aligned}
 \tag{4.6}$$

We present the first 25 fine structure energy levels in Table 4.1 computed with experimental spectroscopic constants from the literature [212].

Level	N	j	E (cm ⁻¹)
1	0	1	0.000
2	1	0	30.326
3	1	2	32.415
4	1	1	34.439
5	2	1	97.550
6	2	3	97.769
7	2	2	100.055
8	3	4	195.867
9	3	2	196.275
10	3	3	198.364
11	4	5	326.544
12	4	3	327.400
13	4	4	329.227
14	5	6	489.603
15	5	4	490.845
16	5	5	492.462
17	6	7	684.810
18	6	5	686.408
19	6	6	687.837
20	7	8	911.887
21	7	6	913.822
22	7	7	915.076
23	8	9	1170.510
24	8	7	1172.771
25	8	8	1173.858

Table 4.1 – The first 25 fine structure energy levels of OH⁺

The presence of the hydrogen atom involves a nonzero nuclear spin $I(\text{H}) = 1/2$. This quantum number will couple to the rotation and the electronic spin giving the scheme

$$F = j + I$$

The rotational structure of the molecule becomes more and more complex with the

splitting of each fine structure component into two hyperfine energy levels labeled as N_{jF} . The spectroscopic parameters describing the rotational structure of OH^+ are summarized in Table 4.2 [212].

Constant	Value (MHz)
B_0	492346.278(146)
D_0	57.6166(52)
λ_0	64246.00(55)
γ_0	-4533.85(34)
$b_F(^1\text{H})$	-75.14(50)
$c(^1\text{H})$	126.01(87)

Table 4.2 – Experimental spectroscopic constants of OH^+ [212].

4.2 Fine structure excitation of OH^+ by atomic hydrogen

Since the $\text{OH}^+\text{-H}$ collisional system has been already studied and collisional data are available, it is a suitable case to test the validity of SACM approach for considering fine structure excitation. We describe below the PES we based this work on. A comparison between CC calculations with SACM results will follow.

4.2.1 Potential energy surface

The $\text{OH}^+ + \text{H}$ interaction involves a quartet [240] and doublet [241] PESs. First, these potentials have an endothermic reactive channel with an enthalpy of $\Delta H = 0.47$ eV for the quartet and 2.32 eV for the doublet. We considered these reactive channels as closed at low collisional energies. Second, in order to compare our results to CC calculations, we needed to consider OH^+ as a rigid rotor. In the quartet PES, the O–H bond length is $r(\text{OH}^+) = 2.15a_0$ at the global minimum which is reasonably different from the equilibrium distance $r_e(\text{OH}^+) = 1.94a_0$ [234], [239]. This means that the rigid rotor should be a reasonable assumption. Finally, the global minimum of the potential is about 0.39 eV (~ 3000 cm^{-1}) which should be deep enough to favor a statistical behavior of the collisional process, as it is the case for the consideration of the rotational structure [97]. Then, this work will only focus on calculations involving the quartet PES as we intended to test the methods and not to produce collisional data that are already available.

4.2.2 Statistical Adiabatic Channel Model (SACM)

In the SACM approach [97], as presented in section 2.4, we compute cross sections in two steps. The first step is to diagonalize the molecular Hamiltonian of Eq. (2.72), excluding the kinetic term¹:

$$\sum_{\alpha'} \left\langle \alpha' \left| \frac{\hat{j}_1^2}{2I_1} + \hat{V} + \frac{\hat{L}^2}{2\mu R^2} \right| \alpha \right\rangle F_{\alpha}^J(R) = 0 \quad (4.7)$$

where here we set $j_2 = 0$ in Eq. (4.7) to consider a linear molecule-atom interaction. The diagonalization is done for each total angular momentum J , resulting in adiabats where their asymptotic value corresponds to the energy level of a given channel. In the case of a non-reactive collision, a schematic view of this process can be seen in Fig. 4.1.

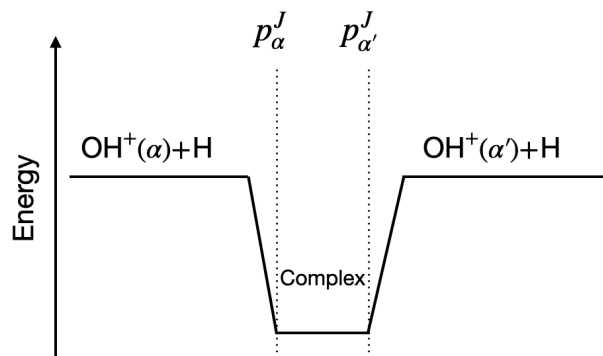


Figure 4.1 – Schematic view of a non-reactive collision with the SACM approach.

The probability to transit from an initial to a final state is given from the S -matrix elements as:

$$|\langle \alpha' | S^J(E) | \alpha \rangle|^2 = \frac{p_{\alpha}^J(E) p_{\alpha'}^J(E)}{\sum_{\alpha''} p_{\alpha''}^J(E)} \quad (4.8)$$

where the $p_{\alpha}^J(E)$ are the probabilities associated to initial and final states. For an inelastic transition, the transition probability is given by the total number of open channels $N_{tot}(E, J)$ for a given total energy and total angular momentum (E, J) . Each channel is assigned with the same weight and the S -matrix elements are given by

1. The case molecule-molecule can be related to the molecule-atom interaction by setting $j_2 = 0$ giving similar result as Corey & McCourt [81].

$$|\langle \alpha' | S^J(E) | \alpha \rangle|^2 = \begin{cases} \frac{1}{N_{tot}(E, J)} & \text{open channels} \\ 0 & \text{otherwise} \end{cases} \quad (4.9)$$

The total cross section for a inelastic collision is similar to Eq. (2.75):

$$\sigma_{\alpha \rightarrow \alpha'}^{\text{SACM}} = \frac{\pi}{k_{\alpha}^2 g_{\alpha}} \sum_J [J] \frac{N_{\alpha}(E, J) N_{\alpha'}(E, J)}{N_{tot}(E, J)} \quad (4.10)$$

where g_{α} is the degeneracy of the initial level. Then, the second step of this method is to count properly the number of open channels. I implemented a script which follow this procedure, as described in section 2.4.3.

4.2.3 Results

The use of the SACM for studying the rotational excitation of OH^+ by H was investigated by Loreau *et al.* [97]. They found an excellent agreement with CC calculations for temperatures between 50 and 1000 K. Most of rate coefficients reproduce quantum calculations within 50% of accuracy. Moreover, rotational rate coefficients show small deviations for $\Delta j = \pm 1$ but all other propensity rules were matching between SACM and CC. They concluded that a statistical behavior is satisfactory for describing the rotational excitation in the OH^+ -H collisional system.

To estimate the validity of fine structure resolved cross sections computed with the SACM approach, we will compare them to those determined through the CC approach by François Lique (not published). Tests have been done for total energies in the range $E_{tot} = 0\text{--}2300 \text{ cm}^{-1}$, considering fine structure energy levels converged up to $N = 6$ (see *e.g.* Table 4.1).

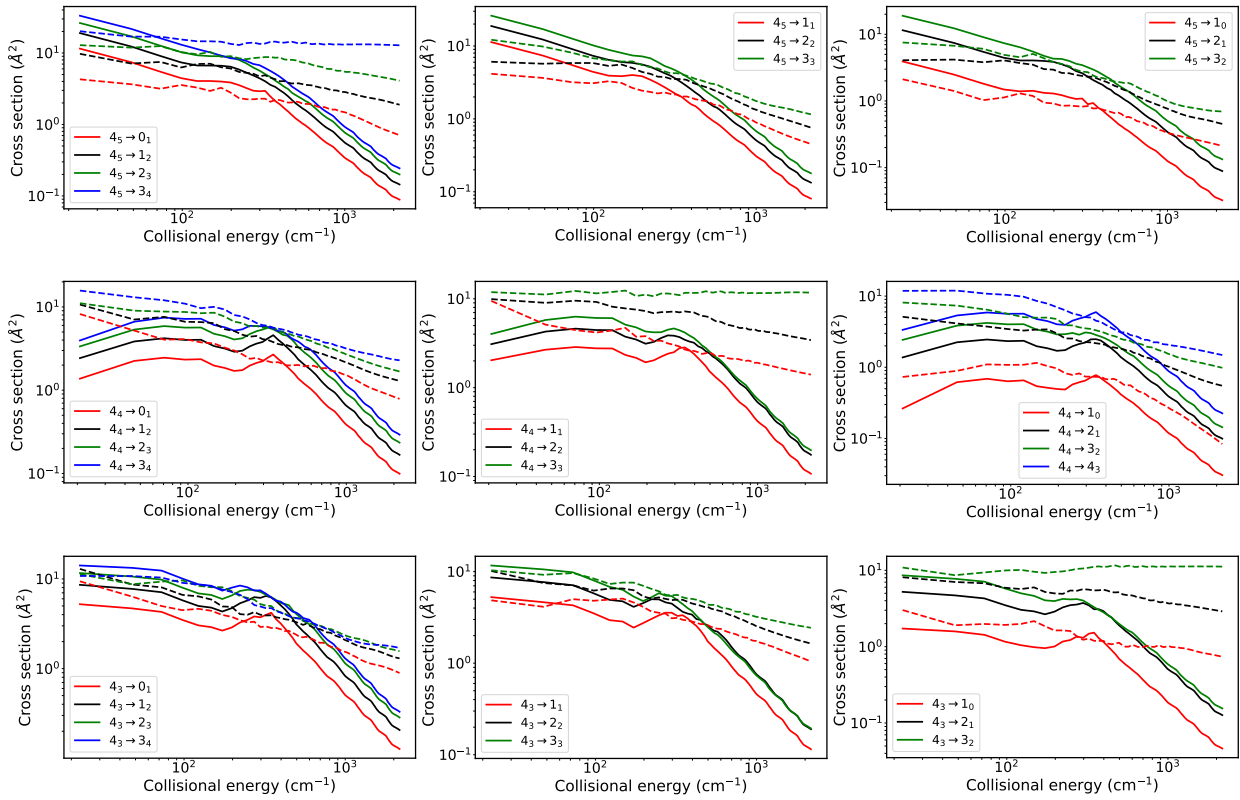


Figure 4.2 – Comparison between fine structure cross sections computed with SACM (solid) and with CC (dashed) methods. For initial levels: 4_5 (top), 4_4 (middle) and 4_3 (bottom). For final levels: $N'_{N'+1}$ (left), $N'_{N'}$ (middle) and $N'_{N'-1}$ (right).

Figs. 4.2, 4.3 and 4.4 present cross sections for fine structure transitions out of the $N = 4, 5$ and 6 levels as a function of the collisional energy. As a general comment, the SACM set of data reproduces rather well the general behavior of the cross sections, decreasing in magnitude as the transfer of angular momentum increases. Discrepancies become more and more important at high energies, which is expected because the collision becomes too fast to get a long-lived intermediate complex. More specifically, we can see that SACM transitions out of the N_{N+1} level have the best agreement with CC cross sections within a factor of 3 at low collisional energy ($\leq 1000 \text{ cm}^{-1}$). Disagreement between the two methods persists for transitions out of the N_{N-1} level, and is worst for transitions out of the N_N level. It is interesting to see that such failing of SACM is increasing with the rotational quantum number N .

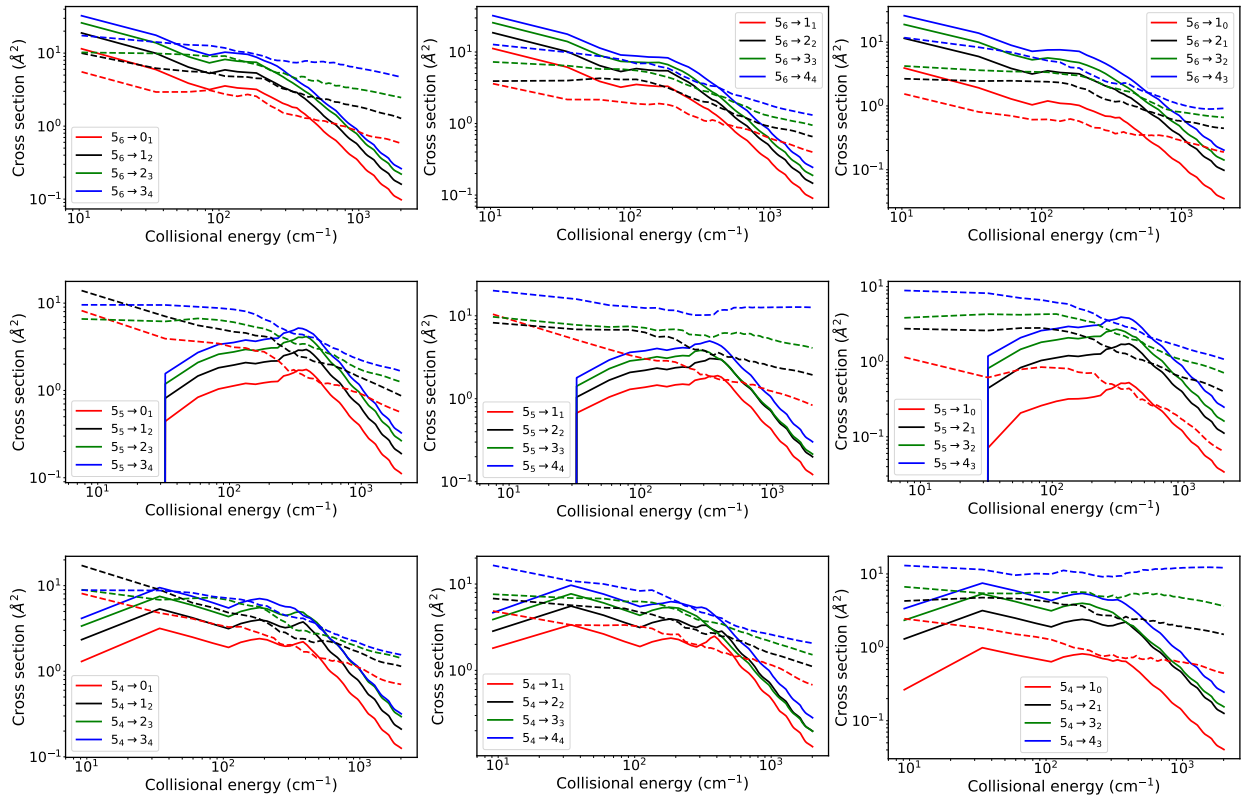


Figure 4.3 – Comparison between fine structure cross sections computed with SACM (solid) and with CC (dashed) methods. For initial levels: 5_6 (top), 5_5 (middle) and 5_4 (bottom). For final levels: $N'_{N'+1}$ (left), $N'_{N'}$ (middle) and $N'_{N'-1}$ (right).

The origin of the particular disagreement of transitions out of the N_N initial level is not obvious and easy to understand but we can still investigate some aspects to at least propose a partial cause. Fig. 4.5 shows some adiabatic curves for a given total angular momentum J . Adiabats can be described in different regimes: a repulsive part for $R \leq 4a_0$, an attractive region for $R = 4-10a_0$, and the long range from $R \geq 10a_0$. Each asymptotic value will correspond to the energy of a given channel, especially to a fine structure energy level of the target. The number of counted adiabats will depend on the energy threshold in which we classically consider the adiabat as open and will have an impact on the magnitude of cross sections. The barrier appearing in the long range results from the centrifugal distortion, increases with the total angular momentum and will have a larger magnitude for a light collisional system. However, we can see an additional barrier in the intermediate range, resulting from avoiding crossing between curves. This may create miss counting of some adiabats when this barrier becomes larger than the centrifugal one. It should be noted that the ΔE is defined according to the difference of energy between the two barriers for the highest channel of the fine structure components, corresponding to the N_N level, showing the most differences with CC results.

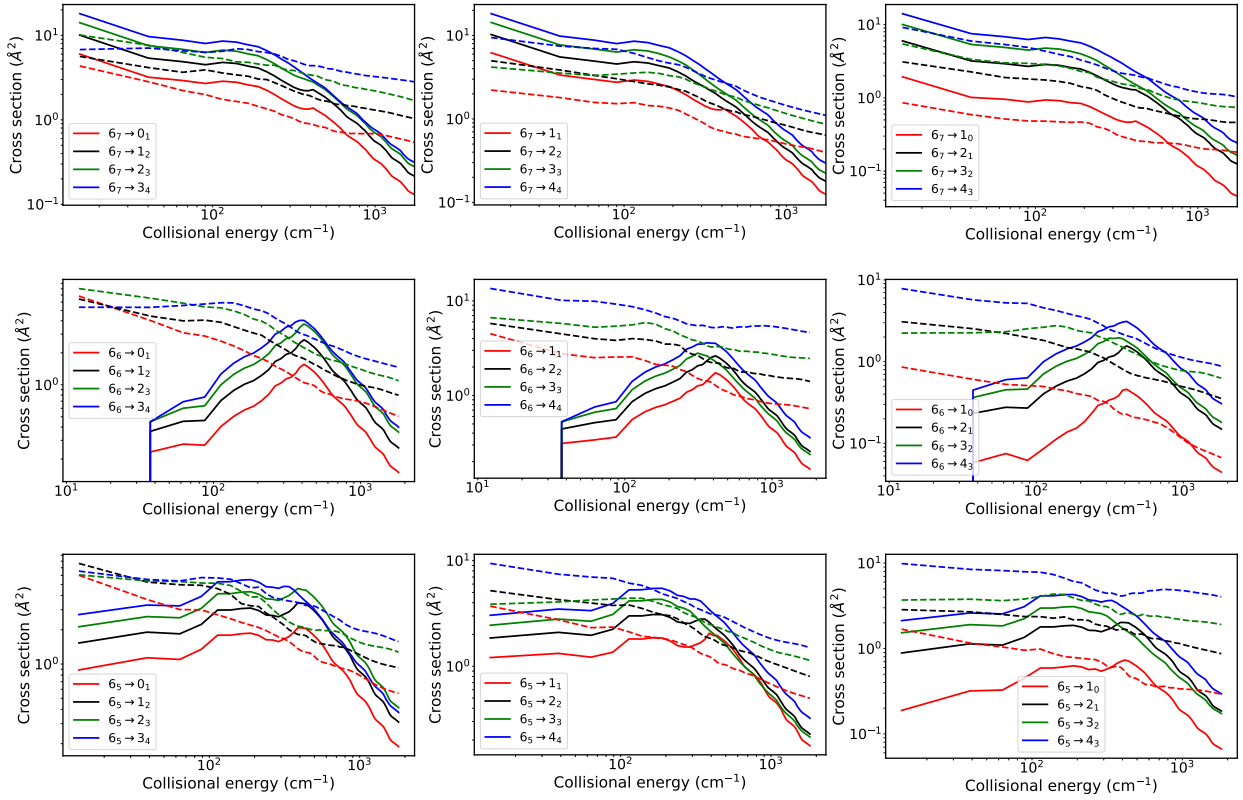


Figure 4.4 – Comparison between fine structure cross sections computed with SACM (solid) and with CC (dashed) methods. For initial levels: 6_7 (top), 6_6 (middle) and 6_5 (bottom). For final levels: $N'_{N'+1}$ (left), $N'_{N'}$ (middle) and $N'_{N'-1}$ (right).

The difference of energy between the maxima of these two barriers becomes larger and larger with increasing N , which is correlated to what was previously observed for the agreement between cross sections. This may be one of the aspects explaining these fail of the SACM for these transitions, at least participating in amplification of these deviations.

We can analyze a more systematic comparison between all rate coefficients for several temperatures as in Fig. 4.6. In this figure, we computed the *weighted mean error factor* (WMEF) as:

$$\text{WMEF} = \frac{\sum_i k_i^{\text{CC}} r_i}{\sum_i k_i^{\text{CC}}}; \quad r_i = \max(k_i^{\text{CC}}/k_i^{\text{SACM}}, k_i^{\text{SACM}}/k_i^{\text{CC}}) \quad (4.11)$$

with r_i defined so that we always have $\text{WMEF} \geq 1$. This error factor quantifies deviations between SACM and CC results according to the magnitude of rate coefficients. We can see a moderate agreement for temperatures $T \geq 50$ K, with a re-increasing of the WMEF at 300 K corresponding to the bad agreement of the high energy regime. Most of rate coefficients agree within a factor of 3, even for the most dominant transitions.

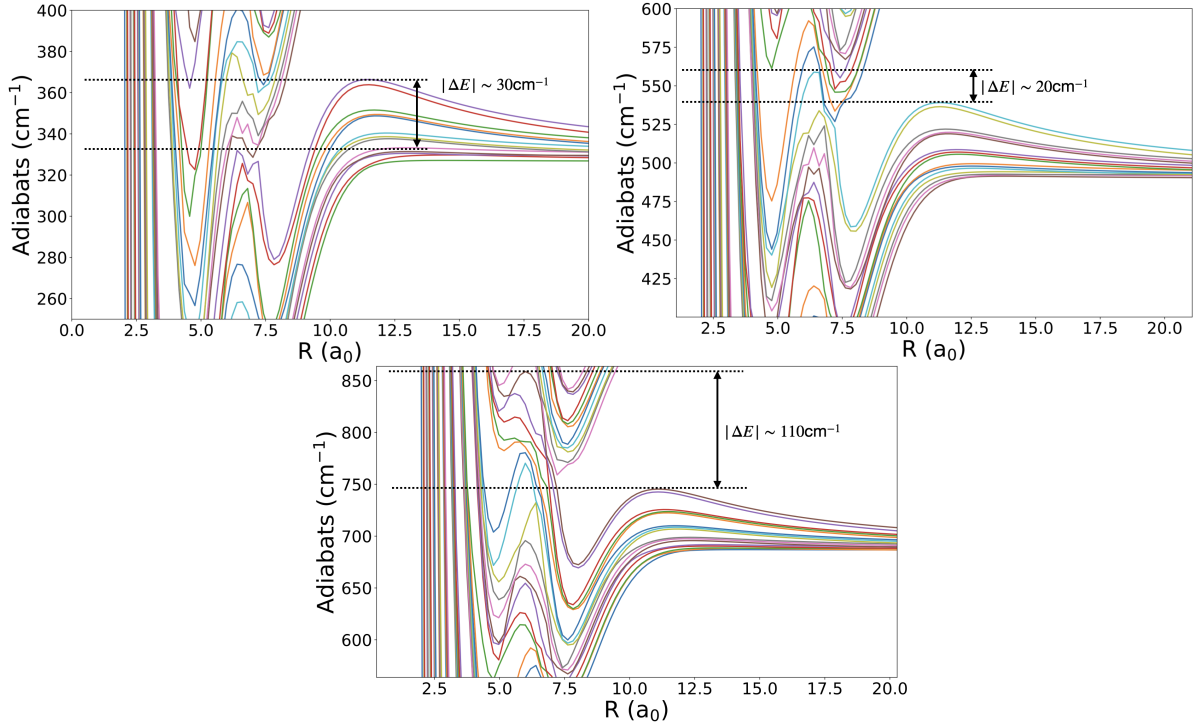


Figure 4.5 – Cuts of several adiabatic curves as a function of the distance for $J = 5$. The asymptotic values correspond to fine structure components for the $N = 4$ (left), $N = 5$ (right) and $N = 6$ (bottom) energy level.

We can follow the overall evolution of the WMEF in Fig. 4.7 to get a rough estimation of the validity temperature range of the SACM for the $\text{OH}^+ + \text{H}$ collisional system including the fine structure. The best agreement with CC results would be between 100 and 250 K. Such comparisons have been done by Loreau *et al.* [97] for the same collisional system for rotational transitions. They show a much better agreement of the SACM with CC for rotational rate coefficients between 50 K (WMEF = 1.18) and 500 K (WMEF = 1.37). The only difference is the inclusion of the fine structure and has clearly an impact on the disagreement with CC. In a pure statistical approach, the number of adiabats should be proportional to the degeneracy of the given energy level. This aspect should tend SACM cross sections to be proportional to the degeneracy of the final level and independent of the initial level. Such behavior would be similar to that of the M_J -random approximation, where the reorientation of the angular momentum is supposed to be statistically randomized [82]. This will not be the case when employing the CC approach, where the rotational angular momentum and electronic spin are coupled; and together with the independence of the potential to the electronic spin, will not affect the orientation of S but create changes in the magnitude of N during a collision [81].

We can also extract some information from fine structure rate coefficients. In Fig. 4.6,

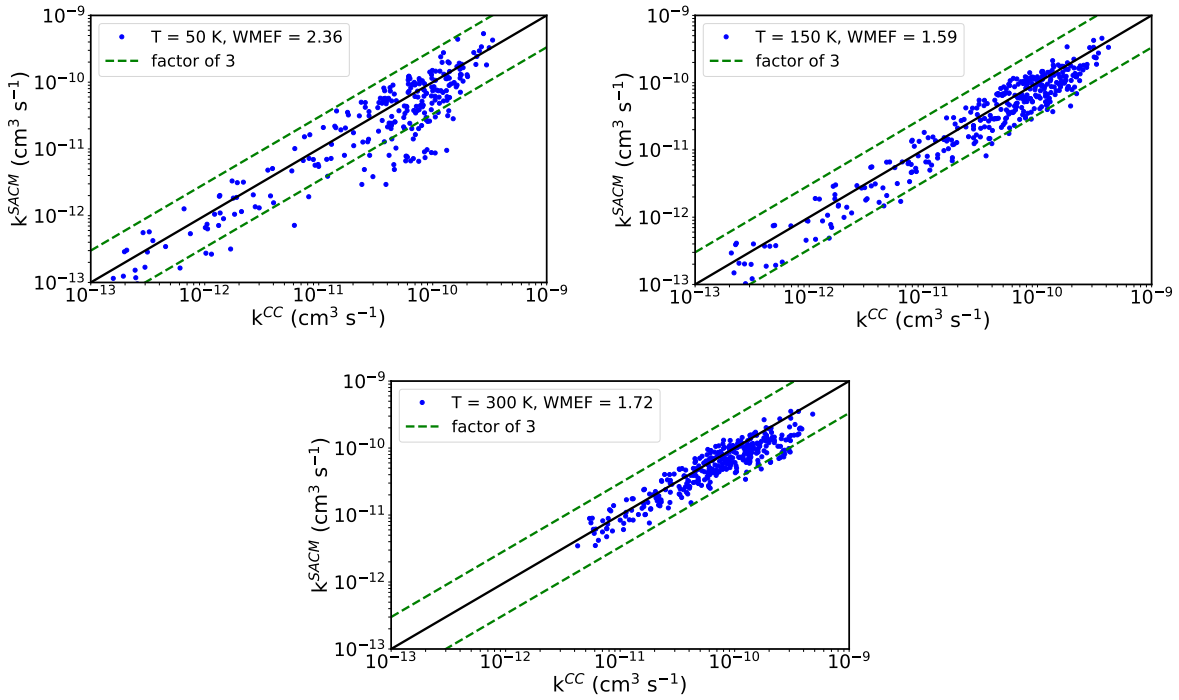


Figure 4.6 – Systematic comparison of fine structure rate coefficients computed with the SACM and CC approaches. Dashed lines represent deviations of a factor of 3.

some CC transitions with intensities larger than $10^{-11} \text{ cm}^3 \text{ s}^{-1}$ deviate much more than a factor of 3 at 50 K. They were identified and most of them correspond to transitions out of the 6_6 and 5_5 energy levels or toward these levels, as expected from cross sections in Fig. 4.4.

We can see in Fig. 4.8 the fine structure propensity rules governing rate coefficients for 50 K and 150 K. Regardless the temperature, CC transitions follow the expected $\Delta N = \Delta j$ propensity rule for an open-shell molecule, at least for $N_{N+1} \rightarrow N'_{N'+1}$ transitions. Even if SACM rate coefficients mostly reproduce these tendencies, the global magnitudes of transitions out of the N_N level are not matching at all with CC results. This effect becomes less and less visible with the temperature, but deviations increase with the initial energy level.

We can partially conclude that SACM calculations are not in good agreement with the CC method, because of the inclusion of the fine structure levels in the $\text{OH}^+ + \text{H}$ collisional study. Even if most of SACM transitions reproduce CC results within a factor of 3, we observe too many discrepancies for transitions with the largest magnitudes which are the most important in astrophysical applications, especially at 50 K which are related to typical interstellar clouds conditions. We have shown that SACM fails at reproducing trend and intensities of some fine structure transitions. Of course, more studies have to be

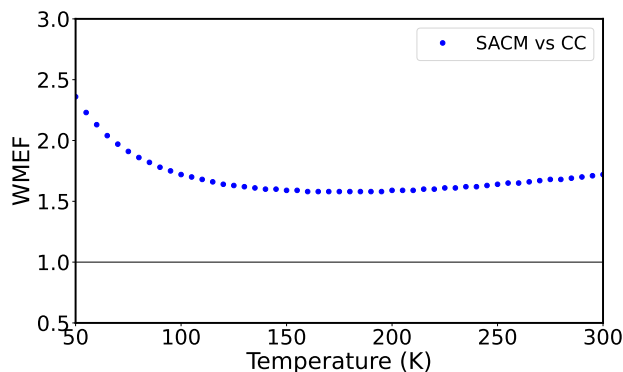


Figure 4.7 – Evolution of the WMEF between SACM and CC results as a function of the temperature. The solid line represent perfect agreement between results.

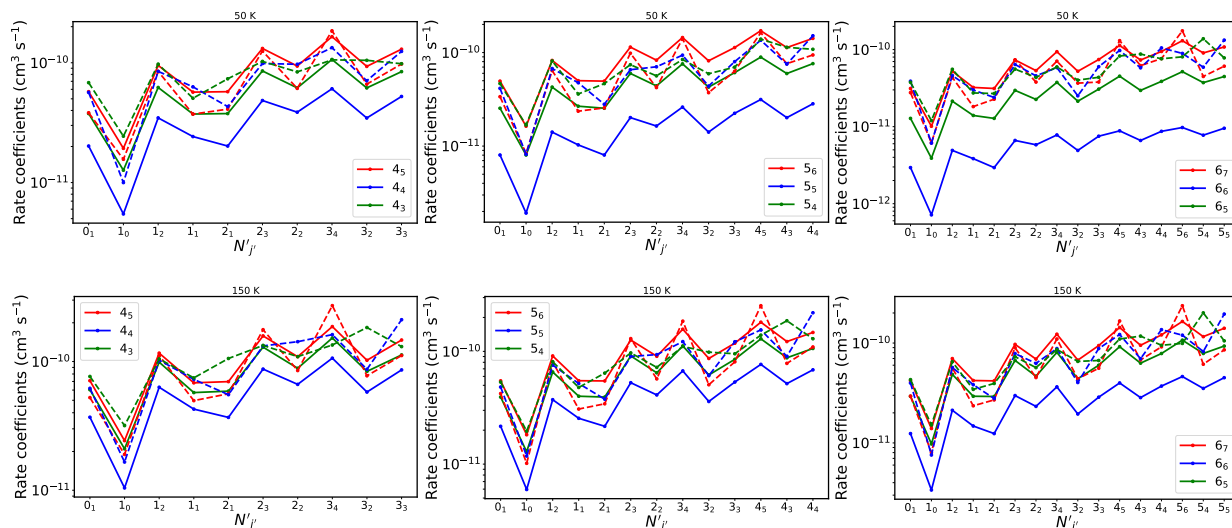


Figure 4.8 – Comparison between fine structure rate coefficients computed with SACM (solid) and with CC (dashed) methods at 50 K (upper) and 150 K (lower).

done with other collisional systems including open-shell molecules to better understand and quantify limits of the SACM. As an alternative, the determination of (hyper)fine rate coefficients for such molecules can be undertaken using IOS approaches, already widely benchmarked for many collisional systems, usually showing agreement with CC by $\sim 30\text{--}50\%$ and with more systematic deviations, which make uncertainties better quantifiable.

4.3 Reactive collisions of OH^+ with H_2

Here, we will explore the impact of the SACM when including both inelastic and reactive channels using the $\text{OH}^+ + \text{H}_2 \rightarrow \text{H}_2\text{O}^+ + \text{H}$ reaction as a test case. We describe below the features of the PES we are using, the steps of the implementation to our

approach and comparisons with the literature. For dynamical calculations, we will only consider the rotational structure of OH^+ , since we found a bad performance of the SACM when incorporating fine structure in section 4.2.3. From these results, we will be able to quantify the collisional excitation of OH^+ by H_2 , including both inelastic and reactive processes; and propose a new set of rotational state-to-state rate coefficients for this collisional system up to 300 K for astrophysical applications.

4.3.1 Potential energy surface

The full-dimensional reactive PES for the H_3O^+ system was computed by Li & Guo [242]. The molecular complex is described using internal coordinates, where each atom is represented by an (x, y, z) set of coordinates. These authors computed up to $\sim 30\,000$ *ab initio* points using the Multi Reference Configuration Interaction method (MRCI) with an aVQZ basis set using the MOLPRO software [112]. A calculation of the harmonic frequencies have shown a good agreement with experimental measurements [239], [243], [244]. The analytical representation of the PES was done with the permutation invariant polynomial-neural network (PIP-NN) approach [115] with a root-mean-square error of $\sim 24\text{ cm}^{-1}$. They found two potential wells for the $\text{OH}^+\dots\text{H}_2$ and $\text{H}_2\text{O}^+\dots\text{H}$ complexes with a saddle point between them. The PES has been through validation with experimental measurements [245], [246] by calculation of the thermal rate coefficient at room temperature using Quasi-Classical Trajectories (QCT) method.

The first step is to adapt the reactive PES in order to make it suitable for adiabats calculations for the SACM application. We computed adiabats with the HIBRIDON code [80], requiring the PES to be described in Jacobi coordinates. We used the following transformation coordinates from cartesian to Jacobi (see Fig. 4.9):

$$\begin{aligned}
 x_1 &= \frac{r_{\text{OH}}}{17} \cos(\theta_1) & ; & & x_2 &= -\frac{16}{17} r_{\text{OH}} \cos(\theta_1) \\
 y_1 &= \frac{r_{\text{OH}}}{17} \sin(\theta_1) & ; & & y_2 &= -\frac{16}{17} r_{\text{OH}} \sin(\theta_1) \\
 z_1 &= 0 & ; & & z_2 &= 0 \\
 \\
 x_3 &= \frac{r_{\text{HH}}}{2} \cos(\theta_2) + R & ; & & x_4 &= -\frac{r_{\text{HH}}}{2} \sin(\theta_2) + R \\
 y_3 &= \frac{r_{\text{HH}}}{2} \sin(\theta_2) \cos(\phi) & ; & & y_4 &= -\frac{r_{\text{HH}}}{2} \sin(\theta_2) \cos(\phi) \\
 z_3 &= \frac{r_{\text{HH}}}{2} \sin(\theta_2) \sin(\phi) & ; & & z_4 &= -\frac{r_{\text{HH}}}{2} \sin(\theta_2) \sin(\phi)
 \end{aligned}$$

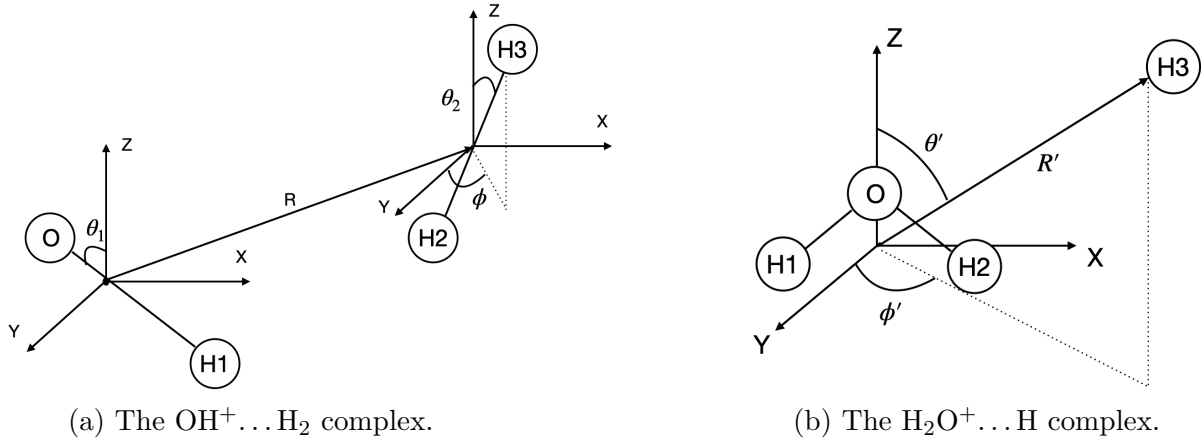


Figure 4.9 – Representation of the reactants (a) and products (b) of the H_3O^+ reactive PES in Jacobi coordinates.

with the sets of coordinates (x, y, z) are associated to the oxygen $\text{O}(x_1, y_1, z_1)$, the hydrogen atom of the target $\text{H1}(x_2, y_2, z_2)$ and the two other hydrogens of H_2 as $\text{H2}(x_3, y_3, z_3)$ and $\text{H3}(x_4, y_4, z_4)$. Here, we consider both OH^+ and H_2 as rigid rotors and we fix $r_{\text{OH}} = 1.029 \text{ \AA}$ [239] and $r_{\text{HH}} = 0.741 \text{ \AA}$ [190] the internuclear equilibrium distances of the OH^+ and H_2 in their respective vibrational ground state. For the $\text{H}_2\text{O}^+ \dots \text{H}$ complex, the transformation coordinates used is as follow:

$$\begin{aligned}
 x_1 &= 0 & ; & \quad x_2 = r'_{\text{OH}} \sin\left(\frac{\alpha}{2}\right) \\
 y_1 &= 0 & ; & \quad y_2 = 0 \\
 z_1 &= \frac{2}{18} r'_{\text{OH}} \cos\left(\frac{\alpha}{2}\right) & ; & \quad z_2 = -\frac{16}{18} r'_{\text{OH}} \cos\left(\frac{\alpha}{2}\right) \\
 \\
 x_3 &= -r'_{\text{OH}} \sin\left(\frac{\alpha}{2}\right) & ; & \quad x_4 = R' \sin(\theta') \cos(\phi') \\
 y_3 &= 0 & ; & \quad y_4 = R' \sin(\theta') \sin(\phi') \\
 z_3 &= -\frac{16}{18} r'_{\text{OH}} \cos\left(\frac{\alpha}{2}\right) & ; & \quad z_4 = R' \cos(\theta')
 \end{aligned}$$

with $r'_{\text{OH}} = 1.006 \text{ \AA}$ and $\alpha = 109.8^\circ$ [247] are the equilibrium structures of the H_2O^+ molecule. We can now generate the new PESs in Jacobi coordinates and extract several values of these potential to determine the expansion coefficients that will be used in the scattering program.

Using a Gauss-Legendre quadrature, expansion coefficients have been extracted up to $\lambda_{1,max} = 10$ and $\lambda_{2,max} = 4$, leading to a total number of 86 expansion coefficients for the $\text{OH}^+ - \text{H}_2$ PES. We found a global minimum for $R = 1.75 \text{ \AA}$, $\theta_1 = 73^\circ$, $\theta_2 = 0^\circ$ and $\phi = 0^\circ$

with a well depth $D_e = 3815.87 \text{ cm}^{-1}$. A second minimum is found for $R = 2.42 \text{ \AA}$, $\theta_1 = 180^\circ$, $\theta_2 = 90^\circ$ and $\phi = 0^\circ$ and a well depth of $D_e = 3412.91 \text{ cm}^{-1}$.

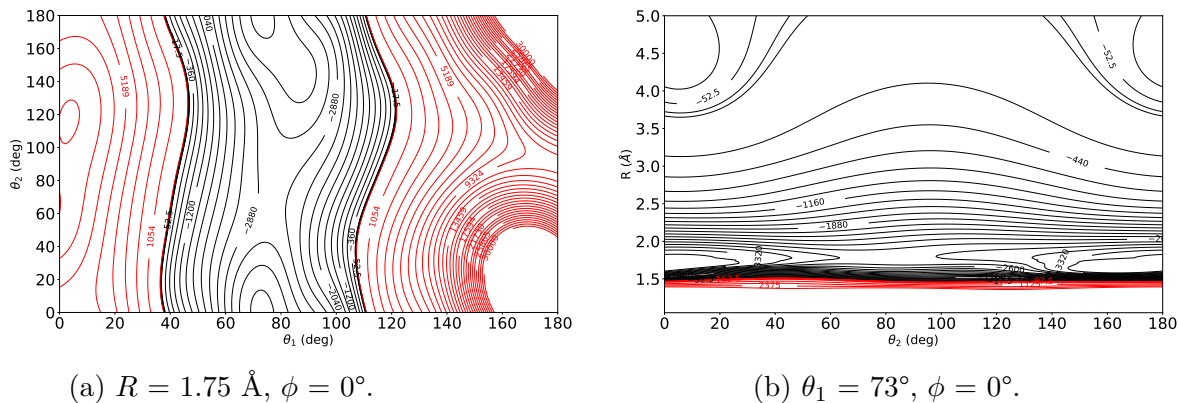


Figure 4.10 – Contour plots of the $\text{OH}^+\text{-H}_2$ PES for geometries corresponding to the global minimum.

We can see some features of the fitted PES by showing contour plots for geometries related to the global minimum in Fig. 4.10. We can see on panel (a) a much more repulsive region for linear orientations where one of the two hydrogens of H_2 are pointed toward the hydrogen end of the O-H bond. The center of mass of OH^+ being close to the oxygen, the hydrogen will be very close to H_2 for $\theta_1 = 180^\circ$. We can see also that the potential is very abrupt when going from repulsive from attractive regime. This effect can be also seen in panel (b) between $R = 1.5\text{-}1.7 \text{ \AA}$, where some oscillations are visible. We expect that these features will have minor impact in scattering calculations. We notice also a quasi-symmetry of the PES about $\theta_2 = 90^\circ$. This should be completely symmetric due to the homonuclearity of H_2 , however small deviations are observed despite developing the potential only using even λ_2 related expansion coefficients. This effect is probably due to the transformation of coordinates.

For the $\text{H}_2\text{O}^+\text{-H}$ PES, the quadrature procedure was performed to ensure extraction of expansion coefficients up to $\lambda_{max} = 10$, involving the index $\mu = [0, \lambda]$ by a step of 2 because of the symmetry of the H_2O^+ molecule. It results that 36 expansion coefficients can be used to develop the PES. We found the minimum of the PES for $R = 2.55 \text{ \AA}$, $\theta' = 122^\circ$ and $\phi' = 0^\circ$ with a well depth of $D_e = 1655.75 \text{ cm}^{-1}$.

Fig. 4.11 displays some features of the $\text{H}_2\text{O}^+\text{-H}$ PES for geometries of the minimum. Both panels (a) and (b) are symmetric about $\phi' = 90^\circ$ due to the symmetry of H_2O^+ . With the reduction of the colliders to rigid rotor systems, we may lose some information in the electronic interaction compared to the original PES. Even if comparisons between the two configurations cannot be direct, it is interesting to look at their principal differ-

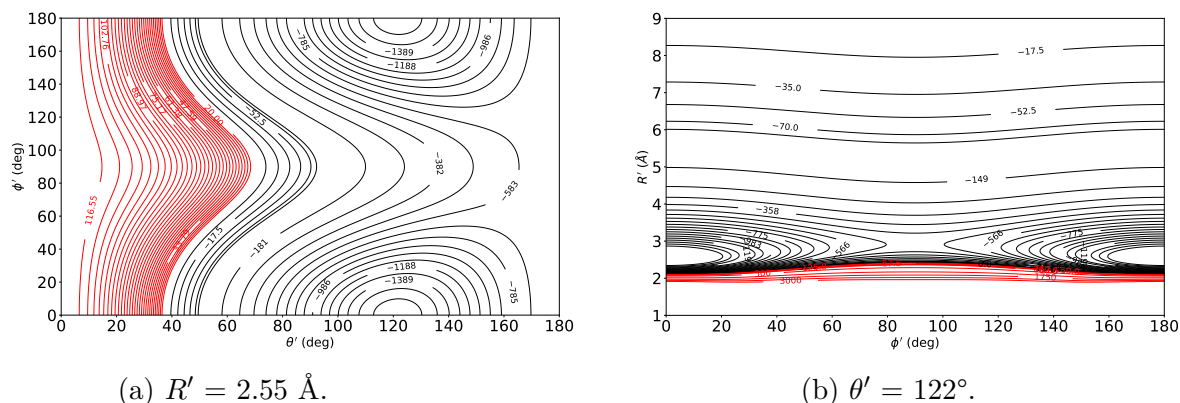


Figure 4.11 – Contour plots of the $\text{H}_2\text{O}^+\text{-H}$ PES for geometries corresponding to the global minimum.

ences. These are summarized in Table 4.3.

	Complex	r_{OH} (Å)	r_{HH} (Å)	D_e (cm^{-1})
Li & Guo 2014	$(\text{OH}^+)\dots\text{H}_2$	1.101	0.762	3822.86
This work	$(\text{OH}^+)\dots\text{H}_2$	1.029	0.741	3815.87
	Complex	r'_{OH} (Å)	α (deg)	D_e (cm^{-1})
Li & Guo 2014	$(\text{H}_2\text{O}^+)\dots\text{H}$	0.998	109.32	1739.02
This work	$(\text{H}_2\text{O}^+)\dots\text{H}$	1.006	109.8	1655.75

Table 4.3 – Comparisons between the full-dimensional H_3O^+ PES and the rigid rotor approximation.

It results that even when changing the equilibrium distances of the molecules for all complexes, the well depth do not change too much between the full dimension PES and the rigid rotor approach, even though differences of $\sim 5\%$ are seen for the $\text{H}_2\text{O}^+\text{-H}$ PES. We expect minor impact on cross sections since the counting on adiabats depends most on the description of the well and the long range.

4.3.2 Dynamical calculations

Scattering calculations for the rotational excitation of OH^+ by H_2 are very similar compared to those performed in section 4.2.2 but using angular functions (2.51). We will not develop these aspects anymore but focus on some features of the $\text{OH}^+ + \text{H}_2 \rightarrow \text{H}_2\text{O}^+ + \text{H}$ reaction. A schematic view of this process can be seen in Fig. 4.12.

In the specific case of the $\text{OH}^+ + \text{H}_2 \rightarrow \text{H}_2\text{O}^+ + \text{H}$ reaction, the $(\text{OH}^+)\cdots\text{H}_2$ and the $(\text{H}_2\text{O}^+)\cdots\text{H}$ complexes are connected by a submerged saddle point. Li & Guo [242] have shown that this barrier enhance the reactivity with the rotational excitation of OH^+ . In the SACM approach, we take only into account the number of entrance and exit channels

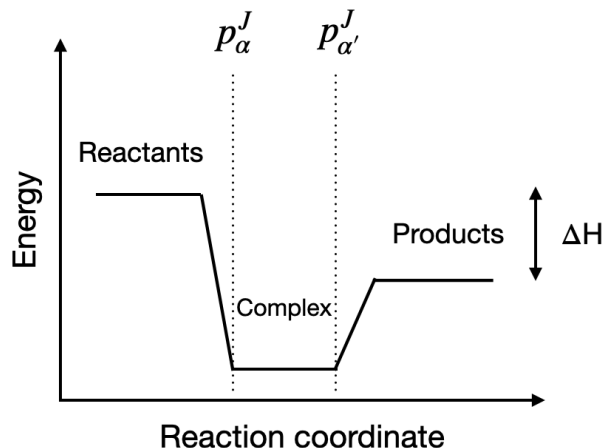


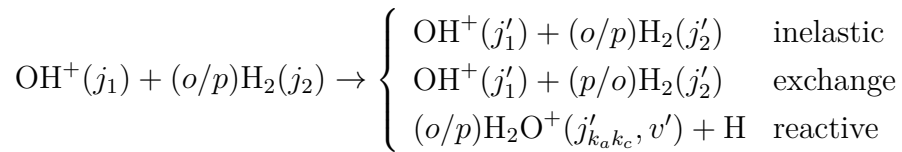
Figure 4.12 – Schematic view of a typical exothermic reaction by a given enthalpy ΔH .

represented by probabilities p_{α}^J and $p_{\alpha'}^J$, respectively and the PES is considered deep enough to ignore effects occurring in the complex region. Also, the reaction is exothermic by $\Delta H \simeq -1.02$ eV [246]. It means that adiabats associated to the $\text{H}_2\text{O}^+\text{-H}$ PES will be subtracted by this value during the counting. However, such exothermicity leads to open vibrational levels of H_2O^+ . Since we describe this molecule within the rigid rotor approach, a first approximation is to compute vibrational energy levels and modes ν_i of the molecules and duplicate all open adiabats from the fundamental level $v = 0$ for the excited vibrational states. To do so, we took into account the H_2O^+ harmonic frequencies $\omega_1 = 3259$ cm^{-1} [243], $\omega_2 = 3212.9$ cm^{-1} [243] and $\omega_3 = 1401.7$ cm^{-1} [248], and computed vibrational energies as $E_{v,i} = \omega_i(v + 1/2)$. We summarized the computed energies used in this work in Table 4.4. It should be noted that we considered the zero-point energies of both $\text{OH}^+ + \text{H}_2$ and $\text{H}_2\text{O}^+ + \text{H}$ in the counting procedure. In our tests and data production, we took into account H_2O^+ energy levels up to maximum ~ 12000 cm^{-1} .

v	$E_{v,1}$	$E_{v,2}$	$E_{v,3}$
0	1629.5	1606.45	700.85
1	4888.5	4819.35	2102.55
2	8147.5	8032.25	3504.25
3	11406.5	11245.15	4905.95
4	×	×	6307.65
5	×	×	7709.35
6	×	×	9111.05
7	×	×	10512.75
8	×	×	11914.45

Table 4.4 – Vibrational energies (in cm^{-1}) of the H_2O^+ molecule.

The reaction of interest can be described as:



where (o/p) indicates if the collision involves H_2 in its *ortho*- or *para*- form. For a non-reactive process, the nuclear spin of H_2 cannot change to keep exchange symmetry properties of the wave function with respect to identical particles. However, such conversion $o \rightleftharpoons p$ is possible through a reactive process. In particular, we will consider that the conversion is possible through the SACM assumptions. We also performed calculations assuming all particles as distinguishable. For very low energy applications, the inclusion of both *ortho*- and *para*- H_2 channels should induce a minor error due to the much larger expected amount of reactive channels, and increase with the energy due to more and more contribution of inelastic channels. In the following sections, we will check the reliability of the SACM approach in two steps:

1. Compare pure rotational inelastic cross sections between SACM and CC calculations, neglecting fine structure.
2. Then, including reactive channels and compare the total rate coefficient with experimental measurements.

4.3.3 Pure inelastic collisions

The validation of the SACM results will be performed by comparing cross sections for several collisional energies with CC calculations. In this step, we exclude reactive processes and will consider only rotational excitation of OH^+ by both *ortho*- and *para*- H_2 separately, based on the PES presented previously. For such tests, we performed cross section calculations with these two methods in order to converge transitions for collisional energies up to 500 cm^{-1} .

We show in Fig. 4.13 a comparison between all converged cross sections computed with the SACM and CC methods for three samples of collisional energies. We can see that the most dominant transitions reproduce very well CC results and generally most cross sections are well predicted within a factor of 2. Such results are similar to those found by Loreau *et al.* [97] for the rotational excitation of OH^+ by H. The inclusion of a larger basis for molecular hydrogen did not impact the present results.

We can conclude that a pure rotational excitation of OH^+ by H_2 can follow a statistical behavior for low and intermediate collisional energies. This was expected because of the large well depth ($D_e \sim 3800 \text{ cm}^{-1}$) of the collisional system that should favor the use of a statistical approach.

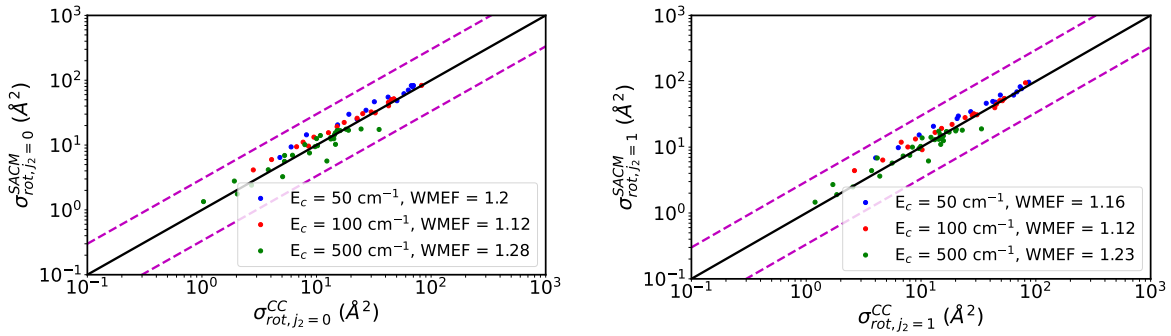


Figure 4.13 – Systematic comparison of rotational cross sections computed with the SACM and CC approaches. Transitions are determined considering *para*-H₂ collisions (left) and *ortho*-H₂ collisions (right). Dashed lines represent deviations by a factor of 3.

4.3.4 Inclusion of reactive processes

Now, we investigate the validity of the SACM when including reactive channels. To do so, we will compute the rate coefficient k_{OH^+} for the OH⁺ reaction with normal H₂ and compare to experimental measurements [236]. In this case, we use normal H₂ to be consistent with experimental conditions. This means that the statistical population of three-fourths of *ortho*-H₂ and one-fourth of *para*-H₂ at 300 K was used throughout the temperature range (5–300 K). The reactive rate coefficient was computed as follow:

$$\begin{aligned}
 k_{\text{OH}^+}(T) &= \sum_{j_1} n_{j_1}(T) \sum_{j_2} n_{j_2}(T) \sum_{\alpha'} k_{j_1 j_2 \rightarrow \alpha'}(T) \\
 &\equiv \frac{\sum_{j_1} [j_1] e^{-E_{j_1}/(k_B T)}}{\sum_{j_1''} [j_1''] e^{-E_{j_1''}/(k_B T)}} \left[\frac{3}{4} \sum_{\alpha'} k_{j_1 j_2, \text{odd} \rightarrow \alpha'}(T) + \frac{1}{4} \sum_{\alpha'} k_{j_1 j_2, \text{even} \rightarrow \alpha'}(T) \right] \quad (4.12)
 \end{aligned}$$

where $n_{j_1}(T) = \frac{[j_1] e^{-E_{j_1}/(k_B T)}}{\sum_{j_1''} [j_1''] e^{-E_{j_1''}/(k_B T)}}$ is the thermal distribution of the population of the target for each temperature. Here we took rotational energy levels E_{j_1} up to $j_1 = 14$. Finally, α' regroups all quantum numbers describing any H₂O⁺ state as $\alpha' \equiv j'_{k'_a k'_c}, v', \nu'_i$; and $k_{j_1 j_2 \rightarrow \alpha'}$ is a state-to-state reactive rate coefficient. Calculations of the $k_{j_1 j_2 \rightarrow \alpha'}$ rate coefficients have been done up to a total energy $E_{\text{tot}}^{\text{max}}$ of 5000 cm⁻¹ to ensure convergence of the 14 first OH⁺ energy levels and up to $j_2 = 0, 1$ for H₂.

We show in Fig. 4.14 a comparison of the total rate coefficient computed with Eq. (4.12) to results of the literature. SACM calculation is reproducing experimental measurements of Tran *et al.* up to a factor ~ 2 at 15 K, and shows even better agreement with those of Kumar *et al.*. Experimental and computed rate coefficients show a temperature dependence compared to the Langevin collisional rate k_L and increase up to ~ 60 K, following

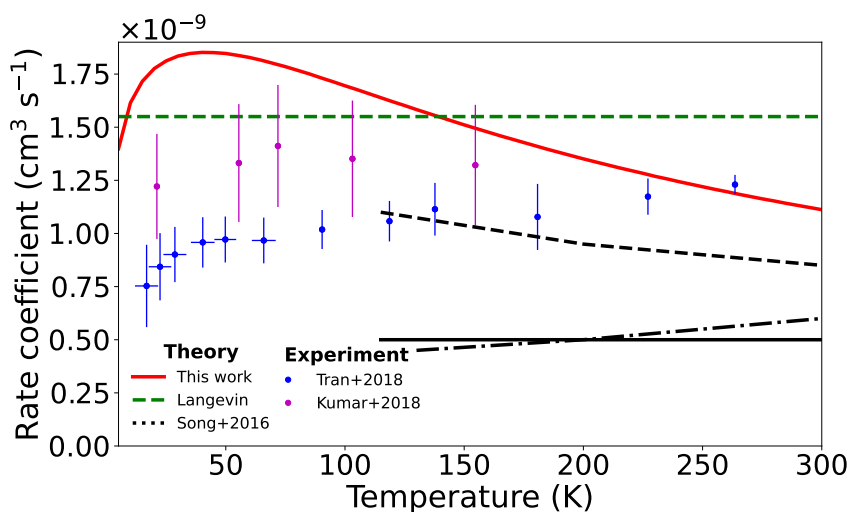


Figure 4.14 – Evolution of the temperature of the rate coefficient k_{OH^+} for the reaction of OH^+ with normal H_2 . Red line represents theoretical calculation with the SACM approach, green curve is the Langevin model of the reaction, blue dots are experimental measurements by Tran *et al.* [236], purple dots are measurements from Kumar *et al.* [237]. Dark data are the k_{j_1, j_2} rate coefficients from Song *et al.* [238] computed with a WP method, where $k_{0,0}$, $k_{2,0}$ and $k_{0,1}$ are in solid, dashed and dashed/dotted lines.

the same behavior. Then, the SACM rate coefficient starts to decrease at high temperatures, showing also similar tendency with the measurements of Kumar *et al.* up to ~ 150 K. Further decreasing of the SACM rate at higher temperatures may be due to either more and more channels of reactants opening toward high energies, promoting non-reactive processes, or the expected fail of the SACM at high temperatures. It is interesting to see that state specific rate coefficients computed by Song *et al.* [238] corroborate also measurements within a factor of 2. A calculation of the total reaction rate would give a similar accuracy.

We can look in more details the contribution of the initial state of OH^+ to the total rate coefficient as plotted in Fig. 4.15. All transitions follow the same behavior as in Fig. 4.14 for the same previous reasons. On the other hand, it seems that the largest contribution comes from the OH^+ ground rotational state $j_1 = 0$ and for $j_2 = 0$. This is expected since these are the most populated levels especially at low temperatures. Most of transitions for $j_2 = 1$ are of the same order of magnitude than those for $j_2 = 0$. Then, contribution to the total rate decreases with the OH^+ energy level. However, this is in contradiction with results determined in previous theoretical studies [238], [242] where the rotational excitation of both OH^+ and H_2 enhance the reaction. This can be due to the rigid rotor approximation used in this work, where we restrict internal motions of the system and potentially miss effects related to the saddle point which should act like a

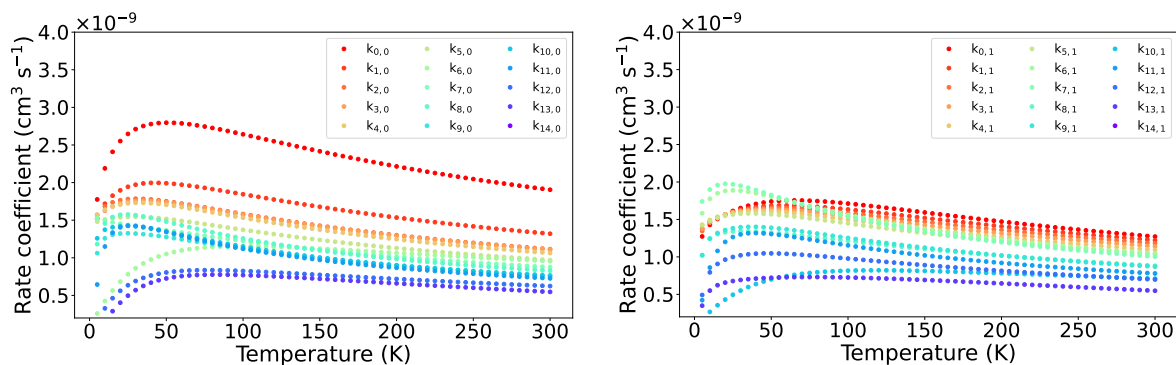


Figure 4.15 – Evolution of SACM reactive rate coefficients with temperature. Each rate $k_{j_1 j_2}$ is summed over products states for simplicity. Left panel shows reactions involving *para*-H₂ ($j_2 = 0$). Right panel stands for *ortho*-H₂ ($j_2 = 1$).

bottleneck and have influence on the rotational excitation to enhance the reactivity.

Overall, regarding the good agreement of pure scattering calculations with CC and reasonable match of the reactivity with experiments, we can be confident in the use of the SACM approach for rotational excitation involving reactive processes for data production as a reliable alternative to more accurate approaches when these cannot be applied, especially at low temperatures.

4.3.5 Rotational state-to-state rate coefficients of OH⁺ induced by collisions with H₂

For data production, we performed SACM calculations up to 300 K to cover environments where OH⁺ is detected. This necessitated to reach a total energy E_{tot}^{max} of 5000 cm⁻¹ and a OH⁺ rotational basis of $j_{1,max} = 17$ and H₂ rotational basis of $j_{2,max} = 8,9$ to expect convergence of rotational cross sections involving OH⁺ energy levels up to $j_1 = 14$ and $j_2 = 1,2$.

Fig. 4.16 displays several rotational cross sections with their corresponding rate coefficients for OH⁺ collisions with *ortho*- and *para*-H₂. Only abrupt different behavior is seen for cross sections at high energies ($E_c \geq 1000$ cm⁻¹), reflecting the limits of the SACM. However, this failure has a minor effect on rate coefficients since these energies do not play an important role in the Boltzmann integration at 300 K. From similarities between *ortho*- and *para*-H₂, we cannot conclude on clear propensity rules, as seen usually for collisions involving neutral species. Another point is the behavior of cross sections. For low collisional energies up to ~ 30 -40 cm⁻¹, the decreasing magnitudes are related to the large inclusions of reactive channels, dominating inelastic collisions in this regime. Beyond

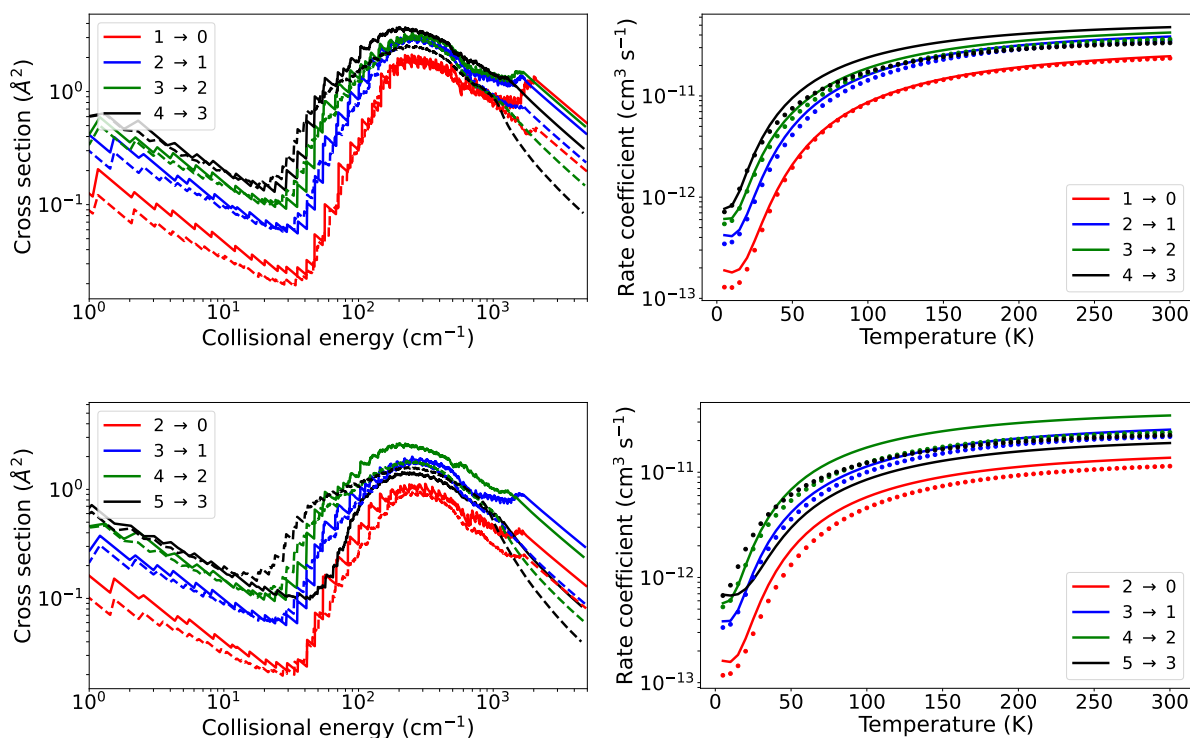


Figure 4.16 – Left panel shows the evolution of cross sections of OH^+ with *para*- H_2 (solid) and *ortho*- H_2 (dotted) with the collisional energy for rotational transitions where $\Delta N = 1$ (top) and $\Delta N = 2$ (bottom). Right panel shows the corresponding rate coefficients.

40 cm^{-1} , the magnitude of cross sections starts to increase due to larger contributions coming from inelastic channels compared to reactive ones. For example, the total number of JTOT parameter needed in the counting of the adiabats for reactants was $\text{JTOT} = 64$ (for both *ortho*- and *para*- H_2) whereas only $\text{JTOT} = 25$ was enough to count adiabats for products.

We can illustrate the differences between inelastic and reactive rate coefficients in Fig. 4.17. It is clear that the reactivity dominates over the range of temperature and still by ~ 2 orders of magnitudes at 300 K, independently of the initial or the final state. This can be attributed to the large exothermicity, resulting in a description of ~ 2300 energy levels for *ortho*- H_2O^+ and *para*- H_2O^+ each; and the inclusion of a larger number of channels for these products than those for OH^+ final states. Then, the summation over all products is naturally giving larger intensities for reactive rate coefficients than those describing inelastic transitions.

It is interesting to look at differences between collisional rate coefficients processed with only non-reactive channels with those computed including reactivity. Fig. 4.18 displays a very significant difference of magnitude in rate coefficients between the two sets of data. This can go from ~ 2 -3 orders of magnitude at low temperature up to a factor

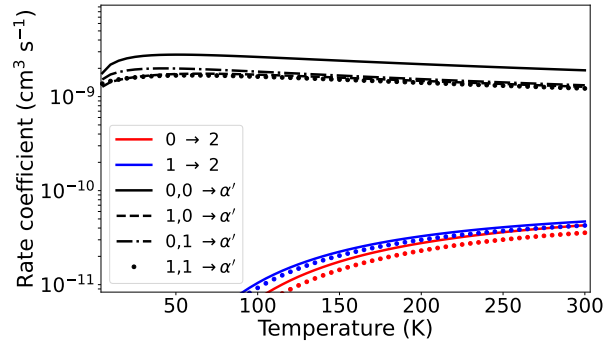


Figure 4.17 – Temperature evolution of several rate coefficients for the $\text{OH}^+\text{-H}_2$ collisional system. Blue and red lines stands for inelastic rate coefficients $k_{j_1 \rightarrow j'_1}$ involving *para*- H_2 (solid) and *ortho*- H_2 (dotted) including reactive channels. All black curves represent reactive rate coefficients $k_{j_1, j_2 \rightarrow \alpha'}$ where α' designates all quantum numbers for the products. All state-to-state reactive rates have been summed over products for clarity.

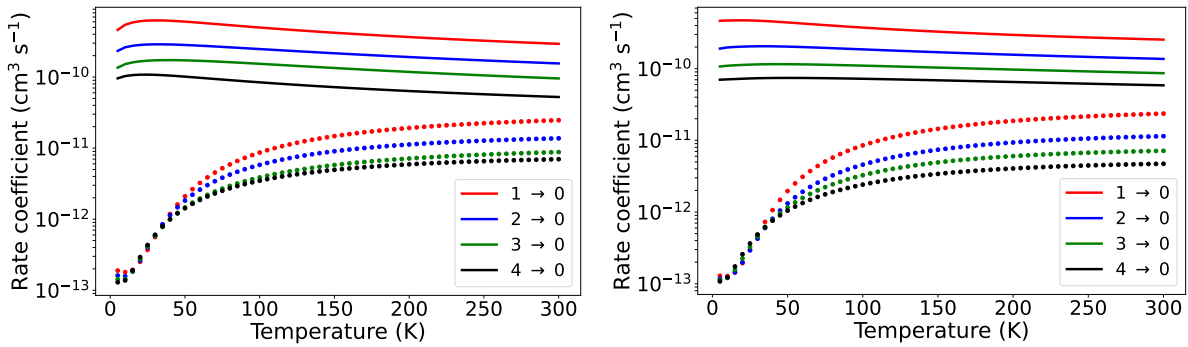


Figure 4.18 – Temperature dependence of rotational de-excitation rate coefficients of OH^+ ($N \rightarrow N'$) with *para*- H_2 ($j_2 = 0$) (left) and *ortho*- H_2 ($j_2 = 1$) (right). Solid lines are related to pure inelastic collisions whereas dotted lines stands for inelastic transitions including reactive channels.

of 10 at high temperatures for *ortho*- and *para*- H_2 collisions. Below 50 K, the number of reactive channels dominates by orders of magnitudes over inelastic ones. For temperatures beyond 50 K, energy levels for reactants start to be more and more populated; and non-reactive channels will compete with reactive processes.

We presented the first set of rotational state-to-state rate coefficients for the $\text{OH}^+\text{-H}_2$ collisional system, including reactive processes. OH^+ being detected in the ISM through hyperfine lines, the next step will be to use this set of data to determine hyperfine resolved rate coefficients to be useful for astrophysical applications. To do so, we project to use IOS methods. However, unlike the case of NH , we will use rotational transitions and not fine structure ones to perform this method so we cannot be sure of a similar agreement

with CC; and tests must be done prior to data production. Finally, we saw that the general order of magnitude of reactive rate coefficients are of the order of $10^{-9} \text{ cm}^{-3}\text{s}^{-1}$ contrary to inelastic collisions, about 10^{-13} – $10^{-12} \text{ cm}^{-3}\text{s}^{-1}$ below 50 K. This is much below than typical intensities reported for the collisional excitation of OH^+ by He [230] and by atomic hydrogen ($\sim 10^{-11}$ – $10^{-10} \text{ cm}^{-3}\text{s}^{-1}$) [228], [234], [249]. We can suggest that collisional excitation induced by molecular hydrogen would be unprobable in the very cold ISM.

CONCLUSIONS AND OUTLOOKS

This thesis presented results for the collisional excitation of radicals by molecular hydrogen for astrophysical applications. This work has two main objectives: to explore state of the art methods and their limits for non-reactive systems; and the impact of statistical approach when including both inelastic and reactive channels in scattering calculations.

In the first part of the thesis, we used the close-coupling approach to carry out time independent scattering calculations in order to provide fine structure resolved rate coefficients for the NH–H₂, ND–H₂, C₂H–H₂, C₂D–H₂, ¹³CCH–H₂ and C¹³CH–H₂ collisional systems. These calculations were based on the PESs that we used to derive those for the treatment of isotopologues. We showed that the most accurate approach can be used for such treatment including the internal structure of the projectile. Differences in rate coefficients are found to be significant when considering *ortho*- or *para*-H₂, from a factor 2 to 10 for all systems considered. We explored the impact of the isotopic substitution on rate coefficients. It results that differences between isotopologues are very minor, up to a factor of 2, for heavy molecules possessing similar energetic structures like C₂H and C₂D. Discrepancies are even lower when the isotopic substitution is attributed to a heavy atom, showing deviations between ¹³CCH, C¹³CH and C₂H less than 30%. For light systems like NH and ND, we saw differences between a factor of 3–5, mostly attributed to the different rotational structures of the colliders. We also corroborate the disagreement between collisions involving He or H₂ projectiles that is usually observed in the literature. This is mostly attributed to the differences in the PESs, showing larger anisotropies for H₂ collisions than for He ones and involving more contributions in cross sections. Mismatches in propensity rules can also be observed between the two projectiles.

For the hyperfine structure treatment, the recoupling method remains the best approach. However, the coupling of electronic spin and one or two nuclear spins to the rotation, including the structure of the projectile is leading to a large number of channels to include in calculations and is computationally expensive and do not permit calculations with nowadays facilities. For the case of ¹³CCH–H₂ and C¹³CH–H₂, we explored strategies to face this challenge that we validated using the C₂H–H₂ collisional system as our reference. We showed that both the dimensional reduction approximation and the IOS limit are leading

to difference of about 20% with respect to the recoupling including one nuclear spin and the structure of the projectile. Then, we chose the dimensional reduction approach for data production of $^{13}\text{CCH-H}_2$ and $\text{C}^{13}\text{CH-H}_2$ hyperfine resolved rate coefficients. In the case of NH and ND, we implemented a description for hyperfine rate coefficients between $^3\Sigma$ systems in collision with a projectile with $j_2 \neq 0$ using the IOS approximation. These formulae take into account fundamental fine structure transitions that was missing in the literature. We compared it to the reference method for both systems and found deviations by less than 50% for all selected cross sections. We assumed that the inclusion of the second nuclear spin do not involve more errors. All the computed collisional data have been submitted to the two most active databases BASECOL [50] and EMAA.

The computed rate coefficients have been used in simple radiative transfer modeling. We showed that the inclusion of both *ortho*- and *para*- H_2 collisions can have an impact in excitation temperatures and critical densities. For conditions similar to those of TMC-1 or L1527, the computed column density of C_2D is consistent within a factor 1.5 with the one computed by Yoshida *et al.* [140] assuming LTE conditions. Finally, we studied the excitation of NH in the η Carinae binary system [164]. The present computed column density differs by a factor of 5 with the previous value where rate coefficients were not available and were then estimated.

The presented results for non-reactive systems led to four peer-reviewed articles, namely Pirlot Jankowiak *et al.* [189], [193]–[195] and can be found also in appendix C.

The second part of this thesis was devoted to the calculation of collisional rate coefficients for reactive systems, when both inelastic and reactive channels must be taken into account simultaneously. This work was done in two substeps. First, we explored the validity of the SACM approach for describing fine structure transitions, where this consideration is missing in the literature. We tested this method with respect to CC calculations through inelastic collisions using the $\text{OH}^+\text{-H}$ collisional system as a test case. We showed a moderate agreement between the two methods by a factor of 3. However, the SACM fails to reproduce specific fine structure transitions and we doubt about its usage for data production. Second, we explored the impact of the SACM in the rotational excitation of OH^+ by H_2 when including both inelastic and reactive processes. We started by showing that SACM successfully reproduce pure inelastic CC calculations. For the reactivity, we compared the total reactive rate coefficient for the OH^+ reaction with normal- H_2 with experimental measurements done by Tran *et al.* [236] and found agreement at low temperature by a factor of 2. The computed inelastic and reactive rate coefficients with the SACM were found to be significantly different by 2 orders of magnitudes, showing domination of reactive collisions for the $\text{OH}^+\text{-H}_2$ collisional system and the importance of considering the reactive path in inelastic calculations. Also, comparisons between pure

inelastic collisions with those including reactive channels show discrepancies up to 3 orders of magnitude at 10–50 K. This suggests that the collisional excitation of OH⁺ by H₂ is weak, contrary to H or He, being endothermic or non-reactive collisions.

For non-reactive systems, a natural extension of this work is to use the new collisional data for C₂D–H₂ collisions to perform radiative transfer modeling for sources with a lower density than L1527, where non-LTE effects should be more significant. In the case of NH, it can be interesting to revise the abundance of both NH and ND. In the study by Bacmann *et al.* [161], both detected have been detected in absorption towards the IRAS16293 protostar, tracing the colder envelope surrounding the protostar. In this study, the lines were fitted using the CLASS HFS method, assuming LTE conditions. In a second study by Bacmann *et al.* [157], detections were reported in the prestellar core 16293E, where both NH and ND were observed. ND was detected in emission, while NH appeared in absorption against the continuum originating from cold dust emission. The model revealed that the ND emission and NH absorption arise from distinct layers within the cloud, as indicated by their differing velocities. In the central region of the core, a lower limit for the [ND]/[NH] ratio of $\geq 2\%$ was established using collision data computed by Dumouchel *et al.* [173] using He as a proxy for H₂.

For reactive systems, the study of OH⁺–H₂ collisions will be completed by computing hyperfine rate coefficients using the IOS approach. Validation must be done prior to data production since we did not include fine structure transitions in SACM calculations. These data will be provided to the BASECOL, EMAA and LAMDA databases and the synthesis of this work will be submitted in a peer-review journal. However, the success of this statistical method to take into account both rotational excitation and reactive processes invite to use it for further reactive molecules like CH⁺ or other hydrides in collision with H or H₂, being important species for the formation of heavier molecules and eventually to prebiotic molecules. Also, the SACM approach saves dramatical computational time compared to CC calculations and it can serve as a useful and promising alternative to provide collisional data for heavy polyatomic systems. Especially, the detection of ro-vibrational transitions in the next years will be more and more significant thanks to advancement in resolution of instruments, exact approaches will not be exploitable to meet astrophysical needs. The SACM can be a starting point toward the development of new theoretical methods for studying reactive and heavy systems which can have a high impact on astrochemistry.

Finally, we expect all computed collisional data and the methodologies used in this

thesis to be useful for future investigations, constraining the questions of astrochemistry; and bring better knowledge about the molecular excitation in space, chemical diversity and star formation.

Appendix

NOTES ON THE V -MATRIX ELEMENTS FOR $2S+1\Sigma - 1\Sigma$ INTERACTIONS

By taking the form of Eqs. (3.15) and (3.31), we can open the V -matrix elements:

$$\begin{aligned}
\langle \alpha'' j''_{12} L'' | \hat{V} | \alpha' j'_{12} L' \rangle &= \sum_{\lambda_1 \lambda_2 \lambda} v_{\lambda_1 \lambda_2 \lambda}(R) \sum_{(m)} C_{m_{\lambda_1} m_{\lambda_2} m}^{\lambda_1 \lambda_2 \lambda} C_{m'_{12} m'_L M}^{j''_{12} L' J} C_{m'_1 m'_2 m'_{12}}^{j'_1 j'_2 j'_{12}} C_{m'_N m_S m'_1}^{N' S j'_1} C_{m''_{12} m''_L M}^{j''_{12} L'' J} \\
&\times C_{m'_1 m'_2 m''_{12}}^{j''_{12} j'_2 j'_{12}} C_{m''_N m_S m'_1}^{N'' S j''_1} \langle N'' m''_N | Y_{\lambda_1 m_{\lambda_1}} | N' m'_N \rangle \\
&\times \langle j''_2 m''_2 | Y_{\lambda_2 m_{\lambda_2}} | j'_2 m'_2 \rangle \langle L'' m''_L | Y_{\lambda m}^* | L' m'_L \rangle
\end{aligned} \tag{A.1}$$

Using the spherical harmonics addition theorem, terms in brackets can be written as [250]:

- $\langle N'' m''_N | Y_{\lambda_1 m_{\lambda_1}} | N' m'_N \rangle = \left(\frac{[N' \lambda_1]}{[N''] 4\pi} \right)^{1/2} C_{m'_N m_{\lambda_1} m''_N}^{N' \lambda_1 N''} C_{000}^{N' \lambda_1 N''}$
- $\langle j''_2 m''_2 | Y_{\lambda_2 m_{\lambda_2}} | j'_2 m'_2 \rangle = \left(\frac{[j'_2 \lambda_2]}{[j''_2] 4\pi} \right)^{1/2} C_{m'_2 m_{\lambda_2} m''_2}^{j'_2 \lambda_2 j'_2} C_{000}^{j'_2 \lambda_2 j''_2}$
- $\langle L'' m''_L | Y_{\lambda m}^* | L' m'_L \rangle = \left(\frac{[L'' \lambda]}{[L'] 4\pi} \right)^{1/2} C_{m''_L m m'_L}^{L'' \lambda L'} C_{000}^{L'' \lambda L'}$

The V -matrix elements can be re-written:

$$\begin{aligned}
\langle \alpha'' j''_{12} L'' | \hat{V} | \alpha' j'_{12} L' \rangle &= (4\pi)^{-3/2} \left(\frac{[N' \lambda_1 j'_2 \lambda_2 L'' \lambda]}{[N'' j''_2 L']} \right)^{1/2} \sum_{\lambda_1 \lambda_2 \lambda} v_{\lambda_1 \lambda_2 \lambda}(R) \\
&\times \sum_{(m)} C_{m_{\lambda_1} m_{\lambda_2} m}^{\lambda_1 \lambda_2 \lambda} C_{m'_{12} m'_L M}^{j''_{12} L' J} C_{m'_1 m'_2 m'_{12}}^{j'_1 j'_2 j'_{12}} C_{m'_N m_S m'_1}^{N' S j'_1} C_{m''_{12} m''_L M}^{j''_{12} L'' J} C_{m'_1 m'_2 m''_{12}}^{j''_{12} j'_2 j'_{12}} \\
&\times C_{m''_N m_S m'_1}^{N'' S j''_1} C_{m'_N m_{\lambda_1} m''_N}^{N' \lambda_1 N''} C_{m'_2 m_{\lambda_2} m''_2}^{j'_2 \lambda_2 j'_2} C_{m''_L m m'_L}^{L'' \lambda L'} \\
&\times C_{000}^{N' \lambda_1 N''} C_{000}^{j'_2 \lambda_2 j''_2} C_{000}^{L'' \lambda L'}
\end{aligned} \tag{A.2}$$

All Clebsch-Gordan coefficients can be open and expressed in term of the $3j$ symbols. It is possible to take advantage of their symmetry rules and by using recoupling angular momentum algebra we can use the identity [251]:

$$j_1 + j_2 = J_{12} \quad j_3 + j_4 = J_{34} \quad J_{12} + J_{34} = J_T$$

$$j_1 + j_3 = J_{13} \quad j_2 + j_4 = J_{24} \quad J_{13} + J_{24} = J_T$$

$$\begin{aligned} \begin{pmatrix} J_{13} & J_{24} & J_T \\ M_{13} & M_{24} & M \end{pmatrix} \begin{Bmatrix} j_1 & j_2 & J_{12} \\ j_3 & j_4 & J_{34} \\ J_{13} & J_{24} & J_T \end{Bmatrix} &= \sum_{\substack{m_1 m_2 m_3 m_4 \\ M_{12} M_{34}}} \begin{pmatrix} j_1 & j_2 & J_{12} \\ m_1 & m_2 & M_{12} \end{pmatrix} \begin{pmatrix} j_3 & j_4 & J_{34} \\ m_3 & m_4 & M_{34} \end{pmatrix} \\ &\times \begin{pmatrix} j_1 & j_3 & J_{13} \\ m_1 & m_3 & M_{13} \end{pmatrix} \begin{pmatrix} j_2 & j_4 & J_{24} \\ m_2 & m_4 & M_{24} \end{pmatrix} \begin{pmatrix} J_{12} & J_{34} & J_T \\ M_{12} & M_{34} & M \end{pmatrix} \end{aligned} \quad (\text{A.3})$$

By taking the correspondence:

$$(j_1, j_2) \equiv (j'_1, j''_1); \quad (j_3, j_4) \equiv (j'_2, j''_2)$$

$$(J_{12}, J_{34}) \equiv (\lambda_1, \lambda_2); \quad (J_{13}, J_{24}) \equiv (j'_{12}, j''_{12}); \quad J_T \equiv \lambda$$

We can replace in Eq. (A.3) to get:

$$\begin{aligned} \begin{pmatrix} j'_{12} & j''_{12} & \lambda \\ m'_{12} & m''_{12} & m \end{pmatrix} \begin{Bmatrix} j'_1 & j''_1 & \lambda_1 \\ j'_2 & j''_2 & \lambda_2 \\ j'_{12} & j''_{12} & \lambda \end{Bmatrix} &= \sum_{\substack{m'_1 m''_1 m'_2 m''_2 \\ m_{\lambda_1} m_{\lambda_2}}} \begin{pmatrix} j'_1 & j''_1 & \lambda_1 \\ m'_1 & m''_1 & m_{\lambda_1} \end{pmatrix} \begin{pmatrix} j'_2 & j''_2 & \lambda_2 \\ m'_2 & m''_2 & m_{\lambda_2} \end{pmatrix} \\ &\times \begin{pmatrix} j'_1 & j'_2 & j'_{12} \\ m'_1 & m'_2 & m'_{12} \end{pmatrix} \begin{pmatrix} j''_1 & j''_2 & j''_{12} \\ m''_1 & m''_2 & m''_{12} \end{pmatrix} \begin{pmatrix} \lambda_1 & \lambda_2 & \lambda \\ m_{\lambda_1} & m_{\lambda_2} & m \end{pmatrix} \end{aligned} \quad (\text{A.4})$$

The first $3j$ symbol in the right hand side (RHS) of Eq. (A.4) is not present in Eq. (A.2). But we can multiply the RHS by [202]:

$$\sum_{\substack{m_1 m'_1 \\ m_{\lambda_1}}} \begin{pmatrix} j'_1 & j''_1 & \lambda_1 \\ m'_1 & m''_1 & m_{\lambda_1} \end{pmatrix}^2 = 1$$

The V -matrix elements can be simplified as:

$$\begin{aligned}
\langle \alpha'' j''_{12} L'' | \hat{V} | \alpha' j'_{12} L' \rangle &= (4\pi)^{-3/2} \left([\lambda_1 \lambda_2 N' j'_1 j'_2 j'_{12} j''_1 j''_{12} L''] \right)^{1/2} [\lambda J] \sum_{\lambda_1 \lambda_2 \lambda} v_{\lambda_1 \lambda_2 \lambda}(R) \\
&\times C_{000}^{N' \lambda_1 N''} C_{000}^{j'_2 \lambda_2 j''_2} C_{000}^{L'' \lambda L'} \\
&\times \sum_{(m)} (-1)^{j'_1 + j'_2 + j'_{12} - L' + N'' + j''_1 + j''_{12} + \lambda_2 - \lambda + m'_1 + m'_{12} + m'_L + m''_N + m''_1 + m''_2 + m''_{12} + m} \\
&\times \begin{pmatrix} N' & S & j'_1 \\ m'_N & m_S & m'_1 \end{pmatrix} \begin{pmatrix} N'' & S & j''_1 \\ m''_N & m_S & m''_1 \end{pmatrix} \begin{pmatrix} N' & \lambda_1 & N'' \\ m'_N & m_{\lambda_1} & m''_N \end{pmatrix} \\
&\times \begin{pmatrix} j'_1 & j''_1 & \lambda_1 \\ m'_1 & m''_1 & m_{\lambda_1} \end{pmatrix} \begin{pmatrix} j'_{12} & L' & J \\ m'_{12} & m'_L & M \end{pmatrix} \begin{pmatrix} j''_{12} & L'' & J \\ m''_{12} & m''_L & M \end{pmatrix} \\
&\times \begin{pmatrix} L'' & \lambda & L' \\ m''_L & m & m'_L \end{pmatrix} \begin{pmatrix} j'_{12} & j''_{12} & \lambda \\ m'_{12} & m''_{12} & m \end{pmatrix} \left\{ \begin{matrix} j'_1 & j''_1 & \lambda_1 \\ j'_2 & j''_2 & \lambda_2 \\ j'_{12} & j''_{12} & \lambda \end{matrix} \right\} \quad (\text{A.5})
\end{aligned}$$

Eq. (A.5) can be more compacted into $6j$ symbols by using the identity [251]:

$$\begin{aligned}
\delta_{j_3 j'_3} \delta_{m_3 m'_3} \frac{1}{[j_3]} \left\{ \begin{matrix} j_1 & j_2 & j_3 \\ J_1 & J_2 & J_3 \end{matrix} \right\} &= \sum_{\substack{m_1 m_2 \\ M_1 M_2 M_3}} (-1)^{J_1 + J_2 + J_3 + M_1 + M_2 + M_3} \begin{pmatrix} J_1 & J_2 & j_3 \\ M_1 & M_2 & m_3 \end{pmatrix} \\
&\times \begin{pmatrix} J_2 & J_3 & j_1 \\ M_2 & M_3 & m_1 \end{pmatrix} \begin{pmatrix} J_3 & J_1 & j_2 \\ M_3 & M_1 & m_2 \end{pmatrix} \begin{pmatrix} j_1 & j_2 & j'_3 \\ m_1 & m_2 & m'_3 \end{pmatrix} \quad (\text{A.6})
\end{aligned}$$

and can be applied on the four first explicit $3j$ symbols and the four next ones, respectively by writing the correspondences:

$$\begin{aligned}
\delta_{JJ'} \delta_{MM'} \frac{1}{[J]} \left\{ \begin{matrix} j''_{12} & L'' & J \\ L' & j'_{12} & \lambda \end{matrix} \right\} &= \sum_{\substack{m''_{12} m''_L \\ m'_L m'_{12} m}} (-1)^{L' + j'_{12} + \lambda + m'_L + m'_{12} + m} \begin{pmatrix} L' & j'_{12} & J \\ m'_L & m'_{12} & M \end{pmatrix} \\
&\times \begin{pmatrix} j'_{12} & \lambda & j''_{12} \\ m'_{12} & m & m''_{12} \end{pmatrix} \begin{pmatrix} \lambda & L' & L'' \\ m & m'_L & m''_L \end{pmatrix} \begin{pmatrix} j''_{12} & L'' & J \\ m''_{12} & m''_L & M \end{pmatrix} \quad (\text{A.7})
\end{aligned}$$

$$\begin{aligned}
\delta_{SS'} \delta_{m_S m'_S} \frac{1}{[S]} \left\{ \begin{matrix} j'_1 & N' & S \\ N'' & j''_1 & \lambda_1 \end{matrix} \right\} &= \sum_{\substack{m'_1 m'_N \\ m''_N m''_1 m_{\lambda_1}}} (-1)^{N'' + j''_1 + \lambda_1 + m''_N + m''_1 + m_{\lambda_1}} \begin{pmatrix} N'' & j''_1 & S \\ m''_N & m''_1 & m_S \end{pmatrix} \\
&\times \begin{pmatrix} j'_1 & \lambda_1 & j'_1 \\ m'_1 & m_{\lambda_1} & m'_1 \end{pmatrix} \begin{pmatrix} \lambda_1 & N'' & N' \\ m_{\lambda_1} & m''_N & m'_N \end{pmatrix} \begin{pmatrix} j'_1 & N' & S \\ m'_1 & m'_N & m_S \end{pmatrix} \quad (\text{A.8})
\end{aligned}$$

and taking into account the symmetry rules of the $3j$ symbols when applying an odd permutation of two columns:

$$\begin{pmatrix} J_1 & J_2 & J_3 \\ M_1 & M_2 & M_3 \end{pmatrix} = (-1)^{J_1+J_2+J_3} \begin{pmatrix} J_2 & J_1 & J_3 \\ M_2 & M_1 & M_3 \end{pmatrix} \quad (\text{A.9})$$

By reintroducing (A.7) and (A.8) into (A.5) we have:

$$\begin{aligned} \langle \alpha'' j''_{12} L'' | \hat{V} | \alpha' j'_{12} L' \rangle &= (4\pi)^{-3/2} \left([\lambda_1 \lambda_2 N' j'_1 j'_2 j'_{12} j''_1 j''_{12} L''] \right)^{1/2} \frac{[\lambda]}{[S]} \sum_{\lambda_1 \lambda_2 \lambda} v_{\lambda_1 \lambda_2 \lambda}(R) \\ &\times C_{000}^{N' \lambda_1 N''} C_{000}^{j'_2 \lambda_2 j''_2} C_{000}^{L'' \lambda L'} (-1)^A \\ &\times \left\{ \begin{matrix} j'_1 & N' & S \\ N'' & j''_1 & \lambda_1 \end{matrix} \right\} \left\{ \begin{matrix} j''_{12} & L'' & J \\ L' & j'_{12} & \lambda \end{matrix} \right\} \left\{ \begin{matrix} j'_1 & j''_1 & \lambda_1 \\ j'_2 & j''_2 & \lambda_2 \\ j'_{12} & j''_{12} & \lambda \end{matrix} \right\} \quad (\text{A.10}) \end{aligned}$$

with $A = j'_1 + j'_2 + S + L' + N'' + j''_1 + j''_{12} - \lambda_1 + \lambda_2 + \lambda + J - m_{\lambda_1} + m'_1 + m''_2 + m''_{12}$. The (m) coefficients are zero by using that $m'_1 + m''_1 + m_{\lambda_1} = 0$ and $m''_1 + m''_2 + m''_{12} = 0$. When opening the remained Clebsch-Gordan coefficients, we obtain the final form of the V -matrix elements:

$$\begin{aligned} \langle \alpha'' j''_{12} L'' | \hat{V} | \alpha' j'_{12} L' \rangle &= (4\pi)^{-3/2} \sum_{\lambda_1 \lambda_2 \lambda} v_{\lambda_1 \lambda_2 \lambda}(R) \frac{[\lambda]}{[S]} [\lambda_1 \lambda_2 N'' N' j'_1 j'_2 j''_1 j''_2 j'_{12} j''_{12} L'' L']^{1/2} \\ &\times (-1)^{N'+j'_1+S+L'+N''+j''_1+j''_{12}+L''+J} \\ &\times \begin{pmatrix} N' & \lambda_1 & N'' \\ 0 & 0 & 0 \end{pmatrix} \begin{pmatrix} j'_2 & \lambda_2 & j''_2 \\ 0 & 0 & 0 \end{pmatrix} \begin{pmatrix} L' & \lambda & L'' \\ 0 & 0 & 0 \end{pmatrix} \\ &\times \left\{ \begin{matrix} j'_1 & N' & S \\ N'' & j''_1 & \lambda_1 \end{matrix} \right\} \left\{ \begin{matrix} j''_{12} & L'' & J \\ L' & j'_{12} & \lambda \end{matrix} \right\} \left\{ \begin{matrix} j'_1 & j''_1 & \lambda_1 \\ j'_2 & j''_2 & \lambda_2 \\ j'_{12} & j''_{12} & \lambda \end{matrix} \right\} \quad (\text{A.11}) \end{aligned}$$

NOTES ON EINSTEIN COEFFICIENTS FOR LINEAR OPEN-SHELL MOLECULES

The following notes are based on Sobelman [252].

For a linear open-shell molecule in the $2S+1\Sigma$ electronic state, the general expression of the spontaneous emission of a photon given by the Einstein coefficient A_{ij} can be written in terms of the line strength factor $S'(NjS, N'j'S)$ ¹:

$$A_{Nj \rightarrow N'j'} = \frac{64\pi^4 \nu_{Nj \rightarrow N'j'}^3}{3hc^3} \frac{S'(NjS, N'j'S)}{[j]} \quad (\text{B.1})$$

with $S'(NjS, N'j'S) = |\langle N'j'S | \hat{\mu} | NjS \rangle|^2$ and $\hat{\mu}$ is the dipole moment operator. Since $\hat{\mu}$ commutes with \hat{S} we can express the dipole moment matrix elements as [202]:

$$\langle N'j'S | \hat{\mu} | NjS \rangle = (-1)^{S+1+N+j} [jj']^{1/2} \left\{ \begin{matrix} N & j & S \\ j' & N' & 1 \end{matrix} \right\} \delta_{SS'} \langle N' | \hat{\mu} | N \rangle \quad (\text{B.2})$$

The $6j$ symbol appearing in relation (B.2) imposes selection rules in radiative transitions as:

- $\Delta S = 0$
- $\Delta N = \pm 1$

We can rewrite the expression of $S'(NjS, N'j'S)$:

$$S'(NjS, N'j'S) = [jj'] \left\{ \begin{matrix} N & j & S \\ j' & N' & 1 \end{matrix} \right\}^2 |\langle N' | \hat{\mu} | N \rangle|^2 \quad (\text{B.3})$$

The term $\langle N' | \hat{\mu} | N \rangle$ is the dipole moment matrix element for a closed-shell molecule, and can be expressed as:

1. Here we explicitly express the line strength factor by a prime and systematically adding its dependence to the quantum numbers as $S'(NjS, N'j'S)$ to avoid confusion with the electronic spin S .

$$|\langle N' | \hat{\mu} | N \rangle|^2 = \mu_D^2 S'(N, N') = \mu_D^2 [NN'] \begin{pmatrix} N' & 1 & N \\ 0 & 0 & 0 \end{pmatrix}^2 = \mu_D^2 \max(N, N') \quad (\text{B.4})$$

with μ_D being the dipole moment of the molecule. From the selection rules imposed to radiative transitions, we have $\max(N, N') = N$. The Einstein coefficient (B.1) can be simplified:

$$A_{Nj \rightarrow N'j'} = \frac{64\pi^4 \nu_{Nj \rightarrow N'j'}^3}{3hc^3} \mu_D^2 N[j'] \begin{Bmatrix} N & j & S \\ j' & N' & 1 \end{Bmatrix}^2 \quad (\text{B.5})$$

PEER-REVIEWED ARTICLES

The following sections regroups the publications related to the work summarized in chapter 3.

Appendix C.1 presents the 4D PES for the NH–H₂ collisional system. This PES has been computed several years before this thesis and my contribution was related to the validation of the PES by computing bound states of the NH⋯H₂ complex and preliminary scattering calculations including the fine structure of NH. We provided all collisional data for (hyper)fine resolved transitions in the article in appendix C.5. This article contains also all the treatment about fine and hyperfine rate coefficients for the ND–H₂ collisional system using the IOS approximation. We compare the differences between the two sets of data and also with previous data using He as a collisional partner. Finally, the impact of the collisional data for NH–H₂ is tested in radiative transfer modeling for an astrophysical application on the η Carinae system and the Orion Bar PDR.

Appendix C.3 presents the work about C₂H–H₂ and C₂D–H₂ calculations. The PES used was already computed and my contribution was to re-expand this potential to describe the C₂D–H₂ PES. We provided the new collisional data for the C₂D–H₂ collisional system including the structure of H₂, and extended fine and hyperfine structure calculations for the C₂H–H₂ collisional system. The impact of the C₂D–H₂ rate coefficients have been checked in radiative transfer modeling.

Appendix C.2 presents the publication about the hyperfine treatment of carbon-bearing isotopologues of C₂H. We also used the 4D PES for the C₂H–H₂ collisional system to determine the ¹³CCH–H₂ and C¹³CH–H₂ PESs. We reduced the dimension of these PESs to exclude the structure of H₂ in order to perform scattering calculations including into account the two nuclear spins of the isotopologues. The new collisional data have been used for radiative transfer calculation.

Finally, appendix C.4 presents an update of the BASECOL database, where the aim is to provide accurate state-to-state rate coefficients for the astrophysical community. My contribution was to furnish all collisional data computed in this thesis.

C.1 Collisional excitation of NH by H₂: Potential energy surface and scattering calculations

Collisional excitation of NH by H₂: Potential energy surface and scattering calculations

Cite as: J. Chem. Phys. **155**, 134303 (2021); <https://doi.org/10.1063/5.0066161>

Submitted: 09 August 2021 • Accepted: 07 September 2021 • Published Online: 01 October 2021

 Paul Pirlot Jankowiak, Yulia N. Kalugina,  Ragav Ramachandran, et al.



View Online



Export Citation



CrossMark

ARTICLES YOU MAY BE INTERESTED IN

[Rotational excitation of CO₂ induced by He: New potential energy surface and scattering calculations](#)

The Journal of Chemical Physics **156**, 104303 (2022); <https://doi.org/10.1063/5.0085094>

[Collisional excitation of interstellar PN by H₂: New interaction potential and scattering calculations](#)

The Journal of Chemical Physics **154**, 034304 (2021); <https://doi.org/10.1063/5.0039145>

[Fully quantum calculations of O₂-N₂ scattering using a new potential energy surface: Collisional perturbations of the oxygen 118#GHz fine structure line](#)

The Journal of Chemical Physics **155**, 124307 (2021); <https://doi.org/10.1063/5.0063006>

Learn More

The Journal of Chemical Physics **Special Topics** Open for Submissions

Collisional excitation of NH by H₂: Potential energy surface and scattering calculations

Cite as: J. Chem. Phys. 155, 134303 (2021); doi: 10.1063/5.0066161

Submitted: 9 August 2021 • Accepted: 7 September 2021 •

Published Online: 1 October 2021







View Online



Export Citation



CrossMark

Paul Pirlot Jankowiak,¹  Yulia N. Kalugina,^{2,a)} Ragav Ramachandran,³  Guillaume Raffy,¹
Paul J. Dagdigian,⁴  and François Lique^{1,3,b)} 

AFFILIATIONS

¹ University Rennes, CNRS, IPR (Institut de Physique de Rennes)—UMR 6251, F-35000 Rennes, France

² Institute of Spectroscopy, Russian Academy of Sciences, Fizicheskaya St. 5, 108840 Troitsk, Moscow, Russia

³ LOMC-UMR 6294, CNRS-Université du Havre, 25 Rue Philippe Lebon, BP 1123, Le Havre, France

⁴ Department of Chemistry, The Johns Hopkins University, Baltimore, Maryland 21218-2685, USA

^{a)} Also at: Département de Chimie, Université de Sherbrooke, Sherbrooke J1K 2R1, Canada.

^{b)} Author to whom correspondence should be addressed: francois.lique@univ-rennes1.fr

ABSTRACT

Collisional data for the excitation of NH by H₂ are key to accurately derive the NH abundance in astrophysical media. We present a new four-dimensional potential energy surface (PES) for the NH–H₂ van der Waals complex. The *ab initio* calculations of the PES were carried out using the explicitly correlated partially spin-restricted coupled cluster method with single, double, and perturbative triple excitations [RCCSD(T)-F12a] with the augmented correlation-consistent polarized valence triple zeta basis set. The PES was represented by an angular expansion in terms of coupled spherical harmonics. The global minimum corresponds to the linear structure with a well depth $D_e = 149.10$ cm⁻¹. The calculated dissociation energy D_0 is found to be 30.55 and 22.11 cm⁻¹ for *ortho*-H₂ and *para*-H₂ complexes, respectively. These results are in agreement with the experimental values. Then, we perform quantum close-coupling calculations of the fine structure resolved excitation cross sections of NH induced by collisions with *ortho*-H₂ and *para*-H₂ for collisional energies up to 500 cm⁻¹. We find strong differences between collisions induced by *ortho*-H₂ and *para*-H₂. Propensity rules are discussed. The cross sections are larger for fine structure conserving transitions than for fine structure changing ones, as predicted by theory. These new results should help in interpreting NH interstellar spectra and better constrain the abundance of NH in interstellar molecular clouds.

Published under an exclusive license by AIP Publishing. <https://doi.org/10.1063/5.0066161>

I. INTRODUCTION

Collisional studies involving open-shell molecules are of great interest from both theoretical and experimental points of view as well as for applications in many fields, such as atmospheric chemistry and astrophysics.^{1,2} Among the numerous existing studies, those involving the NH($X^3\Sigma^-$) radical have been extensively explored. From a fundamental point of view, owing to its large rotational energy level spacing, NH is very useful for cold and ultracold collisional studies. The magnetic moment of the $^3\Sigma^-$ ground electronic state makes it a possible species that can be trapped in buffer gas magnetic field environments.³ This explains why NH–Rare gas (Rg) complexes were the object of numerous energy transfer theoretical and experimental studies.^{4–9} Collisional studies with rare gas also provide information on the

structure and internal properties of complexes and van der Waals interactions.

Collisional studies involving NH radicals are also of great interest from an astrophysical point of view since NH has been observed in several regions of the interstellar medium (ISM).^{10–13} Collisional data are needed for molecular spectra modeling in order to derive the physical conditions in molecular clouds, such as density, temperature, and molecular abundance. Indeed, since these environments do not reach local thermodynamic equilibrium (LTE), the population of NH levels has to be modeled through the competition between radiative and collisional processes.² Without collisional data, astrophysical models are performed using the LTE hypothesis, which does not allow one to fully exploit the highly resolved molecular spectra presently detected.¹³

In addition, the divergence between the NH abundance in observations and chemical models is huge in diffuse molecular clouds.^{10,14} Such divergences may be due to the lack of accurate collisional data for modeling the observational spectra. Indeed, there is still a lack of collisional data of NH with H₂, the main collider in the molecular clouds. Up to now, He was used as a proxy for scattering with H₂ in the ISM studies since only collisional data of NH with He were available,^{4,6} but it is well established that He can be a bad proxy for H₂ in the case of collisions with light hydrides.² To the best of our knowledge, there is only one very recent theoretical study of the NH–H₂ collisional system¹⁵ dealing with non-reactive collisions. These authors performed classical dynamic calculations in order to study NH–H₂ inelastic collisions. However, they did not provide any temperature variation in the collisional data and in addition, the fine structure splitting of the NH has been neglected so that the data cannot be used in astrochemical modeling.

In order to overcome this lack of data, we present in this paper a new 4D potential energy surface (PES) for studying the rotational excitation of NH by H₂. Then, we report inelastic cross sections of the collisional system from quantum close-coupling (CC) calculations taking into account the fine structure of NH. This paper is organized as follows: in Sec. II, we present the new NH–H₂ PES. Section III describes the bound state calculations of the collisional complex in order to validate the accuracy of the new PES. In Sec. IV, we present the inelastic cross sections obtained from our new PES. Finally, Sec. V summarizes and concludes the present work.

II. POTENTIAL ENERGY SURFACE

Collisions between NH and H₂ molecules can be either reactive or inelastic.¹⁵ The NH + H₂ → NH₂ + H reaction is found to be endothermic with an activation energy of ~4000 cm⁻¹.¹⁶ In the low temperature regime relevant to ISM ($T < 300$ K), the reactive process can be safely neglected since the reaction rate coefficient is expected to be completely negligible. In the following, we only focus on the NH–H₂ van der Waals complex.

Fawzy *et al.*¹⁷ previously studied the interaction potential between NH and H₂ molecules. They computed an *ab initio* PES but only for the complex in the planar geometry. The authors performed a search for minima on the PES and computed vibrational frequencies for each minimum. The calculations were carried out at the spin-restricted single and double excitation coupled cluster approach with noniterative perturbational treatment of triples [RCCSD(T)].^{18,19} The basis set for these electronic structure calculations was the augmented correlation-consistent polarized valence double zeta (aug-cc-pVDZ)²⁰ with and without the Basis Set Superposition Error (BSSE) correction. They have found the global minimum corresponding to the linear arrangement and a secondary minimum corresponding to the T-shaped arrangement. This PES, in addition to being obtained at a low level of theory, cannot be used for inelastic collision studies because the out-of-plane movements were not considered.

In the present work, the Jacobi coordinate system presented in Fig. 1 was used. The origin of the coordinate system coincides with the center of mass of the NH molecule. The intermolecular vector **R** connects the centers of mass of NH and H₂ molecules and lies along the *z*-axis. Angle θ_1 defines the rotation of the NH molecule

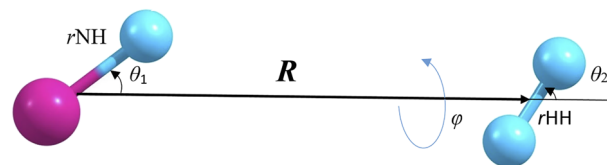


FIG. 1. Coordinate system of the NH–H₂ complex.

with respect to the *z* axis while the rotation of the H₂ molecule is defined by angles θ_2 and φ . Thus, the mutual orientation and position of the H₂ and NH molecules are described by the intermolecular separation, *R*, and the set of three angles (*R*, θ_1 , θ_2 , φ).

The interacting molecules are assumed to be rigid with geometrical structures corresponding to the ground vibrational state for the H₂ molecule $r_{\text{HH}} = 1.449a_0$ and corresponding to the equilibrium geometry for the NH molecule $r_{\text{NH}} = 1.958a_0$.²¹

The *ab initio* calculations of the PES of the NH($X^3\Sigma^-$)–H₂($X^1\Sigma_g^+$) complex in its ground electronic state were carried out at the explicitly correlated partially spin-restricted coupled cluster with the single, double, and perturbative triple excitations [RCCSD(T)-F12a] method²² level of theory with augmented correlation-consistent polarized valence triple zeta (aug-cc-pVTZ) (hereafter, aVTZ) basis set²⁰ using a MOLPRO 2010 package.²³ The exponent in the correlation factor F12 was set to 1.3. The standard auxiliary basis sets and density fitting functions^{24,25} [CABS(OptRI) basis sets] were used during calculations. The BSSE correction was taken into account using the Boys and Bernardi counterpoise scheme.²⁶ We note that the RCCSD(T)-F12/aVTZ method is not size consistent due to the inclusion of noniterative triple excitation. The interaction potential calculated with this method has then been uniformly shifted by subtracting the potential energy at the distance of $R = 1000a_0$, which is 6.3575 cm⁻¹.

The comparison of the radial potential energy cuts obtained using different methods and different basis sets is presented in Fig. 2. The energies extrapolated to the Complete Basis Set (CBS) limit were obtained using the following extrapolation scheme of Peterson *et al.*:²⁷

$$E_X = E_{\text{CBS}} + Ae^{-(X-1)} + Be^{-(X-1)^2}, \quad (1)$$

where *X* is the cardinal number of the aug-cc-pVXZ basis set, E_X is the energy corresponding to the aug-cc-pVXZ basis set, E_{CBS} is the energy extrapolated to the CBS limit, and *A* and *B* are the parameters to be adjusted.

According to the test results presented in Fig. 2, the choice of the RCCSD(T)-F12a method in conjunction with the aVTZ basis set is justified by a good convergence with the RCCSD(T)/CBS, which is the reference in our case. In addition, the selected method allows for a much lower consumption of computer resources in comparison with RCCSD(T)/CBS one.

The *ab initio* calculations were carried out for angles θ_1 from 0° to 180° by 10°, θ_2 from 0° to 90° by 15°, and φ from 0° to 90° by 15°. *R*-distances were varied from 3.75 a_0 to 30 a_0 (36 *R*-values). In total, the calculations were performed for 33 516 geometries (including repeating ones).

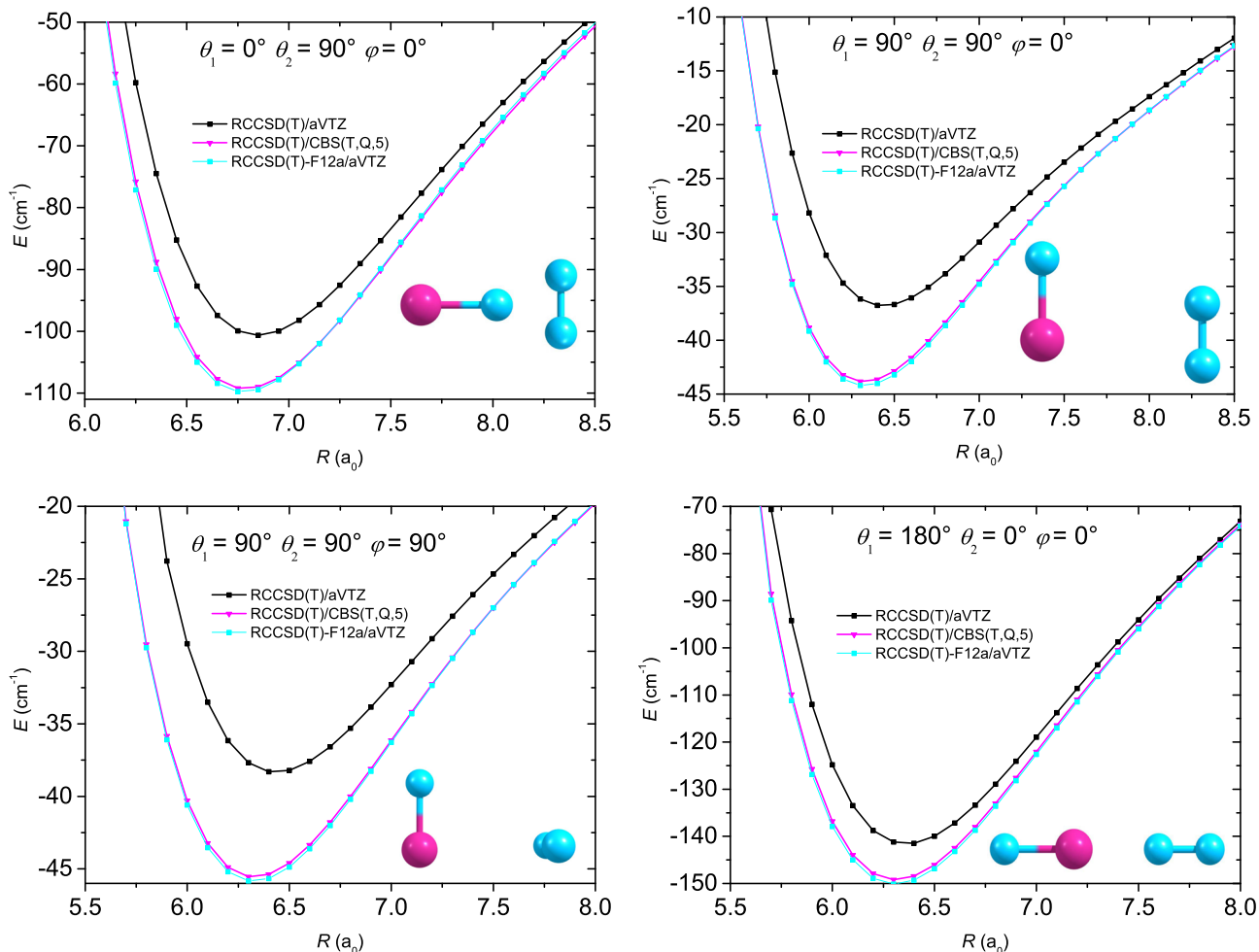


FIG. 2. Potential energy cuts of 4D PES for selected angular orientations. Energy is in cm^{-1} .

The interaction potential $E(R, \theta_1, \theta_2, \varphi)$ was expanded in bispherical harmonics $A_{L_1 L_2 L}(\theta_1, \theta_2, \varphi)$ defined as

$$A_{L_1 L_2 L}(\theta_1, \theta_2, \varphi) = \sqrt{\frac{2L_1 + 1}{4\pi}} \left[\begin{pmatrix} L_1 & L_2 & L \\ 0 & 0 & 0 \end{pmatrix} \right. \\ \times P_{L_1 0}(\theta_1) P_{L_2 0}(\theta_2) + 2 \sum_{M=1}^{\min(L_1, L_2)} \begin{pmatrix} L_1 & L_2 & L \\ M & -M & 0 \end{pmatrix} \\ \left. \times P_{L_1 M}(\theta_1) P_{L_2 M}(\theta_2) \cos(M\varphi) \right], \quad (2)$$

where $L = |L_1 - L_2|, \dots, L_1 + L_2$, where L_1 and L_2 correspond to the θ_1 and θ_2 angular dependences of the PES, while M is related to the dihedral angle φ . The homonuclear symmetry of the H_2 molecule forces the index L_2 to be even. The P_{lm} functions are related

to coupled spherical harmonics through $Y_{lm}(\theta, \phi) = P_{lm}(\theta)e^{im\phi}$. The potential in this basis is written as follows:

$$E(R, \theta_1, \theta_2, \varphi) = \sum_{L_1 L_2 L} v_{L_1 L_2 L}(R) A_{L_1 L_2 L}(\theta_1, \theta_2, \varphi). \quad (3)$$

The expansion coefficients $v_{L_1 L_2 L}(R)$ at each point R were obtained by means of a linear least-squares fit. The chosen number of grid points allows us to expand the potential in bispherical harmonics with $L_1^{\max} = 10$ and $L_2^{\max} = 4$. This gives a total of 86 radial expansion coefficients $v_{L_1 L_2 L}(R)$.

The radial coefficients $v_{L_1 L_2 L}(R)$ in the present work have the following piecewise form:

$$v_{L_1 L_2 L}(R) \left\{ \begin{array}{l} = \sum_{n=2}^{12} a_n(L_1, L_2, L)/R^n, \quad R \leq R_L \\ = \sum_{n=4}^5 c_n(L_1, L_2, L)/R^n, \quad R > R_L, \end{array} \right. \quad (4)$$

where the linking distance R_L was chosen to be $16 a_0$. The coefficients $a_n(L_1, L_2, L)$ were optimized using least-square fitting to *ab initio* points, and coefficients $a_n(L_1, L_2, L)$ were obtained at the condition that the functions from the left and right side of the linking distance and their first derivatives and second derivatives are equal at linking point R_L . We have varied the number of $a_n(L_1, L_2, L)$ coefficients, and it was the best representation obtained for 12 coefficients. Only two coefficients (c_4 and c_5) were used to describe the PES at large R -distances because they correspond to the leading term in the long range expansion of the NH-H₂ interaction: dipole-quadrupole interactions ($\sim R^{-4}$) and quadrupole-quadrupole interaction ($\sim R^{-5}$). The root-mean-square error of the fits in the long and medium-range was in the order of 10^{-3} – 10^{-2} cm^{-1} . The repulsive wall (energies of the order of 10^3 cm^{-1}) was reproduced with a relative error of 0.01%–10%.

The global minimum of the 4D PES corresponds to a linear structure with $\theta_1 = 180^\circ$, $\theta_2 = 0^\circ$, $\varphi = 0^\circ$, and $R = 6.30a_0$ with $D_e = 149.10$ cm^{-1} . This finding is in reasonable agreement with the work of Fawzy *et al.*,¹⁷ where the minimum geometry corresponds to $D_e = 116$ cm^{-1} and $R = 7.9a_0$. The local secondary minimum corresponds to a T-shaped structure with $R = 6.77a_0$, $\theta_1 = 0^\circ$, $\theta_2 = 90^\circ$, and $\varphi = 0^\circ$ with the well depth of 109.52 cm^{-1} . The secondary minimum in the work of Fawzy *et al.*¹⁷ was found to have a well depth of 73 cm^{-1} .

In Fig. 3, we present the contour plots of our 4D PES of the NH-H₂ complex. This plot shows the anisotropy of the interaction with respect to the NH and H₂ rotations. The anisotropy with respect to the NH in-plane rotation is found to be quite important. The anisotropy with respect to H₂ rotation is also found to be large.

III. BOUND STATE CALCULATIONS

In order to check the validity of our new 4D PES, it is of interest to determine the dissociation energy D_0 of the complex and to compare it with the available experimental data of Fawzy *et al.*¹⁷ Hence, we compute bound energy levels of the NH-H₂ complex. They were calculated using the coupled-channel approach, where the coupled equations are solved by the log derivative method,²⁸ as implemented in the bound code.²⁹ The calculations are performed for both NH-*ortho*-H₂ and NH-*para*-H₂ complexes separately. The coupling between the NH rotational states and the electron spin was not taken into account.

Calculations are performed using a starting propagator distance of $R = 4.25a_0$. The asymptotic propagator distance is $20a_0$ to take into account all the attractive part of the potential. The middle propagator distance used is $6.25a_0$, which corresponds roughly to the distance where the global minimum is reached. The propagator step size given for the NH-*ortho*-H₂ configuration was $0.05a_0$ and $0.03a_0$ for the NH-*para*-H₂ complex. The rotational bases of NH and H₂ were extended up to $n_1 = 10$ and $j_2 = 7$, respectively, for the NH-*ortho*-H₂ calculations, whereas $n_1 = 9$ and $j_2 = 8$ were used for the NH-*para*-H₂ ones. The energy of the lowest bound energy levels is given in Table I for both NH-*ortho*-H₂ and NH-*para*-H₂. The bound state energy values are related to the ground state rotational states of the NH-H₂ complex according to the nuclear spin modification of H₂.

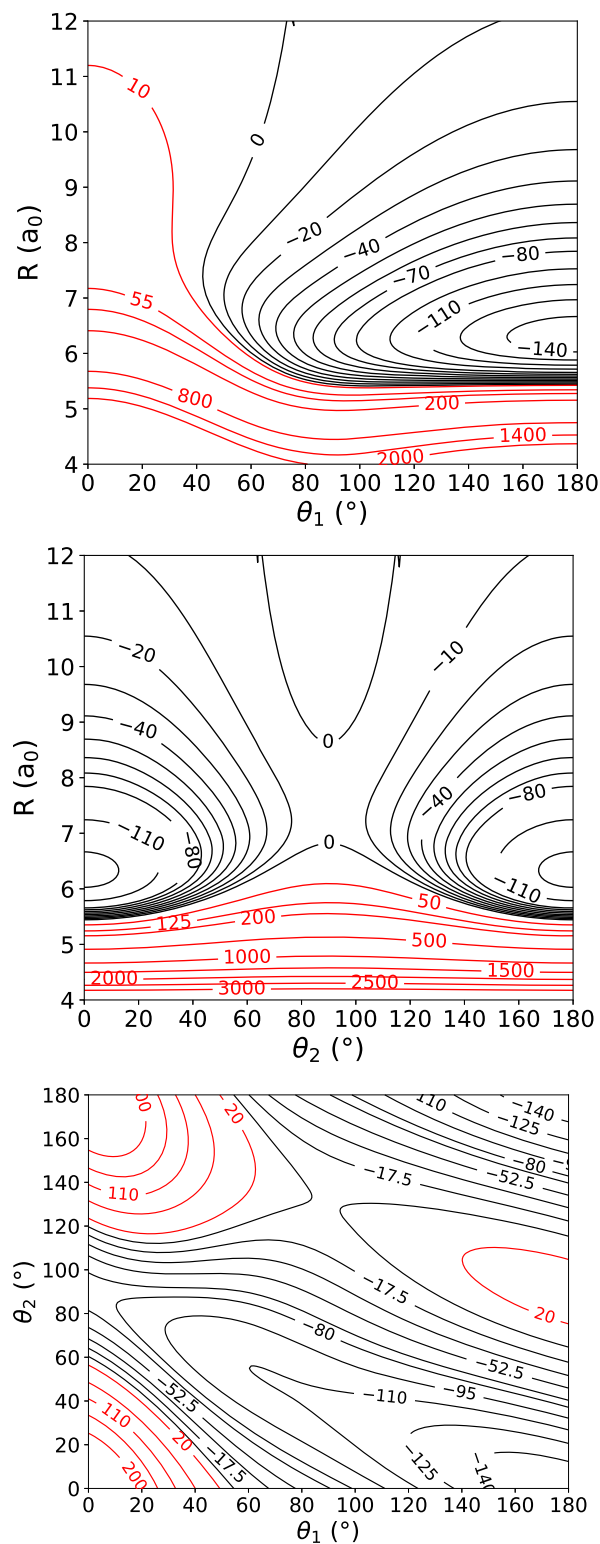


FIG. 3. Potential energy cuts of 4D PES: two coordinates are changing, while others are fixed at their equilibrium values. Energy is in cm^{-1} .

TABLE I. NH–H₂ lower bound energy levels. Energies are relative to the ground state energy of the dissociated fragments, and J represents the total angular momentum of the complex.

NH- <i>ortho</i> -H ₂		NH- <i>para</i> -H ₂	
J	E (cm ⁻¹)	J	E (cm ⁻¹)
0	-30.55	0	-22.11
1	-23.76	1	-20.79
2	-27.26	2	-18.19
3	-23.89	3	-14.33

The total number of the bound states calculated is 6 for NH-*para*-H₂ and 21 for NH-*ortho*-H₂. This is due to the fact that *para*-H₂ in its rotational ground state $j_2 = 0$ admits only a single state, whereas *ortho*-H₂ in its rotational ground state $j_2 = 1$ admits three different orientations. That is why an average of approximately three times more states is found for calculations with *ortho*-H₂.

The dissociation energies D_0 computed in this work are 30.55 cm⁻¹ for NH-*ortho*-H₂ and 22.11 cm⁻¹ for NH-*para*-H₂. One can see that these values are five to ten times larger than the dissociation energy calculated for the NH–He complex.⁴ This indicates that the complex is more stable with H₂ than with He. Fawzy *et al.*¹⁷ studied transitions to the H₂ + NH(A) dissociation continuum via laser excitation. They found a dissociation energy of $D_0 = 32 \pm 2$ cm⁻¹. Our value is in good agreement with the experiment for the NH-*ortho*-H₂. Such agreement suggests that our new PES is reasonably accurate in the van der Waals well region.

Because of the linear equilibrium structure of the complex, it is possible to calculate NH–H₂ rotational constants starting from the formula $E_J = E_0 + BJ(J+1) - DJ^2(J+1)^2$, where E_J is the bound energy level related to the total angular momentum J , E_0 is the ground energy of the complex, B is the rotational constant of the configuration of the complex, and D is the centrifugal constant. For the NH-*para*-H₂ complex, B is equal to 0.6577 cm⁻¹, whereas for the NH-*ortho*-H₂ complex, B is equal to 0.5378 cm⁻¹. To the best of our knowledge, there is no experiment to support these values; however, they can serve as a guideline for future measurements.

IV. FINE STRUCTURE EXCITATION OF NH BY H₂

A. Scattering calculations

In the NH(³Σ⁻) electronic ground state, the rotational levels are split by the spin–spin interaction. In the intermediate coupling scheme, the rotational wave function of NH can be written for $j_1 \geq 1$ as³⁰

$$|F_1jm\rangle = \cos \alpha |n_1 = j_1 - 1, s_1 j_1 m\rangle + \sin \alpha |n_1 = j_1 + 1, s_1 j_1 m\rangle, \\ |F_2jm\rangle = |n_1 = j_1, s_1 j_1 m\rangle, \quad (5)$$

$$|F_3jm\rangle = -\sin \alpha |n_1 = j_1 - 1, s_1 j_1 m\rangle + \cos \alpha |n_1 = j_1 + 1, s_1 j_1 m\rangle,$$

where $|n_1, s_1 j_1 m\rangle$ denotes pure Hund's case (b) basis functions and the mixing angle α is obtained by diagonalization of the molecular Hamiltonian. In this relation corresponding to Hund's case (b), the total molecular angular momentum j_1 is defined by

$$\mathbf{j}_1 = \mathbf{n}_1 + \mathbf{s}_1, \quad (6)$$

where n_1 and s_1 are the nuclear rotational and the electron spin angular momenta. In the pure case (b) limit, $\alpha \rightarrow 0$, the F_1

TABLE II. Influence of the *para*-H₂ rotational basis j_2 on excitation cross sections (in Å²) for collisions of NH with *para*-H₂. Numbers in parentheses represent the j_2 rotational basis.

Transition	E = 35 cm ⁻¹			E = 200 cm ⁻¹			E = 500 cm ⁻¹		
	(0)	(0, 2)	(0, 2, 4)	(0)	(0, 2)	(0, 2, 4)	(0)	(0, 2)	(0, 2, 4)
$n_1, F_i, j_2 \rightarrow n'_1, F'_i, j'_2$									
1, F ₃ , 0 → 0, F ₁ , 0	0.054	8.447	7.683	0.347	0.413	0.412	0.457	0.494	0.494
0, F ₁ , 0 → 1, F ₁ , 0	0.006	0.128	0.117	0.629	0.681	0.681	1.102	1.163	1.163
1, F ₂ , 0 → 1, F ₃ , 0	0.038	0.035	0.035	0.008	0.011	0.011	0.011	0.010	0.010
1, F ₃ , 0 → 2, F ₁ , 0	0.459	0.610	0.609	0.383	0.377	0.376
0, F ₁ , 0 → 2, F ₂ , 0	3.206	3.135	3.134	3.721	3.804	3.804
1, F ₂ , 0 → 2, F ₃ , 0	0.422	0.750	0.752	1.151	1.156	1.156
1, F ₃ , 0 → 3, F ₁ , 0	0.100	0.125	0.125	1.368	1.159	1.152
0, F ₁ , 0 → 3, F ₂ , 0	0.037	0.041	0.413	0.542	0.472	0.470
1, F ₂ , 0 → 3, F ₃ , 0	0.019	0.064	0.065	0.200	0.202	0.202
1, F ₃ , 0 → 4, F ₁ , 0	0.160	0.132	0.131
0, F ₁ , 0 → 4, F ₂ , 0	0.501	0.477	0.476
1, F ₂ , 0 → 4, F ₃ , 0	0.064	0.078	0.078
1, F ₃ , 0 → 5, F ₁ , 0	0.012	0.018	0.018
0, F ₁ , 0 → 5, F ₂ , 0	0.010	0.010	0.010
1, F ₃ , 0 → 0, F ₁ , 2	0.075	0.082
0, F ₁ , 0 → 1, F ₁ , 2	0.038	0.042
1, F ₃ , 0 → 2, F ₁ , 2	0.017	0.019
1, F ₂ , 0 → 2, F ₃ , 2	0.021	0.021

TABLE III. Influence of the *ortho*-H₂ rotational basis j_2 on excitation cross sections (in Å²) for collisions of NH with *ortho*-H₂. Numbers in parentheses represent the j_2 rotational basis.

Transition $n_1, F_i, j_2 \rightarrow n'_1, F'_i, j'_2$	E = 35 cm ⁻¹		E = 200 cm ⁻¹		E = 500 cm ⁻¹	
	(1)	(1, 3)	(1)	(1, 3)	(1)	(1, 3)
1, F ₃ , 1 → 0, F ₁ , 1	38.556	41.215	10.545	10.656	4.861	4.868
0, F ₁ , 1 → 1, F ₁ , 1	4.562	4.605	14.938	15.074	8.160	8.219
1, F ₂ , 1 → 1, F ₃ , 1	12.458	12.071	0.843	0.850	0.291	0.290
1, F ₃ , 1 → 2, F ₁ , 1	1.362	1.264	1.446	1.437
0, F ₁ , 1 → 2, F ₂ , 1	2.462	2.468	2.909	2.930
1, F ₂ , 1 → 2, F ₃ , 1	0.749	0.735	1.082	1.083
1, F ₃ , 1 → 3, F ₁ , 1	0.108	0.116	1.027	0.972
0, F ₁ , 1 → 3, F ₂ , 1	0.105	0.108	1.148	1.145
1, F ₂ , 1 → 3, F ₃ , 1	0.052	0.045	0.338	0.342
1, F ₃ , 1 → 4, F ₁ , 1	0.260	0.242
0, F ₁ , 1 → 4, F ₂ , 1	0.454	0.443
1, F ₂ , 1 → 4, F ₃ , 1	0.088	0.088
1, F ₃ , 1 → 5, F ₁ , 1	0.014	0.015
0, F ₁ , 1 → 5, F ₂ , 1	0.016	0.015

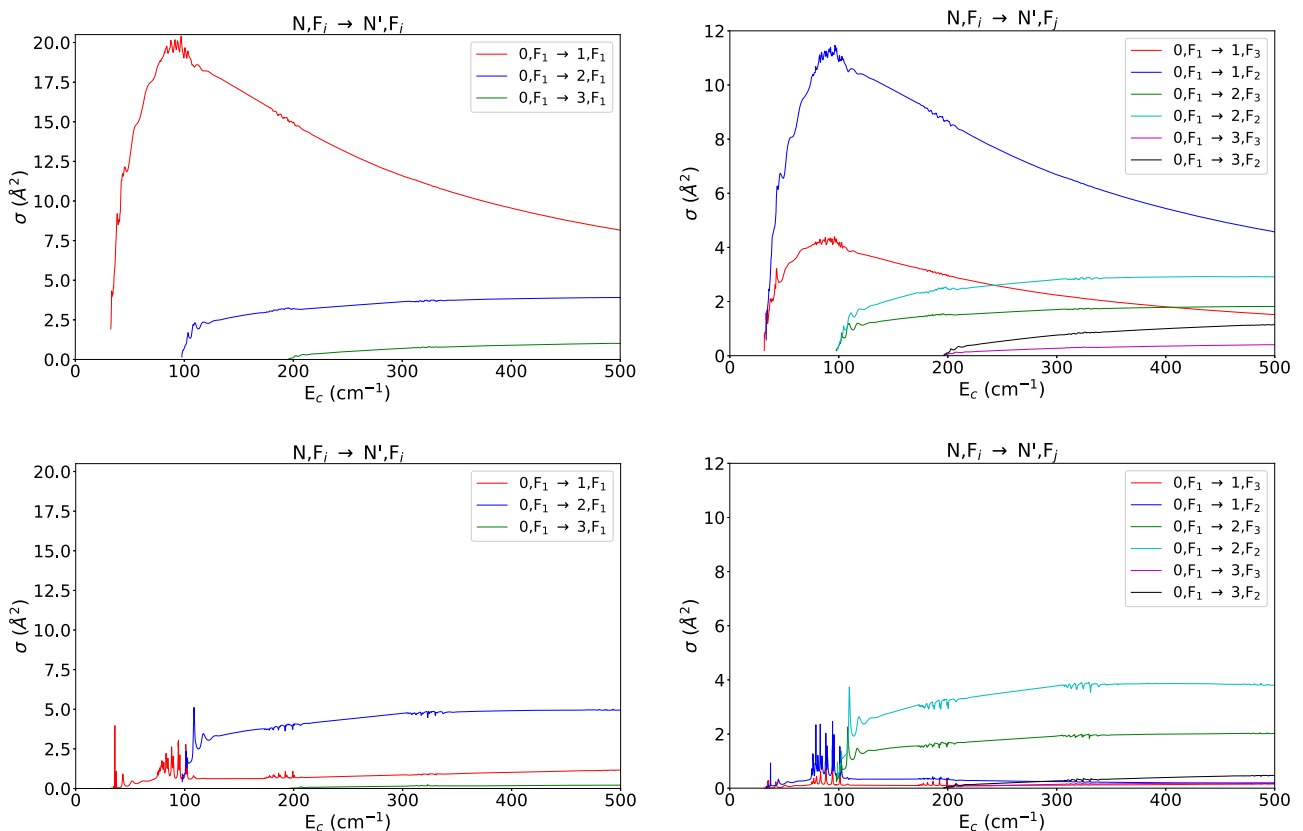
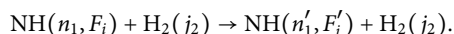


FIG. 4. Fine structure excitation cross sections of NH by *ortho*-H₂ (upper panels) and *para*-H₂ (lower panels) for fine structure conserving transitions (left panels) and for fine structure changing transitions (right panels).

level corresponds to $n_1 = j_1 - 1$ and the F_3 corresponds level to $n_1 = j_1 + 1$.

Energy levels were computed with the use of NH spectroscopic parameters: $B = 16.3433 \text{ cm}^{-1}$, $D = 1.703 \times 10^{-3} \text{ cm}^{-1}$, $\lambda = 0.92 \text{ cm}^{-1}$, and $\gamma = -0.0549 \text{ cm}^{-1}$.³¹ The levels in the spin multiplets are usually labeled by the nuclear rotational quantum number n_1 [corresponding to the Hund's case (b) limit] and the spectroscopic index F_i , and this notation will be used hereafter.

In this study, we consider scattering calculations, including the fine structure of NH such that



Calculations are carried out with both *ortho*-H₂ and *para*-H₂ in their ground rotational levels $j_2 = 0$ and $j_2 = 1$, respectively. We do not present results for the excitation of H₂ even if fully included in the calculations.

Scattering calculations are performed with the close-coupling approach in the intermediate coupling scheme³² as implemented in the HIBRIDON code.³³ The new 4D PES developed in this work has been used for these calculations. The hybrid log-derivative/Airy propagator implemented in the HIBRIDON code has been used. Parameters optimized to ensure the convergence of the inelastic cross sections are $R_{\min} = 4.25a_0$ and $R_{\max} = 50a_0$ for the propagator distances with a step propagator between 0.1 and $0.2a_0$. All these parameters were adequate to ensure a convergence of cross sections to better than 1%. These calculations have been performed for total energies up to 500 cm^{-1} . The energy grid has been calculated with a variable step. For energies between 0.1 and 100 cm^{-1} , the step is 0.1 cm^{-1} . Then, between 100 and 300 cm^{-1} , the step is increased to 0.2 cm^{-1} . Finally, between 300 and 500 cm^{-1} , the step is increased to 0.5 cm^{-1} . We choose a small energy step for small energies so that the resonances can be well described. H₂ rotational constant used in the calculations is $B = 59.332 \text{ cm}^{-1}$.³⁴ The reduced mass of the complex was $\mu = 1.777 \text{ amu}$.

The main difficulty for calculations was the optimization of the H₂ rotational basis. It has a great influence on the convergence of cross sections and on the central processing unit (CPU) time. We considered a rotational basis of NH $n_1^{\max} = 10$ and $j_2 = 0, 2$ for *para*-H₂. The maximum total angular momentum considered was $J = 60$ at a total energy of 500 cm^{-1} . The rotational basis for *ortho*-H₂ was $j_2 = 1$, and we considered a total angular momentum of $J = 70$ at the highest energy. In order to illustrate the convergence of the inelastic cross sections with respect to the H₂ rotational basis, we report some tests in Tables II and III for both *ortho*-H₂ and *para*-H₂ configurations at three values of total energies.

It can be noticed that the mean error between the results obtained with the *para*-H₂ rotational basis $j_2 = 0$ and $j_2 = 0, 2$ is up to 40%. This is due to the fact that at small energies, shape and Feshbach resonances may not be well represented by cross sections and strongly depend on the H₂ basis. It appears essential when studying collisional excitation induced by H₂ ($j_2 = 0$) to take into account at least one more H₂ rotational level in the rotational basis. On the other hand, the mean error of the results obtained using the $j_2 = 0, 2$ and $j_2 = 0, 2, 4$ basis is less than 2–3%. Hence, the H₂ level $j_2 = 4$ has not been taken into account in the H₂ rotational basis. As far as *ortho*-H₂ is concerned, the mean error of the calculations involving the two basis for these three energies is less than 5%. As calculations

with $j_2 = 1, 3$ basis would not have been feasible in a reasonable time and considering the good convergence of the results obtained with the $j_2 = 1$ rotational basis, we have decided to retain only the level $j_2 = 1$ in the basis. It is interesting to note that at the highest energy considered in the work, the cross sections for the rotationally inelastic transitions in H₂ are at least two orders of magnitude lower than the elastic one and can be safely neglected in the astrophysical media modeling.

B. Results

Figure 4 presents the state-to-state cross sections related to collisions of NH with both *ortho*-H₂ and *para*-H₂ as a function of the

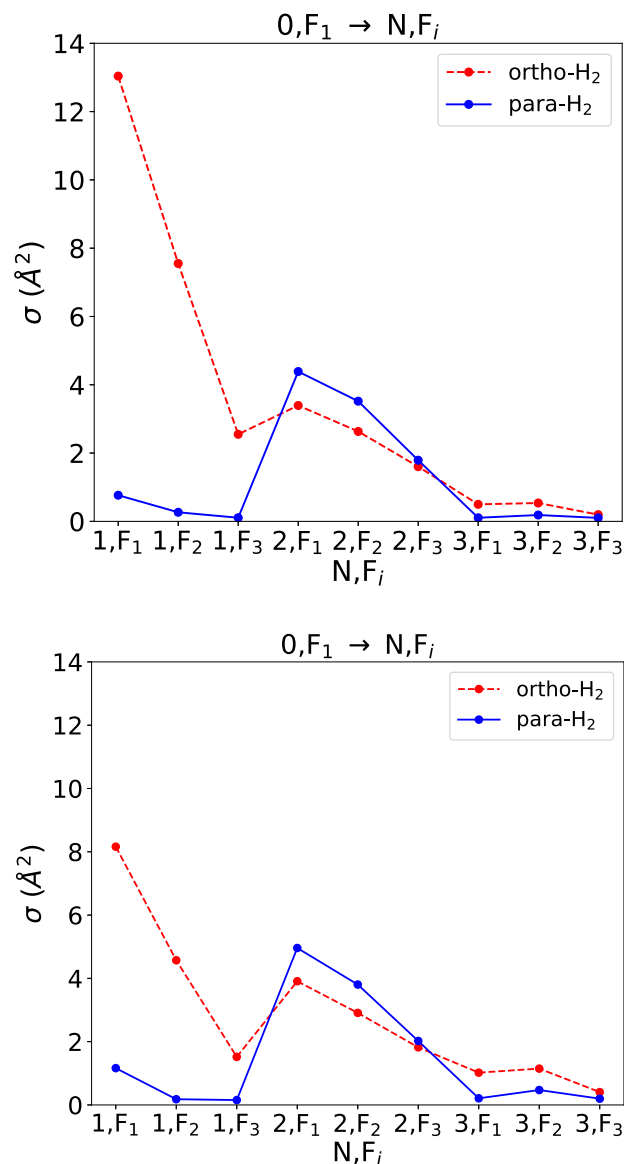


FIG. 5. Propensity rules for transitions from the fundamental state of NH with *ortho*-H₂ (dashed lines) and *para*-H₂ (solid lines) for a total energy of 250 cm^{-1} (upper panel) and 500 cm^{-1} (lower panel).

collisional energy. One can see the shape and Feshbach resonances at low energies for all transitions. These peaks in the cross sections are related to the well depth of the potential of 148.83 cm^{-1} that allows H_2 to be temporarily trapped so that the complex is formed in a (quasi-) bound state before it dissociates.^{35,36}

One can also see that state-to-state cross sections, displayed in part in Figs. 4 and 5, exhibit several propensity rules. First, we can see that fine structure conserving transitions are larger than fine structure changing ones by a factor of ~ 2 . This is due to the fact that the system tends to keep the same orientation of its electron spin during the collision. A direct consequence is that transitions involving $F_{1/3} \rightarrow F_2$ are stronger than $F_1 \rightarrow F_3$ transitions. This effect is more apparent in Fig. 5, which shows cross section intensities as a function of the NH energy levels. This result is predicted by the theory³⁷ and has already been seen for several studies involving the NH radicals, such as $\text{NH}(X^3\Sigma^-)\text{-He}^4$ or $\text{NH}(X^3\Sigma^-)\text{-Ar}^8$.

Figures 4 and 5 also show that transitions induced by collisions with *ortho*- H_2 are larger than the ones induced by *para*- H_2 . More precisely, odd Δn_1 transitions are larger for collisions with *ortho*- H_2 by almost an order of magnitude. However, this tendency is not seen for even Δn_1 transitions, where the cross sections are of similar magnitude whatever the collider is, *para*- H_2 or *ortho*- H_2 . This result can be interpreted from the anisotropy of the PES with the rotation of H_2 and the amplitude of the radial coefficients $v_{L_1 L_2 L}(R)$ [Eq. (4)].

In Fig. 6, the leading radial coefficients $v_{L_1 L_2 L}(R)$ of the PES are plotted as a function of the intermolecular distance. The direct coupling of rotational levels by the interaction potential is related to the rotational quantum numbers and the anisotropic terms of given values of L_1 and L_2 as follows: for a given $n_1 \rightarrow n'_1$ transition, terms with $|n_1 - n'_1| \leq L_1 \leq n_1 + n'_1$ can contribute directly. Similarly, terms with $|n_2 - n'_2| \leq L_2 \leq n_2 + n'_2$ can contribute to $j_2 \rightarrow j'_2$ transitions.

We see in Fig. 6 that the largest cross sections for $n_1 = 0 \rightarrow n'_1$ fine structure conserving and fine structure changing transitions involve final rotational levels with $n'_1 = 1$. This is consistent with the fact that the largest coefficient ($L_1 = 1, L_2 = 0, L = 1$) in the angular expansion of the interaction potential has $L_1 = 1$.

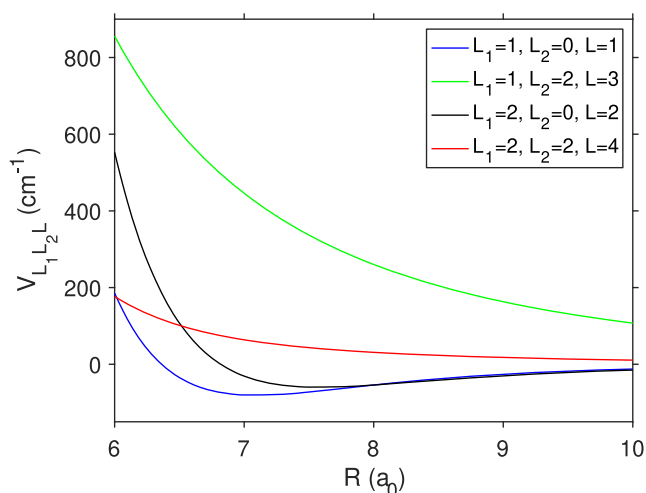


FIG. 6. The larger radial coefficients $v_{L_1 L_2 L}(R)$ as a function of the intermolecular distance R .

Such propensity rules have been observed for several collisional systems, such as $\text{CN}(X^2\Sigma^+)\text{-H}_2$,³⁸ $\text{PN}(X^1\Sigma)\text{-H}_2$,³⁹ or $\text{HCl}\text{-H}_2$.⁴⁰

V. CONCLUSION

We have calculated a new 4D PES of the $\text{NH}\text{-H}_2$ van der Waals complex at the RCCSD(T)-F12a/aVTZ level of theory. The calculated dissociation energy D_0 of the complex with *ortho*- H_2 was found to be in good agreement with the available experimental study.¹⁷ From the bound state calculation, we also deduced a new rotational constant. New experiments are expected to constrain the value obtained.

Using the new PES, we have performed close-coupling calculations in order to determine collisional excitation cross sections of NH by *ortho*- H_2 ($j_2 = 1$) and *para*- H_2 ($j_2 = 0$), including the fine structure of NH. Cross sections were obtained for total energies up to 500 cm^{-1} . We noticed that the rotational basis of H_2 strongly influences cross sections, especially at small collisional energies between $j_2 = 0$ and $j_2 = 0, 2$ bases. The results show that fine structure conserving transitions are larger than fine structure changing ones, which is a typical behavior of $^3\Sigma$ molecules and has already been seen in previous studies. We also found that Δn odd transitions are larger for collisions induced by *ortho*- H_2 and that Δn even transitions are larger for collisions induced by *para*- H_2 .

We expect that this work will encourage more experiments on NH excitation by H_2 with fine structure resolution. In addition, it is of great astrophysical interest to carry out theoretical studies of NH with H_2 to determinate properties and conditions in diffuse and dark clouds, as H_2 is the major collider in the ISM and He is actually used as a proxy for H_2 in astrophysical applications. Calculations at higher collisional energies are in progress, and $\text{NH}\text{-H}_2$ state-to-state rate coefficients at typical interstellar temperatures (5–300 K) will be soon provided in a forthcoming publication.

SUPPLEMENTARY MATERIAL

A Fortran subroutine of the potential energy surface is available as the [supplementary material](#).

ACKNOWLEDGMENTS

This project received funding from the European Research Council (ERC) under the European Union's Horizon 2020 research and innovation program (Grant Agreement No. 811363). We acknowledge the Programme National Physique et Chimie du Milieu Interstellaire (PCMI) of CNRS/INSU with INC/INP co-funded by CEA and CNES. F.L. acknowledges financial support from the Institut Universitaire de France. The results of *ab initio* calculations and fit of the PES in Sec. II have been obtained under support of RSF Grant No. 17-12-01395.

AUTHOR DECLARATIONS

Conflict of Interest

The authors have no conflicts to disclose.

DATA AVAILABILITY

The data that support the findings of this study are available from the corresponding author upon reasonable request.

REFERENCES

- ¹C. A. R. Sá de Melo, *Phys. Today* **61**(10), 45 (2008).
- ²E. Roueff and F. Lique, *Chem. Rev.* **113**, 8906 (2013).
- ³D. Egorov, W. C. Campbell, B. Friedrich, S. E. Maxwell, E. Tsikata, L. D. van Buuren, and J. M. Doyle, *Eur. Phys. J. D* **31**, 307 (2004).
- ⁴R. Ramachandran, J. Klos, and F. Lique, *J. Chem. Phys.* **148**, 084311 (2018).
- ⁵F. Dumouchel, J. Klos, R. Tobiola, A. Bacmann, S. Maret, P. Hily-Blant, A. Faure, and F. Lique, *J. Chem. Phys.* **137**, 114306 (2012).
- ⁶R. Tobiola, F. Dumouchel, J. Klos, and F. Lique, *J. Chem. Phys.* **134**, 024305 (2011).
- ⁷N. Bouhafs and F. Lique, *J. Chem. Phys.* **143**, 184311 (2015).
- ⁸D. Prudenzano, F. Lique, R. Ramachandran, L. Bizzocchi, and P. Caselli, *J. Chem. Phys.* **150**, 214302 (2019).
- ⁹P. J. Dagdigian, *J. Chem. Phys.* **90**, 6110 (1989).
- ¹⁰D. M. Meyer and K. C. Roth, *Astrophys. J., Lett.* **376**, L49 (1991).
- ¹¹I. A. Crawford and D. A. Williams, *Mon. Not. R. Astron. Soc.* **291**, L53 (1997).
- ¹²T. Weselak, G. A. Galazutdinov, Y. Beletsky, and J. Krelowski, *Mon. Not. R. Astron. Soc.* **400**, 392 (2009).
- ¹³A. Bacmann, F. Daniel, P. Caselli, C. Ceccarelli, D. Lis, C. Vastel, F. Dumouchel, F. Lique, and E. Caux, *Astron. Astrophys.* **587**, A26 (2016).
- ¹⁴R. Wagenblast, D. A. Williams, T. J. Millar, and L. A. M. Nejad, *Mon. Not. R. Astron. Soc.* **260**, 420 (1993).
- ¹⁵R. Padash and S. Ramazani, *Mol. Astrophys.* **20**, 100085 (2020).
- ¹⁶D. P. Linder, X. Duan, and M. Page, *J. Chem. Phys.* **99**, 11458 (1995).
- ¹⁷W. M. Fawzy, G. Kerenskaya, and M. C. Heaven, *J. Chem. Phys.* **122**, 144318 (2005).
- ¹⁸P. J. Knowles, C. Hampel, and H. J. Werner, *J. Chem. Phys.* **99**, 5219 (1993).
- ¹⁹P. J. Knowles, C. Hampel, and H.-J. Werner, *J. Chem. Phys.* **112**, 3106 (2000).
- ²⁰T. H. Dunning, *J. Chem. Phys.* **90**, 1007 (1989).
- ²¹K. P. Huber and G. Herzberg, *Molecular Spectra and Molecular Structure. IV. Constants of Diatomic Molecules* (Van Nostrand Reinhold, New York, 1979).
- ²²G. Knizia, T. B. Adler, and H.-J. Werner, *J. Chem. Phys.* **130**, 054104 (2009).
- ²³H.-J. Werner, P. J. Knowles, G. Knizia, F. R. Manby, M. Schütz *et al.*, MOLPRO, version 2010.1, a package of *ab initio* programs, 2010.
- ²⁴W. Klopper, *Mol. Phys.* **99**, 481 (2001).
- ²⁵F. Weigend, A. Köhn, and C. Hättig, *J. Chem. Phys.* **116**, 3175 (2002).
- ²⁶S. F. Boys and F. Bernardi, *Mol. Phys.* **19**, 553 (1970).
- ²⁷K. A. Peterson, D. E. Woon, and T. H. Dunning, *J. Chem. Phys.* **100**, 7410 (1994).
- ²⁸D. E. Manolopoulos, *J. Chem. Phys.* **85**, 6425 (1986).
- ²⁹J. M. Hutson, Bound computer code, version 5, distributed by collaborative computational project No. 6 of the science and engineering research council (UK), 1993.
- ³⁰W. Gordy and R. L. Cook, *Microwave Molecular Spectra* (Wileys and Sons, 1984).
- ³¹F. D. Wayne and H. E. Radford, *Mol. Phys.* **32**, 1407 (1976).
- ³²P. J. Dagdigian, *J. Chem. Phys.* **150**, 084308 (2019).
- ³³M. H. Alexander, D. E. Manolopoulos, H.-J. Werner, B. Follmeg, P. J. Dagdigian *et al.*, Hibridon is a package of programs for the time-independent quantum treatment of inelastic collisions and photodissociation, For more information and/or a copy of the code can be obtained from the website <http://www2.chem.umd.edu/groups/alexander/hibridon>, 2012.
- ³⁴I. F. Silvera, *Rev. Mod. Phys.* **52**, 393 (1980).
- ³⁵K. M. Christoffel and J. M. Bowman, *J. Chem. Phys.* **78**, 3952 (1983).
- ³⁶L. N. Smith, D. J. Malik, and D. Secrest, *J. Chem. Phys.* **71**, 4502 (1979).
- ³⁷M. H. Alexander and P. J. Dagdigian, *J. Chem. Phys.* **79**, 302 (1983).
- ³⁸Y. Kalugina, J. Klos, and F. Lique, *J. Chem. Phys.* **139**, 074301 (2013).
- ³⁹B. Desrousseaux, E. Quintas-Sánchez, R. Dawes, S. Marinakis, and F. Lique, *J. Chem. Phys.* **154**, 034304 (2021).
- ⁴⁰M. Lanza and F. Lique, *J. Chem. Phys.* **141**, 164321 (2014).

C.2 Hyperfine excitation of ^{13}CCH and C^{13}CH by collisions with *para*- H_2

Hyperfine excitation of ^{13}CCH and C^{13}CH by collisions with *para*- H_2

P. Pirlot Jankowiak¹,^{*} F. Lique¹,^{*} and P. J. Dagdigan²

¹Univ Rennes, CNRS, IPR (Institut de Physique de Rennes) – UMR 6251, F-35000 Rennes, France

²Department of Chemistry, The Johns Hopkins University, Baltimore, MD 21218-2685, USA

Accepted 2023 May 31. Received 2023 May 31; in original form 2023 May 2

ABSTRACT

The computation of hyperfine resolved cross sections and rate coefficients for open-shell molecules in collision with H_2 is a true methodological and numerical challenge. Such collisional data are however required to interpret astrophysical observations. We report the first hyperfine resolved rate coefficients for (de-)excitation of ^{13}CCH and C^{13}CH isotopologues induced by collisions with *para*- H_2 . These calculations have been performed using a recently published $\text{C}_2\text{H}-\text{H}_2$ potential energy surface. Hyperfine resolved cross sections and rate coefficients between the first 98 energy levels of the two isotopologues were determined using a recoupling technique for temperatures ranging from 5 to 100 K. Significant isotopic substitution effects were found, showing the necessity of computing isotopologue specific collisional data. These rate coefficients have then been used in a simple radiative transfer modelling for typical molecular cloud conditions.

Key words: molecular data – molecular processes – radiative transfer.

1 INTRODUCTION

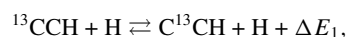
Among the hydrocarbons detected in the interstellar medium (ISM), the ethynyl radical (C_2H) is one of the most abundant. The first detection of this radical has been reported by Tucker, Kutner & Thaddeus (1974) in 13 Galactic sources through hyperfine resolved observations of its rotational emission-line $n = 1 \rightarrow 0$, prior to its study in laboratory (Sastry et al. 1981). This identification was confirmed later by Ziurys et al. (1982) with the detection of the $n = 3 \rightarrow 2$ emission-line. This radical has been observed over the past decades in several astrophysical environments including pre-stellar cores (Padovani et al. 2009), photodissociated regions (PDRs) (Teyssier et al. 2003; Cuadrado et al. 2015), protoplanetary discs (Dutrey, Guilloteau & Guélin 1996), high-mass star-forming regions (Beuther et al. 2008), and dark clouds (Sakai et al. 2010).

The high abundance of C_2H in the ISM also made possible the detection of its carbon-based isotopologues ^{13}CCH and C^{13}CH . Indeed, Salek et al. (1994) detected them through hyperfine resolved observations of the $n = 2 \rightarrow 1$ and $n = 1 \rightarrow 0$ rotational lines, respectively. Observations of the ^{13}C isotopologues can provide interesting insight into the formation path of C_2H and the $^{12}\text{C}/^{13}\text{C}$ isotopic fractionation in the ISM.

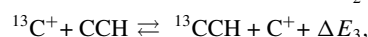
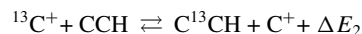
It has been shown that this $^{12}\text{C}/^{13}\text{C}$ ratio in C_2H isotopologues deviates from the $^{12}\text{C}/^{13}\text{C} = 60$ elemental value (Lucas & Liszt 1998), depending on environments and on the isotopologues. Sakai et al. (2010) derived $[\text{CCH}/^{13}\text{CCH}]$ and $[\text{CCH}/\text{C}^{13}\text{CH}]$ ratios higher than 170 and 250 in the Taurus Molecular Cloud (TMC-1) and higher than 80 and 135 in L1527. Additionally, these authors found a $[\text{C}^{13}\text{CH}/^{13}\text{CCH}]$ ratio to be 1.6 in both sources. Such behaviour has

been also found by Salek et al. (1994) and later by Cuadrado et al. (2015); Taniguchi et al. (2019); Yoshida et al. (2019).

Sakai et al. (2010) suggest that the $[\text{C}^{13}\text{CH}/^{13}\text{CCH}]$ ratio might be due to the different production mechanisms of C_2H in cold environments, especially that the two carbons are not equivalent in its pathway through neutral–neutral reactions, or to exchange reactions between ^{13}CCH and C^{13}CH after their formation through the following process:



where $\Delta E_1 \sim 8$ K corresponds to the difference of the zero-point energy of ^{13}CCH with respect to C^{13}CH . The detection of the isotopologues by Cuadrado et al. (2015) in the Orion Bar PDR suggests also that reactions with $^{13}\text{C}^+$ can explain the observed fractionation in warmer objects through processes such as



where $\Delta E_2 \sim 63$ K and $\Delta E_3 \sim 55$ K are the differences of zero-point energy of both isotopologues with respect to C_2H .

In the ISM, especially in cold environments, the density is low, and the populations of molecular levels do not follow a Maxwell–Boltzmann distribution. This non-local thermal equilibrium (non-LTE) behaviour implies a competition between radiative and collisional processes in these environments. Radiative transfer modelling, to interpret the observed spectroscopic intensities, requires then both radiative and collisional data for the observed molecules. While Einstein coefficients depend on the dipole moment and the energetic structure of the molecule that can be found in data bases, rate coefficients must be computed through scattering calculations for each collisional system. These calculations require the prior determination of the potential energy surface (PES) through *ab initio*

* E-mail: paul.pirlot@univ-rennes.fr (PPJ); francois.lique@univ-rennes.fr (FL)

calculations describing the electronic interaction of the observed molecules with the main collider in molecular clouds, generally H_2 .

To the best of our knowledge, there are no collisional data for collisions of ^{13}CCH and C^{13}CH . Indeed, the determination of hyperfine resolved rate coefficients of ^{13}CCH and C^{13}CH in collision with H_2 is a true computational challenge. The coupling of the two non-zero nuclear spins of both the ^{13}C and H atoms to the molecular rotation of C_2H isotopologues leads to a large number of hyperfine energy levels. Scattering calculations with the H_2 collider would imply a very large number of coupled channels to include, and such calculations would overly tax current computational resources. Because of this lack of collisional data, scaled HCN–He collisional data from Green & Thaddeus (1974) have been used by Sakai et al. (2010), including the hyperfine structure of C_2H isotopologues through infinite order sudden (IOS) scaling techniques for non-LTE analysis of ^{13}CCH and C^{13}CH observations. At the present time, the same scaling techniques can be applied on C_2H – H_2 data but isotopic substitution effect have been shown to be non-negligible (Dumouchel et al. 2017).

Presently, hyperfine scattering calculations of molecule–molecule collisions involving only one nuclear spin are feasible in terms of CPU time and memory. Such studies have been performed using the recoupling method for the OH/OD– H_2 (Offer, van Hemert & van Dishoeck 1993; Klos et al. 2020; Dagdigian 2021), SH^+ – H_2 (Dagdigian 2019), and C_2H – H_2 (Dagdigian 2018b) collisional systems. For molecules with two non-zero nuclear spins, a few investigations have been carried out using the recoupling method, considering the projectile as a structureless collider for the NH/ND–He (Dumouchel et al. 2012), C_3N –He (Lara-Moreno, Stoecklin & Halvick 2021), and N_2H^+ –He (Daniel et al. 2005) systems.

The purpose of this paper is to overcome this challenging problem and provide accurate hyperfine rate coefficients of ^{13}CCH and C^{13}CH in collisions with H_2 for temperatures up to 100 K. To do so, two approaches (recoupling based methods and IOS) will be considered. Since ^{13}CCH and C^{13}CH have been detected mostly in cold molecular clouds, it can be assumed that at the low temperature of the clouds only *para*- H_2 in its ground rotational state ($j_2 = 0$, j_2 being the rotational state of H_2) is populated.

This paper is organized as follow: The methodology and especially the selection of a suitable scattering approach are presented in Section 2. Then, a presentation of the features of the C_2H – H_2 PES used in this work is given with also a description of the transformation of the C_2H – H_2 PES to consider isotopic substitution. Section 3 presents and compares the hyperfine rate coefficients for the C_2H isotopologues in collision with H_2 . An application to radiative transfer modelling is carried out in Section 4. This paper follows with a conclusion in Section 5.

2 METHODOLOGY

2.1 Energy levels of C_2H and ^{13}C isotopologues

C_2H is a radical with a $^2\Sigma^+$ ground electronic state. Its rotational levels are split by the spin–rotation interaction. The corresponding angular momentum j can be defined by

$$j = n + S,$$

where n is the nuclear rotational angular momentum and $S = 1/2$ the electronic spin. The presence of non-zero nuclear spin for the H [$I(\text{H}) = 1/2$] atom involves a coupling of the nuclear spin with the angular momentum j . Thus, the hyperfine splitting in C_2H is

Table 1. The lower hyperfine energy levels of ^{13}CCH and C^{13}CH .

Level	n	j	F_1	F	E (cm $^{-1}$)	
					^{13}CCH	C^{13}CH
1	0	0.5	0	0.5	0.000000	0.000000
2	0	0.5	1	0.5	0.029385	0.0004836
3	0	0.5	1	1.5	0.030483	0.005863
4	1	1.5	1	0.5	2.806987	2.843558
5	1	1.5	1	1.5	2.807052	2.843867
6	1	1.5	2	1.5	2.835465	2.847896
7	1	1.5	2	2.5	2.836402	2.848807
8	1	0.5	0	0.5	2.83746	2.850608
9	1	0.5	1	0.5	2.838841	2.851297
10	1	0.5	1	1.5	2.83932	2.851413
11	2	2.5	2	1.5	8.420948	8.530995
12	2	2.5	2	2.5	8.421056	8.531445
13	2	2.5	3	2.5	8.448568	8.534911
14	2	2.5	3	3.5	8.449434	8.535765
15	2	1.5	2	1.5	8.452741	8.539588
16	2	1.5	2	2.5	8.45246	8.53980
17	2	1.5	1	1.5	8.453786	8.540354
18	2	1.5	1	0.5	8.453825	8.540546

described by the F quantum number where

$$F = j + I(\text{H}).$$

Since, the ^{13}CCH and C^{13}CH isotopologues possess the same electronic structure as C_2H , they have a similar fine structure, with just slight differences in the spectroscopic constants. However, both H and ^{13}C atoms have non-zero nuclear spins which couple to the rotation. The hyperfine coupling scheme can now be described as

$$F_1 = j + I(\text{H}), \quad F = F_1 + I(^{13}\text{C}),$$

where F_1 and F now label the hyperfine levels. The nuclear spin of the ^{13}C nucleus equals $I(^{13}\text{C}) = 1/2$. The energy levels have been taken from the CDMS data base (Endres et al. 2016). For ^{13}C isotopologues, each rotational level ($n > 1$) is split in eight hyperfine components except $n = 0$ and 1 which are split in 3 and 7 levels, respectively (see Table 1).

2.2 Selection of suitable approach for scattering calculations: validation with the C_2H – H_2 collisional system

Excitation in molecule–molecule collisions involving an open-shell molecule is a computational challenge. Indeed, the presence of fine and hyperfine structure can lead to a large number of energy levels to take into account in scattering calculations. Especially, when these molecules possess more than one non-zero nuclear spin, quantum calculations are almost not doable, since hyperfine resolved cross sections require a large number of coupled channels to take into account.

The purpose of this paper is to provide hyperfine resolved collisional data for ^{13}CCH and C^{13}CH with H_2 using nuclear spin-free S -matrices. In order to choose the most suitable method to perform such intensively demanding calculations, comparison of both reduced dimension recoupling (Corey & McCourt 1983; Alexander & Dagdigian 1985; Offer et al. 1993) and IOS (Faure & Lique 2012) methods will be performed on the C_2H – H_2 collisional system.

In the case of the IOS approximation, nuclear spin-free cross sections and rate coefficients have been calculated with the 4D PES from Dagdigian (2018b) and taking into account the inclusion of

the rotational levels of $\text{H}_2 j_2 = 0$ and 2, in the scattering basis. IOS hyperfine resolved rate coefficients are determined using the correction of Neufeld & Green (1994) ($k_{njF \rightarrow n'j'F'}^{\text{NG}}$) described in Appendix A.

For the reduced dimension approach, nuclear spin-free cross sections were computed by reducing the dimension of the $\text{C}_2\text{H}-\text{H}_2$ 4D PES of Dagdigan (2018a) to 2D. To do so, we restrict the l_2 index to zero (see equation 3 and text below for details). This is equivalent of restricting the H_2 scattering basis to $j_2 = 0$. Hyperfine cross sections are then computed through the recoupling method. Rate coefficients ($k_{njF \rightarrow n'j'F'}^{2\text{D-rec}}$) from an initial level i to a final level f were determined by integrating the cross sections over a Maxwell–Boltzmann distribution over the collisional energies E_c :

$$k_{i \rightarrow f}(T) = \left(\frac{8}{\pi \mu (k_B T)^3} \right)^{1/2} \int_0^\infty \sigma_{i \rightarrow f}(E_c) E_c e^{-E_c/k_B T} dE_c. \quad (1)$$

These two approaches will be compared with the full calculations (Dagdigan 2018b) for the $\text{C}_2\text{H}-\text{H}_2$ collisional system.¹ These data ($k_{njF \rightarrow n'j'F'}^{4\text{D-rec}}$) have been taken as the reference.

Hyperfine cross sections are determined up to total energies of 500 cm^{-1} ; this ensures convergence of the rate coefficients up to 50 K, for levels up to $n = 7$. Spectroscopic constants were taken from Gottlieb, Gottlieb & Thaddeus (1983) and the reduced mass $\mu = 1.865 \text{ a.m.u.}$ All calculations have been performed using the HIBRIDON scattering code (Alexander et al. 2023).

Fig. 1 presents a comparison at 10 and 50 K of 2D and scaled IOS $\text{C}_2\text{H}-\text{H}_2$ hyperfine rate coefficients with those computed with the 4D PES and the recoupling approach. The dashed lines represent deviations of the rate coefficients within a factor of 2. One can see that the 2D rate coefficients are almost systematically overestimating the 4D ones by ~ 20 per cent, whereas the scaled IOS data are spread up to a factor of 2 for some transitions, despite the fact that the dominant transitions are however well-reproduced.

It is possible to quantify better the deviations of the results by computing the weighted mean error factor (WMEF) such as (Loreau, Lique & Faure 2018)

$$\text{WMEF} = \frac{\sum_{i,f} k_{i \rightarrow f}^{4\text{D-rec}} r_i}{\sum_i k_i^{4\text{D-rec}}}, \quad (2)$$

where $k_i^{4\text{D-rec}}$ is the rate coefficient for the i^{th} transition computed with the 4D PES and using the recoupling technique and $r_i = \max(k_i^{4\text{D-rec}}/k_i^{2\text{D}/\text{NG}}, k_i^{2\text{D}/\text{NG}}/k_i^{4\text{D-rec}})$ so that $r_i \geq 1$. Taking this quantity into account, both approaches have a very similar WMEF. Especially in the case of the IOS approximation, the largest transitions ($> 10^{-11} \text{ cm}^3 \text{ s}^{-1}$) are almost matching perfectly the corresponding 4D transitions.

None of these methods seems to stand out more than another, and it was assumed that these differences would be the same for the study of the ^{13}C isotopologues. Then, for the next step of this work, hyperfine rate coefficients of ^{13}CCH and C^{13}CH with H_2 will be computed using the reduced dimension approach. Several arguments tend to explain this choice:

(i) According to Fig. 1, the quantification of the deviation is better defined for the 2D approach since deviations are more systematic.

(ii) From a theoretical point of view, there is only one approximation made with the 2D approach (neglecting the structure of H_2 and the corresponding coupling terms in the PES), whereas IOS

¹An error of a factor ~ 1.4 has been found in these computed rate coefficients and has been corrected.

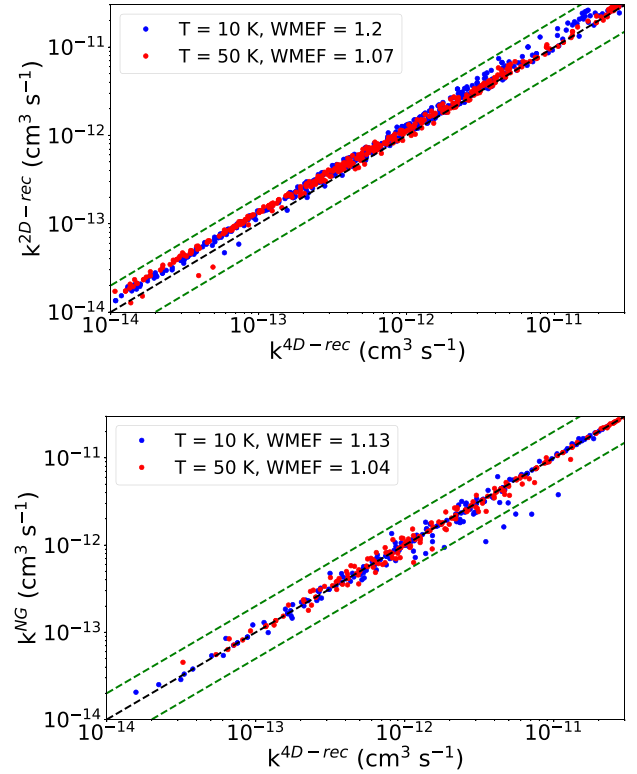


Figure 1. Systematic comparison at 10 and 50 K of $\text{C}_2\text{H}-\text{sph}-\text{H}_2$ recoupling hyperfine rate coefficients with $\text{C}_2\text{H}-\text{para}-\text{H}_2$ ones (upper panel) and corrected IOS hyperfine rate coefficients with $\text{C}_2\text{H}-\text{para}-\text{H}_2$ ones (lower panel). The green dashed lines represent deviations of the rate coefficients within a factor of 2.

approximation is subject to additional approximations: neglect of the rotational structure of the target, scaling relation based on the assumption of a similar error between IOS and close-coupling (CC) to describe rate coefficients among relative hyperfine levels. Also, the correction of Neufeld & Green (1994) requires the calculation of elastic cross sections in order to predict quasi-elastic hyperfine transitions ($n = n', j = j', F \neq F'$). However, CC elastic cross sections are usually not fully converged, and a scaled application of IOS limit is not able to provide quasi-elastic transitions properly. One should note that in Fig. 1, some rate coefficients higher than $3 \times 10^{-12} \text{ cm}^3 \text{ s}^{-1}$ deviate more than a factor of 2. They are related to quasi-elastic transitions, which can only be extrapolated through pure IOS calculations.

(iii) The reduced dimension approach leads to a reasonable error according to astrophysical modelling. The use of the IOS approach would have been more suitable if there was a strong dependence of the orientation of H_2 in the cross sections as in the case for $\text{NH}-\text{H}_2$ collisions (Pirlo Jankowiak et al. 2021) where taking only $j_2 = 0$ leads to a mean error of 40 per cent.

2.3 The excitation of ^{13}C isotopologues

2.3.1 Potential energy surface

C_2H and its isotopologues differ only by the composition of their nucleus and have the same electronic structure. Then, through the Born–Oppenheimer approximation, it is possible to use the $\text{C}_2\text{H}-\text{H}_2$ PES to describe the interaction of ^{13}CCH and C^{13}CH with molecular hydrogen. The $\text{C}_2\text{H}-\text{H}_2$ interaction potential has been computed by

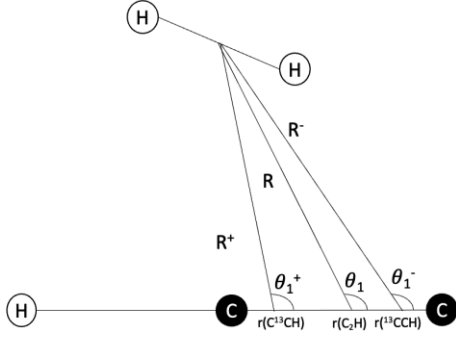


Figure 2. Representation of the $\text{C}_2\text{H}-\text{H}_2$, $^{13}\text{CCH}-\text{H}_2$, and $\text{C}^{13}\text{CH}-\text{H}_2$ interactions in Jacobi coordinates.

one of the authors (Dagdikian 2018a). This author used the restricted coupled cluster method with single, double, and (perturbative) triple excitations [RCCSD(T); Knowles, Hampel & Werner 1993] with the aug-cc-pVQZ basis set. C_2H has a linear geometry, and the PES has been determined assuming that C_2H and H_2 have rigid structures, with their bond lengths taken as the average value of their respective ground vibrational states.

In order to be suitable for time-independent scattering calculations, the analytical representation of the potential has been given in terms of an expansion in bispherical harmonics $A_{l_1 l_2 l}(\theta_1, \theta_2, \phi)$:

$$V(R, \theta_1, \theta_2, \phi) = \sum_{l_1 l_2 l} v_{l_1 l_2 l}(R) A_{l_1 l_2 l}(\theta_1, \theta_2, \phi), \quad (3)$$

where

$$A_{l_1 l_2 l}(\theta_1, \theta_2, \phi) = \left[\frac{(2l+1)}{4\pi} \right]^{1/2} \sum_m (l_1 m l_2, -m | l 0) \times Y_{l_1 m}(\theta_1, 0) Y_{l_2, -m}(\theta_2, \phi). \quad (4)$$

Here, the intermolecular distance between the centres of mass of C_2H and H_2 is represented by the Jacobi vector \mathbf{R} , θ_1 is the angle between C_2H molecular axis and \mathbf{R} (with the carbon end of C_2H pointing toward H_2 for $\theta_1 = 0$), θ_2 is the angle between H_2 molecular axis and \mathbf{R} , and ϕ is the dihedral angle. The terms $v_{l_1 l_2 l}(R)$ are the expansion coefficients of the potential for a given intermolecular separation R , l_1, l_2 are the expansion indexes for C_2H and H_2 , respectively and l was selected as $|l_1 - l_2| < l < l_1 + l_2$.

The transformation of the $\text{C}_2\text{H}-\text{H}_2$ PES to the ^{13}CCH or $\text{C}^{13}\text{CH}-\text{H}_2$ PES requires a shift of the origin of their centre of mass δr . The centres of mass are shifted by $-0.049a_0$ for ^{13}CCH and $+0.039a_0$ for C^{13}CH . The negative value means that the shift is toward the carbon end, and positive if the shift is toward the hydrogen end (see Fig. 2). The ‘+ / -’ notation represents the coordinates in the corresponding isotopologue frame. Then, the transformation of the Jacobi coordinates takes the form

$$\delta r^{+/-} = r(\text{C}^{13}\text{CH}/^{13}\text{CCH}) - r(\text{C}_2\text{H}) \quad (5)$$

$$R^{+/-} = \sqrt{R^2 + \delta r^2 + 2R\delta r^{+/-} \cos(\theta_1)} \quad (6)$$

$$\theta_1^{+/-} = \arcsin \left(\frac{R \sin(\theta_1)}{R^{+/-}} \right). \quad (7)$$

The transformation of angles describing H_2 orientation (θ_2, ϕ) has been neglected since H_2 will be considered as a pseudo-structureless projectile (see the discussion in the following paragraphs). The shift of the centre of mass implies a new expansion of the potential for the interaction of the isotopologues with H_2 . This has been carried out

in this work using a Gauss–Legendre quadrature with 686 different geometries in order to obtain 174 coefficients up to $l_1 = 12$ and $l_2 = 6$ to be consistent with the number of coefficients employed by Dagdigian (2018a).

In order to model H_2 as a pseudo atom, a reduction of the dimensionality of the PES was performed so that only *para*- H_2 ($j_2 = 0$) is involved as a collider (hereafter *sph*- H_2). One can simplify equation (3) using only terms where $l_2 = 0$. This simplification yields the following form for the potential appropriate to treating collisions of a $^2\Sigma^+$ molecule with a (pseudo)atom:

$$V(R, \theta_1) = \sum_{l_1} \left(\frac{[l_1]}{4\pi^{3/2}} \right) v_{l_1 0 l_1} P_{l_1}(\cos \theta_1) \quad (8)$$

with $[l_1] \equiv 2l_1 + 1$. Then, instead of 174 expansion coefficients, only 13 coefficients are needed for the CC calculations. This transformation is used to determine hyperfine cross sections through the recoupling method, as described in Section 2.3.2. The lower order expansion coefficients are presented in Fig. 3.

Most of the coefficients are very close for all three (C_2H , ^{13}CCH , and C^{13}CH) isotopologues interacting with H_2 . Slight differences can be seen for odd l_1 indexes, especially for $l_1 = 1$, where the repulsive behaviour is dominant for ^{13}CCH . Since the shift of the centre of mass is closer to the edge of the molecule, this term characterizes a larger odd anisotropy for the $^{13}\text{CCH}-\text{H}_2$ potential.

2.3.2 Scattering formalism: the recoupling method

With the reduction to two nuclear degrees of freedom, the formalism of atom–molecule collisions with two non-zero nuclear spins can be readily applied. It should be noted that the recoupling method is rigorous if the hyperfine splittings are negligible compared to the rotational energy spacings.

In the recoupling method, the T -matrix elements for a molecule–(pseudo)atom collision with inclusion of the nuclear spins can be obtained from the nuclear spin-free T -matrix elements as described below. The total angular momentum \mathbf{J}_H of the complex when the H nuclear spin is included equals $\mathbf{J} + \mathbf{I}(\text{H})$, where \mathbf{J} is the total angular momentum of the complex without the H nuclear spin. In this case, the T -matrix element is given by (Corey & McCourt 1983)

$$T_{n'j'F_1'L',njF_1L}^{\text{JH}} = (-1)^{j'-j+L'-L} \sum_J [J] \times \left\{ \begin{array}{ccc} I(\text{H}) & j & F_1 \\ L & J_\text{H} & J \end{array} \right\} \left\{ \begin{array}{ccc} I(\text{H}) & j' & F_1 \\ L' & J_\text{H} & J \end{array} \right\} T_{n'j'L',njL}^{\text{J}}, \quad (9)$$

where $[x] = 2x + 1$. The nuclear spin $\mathbf{I}(\text{H})$ equals $1/2$.

We now apply a second recoupling to include the ^{13}C nuclear spin. The total angular momentum \mathbf{J}_T of the complex when both nuclear spins are included equals $\mathbf{J}_\text{H} + \mathbf{I}(^{13}\text{C})$. We note that $\mathbf{I}(^{13}\text{C})$ equals $1/2$. The T -matrix element in this case can be written as

$$T_{n'j'F_1'L',njF_1L}^{\text{JT}} = (-1)^{F'-F+L'-L} \sum_{J_\text{H}} [J_\text{H}] \times \left\{ \begin{array}{ccc} I(^{13}\text{C}) & F_1 & F \\ L & J_\text{T} & J_\text{H} \end{array} \right\} \left\{ \begin{array}{ccc} I(^{13}\text{C}) & F_1' & F \\ L' & J_\text{T} & J_\text{H} \end{array} \right\} \times T_{n'j'F_1'L',njF_1L}^{\text{JH}}. \quad (10)$$

The hyperfine cross sections may be calculated with the T -matrix elements given in equation (10)

$$\sigma_{n'j'F_1'F_1 \rightarrow njF_1F} = \frac{\pi}{k^2 [F]} \sum_{J_\text{T}} [J_\text{T}] \left| T_{n'j'F_1'F_1L',njF_1L}^{\text{JT}} \right|^2 \quad (11)$$

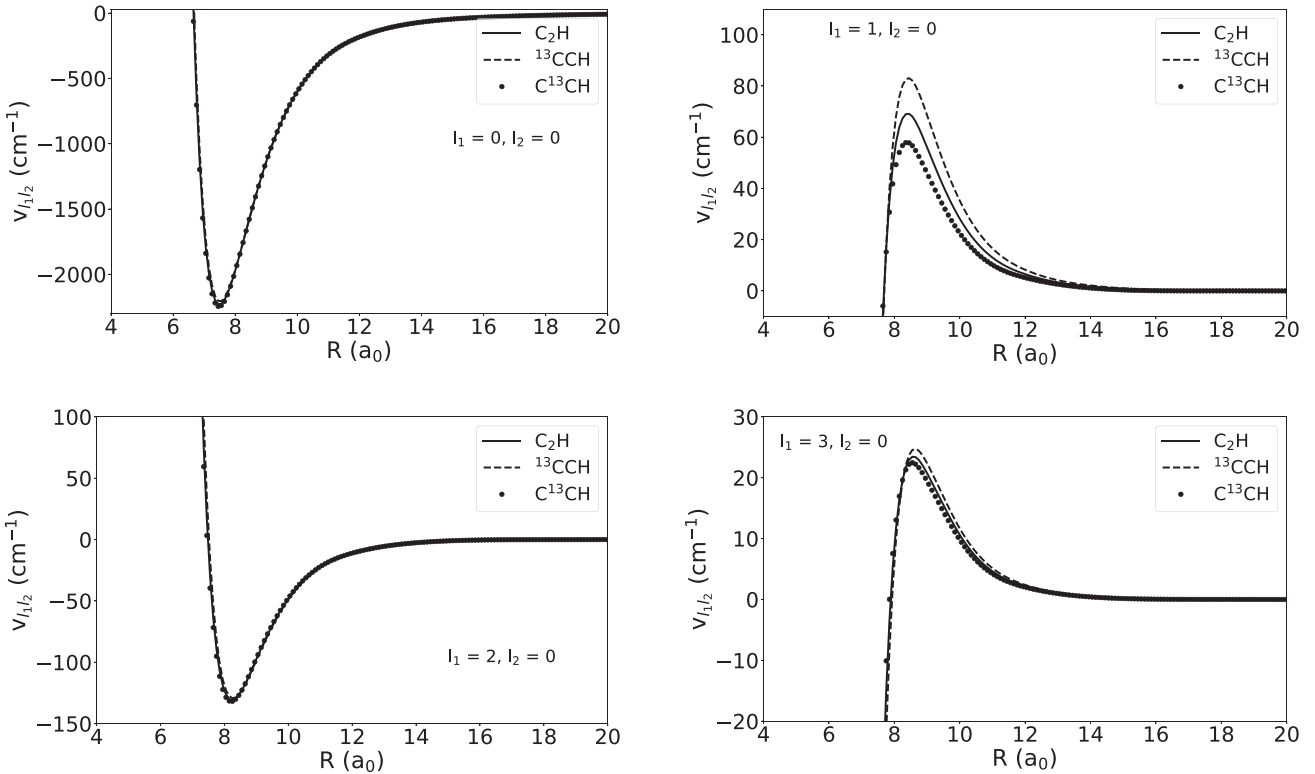


Figure 3. Radial dependence of the lower-order expansion coefficients for C_2H and isotopologues interaction with H_2 . Solid lines are applied to C_2H , dashed lines to ^{13}CCH , and dotted lines to C^{13}CH .

Lara-Moreno et al. (2021) have carried out the equivalent calculation using $12j$ symbols of the second kind. In fact, this $12j$ symbol is defined as the product of four $6j$ symbols, similar to those seen in equations (9) and (10).

3 $^{13}\text{CCH}-\text{H}_2$ AND $\text{C}^{13}\text{CH}-\text{H}_2$ RATE COEFFICIENTS

Scattering calculations have been carried out for the 98 first ^{13}CCH and C^{13}CH hyperfine levels up to $n = 12$ and for a total energy up to $E = 1370 \text{ cm}^{-1}$. Details about scattering parameters are given in Appendix B. Rate coefficients have been computed up to 100 K to cover the range of temperatures where these species are observed. Scattering calculations have been performed using the HIBRIDON software (Alexander et al. 2023).

Fig. 4 presents the temperature variation of several state-to-state hyperfine rate coefficients for $^{13}\text{CCH}-\text{sph}-\text{H}_2$ and $\text{C}^{13}\text{CH}-\text{sph}-\text{H}_2$ collisional systems. One can see a strong propensity rule for $\Delta n = \Delta j = \Delta F_1 = \Delta F$ transitions. The smallest rate coefficients are characterized by $\Delta n \neq \Delta j$. These trends have been already found before by Flower & Lique (2015) for ^{13}CN and C^{15}N in collision with *para*- H_2 . A similar behaviour is also observed in the case of $\text{NH}/\text{ND}-\text{He}$ (Dumouchel et al. 2012) in the case of two nuclear spins. The $\Delta F = \Delta j$ propensity rule (Alexander & Dagdigian 1985) is also highlighted for open-shell molecules with one nuclear spin such as $\text{C}_2\text{H}/\text{C}_2\text{D}-\text{H}_2$ (Dumouchel et al. 2017; Dagdigian 2018b) or $\text{CN}-\text{H}_2$ (Kalugina, Lique & Klos 2012). This propensity rule is a consequence of the fact that the nuclear spin is a spectator in the collision.

In addition, a general trend is that almost all hyperfine transitions for $^{13}\text{CCH}-\text{sph}-\text{H}_2$ collisional system are greater than the ones for

the $\text{C}^{13}\text{CH}-\text{sph}-\text{H}_2$ collisional system. This behaviour mostly comes from the shift of the centre of mass toward the edge of the molecule, leading to a greater anisotropy in the interaction of ^{13}CCH with H_2 (see Fig. 2). Indeed, this effect looks systematic as one can see in Fig. 5. The differences are estimated within a factor 1.5, which is higher than the observed errors between the methodologies compared in Section 2.2. Also, these differences are relatively high regarding the small shift of the centre of mass and the similarity of their rotational constants [$B(^{13}\text{CCH}) = 1.404 \text{ cm}^{-1}$ and $B(\text{C}^{13}\text{CH}) = 1.422 \text{ cm}^{-1}$; McCarthy, Gottlieb & Thaddeus 1995].

It is also interesting to investigate the impact of the isotopic substitution against the main isotopologue C_2H . Since ^{13}CCH , C^{13}CH , and C_2H do not have the same hyperfine structure, the discussion will focus on the fine-structure excitation of these molecules with *sph*- H_2 to keep results on the same level of theory.

Fig. 6 presents the temperature variation of fine-structure-resolved rate coefficients for the three collisional systems. The largest differences in the PES's appear for terms involving the $l_1 = 1$ expansion index, leading a larger odd anisotropy of the PES for ^{13}CCH (see Fig. 3). Therefore, it is not surprising to observe larger rate coefficients for $^{13}\text{CCH}-\text{sph}-\text{H}_2$ than for $\text{C}_2\text{H}-\text{sph}-\text{H}_2$ and $\text{C}^{13}\text{CH}-\text{sph}-\text{H}_2$ for $\Delta n = \Delta j = 1$. It is interesting to note that rate coefficients look similar for $\Delta n = \Delta j = 2$ with a moderated inversion of behaviour between ^{13}CCH and C^{13}CH . It looks clear that C_2H cannot be used as a substitute molecule for the other isotopologues.

4 ASTROPHYSICAL APPLICATION

With the present collisional data, it is possible to perform simple radiative transfer calculations. The aim is to check the possible impact of the isotopic substitution on radiative transfer modelling under

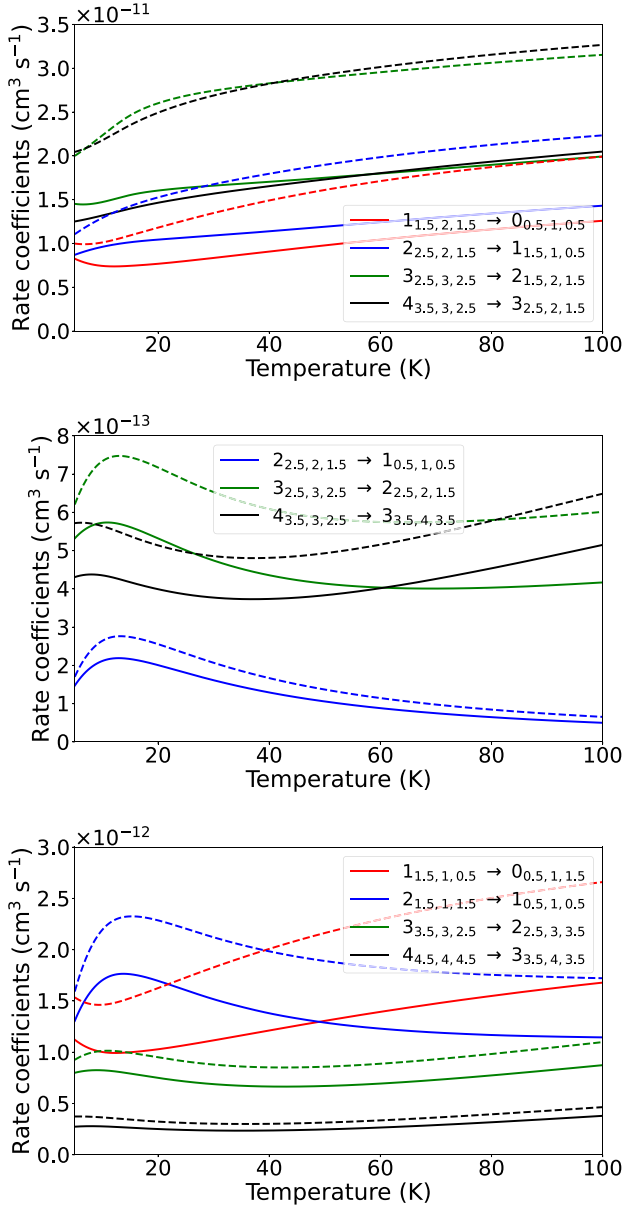


Figure 4. Temperature dependence of ^{13}CCH -*sph*- H_2 (dashed lines) and C^{13}CH -*sph*- H_2 (solid lines) hyperfine rate coefficients for $\Delta n = \Delta j$ (upper), $\Delta n \neq \Delta j$ (middle), and $\Delta F_1 = \Delta j \pm 1$ (lower) transitions.

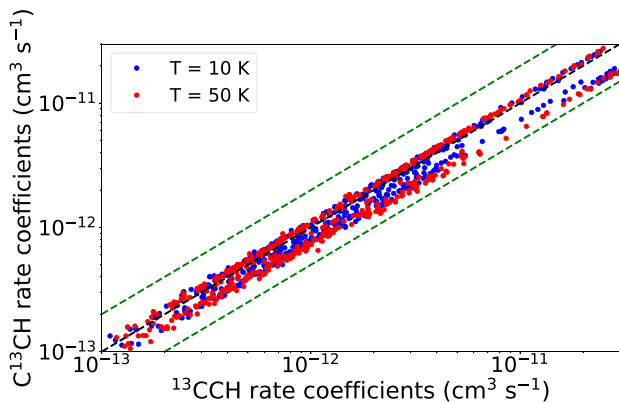


Figure 5. Comparison at 10 and 50 K of hyperfine rate coefficients for all de-excitations of ^{13}CCH -*sph*- H_2 and C^{13}CH -*sph*- H_2 . The green dashed lines represent deviations of the rate coefficients within a factor of 2.

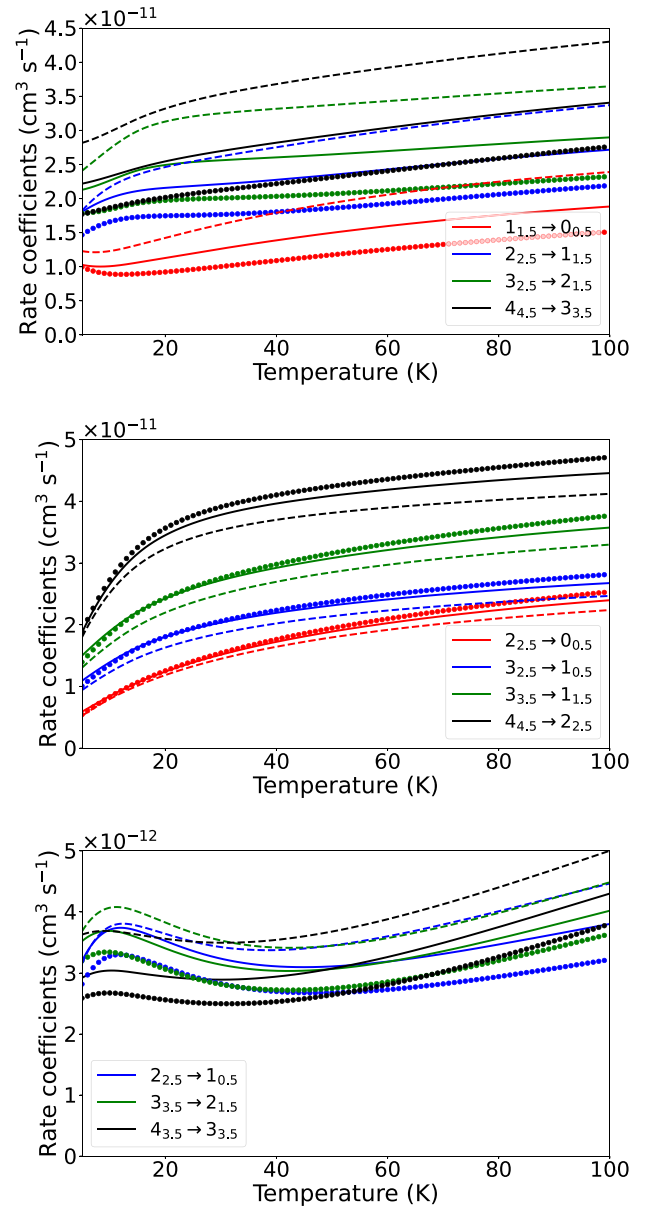


Figure 6. Temperature dependence of C_2H -*sph*- H_2 (solid lines), ^{13}CCH -*sph*- H_2 (dashed lines), and C^{13}CH -*sph*- H_2 (dotted lines) hyperfine rate coefficients for $\Delta n = \Delta j = 1$ (upper), $\Delta n = \Delta j = 2$ (middle), and $\Delta n \neq \Delta j$ (lower) transitions.

non-LTE conditions. These calculations have been performed with the RADEX code (van der Tak et al. 2007) using the escape probability approximation. In order to model astrophysical environments where these molecules are detected, such as TMC-1 (Sakai et al. 2010), L134N (Taniguchi et al. 2019), L1527 (Yoshida et al. 2019) or the Orion bar PDR (Cuadrado et al. 2015), kinetic temperatures were set at 10, 30, and 50 K. The temperature of the background is set to 2.73 K to represent the cosmic microwave background (CMB). The column-density is taken as $1 \times 10^{13} \text{ cm}^{-2}$, which is representative of the typical abundance of C_2H isotopologues in cold molecular clouds. The line width is assumed to be 1 km s^{-1} . It is also assumed that the medium is cold enough so that only *para*- H_2 is populated. Then, explorations at $T_{\text{kin}} = 50 \text{ K}$ in the following paragraphs must be taken with caution since *ortho*- H_2 abundance is not negligible at

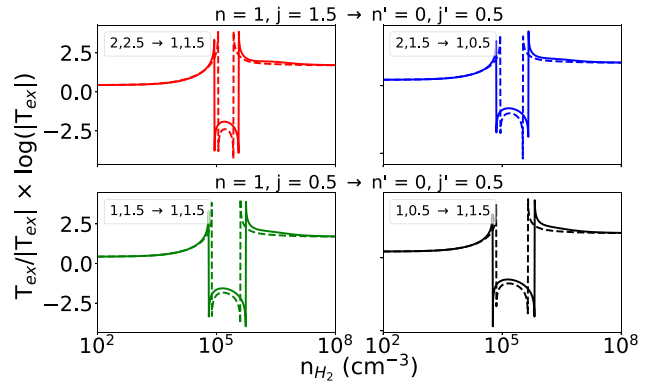
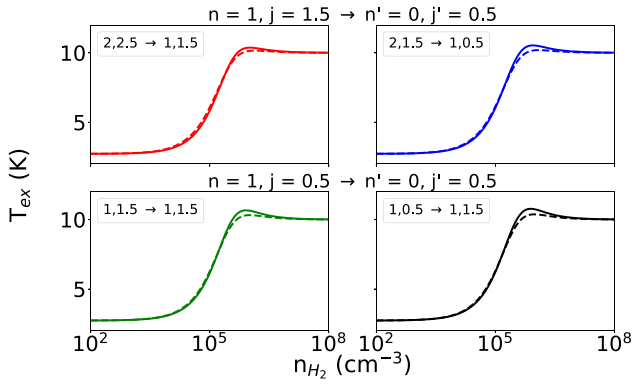


Figure 7. H_2 density dependence of excitation temperatures for selected hyperfine transitions of ^{13}CCH (dashed lines) and C^{13}CH (solid lines) for $T_{\text{kin}} = 10$ K (left) and $T_{\text{kin}} = 50$ K (right). The numbers in legend correspond to the $F_1, F \rightarrow F'_1, F'$ quantum numbers.

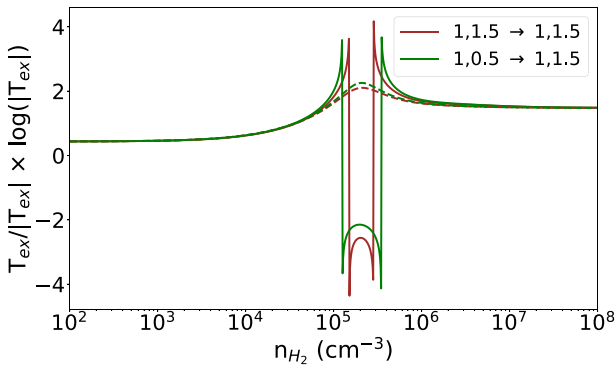


Figure 8. Excitation temperatures for the $n = 1, j = 0.5 \rightarrow n' = 0, j' = 0.5$ hyperfine transitions of ^{13}CCH (dashed lines) and C^{13}CH (solid lines) for $T_{\text{kin}} = 30$ K. The numbers in legend correspond to the $F_1, F \rightarrow F'_1, F'$ quantum numbers.

this temperature. The Einstein coefficients A_{ul} were taken from the CDMS data base (Endres et al. 2016).

Excitation temperatures of observed hyperfine components of the $n = 1 \rightarrow 0$ line of ^{13}CCH and C^{13}CH are plotted in Fig. 7 as a function of the *para*- H_2 density. As a general comment, all excitation temperatures strongly depend on the H_2 density, increasing from radiative (CMB temperature) to thermal equilibrium, where $T_{\text{ex}} = T_{\text{kin}}$. At $T_{\text{kin}} = 10$ K, one can see that relative differences of excitation temperatures of hyperfine transitions between the two isotopologues are very small, not exceeding 15 per cent. However, for $T_{\text{kin}} = 50$ K, a weak maser effect is observed for transitions involving both isotopologues in the intermediate density range of $n_{\text{H}_2} = 10^5 - 10^6 \text{ cm}^{-3}$. One can notice in Fig. 8, a weak maser effect for excitation temperatures of C^{13}CH for the $n = 1, j = 0.5 \rightarrow n' = 0, j' = 0.5$ lines, whereas only a suprathermal effect is seen for ^{13}CCH for the same transitions.

It is also interesting to look at the impact of the rate coefficients on the brightness temperature T_{B} . Table 2 shows brightness temperatures for selected transitions at typical molecular cloud densities. The LTE modelling represents conditions where rate coefficients do not have influence anymore. Then, differences can only come from the magnitude of the Einstein coefficients and of the slight difference in the energy structure of the two isotopologues.

Even if brightness temperatures for all transitions are far from the LTE regime, differences between ^{13}CCH and C^{13}CH remain very close to the ratio of the corresponding Einstein coefficients. Since

rate coefficients for $^{13}\text{CCH-sph-H}_2$ are larger than for $\text{C}^{13}\text{CH-sph-H}_2$ ones, almost systematically $\frac{T_{\text{B}}(\text{C}^{13}\text{CH})}{T_{\text{B}}(^{13}\text{CCH})} < \frac{A_{ul}(\text{C}^{13}\text{CH})}{A_{ul}(^{13}\text{CCH})}$. However, these discrepancies are too low compared to the uncertainties in rate coefficients and astrophysical models to conclude on the possible impact of the isotopic substitution in the rate coefficients for the brightness temperature.

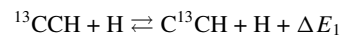
5 DISCUSSION AND CONCLUSION

We have calculated hyperfine-resolved rate coefficients of ^{13}CCH and C^{13}CH for collisions with H_2 including both non-zero nuclear spins of the H and the ^{13}C nuclei. Hyperfine cross sections and rate coefficients have been carried out using the PES of Dagdikian (2018a) and the recoupling technique (Alexander & Dagdikian 1985).

Rate coefficients for $^{13}\text{CCH-sph-H}_2$ and $\text{C}^{13}\text{CH-sph-H}_2$ show a similar propensity rule in favour of $\Delta n = \Delta j = \Delta F_1 = \Delta F$ transitions. Transitions with larger rate coefficients are especially seen with ^{13}CCH for $\Delta n = 1$ transitions, which is a direct consequence of the anisotropy of the PES with a shifted centre of mass. $^{13}\text{CCH-sph-H}_2$ rate coefficients have been found to be generally larger than $\text{C}^{13}\text{CH-sph-H}_2$ ones within a factor 1.5. Even if this effect is moderate, it is still of importance regarding the small shift $|\delta r| = 0.04\text{--}0.05a_0$ of the centre of mass.

Finally, we carried out radiative transfer modelling using these sets of data. For modelling environments at $T_{\text{kin}} = 10$ K, almost no differences have been found between ^{13}CCH and C^{13}CH excitation temperatures of observed lines. However, maser effects are found for ^{13}CCH and C^{13}CH at $T_{\text{kin}} = 30$ and 50 K. Brightness temperatures differ by a maximum of ~ 10 per cent from LTE conditions. Brightness temperatures ratios are almost systematically larger for C^{13}CH which is directly due to differences in the order of magnitude of the Einstein coefficients.

Then, the isotopic substitution does not have a significant impact on radiative transfer modelling and are not able to explain the $[\text{C}^{13}\text{CH}/^{13}\text{CCH}]$ abundance ratio found in cold environments for the observed transitions (Sakai et al. 2010; Cuadrado et al. 2015; Taniguchi et al. 2019; Yoshida et al. 2019). One possible explanation would be that at very low temperature, the exchange reaction of the isotopic carbon



could have a larger contribution than excitation. It has been shown in a chemical model that this exchange reaction has an important impact

Table 2. Comparison of ratio of brightness temperatures T_B (in mK) of ^{13}CCH and C^{13}CH for several hyperfine transitions.

Transition (n, j, F_1, F) \rightarrow (n', j', F'_1, F')	n_{H_2} (cm^{-3})	Ratio of T_B			Ratio of A_{ul}
		$T_{\text{kin}} = 10$ K	$T_{\text{kin}} = 30$ K	$T_{\text{kin}} = 50$ K	
(1,1.5,2,2.5) \rightarrow (0,0.5,1,1.5)	3×10^4	0.92	0.98	1.00	1.04
	3×10^5	1.03	1.05	1.05	
	LTE	1.02	1.02	1.02	
(1,1.5,2,1.5) \rightarrow (0,0.5,1,0.5)	3×10^4	0.98	1.04	1.06	1.07
	3×10^5	1.07	1.09	1.09	
	LTE	1.05	1.05	1.04	
(1,0.5,1,0.5) \rightarrow (0,0.5,1,1.5)	3×10^4	1.33	1.42	1.45	1.41
	3×10^5	1.42	1.46	1.46	
	LTE	1.39	1.38	1.38	
(1,0.5,0,0.5) \rightarrow (0,0.5,1,0.5)	3×10^4	1.29	1.36	1.39	1.41
	3×10^5	1.40	1.43	1.42	
	LTE	1.38	1.38	1.37	
(2,1.5,1,1.5) \rightarrow (1,0.5,1,0.5)	3×10^4	–	1.32	1.33	1.50
	3×10^5	–	1.44	1.45	
	LTE	–	1.47	1.47	

on the $[\text{C}^{13}\text{CH}/^{13}\text{CCH}]$ ratio (Furuya et al. 2011). This reaction could have less impact at higher kinetic temperatures and then allow excitation mechanisms to be more competitive. Nevertheless, these explorations should be looked more carefully in a more complete radiative transfer modelling.

ACKNOWLEDGEMENTS

We acknowledge financial support from the European Research Council (Consolidator Grant COLLEXISM, Grant Agreement No. 811363). We wish to acknowledge the support from the CEA/GENCI (Grand Equipement National de Calcul Intensif) for awarding us access to the TGCC (Très Grand Centre de Calcul) Joliot Curie/IRENE supercomputer within the A0110413001 project. We also acknowledge Guillaume Raffy and Benjamin Desrousseaux for recent and wide improvements on the HIBRIDON scattering code to make it suitable for this work.

DATA AVAILABILITY

The computed collisional data for both $^{13}\text{CCH-sph-H}_2$ and $\text{C}^{13}\text{CH-sph-H}_2$ will be available on the following data bases: EMAX (<https://dx.doi.org/10.17178/EMAX>), BASECOL (Dubernet et al. 2013), and LAMDA (van der Tak et al. 2020)

REFERENCES

Alexander M. H., 1982, *J. Chem. Phys.*, 76, 3637
 Alexander M. H., Dagdigian P. J., 1985, *J. Chem. Phys.*, 83, 2191
 Alexander M. H., Dagdigian P. J., Werner H. J., Klos J., Desrousseaux B., Raffy G., Lique F., 2023, *Comput. Phys. Commun.*, 289, 108761
 Beuther H., Semenov D., Henning Th., Linz H., 2008, *ApJ*, 675, 33
 Corey G. C., McCourt F. R., 1983, *J. Chem. Phys.*, 87, 2723
 Cuadrado S., Pilleri P., Cernicharo J., Fuente A., Joblin C., 2015, *A&A*, 575, A82
 Dagdigian P. J., 2018a, *J. Chem. Phys.*, 148, 024304
 Dagdigian P. J., 2018b, *MNRAS*, 479, 3227
 Dagdigian P. J., 2019, *MNRAS*, 487, 3427
 Dagdigian P. J., 2021, *MNRAS*, 505, 1987
 Daniel F., Dubernet M. L., Meuwly M., Cernicharo J., Pagani L., 2005, *MNRAS*, 363, 1083
 Dubernet M. L. et al., 2013, *A&A*, 553, A50

Dumouchel F., Klos J., Toboła R., Bacmann A., Maret S., Hily-Blant P., Faure A., Lique F., 2012, *J. Chem. Phys.*, 137, 114306
 Dumouchel F., Lique F., Spieddiel A., Feautrier N., 2017, *MNRAS*, 471, 1849
 Dutrey A., Guilloteau S., Guélin M., 1996, *A&A*, 317, L55
 Endres C. P., Schlemmer S., Schilke P., Stutzki J., Müller H. S. P., 2016, *J. Mol. Spectrosc.*, 327, 95
 Faure A., Lique F., 2012, *MNRAS*, 425, 740
 Flower D. R., Lique F., 2015, *MNRAS*, 446, 1750
 Furuya K., Aikawa Y., Sakai N., Yamamoto S., 2011, *ApJ*, 731, 38
 Goldflam R., Kouri D. J., Green S., 1977, *J. Chem. Phys.*, 67, 5661available at: <http://dx.doi.org/10.1063/1.434820>
 Gottlieb C. A., Gottlieb E. W., Thaddeus P., 1983, *ApJ*, 264, 740
 Green S., Thaddeus P., 1974, *ApJ*, 191, 653
 Kalugina Y., Lique F., Klos J., 2012, *MNRAS*, 422, 812
 Klos J., Dagdigian P. J., Alexander M. H., Faure A., Lique F., 2020, *MNRAS*, 493, 3491
 Knowles P. J., Hampel C., Werner H. J., 1993, *J. Chem. Phys.*, 99, 5219
 Lara-Moreno M., Stoecklin T., Halvick P., 2021, *MNRAS*, 507, 4086
 Loreau J., Lique F., Faure A., 2018, *ApJL*, 853, 5
 Lucas R., Liszt H., 1998, *A&A*, 337, 246
 McCarthy M. C., Gottlieb C. A., Thaddeus P., 1995, *J. Mol. Spectrosc.*, 173, 303
 Neufeld D. A., Green S., 1994, *ApJ*, 432, 158
 Offer A. R., van Hemert M. C., van Dishoeck E. W., 1993, *J. Chem. Phys.*, 100, 362
 Padovani M., Walmsley C. M., Tafalla M., Galli D., Müller H. S. P., 2009, *A&A*, 505, 1199
 Pirlot Jankowiak P., Kalugina Y., Ramachandran R., Raffy G., Dagdigian P. J., Lique F., 2021, *J. Chem. Phys.*, 155, 134303
 Sakai N., Saruwatari O., Sakai T., Takano S., Yamamoto S., 2010, *A&A*, 512, A31
 Salek A. H., Simon R., Winnewisser G., Wouterloot J. G. A., 1994, *Can. J. Phys.*, 72, 747
 Sastry K. V. L. N., Helminger P., Charo A., Herbst E., De Lucia F. C., 1981, *ApJ*, 251, 119
 Taniguchi K., Herbst E., Ozeki H., Saito M., 2019, *ApJ*, 884, 167
 Teyssier D., Fossé D., Gerin M., Pety J., Abergel A., Roueff E., 2003, *A&A*, 417, 135
 Tucker K. D., Kutner M. L., Thaddeus P., 1974, *ApJ*, 193, 115
 van der Tak F. F. S., Black J. H., Schöier F. L., Jansen D. J., van Dishoeck E. F., 2007, *MNRAS*, 468, 627
 van der Tak F. F. S., Lique F., Faure A., Black J. H., van Dishoeck E. F., 2020, *Atoms*, 8, 15
 Yoshida K., Sakai N., Nishimura Y., Tokumode T., Watanabe Y., Sakai T., Takano S., 2019, *PASJ*, 71, S18

Ziurys L. M., Saykally R. J., Plambeck R. L., Erickson N. R., 1982, *ApJ*, 254, 94

APPENDIX A: INFINITE ORDER SUDDEN LIMIT

The IOS method can be applied if the collision energy is larger than the rotational spacings, and hence the rotational motion can be neglected (Goldflam, Kouri & Green 1977). In this case, it is possible to employ the transitions out of the lowest rotational level $j = 0$ to derive hyperfine resolved rate coefficients for the targeted isotopologue. This approach has been generalized by Alexander (1982) for the case of a linear molecule in a $^2\Sigma^+$ electronic state

$$k_{njF \rightarrow n'j'F'}^{\text{IOS}} = [j][j'][F'] \sum_L \frac{[L]}{L+1} \times \left(\begin{array}{ccc} j' & L & j \\ -1/2 & 0 & 1/2 \end{array} \right)^2 \left\{ \begin{array}{ccc} j & j' & L \\ F' & F & I(\text{H}) \end{array} \right\}^2 \times 1/2[1 + \epsilon(-1)^{j+j'+L}]k_{0,1/2 \rightarrow L, L+1/2}^{\text{CC}} \quad (\text{A1})$$

where $|j - j'| < L < j + j'$ and ϵ is the parity index.

For the purpose of this work, equation (A1) has been adapted to take into account one nuclear spin and where $k_{0,1/2 \rightarrow L, L+1/2}^{\text{IOS}}$ have been replaced by the exact fundamental transitions $k_{0,1/2 \rightarrow L, L+1/2}^{\text{CC}}$ as is can be seen in earlier works (Daniel et al. 2005; Faure & Lique 2012).

One issue is that for low collisional energies, spacings between rotational energy levels are not negligible. This approximation is expected to fail at low temperature. Neufeld & Green (1994) suggested a scaling procedure to provide a correction at low temperature

$$k_{njF \rightarrow n'j'F'}^{\text{NG}}(T) = \frac{k_{njF \rightarrow n'j'F'}^{\text{IOS}}(T)}{k_{nj \rightarrow n'j'}^{\text{IOS}}(T)} k_{nj \rightarrow n'j'}^{\text{CC}}(T). \quad (\text{A2})$$

This scaling relation satisfies the condition

$$\sum_{F'} k_{njF \rightarrow n'j'F'}^{\text{NG}}(T) = k_{nj \rightarrow n'j'}^{\text{CC}}(T). \quad (\text{A3})$$

However, this correction needs converged CC elastic transitions in order to provide hyperfine quasi-elastic transitions ($n = n'$, $j = j'$, $F \neq F'$), which is usually not the case in scattering calculations. Then, this correction is not suitable to describe such transitions.

APPENDIX B: DETAILS ABOUT THE CONVERGED PARAMETERS USED IN SCATTERING CALCULATIONS

In order to determine accurate cross sections in scattering calculations, it is necessary to optimize the parameters used in the CC equations. We provide in Table B1 the rotational basis of the target n_{max} , the largest total angular momentum J_{TOT} and the step ΔE between total energies intervals E_{TOT} . The neglect of the structure of H_2 imply that rotational basis of H_2 is chosen as $j_2 = 0$ and its rotational constant omitted. For both collisional systems, the radial propagation was considered between $R_{\text{min}} = 4.25a_0$ and $R_{\text{max}} = 60a_0$. Each parameter has been determined to ensure converged cross sections within 1 percent of deviation. Hyperfine calculations were then computed using the nuclear spin-free S -matrices determined with these convergence parameters.

Table B1. Rotational basis set n_{max} and optimized total angular momentum J_{TOT} used for scattering calculations. These parameters are chosen for several total energies E_{TOT} with different steps ΔE .

E_{TOT} (cm $^{-1}$)	ΔE (cm $^{-1}$)	$^{13}\text{CCH-sph-H}_2$		$\text{C}^{13}\text{CH-sph-H}_2$	
		n_{max}	J_{TOT}	n_{max}	J_{TOT}
0.1–50	0.1	10	18	11	15
50–100	0.1	12	24	11	24
100–200	0.1	16	30	15	30
200.5–500	0.5	22	45	22	42
501–700	1	24	51	23	48
705–1000	5	27	57	27	54
1010–1370	10	33	63	32	60

This paper has been typeset from a \LaTeX file prepared by the author.

C.3 Collisional excitation of C₂H and C₂D by molecular hydrogen

Collisional excitation of C₂H and C₂D by molecular hydrogen

P. Pirlot Jankowiak¹, F. Lique^{1*} and P. J. Dagdigan²

¹Univ Rennes, CNRS, IPR (Institut de Physique de Rennes) - UMR 6251, F-35000 Rennes, France

²Department of Chemistry, The Johns Hopkins University, Baltimore, MD 21218-2685, USA

Accepted 2023 September 13. Received 2023 September 13; in original form 2023 July 21

ABSTRACT

The determination of physical conditions in interstellar clouds requires reliable estimation of radiative and collisional data for molecules detected in space. In this work, rate coefficients for de-excitation of C₂H and C₂D induced by collisions with both *ortho*- and *para*-H₂ are presented. Calculations have been carried out using a recently published four-dimensional C₂H–H₂ potential energy surface. Fine-structure resolved cross-sections were computed with the time-independent close-coupling approach. We report cross-sections for transitions between the first 41 levels of C₂H and corresponding rate coefficients up to 500 K. We also computed cross-sections for transitions between the first 31 levels of C₂D and corresponding rate coefficients up to 200 K. Then, hyperfine structure resolved cross-sections and rate coefficients were computed using the recoupling technique. The hyperfine structure resolved rate coefficients for C₂H–H₂ and C₂D–H₂ are calculated for the first 38 hyperfine C₂H energy levels and first 55 hyperfine C₂D energy levels both for temperatures up to 100 K. These collisional data were used in a simple radiative transfer modelling.

Key words: molecular data – radiative transfer – scattering.

1 INTRODUCTION

The ethynyl radical C₂H was first detected by Tucker, Kutner & Thaddeus (1974) in the interstellar medium (ISM) through the $n = 1 \rightarrow 0$ rotational line. Later, experimental studies (Sastry et al. 1981; Gottlieb, Gottlieb & Thaddeus 1983) reported spectroscopic measurements for the $n = 2 \rightarrow 1$ and $n = 3 \rightarrow 2$ lines, providing accurate spectroscopic data for the X²Σ⁺ electronic state of this radical. Since then, C₂H has been detected in a wide range of astrophysical environments such as molecular clouds (Wootten et al. 1980; Sakai et al. 2010), star-forming regions (Beuther et al. 2008; Treviño-Morales et al. 2014; Yoshida et al. 2019), pre-stellar cores (Padovani et al. 2009), protoplanetary discs (Dutrey, Guilloteau & Guélin 1996) and photodissociation regions (PDRs; Ziurys et al. 1982; Teyssier et al. 2003; Cuadrado et al. 2015; Nagy et al. 2015) and is one of the most abundant hydrocarbon molecules in the ISM.

Also, the high abundance of C₂H in the ISM makes possible the observation of its deuterated isotopologue C₂D. Indeed, the first detection of the C₂D radical in the ISM was reported by Combes et al. (1985) in the Kleinman–Low nebula through the $n = 3 \rightarrow 2$ rotational line. This observation was corroborated by two parallel laboratory studies (Bogey, Demuynck & Destombes 1985; Vrtilek et al. 1985). This isotopologue has been subject to additional detections in molecular clouds (Turner 2001), PDR (Parise et al. 2009), and star-forming regions (Treviño-Morales et al. 2014).

The abundance ratio between hydrogenated and deuterated molecules is usually found to deviate from the cosmological elemental ratio [D/H] $\sim 2 \times 10^{-5}$ (Linsky et al. 2006). This abundance ratio can vary by several orders of magnitude from a source to another

and also on the molecule, since the abundance of a molecule depends on its formation path and on the physical conditions of the medium. An accurate determination of the abundance of C₂H and C₂D is of interest to better understand and constrain the deuteration fraction in the ISM. That can give an insight on the evolution of molecular clouds, the abundance of deuterated molecules showing to strongly depend on the age of these objects in chemical models (Treviño-Morales et al. 2014).

The knowledge of the physical conditions of the ISM and especially molecular abundances relies on the interpretation of observational spectra through radiative transfer modelling. Notwithstanding, interstellar environments are subject to low density and energy levels of the detected molecules are out of the local thermodynamic equilibrium (LTE; Roueff & Lique 2013). Then, it is necessary to study excitation mechanisms including both radiative and collisional processes. On one hand, radiative mechanisms are related to Einstein coefficients which depend on the dipole moment of the molecule involved and are determined through spectroscopic analysis. On the other hand, collisional processes are quantified by rate coefficients and can be determined through (quantum) calculations for a given collisional system. It is then of interest to study the excitation of both C₂H and C₂D with molecular hydrogen which is the main collider in molecular clouds where these two isotopologues are mainly observed.

The first collisional study implying C₂H target was done by Spielfiedel et al. (2012), providing fine and hyperfine rate coefficients for transitions induced by He as a substitute of H₂. Najar et al. (2014) provided rate coefficients up to 100 K for the C₂H–*para*-H₂ collisional system, taking into account only the fine-structure splitting of C₂H. To do so, they computed a potential energy surface (PES) based on the rigid rotor approximation, considering *para*-H₂ as a pseudo-atom. This approach excluded the contribution of excited

* E-mail: francois.lique@univ-rennes.fr

levels of H_2 ($j_2 \geq 1$, j_2 being the rotational state of H_2) in the scattering calculations. This potential has also been used by Dumouchel et al. (2017) to compute hyperfine resolved rate coefficients of C_2H and C_2D with *para*- H_2 up to 80 K. In a more recent work, Dagdigian (2018a) used the coupled cluster theory to compute a new 4D PES of the C_2H-H_2 collisional system. This author employed this PES to provide hyperfine rate coefficients of C_2H with *para*- H_2 and the first collisional data with *ortho*- H_2 up to 300 K (Dagdigian 2018b). A reasonable agreement was found with the work from Najar et al. (2014) for C_2H -*para*- H_2 fine-structure resolved rate coefficients. The differences between these results mostly come from the size of H_2 rotational basis in scattering calculations. One can expect that these discrepancies would impact results for the C_2D-H_2 collisional system as well, and new calculations with the 4D PES can be useful.

As far as we know, there are no data about collisional excitation of C_2D with *ortho*- H_2 . Such data are necessary for modelling environments where *ortho*- H_2 is significantly populated (Treviño-Morales et al. 2014). The purpose of this paper is to fill this lack of data. We report the first hyperfine resolved rate coefficients for C_2D collisions with *ortho*- H_2 and improved C_2D -*para*- H_2 collisional data up to 100 K using the 4D PES computed by Dagdigian (2018a). We also recompute hyperfine resolved rate coefficients for the C_2H-H_2 collisional system up to 100 K.¹ We also extend the range of temperature of fine-structure C_2H-H_2 collisional data up to 500 K. New fine-structure rate coefficients have been computed for the C_2D-H_2 collisional system up to 200 K. These data are expected to cover the temperature range of environments where C_2H and C_2D are detected (Treviño-Morales et al. 2014; Nagy et al. 2015).

The paper is organized as follows: Section 2 presents the features of the PES used in scattering calculations and how to make it suitable for molecular dynamics of the C_2D-H_2 collisional system. State-to-state de-excitation rate coefficients of both C_2H and C_2D in collision with molecular hydrogen are presented in Section 3 (It should be noted that excitation rate coefficients can be obtained from the de-excitation rate coefficients through detailed balance). As an application of this new data, we perform a simple radiative transfer application in Section 4. A conclusion summarizes this work in Section 5.

2 METHODOLOGY

2.1 Potential energy surface

The PES describing the electronic interaction of the C_2H-H_2 collisional system has been computed by one of the authors of the present paper (Dagdigian 2018a). This author used the restricted coupled cluster formalism including single, double, and (perturbative) triple excitations [RCCSDT] (Knowles, Hampel & Werner 1993) to perform *ab initio* calculations using the MOLPRO software (Werner, Knowles & et al. 2020). The aug-cc-pVQZ basis set (Dunning 1989) was used to ensure convergence of the interaction potential around the global minimum. The interaction energy of the bimolecular complex depends on four degrees of freedom: The separation R between the centres of mass of C_2H and H_2 PES; the angle θ_1 between the C_2H internuclear axis and the Jacobi vector \mathbf{R} ; the angle θ_2 between

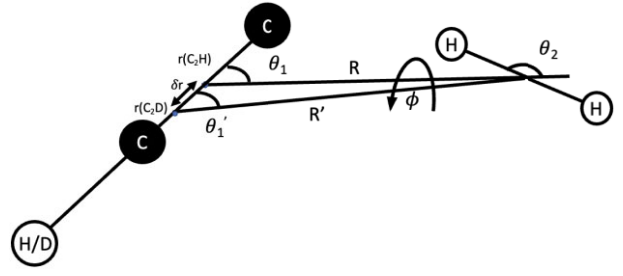


Figure 1. Representation of the C_2H-H_2 and C_2D-H_2 geometries. The unprimed and primed quantities refer to C_2H and C_2D respectively.

the H_2 internuclear axis and the Jacobi vector \mathbf{R} ; and the dihedral angle ϕ between the (C_2H, \mathbf{R}) plane and H_2 axis. Both C_2H and H_2 are considered as rigid rotors, where their nuclear geometries are taken as their respective equilibrium configurations in the ground vibrational state.

The fit of the PES was represented by an expansion in bispherical harmonics:

$$V(R, \theta_1, \theta_2, \phi) = \sum_{l_1 l_2 l} v_{l_1 l_2 l}(R) A_{l_1 l_2 l}(\theta_1, \theta_2, \phi). \quad (1)$$

The $A_{l_1 l_2 l}(\theta_1, \theta_2, \phi)$ in equation (1) depend on the angular coordinates of the system, defined as:

$$A_{l_1 l_2 l}(\theta_1, \theta_2, \phi) = \left(\frac{[l_1]}{4\pi} \right)^{1/2} \sum_m (l_1 m l_2, -m | l 0) \times Y_{l_1 m}(\theta_1, 0) Y_{l_2, -m}(\theta_2, \phi), \quad (2)$$

where the Y_{lm} are spherical harmonics, $(\dots | \dots)$ are Clebsch–Gordan coefficients, $[x] \equiv (2x + 1)$. The $v_{l_1 l_2 l}(R)$ are the radial coefficients for a given distance R , and l_1, l_2, l are chosen such that $|l_1 - l_2| < l < l_1 + l_2$. Equations (1) and (2) are the most suitable form of the PES for time-independent scattering calculations. The global minimum was found for $R = 7.82a_0$ and the $\theta_1 = 180^\circ$, $\theta_2 = 90^\circ$, $\phi = 0^\circ$ orientation with an associated well depth D_e of 133.4 cm^{-1} .

Within the Born–Oppenheimer approximation, it is possible to use the C_2H-H_2 PES to describe the interaction of the C_2D-H_2 complex. This can be performed with a transformation of the coordinates through a shift δr of the centre of mass of the targeted molecule (see Fig. 1). The transformation from one isotopologue frame to the other one can be obtained through:

$$\delta r = r(C_2D) - r(C_2H), \quad (3)$$

$$R' = \sqrt{R^2 + \delta r^2 + 2R\delta r \cos(\theta_1)}, \quad (4)$$

$$\theta_1' = \cos^{-1} \left(\frac{R \cos(\theta_1) - \delta r}{R'} \right), \quad (5)$$

where $r(C_2H)$ and $r(C_2D)$ are the positions of the centre of mass of C_2H and C_2D respectively along the internuclear axis (see Fig. 1). The same bond lengths are assumed for C_2D than for C_2H since the molecule is assumed to be rigid. The transformation of the coordinates θ_2 and ϕ was not necessary since the impact on the dynamics is found to be negligible. The centre of mass is shifted by $\delta r = +0.1157a_0$, toward the deuterium end. This transformation leads to a new expansion of the PES for the C_2D-H_2 complex. Dagdigian (2018a) obtained a fit for $l_1 = 12$ and $l_2 = 6$, leading to 174 radial coefficients for C_2H-H_2 . For the C_2D-H_2 collisional system, we expanded the PES with the same number of coefficients as for C_2H-H_2 using a Gauss–Legendre quadrature with 686 geometries.

¹ It has been found that the most recent available collisional data (Dagdigian 2018b) was overestimated by a factor ~ 1.4 . Also, we figured out a bug in the recoupling approach from the scattering software used in this work did not correctly calculate quasi-elastic transitions.

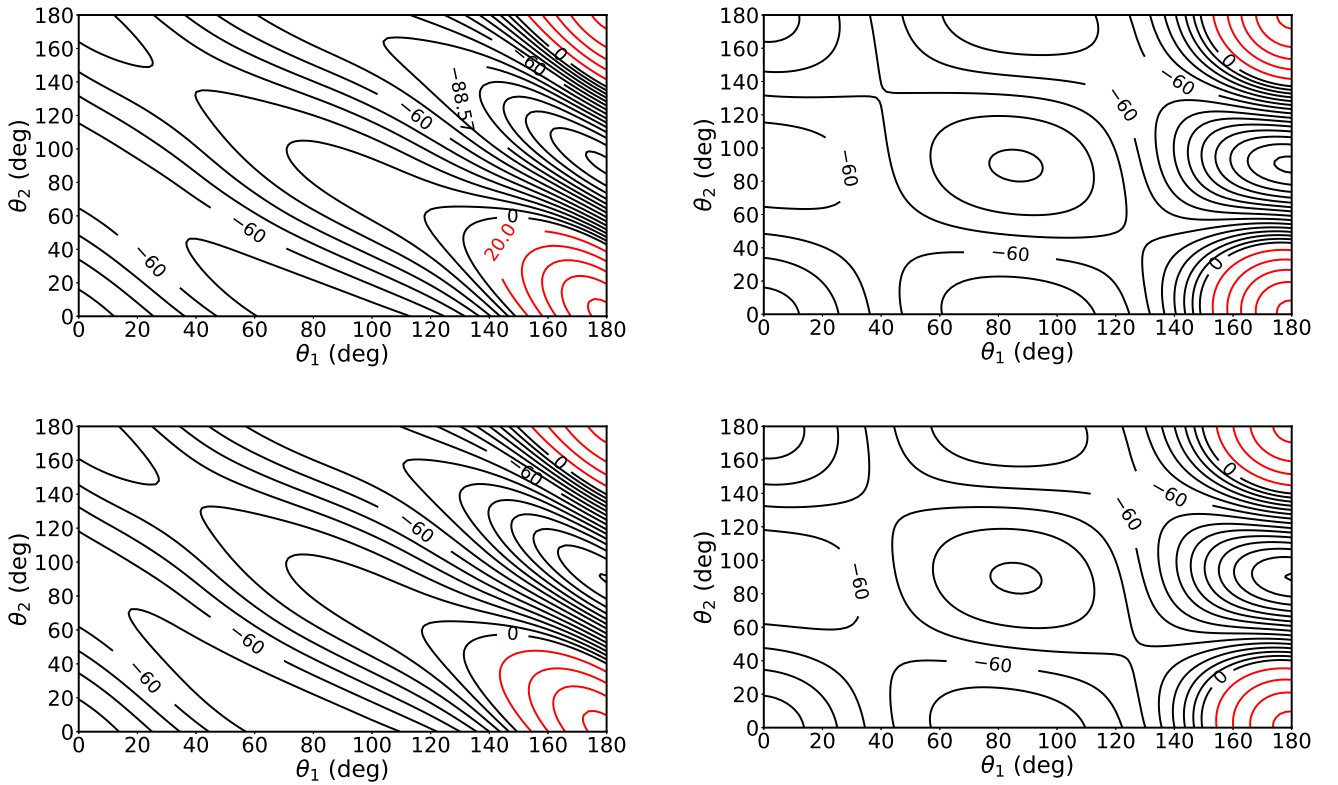


Figure 2. Contour plots of the interaction potential of C_2H (upper panels) and C_2D (lower panels) for an intermolecular separation $R = 7.82a_0$. The left and right panels have $\phi = 0^\circ$ (left panels) and 30° (right panels). Contours in red represent a repulsive interaction, contours in black an attractive interaction. The values of the potential are given in cm^{-1} .

It is interesting to check the impact of the isotopic substitution on the contour plots of the PES for given geometries. Fig. 2 shows the angular dependence of the PES of the C_2H-H_2 and C_2D-H_2 complexes for two geometries around the global minimum. One can see that for both isotopologues, the most repulsive interaction occurs when $\theta_1 = 180^\circ$, corresponding to the orientation of the targeted hydrogen/deuterium toward the collider, and for $\theta_2 = 0^\circ$ and $\theta_2 = 180^\circ$.

The most attractive part of the PES corresponds to a T-shaped structure of the complexes ($\theta_1 = 180^\circ$, $\theta_2 = 90^\circ$), where the global minimum is reached. These contour plots illustrate the large anisotropy of the PES. Even if the shapes of the interaction energy look very similar in both isotopologue frames, one can see slight differences in the range $\theta_1 = 140-180^\circ$, where larger anisotropy is seen for the C_2H-H_2 complex. Such differences will have impact on the magnitude of the C_2H-H_2 and C_2D-H_2 excitation cross-sections as will be seen in Section 3.

2.2 Scattering formalism

Both C_2H and C_2D are open-shell molecules with a $^2\Sigma^+$ electronic ground state. The unpaired electron, with spin $S_1 = 1/2$, couples with the rotational angular momentum n_1 to yield the total angular momentum j_1 of the molecule:

$$\mathbf{n}_1 + \mathbf{S}_1 = \mathbf{j}_1.$$

During the collision, j_1 and the rotational angular momentum j_2 of the projectile will be coupled with the rotation of the target. The total

angular momentum J of the complex thus equals

$$\mathbf{J} = \mathbf{j}_{12} + \mathbf{L},$$

where \mathbf{L} is the orbital angular momentum and $\mathbf{j}_{12} = \mathbf{j}_1 + \mathbf{j}_2$ is the vector sum of the molecular angular momenta. This coupling scheme has been used in quantum time-independent calculations with the close coupling method (CC) to determine fine-structure resolved cross-sections in the same way as employed by Dagdigian (2018b).

In addition, both C_2H and C_2D possess a non-zero nuclear spin due to the H and D nuclei. The coupling of the nuclear spin to the rotation yields a hyperfine splitting of the fine-structure energy levels where

$$\mathbf{F}_1 = \mathbf{j}_1 + \mathbf{I}_X,$$

where \mathbf{F}_1 denotes the total angular momentum of the targeted isotopologue including its nuclear spin, \mathbf{I}_X is the nuclear spin ($X = H$ or D), $I_H = 1/2$, and $I_D = 1$. When the hyperfine splittings are small, it is possible to consider them as degenerate and carry out hyperfine structure calculations using a recoupling technique (Alexander & Dagdigian 1985). Then, the nuclear spin can be recoupled to the total angular momentum of the complex as $\mathbf{J} + \mathbf{I}_X = \mathbf{J}_T$.

This approach consists of using nuclear spin-free T -matrix elements $T_{n_1 j_1 j_2 j_{12} L, n'_1 j'_1 j'_2 j'_{12} L'}$ computed by the CC method to determine hyperfine resolved cross-sections. The T -matrix elements including the nuclear spin can be obtained using the spin-free T -matrix elements

(Offer, van Hemert & van Dishoeck 1993):

$$\begin{aligned}
 T_{n_1 j_1 F_1 j_2 j_R L, n'_1 j'_1 F'_1 j'_2 j'_R L'}^{J_T} &= \sum_{J j_1 j'_1} (-1)^{j_2 + j'_2 + j_R + j'_R + L + L'} \\
 &\times \left([j_{12}] [j'_{12}] [j_R] [j'_R] [F_1] [F'_1] \right)^{1/2} [J] \\
 &\times \begin{Bmatrix} j_1 & j_2 & j_{12} \\ L & J & j_R \end{Bmatrix} \begin{Bmatrix} j'_1 & j'_2 & j'_{12} \\ L' & J & j'_R \end{Bmatrix} \\
 &\times \begin{Bmatrix} j_R & j_1 & J \\ I_X & J_T & F_1 \end{Bmatrix} \begin{Bmatrix} j'_R & j'_1 & J \\ I_X & J_T & F'_1 \end{Bmatrix} \\
 &\times T_{n_1 j_1 j_2 j_R L, n'_1 j'_1 j'_2 j'_R L'}^J. \quad (6)
 \end{aligned}$$

Here, $j_2 + L = j_R$ and $j_R + F_1 = J_T$. The T -matrix elements in equation (6) can be used to compute hyperfine resolved cross-sections:

$$\begin{aligned}
 \sigma_{n_1 j_1 F_1, n'_1 j'_1 F'_1} &= \frac{\pi}{k^2 [F_1] [j_2]} \\
 &\times \sum_{J_T j_R j'_R L L'} [J_T] \left| T_{n_1 j_1 F_1 j_2 j_R L, n'_1 j'_1 F'_1 j'_2 j'_R L'}^{J_T} \right|^2, \quad (7)
 \end{aligned}$$

where k^2 is the wave vector of the initial state.

Nuclear spin-free calculations have been carried out for C_2D collisions with both *ortho*- and *para*- H_2 up to 1618.7 cm^{-1} and 1500 cm^{-1} , respectively, for energy levels up to $n_1 \leq 15$ (see Appendix A for more details about the used parameters in scattering calculations). These calculations have been performed including a rotational basis of $j_2 = 0, 2$ for *para*- H_2 . In the case of *ortho*- H_2 collisions, only a basis $j_2 = 1$ was necessary.

For collisions of C_2D with *ortho*- H_2 and *para*- H_2 , hyperfine rate coefficients have been computed for 55 energy levels up to $n_1 = 9$ and for temperatures between 5 and 100 K. For the C_2H - H_2 collisional system, fine-structure calculations were performed up to a total energy of 3500 cm^{-1} for collisions with *para*- H_2 and 3618.7 cm^{-1} for collisions with *ortho*- H_2 . Energy levels with n_1 up to 20 were taken into account in the CC calculations. Fine-structure rate coefficients were then computed up to 500 K. All scattering calculations (both CC and recoupling) were performed with the HIBRIDON scattering code (Alexander et al. 2023). For the highest total energies considered, greater than 1500 cm^{-1} , the convergence of cross-sections with respect to the H_2 basis used is moderate, up to a few tens of percents of mean absolute deviation. Such intensive calculations may be accomplished by using the coupled state approximation. However, this method is not implemented yet in the HIBRIDON code for molecule–molecule collisions. However, this truncated H_2 basis moderately impacts the rate coefficients presently computed.

The rate coefficient from an initial level i to a final level f consists in integrating the cross-section in equation (7) over a Maxwell–Boltzmann distribution of the collisional energies E_c :

$$k_{i \rightarrow f}(T) = \left(\frac{8}{\pi \mu (k_B T)^3} \right)^{1/2} \int_0^\infty \sigma_{i \rightarrow f}(E_c) E_c e^{-E_c/k_B T} dE_c, \quad (8)$$

where μ is the reduced mass of the given collisional system and k_B is the Boltzmann's constant.

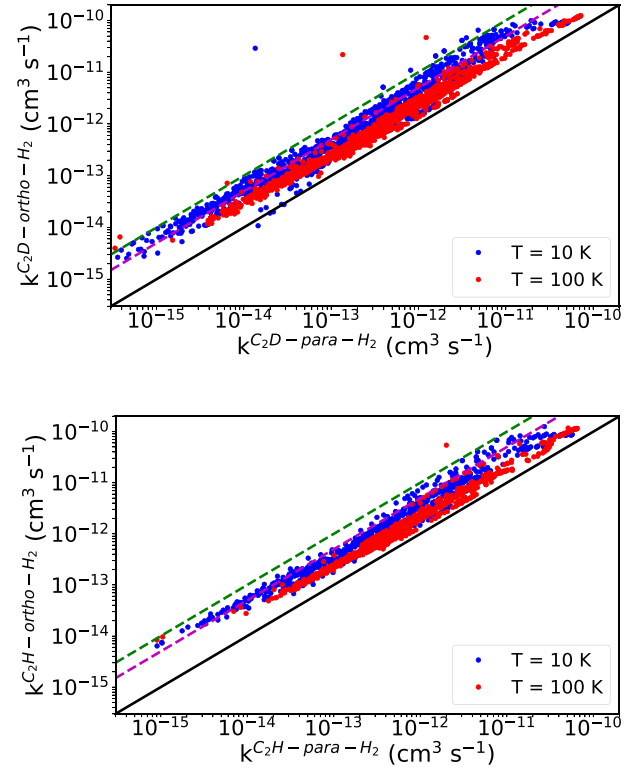


Figure 3. Systematic comparison of hyperfine rate coefficients for C_2D –*ortho*- and *para*- H_2 collisions (upper panel) and for C_2H –*ortho*- and *para*- H_2 collisions (lower panel) at 10 K and 100 K. Magenta and green dashed lines represent deviations within a factor of 5 and 10, respectively.

3 RATE COEFFICIENTS

3.1 C_2H – H_2 rate coefficients

Both fine and hyperfine structure resolved rate coefficients calculated in this work for the C_2H – H_2 collisional system are essentially the same with the same propensity rules as in the calculations by Dagdigan (2018b) and will not be discussed in details here. We just review the main features of these collisional data. It is found that the rate coefficients for collisions involving *ortho*- H_2 are larger than those with *para*- H_2 (see also Fig. 3). For fine-structure transitions induced by *para*- and *ortho*- H_2 , propensity rules (Alexander 1982) are observed for $\Delta n_1 = \Delta j_1$ transitions (see Fig. 6) with $\Delta n_1 = \Delta j_1 = 2$ transitions dominating over $\Delta n_1 = \Delta j_1 = 1$ transitions. These effects have an impact on the behaviour of hyperfine structure transitions, where fine structure conserving transitions displayed larger intensities for $\Delta j_1 = \Delta F_1$ transitions than for $\Delta n_1 \neq \Delta j_1$ ones.

3.2 C_2D – H_2 rate coefficients

Fig. 3 shows a comparison between hyperfine resolved C_2D –*ortho*- H_2 and C_2D –*para*- H_2 rate coefficients at 10 K and 100 K. One can see that all rate coefficients are larger for C_2D –*ortho*- H_2 collisions by a factor of 10 at low temperatures. Such deviations come from the PES features, where larger anisotropies are expected for the *ortho*- H_2 collider. These differences are still an order of a factor of 5 at 100 K. This also can be seen in Fig. 4, where *ortho*- H_2 rate coefficients are dominating the corresponding *para*- H_2 quantities. Such effect is well

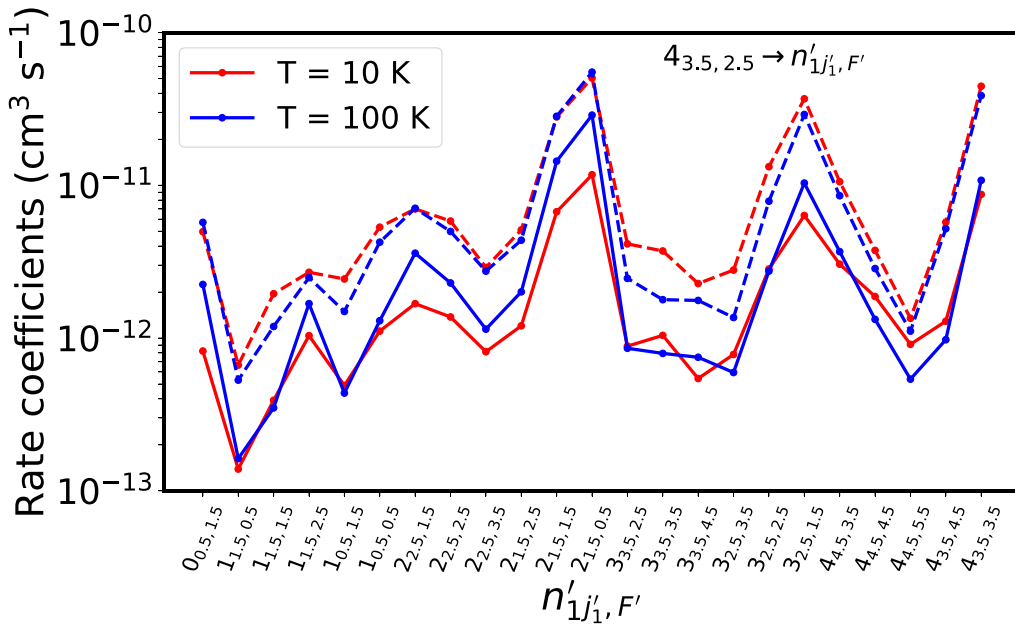


Figure 4. Hyperfine structure resolved transitions for C_2D in collision with *para*- H_2 (solid lines) and *ortho*- H_2 (dashed lines) from the $4_{3,5,2,5}$ energy level toward lower levels.

known for neutral collisional systems such as $PN-H_2$ (Desrousseaux et al. 2021) or HC_2NC-H_2 and HNC_3-H_2 (Bop et al. 2021).

It is also possible to see a propensity rule in favour of fine structure conserving ($\Delta n_1 = \Delta j_1$) transitions, which is consistent with results observed in C_2H collisions (Dagdikian 2018b). This propensity rule results from the fact that the electron spin is a spectator in the collision. This effect is generally observed for open-shell molecules such as CCS (Godard Palluet & Lique 2023), CN (Kalugina, Klos & Lique 2013) or SH^+ (Dagdikian 2019). A propensity rule for even $\Delta n_1 = \Delta j_1$ transitions is observed.

More specifically, in the case of the hyperfine structure excitation, a propensity rule (Alexander & Dagdigian 1985) is also observed for $\Delta j_1 = \Delta F_1$ transitions. Similar to the propensity rule for fine-structure transitions, this hyperfine propensity rule results from the spectator role that nuclear spin plays in the collision. With the propensity rule for fine-structure transitions, the largest rate coefficients occur for $\Delta n_1 = \Delta j_1 = \Delta F_1$ transitions. The weakest transitions occur when $\Delta n_1 \neq \Delta j_1 \neq \Delta F_1$, sometimes by one order of magnitude compared to the dominant transitions.

It is interesting to compare the C_2D-H_2 rate coefficients with the previous study of Dumouchel et al. (2017). In their work, the 2D averaged PES computed by Najjar et al. (2014) for the C_2H-H_2 collisional system and transformed to describe the C_2D-H_2 system was used for scattering calculations. The computed rate coefficients were computed with only $j_2 = 0$ in the H_2 rotational basis. Fig. 5 shows a comparison between the two sets of collisional data for two given temperatures. One can see that most of the transitions are contained within a factor of 2 of differences, whereas the largest ones are relatively well reproduced. Such differences can come from several possibilities. First, the inclusion of two more degrees of freedom in the C_2H-H_2 interaction potential leads to more anisotropies (see Fig. 2) and radial coefficients to take into account in scattering calculations. Second, the inclusion of $j_2 = 0, 2$ rotational basis is often necessary to converge cross-sections computed with the CC approach.

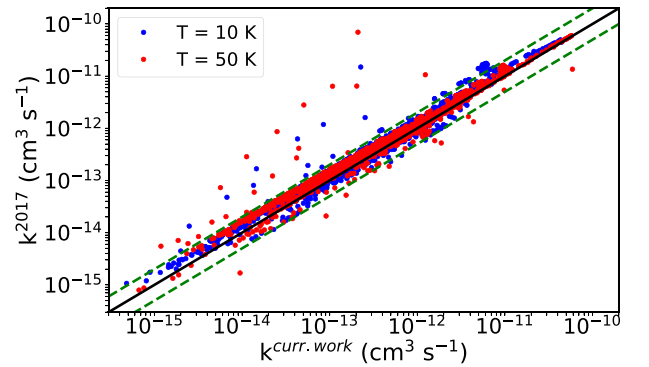


Figure 5. Systematic comparison of C_2D -*para*- H_2 hyperfine rate coefficients computed in this work and the previous study by Dumouchel et al. (2017) for transitions at 10 K and 50 K. Green dashed lines represent deviations within a factor of 2.

3.3 C_2H-H_2 versus C_2D-H_2 rate coefficients

Fig. 6 presents comparisons of several fine-structure rate coefficients of C_2H and C_2D in collisions with both *ortho*- and *para*- H_2 . It should be noted that the isotopologues have different numbers of hyperfine transitions because of the differences values of the H and D nuclear spins. The strongest impact of the isotopic substitution can be observed for $\Delta n_1 = \Delta j_1 = 1$ transitions for both H_2 colliders, in a more moderate way for *ortho*- H_2 than *para*- H_2 . Such differences mostly come from the shift of the centre of mass of the PES, leading to significant differences in expansion coefficients $v_{l_1 l_2}$. Especially, radial coefficients with odd l_1 indexes are larger for the C_2H-H_2 complex than the C_2D-H_2 one. This is related to the fact that the centre of mass is closer of the centre of the molecule in the case of C_2D and leads to less anisotropy in the PES (see Fig. 1).

For the other cases ($\Delta n_1 = \Delta j_1 = 2$ and $\Delta n_1 \neq \Delta j_1$), the impact of isotopic substitution is moderate and rate coefficients are of the same order of magnitude for both collisional systems. Since the PES expansion coefficients involved in the CC equations for these types

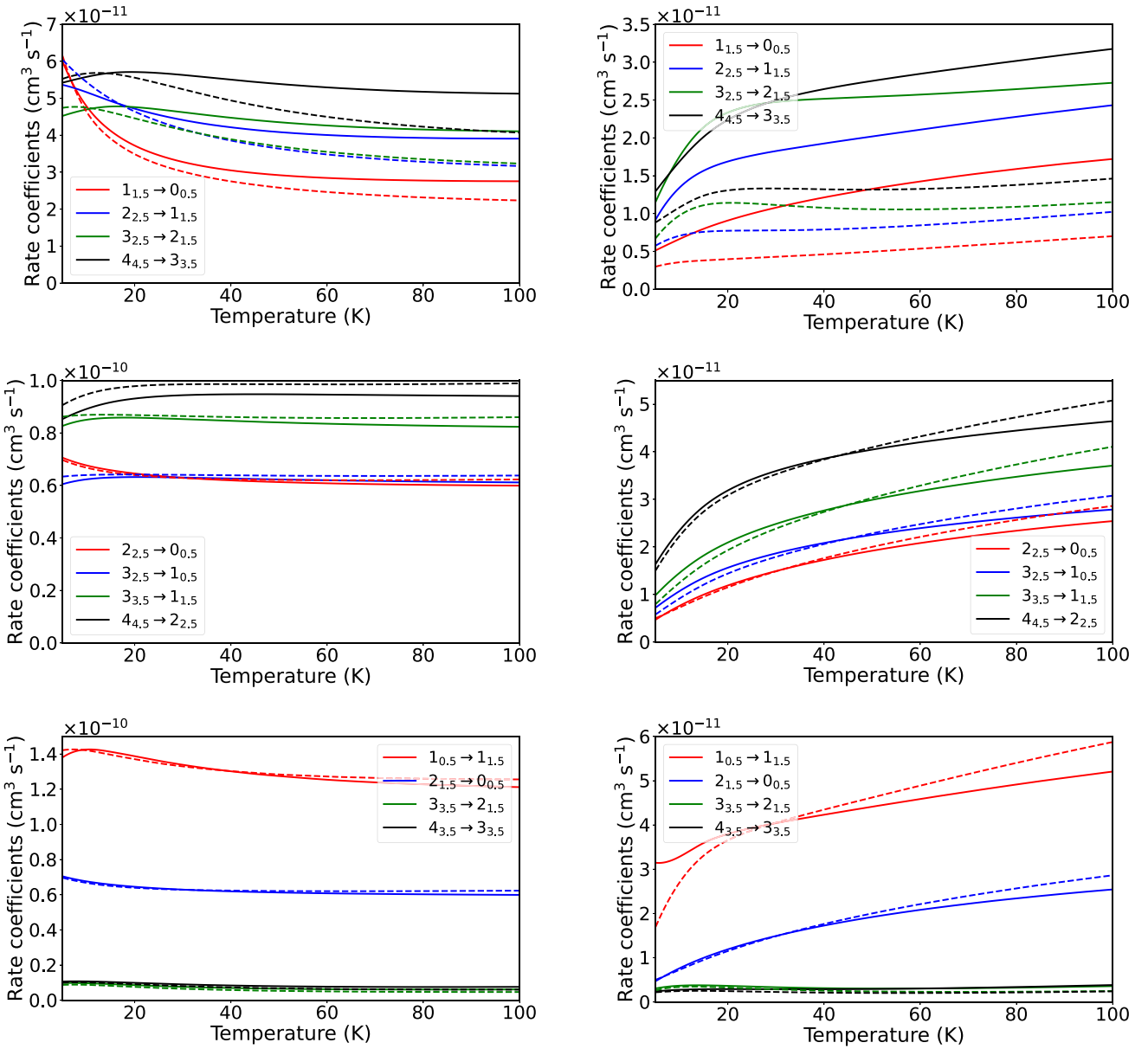


Figure 6. Temperature dependence of fine-structure resolved rate coefficients for C_2H (solid lines) and C_2D (dashed lines) in collision with *ortho*- H_2 (left panel) and *para*- H_2 (right panel). Comparisons are done for $\Delta n_1 = \Delta j_1 = 1$ (upper), $\Delta n_1 = \Delta j_1 = 2$ (middle), and $\Delta n_1 \neq \Delta j_1$ (lower) transitions.

of transitions are very similar, these slight differences can mostly come from the spectroscopic structure of the two targets since their rotational constant are quite different, where $B_{C_2H} = 1.457 \text{ cm}^{-1}$ and $B_{C_2D} = 1.203 \text{ cm}^{-1}$ (Gottlieb et al. 1983; Vrtilek et al. 1985).

4 EXCITATION OF C_2D IN THE ISM

Once hyperfine resolved rate coefficients are computed, it is possible to illustrate the impact of the new set of collisional data on radiative transfer modelling. Such modelling has already been done for the C_2H – H_2 collisional system (Dagdigan 2018b) and will not be discussed here. The following discussion will focus on the new data of the C_2D – H_2 collisional system. This was carried out using the RADEX code (Van der Tak et al. 2007) with the escape probability approximation. Calculations were performed in order to model typical cold environments where C_2D is detected, such as TMC-1 (Turner 2001)

or L1527 (Yoshida et al. 2019). The kinetic temperature T_{kin} was set to 10 K, a linewidth of 0.5 km s^{-1} , and a typical column density of $1 \times 10^{13} \text{ cm}^{-2}$. A background temperature T_{bg} was assumed to be 2.73 K, representing the cosmic microwave background. Einstein coefficients were taken from the Cologne Database for Molecular Spectroscopy (Endres et al. 2016). Another calculation has been done at $T_{\text{kin}} = 50 \text{ K}$ to model warmer environments such as Monoceros R2 (Treviño-Morales et al. 2014), with a typical linewidth of 1 km s^{-1} .

Fig. 7 shows the dependence of excitation temperatures upon the density of H_2 for several hyperfine transitions of the C_2D $n_1 = 1-0$ rotational line for kinetic temperature (T_{kin}) of 10 K and $n_1 = 2-1$ for $T_{\text{kin}} = 50 \text{ K}$. The range of excitation temperature varies from $T_{\text{ex}} = T_{\text{bg}}$ at very low densities where radiative processes are dominant, to $T_{\text{ex}} = T_{\text{kin}}$ at high densities, where the LTE is reached due to the domination of collisional processes.

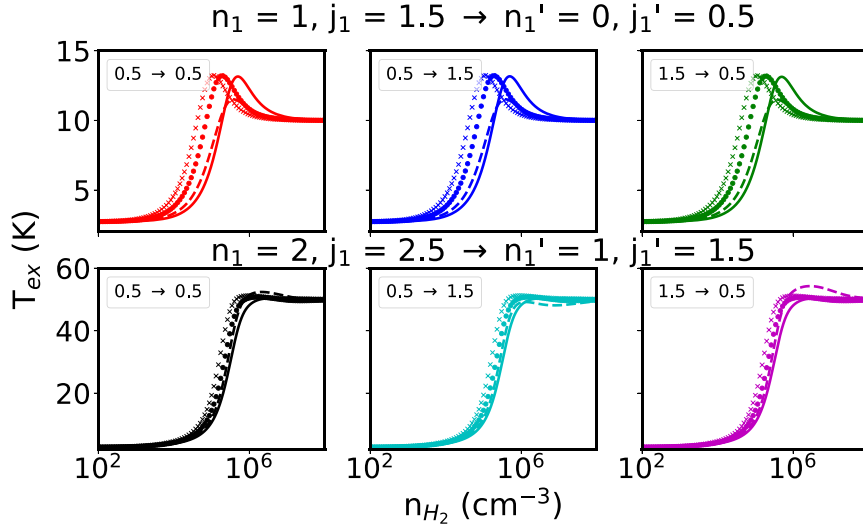


Figure 7. Excitation temperatures as a function of the density of H₂ at $T_{\text{kin}} = 10$ K (upper panels) and 50 K (lower panels) for several hyperfine radiative transitions of C₂D. Numbers in legend represent $F \rightarrow F'$ quantum numbers. Dashed lines are related to the set of data from Dumouchel et al. (2017), solid lines the set of data of the present work with 100 per cent of *para*-H₂ density, dotted lines with 25 per cent of *ortho*-H₂ and crossed lines with 75 per cent of *ortho*-H₂.

Comparisons were carried out with the set of data for C₂D–*para*-H₂ from Dumouchel et al. (2017). Also, the impact of the new *ortho*-H₂ collisions will be assessed with different *ortho*-to-*para*-H₂ ratio (OPR) taken for the radiative transfer calculations. For $T_{\text{kin}} = 10$ K, one can see that for 100 per cent of *para*-H₂, excitation temperatures coincide with the kinetic temperature at $n_{\text{H}_2} \sim 2 \times 10^7$ cm⁻³, showing that a very dense gas is needed to thermalize, whereas modelling obtained using Dumouchel et al. (2017) reaches LTE conditions at $n_{\text{H}_2} \sim 8 \times 10^6$ cm⁻³. This is not surprising since most of rate coefficients for C₂D–*para*-H₂ of Dumouchel et al. (2017) are larger by up to a factor of 2, making collisions more efficient than the set of data provided in this work. However, most of the differences in this modelling are not more than 20 per cent. The increasing of the OPR to 25 per cent and 75 per cent involves the contribution of C₂D–*ortho*-H₂ rate coefficients. It has an impact on the critical density because of the differences between *ortho*- and *para*-H₂ collisions. In addition, excitation temperatures of the presented transitions at $T_{\text{kin}} = 50$ K are less sensitive to *ortho*-H₂ collisions. For most of the models, LTE is reached around 10^6 cm⁻³. That can also be related to the order of magnitude of the rate coefficients, having a strongly different behaviour at 10 K between *ortho*- and *para*-H₂ collisions than at higher temperatures (see Fig. 3) and be less sensitive to the modelling.

It is interesting to reinterpret C₂D observations made on L1527 by Yoshida et al. (2019) and to derive the C₂D column density with our new set of rate coefficients. We determined the column density range of C₂D by computing integrated intensity of different detected lines that best reproduce these observations (see Table 1), minimizing the following χ^2 parameter

$$\chi^2 = \sum_{i=1}^N \left(\frac{F_i^{\text{obs}} - F_i^{\text{calc}}}{\sigma_i} \right)^2, \quad (9)$$

where N denotes the number of observed lines, F_i^{obs} and F_i^{calc} are the integrated intensities observed and calculated respectively, and σ_i is the uncertainty of the i^{th} observation. We varied the column density in the range $[10^{12} - 10^{14}]$ cm⁻² and the H₂ density $[5 \times 10^5 - 3 \times 10^6]$ cm⁻³ for two fixed kinetic temperatures of 10 K and 15 K.

Table 1. Line parameters for C₂D observations done by Yoshida et al. (2019).

Frequency (GHz)	Transition ($n_1, j_1, F \rightarrow n_1', j_1', F'$)	$\int T_{\text{mb}} dv$ (K km s ⁻¹)
72.101715	(1,1.5,1.5) → (0,0.5,1.5)	0.147(16) ^a
72.107700	(1,1.5,2.5) → (0,0.5,1.5)	0.395(16)
72.109114	(1,1.5,0.5) → (0,0.5,0.5)	0.117(14)
72.112399	(1,1.5,1.5) → (0,0.5,0.5)	0.144(15)
72.187704	(1,0.5,1.5) → (0,0.5,1.5)	0.165(20)
72.189505	(1,0.5,0.5) → (0,0.5,1.5)	0.12(3)
72.198388	(1,0.5,1.5) → (0,0.5,0.5)	0.065(16)

Note. ^aParenthesis represent the errors of last significant digits.

Fig. 8 shows the dependence of the χ^2 parameter upon the H₂ density and the range of derived C₂D column densities for the best reproduced observations. One can see that for both kinetic temperatures, this procedure was not able to constrain the H₂ density within the proposed grid. For $T_{\text{kin}} = 10$ K, the column density is determined as $N = (3.2 - 4.9) \times 10^{13}$ cm⁻² within a confidence level of 99 per cent, where observations derived a value of $N = (4.7 \pm 0.3) \times 10^{13}$ cm⁻². For $T_{\text{kin}} = 15$ K, the column density is found to be $N = (3.6 - 5.8) \times 10^{13}$ cm⁻² compared with observations where $N = (5.6 \pm 1.1) \times 10^{13}$ cm⁻². These calculations agree with the literature within a factor ~ 1.5 which is relatively consistent regarding the used methods and uncertainties involved. The column densities derived from observations were carried out in the LTE conditions, finding that lines are optically thin so no corrections need to be applied on brightness temperatures and used a least-squares fitting method. In our calculations, the computed opacities are never greater than 0.1 for all lines and the two kinetic temperatures. However, it should be noted that the density influences excitation temperatures. The considered lines reproduced observations for excitation temperatures varying from ~ 11 to 13 K and from ~ 16 to 26 K for $T_{\text{kin}} = 10$ K and $T_{\text{kin}} = 15$ K respectively. This corresponds to a regime where lines are in a slight suprathermal effect and close to LTE conditions. Since the excitation temperatures do not match

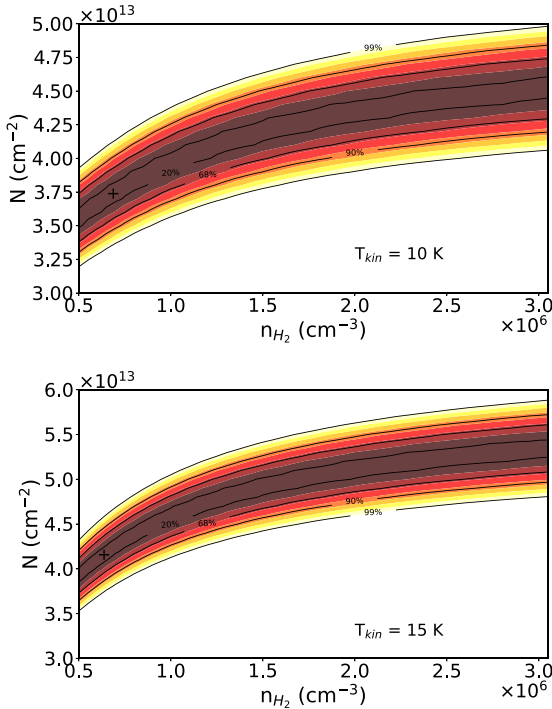


Figure 8. Dependence of the χ^2 parameter with the column density and the H_2 density for kinetic temperatures at 10 K (upper panel) and 15 K (lower panel). Values are shown for 20 percent, 68 percent, 90 percent, and 99 percent levels of confidence representing $\chi_{\min}^2 + (0.45, 2.3, 4.61, 9.21)$; Lampton, Margon & Bowyer 1976; Schöier et al. 2002). The crossed dot represents the minimum of the χ^2 .

with the kinetic temperature, one can see that the derived ranges of column densities tends to decrease the observed values. Our best solutions where the χ_{\min}^2 is reached correspond to $N = 4.1 \times 10^{13} \text{ cm}^{-2}$, $n_{\text{H}_2} = 6 \times 10^5 \text{ cm}^{-3}$ and $T_{\text{ex}} \sim 24 \text{ K}$ for all hyperfine lines for $T_{\text{kin}} = 15 \text{ K}$. For the case where $T_{\text{kin}} = 10 \text{ K}$, χ_{\min}^2 is reached when $N = 3.7 \times 10^{13} \text{ cm}^{-2}$, $n_{\text{H}_2} = 6.5 \times 10^5 \text{ cm}^{-3}$, and $T_{\text{ex}} \sim 13 \text{ K}$ for the multiplet. This would mean that the population of these states under LTE conditions are underestimated compared to non-LTE modelling. In our case, we increase the population of the lower levels of these lines by ~ 14 per cent and ~ 20 per cent at $T_{\text{kin}} = 10 \text{ K}$ and $T_{\text{kin}} = 15 \text{ K}$, respectively.

5 CONCLUSION

We computed hyperfine resolved rate coefficients for C_2H and C_2D in collision with both *ortho*- and *para*- H_2 . These data take into account the first 38 C_2H hyperfine levels and the first 55 C_2D hyperfine levels up to 100 K. We also extended the range of temperature for fine-structure $\text{C}_2\text{H}-\text{H}_2$ collisions up to 500 K for levels up to $n_1 = 20$. We also computed $\text{C}_2\text{D}-\text{H}_2$ fine-structure resolved rate coefficients for levels up to $n_1 = 15$ and for temperatures up to 200 K. These data were computed using the 4D PES of Dagdigian (2018a) and the recoupling method (Alexander & Dagdigian 1985; Offer et al. 1993). $\text{C}_2\text{D}-\text{ortho}-\text{H}_2$ and $\text{C}_2\text{D}-\text{para}-\text{H}_2$ rate coefficients show very different behaviours, where differences are observed up to a factor of 10. This is a standard observation for neutral systems, showing the importance of taking into account the internal structure of H_2 in scattering calculations. We observed more specifically that fine-structure conserving transitions are larger than fine-structure

changing ones for C_2D collisions and display even larger rate coefficients for the $\Delta n_1 = \Delta j_1 = \Delta F = 2$ propensity rule.

With isotopic substitution C_2H and C_2D rate coefficients can differ up to factor of 2 for $\Delta n_1 = \Delta j_1 = 1$ transitions, especially when collisions occur with *para*- H_2 . For $\Delta n_1 = \Delta j_1 = 2$ transitions, both isotopologues with *ortho*- and *para*- H_2 are the same order of magnitude. Such results reflect the shift of the centre of mass between the two isotopologues in the PES, their energetic structure and the larger anisotropies of the PES for the *ortho*- H_2 collider.

This new set of data has been compared with the previous work done by Dumouchel et al. (2017), where they used a transformed 2D PES for the $\text{C}_2\text{D}-\text{H}_2$ system (i.e. neglecting the internal structure of H_2). It has been shown that the inclusion of $j_2 = 0, 2$ in the rotational basis for scattering calculations lead differences up to a factor of 2.

We carried out a radiative transfer modelling to illustrate the impact of the new set of $\text{C}_2\text{D}-\text{H}_2$ rate coefficients. Differences in excitation temperatures are moderate between the new set of data and the one obtained by Dumouchel et al. (2017) compared to the usual uncertainties involved in astrophysical applications when only *para*- H_2 collisions occur. However, larger differences are observed when collisions with *ortho*- H_2 take place. We computed and reinterpreted the column density of C_2D under non-LTE conditions with the literature in the case of the low-mass star-forming region L1527 (Yoshida et al. 2019). The agreement with observations was found to be within a factor ~ 1.5 , which can be considered good regarding the uncertainties due to, on one hand, the methods used for calculations of the PES and rate coefficients, assumptions made by non-LTE modelling, and on the other hand uncertainties of the measurements and the methods used to compute column densities under the LTE assumption. Especially, LTE modelling are underestimating the population of the lower levels of a given transition compared to calculations done under non-LTE conditions.

These data are expected to be used for the interpretation of astronomical observations in order to determine physical conditions in regions where *ortho*- H_2 is significantly populated.

ACKNOWLEDGEMENTS

We acknowledge financial support from the European Research Council (Consolidator grant COLLEXISM, grant agreement no. 811363). We wish to acknowledge the support from the CEA/GENCI (Grand Equipement National de Calcul Intensif) for awarding us access to the TGCC (Très Grand Centre de Calcul) Joliot Curie/IRENE supercomputer within the A0110413001 project.

DATA AVAILABILITY

Fine and hyperfine structure resolved rate coefficients for $\text{C}_2\text{H}-\text{H}_2$ and $\text{C}_2\text{D}-\text{H}_2$ will be available on the following databases: EMAA (<https://dx.doi.org/10.17178/EMAA>), LAMDA (Van der Tak et al. 2020), and BASECOL (Dubernet et al. 2012).

REFERENCES

- Alexander M. H., 1982, *J. Chem. Phys.*, 76, 3637
- Alexander M. H., Dagdigian P. J., 1985, *J. Chem. Phys.*, 83, 2191
- Alexander M. H., Dagdigian P. J., Werner H. J., Klos J., Desrousseaux B., Raffy G., Lique F., 2023, *Comput. Phys. Commun.*, 289, 108761
- Beuther H., Semenov D., Henning Th., Linz H., 2008, *ApJ*, 675, 33
- Bogey M., Demuynck C., Destombes J. L., 1985, *A&A*, 144, 15
- Pop C. T., Lique F., Faure A., Quintas-Sánchez E. L., Dawes R., 2021, *MNRAS*, 501, 1911

- Combes F., Encrenaz P. J., Gerin M., Bogey M., Demuynck C., Destombes J. L., 1985, *A&A*, 147, 25
- Cuadrado S., Goicoechea J. R., Pilleri P., Cernicharo J., Fuente A., Joblin C., 2015, *A&A*, 575, A82
- Dagdigian P. J., 2018a, *J. Chem. Phys.*, 148, 024304
- Dagdigian P. J., 2018b, *MNRAS*, 479, 3227
- Dagdigian P. J., 2019, *MNRAS*, 487, 3427
- Desrousseaux B., Quintas-Sánchez E. L., Dawes R., Marinakis S., Lique F., 2021, *J. Chem. Phys.*, 154, 034304
- Dubernet M. L. et al., 2012, *A&A*, 553, 50
- Dumouchel F., Lique F., Spiediedel A., Feautrier N., 2017, *MNRAS*, 471, 1849
- Dunning T. H., 1989, *J. Chem. Phys.*, 90, 1007
- Dutrey A., Guilloteau S., Guélin M., 1997, *A&A*, 317, L55
- Endres C. P., Schlemmer S., Schilke P., Stutzki J., Müller H. S. P., 2016, *J. Mol. Spectrosc.*, 327, 95
- Godard Palluet A., Lique F., 2023, *J. Chem. Phys.*, 158, 044303
- Gottlieb C. A., Gottlieb E. W., Thaddeus P., 1983, *ApJ*, 264, 740
- Kalugina Y., Klos J., Lique F., 2013, *J. Chem. Phys.*, 139, 074301
- Knowles P. J., Hampel C., Werner H. J., 1993, *J. Chem. Phys.*, 99, 5219
- Lampton M., Margon B., Bowyer S., 1976, *ApJ*, 208, 177
- Linsky J. L. et al., 2006, *ApJ*, 647, 1106
- Nagy Z., Ossenkopf V., Van der Tak F. F. S., Faure A., Makai Z., Bergin E. A., 2015, *A&A*, 578, A124
- Najar F., Ben Abdallah D., Spiediedel A., Dayou F., Lique F., Feautrier N., 2014, *Chem. Phys. Lett.*, 614, 251
- Offer A. R., van Hemert M. C., van Dishoeck E. W., 1993, *J. Chem. Phys.*, 100, 362
- Padovani M., Walmsley C. M., Tafalla M., Galli D., Müller H. S. P., 2009, *A&A*, 505, 1199
- Parise B., Leurini S., Schlike P., Roueff E., Thorwirth S., Lis D. C., 2009, *A&A*, 508, 737
- Roueff E., Lique F., 2013, *Chem. Rev.*, 113, 8906
- Sakai N., Saruwatari O., Sakai T., Takano S., Yamamoto S., 2010, *A&A*, 512, A31
- Sastry K. V. L. N., Helminger P., Charo A., Herbst E., De Lucia F. C., 1981, *ApJ*, 251, 119
- Schöier F. L., Jørgensen J. K., van Dishoeck E. F., Blake G. A., 2002, *A&A*, 390, 1001
- Spiediedel A., Feautrier N., Najar F., Ben Abdallah D., Dayou F., Senent M. L., Lique F., 2012, *MNRAS*, 421, 1891
- Teyssier D., Fossé D., Gerin M., Pety J., Abergel A., Roueff E., 2003, *A&A*, 417, 135
- Treviño-Morales S. P. et al., 2014, *A&A*, 569, A19
- Tucker K. D., Kutner M. L., Thaddeus P., 1974, *ApJ*, 193, 115
- Turner B. E., 2001, *ApJ*, 136, 579
- Van der Tak F. F. S., Black J. H., Schöier F. L., Jansen D. J., van Dishoeck E. F., 2007, *MNRAS*, 468, 627
- Van der Tak F. F. S., Lique F., Faure A., Black J. H., van Dishoeck E. F., 2020, *Atoms*, 8, 15
- Vrtilek J. M., Gottlieb C. A., Langer W. D., Thaddeus P., Wilson R. W., 1985, *A&A*, 296, 35
- Werner H. J., Knowles P. J., et al. F. R. M., 2020, *J. Chem. Phys.*, 152, 144107
- Wootton A., Bozyan E. P., Garrett D. B., Loren R. B., Snell R. L., 1980, *ApJ*, 239, 844
- Yoshida K., Sakai N., Nishimura Y., Tokumode T., Watanabe Y., Sakai T., Takano S., 2019, *PASJ*, 71, S18
- Ziurys L. M., Saykally R. J., Plambeck R. L., Erickson N. R., 1982, *ApJ*, 254, 94

APPENDIX: DISCUSSION ON THE SCATTERING CONVERGED PARAMETERS

Fine-structure resolved cross-sections for C₂H and C₂D in collision with both *ortho*- and *para*-H₂ were determined through solution of the CC equations. To do so, the rotational basis of the targeted molecule n_{\max} and the total angular momentum J_{tot} are converged for different total energies E_{tot} at different energy steps ΔE . For all collisional systems, the rotational basis of the H₂ collider was chosen to be $j_{2,\max} = 0, 2$ for *para*-H₂ and $j_{2,\max} = 1$ for *ortho*-H₂. The largest parameters are presented in Tables A1–A2. Optimization was done in order to converge cross-sections within 1 percent of accuracy for each parameter. The propagation of the partial waves was done from $R_{\min} = 4.25a_0$ to $R_{\max} = 50a_0$ for C₂H collisions, and from $R_{\min} = 4.25a_0$ to $R_{\max} = 60a_0$ for C₂D collisions. Then, hyperfine calculations were done using the nuclear spin-free S -matrices computed with these parameters.

Table A1. Values of the converged parameters used for scattering calculations for the C₂H–H₂ collisional system. The rotational basis n_{\max} of the targeted molecule, total angular momentum J_{tot} and total energies E_{tot} with energy steps ΔE are presented.

E_{tot} (cm ⁻¹)	C ₂ H– <i>ortho</i> -H ₂			C ₂ H– <i>para</i> -H ₂			
	ΔE (cm ⁻¹)	n_{\max}	J_{tot}	E_{tot} (cm ⁻¹)	ΔE (cm ⁻¹)	n_{\max}	J_{tot}
118.8–168.7	0.1	9	18	0.1–50	0.1	10	18
168.8–218.7	0.1	12	24	50.1–100	0.1	12	24
218.9–318.7	0.1	15	30	100.1–200	0.1	15	27
319.7–618.7	0.1	17	42	200.2–300	0.1	19	39
620.7–818.7	2	20	48	301–500	1	19	39
823.7–1118.7	5	24	57	505–700	5	22	45
1128.7–1618.7	10	27	69	710–1000	10	25	51
1718.7–2118.7	100	27	85	1050–1500	50	28	60
2318.7–3118.7	200	27	100	1600–2000	100	28	81
3618.7	500	27	100	2200–3000	200	28	100
–	–	–	–	3500	500	28	100

Table A2. Values of the converged parameters used for scattering calculations for the C₂D–H₂ collisional system. The rotational basis n_{\max} of the targeted molecule, total angular momentum J_{tot} , and total energies E_{tot} with energy steps ΔE are presented.

E_{tot} (cm ⁻¹)	C ₂ D– <i>ortho</i> -H ₂			E_{tot} (cm ⁻¹)	C ₂ D– <i>para</i> -H ₂		
	ΔE (cm ⁻¹)	n_{\max}	J_{tot}		ΔE (cm ⁻¹)	n_{\max}	J_{tot}
118.8–168.7	0.1	12	18	0.1–50	0.1	11	18
168.8–218.7	0.1	12	24	50.1–100	0.1	13	24
218.9–318.7	0.1	13	30	100.1–200	0.1	16	30
318.9–618.7	0.2	15	45	200.2–500	0.2	20	42
619.2–818.7	0.5	18	51	500.5–700	1	23	48
819.7–1118.7	1	21	57	705–1000	5	28	54
1123.7–1618.7	5	25	66	1010–1500	10	34	60

This paper has been typeset from a $\text{\TeX}/\text{\LaTeX}$ file prepared by the author.

C.4 BASECOL2023 scientific content

BASECOL2023 scientific content

M. L. Dubernet¹, C. Boursier¹, O. Denis-Alpizar³, Y. A. Ba¹, N. Moreau¹, C. M. Zwölf¹, M. A. Amor⁴, D. Babikov⁵, N. Balakrishnan⁶, C. Balança¹, M. Ben Khalifa⁷, A. Bergeat², C. T. Bop⁸, L. Cabrera-González⁹, C. Cárdenas^{10,11}, A. Chefai⁴, P. J. Dagdigan¹², F. Dayou¹, S. Demes⁸, B. Desrousseaux⁸, F. Dumouchel¹³, A. Faure¹⁴, R. C. Forrey¹⁵, J. Franz¹⁶, R. M. García-Vázquez^{2,26}, F. Gianturco¹⁷, A. Godard Palluet⁸, L. González-Sánchez¹⁹, G. C. Groenenboom²⁰, P. Halvick², K. Hammami⁴, F. Khadri⁴, Y. Kalugina⁸, I. Kleiner²¹, J. Kłos^{22,23}, F. Lique⁸, J. Loreau⁷, B. Mandal⁵, B. Mant¹⁷, S. Marinakis¹⁸, D. Ndaw²⁴, P. Pirlot Jankowiak⁸, T. Price¹⁵, E. Quintas-Sánchez²⁷, R. Ramachandran^{13,28}, E. Sahnoun⁴, C. Santander³, P. C. Stancil²⁵, T. Stoecklin², J. Tennyson²⁹, F. Tonolo^{30,31}, R. Urzúa-Leiva³, B. Yang²⁵, E. Yurtsever³², and M. Żóltowski^{8,13}

(Affiliations can be found after the references)

Received 11 October 2023 / Accepted 5 November 2023

ABSTRACT

Context. The global context of making numerous data produced by researchers available requires collecting and organising the data, assigning meaningful metadata, and presenting the data in a meaningful and homogeneous way. The BASECOL database, which collects inelastic rate coefficients for application to the interstellar medium and to circumstellar and cometary atmospheres, meets those requirements.

Aims. We aim to present the scientific content of the BASECOL2023 edition.

Methods. While the previous versions relied on finding rate coefficients in the literature, the current version is populated with published results sent by the producers of data. The paper presents the database, the type of data that can be found, the type of metadata that are used, and the Virtual Atomic and Molecular Data Centre (VAMDC) standards that are used for the metadata. Finally, we present the different datasets species by species.

Results. As the BASECOL database, interconnected with the VAMDC e-infrastructure, uses the VAMDC standards, the collisional data can be extracted with tools using VAMDC standards and can be associated with spectroscopic data extracted from other VAMDC connected databases such as the Cologne database for molecular spectroscopy (CDMS), the jet propulsion laboratory molecular spectroscopy database (JPL), and the high-resolution transmission molecular absorption database (HITRAN).

Key words. standards – astrochemistry – molecular data – molecular processes – astronomical databases: miscellaneous

1. Introduction

The paper presents the scientific content of the BASECOL2023 edition¹. BASECOL provides state-to-state inelastic atomic and molecular collisional rate coefficients with energy transfer in both the target and the projectile, in a temperature range suitable for radiative transfer modelling in the interstellar medium (ISM) or circumstellar atmospheres and cometary atmospheres, where local thermodynamic equilibrium (LTE) conditions are not fulfilled. In addition, the BASECOL format provides effective and thermalised rate coefficients, as stated below (Sect. 2.4). BASECOL provides a wide overview of the field of rate coefficient calculations for the above applications, and it follows the VAMDC standards (Albert et al. 2020; Dubernet et al. 2016). BASECOL is therefore accessible from VAMDC applications such as the VAMDC portal², the species database service³, and other user tools that use VAMDC standards. One of the tools is the SPECTCOL tool⁴, the latest edition of which will be published in 2024.

¹ <https://basecol.vamdc.org>

² <https://portal.vamdc.eu>

³ <https://species.vamdc.eu>

⁴ <https://vamdc.org/activities/research/software/spectcol/>

Other databases, such as the Leiden atomic and molecular database (LAMDA; van der Tak et al. 2020)⁵ and the excitation of molecules and atoms for astrophysics database (EMAA)⁶, provide ready-to-use ASCII data files that combine selected rate coefficients and spectroscopic datasets. EMAA in particular allows the user to select the projectile(s) of interest, and a digital object identifier (DOI) is provided as a persistent identifier for each dataset.

Contents of the BASECOL2012 edition (Dubernet et al. 2013) were created by the scientific maintainer using rate coefficients mostly extracted from the literature. It was recently underlined by Dubernet et al. (2023) that this method is no longer sustainable. Therefore, the producers of rate coefficients are now invited to send their data formatted in a requested template. The current scientific content of the BASECOL database, called BASECOL2023, corresponds to the efforts of the various co-authors in providing their data with that template; in doing so, they contribute to the long-term preservation of the data and to the data indexation with relevant and community standard metadata for atomic and molecular data, that is VAMDC

⁵ <https://home.strw.leidenuniv.nl/~moldata/>

⁶ <https://emaa.osug.fr>

standards (Albert et al. 2020; Dubernet et al. 2016, 2010)⁷. From surveys of the literature, we know that there are still missing rate coefficient datasets, and producers are welcome to contact the next BASECOL scientific leader, Dr Otoniel Denis-Alpizar, in order to include their data.

We would like to emphasise that BASECOL2023 provides an environment where the numerical data are not manipulated prior to their ingestion in the database, and if inconsistencies are noticed, the producers of the data are invited to provide new numerical data. In addition, prior to public access, the producers of the data privately visualise the display of their numerical and text data, and can ask that the BASECOL maintainer changes the text data. Finally, the references to the main papers for both the rate coefficients and the potential energy surfaces are provided, and the BASECOL home page emphasises that users must cite the original papers. The BASECOL technical design has been entirely updated: in particular, a versioning feature that allows accessibility to all versions has been added, and the dataset ingestion procedure has been reviewed in order to directly include the VAMDC metadata and to check the consistency of the datasets. A full description of the new BASECOL technical infrastructure is provided in Ba et al. (2020). From a scientific point of view, BASECOL2023 has been intensively updated in the past three years, and this paper provides the current status. BASECOL2023 contains a total of 491 collisional datasets of which 358 datasets correspond to the last version of the recommended datasets. It includes information on the collisional inelastic de-excitation of 103 atomic and molecular, neutral, and ionic species colliding mainly with projectiles such as H, He, H₂, and H₂O.

2. Description of the datasets found in BASECOL

2.1. Composition and display of datasets

The BASECOL data are organised and displayed in a collisional dataset. A dataset corresponds to a collision between two colliding species: the target and the projectile species. As the product species are formally the same as the colliding species (target and the projectile), BASECOL can handle elastic, inelastic, and possibly rearrangement processes if the product species are the same as the colliding species.

The species can either be neutral or charged and atomic or molecular in nature. It is described by its usual chemical formula and is internally uniquely identified by its InChIkey and InChI number⁸, possibly supplemented by the nuclear spin symmetry (ortho, para, meta, etc.). The species database website⁹ makes it possible to find the VAMDC species including the InChIkey and InChI number expressions.

Once the colliding species are identified, a dataset corresponds to three numerical tables: one table containing the process rate coefficients of the state-to-state energy level transitions of the two colliding species (in cm³ s⁻¹) as a function of temperature (in kelvin), and one table per species containing the energy levels whose labels characterise the transitions in the rate coefficient table (see Sect. 2.4 for the specific issues of labelling the energy levels transitions for effective and thermalised rate coefficients).

⁷ <https://vamdc.org/activities/research/documents/standards/>

⁸ <https://iupac.org/who-we-are/divisions/division-details/inchi/>

⁹ <https://species.vamdc.eu>

The unique dataset is associated with its ‘main’ publication, that is, the one in which it was published¹⁰, and it is complemented by a short description of the methodologies used in the potential energy surface (PES) and the dynamical calculations wherever relevant. The PES’s references are systematically cited, as well as references linked to the energy levels (for the latter it depends on the availability of the information provided by the data producer). Additional references – such as references linked to methodologies or to a historical review of the collisional system – that might be associated with the dataset are also cited. Additional information about precision or review of data is sometimes included. In particular, datasets are labelled as ‘outdated’ whenever this is the case, or are labelled ‘not recommended’ when the datasets have errors either mentioned in a published erratum or mentioned privately by the authors.

As part of the newly designed BASECOL structure (Ba et al. 2020), the versioning of the dataset has been introduced. A new version is created when the rate coefficient table and/or the associated energy table are changed, and BASECOL provides access to the previous versions of the datasets in order to guarantee traceability of data and reproducibility of usage. We comment on the modifications between versions.

2.2. Discussion on BASECOL recommendation

The BASECOL interfaces, which display the list of available datasets corresponding to a query, indicate the status, ‘Recommended: yes or no’. ‘Recommended: no’ corresponds both to outdated datasets and to datasets with errors (see previous paragraph). It should be noted that VAMDC accesses the last version of the recommended datasets only to avoid confusing users. The current choice of BASECOL2023 is to provide access to ‘recommended sets’ only, but this paradigm could be changed upon a user’s request.

A priori, all datasets are recommended when they are first included in the BASECOL database. The outdated datasets are ‘non-recommended’ for the following reasons: 1) new calculations are performed with a clearly more sophisticated potential energy surface, 2) new calculations are performed with more sophisticated scattering methodologies (e.g. the basis set is larger, the scattering method has less approximation). Nevertheless, some datasets are still recommended even if they do not fit the above criteria, as they offer alternative realistic datasets that can be used to test the influence of rate coefficients in radiative transfer studies.

The detailed description of the datasets given in the following paragraphs explains the choices.

2.3. BASECOL2023 molecular quantum number description

The description of BASECOL2023 quantum numbers follows the VAMDC standards¹¹. Within VAMDC standards the molecules are classified by fourteen so-called cases¹². Each case corresponds to a specific type of molecule: diatomic, linear triatomic, non-linear triatomic, linear polyatomic, symmetric top, spherical, and asymmetric molecules, combined with its electronic state separated into closed-shell and open-shell states. Diatomic open-shell molecules can be described in two possible

¹⁰ The main publication is marked in red on the BASECOL website.

¹¹ <https://standards.vamdc.eu/#data-model>

¹² <https://amdis.iaea.org/cbc/>

cases: *hunda* (Hund's a coupling) and *hundb* (Hund's b coupling). Table A.1 indicates the BASECOL2023 molecules and their cases.

Currently, three molecules have issues with the VAMDC cases because the energy tables provided by the authors cannot be described with the current VAMDC cases. The *hundb* case has been assigned to the C₄ (X³Σ_g⁻) energy table (ID = 127) because the SpinComponentLabel label does not exist in the linear polyatomic open shell (lpos) case. The *hunda* has been assigned to the C₆H (X²Π) energy tables (ID = 154, 155) because the authors used (J,Ω) quantum numbers and the lpos case does not include Ω. This is a temporary solution while the VAMDC standards evolve. The CH₃OH molecule is described with a spherical top closed shell (stcs) case, in which the label rovibSym is used for the symmetry of the torsional function (see Sect. 9.9 for more information).

2.4. Rate coefficients

The collisional rate coefficients provided by BASECOL are state-to-state rate coefficients, effective rate coefficients, and thermalised rate coefficients, each of which is defined below. In most cases, state-to-state (de-)excitation rate coefficients ($R(T)$) are obtained at a given temperature from Boltzmann thermal averages of the calculated state-to-state inelastic cross-sections obtained on a grid of kinetic energies E :

$$R(\alpha \rightarrow \alpha'; \beta \rightarrow \beta')(T) = \left(\frac{8}{\pi\mu}\right)^{1/2} \frac{1}{(k_B T)^{3/2}} \int_0^\infty \sigma_{\alpha \rightarrow \alpha'; \beta \rightarrow \beta'}(E) E e^{-E/k_B T} dE, \quad (1)$$

where k_B is the Boltzmann constant, μ is the reduced mass of the colliding system, and (α, β) , (α', β') represent the initial and final levels of the target (α) and projectile (β). Therefore, a typical BASECOL rate coefficient table is composed of the following items: Cols. 1 and 2 contain the initial α and final α' levels of the target, Cols. 3 and 4 contain the initial β and final β' levels of the projectile, the subsequent columns give the state-to-state rate coefficients (Eq. (1)) at different temperatures (in kelvin).

These state-to-state collisional rate coefficients follow the principle of detailed balance, and reverse rate coefficients $R(\alpha' \rightarrow \alpha; \beta' \rightarrow \beta)(T)$ can be obtained from forward rate coefficients by the usual formula:

$$g_{\alpha'} g_{\beta'} e^{-\frac{E_{\text{int}}(\alpha')}{k_B T}} e^{-\frac{E_{\text{int}}(\beta')}{k_B T}} R(\alpha' \rightarrow \alpha; \beta' \rightarrow \beta) = g_\alpha g_\beta e^{-\frac{E_{\text{int}}(\alpha)}{k_B T}} e^{-\frac{E_{\text{int}}(\beta)}{k_B T}} R(\alpha \rightarrow \alpha'; \beta \rightarrow \beta'), \quad (2)$$

where g_α and g_β are the statistical weights related to the ro-vibrational levels of the target and projectile, respectively, and the different E_{int} are the ro-vibrational energies of the species. When the projectile is an electron or an atom whose internal energy does not change during the collision, the state-to-state (de-)excitation rate coefficient is Eq. (1) with $\beta = \beta' = 1$.

When the projectile is a molecule, such as H₂ or H₂O, transitions are possible in the projectile molecule. Nevertheless, most published calculations with H₂ do not allow excitation of H₂, thereby fixing H₂ in its lowest para (-p) ($j = 0$) and ortho (-o) ($j = 1$) states. Within this approximation, the state-to-state (de-)excitation rate coefficient is Eq. (1) with $\beta = \beta' = 1$, similarly to atoms.

BASECOL allows the inclusion of the so-called effective rate coefficients $\hat{R}_\beta(\alpha \rightarrow \alpha')$ that are given by the sum of the state-to-state rate coefficients (Eq. (1)) over final projectile states, β' for

a given initial β :

$$\hat{R}_\beta(\alpha \rightarrow \alpha')(T) = \sum_{\beta'} R(\alpha \rightarrow \alpha'; \beta \rightarrow \beta')(T). \quad (3)$$

In BASECOL the effective rate coefficients are identified as 'effective' in the title of the dataset, and the table's entry for the projectile initial level indicates the β level of Eq. (3), while the projectile's final level is meaningless and is currently set equal to the initial level for convenience. It should be mentioned that these effective rate coefficients do not follow the principle of detailed balance, so both excitation and de-excitation rate coefficients should be calculated explicitly.

Finally, thermalised de-excitation rate coefficients can be obtained by averaging over the initial ro-vibrational levels of the projectile:

$$\bar{R}(\alpha \rightarrow \alpha')(T) = \sum_{\beta} \rho(\beta) \hat{R}_\beta(\alpha \rightarrow \alpha')(T), \quad (4)$$

with $\rho(\beta) = g_\beta e^{-\frac{E_{\text{int}}(\beta)}{k_B T}} / Z(T)$, where $Z(T)$ is the partition function obtained as a sum over the β states. Such rate coefficients follow the principle of detailed balance automatically if an accurate quantum scattering methodology – such as the close-coupling (CC) or coupled states (CS) method – is employed. If the approximate scattering methodology is employed (such as classical, semi-classical, or mixed quantum/classical), the values of computed rate coefficients for excitation and quenching may need to be 'symmetrised' first to ensure that they satisfy the principle of detailed balance. The examples of such a symmetrisation procedure can be found in Boursier et al. (2020) and Mandal & Babikov (2023a).

For projectiles with ortho and para species such as H₂ or H₂O, the datasets can be calculated considering the two nuclear symmetries as independent. For example, the quasi-classical calculations (QCT) calculations by Faure et al. (2007b) directly calculate the rotational de-excitation rate coefficients of H₂O by thermalised ortho and para H₂ considered as separate species (labelled o/p-t-H₂ in the tables of the Appendix). Another example is the quantum de-excitation of HCN by a thermalised para-H₂O dataset (Dubernet & Quintas-Sánchez 2019; labelled p-t-H₂O in the tables of the Appendix).

In some cases, the calculations are provided for a thermalisation over both the para- and ortho-projectile species. An example is the ro-vibrational de-excitation (Faure & Josselin 2008) of o/p-H₂O with thermalised H₂ over the two nuclear species (labelled t-H₂ in the tables of the Appendix) and the calculations for the de-excitation of o/p-H₂O by H₂O (Boursier et al. 2020; Mandal & Babikov 2023a) thermalised over both para- and ortho-H₂O projectiles (labelled t-H₂O in the tables of the Appendix). The user is referred to the papers to see how the thermalisation was performed.

In BASECOL, the thermalised rate coefficients are identified as thermalised in the title of the dataset, and the entries for the projectile's initial and final levels are meaningless. They are always denoted as the $\beta = \beta' = 1$ level for convenience.

2.5. Fitting information of the datasets

BASECOL2012 had fitting features that made it possible to download and to visualise fitting functions for rate coefficient datasets; those fits were either provided in the authors publications (mainly for electron impact collisions), or were mostly calculated by one of the former BASECOL maintainers (F. Daniel)

for collisions with the heavy projectiles. The list of fitted datasets is indicated in Table A.1 of our previous publication (Dubernet et al. 2013).

No additional set has been fitted since 2013 as the astrophysical users prefer to use their own fitting functions, but BASECOL2023 has been upgraded with a new graphical display of fits that allows us to visualise the quality of the fits.

The electron impact rate coefficients for D₂O, H₂O, and HDO datasets (Faure et al. 2004); HCN, HNC, DCN, and DNC datasets (Faure et al. 2007b); SiO (Varambhia et al. 2009); the HC₃N-p-H₂ dataset (Wernli et al. 2007a,b); and the o-H₂CO-o/p-H₂ datasets (Troscompt et al. 2009) use the following fitting equation introduced by Balakrishnan et al. (1999a):

$$\log(R(T)) = \sum_{k=0}^4 a_k \left[\frac{1}{T^{(1/6)}} \right]^k, \quad (5)$$

where $R(T)$ is the rate coefficient in cm³ s⁻¹, T the temperature in kelvin, and a_k the fitted coefficients.

The electron impact rate coefficients for the CO⁺, HCO⁺, NO⁺, o/p-H₂⁺ (Faure & Tennyson 2001), o/p-H₃⁺, and o/p-H₃O⁺ datasets (Faure & Tennyson 2003) used the following fitting function with $T_0 = 300$ K:

$$\log(R(T)) = a \left[\frac{T}{T_0} \right]^b \exp(-c/T), \quad (6)$$

where $R(T)$ is the rate coefficient in cm³ s⁻¹, T the temperature in kelvin, and a , b , c the fitted coefficients. The electron-H₂⁺ rate coefficients dataset of Sarpal & Tennyson (1993) is fitted with the latter formula where $T_0 = 1$ K (in BASECOL we used $\exp(c/T)$, so the coefficient c is negative for that particular dataset). The dataset (Lim et al. 1999) for the collision of CH⁺ with electrons is fitted with

$$\log(R(T)) = a [T]^{[b+c \ln(T)]}, \quad (7)$$

where $R(T)$ is the rate coefficient in cm³ s⁻¹, T is the temperature in kelvin, and a , b , c are the fitted coefficients.

Apart from the above cited datasets, BASECOL2012 datasets for collisions with heavy projectiles have been internally fitted with the so-called common fit equation⁷ (please note that there was a typo in the formula for this equation in Ba et al. (2020), which is corrected below):

$$\log(R(T)) = \sum_{k=1}^{N-1} a_k \left[\log \left(\frac{T}{\epsilon T_0} \right) \right]^{k-1} + a_N \left(\frac{1}{\frac{T}{\epsilon T_0} + \epsilon} - 1 \right), \quad (8)$$

where $R(T)$ is the rate coefficient in cm³ s⁻¹, T is the temperature in kelvin, and ϵ , a_k are the fitted coefficients (in addition $T_0 = 1$ K is formally introduced for homogeneity purposes).

2.6. Search for the datasets

The search feature has evolved since the description of Ba et al. (2020). The ‘collision’ search of Ba et al. (2020) has been renamed ‘browse collision’, and a ‘search collision’ has been added. The latter search requires clicking on the fields in order to perform the selection, as can be seen in Fig. 1. This search collisions interface is extremely useful for rapidly querying the content of the database as one can access all datasets for a single or several target species, or for a single or several projectile species. One can find all datasets related to a given collisional

Fig. 1. Query interface for collisional rate coefficients for HCN-He with hyperfine selection. This interface is accessible from the ‘search collisions’ item in the black band.

process (rotation, vibration, ro-vibration, fine, and hyperfine). One can select a given range of years, the name of an author, or part of the name of an author. The implicit rule of selection between the year, target, target symmetry, collider (i.e. projectile), and collider symmetry (i.e. projectile symmetry) fields is an ‘and’ rule, and the explicit rule for a given field is an ‘or’ rule.

3. Bibliographic database

The 2023 bibliographic database can be independently searched in the search articles section (see Fig. 1). The bibliographic database includes the references attached to the collisional datasets only. The references are classified in five categories: category 1 corresponds to the main publication where the data are published, category 2 corresponds to the references of the potential energy surfaces used to calculate the rate coefficients, category 3 corresponds to references linked to the spectroscopy of the molecules (energy tables), category 4 is used whenever a methodology or a code is mentioned, and category 5 corresponds to the context. This category index selects which references are sent to VAMDC. Currently, we transfer all references up to and including category 3.

Each reference is indexed with keywords that allow us to narrow the search of references in the database, for example with respect to the target or projectile species, the type of data that can be found (cross-sections, rate coefficients, potential energy surfaces), the type of transitions (rotation, fine, hyperfine, etc.), or even the programs used (this can be found via the key term miscellaneous: program). The outputs of the bibliographic database are in BibTeX and in BASECOL internal format.

4. BASECOL policies

When the data producer submits the paper related to the datasets to a journal, he/she should contact the BASECOL scientific leader whose credentials are in the contact section of the

BASECOL website. In return, the data producer receives the instructions and a directory containing examples of the files to be sent. We prefer not to provide the information online as items might change over time, and we stress the importance of following the instructions in order to speed up the procedure. Once the publication is accepted by a journal, the data producer sends the package of information that includes numerical data and text data. The numerical data are composed of the rate coefficients table and the energy table that allows to identify the transitions in the rate coefficients table. To this effect, the producer is invited to follow VAMDC standards for the quantum numbers' designation. The text data are composed of a description of the main features of the methodology used in the calculations and a file containing the references cited in the methodology. The producer includes the relevant publications linked to the dataset in the package. The text data, references, energy table values, and additional metadata are included in the original producers' file, which contains the numerical values of the rate coefficients, and a so-called ingestion file is created. The BASECOL manager uploads this ingestion file to the database through a script that parses the file. The parsing procedure checks the consistency of the numerical data. Many items related to the structure of the ingestion file and to the ingestion procedure are already described in the BASECOL technical paper by Ba et al. (2020). During the process of creating the entries for BASECOL, the scientific maintainer interacts with the producer in order to verify any issues that might be raised in the various data. At the end, the producer verifies the data on a password-protected private website and gives his/her agreement for publication on the public website. From 2021 the BASECOL business model relies on the data producers sending data to the maintainer and following the above described policies. The data producer is informed and agrees that his/her mail credentials are kept so that the person who prepared the initial numerical data can be contacted.

5. Collisions with electrons

Table B.1 provides the collisional systems with electrons as projectiles; no new dataset has been added since BASECOL2012, indeed no authors sent their data in the requested format. BASECOL2023 datasets have been upgraded with VAMDC standards for the description of quantum numbers, and the energy levels unit has been changed to wavenumbers whenever it was necessary. The electron impact rate coefficients are labelled 'recommended' in BASECOL, even if newer datasets can be found in the literature. For more recent information on electron impact collision for astrophysical applications, a review can be found in Tennyson & Faure (2019). In addition, several academic and open science databases, mainly aimed at plasma application, contain rate coefficients for the collisional excitation of atoms and molecules by electrons (see VAMDC; Albert et al. 2020; and the LAMDA; van der Tak et al. 2020¹³; and EMAA¹⁴ databases for astrophysical applications).

6. Atoms and atomic ions with heavy partners (H, He, o/p-H₂)

Table B.2 provides the list of datasets for the excitation of the fine structure of C and C⁺ (sometimes referred to as C I and C II, respectively), of O (OI), of S (S I), and of Si and Si⁺ (Si I and Si II, respectively). We say that an atomic species has

a complete collisional panel when datasets are available for the four projectiles: H, He, o/p-H₂.

The carbon atom C has a complete collisional panel. BASECOL2023 has been updated with a dataset (Bergeat et al. 2018) for the de-excitation of C(³P_{*j*}) by He for temperatures up to 350 K. We consider that this dataset supersedes the dataset by Staemmler & Flower (1991) as the theoretical cross-sections reproduce most of the resonances found in the experimental results well; thus, we assume that the theoretical potential energy surfaces (PES) are accurate enough to provide reliable cross-sections and rate coefficients. BASECOL2012 already included the dataset from Abrahamsson et al. (2007) for C(³P_{*j*}) in collision with H that superseded the non-recommended dataset of Launay & Roueff (1977) and a dataset (Schröder et al. 1991) for C(³P_{*j*}) impacted by o/p-H₂ for temperatures up to 1000 K/1200 K.

The carbon C⁺(²P_{1/2}) ion has an incomplete collisional panel. The dataset C⁺(²P_{1/2})-H comes from Barinovs et al. (2005) for temperatures up to $T = 2000$ K. BASECOL2023 has been updated with two datasets (Kłos et al. 2020a) for the quenching of the spin-orbit transition of C⁺(²P_{1/2}) by o/p-H₂ for temperature up to 500 K; those datasets have been calculated with a newly calculated PES (Kłos et al. 2020a) and with CC calculations using a basis set that includes rotational levels of ortho-H₂ up to $j=15$ or of para-H₂ up to $j = 16$. The dataset with ortho-H₂ corresponds to state-to-state rate coefficients restrained to o-H₂ remaining in its lowest rotational level ($j = 1$), while the dataset for para-H₂ corresponds to thermalised rate coefficients (see Eq. (4)) calculated with state-to-state rate coefficients involving transitions between para-H₂ rotational levels.

The oxygen atom O(³P_{*j*}) has a complete collisional panel. The quenching of the spin-orbit transition of O(³P_{*j*}) by H has been revisited by two groups (Lique et al. 2017; Vieira & Krems 2017), and new calculations for the de-excitation of O(³P_{*j*}) by o/p-H₂ (Lique et al. 2017) and by He (Lique et al. 2017) have been performed. BASECOL2023 has been updated with these five recommended datasets. Therefore, the old datasets for O-H (Abrahamsson et al. 2007; Launay & Roueff 1977) and O-o/p-H₂ (Jaquet et al. 1992) are now obsolete and labelled as non-recommended.

For the quenching of the oxygen atom O(³P_{*j*}) by H, the competing datasets (Lique et al. 2017; Vieira & Krems 2017) calculated the same year, use different potential energy surfaces, but identical spin-coupling terms (Parlant & Yarkony 1999): the calculation of Lique et al. (2017) uses the recent PES from Dagdigian et al. (2016), and the calculations of Vieira & Krems (2017) use the PES from Parlant & Yarkony (1999). Vieira & Krems (2017) mentioned that they corrected some errors made by Abrahamsson et al. (2007), and with the help of machine learning techniques they provide error bars on the rate coefficients.

For the S(³P), Si(³P) atoms and the Si⁺(²P_{1/2}) ion, the collisional panel is incomplete since only one projectile is available: either H or He. The dataset (Barinovs et al. 2005) for the quenching of the spin-orbit transition of Si⁺ by H for temperatures up to 2000 K was already in BASECOL2012. BASECOL2023 has been updated with two recent datasets (Lique et al. 2018) for the de-excitation of S(³P) by He and of Si(³P) by He for temperatures up to 1000 K.

7. Diatomic molecules with heavy partners

The diatomic species Table B.3 includes neutral molecules, cations and anions in collision with He, H and H₂ for

¹³ <https://home.strw.leidenuniv.nl/~moldata/>

¹⁴ <https://emaa.osug.fr>

astrophysical applications, as well as some collisional datasets concerning excitation by Ar and Ne.

7.1. Anions and cations

BASECOL2012 had three ionised species only. It included the rotational de-excitation of CH^+ by He with two recommended datasets: one dataset (Turpin et al. 2010) for transitions among six rotational levels ($T = 1\text{--}200$ K) and another dataset (Hammami et al. 2009) for transitions among 11 levels ($T = 20\text{--}2000$ K). The latter dataset already superseded an older dataset (Hammami et al. 2008a) marked as non-recommended. BASECOL2012 also included the rotational de-excitation among eleven rotational levels of CN^- by o/p- H_2 (Kłos & Lique 2011) and among eleven levels of SiH^+ by He (Nkem et al. 2009). BASECOL2023 has been updated with nine additional datasets concerning the rotational and vibrational excitation of C_2^- (Mant et al. 2020a,c,b) in collision with He, Ar, and Ne, and of CN^- (González-Sánchez et al. 2020, 2021; Mant et al. 2021) in collision with He and Ar. As far as cations are concerned, the new additions mainly concern rotational de-excitation of the following species: AlO^+ by He (Denis-Alpizar et al. 2018c); $^{36}\text{ArH}^+$ by He (Bop et al. 2016); $^{36}\text{ArD}^+$ by He (García-Vázquez et al. 2019); CF^+ by He (Denis-Alpizar et al. 2018a), by p- H_2 (Denis-Alpizar & Rubayo-Soneira 2019; Desrousseaux et al. 2021), and by o- H_2 (Desrousseaux et al. 2021); HeH^+ by H (Desrousseaux & Lique 2020); NeH^+ by He (Bop et al. 2017); NO^+ by He (Denis-Alpizar & Stoecklin 2015) and by p- H_2 (Cabrera-González et al. 2020); and NS^+ by He (Cabrera-González et al. 2018).

In the case of the collisional rotational excitation of CF^+ with p- H_2 (Denis-Alpizar & Rubayo-Soneira 2019; Desrousseaux et al. 2021), a good agreement was found between the two new sets of data despite the use of a less accurate PES by Denis-Alpizar & Rubayo-Soneira (2019). The dataset of Denis-Alpizar & Rubayo-Soneira (2019) provides rate coefficients for roughly the same transitions, but for temperatures between $T = 10$ K and $T = 300$ K, while Desrousseaux et al. (2021) provide data between $T = 5$ K and $T = 150$ K.

The de-excitation among rotational levels of NS^+ cation by H_2 has been included with several datasets: a first dataset (Bop 2019; 24 levels; $T = 5\text{--}100$ K) of NS^+ in collision with p- H_2 ($j = 0$) that was calculated with a PES spherically averaged over the H_2 directions, and two datasets (Bop et al. 2022a; 15 levels; $T = 5\text{--}50$ K) in collision with p- H_2 ($j = 0$) and with o- H_2 ($j = 1$); both datasets were calculated with a 4D PES (Bop et al. 2022a). For these datasets, the authors (Bop et al. 2022a) performed some interesting precision tests related to the dimension of the H_2 rotational basis in the dynamical calculations. They found that the neglect of higher H_2 rotational levels induced differences up to 30% in the rate coefficients.

The rate coefficients among hyperfine levels, obtained via IOS recoupling techniques, are added for CF^+ by He (Denis-Alpizar et al. 2018a), for NS^+ by He (Cabrera-González et al. 2018), and for NS^+ by p- H_2 ($j = 0$) (Bop 2019). The rovibrational excitation of $^{36}\text{ArH}^+$ by He (García-Vázquez et al. 2019) has been added as well.

7.2. CH

BASECOL2023 is enriched with the CH species with two datasets: the fine structure resolved excitation of $\text{CH}(^2\Pi)$ by He (Marinakos et al. 2015) and the hyperfine structure resolved excitation for $\text{CH}(^2\Pi)\text{--He}$ (Marinakos et al. 2019). The hyperfine

results are obtained with a recoupling technique using the data from Marinakis et al. (2015).

7.3. CN, ^{13}CN , C^{15}N

The current CN data (Table B.3) include collisions with He and H_2 and tackle rotational, fine and hyperfine resolved de-excitation processes. Nine recommended datasets are available for CN, one for ^{13}CN and one for C^{15}N .

7.3.1. CN-He

BASECOL2012 included the CN-He system with two datasets: one for transitions among the lowest 41 fine levels of CN for temperatures between 5 and 350 K (Lique et al. 2010b) and for transitions among the lowest 37 hyperfine levels of CN for temperatures between 5 and 30 K (Lique & Kłos 2011).

7.3.2. CN and isotopologues with H_2

BASECOL2023 has been enriched with collisional processes involving the H_2 projectile for CN, ^{13}CN , and C^{15}N . The CN- H_2 saga includes a first publication by Kalugina et al. (2012b), where they calculated a 4D PES and then reduced the dimensionality to a 3D PES in order to calculate rate coefficients among hyperfine levels of CN in collision with p- H_2 ($j = 0$). This dataset, included in BASECOL2012, is now superseded by the new calculations cited thereafter and marked as non-recommended. In a subsequent publication, Kalugina et al. (2013) calculated a 4D PES, and using this 4D PES they calculated rate coefficients among rotational and fine resolved structure of CN in collision with o- H_2 ($j = 1$) and with para- H_2 ($j = 0, 2$); for the fine resolved structure calculations they used a recoupling technique. For para- H_2 they provided state-to-state rate coefficients that include transitions $j(\text{H}_2) = 0\text{--}0, 2\text{--}2$ and $2\text{--}0$ (note that separate fine structure datasets are provided for $j(\text{H}_2) = 0\text{--}0$ and $j(\text{H}_2) = 2\text{--}0, 2\text{--}2$ as the $0\text{--}0$ dataset includes 25 transitions among 25 fine levels of CN, while the $j(\text{H}_2) = 2\text{--}0, 2\text{--}2$ datasets involve 17 fine levels). Finally, Kalugina & Lique (2015) used the PES from Kalugina et al. (2013) to calculate rate coefficients among hyperfine levels of CN using a recoupling technique. The hyperfine rates from Kalugina & Lique (2015) are within a factor of two of those reported in Kalugina et al. (2012b) due primarily to the use of a reduced PES in the latter case. Two new datasets have been added for the hyperfine excitation of ^{13}CN and of C^{15}N by para- H_2 (Flower & Lique 2015), where the PES of Kalugina et al. (2013) is used.

7.4. CO

The current CO data (Table B.3) include collisions with H, He, H_2 , and H_2O , and tackle rotational, vibrational, and rovibrational de-excitation processes. 17 recommended datasets are available.

7.4.1. CO-He

BASECOL2012 already had datasets (Cecchi-Pestellini et al. 2002) for the de-excitation of 15 rotational levels of CO ($T = 5\text{--}500$ K) and of seven vibrational levels of CO ($T = 500\text{--}5000$ K).

7.4.2. CO-H

BASECOL2012 had a dataset by Balakrishnan et al. (2002) for the de-excitation of five vibrational levels of CO in the

temperature range from 100 K to 3000 K. BASECOL2012 also included two datasets (Balakrishnan et al. 2002) calculated with the CC method; they span the low-temperature range ($T = 5\text{--}100$ K) among eight rotational levels and the high-temperature range ($T = 100\text{--}3000$ K) among 17 rotational levels. These three datasets were calculated with the PES of Keller et al. (1996); they are kept as recommended in order to provide meaningful comparisons with the more recent data cited below. New datasets for the CO-H system have been added to BASECOL2023 for rotational de-excitation (Walker et al. 2015) and for ro-vibrational de-excitation (Song et al. 2015b,a); both datasets use the PES of Song et al. (2013).

The rotational de-excitation rate coefficients (Walker et al. 2015) for temperatures ranging from 2 K to 3000 K are obtained for CO ($v = 0, j$) quenching from $j = 1\text{--}45$ to all lower j' levels, where j is the rotational quantum number. CC and CS calculations were performed in full dimension for $j = 1\text{--}5, 10, 15, 20, 25, 30, 35, 40,$ and 45 , while scaling approaches were used to estimate rate coefficients for all other intermediate rotational states.

For the ro-vibrational de-excitation process in the temperature range from 2 to 3000 K, the dataset (Song et al. 2015b) provides the rate coefficients from initial states ($v = 1\text{--}5, j = 0\text{--}30$) to (v', j'), where $v' = 0, 1, \dots, v - 1$, and $j' = 0, 1, \dots$, the highest final $j' = 27\text{--}42$, depending on the initial j . The transitions for larger final j' are not reported, either because they are negligibly small, or because they were not completely converged. It should be noted that the rate coefficients for ro-vibrational ($v = 1, j = 0\text{--}30$) \rightarrow ($v' = 0, j'$) transitions were obtained from scattering cross-sections previously computed with the CC method by Song et al. (2015a). Combining these with the rate coefficients for vibrational $v = 1\text{--}5 \rightarrow v' < v$ quenching obtained with the infinite-order sudden approximation, Song et al. (2015b) used an extrapolation scheme that yields the rate coefficients for ro-vibrational $v = 2\text{--}5, j = 0\text{--}30$, de-excitation.

7.4.3. CO-H₂

BASECOL2012 already contained datasets (Yang et al. 2010) calculated with the PES of Jankowski & Szalewicz (1998), which provided the rotational de-excitation of CO by o/p-H₂ among the lowest 41 rotational CO levels and for temperature between 1 K and 3000 K. The above datasets provide a larger number of transitions for a larger temperature range than previous datasets (Wernli et al. 2006; Flower 2001a) calculated with the same PES (Jankowski & Szalewicz 1998). All datasets are kept as recommended, as no strong argument can distinguish between the methodologies.

New datasets for the ro-vibrational de-excitation of CO by o/p-H₂ have been added to BASECOL2023 (Yang et al. 2016): the ro-vibrational de-excitation rate coefficients for all transitions from CO ($v = 1, j = 1\text{--}5$) to ($v' = 0, j' = 0\text{--}22$) in collisions with para-H₂ ($j = 0$) and ortho-H₂ ($j = 1$) are provided. In addition, the state to state rate coefficients for vibrational transitions of CO from ($v = 2, j = 0$) to ($v' = 1$ and $0, j' = 0\text{--}20$) are also provided for para-H₂ remaining in its ground rotational state ($j = 0$) and for para-H₂ excited from $j = 0$ to $j = 2$. Those calculations are based on the PES of Yang et al. (2015b).

7.4.4. CO-H₂O

For cometary applications, BASECOL2023 has been updated with two datasets (Faure et al. 2020) with thermalised rate

coefficients for the de-excitation of CO by o/p-H₂O (11 levels; $T = 5\text{--}100$ K). The calculations use a new 5D PES (Kalugina et al. 2018) and the statistical approach of Loreau et al. (2018). The thermalised rate coefficients are obtained from the state-to-state rate coefficients summing over the final states of o/p-H₂O and averaging over the initial rotational states of o/p-H₂O where p-H₂O and o-H₂O are independent species.

7.5. CS

The CS data (Table B.3) include collisions with He and H₂, and tackle rotational and ro-vibrational processes; six recommended datasets are available.

7.5.1. CS-He

BASECOL2012 already included collisions of CS with He that are still recommended: one dataset (Lique et al. 2006b) for the de-excitation among the lowest 31 rotational levels of CS ($T = 10\text{--}300$ K) and another one (Lique & Spielfiedel 2007) for the de-excitation among the lowest 114 ro-vibrational levels ($T = 300\text{--}1500$ K).

7.5.2. CS-H₂

BASECOL2023 has been updated with collisional processes with the H₂ molecule. The recent rotational de-excitation datasets for CS by o/p-H₂ of Denis-Alpizar et al. (2018b) have been added and supersede previous results (Turner et al. 1992; Green & Chapman 1978) calculated with an old PES (Green & Chapman 1978).

Two new datasets by Yang et al. (2018a) have been included for the ro-vibrational de-excitation of CS by o/p-H₂. Those datasets cover the ro-vibrational de-excitation rate coefficients from the CS ro-vibrational states ($v = 1, j = 1\text{--}5$) to the ($v' = 0, j' = 0\text{--}35$) levels in collision with para-H₂ ($j = 0$) and with ortho-H₂ ($j = 1$). In addition, the state-to-state rate coefficients for ro-vibrational transitions of CS from ($v = 1, j = 1\text{--}5$) to ($v' = 0, j' = 0\text{--}33$) are also provided for para-H₂ excited from $j = 0$ to $j = 2$, as well as the state-to-state rate coefficients for ro-vibrational transitions of CS from ($v = 1, j = 1\text{--}5$) to ($v' = 0, j' = 0\text{--}28$) for ortho-H₂ excited from $j = 1$ to $j = 3$. Within those two datasets, the rotational de-excitation rate coefficients among the first six rotational levels of CS are also provided for $v = 0$ for collisions with both para-H₂ ($j = 0$) and ortho-H₂ ($j = 1$).

7.6. HCl

The current HCl data (Table B.3) include collisions with He, H₂, and H, and tackle rotational and hyperfine resolved de-excitation processes. Six recommended datasets are available.

7.6.1. HCl-He

BASECOL2023 has been updated with three datasets: two datasets for the de-excitation among rotational levels of HCl, those sets have been calculated by Lanza & Lique (2012) (11 levels; $T = 10\text{--}300$ K) and by Yang & Stancil (2014) (21 levels; $T = 1\text{--}3000$ K), and a dataset for the de-excitation from hyperfine resolved transitions (40 levels; $T = 10\text{--}300$ K; Lanza & Lique 2012) obtained by a recoupling technique. The rotational datasets of Lanza & Lique (2012) and of Yang & Stancil (2014) are of comparable quality and are both recommended; in addition, the hyperfine rate coefficients could be obtained from the

latter dataset (Yang & Stancil 2014) using the usual recoupling techniques (Lanza & Lique 2012). These datasets supersede the previous rotational and hyperfine datasets of Neufeld & Green (1994) as Lanza & Lique (2012) and Yang & Stancil (2014) use more recent PES and better methodologies for the scattering calculations. The datasets of Neufeld & Green (1994) are now marked as non-recommended.

7.6.2. HCl–H₂

BASECOL2023 has been updated with two rotational datasets (Lanza et al. 2014a) for the de-excitation among the eleven lowest rotational levels of HCl ($T = 10\text{--}300\text{ K}$) with o/p-H₂. Those rotational state-to-state rate coefficients were obtained with rotational basis sets that include, respectively, the $j_2 = 3$ and $j_2 = 2$ levels of H₂. It should be mentioned that the dataset with para-H₂ includes transitions among the $j_2 = 0, 2$ levels of H₂ projectile.

7.6.3. HCl–H

More recently, calculations including dissociation were performed by Lique & Faure (2017) for the rotational excitation of HCl–H system. Their rotational de-excitation rate coefficients (Lique & Faure 2017; 11 levels; $T = 10\text{--}500\text{ K}$) are now in BASECOL2023.

7.7. HF

The current HF data (Table B.3) include collisions with He, H₂, H, and H₂O, and tackle rotational de-excitation processes. Seven recommended datasets are available.

7.7.1. HF–He

BASECOL2023 has been updated with a dataset (Yang et al. 2015a) for the rotational de-excitation of HF by He (21 levels and $T = 1\text{--}3000\text{ K}$), this dataset is calculated with the PES of Moszynski et al. (1994). BASECOL2012 already included the dataset (10 levels; $T = 0.1\text{--}300\text{ K}$) of Reese et al. (2005) that was calculated with the more recent PES of Stoecklin et al. (2003). Yang et al. (2015a) presented a comparison with the results obtained by Reese et al. (2005); they indicate a percentage difference from 20% to 75% at 50 K for most of the strongest transitions. As no objective quality arguments can be put forward, the two datasets are kept as recommended.

7.7.2. HF–H₂

BASECOL2023 has also been updated with two datasets (Guillon & Stoecklin 2012) for the de-excitation of six rotational levels of HF in collision with o/p-H₂ ($T = 0.1\text{--}150\text{ K}$): these datasets include some transitions within the H₂ rotational levels.

7.7.3. HF–H

A recent dataset (Desrousseaux & Lique 2018) for the rotational de-excitation of HF by H (9 levels $T = 10\text{--}500\text{ K}$) has been added to BASECOL2023; it uses the PES of Li et al. (2007).

7.7.4. HF–H₂O

For cometary applications, BASECOL2023 has been updated with two datasets (Loreau et al. 2022) with thermalised rate

coefficients for the de-excitation of HF by o/p-H₂O (7 levels; $T = 5\text{--}150\text{ K}$). The calculations use a new 5D PES (Loreau et al. 2020) and the statistical approach of Loreau et al. (2018). The thermalised rate coefficients are obtained from the state-to-state rate coefficients summing over the final states of o/p-H₂O and averaging over the initial rotational states of o/p-H₂O where p-H₂O and o-H₂O are independent species.

7.8. HD

The current HD data (Table B.3) include collisions with He, H₂, and H, and tackle rotational and ro-vibrational de-excitation processes. Ten recommended datasets are available.

7.8.1. HD–He

All the BASECOL datasets concerning HD in collision with He had been calculated using the PES of Muchnick & Russek (1994). BASECOL2012 already had the rotational de-excitation of HD by He (10 levels; $T = 80\text{--}2000\text{ K}$) by Roueff & Zeippen (1999). BASECOL2023 has been updated with two datasets from Nolte et al. (2011) for the ro-vibrational de-excitation of HD by He: those two datasets span different temperature range and transitions. In those calculations, Nolte et al. (2011) extended the calculations of Roueff & Zeippen (2000) to include transitions with $j = 0$ and 1 for $v = 0\text{--}17$, and for which $\Delta v = 0, -1, -2$. Compared to Roueff & Zeippen (2000), significant discrepancies were found for the highest previously considered vibrational state of $v = 3$, but for $v = 0, 1, 2$, the new results are very close to previous results. The ro-vibrational data from Roueff & Zeippen (2000) were never provided to BASECOL.

7.8.2. HD with H₂ projectile

Two new datasets, calculated with the PES of Patkowski et al. (2008), have been included in BASECOL2023 for the de-excitation of nine rotational levels of HD by o/p-H₂ (Wan et al. 2019) for temperatures up to 10 000 K. These results supersede the results (9 levels; $T = 50\text{--}500\text{ K}$) of Flower (1999a) as the latter calculations used on older PES (Schwenke 1988) and did not take into account the excitation of the H₂ molecule in the rotational basis set. Therefore, the rotational dataset from Flower (1999a) is now indicated as non-recommended. The BASECOL2012 datasets for the ro-vibrational de-excitation of HD by o/p-H₂ by Flower & Roueff (1999a) with the PES of Schwenke (1988) have not been revisited and to our knowledge are currently the only available datasets.

7.8.3. HD–H

A new dataset for the rotational de-excitation of eleven rotational levels of HD by H (Desrousseaux et al. 2018) was added to BASECOL2023 in the temperature range between 10 K and 1000 K; calculations were performed with the PES of Mielke et al. (2002). BASECOL2012 already included the rotational de-excitation of HD by H for ten rotational levels and a temperature range from 100 K to 2000 K (Roueff & Flower 1999) where the PES of Boothroyd et al. (1996) was used. The rotational dataset of Roueff & Flower (1999) is kept as recommended to keep the coherence with the ro-vibrational de-excitation rate coefficients of HD by H (Flower & Roueff 1999a) calculated with the same PES (Boothroyd et al. 1996). In addition, there is no strong argument about the difference of quality of the PES of Boothroyd et al. (1996) and the one of Mielke et al. (2002).

7.9. H₂

The current H₂ data (Table B.3) include collisions with He, H₂, and H, and they tackle rotational and ro-vibrational de-excitation processes. Eleven recommended datasets are available.

BASECOL2023 was updated with one new dataset for the collision of H₂ with H (Lique et al. 2012), where the ortho-para conversion was tackled. All the other datasets were already included in BASECOL2012, and they form a very complete manifold of datasets calculated at the end of the last century.

7.9.1. H₂ with He projectile

The ro-vibrational de-excitation datasets of o/p-H₂ by He calculated with the PES of Muchnick & Russek (1994) are currently the only available datasets (Flower et al. 1998) in BASECOL. These results can be used for the rotational de-excitation of o/p-H₂ by He. Flower et al. (1998) provided ro-vibrational rate coefficients for all transitions among levels below ($v = 3, j \leq 8, E = 15228.88 \text{ cm}^{-1}$) for para-H₂ and below ($v = 3, j \leq 7, E = 14495.46 \text{ cm}^{-1}$) for ortho-H₂ ($T = 100\text{--}6000 \text{ K}$). It should be noted that for para-H₂ the rate coefficients had not been calculated for transitions involving the 27th level of para-H₂, (i.e. $v = 1, j = 14$), but they were available for transitions involving the 28th level ($v = 3, j = 8$); so, in BASECOL2023 we decided to limit the data set at the 26th level. For ortho-H₂, the rate coefficients had not been calculated for transitions involving level 24 (i.e. $v = 2, j = 11$), but they were calculated for transitions involving level 25 ($v = 3, j = 7$), so in BASECOL2023 we limited the dataset at level 23. In BASECOL2012, the rate coefficients for the missing transitions were set to zero. Nevertheless, another work has been carried out for this system. Balakrishnan et al. (1999b) calculated ro-vibrational de-excitation rate coefficients from $v = 2$ to 6, with $\Delta v = -1$, for temperatures between 100 K and 4000 K. For ortho-H₂ the transitions involve de-excitation from ($v, j = 1\text{--}7$) to ($v - 1, j = 1\text{--}11$) and to ($v, j = 1\text{--}5$). For para-H₂ the transitions involve de-excitation from ($v, j = 0\text{--}6$) to ($v - 1, j = 0\text{--}10$) and to ($v, j = 0\text{--}4$). These calculations are an extension for $v = 4, 5, 6$ of the work of Flower et al. (1998) using the same PES (Muchnick & Russek 1994). It should be noted that the calculations of Balakrishnan et al. (1999b) are an extension of the calculations by Balakrishnan et al. (1999a), but with a larger ro-vibrational basis set. Ro-vibrational results of Balakrishnan et al. (1999b) and Flower et al. (1998) show discrepancies for ro-vibrational results with large Δj transitions, but there is no conclusion about the respective quality of results. As far as pure rotational calculations are concerned, Flower et al. (1998) and Balakrishnan et al. (1999a) agree well at the published temperature (100 K and higher). For unknown reasons, those data have never been included in BASECOL, and if the authors (Balakrishnan et al. 1999a) provide their data in the BASECOL format, we are happy to include them.

7.9.2. H₂ with o/p-H₂ projectile

BASECOL2023 includes four datasets (Flower & Roueff 1998a, 1999b) with the o/p-H₂ projectile; those datasets have been obtained with the PES of Schwenke (1988). With the p-H₂ projectile kept in its ground state ($v = 0, j = 0$), two datasets (Flower & Roueff 1998a) provide ro-vibrational rate coefficients between 100 K and 6000 K for the de-excitation from the 26 lowest target para-H₂ levels, and from the 23 lowest target ortho-H₂ levels. Flower & Roueff (1998a) calculated more levels: for para-H₂ such that $j \leq 16$ in $v = 0$, $j \leq 12$ in $v = 1$, and $j \leq 8$ in $v = 2$ and for target ortho-H₂ levels such that $j \leq 15$ in $v = 0$, $j \leq 13$ in

$v = 1, j \leq 9$ in $v = 2$, and $j \leq 7$ in $v = 3$. For the reasons developed above for H₂-He, BASECOL2023 truncates the datasets.

With the ortho-H₂ projectile kept in its ground state ($v = 0, j = 1$), two datasets (Flower & Roueff 1999b) provide ro-vibrational rate coefficients between 100 K and 6000 K for the de-excitation from the 19 lowest target para-H₂ levels, and from the 17 lowest target ortho-H₂ levels. Flower & Roueff (1999b) calculated ro-vibrational rate coefficients for more levels in the case of ortho-H₂ such that $j \leq 15$ in $v = 0$, $j \leq 13$ in $v = 1$ and $j \leq 9$ in $v = 2$. But rate coefficients have not been calculated for transitions involving the 18th and 20th levels of the ortho-H₂ target (i.e. $v = 3, j = 1; v = 3, j = 3$). Therefore, BASECOL2023 provides the data set up to level 17 of the ortho-H₂ target. We are aware of the recent calculations by Hernández et al. (2021) of rotational H₂-H₂ de-excitation rate coefficients and we invite the authors to provide the data in our format.

7.9.3. H₂ with H projectile

Currently, BASECOL2023 includes two datasets (Flower & Roueff 1998b) for the ro-vibrational de-excitation of o/p-H₂ by H; those datasets have been calculated with the PES of Boothroyd et al. (1996) and provide rate coefficients from 100 K to 6000 K: one dataset for p-H₂ with 26 ro-vibrational levels and another one for o-H₂ with 23 ro-vibrational levels (see the paragraph on H₂-He above for explanations on the number of levels in the datasets).

The above results could be used for the rotational excitation of o/p-H₂ by H, but the pure rotational rate coefficients have differences as much as a factor of 2 compared to the results of Forrey et al. (1997) and the contribution of the reactive channel to the inelastic rate coefficients is not included as been done in Lique et al. (2012).

BASECOL includes the two datasets calculated by Forrey et al. (1997) that provide rotational de-excitation among the lowest three rotational levels of either p-H₂ or o-H₂ between 100 K and 1000 K. These datasets have been calculated with the same 3D PES (Boothroyd et al. 1996) as the ro-vibrational datasets of Flower & Roueff (1998b), but an exact wave function for H₂ is used instead of a harmonic approximation. This approximation is likely to explain the difference of factor of two between the two types of calculations. Indeed, Forrey et al. (1997) compared various ways to reduce a 3D PES to a 2D PES: a rigid rotor approximation, an average of 3D PES over the harmonic oscillator approximation, an average of 3D PES over the exact ro-vibrational wave function. They found that the rigid rotor approximation and the harmonic oscillator wave function strongly underestimate the rotational cross-sections (about a factor of two).

Finally, the combination of inelastic scattering of H₂ by H and ortho-para conversion of H₂ via H exchange has been studied by Lique et al. (2012) using the PES of Mielke et al. (2002). BASECOL2023 has been updated with the corresponding dataset of collisional rate coefficients among the first nine rotational levels of H₂ in collision with H for temperatures between 300 K and 1500 K (Lique et al. 2012). The differences between the data-sets of Forrey et al. (1997), Flower & Roueff (1998b), and Lique et al. (2012) are given in Fig. C.1 and show the importance of considering the exchange channel for this collision.

7.10. KCl

BASECOL2023 was updated with the KCl molecule and with a single dataset (Sahnoun et al. 2018) concerning the de-excitation

of KCl by p-H₂ ($j = 0$) among the 16 lowest rotational levels of KCl ($T = 2\text{--}50$ K).

7.11. NaH

Another new molecule is NaH, and the current unique dataset (Bop et al. 2019b) concerns the rotational de-excitation of NaH by He (11 levels; $T = 5\text{--}200$ K) calculated with a PES averaged over the ground vibrational wave function of NaH (Bop et al. 2019b).

7.12. NH

The NH($X^3\Sigma^+$) data (Table B.3) include collisions with He and tackle the rotational fine structure process; two recommended datasets are available, and no strong arguments could be used to distinguish between them. BASECOL2023 has been updated with a new dataset (Ramachandran et al. 2018) for the fine structure rotational excitation of NH by He (25 levels; $T = 10\text{--}350$ K). This dataset has been calculated with a 2D PES averaged over a 3D PES that included the vibrational coordinate of NH when the previous dataset of Toboła et al. (2011), already in BASECOL2012, had been calculated with a 2D PES. It should be noted that both datasets agree reasonably well with the experimental rate coefficients of Rinnenthal & Gericke (2002); they both provide transitions among the lowest 25 rotational levels and in the same temperature range up to 350 K. Figure C.2 displays the differences between the two calculated rate coefficient datasets: as it appears that they do not show any significant differences (the average percentage difference between the two data sets is less than 40% for the $\Delta N = \Delta F$ transition), and it is worth noting that the differences are not homogeneous. Both datasets are marked as recommended in BASECOL2023.

7.13. NO

The NO data (Table B.3) include collisions with He and H₂ and tackle fine and hyperfine processes; two recommended datasets are available. BASECOL2012 already had the dataset (Kłos et al. 2008) for the rotational de-excitation of the fine structure levels of NO by He (98 levels; $T = 10\text{--}500$ K). On that dataset (Kłos et al. 2008), BASECOL2023 has updated the notation for the Kronig parity labels in order for them to agree with VAMDC standards, and the energy levels have been put in increasing order, but the scientific content is not changed; the final version of the dataset has changed to v4. BASECOL2023 has been updated with a dataset (Ben Khalifa & Loreau 2021) for the rotational de-excitation of the hyperfine structure of NO by p-H₂ (100 levels; $T = 7\text{--}100$ K), the authors use the new PES of Kłos et al. (2017a).

7.14. OH, OD

The OH data (Table B.3) include collisions with He, H₂, and H, and tackle rotational fine and hyperfine structure resolved processes. Ten recommended datasets are available.

7.14.1. OH–He

The oldest dataset (Kłos et al. 2007), already in BASECOL2012, includes fine structure de-excitation rate coefficients of OH by He using the 2D PES of Lee et al. (2000). BASECOL2023 has been updated with a more recent dataset (Kalugina et al. 2014) that provides rate coefficients for the same system and process.

This is for the same number of transitions (roughly 44) and for the same temperature range ($T = 5\text{--}350$ K), but the authors used the new vibrationally averaged 3D PES of Kalugina et al. (2014). The discussions of Kalugina et al. (2014) seem to show that a vibrationally averaged PES provides some theoretical results in closer agreement with the experimental results. Nevertheless, other tests (Kalugina et al. 2014) show no difference in using either a 2D or an averaged 3D PES. For all the above reasons, the two datasets are indicated as recommended. We checked both sets of rate coefficients at 5, 10, 50, and 300 K. For the transitions up to level 9.5e, the agreement is good, with averaged percentage differences of 28.3, 19, 18.4, and 10.9, respectively. However, for transitions from level 9.5e up to level 10.5e, the averaged percentage differences are 172.2, 130.1, 64.3, and 101, respectively.

BASECOL2023 is further updated with a dataset (Marinakos et al. 2019) that provides hyperfine resolved collisional de-excitation rate coefficients of OH by He. The authors used a recoupling technique together with the nuclear spin-free S matrices of Kalugina et al. (2014).

7.14.2. OH/OD–H₂

The OH–H₂ system has been investigated by Offer et al. (1994), the corresponding datasets can be found on the LAMDA database (LAMDA; van der Tak et al. 2020). BASECOL2023 was updated with two datasets (Kłos et al. 2017b) for the fine structure de-excitation of OH by o/p-H₂ (20 levels; $T = 10\text{--}150$ K) and two datasets (Kłos et al. 2020b) for the hyperfine resolved structure de-excitation of OH by o/p-H₂ (24 levels; $T = 10\text{--}150$ K), the four datasets were obtained with the PES of Ma et al. (2014). The OH–H₂ fine structure rate coefficients for collisions with both para-H₂($j = 0$) and ortho-H₂($j = 1$) differ by a factor of less than three from the older rates by Offer et al. (1994), and the new hyperfine resolved rate coefficients (Kłos et al. 2020b) are found to increase the hyperfine intensities by a factor of about 1–3 in comparison to previous rates of Offer et al. (1994). The new OH–H₂ rate coefficients (Kłos et al. 2017b, 2020b) are expected to be more precise than the previous ones (Offer et al. 1994), as the new datasets were obtained with the recent PES (Ma et al. 2014) that performed fairly well in comparison of theoretical calculations with scattering experiments (Schewe et al. 2015). The OD molecule is new in BASECOL, and two datasets (Dagdikian 2021a) provide hyperfine resolved structure de-excitation of OD by o/p-H₂ (40 levels; $T = 5\text{--}200$ K); they were obtained with the same PES (Ma et al. 2014) as above.

7.14.3. OH–H

BASECOL2023 was updated with a dataset (Dagdikian 2022a) that provides hyperfine resolved collisional de-excitation rate coefficients of OH by H atoms calculated with a recoupling technique and with fine resolved structure excitation results of OH by H (Dagdikian 2022b). These calculations used the potential energy curves of Alexander et al. (2004).

7.15. O₂

The O₂ data (Table B.3) include collisions with He and o/p-H₂, and tackle rotational and fine structure resolved processes; three recommended datasets are available. BASECOL2012 already had the dataset for the rotational fine structure resolved de-excitation of O₂ by He (36 fine levels; $T = 5\text{--}350$ K; Lique 2010), which was calculated using the PES of

Groenenboom & Struniewicz (2000). BASECOL20023 was updated with two datasets from Kalugina et al. (2012a) concerning the rotational de-excitation of O₂ by o/p-H₂ (7 rotational levels; $T = 5\text{--}150\text{ K}$).

7.16. PN

The PN data (Table B.3) include collisions with He and p-H₂ and tackle the rotational process; two recommended datasets are available. BASECOL2012 already had the dataset for the rotational de-excitation of PN by He (31 levels; $T = 10\text{--}300\text{ K}$; Toboła et al. 2007). BASECOL20023 was updated with a dataset from Najjar et al. (2017) concerning the rotational de-excitation of PN by p-H₂ (40 levels; $T = 10\text{--}300\text{ K}$).

7.17. SH

BASECOL2012 already had the dataset for the rotational de-excitation of the fine structure levels of SH by He (Kłos et al. 2009; 60 levels; $T = 5\text{--}350\text{ K}$). On that dataset (Kłos et al. 2009), BASECOL2023 updated the notation for the Kronig parity labels in order for them to agree with VAMDC standards; the scientific content is not changed, but the version of the dataset has changed to v2 and is recommended.

7.18. SiO

The SiO data (Table B.3) include collisions with He and H₂, and tackle the rotational and ro-vibrational processes; eight recommended datasets are available.

7.18.1. SiO–He

BASECOL2023 has been updated with two datasets: a low temperature dataset for rotational de-excitation (Dayou & Balança 2006) among 27 rotational levels ($T = 10\text{--}300\text{ K}$) and a more approximate high temperature dataset for ro-vibrational de-excitation (Balança & Dayou 2017) among 246 levels ($T = 250\text{--}10\,000\text{ K}$).

7.18.2. SiO–H₂

BASECOL2023 was updated with two very rich datasets by Yang et al. (2018b) for collisions with o/p-H₂: the ro-vibrational and rotational de-excitation rate coefficients for SiO ro-vibrational states ($v = 1, j = 1\text{--}10$) to ($v' = 0, j' = 0\text{--}35$) in collisions with ortho-H₂ ($j = 1$) and para-H₂ ($j = 0$). The rate coefficients for rotational transition of SiO from ($v = 1, j = 1\text{--}10$) to ($v' = 1, j' < j$) and among the first six rotational levels in the ground vibrational state are also included in both the para-H₂ and ortho-H₂ datasets. In addition, the para-H₂ dataset provides the ro-vibrational de-excitation rate coefficients for SiO ro-vibrational states ($v = 1, j = 1\text{--}10$) to ($v' = 0, j' = 0\text{--}34$) when para-H₂ is excited from $j(\text{H}_2) = 0$ to $j(\text{H}_2) = 2$.

In addition, BASECOL2023 was updated with four datasets (Balança et al. 2018) for the rotational de-excitation of SiO with o/p-H₂: two low temperature datasets (21 levels; $T = 5\text{--}300\text{ K}$) calculated with the CC method, and two high temperature datasets (30 levels; $T = 5\text{--}1000\text{ K}$) obtained with the more approximate CS method (the sets are identified, respectively, as CC and CS in Table B.3). The above CC and CS SiO–H₂ datasets are recommended as they could be used to test the influence of different datasets on the radiative transfer results. The user should prefer the CC results over the CS or the infinite

order sudden (IOS) approximation results in the relevant temperature range and contact the authors if any doubt. However, the older datasets (Dayou & Balança 2006; Turner et al. 1992) have been set to non-recommended.

7.19. SiS

The SiS data (Table B.3) include collisions with He and H₂ and tackle the rotational and ro-vibrational processes; four recommended datasets are available. BASECOL2012 already included a dataset (Vincent et al. 2007) for the rotational de-excitation of SiS by He (26 levels; $T = 10\text{--}200\text{ K}$), two datasets (Kłos et al. 2008) for the rotational de-excitation of SiS by o/p-H₂ (41 levels; $T = 5\text{--}300\text{ K}$), and one dataset (Toboła et al. 2008) for the ro-vibrational de-excitation of SiS by He (505 levels corresponding to vibration up to $v = 4$ and to rotation up to $j = 100$ with $T = 100\text{--}1500\text{ K}$).

7.20. SO

The SO data (Table B.3) include collisions with He and H₂ and tackle the rotational fine structure and ro-vibrational fine structure processes. Six recommended datasets are available.

7.20.1. SO–He

BASECOL2012 already included two datasets for the rotational fine structure de-excitation of SO by He: one dataset (Lique et al. 2005) for 31 fine levels ($T = 5\text{--}50\text{ K}$) and another one (Lique et al. 2006a) for 91 fine levels ($T = 60\text{--}300\text{ K}$). It also included a dataset (Lique et al. 2006c) for the ro-vibrational fine structure de-excitation of SO by He (236 levels; $T = 300\text{--}800\text{ K}$).

7.20.2. SO–H₂

Recently, new extensive calculations have been performed for the ro-vibrational fine structure de-excitation of SO by o/p-H₂ (Price et al. 2021), where a new 6D PES by Yang et al. (2020) was used. BASECOL2023 has been updated with the corresponding two datasets (Price et al. 2021) that span 273 ro-vibrational transitions up to $v = 2$ for temperatures between 10 K and 3000 K. BASECOL2012 already included the smaller dataset of Lique et al. (2007) for the rotational fine structure de-excitation of SO by p-H₂ (31 levels; $T = 5\text{--}50\text{ K}$), which already superseded an older dataset from Green (1994) as the 1994 calculations used a CS-H₂ PES.

8. Triatomic molecules with heavy partners

BASECOL2023 contains 31 triatomic species (Table B.4) aside from the para-ortho symmetries.

8.1. AICN, AINC

One recommended set is available for AICN and two for AINC. BASECOL2023 was updated with two datasets (Hernández Vera et al. 2013) concerning the de-excitation by He among the 30 rotational levels of AICN and of AINC in the 5 K to 100 K temperature range. A dataset for the rotational de-excitation of AINC by p-H₂ (Urzúa-Leiva & Denis-Alpizar 2020) where H₂ is treated as a spherical atom was also added (27 levels; $T = 5\text{--}105\text{ K}$).

8.2. C_3

Four recommended datasets are available for the C_3 molecule. BASECOL2012 included the dataset (Ben Abdallah et al. 2008) for the de-excitation among six rotational levels of C_3 by impact with He ($T = 5\text{--}15$ K). BASECOL2023 was enriched with three additional datasets: a dataset (Stoecklin et al. 2015) for the rovibrational excitation of C_3 by He (23 levels; $T = 10\text{--}155$ K) and two datasets (Santander et al. 2022) for the rotational de-excitation of C_3 by o/p- H_2 (11 levels; $T = 5\text{--}50$ K).

8.3. C_2H , C_2D , ^{13}CCH , $C^{13}CH$

Five recommended datasets are available for the $C_2H(X^2\Sigma^+)$ molecule: four datasets for $C_2D(X^2\Sigma^+)$, one for $^{13}CCH(X^2\Sigma^+)$, and one for $C^{13}CH(X^2\Sigma^+)$.

8.3.1. $C_2H\text{--}He$

BASECOL2023 has been upgraded with a new version of the dataset (Spielfiedel et al. 2013; version 2, 46 levels; $T = 5\text{--}100$ K) for the de-excitation of the hyperfine levels of C_2H by He, this dataset replaces the previous dataset (version 1, 34 levels; $T = 5\text{--}100$ K; Spielfiedel et al. 2012) which had flaws in the calculations and is not recommended.

8.3.2. $C_2H\text{--}H_2$

This system has been updated with a series of datasets of increasing reliability. BASECOL2023 had been updated with a dataset (Dumouchel et al. 2017) for the de-excitation of the first 17 fine levels of C_2H by p- H_2 , and the corresponding dataset (Dumouchel et al. 2017) for the de-excitation of the first 34 hyperfine levels of C_2H by p- H_2 ($T = 2\text{--}80$ K). These datasets were obtained with a 2D PES (Najar et al. 2014) where H_2 is taken as spherical, and where the PES is averaged over H_2 orientations. Those datasets are now labelled as non-recommended as the PES is crude compared to the calculations of Pirlot Jankowiak et al. (2023b).

BASECOL2023 had also been updated with two datasets (Dagdigian 2018a) for the de-excitation from the first 30 hyperfine levels of C_2H by o/p- H_2 ($T = 10\text{--}300$ K); they were obtained with a newly calculated 4D PES (Dagdigian 2018b). Pirlot Jankowiak et al. (2023b) found an error in those calculations and re-did the dynamical calculations with the same 4D PES (Dagdigian 2018b). BASECOL keeps a trace of the data, and therefore the datasets of Dagdigian (2018a) are kept, but they are labelled as non-recommended. Keeping those datasets of Dagdigian (2018b) is very important, as they were publicly available on both the BASECOL and the LAMDA databases for a certain period of time.

BASECOL2023 was updated with the two recent datasets (Pirlot Jankowiak et al. 2023b) for the de-excitation of 41 fine rotational levels of C_2H by o/p- H_2 ($T = 5\text{--}500$ K) and the two corresponding datasets (Pirlot Jankowiak et al. 2023b) for the de-excitation of the first 38 hyperfine levels of C_2H by o/p- H_2 ($T = 5\text{--}100$ K). Those datasets were obtained with the 4D PES of Dagdigian (2018b). The dynamical calculations with p- H_2 include the first two rotational levels of p- H_2 , but the state-to-state rate coefficients concern the j(p- H_2) 0-0 transition only.

8.3.3. $C_2D\text{--}p\text{--}H_2$

BASECOL2023 had been updated with two datasets (Dumouchel et al. 2017) for the de-excitation from the first

49 hyperfine levels and the first 17 fine levels of C_2D by p- H_2 have been added ($T = 2\text{--}80$ K); these datasets were obtained with the 2D PES of Najar et al. (2014) averaged over H_2 orientations and shifted to take into account the D isotope. Those datasets have been superseded by the datasets of Pirlot Jankowiak et al. (2023b), and they are labelled as non-recommended.

BASECOL2023 had been updated with two datasets (Pirlot Jankowiak et al. 2023b) for the state-to-state de-excitation from the 31 fine structure levels of C_2D with o/p- H_2 ($T = 5\text{--}200$ K), and the corresponding two datasets (Pirlot Jankowiak et al. 2023b) for the state-to-state de-excitation from the first 55 hyperfine levels of C_2D by o/p- H_2 ($T = 5\text{--}100$ K). The dynamical calculations with p- H_2 include the first two rotational levels of p- H_2 , but the state-to-state rate coefficients concern the j(p- H_2) 0-0 transition only.

8.3.4. ^{13}CCH , $C^{13}CH$ with p- H_2

BASECOL2023 has been updated with two datasets (Pirlot Jankowiak et al. 2023a) for the hyperfine and fine resolved rotational de-excitation of $C^{13}CH$ and ^{13}CCH by p- H_2 . Both datasets involve transitions among 98 hyperfine levels for temperatures between 5 K and 100 K. The hyperfine couplings include a first coupling with the ^{13}C nuclear spin leading to the F_1 quantum number and then a coupling to the hydrogen nuclear spin leading to the F quantum number.

8.4. C_2H^-

Two recommended datasets are available for the C_2H^- molecule. BASECOL2023 was updated with two datasets for the rotational de-excitation of C_2H^- by He; one dataset (Gianturco et al. 2019) involves nine rotational levels ($T = 5\text{--}100$ K), and the other dataset (Dumouchel et al. 2012) involves 13 rotational levels ($T = 5\text{--}100$ K). Both datasets were calculated with the same PES (Dumouchel et al. 2012); the cross-sections were obtained over the same range of energies up to 1000 cm^{-1} with the close coupling method; therefore, the rate coefficients should be equivalent, as shown in Fig. C.3.

8.5. C_2N^-

One recommended dataset is available for the open shell $C_2N^- (X^3\Sigma^-)$ molecule. BASECOL2023 was updated with a dataset (Franz et al. 2020) for the de-excitation among rotational levels of C_2N^- in collision with He (16 levels; $T = 5\text{--}100$ K). In that calculation, the electronic structure of C_2N^- has been ignored, and the energy levels are labelled with the spin free quantum number N ; they also calculated a new PES for the C_2N^- -He system.

8.6. C_2O

One recommended dataset is available for the open shell $C_2O(X^3\Sigma^-)$ molecule. BASECOL2023 was upgraded with a dataset (Khadri et al. 2022b) concerning the de-excitation of C_2O in collision with He (31 levels; $T = 2\text{--}80$ K); this dataset was obtained with a newly developed PES (Khadri et al. 2022b). This is part of a series of calculations that explore the excitation of long carbon chains (see below).

8.7. CH_2

Four recommended datasets are available for the asymmetric open shell $CH_2 (X^3B_1)$ molecule.

BASECOL2023 was upgraded with four new datasets (Dagdikian 2021b) for the CH₂ molecule in its para and ortho symmetries: datasets for the de-excitation from the first 69 hyperfine levels of o-CH₂ by o/p-H₂ and from the first 27 rotational levels of p-CH₂ by o/p-H₂ were added for temperatures between 5 K and 300 K. Those four datasets were obtained with a newly calculated PES (Dagdikian 2021c), and the splittings due to the electron spin were treated using a recoupling method. For o-CH₂ the splittings due to the nuclear spin were treated with the M_J randomisation approximation (Alexander & Dagdikian 1985).

8.8. CO₂

One recommended dataset is available for the CO₂ molecule. BASECOL2023 was upgraded with a collisional dataset (Godard Palluet et al. 2022) for the rotational de-excitation of CO₂ by He (21 levels; $T = 4\text{--}300$ K); this dataset was calculated with a newly developed PES (Godard Palluet et al. 2022).

8.9. HCN

Six recommended datasets are available for the HCN molecule.

8.9.1. HCN–He

BASECOL2012 already contained the dataset for the excitation of the 26 rotational levels of HCN by He (Dumouchel et al. 2010; Sarrasin et al. 2010). This dataset uses the sophisticated PES of Toczyłowski et al. (2001) and therefore supersedes the calculations by Green & Thaddeus (1974). When hyperfine resolved lines are observed, the dataset of Monteiro & Stutzki (1986) could be used in the absence of other data, though it is not reliable because of the poor PES used in the dynamical calculations. This dataset is currently indicated as non-recommended, and additional calculations of hyperfine rate coefficients should be performed. As an alternative, the rotational rate coefficients of Dumouchel et al. (2010); Sarrasin et al. (2010) could be used to produce hyperfine levels transitions using an IOS approach (Corey & McCourt 1983).

8.9.2. HCN–H₂

The excitation of HCN by para and ortho-H₂ has led to the two datasets (Hernández Vera et al. 2017) of BASECOL2023, that include the excitation of 26 rotational levels of HCN up to 500 K, with calculations based on the PES of Denis-Alpizar et al. (2013). Part of this work is an extension of the work of Hernández Vera et al. (2014), where the excitation of 13 levels by para H₂ below 100 K was calculated, and the data are identical in the overlapping region. The latter dataset (Hernández Vera et al. 2014) is kept in BASECOL2023, as one objective of BASECOL is to curate data published in journals.

Using those highly accurate rate coefficients and an IOS recoupling method, Goicoechea et al. (2022) calculated the hyperfine resolved rate coefficients for HCN in collision with o/p-H₂, the two corresponding datasets (34 levels; $T = 5\text{--}500$ K; Goicoechea et al. 2022) are in BASECOL2023. Those datasets supersede the hyperfine HCN-p-H₂ dataset by Ben Abdallah et al. (2012) calculated with a simpler PES averaged over three orientations of H₂. It was mentioned in Hernández Vera et al. (2014) that the HCN-p-H₂ calculations of Ben Abdallah et al. (2012) led to significant inaccuracies,

in particular at low temperatures. Therefore, the dataset of Ben Abdallah et al. (2012) is labelled as non-recommended.

Finally, for cometary applications, BASECOL2023 was updated with a dataset (Dubernet & Quintas-Sánchez 2019) with thermalised rate coefficients for the de-excitation of HCN (8 levels; $T = 5\text{--}150$ K) by p-H₂O. The calculations use a new 5D PES (Quintas-Sánchez & Dubernet 2017) and the CS method, where the basis sets are not fully converged (about 20%). The thermalised rate coefficients are obtained from the state-to-state rate coefficients summing over the final states of para-H₂O and averaging over the initial rotational states of para-H₂O.

8.10. HNC

Five recommended datasets are available for the HNC molecule for collisions with He and o/p-H₂. BASECOL2012 already included the dataset (Dumouchel et al. 2010; Sarrasin et al. 2010) for the excitation among the 26 rotational levels of HNC by He calculated with the new PES of Sarrasin et al. (2010; $T = 5\text{--}500$ K), and two datasets (Dumouchel et al. 2010) for the rotational de-excitation among eleven rotational levels of HNC by o/p-H₂ ($T = 5\text{--}100$ K). The p-H₂ dataset included the excitation between the ground level and the first excited state of p-H₂, as well as de-excitation of HCN rotational levels for $j = 2$ of p-H₂. The o-H₂ dataset was calculated with an extended basis for H₂ ($j = 1, 3$).

BASECOL2023 has been updated with two datasets (Hernández Vera et al. 2017) for the de-excitation of HNC by p-H₂ ($j = 0$) and o-H₂ ($j = 1$) (26 levels; $T = 5\text{--}500$ K). The p-H₂ dataset was calculated with an extended basis set for p-H₂ ($j = 0, 2$), but the o-H₂ dataset was calculated with o-H₂ ($j = 1$) only. The new datasets (Hernández Vera et al. 2017) are identical or similar for the 11 lowest transitions and for temperatures below 100 K to the previous datasets of Dumouchel et al. (2010) when H₂ stays, respectively, in its lowest level, $j = 0$ or $j = 1$. The datasets of Dumouchel et al. (2010) are recommended as the quality of the data is identical to those of Hernández Vera et al. (2017) for collision with both p-H₂ and o-H₂; in addition, the dataset of Dumouchel et al. (2010) provides information on the behaviour of rate coefficients with $j(\text{H}_2) = 2$.

8.11. HCO⁺, DCO⁺, HC¹⁷O⁺

Three recommended datasets are available for HCO⁺: one for DCO⁺ and one for HC¹⁷O⁺. BASECOL2023 was upgraded with a dataset (Tonolo et al. 2021) for the de-excitation of six rotational levels of HCO⁺ in collision with He ($T = 5\text{--}100$ K) calculated with their new PES (Tonolo et al. 2021) and with two datasets (Denis-Alpizar et al. 2020) for the rotational de-excitation of HCO⁺ by o/p-H₂ (22 levels; $T = 10\text{--}200$ K), calculated with their new 4D PES (Denis-Alpizar et al. 2020). The previous dataset for the de-excitation of HCO⁺ by p-H₂ ($j=0$) from Flower (1999b), which used an old PES (Monteiro 1985), is now outdated because of the quality of the PES, and it is indicated as non-recommended.

A new dataset (Denis-Alpizar et al. 2020) was added for the rotational de-excitation of DCO⁺ in collision with p-H₂ (22 levels; $T = 10\text{--}200$ K) calculated with the same 4D PES (Denis-Alpizar et al. 2020) as HCO⁺-H₂. BASECOL2012 included a low-quality dataset (Pagani et al. 2012) for the hyperfine structure resolved de-excitation of DCO⁺ by p-H₂ obtained with an IOS recoupling technique using the HCO⁺-p-H₂ rotational rate coefficients of Flower (1999b), the latter being now

superseded. Nevertheless, the dataset of [Pagani et al. \(2012\)](#) is left as recommended as it is the only available dataset. However, we would recommend using the newly calculated rotational dataset of $\text{DCO}^+ - \text{p-H}_2$ ([Denis-Alpizar et al. 2020](#)) to calculate new hyperfine rate coefficients for this system. Finally, we have added a dataset ([Tonolo et al. 2022](#)) for the de-excitation among the 33 first hyperfine levels of HC^{17}O^+ with p-H_2 ; in these calculations, the H_2 projectile has been treated as a spherical body and an average of the potential based on five orientations of H_2 has been employed for the scattering calculations.

8.12. HCO

Two recommended datasets are available for the HCO asymmetric open shell molecule. BASECOL2023 was upgraded with two datasets ([Dagdigian 2020b](#)) for the de-excitation among hyperfine resolved rotational levels of HCO by o/p-H_2 (86 levels; $T = 5\text{--}200$ K). Those rate coefficients were obtained with a new PES ([Dagdigian 2020d](#)), the splittings due to the electron spin was treated using a recoupling method, while the splittings due to the nuclear spin was treated with the M_J randomisation approximation ([Alexander & Dagdigian 1985](#)).

8.13. HCP

Two recommended datasets are available for the HCP molecule. BASECOL2012 already had a dataset ([Hammami et al. 2008b](#)) for the rotational de-excitation of HCP by He (16 levels; $T = 20\text{--}200$ K) and a dataset ([Hammami et al. 2008c](#)) for the rotational de-excitation of HCP by p-H_2 (11 levels; $T = 10\text{--}70$ K). In both systems, a new PES was calculated; for the HCP- p-H_2 system, the H_2 projectile was treated as a spherical body and an average of the potential based on five orientations of H_2 was employed for the scattering calculations.

8.14. HCS⁺

Two recommended datasets are available for the HCS⁺ molecule. BASECOL2023 was updated with a dataset ([Dubernet et al. 2015](#)) for the rotational de-excitation of HCS⁺ by He (20 levels; $T = 5\text{--}100$ K) calculated with a new PES ([Dubernet et al. 2015](#)). This dataset supersedes the dataset of [Monteiro \(1984\)](#) because of better quality of the PES and of the dynamical calculations, the dataset of [Monteiro \(1984\)](#) is indicated as non-recommended.

A new dataset ([Denis-Alpizar et al. 2022](#)) for the rotational de-excitation of HCS⁺ by p-H_2 has been added; this dataset has been obtained with a new PES ([Quintas-Sánchez et al. 2021](#)). The authors mention that this dataset can be used for collisions with o-H_2 to a good approximation.

8.15. H₂O

Twenty-two recommended datasets are currently available for the H_2O molecule.

8.15.1. H₂O–He

BASECOL2023 was updated with two datasets ([Yang et al. 2013](#)) for the de-excitation of rotational levels of $\text{o/p-H}_2\text{O}$ by He (10 levels; $T = 2\text{--}3000$ K); these calculations have used the PES from [Patkowski et al. \(2002\)](#). BASECOL2012 already had the two datasets (45 levels; $T = 20\text{--}2000$ K) from [Green et al. \(1993\)](#) that had been calculated with the PES of

[Maluendes et al. \(1992\)](#). Those datasets are still marked as recommended as they span more transitions, and the agreement between both sets are reasonably good, see Fig. C.4. However, at low temperatures, the data of [Yang et al. \(2013\)](#) show significant differences with the previous rates.

8.15.2. H₂O with o/p-H_2 and thermalised H₂

There are three types of calculation for the rotational de-excitation of H_2O with H_2 : highly accurate quantum calculations (mostly CC calculations; [Daniel et al. 2011, 2010](#); [Dubernet et al. 2009](#)), quasi-classical calculations (QCT; [Faure et al. 2007a](#)), and more approximate quantum CS calculations ([Żóltowski et al. 2021](#)) that provide rate coefficients among twice the number of rotational levels than the two other sets of calculations.

BASECOL2012 contained the four state-to-state rate coefficients datasets ([Daniel et al. 2011, 2010](#); [Dubernet et al. 2009](#)) for the rotational de-excitation of $\text{o/p-H}_2\text{O}$ by $\text{o/p-H}_2(j)$ (45 levels; $T = 5\text{--}1500$ K) where the transitions among H_2 levels have been considered up to $j(\text{H}_2) = 4$ for some water transitions; those datasets have been obtained with a 5D average of the 9D PES of [Valiron et al. \(2008\)](#) and quantum calculations (mostly close coupling) for the dynamics of the nuclei. [Daniel et al. \(2011\)](#) completed calculations of respectively [Dubernet et al. \(2009\)](#) and [Daniel et al. \(2010\)](#). A package is distributed in the ‘tools’ section of the BASECOL website in order to calculate effective and thermalised rate coefficients. Those results superseded the four datasets (5 levels; $T = 20\text{--}140$ K) of [Phillips et al. \(1996\)](#) calculated with the PES of [Phillips et al. \(1994\)](#), which are now marked as non-recommended.

BASECOL2012 contained four datasets ([Faure et al. 2007a](#)) calculated with a 5D average of the 9D PES of [Valiron et al. \(2008\)](#) and with quasi-classical trajectories (45 levels; $T = 20\text{--}2000$ K). Though those data have been obtained with a less precise method than the results of [Daniel et al. \(2011, 2010\)](#); [Dubernet et al. \(2009\)](#), and though they might show differences of as much as a factor of three, they are still marked as recommended as an alternative choice for users.

BASECOL2023 was updated with two datasets ([Żóltowski et al. 2021](#)) for the rotational de-excitation of $\text{o/p-H}_2\text{O}$ by p-H_2 (97 levels; $T = 10\text{--}2000$ K). The authors used the 5D average of the 9D PES of [Valiron et al. \(2008\)](#), but this potential was further approximated using the adiabatic hinder rotor approximation proposed by [Scribano et al. \(2012\)](#), reducing its dimensionality to 3D, where the H_2 molecule is treated as a pseudo-atom. The authors indicate that the precision of the rate coefficients can be between a factor of two and three compared to quantum close coupling calculations using a full 5D PES. The datasets are nevertheless marked recommended, as they provide a very large extension in the number of transitions. BASECOL2012 contained two datasets ([Faure et al. 2007a](#)) calculated with the 9D PES of [Valiron et al. \(2008\)](#) for the ro-vibrational de-excitation of $\text{o/p-H}_2\text{O}$ with fully thermalised H_2 (411 levels; $T = 200\text{--}5000$ K).

8.15.3. H₂O–H

BASECOL2023 was updated with two datasets ([Daniel et al. 2015](#)) for the rotational de-excitation of $\text{o/p-H}_2\text{O}$ by H (45 levels; $T = 5\text{--}1500$ K). These datasets were obtained with the PES of [Dagdigian & Alexander \(2013\)](#).

8.15.4. H₂O–H₂O

BASECOL2023 has been updated with four datasets for the rotational de-excitation of o/p-H₂O by thermalised H₂O; those datasets are intended for cometary and planetary atmospheres applications. Two datasets (Boursier et al. 2020) for transitions among 59 o/p-H₂O levels ($T = 100\text{--}800\text{ K}$) have been obtained with a crude PES and with semi-classical calculations; two other datasets (Mandal & Babikov 2023a) for transitions among 21/22 o/p-H₂O levels ($T = 5\text{--}1000\text{ K}$) were obtained with the MQCT method (Mandal & Babikov 2023b; Mandal et al. 2022), a truncated expansion of the PES of Jankowski & Szalewicz (2005) and extrapolations of cross-sections at low and high collision energy. All of these datasets were obtained using approximate scattering methods that involve the symmetrisation of cross-sections computed for excitation and quenching to ensure that the final data satisfy the principle of detailed balance, as explained in detail in the references cited (Boursier et al. 2020; Mandal & Babikov 2023a).

8.16. D₂O, HDO

Two recommended datasets are currently available for the D₂O molecule, and three are available for the HDO molecule. BASECOL2023 was updated with two datasets (Faure et al. 2012) for the rotational de-excitation of o/p-D₂O by p-H₂ (6 levels; $T = 5\text{--}100\text{ K}$); these datasets were obtained with the PES of Valiron et al. (2008) and with quantum calculations for the dynamics of the nuclei.

BASECOL2012 already included a dataset (Green 1989) for the rotational de-excitation of HDO by He (34 levels; $T = 50\text{--}500\text{ K}$). BASECOL2023 has been updated with two datasets (Faure et al. 2012); one dataset provides thermalised rotational de-excitation rate coefficients of HDO by p-H₂ (30 levels; $T = 5\text{--}300\text{ K}$) and the other includes rotational de-excitation rate coefficients of HDO by o-H₂ ($j = 1$). These datasets were obtained with the PES of Valiron et al. (2008) and with quantum calculations for the dynamics of the nuclei.

8.17. H₂S

Four recommended datasets are available for the closed-shell asymmetric H₂S molecule. BASECOL2023 was updated with four datasets (Dagdigian 2020a) for the rotational de-excitation of o/p-H₂S by o/p-H₂ (19 levels; $T = 5\text{--}500\text{ K}$). These datasets were calculated with a new 4D PES (Dagdigian 2020c).

8.18. MgCN, MgNC

Two recommended datasets are available for MgCN, and there are two for MgNC. BASECOL2023 was updated with two datasets (Hernández Vera et al. 2013) concerning the rotational de-excitation by He among the 36 rotational levels of MgCN and of MgNC ($T = 5\text{--}100\text{ K}$) and with two datasets (Hernández Vera et al. 2013) for the de-excitation among the fine resolved structures of MgCN and MgNC ($T = 5\text{--}100\text{ K}$). The de-excitation among fine levels uses a recoupling technique based on the IOS approximation (Corey & McCourt 1983).

8.19. NH₂

Four recommended datasets are available for the asymmetric open shell NH₂ (X^2B_1) molecule.

The NH₂ (X^2B_1) molecule presents a fine and hyperfine structure, but presently no collisional studies including either the electronic or the nuclear spins have been performed. BASECOL2023 was updated with four datasets (Bouhafs et al. 2017a) for the de-excitation among 15 spin free rotational levels of p-NH₂ and o-NH₂ by o/p-H₂ ($T = 10\text{--}150\text{ K}$); these datasets were obtained with a 4D PES (Bouhafs et al. 2017a) constructed from the 9D global PES of the ground electronic state of NH₄ (Li & Guo 2014).

8.20. N₂H⁺

Four recommended datasets are available for the N₂H⁺ molecule. BASECOL2012 already included two datasets (Daniel et al. 2005) calculated with a new PES (Daniel et al. 2004) for the de-excitation among seven rotational and among 55 hyperfine levels of N₂H⁺ by He. The dataset of Green (1975) was superseded and is labelled as non-recommended.

BASECOL2023 was updated with a dataset (Balança et al. 2020) for the de-excitation among 26 rotational levels of N₂H⁺ by p-H₂ ($T = 5\text{--}500\text{ K}$). The data were obtained with the adiabatic hindered rotor (AHR) approach (Li et al. 2010; Zeng et al. 2011), which reduced the 4D PES of Spielfiedel et al. (2015) to a 2D PES, and thus did not take into account the structure of the H₂ projectile. In addition, BASECOL2023 was updated with a dataset (Lique et al. 2015) for the de-excitation among 64 hyperfine levels of N₂H⁺ by p-H₂. This dataset was obtained with the same AHR approach, the same PES (Spielfiedel et al. 2015), and with a recoupling technique (Daniel et al. 2004).

8.21. OCS

Three recommended datasets are available for the OCS molecule. New work is certainly needed for this molecule. BASECOL2012 already included a dataset (Green & Chapman 1978) for the rotational de-excitation of OCS by p-H₂ (13 levels; $T = 10\text{--}100\text{ K}$), and a dataset (Flower 2001b) for the rotational de-excitation of OCS by He (27 levels; $T = 10\text{--}150\text{ K}$). The dataset with p-H₂ was obtained with a very crude PES and the CS method. BASECOL2023 was updated with a dataset (Chefai et al. 2018) for the de-excitation of OCS by Ar, for which a new PES was calculated (Chefai et al. 2018).

8.22. o-SiC₂

One recommended dataset is available for the o-SiC₂ molecule. BASECOL2012 already included a dataset (Chandra & Kegel 2000) for the rotational de-excitation of o-SiC₂ by He (40 levels; $T = 25\text{--}125\text{ K}$). The authors used an infinite order sudden approximation method, extended the work of Palma & Green (1987), and claimed that their results applied to the H₂ projectile. We re-did the calculations, and it is clear that their results correspond to a collision with He.

8.23. SO₂

Three recommended datasets are available for the SO₂ molecule. BASECOL2012 already included a dataset (Green 1995) for the rotational de-excitation of SO₂ by He (50 levels; $T = 25\text{--}125\text{ K}$) with the PES of Palma (1987) and an IOS method. BASECOL2012 included two datasets (Cernicharo et al. 2011) for the de-excitation of SO₂ by o/p-H₂ (31 levels; $T = 5\text{--}30\text{ K}$). These datasets were obtained with a 5D PES from Spielfiedel et al. (2009) and with the close coupling method.

9. Molecules with more than three atoms with heavy partners

The general table (Table B.5) presents collisional datasets for 26 molecules with more than three atoms.

9.1. C_3H_2

Two recommended datasets are available for the C_3H_2 molecule. BASECOL2012 already included a dataset (Chandra & Kegel 2000) for the rotational de-excitation of o/p- C_3H_2 by He (47/48 levels; $T = 30$ –120 K). The authors used the IOS method, extended the work of Green et al. (1987), and claimed that their excitation rate coefficients applied to the H_2 projectile. We re-did the calculations and it is clear that their results correspond to a collision with He. The current datasets provide the de-excitation rate coefficients obtained by detailed balance using the JPL database (Pearson et al. 2010) spectroscopic data. It should be noted that more precise datasets were calculated by Avery & Green (1989), but for fewer levels. They provided CS rate coefficients among the 16 lowest ortho levels and the 17 lowest para levels for three temperatures ($T = 10, 20, 30$ K); they used the same PES (Green et al. 1987). The latter calculation is not in BASECOL.

9.2. C_3O, C_3S

One recommended dataset is available for C_3O and one for C_3S . BASECOL2023 was updated with a dataset (Bop et al. 2022b) for the rotational de-excitation of C_3O by He (31 levels; $T = 5$ –150 K) calculated with the PES of Khadri & Hammami (2019), and a dataset (Sahnoun et al. 2020) for the rotational de-excitation of C_3S by He (11 levels; $T = 2$ –25 K); in the latter calculation the authors calculated a new PES.

9.3. C_4

One recommended dataset is available for the C_4 ($X^3\Sigma_g^-$) molecule. BASECOL2012 already included a dataset (Lique et al. 2010a) for the fine structure resolved rotational de-excitation of C_4 by He (30 levels; $T = 5$ –50 K). The authors calculated a new PES.

9.4. C_4H^-

Two recommended datasets are available for the C_4H^- molecular ion. BASECOL2023 was updated with two datasets (Balança et al. 2021) for the rotational de-excitation of C_4H^- by o/p- H_2 (30 levels; $T = 5$ –100 K). A new PES was calculated by the authors.

9.5. C_5, C_5O, C_5S

One recommended dataset is available for C_5 , one is available for C_5O , and one is available for C_5S . BASECOL2023 was updated with a dataset (Chefai et al. 2021) for the rotational de-excitation of C_5 by He (15 levels; $T = 5$ –300 K) and a dataset (Khadri et al. 2020) for the rotational de-excitation of C_5S by He (51 levels; $T = 2$ –100 K). In both cases the respective authors calculated a new PES. In addition, it has been updated with a dataset (Bop et al. 2022b) for the rotational de-excitation of C_5O by He (31 levels; $T = 5$ –150 K). These calculations were performed with the PES of Khadri et al. (2022a).

9.6. C_5H^+

One recommended dataset is available for the C_5H^+ molecular ion. BASECOL2023 has been updated with a dataset (Khadri et al. 2023) for the rotational de-excitation of C_5H^+ by He (16 levels; $T = 5$ –100 K). The authors calculated a new 2D PES. This calculation follows the recent discovery of this new molecule in TMC-1 (Cernicharo et al. 2022).

9.7. C_6H^-, C_6H

Two recommended datasets are available for C_6H ($^2\Pi$) and three for C_6H^- . BASECOL2023 was updated with two datasets (Walker et al. 2018): one for the fine resolved rotational de-excitation of C_6H by He (122 levels; $T = 5$ –100 K) and one for the hyperfine resolved de-excitation for the same system (52 levels; $T = 5$ –100 K). The authors calculated a new PES.

Three new datasets (Walker et al. 2017) for the excitation of the close-shell anion C_6H^- were added: one dataset for the rotational de-excitation of C_6H^- by He (11 levels; $T = 5$ –100 K) and two datasets for the rotational de-excitation of C_6H^- by o/p- H_2 (31 levels; $T = 5$ –100 K). The three datasets were obtained with a new PES (Walker et al. 2016).

9.8. CH_3CN, CH_3NC

Two recommended datasets are available for CH_3CN and two are available for CH_3NC . BASECOL2023 was updated with four datasets (Ben Khalifa et al. 2023) for the rotational de-excitation of o/p- CH_3CN (52/75 levels; $T = 7$ –100 K) and of o/p- CH_3NC (66/63 levels; $T = 7$ –100 K) by He. These collisional datasets were calculated with the PES of Ben Khalifa et al. (2022).

9.9. CH_3OH

Fourteen recommended datasets are available for CH_3OH ; they handle rotational processes for three torsional states and for ro-torsional processes. The datasets existed in BASECOL2012, but they were very recently imported to BASECOL2023 as we needed to take decisions about the labelling of the energy levels.

The current BASECOL labelling of levels is J, K ($=K_a$), v_t the torsional quantum number, and the ro-torsional symmetry of the wave function (A or E). In addition, for A states the pseudo-parity is indicated by a + or – symbol; this pseudo-parity comes from the two possible linear combinations of basis set functions as explained in Herbst et al. (1984) and Hougen et al. (1994). Therefore, the VAMDC rovibSym label is used as a ro-torsional symmetry label and follows the convention $A+, A-, E1$ (equivalent to “ E with positive K -sign”) and $E2$ (equivalent to “ E with negative K -sign”) with the symmetric quantum numbers J and K (>0). CH_3OH is currently identified by the stcs VAMDC case (see Table A.1), as no other case can fit this description.

Those notations are implicitly used in the traditional output of the JPL (Pearson et al. 2010) database, and both in the traditional and the VAMDC access of the HITRAN database (Gordon et al. 2022). It should be noted that the JPL quantum numbers are incomplete. The rovibSym label is omitted, and the pseudo-parity quantum number is included for the A -symmetry states only. By deduction, the levels without pseudo-parity belong to the E -symmetry, and JPL uses the K -signed notation.

It is possible to use the usual labelling of the C_{3v} symmetry group, that is the asymmetric rotational quantum numbers (J, K_a ($=K$), K_c), the v_t quantum number, and the ro-torsional A or E symmetry. An example of these notations is provided in

the CDMS (Müller et al. 2005) database; these notations imply that their VAMDC output uses an asymmetric top closed shell (asymcs) case.

Hougen et al. (1994) explained how to transform notations from one label to the other. In addition, the supplementary material of Xu et al. (2008) identifies the energy levels with notations that allow to find the two ways of labelling. For A-symmetry the states are identified with $J, K_a = K, K_c, v_t$ and the pseudo-parity; for the E-symmetry, the states are identified with J, K -signed, and K_c, v_t .

9.9.1. CH₃OH-He

Two datasets (Rabli & Flower 2011) are available for the torsional de-excitation of A-CH₃OH and E-CH₃OH by He (150 levels; $T = 10$ –400 K). The authors used the PES of Pottage et al. (2002). Six datasets (Rabli & Flower 2010b) are available for the rotational de-excitation of A/E-CH₃OH by He, with A/E-CH₃OH in respectively the ground, the $v_t = 1$ and the $v_t = 2$ torsional states (256 levels; $T = 10$ –200 K); the authors used the PES of Pottage et al. (2002). It should be noted that those calculations were carried out with a maximum value of $j = 15$, which means that there are missing higher j rotational levels for energy levels lying above 200 cm^{-1} .

9.9.2. CH₃OH-p-H₂

Six datasets (Rabli & Flower 2010a) are available for the rotational de-excitation of A/E-CH₃OH by p-H₂, with A/E-CH₃OH in the ground, the $v_t = 1$, and the $v_t = 2$ torsional states, respectively (256 levels; $T = 10$ –200 K); the authors used the PES of Pottage et al. (2004). Again, it should be noted that those calculations are carried out with a maximum value of $j = 15$, which means that there are missing higher j rotational levels for energy levels lying above 200 cm^{-1} .

9.10. CNCN

One recommended dataset is available for CNCN. BASECOL2023 was updated with a dataset (Ndaw et al. 2021) for the rotational de-excitation of CNCN by He (30 levels; $T = 5$ –150 K); the authors calculated a new PES.

9.11. H₂CO

Four recommended datasets are available for the H₂CO molecule. BASECOL2012 already included two datasets (Green 1991) for the rotational de-excitation of o/p-H₂CO by He (40/41 levels; $T = 10$ –300 K) that used the PES of Garrison & Lester (1975) and two datasets (Troscmidt et al. 2009) for the rotational de-excitation of o-H₂CO by o/p-H₂ (10 levels; $T = 5$ –100 K), where the authors calculated a new PES.

9.12. H₃O⁺

Four recommended datasets are available for the H₃O⁺ molecular ion. BASECOL2023 has been updated with four datasets (Demes et al. 2022) for the rotational de-excitation of the lowest 11 rotation-inversion levels of o-H₃O⁺ with o/p-H₂ and of the 21 lowest rotation-inversion levels of p-H₃O⁺ with o/p-H₂, for temperatures between 10 K and 300 K. The collisional datasets with p-H₂ include calculations described in Demes et al. (2021, 2022), and all four datasets were calculated with the PES of Demes et al. (2020).

9.13. HC₃N

Seven recommended datasets are available for the HC₃N molecule. BASECOL2012 already included a dataset (Wernli et al. 2007a) for the rotational de-excitation of HC₃N by He (11 levels; $T = 10$ –40 K). This dataset is considered to supersede the dataset (21 levels; $T = 10$ –80 K) of Green & Chapman (1978) as the authors (Green & Chapman 1978) used a Gordon-Kim PES (Gordon & Kim 1972) and the dynamics of the collision is treated with the quasi-classical trajectory approach. Therefore, the dataset of Green & Chapman (1978) is marked as non-recommended.

BASECOL2012 included a dataset (Wernli et al. 2007a) for the rotational de-excitation of HC₃N by p-H₂ ($j = 0$) (51 levels; $T = 10$ –100 K). This dataset suffered from errors in the calculations, and the authors (Wernli et al. 2007b) indicated that the uncertainties on rate coefficients might be around 20%. This dataset is now indicated as non-recommended, as new calculations are available.

BASECOL2023 was updated with three datasets (Faure et al. 2016) for the rotational de-excitation of HC₃N by p-H₂ and o-H₂ (38 levels; $T = 10$ –300 K). One dataset presents the state-to-state rate coefficients of HC₃N by p-H₂ in its ground rotational state $j = 0$; a second dataset presents the thermalised rate coefficients of HC₃N by p-H₂; the third dataset corresponds to the state-to-state rate coefficients of HC₃N by o-H₂ ($j = 1$) that can be used as thermalised rate coefficients. The calculations were not performed for $j(\text{H}_2)$ larger than 1; thus, assumptions were performed in order to obtain the thermalised rate coefficients (see Faure et al. 2016 for the methodology used for the thermalisation). It should be noted that close coupling calculations were used below $j(\text{HC}_3\text{N}) = 30$. For HC₃N levels between $j(\text{HC}_3\text{N}) = 31$ and 37, only QCT rate coefficients for para-H₂ ($j = 0$) were available, and this set was employed directly for both para-H₂ and ortho-H₂ (no thermal averaging).

In addition, BASECOL2023 was updated with three datasets (Faure et al. 2016) for the de-excitation among hyperfine resolved rotational levels of HC₃N by p-H₂ and o-H₂ (61 levels; $T = 10$ –100 K). Those datasets were obtained from the above-mentioned three rotational rate coefficient datasets using the scaled-infinite-order-sudden-limit method (Neufeld & Green 1994; Lanza & Lique 2014), which was checked against recoupling calculations.

9.14. HNCCC, HCCNC

Two recommended datasets are available for the HNCCC molecule, and two are available for HCCNC. BASECOL2023 was updated with two datasets (Bop et al. 2021) for the rotational de-excitation of HNCCC by o/p-H₂ (30 levels; $T = 5$ –80 K) and with two datasets (Bop et al. 2021) for the rotational de-excitation of HCCNC by o/p-H₂ (30 levels; $T = 5$ –80 K). The datasets were obtained with a new PES (Bop et al. 2019a).

9.15. HMgNC

One recommended dataset is available for the HMgNC molecule. BASECOL2023 was updated with a dataset (Amor et al. 2021) for the rotational de-excitation of HMgNC by He (14 levels; $T = 5$ –200 K); the authors calculated a new PES.

9.16. HOCO⁺

One recommended dataset is available for the HOCO⁺ molecule. BASECOL2012 already included a dataset (Hammami et al. 2007) for the rotational de-excitation of HOCO⁺ by He

(25 levels; $T = 10\text{--}30\text{ K}$); the dataset was calculated with the PES of Hammami et al. (2004).

9.17. NCCNH^+

One recommended dataset is available for the NCCNH^+ molecule. BASECOL2023 was updated with a dataset (Bop et al. 2018) for the rotational de-excitation of NCCNH^+ by He (11 levels; $T = 5\text{--}100\text{ K}$); the authors calculated a new PES.

9.18. NH_3

Sixteen recommended datasets are available for the NH_3 molecule.

9.18.1. $\text{NH}_3\text{-He}$

BASECOL 2012 already included two datasets (Machin & Roueff 2005) for the rotational de-excitation of o/p- NH_3 by He (22/16 levels; $T = 5\text{--}300\text{ K}$). Those datasets were obtained with the PES of Hodges & Wheatley (2001).

9.18.2. $\text{NH}_3\text{-H}_2$

The first calculations for the excitation of o/p- NH_3 by para- H_2 were performed by Danby et al. (1986, 1987) in the temperature range from 15 K to 300 K, subsequently improved and extended to 17 levels for ortho- NH_3 and to 24 levels for para- NH_3 by Danby et al. (1988). Therefore, the datasets of Danby et al. (1986, 1987) are marked as non-recommended.

The next set of calculations for the excitation of o/p- NH_3 by p- H_2 were performed by Maret et al. (2009) using their newly calculated PES for ten levels of p- NH_3 and six levels of ortho- NH_3 in the temperature range from 5 K to 100 K; those datasets were already in BASECOL2012.

BASECOL2023 was updated with four datasets (Bouhafs et al. 2017b) for the rotational de-excitation of o/p- NH_3 by o/p- H_2 . The work of Bouhafs et al. (2017b) used the same PES (Maret et al. 2009), extended the number of transitions to 17 o- NH_3 and 34 p- NH_3 levels, and increased the temperature range up to 200 K. The calculations of Bouhafs et al. (2017b) are of better quality than those of Danby et al. (1988), as their basis set included the $j(\text{H}_2) = 2$ level for collision with p- H_2 . However, the calculations of Bouhafs et al. (2017b) did not include the temperature $T = 5\text{ K}$.

Very recently and using the same PES (Maret et al. 2009), close coupling calculations were performed up to 500 K by Demes et al. (2023), where most of the rotation-inversion levels of ammonia were considered below the first vibrational excitation threshold, leading to a total of 33 ortho- and 62 para- NH_3 states. Those calculations were carried out with a basis set that includes $j(\text{H}_2) = 0, 2$ for p- H_2 and $j(\text{H}_2) = 1$ for o- H_2 .

Therefore, BASECOL2023 was updated with four datasets (Demes et al. 2023) for the state-to-state rotational de-excitation of o(33 levels)/p(62 levels)- NH_3 by o/p- H_2 between 100 K and 500 K. It should be noted that the two datasets for o/p- NH_3 with p- H_2 include the state-to-state rate coefficients involving all transitions between $j(\text{p-H}_2) = 0$ and $j(\text{p-H}_2) = 2$ (i.e. 0-0, 0-2, 2-0 and 2-2 transitions). In addition, two datasets (Demes et al. 2023) for thermalised rate coefficients of o(33 levels)/p(62 levels)- NH_3 with p-t- H_2 , built upon the previously mentioned state-to-state rate coefficients ($j(\text{H}_2) = 0, 2$), are included.

As a conclusion, we choose to remove the recommendation of the results of Danby et al. (1988), and we kept the datasets of Maret et al. (2009), of Bouhafs et al. (2017b), and of Demes et al. (2023), as recommended. These should overlap and agree in some regions of temperature and transitions. We did this so that the user can access all those data through VAMDC.

9.18.3. $\text{NH}_3\text{-H}$

BASECOL2023 was updated with two datasets (Bouhafs et al. 2017b) for the de-excitation of 34 levels of p- NH_3 by H and for the de-excitation of 17 levels of o- NH_3 by H. They are calculated with the PES of Li & Guo (2014).

9.19. NH_3 isotopologues

Four recommended datasets are available for the NH_2D , four are available for ND_2H , and three are available for ND_3 . BASECOL2012 already included two datasets (Machin & Roueff 2006) for the rotational de-excitation of o/p- NH_2D by He (9 levels; $T = 5\text{--}100\text{ K}$) and two datasets (Machin & Roueff 2007) for the rotational de-excitation of o/p- ND_2H by He (9 levels; $T = 5\text{--}100\text{ K}$). The four datasets were calculated with a modified version of the PES of Hodges & Wheatley (2001) to account for isotopic shift.

BASECOL2023 was updated with two datasets (Daniel et al. 2014) for the rotational de-excitation of o/p- NH_2D by p- H_2 (79 levels; $T = 5\text{--}300\text{ K}$), two datasets (Daniel et al. 2016) for the rotational de-excitation of o/p- ND_2H by p- H_2 (16 levels; $T = 5\text{--}50\text{ K}$), and three datasets (Daniel et al. 2016) for the rotational de-excitation of o/p/meta- ND_3 by p- H_2 (16/9/9 levels; $T = 5\text{--}50\text{ K}$). The seven new datasets were calculated with a modified version of the PES of Maret et al. (2009) to account for isotopic shift. It should be noted that the collisional treatment ignored the para or meta specificity of ND_3 , so the theoretical results for the para and meta spin isomers are identical. However, specific calculations were performed for the ortho- ND_3 spin isomer.

10. Other information displayed on the BASECOL website

Two other sections are displayed on the BASECOL website: the contacts section, which provides the information about the maintainers of the BASECOL, and the tools section, where tools sent by producers and by other teams are provided. Currently, there is a package called the water rate package, which makes it possible to use the fitting functions of the $\text{H}_2\text{O-H}_2$ rate coefficients (Daniel et al. 2011, 2010; Dubernet et al. 2009) in order to obtain state to state, effective and thermalised rate coefficients; the package contains an option to create outputs in the RADEX format¹⁵.

A link to the VAMDC SPECTCOL tool is also provided; the aim of the client tool SPECTCOL¹⁶ is to associate spectroscopic data extracted from spectroscopic databases through VAMDC, with collisional data provided by collisional databases. It can also be used to display the extracted spectroscopic data (transitions, energy levels, etc.) and the extracted collisional data. The current features of the SPECTCOL tool are described in a forthcoming publication.

¹⁵ <https://personal.sron.nl/~vdtak/radex/index.shtml>

¹⁶ <https://vamdc.org/activities/research/software/spectcol/>

11. Conclusions

BASECOL2023 gives a wide overview of the field of inelastic rate coefficients, mostly for collisions with heavy projectiles and in the temperature range relevant to the ISM, circumstellar atmospheres, and cometary atmospheres. The numerical data sent by the producers of data are not modified. The producers of data have the right to modify the entries prior to their publication, and even later, as the BASECOL versioning system allows us to keep track of the changes at a fine granularity. BASECOL is one of the 40 interconnected databases of the VAMDC e-infrastructure, which ensures that the data can be easily identified and combined, for example by the SPECTCOL tool, with spectroscopic data from other databases such as the CDMS database (Endres et al. 2016) in order to produce ready-to-use outputs for the modelling of non-LTE media. Users can use the VAMDC standards and the java or python libraries in order to create their own access to BASECOL and to other databases in VAMDC.

From a scientific point of view, our main plan for the future is to maintain and further expand this database including new datasets, which is a challenge in itself. In addition, we plan to introduce technical changes that will, for example, allow the user to select data formats when exporting data and make it easier for data producers to prepare files. However, this idea is still in the making, and once implemented, it will be communicated to the astronomical community.

Finally, we stress that the BASECOL database is an international database that is open to all data producers who have published inelastic rate coefficients that fit within the database format. As mentioned in the introduction, Dr O. Denis-Alpizar is the next manager of the BASECOL database.

Acknowledgements. BASECOL has been supported by the VAMDC consortium and by Paris Astronomical Data Center (PADC) from Paris Observatory. For this paper and for the scientific update of BASECOL2023 M.L.D. thanks her collaborator and co-author Corinne Boursier (CB) for her scientific contributions and support, she has been a key motor for the completion of this work. M.L.D. thanks Otoniel Denis-Alpizar for his decision to take over the scientific leadership of BASECOL, and Yaye Awa Ba and Nicolas Moreau for the long term collaboration and their continuous support to the technical platforms. M.L.D. thanks two post-docs who contributed to the maintenance of the database: Dr Sarandis Marinakis and Dr Fabien Daniel, the latter has left the field of research. We are grateful to one of our co-author, Dr Isabelle Kleiner, for very helpful discussions on the spectroscopy of CH₃OH. The list of co-authors includes the scientific team who maintains the database content, the technical team who designed and maintains the technical platforms, the data providers who provided their data in the requested format, thus contributing to the numerical and text information of the BASECOL database and paper.

References

- Abrahamsson, E., Krems, R. V., & Dalgarno, A. 2007, *ApJ*, 654, 1171
- Albert, D., Antony, B. K., Ba, Y. A., et al. 2020, *Atoms*, 8, 76
- Alexander, M. H., & Dagdigian, P. J. 1985, *J. Chem. Phys.*, 83, 2191
- Alexander, M. H., Rackham, E. J., & Manolopoulos, D. E. 2004, *J. Chem. Phys.*, 121, 5221
- Amor, M. A., Hammami, K., & Wiesenfeld, L. 2021, *MNRAS*, 506, 957
- Avery, L. W., & Green, S. 1989, *ApJ*, 337, 306
- Ba, Y.-A., Dubernet, M.-L., Moreau, N., & Zwölf, C. M. 2020, *Atoms*, 8, 69
- Balakrishnan, N., Forrey, R. C., & Dalgarno, A. 1999a, *ApJ*, 514, 520
- Balakrishnan, N., Vieira, M., Babb, J. F., et al. 1999b, *ApJ*, 524, 1122
- Balakrishnan, N., Yan, M., & Dalgarno, A. 2002, *ApJ*, 568, 443
- Balança, C., & Dayou, F. 2017, *MNRAS*, 469, 1673
- Balança, C., Dayou, F., Faure, A., Wiesenfeld, L., & Feautrier, N. 2018, *MNRAS*, 479, 2692
- Balança, C., Scribano, Y., Loreau, J., Lique, F., & Feautrier, N. 2020, *MNRAS*, 495, 2524
- Balança, C., Quintas-Sánchez, E., Dawes, R., et al. 2021, *MNRAS*, 508, 1148
- Barinovs, G., & van Hemert, M. 2004, *Chem. Phys. Lett.*, 399, 406
- Barinovs, G., van Hemert, M. C., Krems, R., & Dalgarno, A. 2005, *ApJ*, 620, 537
- Ben Abdallah, D., Hammami, K., Najar, F., et al. 2008, *ApJ*, 686, 379
- Ben Abdallah, D., Najar, F., Jaidane, N., Dumouchel, F., & Lique, F. 2012, *MNRAS*, 419, 2441
- Ben Khalifa, M., & Loreau, J. 2021, *MNRAS*, 508, 1908
- Ben Khalifa, M., Dagdigian, P. J., & Loreau, J. 2022, *J. Phys. Chem. A*, 126, 9658
- Ben Khalifa, M., Dagdigian, P., & Loreau, J. 2023, *MNRAS*, 523, 2577
- Bergeat, A., Chefdeville, S., Costes, M., et al. 2018, *Nat. Chem.*, 10, 519
- Bian, W., & Werner, H.-J. 2000, *J. Chem. Phys.*, 112, 220
- Boothroyd, A. I., Keogh, W. J., Martin, P. G., & Peterson, M. R. 1996, *J. Chem. Phys.*, 104, 7139
- Bop, C. T. 2019, *MNRAS*, 487, 5685
- Bop, C. T., Hammami, K., Niane, A., Faye, N. A. B., & Jaidane, N. 2016, *MNRAS*, 465, 1137
- Bop, C. T., Hammami, K., & Faye, N. A. B. 2017, *MNRAS*, 470, 2911
- Bop, C. T., Faye, N. A. B., & Hammami, K. 2018, *MNRAS*, 478, 4410
- Bop, C. T., Batista-Romero, F. A., Faure, A., et al. 2019a, *ACS Earth Space Chem.*, 3, 1151
- Bop, C. T., Faye, N., & Hammami, K. 2019b, *Chem. Phys.*, 519, 21
- Bop, C. T., Lique, F., Faure, A., Quintas-Sánchez, E., & Dawes, R. 2021, *MNRAS*, 501, 1911
- Bop, C., Kalugina, Y., & Lique, F. 2022a, *J. Chem. Phys.*, 156, 204311
- Bop, C. T., Khadri, F., & Hammami, K. 2022b, *MNRAS*, 518, 3533
- Bouhafs, N., Lique, F., Faure, A., et al. 2017a, *J. Chem. Phys.*, 146, 064309
- Bouhafs, N., Rist, C., Daniel, F., et al. 2017b, *MNRAS*, 470, 2204
- Boursier, C., Mandal, B., Babikov, D., & Dubernet, M. L. 2020, *MNRAS*, 498, 5489
- Cabrera-González, L., Mera-Adasme, R., Páez-Hernández, D., & Denis-Alpizar, O. 2018, *MNRAS*, 480, 4969
- Cabrera-González, L., Páez-Hernández, D., & Denis-Alpizar, O. 2020, *MNRAS*, 494, 129
- Cecchi-Pestellini, C., Bodo, E., Balakrishnan, N., & Dalgarno, A. 2002, *ApJ*, 571, 1015
- Cernicharo, J., Spielfiedel, A., Balança, C., et al. 2011, *A&A*, 531, A103
- Cernicharo, J., Agúndez, M., Cabezas, C., et al. 2022, *A&A*, 657, A16
- Chandra, S., & Kegel, W. H. 2000, *A&AS*, 142, 113
- Chefai, A., Jellali, C., Hammami, K., & Aroui, H. 2018, *Astrophys. Space Sci.*, 363, 265
- Chefai, A., Ben Khalifa, M., Khadri, F., & Hammami, K. 2021, *Phys. Chem. Chem. Phys.*, 23, 23741
- Corey, G. C., & McCourt, F. R. 1983, *J. Chem. Phys.*, 87, 2723
- Cybulski, S. M., Toczyłowski, R. R., Lee, H.-S., & McCoy, A. B. 2000, *J. Chem. Phys.*, 113, 9549
- Cybulski, S. M., Krems, R. V., Sadeghpour, H. R., et al. 2005, *J. Chem. Phys.*, 122, 094307
- Dagdigian, P. 2018a, *MNRAS*, 479, 3227
- Dagdigian, P. 2018b, *J. Chem. Phys.*, 148, 024304
- Dagdigian, P. J. 2020a, *MNRAS*, 494, 5239
- Dagdigian, P. J. 2020b, *MNRAS*, 498, 5361
- Dagdigian, P. J. 2020c, *J. Chem. Phys.*, 152, 074307
- Dagdigian, P. J. 2020d, *J. Chem. Phys.*, 152, 224307
- Dagdigian, P. J. 2021a, *MNRAS*, 505, 1987
- Dagdigian, P. J. 2021b, *MNRAS*, 508, 118
- Dagdigian, P. J. 2021c, *Mol. Phys.*, 119, 21
- Dagdigian, P. J. 2022a, *MNRAS*, 518, 5976
- Dagdigian, P. J. 2022b, *J. Chem. Phys.*, 157, 104305
- Dagdigian, P. J., & Alexander, M. H. 2013, *J. Chem. Phys.*, 139, 194309
- Dagdigian, P. J., Klos, J., Warehime, M., & Alexander, M. H. 2016, *J. Chem. Phys.*, 145, 164309
- Danby, G., Flower, D. R., Kochanski, E., Kurdi, L., & Valiron, P. 1986, *J. Phys. B: At. Mol. Opt. Phys.*, 19, 2891
- Danby, G., Flower, D. R., Valiron, P., Kochanski, E., & Kurdi, L. 1987, *J. Phys. B: At. Mol. Opt. Phys.*, 20, 1039
- Danby, G., Flower, D. R., Valiron, P., Schilke, P., & Walmsley, C. M. 1988, *MNRAS*, 235, 229
- Daniel, F., Dubernet, M.-L., & Meuwly, M. 2004, *J. Chem. Phys.*, 121, 4540
- Daniel, F., Dubernet, M.-L., Meuwly, M., Cernicharo, J., & Paganí, L. 2005, *MNRAS*, 363, 1083
- Daniel, F., Dubernet, M.-L., Pacaud, F., & Grosjean, A. 2010, *A&A*, 517, A13
- Daniel, F., Dubernet, M.-L., & Grosjean, A. 2011, *A&A*, 536, A76
- Daniel, F., Faure, A., Wiesenfeld, L., et al. 2014, *MNRAS*, 444, 2544
- Daniel, F., Faure, A., Dagdigian, P. J., et al. 2015, *MNRAS*, 446, 2312
- Daniel, F., Rist, C., Faure, A., et al. 2016, *MNRAS*, 457, 1535
- Dayou, F., & Balança, C. 2006, *A&A*, 459, 297
- Demes, S., Lique, F., Faure, A., & Rist, C. 2020, *J. Chem. Phys.*, 153, 094301
- Demes, S., Lique, F., Faure, A., et al. 2021, *MNRAS*, 509, 1252

- Demes, S., Lique, F., Faure, A., & van der Tak, F. F. S. 2022, *MNRAS*, **518**, 3593
- Demes, S., Lique, F., Loreau, J., & Faure, A. 2023, *MNRAS*, **524**, 2368
- Denis-Alpizar, O., & Rubayo-Soneira, J. 2019, *MNRAS*, **486**, 1255
- Denis-Alpizar, O. & Stoecklin, T. 2015, *MNRAS*, **451**, 2986
- Denis-Alpizar, O., Stoecklin, T., Halvick, P., Dubernet, M.-L., & Marinakis, S. 2012, *J. Chem. Phys.*, **137**, 234301
- Denis-Alpizar, O., Kalugina, Y., Stoecklin, T., Vera, M. H., & Lique, F. 2013, *J. Chem. Phys.*, **139**, 224301
- Denis-Alpizar, O., Stoecklin, T., & Halvick, P. 2014, *J. Chem. Phys.*, **140**, 084316
- Denis-Alpizar, O., Inostroza, N., & Castro Palacio, J. 2018a, *MNRAS*, **473**, 1438
- Denis-Alpizar, O., Stoecklin, T., Guilloteau, S., & Dutrey, A. 2018b, *MNRAS*, **478**, 1811
- Denis-Alpizar, O., Trabelsi, T., Hochlaf, M., & Stoecklin, T. 2018c, *MNRAS*, **475**, 783
- Denis-Alpizar, O., Stoecklin, T., Dutrey, A., & Guilloteau, S. 2020, *MNRAS*, **497**, 4276
- Denis-Alpizar, O., Quintas-Sánchez, E., & Dawes, R. 2022, *MNRAS*, **512**, 5546
- Desrousseaux, B., & Lique, F. 2018, *MNRAS*, **476**, 4719
- Desrousseaux, B., & Lique, F. 2020, *J. Chem. Phys.*, **152**, 074303
- Desrousseaux, B., Coppola, C. M., Kazandjian, M. V., & Lique, F. 2018, *J. Phys. Chem. A*, **122**, 8390
- Desrousseaux, B., Quintas-Sánchez, E., Dawes, R., & Lique, F. 2019, *J. Phys. Chem. A*, **123**, 9637
- Desrousseaux, B., Lique, F., Goicoechea, J. R., Quintas-Sánchez, E., & Dawes, R. 2021, *A&A*, **645**, A8
- Dubernet, M.-L., & Quintas-Sánchez, E. 2019, *Mol. Astrophys.*, **16**, 100046
- Dubernet, M.-L., Daniel, F., Grosjean, A., & Lin, C. Y. 2009, *A&A*, **497**, 911
- Dubernet, M. L., Boudon, V., Culhane, J. L., et al. 2010, *JQSRT*, **111**, 2151
- Dubernet, M.-L., Alexander, M. H., Ba, Y. A., et al. 2013, *A&A*, **553**, A50
- Dubernet, M.-L., Quintas-Sánchez, E., & Tuckey, P. 2015, *J. Chem. Phys.*, **143**
- Dubernet, M. L., Antony, B. K., Ba, Y. A., et al. 2016, *J. Phys. B: At. Mol. Opt. Phys.*, **49**
- Dubernet, M., Berriman, G., Barklem, P., et al. 2023, in *Proceedings IAU Symposium No. 371*, Busan, Korea, 9–11 August 2022, eds. D. Soderblom, & G. Nave, Honoring Charlotte Moore Sitterly: Astronomical Spectroscopy in the 21st century, S371 (Cambridge University Press, International Astronomical Union), 72
- Dumouchel, F., Faure, A., & Lique, F. 2010, *MNRAS*, **406**, 2488
- Dumouchel, F., Klos, J., & Lique, F. 2011, *Phys. Chem. Chem. Phys.*, **13**, 8204
- Dumouchel, F., Spielfiedel, A., Senent, M., & Feautrier, N. 2012, *Chem. Phys. Lett.*, **533**, 6
- Dumouchel, F., Lique, F., Spielfiedel, A., & Feautrier, N. 2017, *MNRAS*, **471**, 1849
- Endres, C. P., Schlemmer, S., Schilke, P., Stutzki, J., & Mueller, H. S. P. 2016, *J. Mol. Spectrosc.*, **327**, 95
- Faure, A., & Josselin, E. 2008, *A&A*, **492**, 257
- Faure, A., & Tennyson, J. 2001, *MNRAS*, **325**, 443
- Faure, A., & Tennyson, J. 2003, *MNRAS*, **340**, 468
- Faure, A., Gorfinkiel, J. D., & Tennyson, J. 2004, *MNRAS*, **347**, 323
- Faure, A., Crimier, N., Ceccarelli, C., et al. 2007a, *A&A*, **472**, 1029
- Faure, A., Varambhia, H. N., Stoecklin, T., & Tennyson, J. 2007b, *MNRAS*, **382**, 840
- Faure, A., Wiesenfeld, L., Scribano, Y., & Ceccarelli, C. 2012, *MNRAS*, **420**, 699
- Faure, A., Lique, F., & Wiesenfeld, L. 2016, *MNRAS*, **460**, 2103
- Faure, A., Lique, F., & Loreau, J. 2020, *MNRAS*, **493**, 776
- Flower, D. R. 1999a, *J. Phys. B: At. Mol. Opt. Phys.*, **32**, 1755
- Flower, D. R. 1999b, *MNRAS*, **305**, 651
- Flower, D. R. 2001a, *J. Phys. B: At. Mol. Opt. Phys.*, **34**, 2731
- Flower, D. R. 2001b, *MNRAS*, **328**, 147
- Flower, D. R., & Lique, F. 2015, *MNRAS*, **446**, 1750
- Flower, D. R., & Roueff, E. 1998a, *J. Phys. B: At. Mol. Opt. Phys.*, **31**, 2935
- Flower, D. R., & Roueff, E. 1998b, *J. Phys. B: At. Mol. Opt. Phys.*, **31**, L955
- Flower, D. R., & Roueff, E. 1999a, *MNRAS*, **309**, 833
- Flower, D. R., & Roueff, E. 1999b, *J. Phys. B: At. Mol. Opt. Phys.*, **32**, 3399
- Flower, D. R., Roueff, E., & Zeippen, C. J. 1998, *J. Phys. B: At. Mol. Opt. Phys.*, **31**, 1105
- Forrey, R. C., Balakrishnan, N., Dalgarno, A., & Lepp, S. 1997, *ApJ*, **489**, 1000
- Franz, J., Mant, B. P., González-Sánchez, L., Wester, R., & Gianturco, F. A. 2020, *J. Chem. Phys.*, **152**, 234303
- García-Vázquez, R. M., Márquez-Mijares, M., Rubayo-Soneira, J., & Denis-Alpizar, O. 2019, *A&A*, **631**, A86
- Garrison, B. J., & Lester, W. A. 1975, *J. Chem. Phys.*, **63**, 1449
- Gianturco, F. A., González-Sánchez, L., Mant, B. P., & Wester, R. 2019, *J. Chem. Phys.*, **151**, 144304
- Godard Palluet, A., Thibault, F., & Lique, F. 2022, *J. Chem. Phys.*, **156**, 104303
- Goicoechea, J. R., Lique, F., & Santa-Maria, M. G. 2022, *A&A*, **658**, A28
- González-Sánchez, L., Mant, B. P., Wester, R., & Gianturco, F. A. 2020, *ApJ*, **897**, 75
- González-Sánchez, L., Yurtsever, E., Mant, B. P., Wester, R., & Gianturco, F. A. 2021, *Phys. Chem. Chem. Phys.*, **23**, 7703
- Gordon, R. G., & Kim, Y. S. 1972, *J. Chem. Phys.*, **56**, 3122
- Gordon, I., Rothman, L., Hargreaves, R., et al. 2022, *JQSRT*, **277**, 107949
- Green, S. 1975, *ApJ*, **201**, 366
- Green, S. 1989, *ApJS*, **70**, 813
- Green, S. 1991, *ApJS*, **76**, 979
- Green, S. 1994, *ApJ*, **434**, 188
- Green, S. 1995, *ApJS*, **100**, 213
- Green, S., & Chapman, S. 1978, *ApJS*, **37**, 169
- Green, S., & Thaddeus, P. 1974, *ApJ*, **191**, 653
- Green, S., Defrees, D. J., & McLean, A. D. 1987, *ApJS*, **65**, 175
- Green, S., Maluendes, S., & McLean, A. D. 1993, *ApJS*, **85**, 181
- Groenenboom, G. C., & Struniewicz, I. M. 2000, *J. Chem. Phys.*, **113**, 95621
- Guillon, G., & Stoecklin, T. 2012, *MNRAS*, **420**, 579
- Hammami, K., Jaidane, N., Spielfiedel, A., & Feautrier, N. 2004, *J. Chem. Phys.*, **121**, 1325
- Hammami, K., Lique, F., Jaidane, N., et al. 2007, *A&A*, **462**, 789
- Hammami, K., Owono Owono, L., Jaidane, N., & Ben Lakhdar, Z. 2008a, *J. Mol. Struct.: THEOCHEM*, **853**, 18
- Hammami, K., Owono Owono, L. C., Jaidane, N. J., & Ben Lakhdar, Z. 2008b, *J. Mol. Struct.: THEOCHEM*, **860**, 45
- Hammami, K., Nkem, C., Owono Owono, L. C., Jaidane, N., & Ben Lakhdar, Z. 2008c, *J. Chem. Phys.*, **129**, 204305
- Hammami, K., Owono Owono, L. C., & Stauber, P. 2009, *A&A*, **507**, 1083
- Heijmen, T. G. A., Moszynski, R., Wormer, P. E. S., & van der Avoird, A. 1997, *J. Chem. Phys.*, **107**, 9921
- Herbst, E., Messer, J., De Lucia, F., & Helminger, P. 1984, *J. Mol. Spectrosc.*, **108**, 42
- Hernández, M. I., Tejada, G., Fernández, J. M., & Montero, S. 2021, *A&A*, **647**, A155
- Hernández Vera, M., Lique, F., Dumouchel, F., et al. 2013, *MNRAS*, **432**, 468
- Hernández Vera, M., Kalugina, Y., Denis-Alpizar, O., Stoecklin, T., & Lique, F. 2014, *J. Chem. Phys.*, **140**, 224302
- Hernández Vera, M., Lique, F., Dumouchel, F., Hily-Blant, P., & Faure, A. 2017, *MNRAS*, **468**, 1084
- Higgins, K., & Klemperer, W. 1999, *J. Chem. Phys.*, **110**, 1383
- Hodges, M. P., & Wheatley, R. J. 2001, *J. Chem. Phys.*, **114**, 8836
- Hougen, J., Kleiner, I., & Godefroid, M. 1994, *J. Mol. Spectrosc.*, **163**, 559
- Jankowski, P., & Szalewicz, K. 1998, *J. Chem. Phys.*, **108**, 3554
- Jankowski, P., & Szalewicz, K. 2005, *J. Chem. Phys.*, **123**, 104301
- Jaquet, R., Staemmler, V., Smith, M. D., & Flower, D. R. 1992, *J. Phys. B: At. Mol. Opt. Phys.*, **25**, 285
- Kalemos, A., Mavridis, A., & Metropoulos, A. 1999, *J. Chem. Phys.*, **111**, 9536
- Kalugina, Y., & Lique, F. 2015, *MNRAS*, **446**, L21
- Kalugina, Y., Alpizar, O. D., Stoecklin, T., & Lique, F. 2012a, *Phys. Chem. Chem. Phys.*, **14**, 16458
- Kalugina, Y., Lique, F., & Klos, J. 2012b, *MNRAS*, **2545**
- Kalugina, Y., Klos, J., & Lique, F. 2013, *J. Chem. Phys.*, **139**, 074301
- Kalugina, Y., Lique, F., & Marinakis, S. 2014, *Phys. Chem. Chem. Phys.*, **16**, 13500
- Kalugina, Y. N., Faure, A., van der Avoird, A., Walker, K., & Lique, F. 2018, *Phys. Chem. Chem. Phys.*, **20**, 5469
- Keller, H.-M., Floethmann, H., Dobbyn, A. J., et al. 1996, *J. Chem. Phys.*, **105**, 4983
- Khadri, F., & Hammami, K. 2019, *Phys. Chem. Chem. Phys.*, **21**, 4606
- Khadri, F., Chefai, A., & Hammami, K. 2020, *MNRAS*, **498**, 5159
- Khadri, F., Chefai, A., & Hammami, K. 2022a, *MNRAS*, **513**, 4573
- Khadri, F., Hachani, L., Elabidi, H., & Hammami, K. 2022b, *MNRAS*, **513**, 6152
- Khadri, F., Elabidi, H., & Hammami, K. 2023, *MNRAS*, **522**, 4038
- Klos, J., & Lique, F. 2008, *MNRAS*, **390**, 239
- Klos, J., & Lique, F. 2011, *MNRAS*, **418**, 271
- Klos, J., Chalasinski, G., Berry, M. T., Bukowski, R., & Cybulski, S. M. 2000, *J. Chem. Phys.*, **112**, 2195
- Klos, J., Lique, F., & Alexander, M. H. 2007, *Chem. Phys. Lett.*, **445**, 12
- Klos, J., Lique, F., & Alexander, M. H. 2008, *Chem. Phys. Lett.*, **455**, 1
- Klos, J., Lique, F., & Alexander, M. H. 2009, *Chem. Phys. Lett.*, **476**, 135
- Klos, J., Ma, Q., Alexander, M. H., & Dagdigian, P. J. 2017a, *J. Chem. Phys.*, **146**, 114301
- Klos, J., Ma, Q., Dagdigian, P. J., et al. 2017b, *MNRAS*, **471**, 4249
- Klos, J., Dagdigian, P., & Lique, F. 2020a, *MNRAS*, **501**, L38
- Klos, J., Dagdigian, P. J., Alexander, M. H., Faure, A., & Lique, F. 2020b, *MNRAS*, **493**, 3491
- Lanza, M., & Lique, F. 2012, *MNRAS*, **424**, 1261
- Lanza, M., & Lique, F. 2014, *J. Chem. Phys.*, **141**, 164321

- Lanza, M., Kalugina, Y., Wiesenfeld, L., Faure, A., & Lique, F. 2014a, *MNRAS*, **443**, 3351
- Lanza, M., Kalugina, Y., Wiesenfeld, L., & Lique, F. 2014b, *J. Chem. Phys.*, **140**, 064316
- Launay, J. M., & Roueff, E. 1977, *A&A*, **56**, 289
- Lee, H., McCoy, A. B., Toczyłowski, R. R., & Cybulski, S. M. 2000, *J. Chem. Phys.*, **113**, 5736
- Li, J., & Guo, H. 2014, *Phys. Chem. Chem. Phys.*, **16**, 6753
- Li, G., Werner, H.-J., Lique, F., & Alexander, M. H. 2007, *J. Chem. Phys.*, **127**, 174302
- Li, H., Roy, P. N., & Le Roy, R. J. 2010, *J. Chem. Phys.*, **133**, 104305
- Lim, A. J., Rabadán, I., & Tennyson, J. 1999, *MNRAS*, **306**, 473
- Lique, F. 2010, *J. Chem. Phys.*, **132**, 044311
- Lique, F., & Faure, A. 2017, *MNRAS*, **472**, 738
- Lique, F., & Kłos, J. 2011, *MNRAS*, **413**, L20
- Lique, F., & Spielfiedel, A. 2007, *A&A*, **462**, 1179
- Lique, F., Spielfiedel, A., Dubernet, M.-L., & Feautrier, N. 2005, *J. Chem. Phys.*, **123**, 134316
- Lique, F., Dubernet, M.-L., Spielfiedel, A., & Feautrier, N. 2006a, *A&A*, **450**, 399
- Lique, F., Spielfiedel, A., & Cernicharo, J. 2006b, *A&A*, **451**, 1125
- Lique, F., Spielfiedel, A., Dhont, G., & Feautrier, N. 2006c, *A&A*, **458**, 331
- Lique, F., Senent, M.-L., Spielfiedel, A., & Feautrier, N. 2007, *J. Chem. Phys.*, **126**, 164312
- Lique, F., Kłos, J., & Hochlaf, M. 2010a, *Phys. Chem. Chem. Phys.*, **12**, 15672
- Lique, F., Spielfiedel, A., Feautrier, N., et al. 2010b, *J. Chem. Phys.*, **132**, 024303
- Lique, F., Honvault, P., & Faure, A. 2012, *J. Chem. Phys.*, **137**, 154303
- Lique, F., Daniel, F., Pagani, L., & Feautrier, N. 2015, *MNRAS*, **446**, 1245
- Lique, F., Kłos, J., Alexander, M. H., Le Picard, S. D., & Dagdigan, P. J. 2017, *MNRAS*, **474**, 2313
- Lique, F., Kłos, J., & Le Picard, S. D. 2018, *Phys. Chem. Chem. Phys.*, **20**, 5427
- Loreau, J., Lique, F., & Faure, A. 2018, *ApJ*, **853**, L5
- Loreau, J., Kalugina, Y. N., Faure, A., van der Avoird, A., & Lique, F. 2020, *J. Chem. Phys.*, **153**, 214301
- Loreau, J., Faure, A., & Lique, F. 2022, *MNRAS*, **516**, 5964
- Ma, Q., Kłos, J., Alexander, M. H., van der Avoird, A., & Dagdigan, P. J. 2014, *J. Chem. Phys.*, **141**, 174309
- Machin, L., & Roueff, E. 2005, *J. Phys. B: At. Mol. Opt. Phys.*, **38**, 1519
- Machin, L., & Roueff, E. 2006, *A&A*, **460**, 953
- Machin, L., & Roueff, E. 2007, *A&A*, **465**, 647
- Maluendes, S., McLean, A. D., & Green, S. 1992, *J. Chem. Phys.*, **96**, 8150
- Mandal, B., & Babikov, D. 2023a, *A&A*, **678**, A51
- Mandal, B., & Babikov, D. 2023b, *A&A*, **671**, A51
- Mandal, B., Joy, C., Bostan, D., Eng, A., & Babikov, D. 2022, *J. Phys. Chem. Lett.*, **14**, 817
- Mant, B. P., Gianturco, F. A., González-Sánchez, L., Yurtsever, E., & Wester, R. 2020a, *J. Phys. B: At. Mol. Opt. Phys.*, **53**, 025201
- Mant, B. P., Gianturco, F. A., Wester, R., Yurtsever, E., & González-Sánchez, L. 2020b, *Phys. Rev. A*, **102**, 062810
- Mant, B. P., Gianturco, F. A., Wester, R., Yurtsever, E., & González-Sánchez, L. 2020c, *J. Int. Mass Spectrom.*, **457**, 116426
- Mant, B. P., Yurtsever, E., González-Sánchez, L., Wester, R., & Gianturco, F. A. 2021, *J. Chem. Phys.*, **154**, 084305
- Maret, S., Faure, A., Scifoni, E., & Wiesenfeld, L. 2009, *MNRAS*, **399**, 425
- Marinakakis, S., Dean, I. L., Kłos, J., & Lique, F. 2015, *Phys. Chem. Chem. Phys.*, **17**, 21583
- Marinakakis, S., Kalugina, Y., Kłos, J., & Lique, F. 2019, *A&A*, **629**, A130
- Mielke, S. L., Garrett, B. C., & Peterson, K. A. 2002, *J. Chem. Phys.*, **116**, 4142
- Monteiro, T. 1984, *MNRAS*, **210**, 1
- Monteiro, T. S. 1985, *MNRAS*, **214**, 419
- Monteiro, T. S., & Stutzki, J. 1986, *MNRAS*, **221**, 33P
- Moszynski, R., Wormer, P. E. S., Jeziorski, B., & van der Avoird, A. 1994, *J. Chem. Phys.*, **101**, 2811
- Muchnick, P., & Russek, A. 1994, *J. Chem. Phys.*, **100**, 4336
- Müller, H. S. P., Schlöder, F., Stutzki, J., & Winnewisser, G. 2005, *J. Mol. Struct.*, **742**, 215
- Murdachaw, G., Szalewicz, K., Jiang, H., & Bačić, Z. 2004, *J. Chem. Phys.*, **121**, 11839
- Najar, F., Ben Abdallah, D., Spielfiedel, A., et al. 2014, *Chem. Phys. Lett.*, **614**, 251
- Najar, F., Nouai, M., ElHanini, H., & Jaidane, N. 2017, *MNRAS*, **472**, 2919
- Ndaw, D., Bop, C. T., Dieye, G., Faye, N. B., & Lique, F. 2021, *MNRAS*, **503**, 5976
- Neufeld, D. A., & Green, S. 1994, *ApJ*, **432**, 158
- Nkem, C., Hammami, K., Manga, A., et al. 2009, *J. Mol. Struct.: THEOCHEM*, **901**, 220
- Nolte, J. L., Stancil, P. C., Lee, T.-G., Balakrishnan, N., & Forrey, R. C. 2011, *ApJ*, **744**, 62
- Offer, A. R., van Hemert, M. C., & van Dishoeck, E. F. 1994, *J. Chem. Phys.*, **100**, 362
- Pagani, L., Bourgoïn, A., & Lique, F. 2012, *A&A*, **548**, A4
- Palma, A. 1987, *ApJS*, **64**, 565
- Palma, A., & Green, S. 1987, *ApJ*, **316**, 830
- Palma, A., Green, S., Defrees, D. J., & McLean, A. D. 1988, *J. Chem. Phys.*, **89**, 1401
- Parlant, G., & Yarkony, D. R. 1999, *J. Chem. Phys.*, **110**, 363
- Patkowski, K., Brudermann, J., Steinbach, C., Buck, U., & Moszynski, R. 2002, *J. Chem. Phys.*, **117**, 11166
- Patkowski, K., Cencek, W., Jankowski, P., et al. 2008, *J. Chem. Phys.*, **129**, 094304
- Pearson, J. C., Mueller, H. S. P., Pickett, H. M., Cohen, E. A., & Drouin, B. J. 2010, *JQSRT*, **111**, 1614
- Phillips, T. R., Maluendes, S., McLean, A. D., & Green, S. 1994, *J. Chem. Phys.*, **101**, 5824
- Phillips, T. R., Maluendes, S., & Green, S. 1996, *ApJS*, **107**, 467
- Pirlot Jankowiak, P., Lique, F., & Dagdigan, P. 2023a, *MNRAS*, **523**, 3732
- Pirlot Jankowiak, P., Lique, F., & Dagdigan, P. J. 2023b, *MNRAS*, **526**, 885
- Pottage, J. T., Flower, D. R., & Davis, S. L. 2002, *J. Phys. B: At. Mol. Opt. Phys.*, **35**, 2541
- Pottage, J. T., Flower, D. R., & Davis, S. L. 2004, *MNRAS*, **352**, 39
- Price, T. J., Forrey, R. C., Yang, B., & Stancil, P. C. 2021, *J. Chem. Phys.*, **154**, 034301
- Quintas-Sánchez, E., & Dubernet, M.-L. 2017, *Phys. Chem. Chem. Phys.*, **19**, 6849
- Quintas-Sánchez, E., Dawes, R., & Denis-Alpizar, O. 2021, *Mol. Phys.*, **119**, e1980234
- Rabadan, I., Sarpal, B. K., & Tennyson, J. 1998, *MNRAS*, **299**, 171
- Rabli, D., & Flower, D. R. 2010a, *MNRAS*, **406**, 95
- Rabli, D., & Flower, D. R. 2010b, *MNRAS*, **403**, 2033
- Rabli, D., & Flower, D. R. 2011, *MNRAS*, **411**, 2011
- Ramachandran, C., De Fazio, D., Cavalli, S., Tarantelli, F., & Aquilanti, V. 2009, *Chem. Phys. Lett.*, **469**, 26
- Ramachandran, R., Kłos, J., & Lique, F. 2018, *J. Chem. Phys.*, **148**, 084311
- Reese, C., Stoecklin, T., Voronin, A., & Rayez, J. C. 2005, *A&A*, **430**, 1139
- Rinnenthal, J. L., & Gericke, K.-H. 2002, *J. Chem. Phys.*, **116**, 9776
- Roueff, E., & Flower, D. R. 1999, *MNRAS*, **305**, 353
- Roueff, E., & Zeippen, C. J. 1999, *A&A*, **343**, 1005
- Roueff, E., & Zeippen, C. J. 2000, *A&AS*, **142**, 475
- Sahnoun, E., Nkem, C., Naindoub, A., et al. 2018, *Astrophys. Space Sci.*, **363**, 195
- Sahnoun, E., Ben Khalifa, M., Khadri, F., & Hammami, K. 2020, *ApJS*, **365**, 1
- Santander, C., Denis-Alpizar, O., & Cárdenas, C. 2022, *A&A*, **657**, A55
- Sarpal, B. K., & Tennyson, J. 1993, *MNRAS*, **263**, 909
- Sarrasin, E., Abdallah, D. B., Wernli, M., et al. 2010, *MNRAS*, **404**, 518
- Schewe, H. C., Ma, Q., Vanhaecke, N., et al. 2015, *J. Chem. Phys.*, **142**, 204310
- Schröder, K., Staemmler, V., Smith, M. D., Flower, D. R., & Jaquet, R. 1991, *J. Phys. B: At. Mol. Opt. Phys.*, **24**, 2487
- Schwenke, D. W. 1988, *J. Chem. Phys.*, **89**, 2076
- Scribano, Y., Faure, A., & Lauvergna, D. 2012, *J. Chem. Phys.*, **136**, 094109
- Song, L., van der Avoird, A., & Groenenboom, G. C. 2013, *J. Phys. Chem. A*, **117**, 7571
- Song, L., Balakrishnan, N., van der Avoird, A., Karman, T., & Groenenboom, G. C. 2015a, *J. Chem. Phys.*, **142**, 204303
- Song, L., Balakrishnan, N., Walker, K. M., et al. 2015b, *ApJ*, **813**, 96
- Spielfiedel, A., Senent, M.-L., Dayou, F., et al. 2009, *J. Chem. Phys.*, **131**, 014305
- Spielfiedel, A., Feautrier, N., Najar, F., et al. 2012, *MNRAS*, **421**, 1891
- Spielfiedel, A., Feautrier, N., Najar, F., et al. 2013, *MNRAS*, **429**, 923
- Spielfiedel, A., Senent, M. L., Kalugina, Y., et al. 2015, *J. Chem. Phys.*, **143**, 024301
- Staemmler, V., & Flower, D. R. 1991, *J. Phys. B: At. Mol. Opt. Phys.*, **24**, 2343
- Stoecklin, T., & Voronin, A. 2011, *J. Chem. Phys.*, **134**, 204312
- Stoecklin, T., Voronin, A., & Rayez, J. C. 2003, *Chem. Phys.*, **294**, 117
- Stoecklin, T., Denis-Alpizar, O., & Halvick, P. 2015, *MNRAS*, **449**, 3420
- Tennyson, J., & Faure, A. 2019, in *Gas-phase Chemistry in Space: From Elementary Particles to Complex Organic Molecules*, eds. F. Lique, & A. Faure (AAS-IOP Astronomy)
- Toboła, R., Kłos, J., Lique, F., Chałasiński, G., & Alexander, M. H. 2007, *A&A*, **468**, 1123
- Toboła, R., Lique, F., Kłos, J., & Chałasiński, G. 2008, *J. Phys. B: At. Mol. Opt. Phys.*, **41**, 155702
- Toboła, R., Dumouchel, F., Kłos, J., & Lique, F. 2011, *J. Chem. Phys.*, **134**, 024305
- Toczyłowski, R. R., Doloresco, F., & Cybulski, S. M. 2001, *J. Chem. Phys.*, **114**, 851
- Tonolo, F., Bizzocchi, L., Melosso, M., et al. 2021, *J. Chem. Phys.*, **155**, 234306

- Tonolo, F., Lique, F., Melosso, M., Puzzarini, C., & Bizzocchi, L. 2022, *MNRAS*, **516**, 2653
- Troscompt, N., Faure, A., Wiesenfeld, L., Ceccarelli, C., & Valiron, P. 2009, *A&A*, **493**, 687
- Turner, B. E., Chan, K.-W., Green, S., & Lubowich, D. A. 1992, *ApJ*, **399**, 114
- Turpin, F., Stoecklin, T., & Voronin, A. 2010, *A&A*, **511**, A28
- Urzúa-Leiva, R., & Denis-Alpizar, O. 2020, *ACS Earth Space Chem.*, **4**, 2384
- Valiron, P., Wernli, M., Faure, A., et al. 2008, *J. Chem. Phys.*, **129**, 134306
- van der Tak, F. F. S., Lique, F., Faure, A., Black, J. H., & van Dishoeck, E. F. 2020, *Atoms*, **8**, 15
- Varambhia, H. N., Gupta, M., Faure, A., Baluja, K. L., & Tennyson, J. 2009, *J. Phys. B: At. Mol. Opt. Phys.*, **42**, 095204
- Vieira, D., & Krems, R. V. 2017, *ApJ*, **835**, 255
- Vincent, L. F. M., Spielfiedel, A., & Lique, F. 2007, *A&A*, **472**, 1037
- Walker, K. M., Song, L., Yang, B. H., et al. 2015, *ApJ*, **811**, 27
- Walker, K. M., Dumouchel, F., Lique, F., & Dawes, R. 2016, *J. Chem. Phys.*, **145**, 024314
- Walker, K. M., Lique, F., Dumouchel, F., & Dawes, R. 2017, *MNRAS*, **466**, 831
- Walker, K. M., Lique, F., & Dawes, R. 2018, *MNRAS*, **473**, 1407
- Wan, Y., Balakrishnan, N., Yang, B. H., Forrey, R. C., & Stancil, P. C. 2019, *MNRAS*, **488**, 381
- Wernli, M., Valiron, P., Faure, A., et al. 2006, *A&A*, **446**, 367
- Wernli, M., Wiesenfeld, L., Faure, A., & Valiron, P. 2007a, *A&A*, **464**, 1147
- Wernli, M., Wiesenfeld, L., Faure, A., & Valiron, P. 2007b, *A&A*, **475**, 391
- Xu, L.-H., Fisher, J., Lees, R. M., et al. 2008, *J. Mol. Spectrosc.*, **251**, 305
- Yang, B., & Stancil, P. C. 2014, *ApJ*, **783**, 92
- Yang, B., Stancil, P. C., Balakrishnan, N., & Forrey, R. C. 2010, *ApJ*, **718**, 1062
- Yang, B., Stancil, P. C., Kimura, M., Satomi, W., & Nagao, M. 2013, *ApJ*, **765**, 77
- Yang, B., Walker, K. M., Forrey, R. C., Stancil, P. C., & Balakrishnan, N. 2015a, *A&A*, **578**, A65
- Yang, B. H., Zhang, P., Wang, X. H., et al. 2015b, *Nat. Commun.*, **6**, 6629
- Yang, B. H., Zhang, P., Wang, X. H., et al. 2016, *J. Chem. Phys.*, **145**, 034308
- Yang, B., Zhang, P., Qu, C., et al. 2018a, *Phys. Chem. Chem. Phys.*, **20**, 28425
- Yang, B., Zhang, P., Qu, C., et al. 2018b, *J. Phys. Chem. A*, **122**, 1511
- Yang, B., Zhang, P., Qu, C., et al. 2020, *Chem. Phys.*, **532**, 110695
- Yau, A. W., & Dalgarno, A. 1976, *ApJ*, **206**, 652
- Zeng, T., Li, H., Le Roy, R. J., & Roy, P. N. 2011, *J. Chem. Phys.*, **135**, 094304
- Żóltowski, M., Lique, F., Karska, A., & Żuchowski, P. S. 2021, *MNRAS*, **502**, 5356
- ⁸ Univ. Rennes, CNRS, IPR (Institut de Physique de Rennes) – UMR 6251, 35000 Rennes, France
- ⁹ Department of Chemistry, The University of Manchester, Oxford Road, Manchester M13 9PL, UK
- ¹⁰ Departamento de Física, Facultad de Ciencias, Universidad de Chile, Av. Las Palmeras 3425, Ñuñoa, Santiago, Chile
- ¹¹ Centro para el Desarrollo de la Nanociencia y la Nanotecnología (CEDENNA), Av. Ecuador 3493, Santiago 9170124, Chile
- ¹² Department of Chemistry, The Johns Hopkins University, Baltimore, MD 21218-2685, USA
- ¹³ LOMC – UMR 6294, CNRS-Université du Havre, 25 rue Philippe Lebon, BP 1123, 76063 Le Havre Cedex, France
- ¹⁴ IPAG, Université Grenoble Alpes & CNRS, CS 40700, 38058 Grenoble, France
- ¹⁵ Department of Physics, Penn State University, Berks Campus, Reading, PA 19610, USA
- ¹⁶ Department of Theoretical Physics and Quantum Informatics, Faculty of Applied Physics and Mathematics, Gdansk University of Technology, ul. Narutowicza 11/12, 80-233 Gdansk, Poland
- ¹⁷ Institute for Ion Physics and Applied Physics, University of Innsbruck, Technikerstr. 25/3, 6020 Innsbruck, Austria
- ¹⁸ Department of Chemistry, University of Patras, Patras 26504, Greece
- ¹⁹ Departamento de Química Física, University of Salamanca, Plaza de los Caídos s/n, 37008 Salamanca, Spain
- ²⁰ Theoretical Chemistry, Institute for Molecules and Materials, Radboud University, Heyendaalseweg 135, 6525 AJ Nijmegen, The Netherlands
- ²¹ Université Paris Cité and Univ. Paris Est Creteil, CNRS, LISA, 75013 Paris, France
- ²² Joint Quantum Institute, Department of Physics, University of Maryland, College Park, MD 20742, USA
- ²³ Department of Physics, Temple University, Philadelphia, PA 19122, USA
- ²⁴ Laboratoire Atomes Lasers, Département de Physique, Faculté des Sciences et Techniques, Université Cheikh Anta Diop, Dakar 5005, Senegal
- ²⁵ Depart. of Physics and Astronomy and Center for Simulation Physics, The University of Georgia, Athens, Georgia 30602-2451, USA
- ²⁶ Departamento de Física Atómica y Molecular, Instituto Superior de Tecnologías y Ciencias Aplicadas, Universidad de La Habana, Ave. Salvador Allende No. 1110, 10400 Plaza de la Revolución, La Habana, Cuba
- ²⁷ Department of Chemistry, Missouri University of Science and Technology, Rolla, MO 65409, USA
- ²⁸ Physical Research Laboratory, Ahmedabad, India
- ²⁹ Department of Physics and Astronomy, University College London, London WC1E 6BT, UK
- ³⁰ Scuola Normale Superiore, Piazza dei Cavalieri 7, 56126 Pisa, Italy
- ³¹ Department of Chemistry “Giacomo Ciamician,” University of Bologna, Via F. Selmi 2, 40126 Bologna, Italy
- ³² Department of Chemistry, Koç University, Rumelifeneri Yolu, Sariyer, 34450, Istanbul, Turkey
- ¹ Observatoire de Paris, PSL University, Sorbonne Université, CNRS, LERMA, Paris, France
e-mail: marie-lise.dubernet@observatoiredeparis.obspm.fr
- ² Univ. Bordeaux, CNRS, Bordeaux INP, ISM, UMR 5255, 33400 Talence, France
- ³ Facultad de Ingeniería, Universidad Autónoma de Chile, Av. Pedro de Valdivia 425, 7500912 Providencia, Santiago, Chile
e-mail: otonieldenisalpizar@gmail.com
- ⁴ LSAMA, Department of Physics, Faculty of Sciences, Université Tunis El-Manar, 1060 Tunis, Tunisia
- ⁵ Marquette University, Chemistry Department, Milwaukee, WI 53233, USA
- ⁶ Department of Chemistry and Biochemistry, University of Nevada, Las Vegas, NV 89154, USA
- ⁷ KU Leuven, Department of Chemistry, Celestijnenlaan 200F, 3001 Leuven, Belgium

Appendix A: List of VAMDC cases and BASECOL associated molecules

Table A.1. List of BASECOL2023 molecules with the associated cases.

Cases	Description	Molecules
des	Diatomic cs	$^{36}\text{ArH}^+$, $^{36}\text{ArD}^+$, AlO^+ , CF^+ , CH^+ , CN^- , CO , CS H_2 , HD , HeH^+ , HCl , HF , KCl , NaH , NeH^+ , NO^+ , NS^+ , PN , SiH^+ , SiO , SiS
hunda	Diatomic os: hund's case a	CH ($X^2\Pi$), OH ($X^2\Pi$), OD ($X^2\Pi$), NO ($X^2\Pi$), SH ($X^2\Pi$), C_6H ($X^2\Pi$)
hundb ^(a)	Diatomic os: hund's case b	C_2^- ($X^2\Sigma_g^+$), CN ($X^2\Sigma^+$), ^{13}CN ($X^2\Sigma^+$), C^{15}N ($X^2\Sigma^+$), CO^+ ($X^2\Sigma^+$) C_4 ($X^3\Sigma_g^-$), H_2^+ ($X^2\Sigma_g^+$), NH ($X^3\Sigma^+$), O_2 ($X^3\Sigma_g^-$), SO ($X^3\Sigma^-$)
ltcs	linear triatomic cs	AlCN , AlNC , C_3 , C_2H^- , CO_2 , HCN , HNC , DCN , DNC , HCO^+ , HC^{17}O^+ , DCO^+ , HCP , HCS^+ , N_2H^+ , OCS
nlts	non-linear triatomic cs	D_2O , HDO , H_2O , H_2S , SiC_2 , SO_2
stcs	symmetric top cs	H_3^+ , H_3O^+ , NH_3 , ND_3 , CH_3CN , CH_3NC , CH_3OH
lpcs	linear polyatomic cs	CNCN , C_6H^- , HC_3N , HCCNC , HNCCC , HMgNC , NCCNH^+ , C_3O , C_3S , C_4H^- , C_5 , C_5O , C_5S
asymcs	asymmetric cs	H_2CO , HOCO^+ , C_3H_2 , NH_2D , ND_2H
asymos	asymmetric os	none
sphcs	spherical cs	none
sphos	spherical os	none
ltos	linear triatomic os	C_2H ($X^2\Sigma^+$), C_2D ($X^2\Sigma^+$), C_2N^- ($X^3\Sigma^-$), C_2O ($X^3\Sigma^-$), MgCN ($X^2\Sigma^+$), MgNC ($X^2\Sigma^+$)
lpos	linear polyatomic os	none
nlts	non-linear triatomic os	NH_2 (X^2B_1), CH_2 (X^3B_1), HCO

Notes. cs and os denote closed shell and open shell molecules. The molecules in blue have issues with the case assignment; this is explained in the text (see Sect. 2.3). ^(a) The hundb case includes intermediate coupling based on Hund's case b.

Appendix B: Tables of collisional datasets

This appendix provides tables describing the content of the BASECOL database. The names of the columns are self-explanatory, and each line in the sections corresponds to collisional dataset(s), as described in our technical publication. The current tables display some differences compared to Table 1 of the BASECOL2012 publication. The internal ID is not provided anymore because BASECOL2023 stores the successive versions of a given collisional dataset, and each version has a different ID. It is still possible to navigate through BASECOL with the IDs if the user keeps them in memory, as one ID corresponds to a unique couple collisional dataset/version. To date, we have removed the output flat files corresponding to the combination of collisional and spectroscopic data from the BASECOL interface; therefore, the tables do not include information related to those output files. In the following tables, the columns provide the following information: (1) the atomic or molecular target; (2) the perturbing projectile; (3) the energy levels for which rate coefficients are available: the symbols r, f, v, rv, rt, and h are used to denote rotational, fine, vibrational, ro-vibrational, ro-torsional, and hyperfine transitions, respectively (for example, r7 means that rate coefficients are available for the 7 lowest rotational levels); (4) temperature range in kelvin for which the rates have been calculated; (5 & 6) references to the papers describing, respectively, the collisional calculations and the potential energy surfaces; and (7) the year of publication. For Sect. 5, columns (2) and (6) have been removed. In the tables, the notation o/p-H₂ is a synthetic notation that corresponds to two datasets that have the same characteristics: number (except if marked otherwise) and type of levels, temperature range, and references; however one dataset is for a collision with ortho-H₂, and the other one with para-H₂.

Appendix B.1. Collisional data with electrons

Table B.1. List of collisional data with electrons.

Target	Levels	T (K)	Ref	Year
RECOMMENDED				
CH ⁺	r8	100-15000	Lim et al. (1999)	1999
H ₂ ⁺	v3	100-20000	Sarpal & Tennyson (1993)	1993
o/p-H ₂ ⁺	r2	100-10000	Faure & Tennyson (2001)	2001
o/p-H ₃ ⁺	r2/r4	100-10000	Faure & Tennyson (2003)	2003
o/p-H ₃ O ⁺	r4/r8	100-10000	Faure & Tennyson (2003)	2003
HeH ⁺	r3	100-20000	Rabadan et al. (1998)	1998
HeH ⁺	v3	100-20000	Rabadan et al. (1998)	1998
CO ⁺	r5	100-10000	Faure & Tennyson (2001)	2001
HCO ⁺	r3	100-10000	Faure & Tennyson (2001)	2001
NO ⁺	r5	100-10000	Faure & Tennyson (2001)	2001
o/p-H ₂ O	r18	100-8000	Faure et al. (2004)	2004
o/p-D ₂ O	r18	100-8000	Faure et al. (2004)	2004
o-H ₂ O	rv411	200 - 5000	Faure & Josselin (2008)	2008
p-H ₂ O	rv413	200 - 5000	Faure & Josselin (2008)	2008
HDO	r36 (a-type)	100-8000	Faure et al. (2004)	2004
HDO	r36 (b-type)	100-8000	Faure et al. (2004)	2004
HCN	r9	5-2000	Faure et al. (2007b)	2007
HCN	h10	10-100-1000	Faure et al. (2007b)	2007
HNC	r9	5-2000	Faure et al. (2007b)	2007
HNC	h10	10-1000	Faure et al. (2007b)	2007
DCN	r9	5-2000	Faure et al. (2007b)	2007
DCN	h10	10-100-1000	Faure et al. (2007b)	2007
DNC	r9	5-2000	Faure et al. (2007b)	2007
DNC	h10	10-100-1000	Faure et al. (2007b)	2007
SiO	r41	5-5000	Varambhia et al. (2009)	2009

Notes. This list of datasets has not changed since 2012 (see text).

Appendix B.2. Collisional data of atoms excited by heavy projectiles

Table B.2. List of collisional datasets of atoms and atomic ions/cations excited by heavy projectiles.

Target	Projectile	Levels	T (K)	Ref	PES Ref	Year
RECOMMENDED						
C	H	f3	5-1000	Abrahamsson et al. (2007)	Kalamos et al. (1999)	2007
C	o/p-H₂	f3	10-1200	Schröder et al. (1991)	Schröder et al. (1991)	1991
C	He	f3	5-350	Bergeat et al. (2018)	Bergeat et al. (2018)	2018
C⁺	H	f2	20-2000	Barinovs et al. (2005)	Barinovs & van Hemert (2004)	2005
C⁺	o/p-H₂	f2	5-500	Kłos et al. (2020a)	Kłos et al. (2020a)	2020
O	H	f3	50-1000	Vieira & Krems (2017)	Parlant & Yarkony (1999)	2017
O	H	f3	10-1000	Lique et al. (2017)	Dagdigian et al. (2016)	2017
O	He	f3	10-1000	Lique et al. (2017)	Lique et al. (2017)	2017
O	o/p-H₂	f3	10-1000	Lique et al. (2017)	Dagdigian et al. (2016)	2017
Si	He	f3	5-1000	Lique et al. (2018)	Lique et al. (2018)	2018
S	He	f3	5-1000	Lique et al. (2018)	Lique et al. (2018)	2018
Si ⁺	H	f2	20-2000	Barinovs et al. (2005)	Barinovs et al. (2005)	2005
NOT RECOMMENDED (outdated)						
O	H	f3	50-1000	Launay & Roueff (1977)	Launay & Roueff (1977)	1977
O	H	f3	50-1000	Abrahamsson et al. (2007)	Parlant & Yarkony (1999)	2007
O	o/p-H ₂	f3	20-1500	Jaquet et al. (1992)	Jaquet et al. (1992)	1992
C	H	f3	4-1000	Launay & Roueff (1977)	Yau & Dalgarno (1976)	1977
C	He	f3	10-150	Staemmler & Flower (1991)	Staemmler & Flower (1991)	1991

Notes. The species in bold correspond to the systems added since 2012.

Appendix B.3. Collisional data of diatomic species excited by heavy projectiles

Table B.3. List of neutral and ionic diatomic collisional data.

Target	Coll.	Levels	T (K)	Ref	PES Ref	Year
RECOMMENDED						
AlO⁺	He	r16	10-1005	Denis-Alpizar et al. (2018c)	Denis-Alpizar et al. (2018c)	2018
³⁶ ArH⁺	He	r11	5-300	Bop et al. (2016)	Bop et al. (2016)	2016
³⁶ ArH⁺	He	rv33	10-500	García-Vázquez et al. (2019)	García-Vázquez et al. (2019)	2019
³⁶ ArD⁺	He	r13	10-500	García-Vázquez et al. (2019)	García-Vázquez et al. (2019)	2019
C₂⁻	He	r9	5-100	Mant et al. (2020a)	Mant et al. (2020a)	2020
C₂⁻	Ar	r5	5-100	Mant et al. (2020c)	Mant et al. (2020c)	2020
C₂⁻	Ne	r5	5-100	Mant et al. (2020c)	Mant et al. (2020c)	2020
C₂⁻	He	v3	5-100	Mant et al. (2020b)	Mant et al. (2020b)	2020
C₂⁻	Ne	v3	5-100	Mant et al. (2020b)	Mant et al. (2020b)	2020
C₂⁻	Ar	v3	5-100	Mant et al. (2020b)	Mant et al. (2020b)	2020
CF⁺	He	r22	5-155	Denis-Alpizar et al. (2018a)	Denis-Alpizar et al. (2018a)	2019
CF⁺	He	h29	5-155	Denis-Alpizar et al. (2018a)	Denis-Alpizar et al. (2018a)	2019
CF⁺	p-H₂	r21	10-300	Denis-Alpizar & Rubayo-Soneira (2019)	Denis-Alpizar & Rubayo-Soneira (2019)	2019
CF⁺	p-H₂	r22	5-150	Desrousseaux et al. (2021)	Desrousseaux et al. (2019)	2021
CF⁺	o-H₂	r22	5-150	Desrousseaux et al. (2021)	Desrousseaux et al. (2019)	2021
CH⁺	He	r11	20-2000	Hammami et al. (2009)	Hammami et al. (2008a)	2009
CH⁺	He	r6	0.1-200	Turpin et al. (2010)	Turpin et al. (2010)	2010
CH	He	f30	10-300	Marinakis et al. (2015)	Marinakis et al. (2015)	2015
CH	He	h60	10-300	Marinakis et al. (2019)	Marinakis et al. (2015)	2019
CN⁻	o/p-H₂^(c)	r11	5-100	Klos & Lique (2011)	Klos & Lique (2011)	2011
CN⁻	He	r11	5-100	González-Sánchez et al. (2020)	González-Sánchez et al. (2020)	2020
CN⁻	Ar	r11	5-100	González-Sánchez et al. (2021)	González-Sánchez et al. (2021)	2021
CN⁻	He	v3	5-100	Mant et al. (2021)	Mant et al. (2021)	2021
CN	He	f41	5 - 350	Lique et al. (2010b)	Lique et al. (2010b)	2010
CN	He	h37	5 - 30	Lique & Klos (2011)	Lique et al. (2010b)	2011
CN^(a)	p-H₂	r18	5 - 300	Kalugina et al. (2013)	Kalugina et al. (2013)	2013
CN	o-H₂	r16	5 - 300	Kalugina et al. (2013)	Kalugina et al. (2013)	2013
CN^(b)	p-H₂	f25	5 - 100	Kalugina et al. (2013)	Kalugina et al. (2013)	2013
CN^(c)	p-H₂	f17	5 - 100	Kalugina et al. (2013)	Kalugina et al. (2013)	2013
CN	o-H₂	f17	5 - 100	Kalugina et al. (2013)	Kalugina et al. (2013)	2013
CN	o/p-H₂	h73	5 - 100	Kalugina & Lique (2015)	Kalugina et al. (2013)	2015
¹³ CN	p-H₂	h146	5 - 80	Flower & Lique (2015)	Kalugina et al. (2013)	2015
C¹⁵N	p-H₂	h34	5 - 150	Flower & Lique (2015)	Kalugina et al. (2013)	2015
CO	He	r15	5-500	Cecchi-Pestellini et al. (2002)	Heijmen et al. (1997)	2002
CO	He	v7	500-5000	Cecchi-Pestellini et al. (2002)	Heijmen et al. (1997)	2002
CO	H	r77	2-3000	Walker et al. (2015)	Song et al. (2013)	2015
CO	H	r8	5-100	Balakrishnan et al. (2002)	Keller et al. (1996)	2002
CO	H	r17	100-3000	Balakrishnan et al. (2002)	Keller et al. (1996)	2002
CO	H	rv350	2-3000	Song et al. (2015b)	Song et al. (2013)	2015
CO	H	v5	100-3000	Balakrishnan et al. (2002)	Keller et al. (1996)	2002
CO	o/p-H₂	r41	1-3000	Yang et al. (2010)	Jankowski & Szalewicz (1998)	2010
CO	o/p-H₂	r6	5-70	Wernli et al. (2006)	Jankowski & Szalewicz (1998)	2006
CO	o-H₂	r20	5-400	Flower (2001a)	Jankowski & Szalewicz (1998)	2001
CO	p-H₂	r29	5-400	Flower (2001a)	Jankowski & Szalewicz (1998)	2001
CO	p-H₂	rv45	1-300	Yang et al. (2016)	Yang et al. (2015b)	2016
CO	o-H₂	rv29	1-300	Yang et al. (2016)	Yang et al. (2015b)	2016
CO	o/p-t-H₂0	r11	10-100	Faure et al. (2020)	Kalugina et al. (2018)	2020
CS	He	r31	10-300	Lique et al. (2006b)	Lique et al. (2006b)	2006
CS	He	rv114	300-1500	Lique & Spielfiedel (2007)	Lique & Spielfiedel (2007)	2007
CS	o/p-H₂	rv42	5-1000	Yang et al. (2018a)	Yang et al. (2018a)	2018
CS	o/p-H₂	r30	5-305	Denis-Alpizar et al. (2018b)	Denis-Alpizar et al. (2012)	2018
HCl	He	r21	1-3000	Yang & Stancil (2014)	Murdachaew et al. (2004)	2014
HCl	He	r11	10-300	Lanza & Lique (2012)	Lanza & Lique (2012)	2012
HCl	He	h40	10-300	Lanza & Lique (2012)	Lanza & Lique (2012)	2012
HCl^(a)	p-H₂	r11	10-300	Lanza et al. (2014a)	Lanza et al. (2014b)	2014
HCl	o-H₂	r11	10-300	Lanza et al. (2014a)	Lanza et al. (2014b)	2014

Continued on next page.

Table B.3 – Continued from previous page.

Target	Coll.	Levels	T (K)	Ref	PES Ref	Year
HCl	o/p-H₂	h20	10-300	Lanza & Lique (2014)	Lanza et al. (2014b)	2014
HCl	H	r11	10-500	Lique & Faure (2017)	Bian & Werner (2000)	2017
HF	He	r21	1-3000	Yang et al. (2015a)	Moszynski et al. (1994)	2015
HF	He	r10	0.1-300	Reese et al. (2005)	Stoecklin et al. (2003)	2005
HF	o/p-H₂	r6	0.1-150	Guillon & Stoecklin (2012)	Guillon & Stoecklin (2012)	2012
HF	H	r9	10-500	Desrousseaux & Lique (2018)	Li et al. (2007)	2018
HF	o/p-t-H₂0	r7	10-150	Loreau et al. (2022)	Loreau et al. (2020)	2022
HD	He	r10	80-2000	Roueff & Zeppen (1999)	Muchnick & Russek (1994)	1999
HD	He	rv94	2-100	Nolte et al. (2011)	Muchnick & Russek (1994)	2011
HD	He	rv223	2-1000	Nolte et al. (2011)	Muchnick & Russek (1994)	2011
HD	o/p-H₂	r9	1-10000	Wan et al. (2019)	Patkowski et al. (2008)	2019
HD	o/p-H₂	rv24	100-1940	Flower & Roueff (1999a)	Schwenke (1988)	1999
HD	H	r11	10-1000	Desrousseaux et al. (2018)	Mielke et al. (2002)	2018
HD	H	r10	100-2000	Roueff & Flower (1999)	Boothroyd et al. (1996)	1999
HD	H	rv30	100-2080	Flower & Roueff (1999a)	Boothroyd et al. (1996)	1999
o-H ₂	He	rv23	100-6000	Flower et al. (1998)	Muchnick & Russek (1994)	1998
p-H ₂	He	rv26	100-6000	Flower et al. (1998)	Muchnick & Russek (1994)	1998
o-H ₂	o-H ₂	rv17	100-6000	Flower & Roueff (1999b)	Schwenke (1988)	1999
p-H ₂	o-H ₂	rv19	100-6000	Flower & Roueff (1999b)	Schwenke (1988)	1999
o-H ₂	p-H ₂	rv23	100-6000	Flower & Roueff (1998a)	Schwenke (1988)	1998
p-H ₂	p-H ₂	rv26	100-6000	Flower & Roueff (1998a)	Schwenke (1988)	1998
H ₂	H	r9	300-1500	Lique et al. (2012)	Mielke et al. (2002)	2012
o/p-H ₂	H	r3	100-1000	Forrey et al. (1997)	Boothroyd et al. (1996)	1997
o-H ₂	H	rv23	100-6000	Flower & Roueff (1998b)	Boothroyd et al. (1996)	1998
p-H ₂	H	rv26	100-6000	Flower & Roueff (1998b)	Boothroyd et al. (1996)	1998
HeH ⁺	H	r10	5-500	Desrousseaux & Lique (2020)	Ramachandran et al. (2009)	2020
KCl	p-H₂	r16	2-50	Sahnoun et al. (2018)	Sahnoun et al. (2018)	2018
NaH	He	r11	5-200	Bop et al. (2019b)	Bop et al. (2019b)	2019
NeH ⁺	He	r11	5-300	Bop et al. (2017)	Bop et al. (2017)	2017
NH	He	f25	5- 350	Toboła et al. (2011)	Cybulski et al. (2005)	2011
NH	He	f25	10- 350	Ramachandran et al. (2018)	Ramachandran et al. (2018)	2018
NO ⁺	He	r8	1-205	Denis-Alpizar & Stoecklin (2015)	Stoecklin & Voronin (2011)	2015
NO ⁺	p-H₂	r19	5-300	Cabrera-González et al. (2020)	Cabrera-González et al. (2020)	2020
NO	He	f98	10-500	Kłos et al. (2008)	Kłos et al. (2000)	2008
NO	p-H₂	h100	7-100	Ben Khalifa & Loreau (2021)	Kłos et al. (2017a)	2021
NS ⁺	He	r28	10-305	Cabrera-González et al. (2018)	Cabrera-González et al. (2018)	2018
NS ⁺	He	h40	10-305	Cabrera-González et al. (2018)	Cabrera-González et al. (2018)	2018
NS ⁺	o/p-H₂	r15	5-50	Bop et al. (2022a)	Bop et al. (2022a)	2019
NS ⁺	p-H₂	r24	5-100	Bop (2019)	Bop (2019)	2019
NS ⁺	p-H₂	h67	10-100	Bop (2019)	Bop (2019)	2019
OH	He	f46	5-350	Kłos et al. (2007)	Lee et al. (2000)	2007
OH	He	f44	5-350	Kalugina et al. (2014)	Kalugina et al. (2014)	2014
OH	He	h56	5-350	Marinakakis et al. (2019)	Kalugina et al. (2014)	2019
OH	o/p-H₂	f20	10-150	Kłos et al. (2017b)	Ma et al. (2014)	2017
OH	o/p-H₂	h24	10-150	Kłos et al. (2020b)	Ma et al. (2014)	2020
OD	o/p-H₂	h40	5-200	Dagdigian (2021a)	Ma et al. (2014)	2021
OH	H	h24	5-500	Dagdigian (2022a)	Alexander et al. (2004)	2022
O ₂	He	f36	5-350	Lique (2010)	Groenenboom & Struniewicz (2000)	2010
O ₂	o/p-H₂	r7	5-150	Kalugina et al. (2012a)	Kalugina et al. (2012a)	2012
PN	He	r31	10-300	Toboła et al. (2007)	Toboła et al. (2007)	2007
PN	p-H₂	r40	10-300	Najar et al. (2017)	Najar et al. (2017)	2017
SH	He	f60	5-350	Kłos et al. (2009)	Cybulski et al. (2000)	2009
SiH ⁺	He	r11	5-200	Nkem et al. (2009)	Nkem et al. (2009)	2009
SiO	He	r27	10-300	Dayou & Balança (2006)	Dayou & Balança (2006)	2006
SiO	He	rv246	250-10000	Balança & Dayou (2017)	Balança & Dayou (2017)	2017
SiO	o/p-H₂	rv47	5-1000	Yang et al. (2018b)	Yang et al. (2018b)	2018
SiO ^(d)	o/p-H₂	r21	5-300	Balança et al. (2018)	Balança et al. (2018)	2018
SiO ^(e)	o/p-H₂	r30	5-1000	Balança et al. (2018)	Balança et al. (2018)	2018
SiS	He	r26	10-200	Vincent et al. (2007)	Vincent et al. (2007)	2007
SiS	He	rv505	100-1500	Toboła et al. (2008)	Toboła et al. (2008)	2008
SiS	o/p-H₂	r41	5-300	Kłos & Lique (2008)	Kłos & Lique (2008)	2008

Continued on next page.

Table B.3 – Continued from previous page.

Target	Coll.	Levels	T (K)	Ref	PES Ref	Year
SO	He	f31	5-50	Lique et al. (2005)	Lique et al. (2005)	2005
SO	He	f91	60-300	Lique et al. (2006a)	Lique et al. (2005)	2006
SO	He	rv236	300-800	Lique et al. (2006c)	Lique et al. (2006c)	2006
SO	o/p-H ₂	rv273	5-3000	Price et al. (2021)	Yang et al. (2020)	2021
SO	p-H ₂	r31	5-50	Lique et al. (2007)	Lique et al. (2007)	2007
NOT RECOMMENDED (outdated)						
CH ⁺	He	r11	20-200	Hammami et al. (2008a)	Hammami et al. (2008a)	2008
CN	p-H ₂	h73	5 - 100	Kalugina et al. (2012b)	Kalugina et al. (2012b)	2012
CS	p-H ₂	r21	20-300	Turner et al. (1992)	Green & Chapman (1978)	1992
CS	p-H ₂	r13	10-100	Green & Chapman (1978)	Green & Chapman (1978)	1978
HCl	He	r8	10-300	Neufeld & Green (1994)	Neufeld & Green (1994)	1994
HCl	He	h28	10-300	Neufeld & Green (1994)	Neufeld & Green (1994)	1994
HD	o/p-H ₂	r9	50-500	Flower (1999a)	Schwenke (1988)	1999
SiO	p-H ₂	r21	20-300	Turner et al. (1992)	Turner et al. (1992)	1992
SiO	p-H ₂	r20	10-300	Dayou & Balança (2006)	Dayou & Balança (2006)	2006
SO	p-H ₂	f70	50-350	Green (1994)	Green (1994)	1994

Notes. The species in bold correspond to the systems added since 2012.^(a) The transitions among the first two levels of the projectile are provided. ^(b) In this dataset the projectile remains in its ground state. ^(c) The projectile's transitions $j=2-2$ and $j=2-0$ are provided. ^(d) This SiO dataset from Balança et al. (2018) uses the CC method. ^(e) This SiO dataset from Balança et al. (2018) uses the CS method.

Appendix B.4. Collisional data of triatomic species excited by heavy projectiles

Table B.4. List of triatomic collisional data.

Target	Coll.	Levels	T (K)	Ref	PES Ref	Year
RECOMMENDED						
AICN	He	r30	5-100	Hernández Vera et al. (2013)	Hernández Vera et al. (2013)	2013
AINC	He	r30	5-100	Hernández Vera et al. (2013)	Hernández Vera et al. (2013)	2013
AINC	p-H₂	r27	5-105	Urzúa-Leiva & Denis-Alpizar (2020)	Urzúa-Leiva & Denis-Alpizar (2020)	2020
C ₃	He	r6	5-15	Ben Abdallah et al. (2008)	Ben Abdallah et al. (2008)	2008
C₃	He	rv23	10-155	Stoeklin et al. (2015)	Denis-Alpizar et al. (2014)	2015
C₃	o/p-H₂	r11	5-50	Santander et al. (2022)	Santander et al. (2022)	2022
C₂H	He	h46	5-100	Spielfiedel et al. (2013)	Spielfiedel et al. (2013)	2013
C₂H	o/p-H₂	f41	5-500	Pirlot Jankowiak et al. (2023b)	Dagdgian (2018b)	2023
C₂H	o/p-H₂	h38	5-100	Pirlot Jankowiak et al. (2023b)	Dagdgian (2018b)	2023
C₂D	o/p-H₂	f31	5-200	Pirlot Jankowiak et al. (2023b)	Dagdgian (2018b)	2023
C₂D	o/p-H₂	h55	5-100	Pirlot Jankowiak et al. (2023b)	Dagdgian (2018b)	2023
C¹³CH	p-H₂	h98	5-100	Pirlot Jankowiak et al. (2023a)	Dagdgian (2018b)	2023
¹³CCH	p-H₂	h98	5-100	Pirlot Jankowiak et al. (2023a)	Dagdgian (2018b)	2023
C₂H⁻	He	r13	5-100	Dumouchel et al. (2012)	Dumouchel et al. (2012)	2012
C₂H⁻	He	r9	5-100	Gianturco et al. (2019)	Dumouchel et al. (2012)	2019
C₂N⁻	He	r16	5-100	Franz et al. (2020)	Franz et al. (2020)	2020
C₂O	He	f31	2-80	Khadri et al. (2022b)	Khadri et al. (2022b)	2022
o-CH₂	o/p-H₂	h69	5-300	Dagdgian (2021b)	Dagdgian (2021c)	2021
p-CH₂	o/p-H₂	r27	5-300	Dagdgian (2021b)	Dagdgian (2021c)	2021
CO₂	He	r21	4-300	Godard Palluet et al. (2022)	Godard Palluet et al. (2022)	2022
HCN	He	r26	5-500	Dumouchel et al. (2010)	Toczyłowski et al. (2001)	2010
HCN	p-H₂	r13	5-100	Hernández Vera et al. (2014)	Denis-Alpizar et al. (2013)	2014
HCN	o/p-H₂	r26	5-500	Hernández Vera et al. (2017)	Denis-Alpizar et al. (2013)	2017
HCN	o/p-H₂	h34	5 - 500	Goicoechea et al. (2022)	Denis-Alpizar et al. (2013)	2022
HCN	p-t-H₂0	r8	5 - 150	Dubernet & Quintas-Sánchez (2019)	Quintas-Sánchez & Dubernet (2017)	2019
HNC	He	r26	5-500	^c Dumouchel et al. (2010)	Sarrasin et al. (2010)	2010
HNC	o/p-H ₂	r11	5-100	Dumouchel et al. (2011)	Dumouchel et al. (2011)	2011
HNC	o/p-H₂	r26	5-500	Hernández Vera et al. (2017)	Dumouchel et al. (2011)	2017
HCO⁺	He	r6	5-100	Tonolo et al. (2021)	Tonolo et al. (2021)	2021
HCO⁺	o/p-H₂	r22	10-200	Denis-Alpizar et al. (2020)	Denis-Alpizar et al. (2020)	2020
DCO⁺	p-H₂	r22	10-200	Denis-Alpizar et al. (2020)	Denis-Alpizar et al. (2020)	2020
DCO ⁺	p-H ₂	h31	5-300	Pagani et al. (2012)	Monteiro (1985)	2012
HC¹⁷O⁺	p-H₂	h33	5-100	Tonolo et al. (2022)	Tonolo et al. (2022)	2022
HCO	o/p-H₂	h86	5-200	Dagdgian (2020b)	Dagdgian (2020d)	2020
HCP	p-H ₂	r11	10-70	Hammami et al. (2008c)	Hammami et al. (2008c)	2008
HCP	He	r16	20-200	Hammami et al. (2008b)	Hammami et al. (2008b)	2008

Continued on next page.

Table B.4 – Continued from previous page.

Target	Coll.	Levels	T (K)	Ref	PES Ref	Year
HCS⁺	He	r20	5-100	Dubernet et al. (2015)	Dubernet et al. (2015)	2015
HCS⁺	p-H₂	r31	5-100	Denis-Alpizar et al. (2022)	Quintas-Sánchez et al. (2021)	2022
o/p-H₂O	He	r10	2-3000	Yang et al. (2013)	Patkowski et al. (2002)	1993
o/p-H ₂ O	He	r45	20-2000	Green et al. (1993)	Maluendes et al. (1992)	1993
p-H ₂ O	o/p-H ₂	r45	5-1500	Daniel et al. (2011)	Valiron et al. (2008)	2011
o-H ₂ O	o-H ₂	r45	5-1500	Daniel et al. (2011)	Valiron et al. (2008)	2011
o-H ₂ O	p-H ₂	r45	5-1500	Dubernet et al. (2009)	Valiron et al. (2008)	2011
o/p-H₂O	p-H₂	r97	10-2000	Żóltowski et al. (2021)	Valiron et al. (2008)	2021
o/p-H ₂ O	o/p-t-H ₂	r45	20-2000	Faure et al. (2007a)	Valiron et al. (2008)	2007
o/p-H ₂ O	t-H ₂	rv411	200 - 5000	Faure & Josselin (2008)	Valiron et al. (2008)	2008
o/p-H₂O	H	r45	5-1500	Daniel et al. (2015)	Dagdikian & Alexander (2013)	2015
o/p-H₂O	t-H₂O	r59	100 - 800	Boursier et al. (2020)	Boursier et al. (2020)	2020
o/p-H₂O	t-H₂O	r21/r22	5 - 1000	Mandal & Babikov (2023a)	Jankowski & Szalewicz (2005)	2023
o/p-D₂O	p-H₂	r6	5-100	Faure et al. (2012)	Valiron et al. (2008)	2012
HDO	He	r34	50-500	Green (1989)	Palma et al. (1988)	1989
HDO	p-t-H₂	r30	5 - 300	Faure et al. (2012)	Valiron et al. (2008)	2012
HDO	o-H₂	r30	5 - 300	Faure et al. (2012)	Valiron et al. (2008)	2012
o/p-H₂S	o/p-H₂	r19	5 - 500	Dagdikian (2020a)	Dagdikian (2020c)	2020
MgCN	He	r36	5-100	Hernández Vera et al. (2013)	Hernández Vera et al. (2013)	2013
MgCN	He	f41	5-100	Hernández Vera et al. (2013)	Hernández Vera et al. (2013)	2013
MgNC	He	r36	5-100	Hernández Vera et al. (2013)	Hernández Vera et al. (2013)	2013
MgNC	He	f41	5-100	Hernández Vera et al. (2013)	Hernández Vera et al. (2013)	2013
o/p-NH₂	o/p-H₂	r15	10-150	Bouhafs et al. (2017a)	Li & Guo (2014)	1978
N ₂ H ⁺	He	r7	5-50	Daniel et al. (2005)	Daniel et al. (2004)	2005
N ₂ H ⁺	He	h55	5-50	Daniel et al. (2005)	Daniel et al. (2004)	2005
N₂H⁺	p-H₂	r26	5-500	Balança et al. (2020)	Spielfiedel et al. (2015)	2020
N₂H⁺	p-H₂	h64	5-70	Lique et al. (2015)	Spielfiedel et al. (2015)	2015
OCS	p-H ₂	r13	10-100	Green & Chapman (1978)	Green & Chapman (1978)	1978
OCS	He	r27	10-150	Flower (2001b)	Higgins & Klemperer (1999)	2001
OCS	Ar	r21	5-400	Chefai et al. (2018)	Chefai et al. (2018)	2018
o-SiC ₂	He	r40	25-125	Chandra & Kegel (2000)	Palma & Green (1987)	2000
SO ₂	He	r50	25-125	Green (1995)	Palma (1987)	1995
SO ₂	o/p-H ₂	r31	5-30	Cernicharo et al. (2011)	Spielfiedel et al. (2009)	2011
NON-RECOMMENDED (mostly outdated)						
C₂H	o/p-H₂	h30	10-300	Dagdikian (2018a)	Dagdikian (2018b)	2018
C₂H	p-H₂	f17	5-80	Dumouchel et al. (2017)	Najar et al. (2014)	2017
C₂H	p-H₂	h34	2-80	Dumouchel et al. (2017)	Najar et al. (2014)	2017
C₂D	p-H₂	h49	2-80	Dumouchel et al. (2017)	Najar et al. (2014)	2017
C₂D	p-H₂	f17	5-80	Dumouchel et al. (2017)	Najar et al. (2014)	2017
HCN	He	h13	10-30	Monteiro & Stutzki (1986)	Green & Thaddeus (1974)	1986
HCN	He	r8	5-100	Green & Thaddeus (1974)	Green & Thaddeus (1974)	1974
HCN	p-H ₂	h31	5 - 100	Ben Abdallah et al. (2012)	Ben Abdallah et al. (2012)	2012
HCO ⁺	p-H ₂	r21	5-390	Flower (1999b)	Monteiro (1985)	1999
HCS ⁺	He	r11	10-60	Monteiro (1984)	Monteiro (1984)	1984
o/p-H ₂ O	o/p-H ₂	r5	20-140	Phillips et al. (1996)	Phillips et al. (1994)	1996
N ₂ H ⁺	He	r7	5-40	Green (1975)	Green (1975)	1975

Notes. For H₂O collisional data: t-H₂, t-H₂O means that H₂, H₂O are thermalised over para and ortho species (you should refer to the papers to see how this is done); o/p-t-H₂ or o/p-t-H₂O means that H₂ or H₂O is thermalised over para-species only or ortho-species only. The species in bold correspond to the systems added since 2012.

Appendix B.5. Collisional data of species with more than 3 atoms excited by heavy projectiles

Table B.5. List of collisional datasets for molecules with more than three atoms.

Target	Coll.	Levels	T (K)	Ref	PES Ref	Year
RECOMMENDED						
o/p c-C ₃ H ₂	He	r47/48	30-120	Chandra & Kegel (2000)	Green et al. (1987)	2000
C ₃ O	He	r31	5-150	Bop et al. (2022b)	Khadri & Hammami (2019)	2022
C ₃ S	He	r11	2-25	Sahnoun et al. (2020)	Sahnoun et al. (2020)	2020
C ₄	He	f30	5-50	Lique et al. (2010a)	Lique et al. (2010a)	2010
C ₄ H ⁻	o/p-H ₂	r30	5-100	Balança et al. (2021)	Balança et al. (2021)	2021
C ₅	He	r15	5-300	Chefai et al. (2021)	Chefai et al. (2021)	2021
C ₅ H ⁺	He	r16	5-100	Khadri et al. (2023)	Khadri et al. (2023)	2023
C ₅ O	He	r31	5-150	Bop et al. (2022b)	Khadri et al. (2022a)	2022
C ₅ S	He	r51	2-100	Khadri et al. (2020)	Khadri et al. (2020)	2020
C ₆ H	He	f122	5-100	Walker et al. (2018)	Walker et al. (2018)	2018
C ₆ H	He	h52	5-100	Walker et al. (2018)	Walker et al. (2018)	2018
C ₆ H ⁻	He	r11	5-100	Walker et al. (2017)	Walker et al. (2016)	2017
C ₆ H ⁻	o/p-H ₂	r31	5-100	Walker et al. (2017)	Walker et al. (2016)	2017
p-CH ₃ CN	He	r75	7-100	Ben Khalifa et al. (2023)	Ben Khalifa et al. (2022)	2023
o-CH ₃ CN	He	r52	7-100	Ben Khalifa et al. (2023)	Ben Khalifa et al. (2022)	2023
p-CH ₃ NC	He	r63	7-100	Ben Khalifa et al. (2023)	Ben Khalifa et al. (2022)	2023
o-CH ₃ NC	He	r66	7-100	Ben Khalifa et al. (2023)	Ben Khalifa et al. (2022)	2023
A/E-CH ₃ OH	He	rt150	10-400	Rabli & Flower (2011)	Pottage et al. (2002)	2011
A-CH ₃ OH	He	r256, vt=0	10-200	Rabli & Flower (2010b)	Pottage et al. (2002)	2010
A-CH ₃ OH	He	r256, vt=1	10-200	Rabli & Flower (2010b)	Pottage et al. (2002)	2010
A-CH ₃ OH	He	r256, vt=2	10-200	Rabli & Flower (2010b)	Pottage et al. (2002)	2010
E-CH ₃ OH	He	r256, vt=0	10-200	Rabli & Flower (2010b)	Pottage et al. (2002)	2010
E-CH ₃ OH	He	r256, vt=1	10-200	Rabli & Flower (2010b)	Pottage et al. (2002)	2010
E-CH ₃ OH	He	r256, vt=2	10-200	Rabli & Flower (2010b)	Pottage et al. (2002)	2010
A-CH ₃ OH	p-H ₂	r256, vt=0	10-200	Rabli & Flower (2010a)	Pottage et al. (2004)	2010
A-CH ₃ OH	p-H ₂	r256, vt=1	10-200	Rabli & Flower (2010a)	Pottage et al. (2004)	2010
A-CH ₃ OH	p-H ₂	r256, vt=2	10-200	Rabli & Flower (2010a)	Pottage et al. (2004)	2010
E-CH ₃ OH	p-H ₂	r256, vt=0	10-200	Rabli & Flower (2010a)	Pottage et al. (2004)	2010
E-CH ₃ OH	p-H ₂	r256, vt=1	10-200	Rabli & Flower (2010a)	Pottage et al. (2004)	2010
E-CH ₃ OH	p-H ₂	r256, vt=2	10-200	Rabli & Flower (2010a)	Pottage et al. (2004)	2010
CNCN	He	r30	5-150	Ndaw et al. (2021)	Ndaw et al. (2021)	2021
o/p-H ₂ CO	He	r40/r41	10-300	Green (1991)	Garrison & Lester (1975)	1991
o-H ₂ CO	o/p-H ₂	r10	5-100	Troscompt et al. (2009)	Troscompt et al. (2009)	2009
p-H ₃ O ⁺	o/p-H ₂	r21	10-300	Demes et al. (2022)	Demes et al. (2020)	2022
o-H ₃ O ⁺	o/p-H ₂	r11	10-300	Demes et al. (2022)	Demes et al. (2020)	2022
HC ₃ N	He	r11	10-40	Wernli et al. (2007a,b)	Wernli et al. (2007a,b)	2007
HC ₃ N	o/p-H ₂	r38	10-300	Faure et al. (2016)	Wernli et al. (2007a)	2016
HC ₃ N	t-p-H ₂	r38	10-300	Faure et al. (2016)	Wernli et al. (2007a)	2016
HC ₃ N	o/p-H ₂	h61	10-100	Faure et al. (2016)	Wernli et al. (2007a)	2016
HC ₃ N	t-p-H ₂	h61	10-100	Faure et al. (2016)	Wernli et al. (2007a)	2016
HNCCC	o/p-H ₂	r30	5-80	Bop et al. (2021)	Bop et al. (2019a)	2021
HCCNC	o/p-H ₂	r30	5-80	Bop et al. (2021)	Bop et al. (2019a)	2021
HMgNC	He	r14	5-200	Amor et al. (2021)	Amor et al. (2021)	2021
HOCO ⁺	He	r25	10-30	Hammami et al. (2007)	Hammami et al. (2004)	2007
HNCCN ⁺	He	r11	5-100	Bop et al. (2018)	Bop et al. (2018)	2018
o/p-NH ₃	He	r22/16	5-300	Machin & Roueff (2005)	Hodges & Wheatley (2001)	2005
o/p-NH ₃	o/p-H ₂	r33/62	100-500	Demes et al. (2023)	Maret et al. (2009)	2023
o/p-NH ₃	p-t-H ₂	r33/62	100-500	Demes et al. (2023)	Maret et al. (2009)	2023
o/p-NH ₃	o/p-H ₂	r17/34	10-200	Bouhafs et al. (2017b)	Maret et al. (2009)	2017
o/p-NH ₃	p-H ₂	r6/10	5-100	Maret et al. (2009)	Maret et al. (2009)	2009
o/p-NH ₃	H	r17/34	10-200	Bouhafs et al. (2017b)	Li & Guo (2014)	2017
o/p-NH ₂ D	He	r9	5-100	Machin & Roueff (2006)	Hodges & Wheatley (2001) ^(a)	2006
o/p-NH ₂ D	p-H ₂	r79	5-300	Daniel et al. (2014)	Maret et al. (2009)	2014
o/p-ND ₂ H	He	r9	5-100	Machin & Roueff (2007)	Hodges & Wheatley (2001) ^(a)	2007
o/p-ND ₂ H	p-H ₂	r16	5-50	Daniel et al. (2016)	Maret et al. (2009)	2016
o/p/meta-ND ₃	p-H ₂	r16/r9/r9	5-50	Daniel et al. (2016)	Maret et al. (2009)	2016

NON-RECOMMENDED (mostly outdated)

Continued on next page.

Table B.5 – Continued from previous page.

Target	Coll.	Levels	T (K)	Ref	PES Ref	Year
HC ₃ N	He	r21	10-80	Green & Chapman (1978)	Green & Chapman (1978)	1978
HC ₃ N	p-H ₂	r51	10-100	Wernli et al. (2007a,b)	Wernli et al. (2007a,b)	2007
o-NH ₃	p-H ₂	r9	15-300	Danby et al. (1986)	Danby et al. (1986)	1986
p-NH ₃	p-H ₂	r16	15-300	Danby et al. (1987)	Danby et al. (1986)	1987
o/p-NH ₃	p-H ₂	r17/24	15-300	Danby et al. (1988)	Danby et al. (1986)	1988

Notes. The species in bold correspond to the systems added since 2012. ^(a)The PES of [Hodges & Wheatley \(2001\)](#) was adapted by [Machin & Roueff \(2006\)](#) and [Machin & Roueff \(2007\)](#) to account for the isotopic shift.

Appendix C: Figures

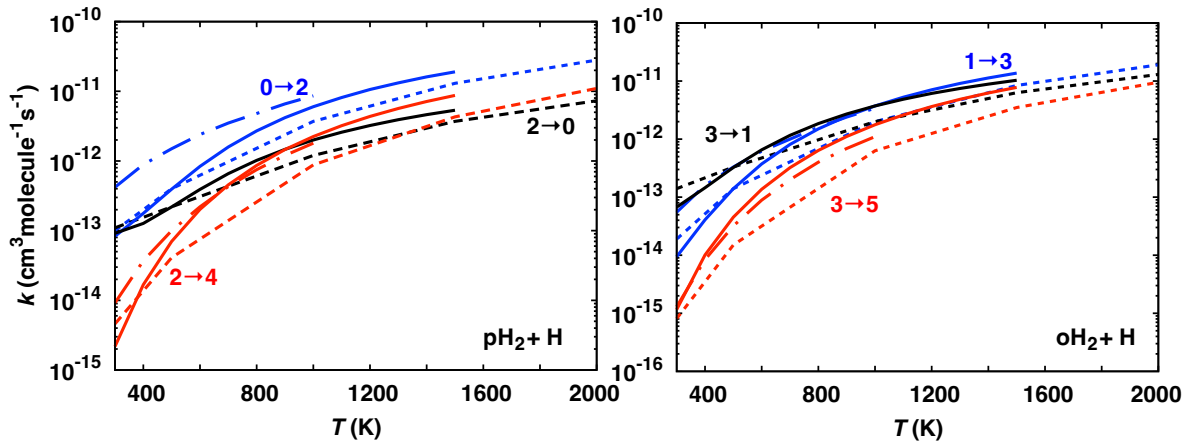


Fig. C.1. Rotational rate coefficients of para-H₂ and ortho-H₂ by H reported by [Forrey et al. \(1997\)](#) (dash-dotted lines), [Flower & Roueff \(1998b\)](#) (dashed lines), and [Lique et al. \(2012\)](#) (solid lines). Rotational transitions of H₂ are labelled as $j_i \rightarrow j_f$.

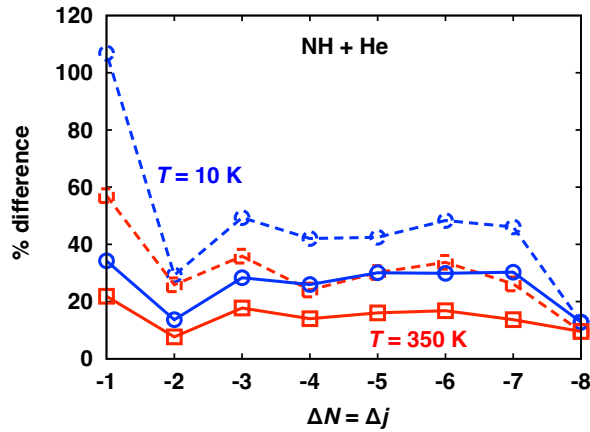


Fig. C.2. Average percentage difference (solid lines) and maximum percentage difference (dashed lines) between the rate coefficients reported by [Toboła et al. \(2011\)](#) and [Ramachandran et al. \(2018\)](#) for the $\Delta N = \Delta j$ transitions in the NH+He collision at 10 K (circles) and 350 K (squares).

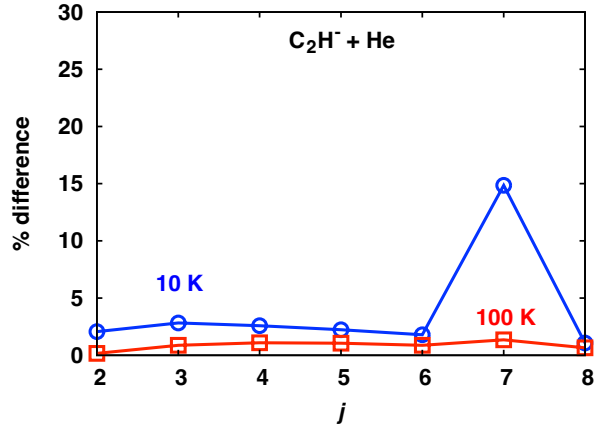


Fig. C.3. Percentage difference between rate coefficients reported by Dumouchel et al. (2012) and Gianturco et al. (2019) for the $\Delta j = 2$ transitions (strong propensity was found for this transition) in the $\text{C}_2\text{H}^+ + \text{He}$ collision at 10 K (circles) and 100 K (squares).

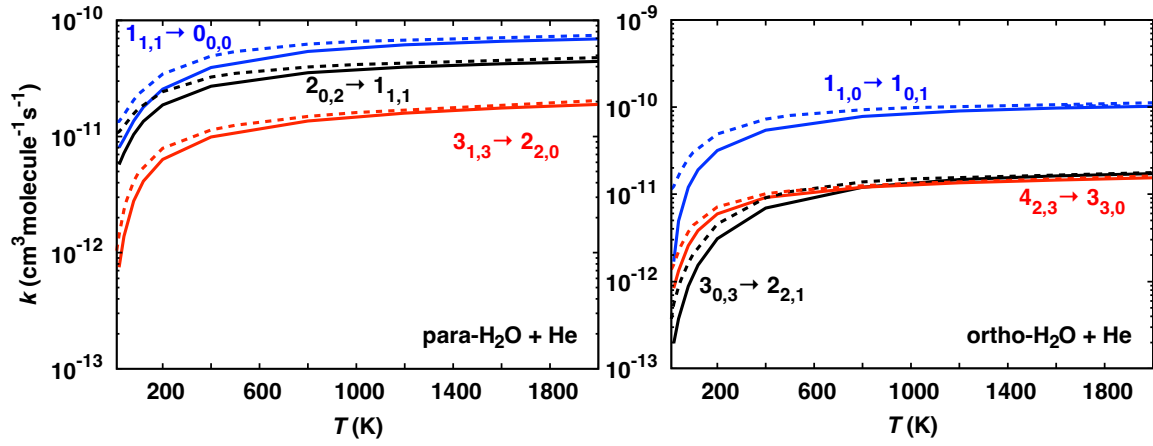


Fig. C.4. Rotational rate coefficient of para- H_2O and ortho- H_2O by He reported by Green et al. (1993) (solid lines), and Yang et al. (2013) (dashed lines). Rotational transitions of H_2O are labelled as $j_{K_a, K_c}^i \rightarrow j_{K_a, K_c}^f$.

C.5 Hyperfine excitation of NH and ND by molecular hydrogen: Rate coefficients and astrophysical modeling

Hyperfine excitation of NH and ND by molecular hydrogen

Rate coefficients and astrophysical modeling

Paul Pirlot Jankowiak¹ , François Lique¹ , and Javier R. Goicoechea² 

¹ Univ. Rennes, CNRS, IPR (Institut de Physique de Rennes) – UMR 6251, 35000 Rennes, France
e-mail: paul.pirlot@univ-rennes.fr; francois.lique@univ-rennes.fr

² Instituto de Física Fundamental (CSIC), Calle Serrano 121-123, 28006 Madrid, Spain

Received 6 December 2023 / Accepted 8 January 2024

ABSTRACT

The NH and ND radicals are of key importance in the comprehension of nitrogen chemistry and the enhancement of deuterated molecules in the interstellar medium. Observations by space telescopes yield spectra that can resolve the fine and hyperfine structure of these radicals, a consequence of the electronic and magnetic interactions of nitrogen, hydrogen, and deuterium nuclei. Accurate rate coefficients, induced by collisions with H₂, are required to interpret spectra of these radicals. We report the first rate coefficients for fine and hyperfine transitions of NH and ND in collision with both ortho- and para-H₂. Based on a recent four-dimensional potential energy surface, fine-structure resolved cross sections and rate coefficients are computed with the time-independent close-coupling method over a temperature range of 5–300 K. Our calculations include the first 25 energy levels of NH and ND. Hyperfine resolved cross sections and rate coefficients are determined using the infinite-order sudden (IOS) approximation between 5 and 200 K for NH and 100 K for ND. We consider the first 71 and 105 energy levels of NH and ND, respectively. General propensity rules are discussed. We found a significant isotopic substitution effect in the rate coefficients. In addition, the rate coefficients for collisions with H₂ are larger than those with He by a factor of up to 5, leading to lower critical densities for collisional excitation with H₂ than He. The impact of the new set of collisional data has been investigated in simple radiative transfer models of the NH emission seen toward the Orion Bar and the ejecta of the η Carinae binary star. We observed significant differences by a factor of 5 between the presently determined column densities for NH compared to those from the literature using He as a collider.

Key words. astrochemistry – molecular data – molecular processes – radiative transfer – scattering

1. Introduction

Nitrogen hydrides are key species in the formation of complex nitrogen-bearing molecules observed in the interstellar medium (ISM; Gerin et al. 2016). An accurate determination of the abundances of these species is essential for understanding nitrogen chemistry, which remains a subject of ongoing exploration (Bacmann et al. 2016). Among nitrogen hydrides, the NH radical is of particular interest since it is an important intermediate in the synthesis of heavier molecules (Bacmann et al. 2010; Gerin et al. 2016). Observations of NH were first reported in comets (Swings et al. 1941) and stellar atmospheres (Schmitt 1969; Lambert & Beer 1972). Meyer & Roth (1991) detected NH in the ISM in ζ Per and HD 27778 diffuse clouds through the A³ Π –X³ Σ UV absorption band. The high rotational constant of NH leads to rotational lines in the submillimeter frequency range (≥ 1 THz), making ground-based observations not suitable for detecting rotational transitions. Thanks to the Infrared Space Observatory (ISO), Cernicharo et al. (2000) and Goicoechea et al. (2004) reported the first detection of far-infrared fine-structure components $2_3 \rightarrow 1_2$ and $2_2 \rightarrow 1_1$ toward the Sgr B2 dense molecular cloud.

From the first detection of NH, large divergences between the determined abundances from observations and those predicted by chemical models were pointed out (Wagenblast et al. 1993). The much higher spectral resolution observations with the heterodyne receiver HIFI on board the *Herschel* space telescope led to the suggestion that the formation of NH in cold

molecular clouds and prestellar cores may occur through dissociative recombination of N₂H⁺ (Hily-Blant et al. 2010; Dislaire et al. 2012; Le Gal et al. 2014) in addition to the well known N⁺ + H₂ reaction followed by dissociative recombination. Various models confirmed the poor understanding of the NH abundance and other nitrogen hydrides despite the many observations in the solar-mass Class 0 protostar IRAS 16293-2422 (Bacmann et al. 2010; Hily-Blant et al. 2010), in the H II region G10.6-0.4 (W31; Persson et al. 2012), the star-forming region W49N (Persson et al. 2012), the binary star η Carinae, and the Homunculus nebula (Gull et al. 2020). Goicoechea & Roncero (2022) recently detected NH emission lines toward the Orion Bar photodissociation region (PDR), where their modeling based on state-specific rate coefficients calculations for the N + H₂(ν) \rightarrow NH + H reaction lead to an enhancement of the NH column density by a factor ~ 25 compared to chemical models using thermal rate coefficients and showing better agreement with observations. The study revealed the importance of UV-pumped vibrationally excited H₂ in the formation of NH in strongly UV-irradiated molecular clouds.

The deuterium fractionation is also a fundamental parameter of the study of the ISM. It is well known that the abundance ratio between a deuterated molecule and its hydrogenated counterpart can deviate by several orders of magnitude from the elemental ratio [D]/[H] $\sim 2 \times 10^{-5}$ (Linsky et al. 2006) depending on the molecule and on the source. High degrees of molecular deuteration have been observed in various cold environments (Ceccarelli et al. 1998; Caselli et al. 2003; Bacmann et al. 2003).

In this context, the study of the ND radical is of interest to infer the deuterium enhancement in the chemistry of nitrogen hydrides. Bacmann et al. (2010) reported the first detection of ND in IRAS 16293-2422 resolving the hyperfine multiplet of the $1 \rightarrow 0$ rotational line and deriving an abundance ratio $[\text{ND}]/[\text{NH}] \geq 30\%$. Bacmann et al. (2016) also detected ND toward the 16293E prestellar core and confirmed the high degree of deuteration of the NH radical.

At low densities, the determination of molecular abundances cannot be achieved assuming local thermodynamic equilibrium (LTE). The computation of reliable state-to-state rate coefficients of NH and ND induced by collisions with the main collider H_2 in molecular clouds is required. Interactions of the molecular electronic spin and nuclear spin of the nitrogen and the hydrogen or deuterium atoms to the molecular rotation leads to a large number of energy levels to consider in scattering calculations. In addition, the inclusion of the internal structure of H_2 requires a large number of channels to consider in quantum dynamical calculations that are not achievable with current computational resources. There are presently no collisional data reported about fine and hyperfine resolved rate coefficients for NH and ND in collision with both ortho- and para- H_2 . Because of this lack of data, Bacmann et al. (2016) used scaled NH/ND-He hyperfine rate coefficients computed by Dumouchel et al. (2012) to model molecular spectra. In addition, Goicoechea & Roncero (2022) scaled fine-structure NH-He rate coefficients from Toboła et al. (2011). These estimations of NH- H_2 rate coefficients may not be accurate enough, especially in the case of light hydrides. Hyperfine line-overlap and opacity effects may also lead to subtle radiative effects and anomalous hyperfine line emission (Goicoechea et al. 2022).

To date, only a few investigations have reported hyperfine resolved rate coefficients for collisions involving a molecule possessing two nonzero nuclear spins such as N_2H^+ -He (Daniel et al. 2005), NH/ND-He (Dumouchel et al. 2012), or $^{13}\text{CCH}/^{13}\text{CH}$ -para- H_2 (Pirlot Jankowiak et al. 2023). Because NH is detected in both cold and warm astrophysical environments, it is essential to take into account explicitly the internal structure of H_2 in the scattering calculations. This work aims to fill this objective by providing fine and hyperfine resolved rate coefficients for NH and ND in collisions with molecular hydrogen (both ortho- and para- H_2). Fine-structure calculations are achieved with the close-coupling (CC) method, while the infinite-order sudden (IOS) approximation (Faure & Lique 2012; Lanza & Lique 2014) is employed to overcome the computational challenges posed by the inclusion of the hyperfine structure in the scattering calculations. The paper is organized as follows. Section 2 presents the potential energy surface (PES) used in this work. Details about the treatment for the ND isotopolog is also highlighted. Section 3 describes the scattering formalism for the obtention of both fine- and hyperfine-structure resolved rate coefficients. Fine-structure results are presented and discussed. Then hyperfine resolved rate coefficients are presented. Section 4 presents an illustration of the impact of the new computed rate coefficients in a simple radiative transfer modeling under non-LTE conditions. A summary of the work and our conclusions are presented in Sect. 5.

2. Potential energy surface

In this work we use the four-dimensional PES computed by Pirlot Jankowiak et al. (2021, hereafter Paper I). Ab initio calculations were done for 33 516 geometries with the explicitly

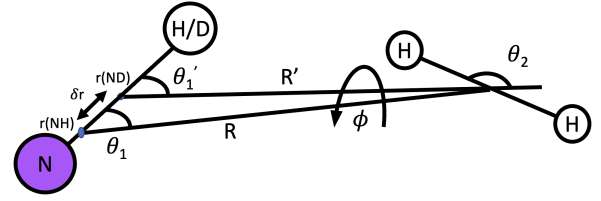


Fig. 1. Description of the NH- H_2 and ND- H_2 complexes in Jacobi coordinates. Unprimed and primed coordinates relate to NH and ND, respectively.

correlated coupled cluster single, double, and a perturbative treatment of triple excitations [RCCSD(T)-F12a] (Knizia et al. 2009) using the MOLPRO software (Werner et al. 2020). The augmented correlation-consistent polarized valence triple zeta (aug-cc-pVTZ) basis set (Dunning 1989) was used and the counterpoise scheme of Boys & Bernardi (1970) was considered to take into account the basis set superposition error.

This PES is provided as a function of the Jacobi coordinate system. The origin of this coordinate system lies at the center of mass of NH, with the intermolecular separation between NH and H_2 centers of mass denoted as the vector \mathbf{R} , aligned along the z -axis. The rotational motion of NH around the R axis is described by the angle θ_1 , while the angles (θ_2, ϕ) specify the orientation of H_2 (see Fig. 1).

In this PES, both NH and H_2 are treated as rigid rotors. We consider the internuclear distances taken in the average of the vibrational ground state for both species, with $r_{\text{NH}} = 1.958a_0$ and $r_{\text{HH}} = 1.449a_0$ (Huber & Herzberg 1979).

To make this PES suitable for time-independent quantum scattering calculations, the analytical representation of the potential was done in terms of bispherical harmonics, given by

$$V(R, \theta_1, \theta_2, \phi) = \sum_{l_1 l_2 l} v_{l_1 l_2 l}(R) A(\theta_1, \theta_2, \phi) \quad (1)$$

$$A(\theta_1, \theta_2, \phi) = \sqrt{\frac{2l+1}{4\pi}} \left[\begin{pmatrix} l_1 & l_2 & l \\ 0 & 0 & 0 \end{pmatrix} P_{l_1 0}(\theta_1) P_{l_2 0}(\theta_2) \right. \\ \left. + 2 \sum_{m=1}^{\min(l_1, l_2)} \begin{pmatrix} l_1 & l_2 & l \\ m & -m & 0 \end{pmatrix} \right. \\ \left. \times P_{l_1 m}(\theta_1) P_{l_2 m}(\theta_2) \cos(m\phi) \right]. \quad (2)$$

Here P_{lm} denotes associated Legendre polynomials, and (\dots) represents 3j-Wigner symbols; l_1 , l_2 , and l are defined such that $|l_1 - l_2| < l < l_1 + l_2$. Then, the expansion coefficients $v_{l_1 l_2 l}(R)$ are determined through a least-squares fitting procedure, setting $l_1^{\text{max}} = 10$ and $l_2^{\text{max}} = 4$ and resulting in a total of 86 terms for subsequent scattering calculations.

The global minimum was found to be $D_e = 149.10 \text{ cm}^{-1}$ corresponding to a linear geometry characterized by $R = 6.30a_0$, $\theta_1 = 180^\circ$, $\theta_2 = 0^\circ$, and $\phi = 0^\circ$, where one hydrogen atom is oriented toward the nitrogen end. Additionally, a secondary minimum was observed for a T-shaped geometry with $R = 6.77a_0$, $\theta_1 = 0^\circ$, $\theta_2 = 90^\circ$, and $\phi = 0^\circ$, exhibiting a well depth $D_e = 109.52 \text{ cm}^{-1}$. This PES has undergone validation, displaying good agreement between bound state calculations and experimental measurements from Fawzy et al. (2005).

The deuteration of NH yields the ND molecule by a displacement of the center of mass of $\delta r = -0.1149a_0$ toward the

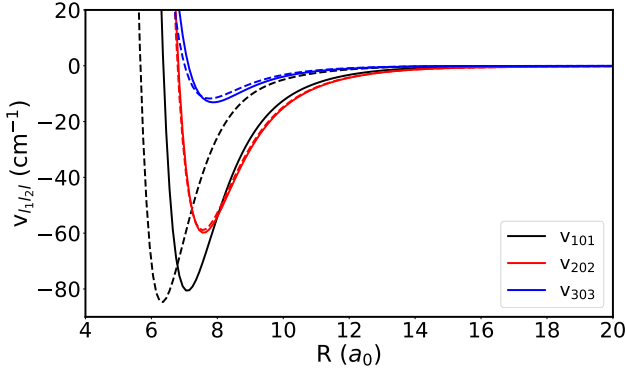


Fig. 2. First expansion coefficients $v_{l_1 l_2 l}(R)$ for the NH–H₂ (solid) and ND–H₂ (dashed) collisional systems.

deuterium end. To assess the interaction potential for the ND–H₂ complex, we introduce new coordinates (R' , θ'_1) and transform the primary isotopolog coordinates as follows:

$$R' = \sqrt{R^2 + \delta r^2 + 2R\delta r \cos(\theta_1)}, \quad (3)$$

$$\theta'_1 = \cos^{-1} \left(\frac{R \cos(\theta_1) - \delta r}{R'} \right). \quad (4)$$

Within the rigid rotor approximation, we assume that the bond lengths for NH and ND remain identical. Notably, we found that the transformation of the (θ_2 , ϕ) angles have no impact on the dynamics calculations and was not necessary. In order to obtain an analytical representation suitable for scattering calculations, a Gauss-Legendre quadrature procedure was performed for 588 geometries from the transformed NH–H₂ PES with $l_1^{\max} = 10$ and $l_2^{\max} = 4$.

Figure 2 displays the first radial coefficients $v_{l_1 l_2 l}(R)$ for both NH–H₂ and ND–H₂ complexes. The most significant difference arises from the v_{101} term. This term exhibits a lower magnitude for the ND–H₂ PES than the NH–H₂ PES, indicating a more pronounced odd anisotropy for the NH–H₂ complex. This effect was already seen for the NH/ND–He collisional systems in the study of Dumouchel et al. (2012). We anticipate that the incorporation of these radial coefficients in scattering calculations will lead to differences in cross sections between the two isotopologs.

3. Scattering calculations

3.1. Fine-structure excitation

The NH and ND radicals are both open-shell molecules, and possess a nonzero electronic spin $S = 1$. This is coupled to the spin-free rotational angular momentum n_1 such that

$$\mathbf{j}_1 = \mathbf{n}_1 + \mathbf{S},$$

where j_1 is the total rotational angular momentum of the target. Then, in the $^3\Sigma^-$ ground electronic state, the NH and ND rotational levels are split by spin-rotation and spin-spin interaction. In the intermediate coupling scheme, the wave function can be defined for $j_1 \geq 1$ as (Gordy & Cook 1984)

$$\begin{aligned} |F_1 j_1 m\rangle &= \cos(\alpha) |j_1 - S, j_1 m\rangle + \sin(\alpha) |j_1 + S, j_1 m\rangle \\ |F_2 j_1 m\rangle &= |j_1, j_1 m\rangle \\ |F_3 j_1 m\rangle &= -\sin(\alpha) |j_1 - S, j_1 m\rangle + \cos(\alpha) |j_1 + S, j_1 m\rangle \end{aligned} \quad (5)$$

Table 1. Spectroscopic constants of NH and ND radicals in their $^3\Sigma^-$ electronic state.

Parameters ^(a)	NH ^(b)	ND ^(c)
B_0	16.343	8.782
D_0	1.703×10^{-4}	4.880×10^{-4}
γ_0	-5.485×10^{-2}	-2.947×10^{-2}
λ_0	0.920	0.919
μ_D	1.39 ^(d)	1.39

Notes. ^(a)The values of the parameters are given in cm^{-1} . ^(b)Flores-Mijangos et al. (2004). ^(c)Takano et al. (1998). ^(d)The value of μ_D is given in Debye (Keun Park & Sun 1993).

where $|n_1, j_1 m\rangle$ denotes the wave function in a pure Hund's case (b), and α is the angle arising from the diagonalization of the molecular Hamiltonian. In the pure Hund's case (b) limit ($\alpha \rightarrow 0$), the F_i labels are associated with $n_1 = j_1 - S$ for F_1 and $n_1 = j_1 + S$ for F_3 . For simplicity, fine-structure levels are labeled as n_{1, j_1} corresponding to the pure Hund's case (b) limit, although all calculations were done in the intermediate coupling scheme. In the CC approach, the NH or ND angular momentum couples with the rotational angular momentum j_2 of the H₂ collider to form the resultant sum j_{12} . This couples to the orbital angular momentum L to yield the total angular momentum J :

$$\mathbf{j}_{12} = \mathbf{j}_1 + \mathbf{j}_2 \quad \mathbf{J} = \mathbf{j}_{12} + \mathbf{L}.$$

This is the general approach used to compute fine-structure resolved cross sections with the CC procedure.

By the resolution of the CC equations, it is possible to determine fine-structure state-to-state cross sections defined as

$$\sigma_{n_1 j_1 j_2 \rightarrow n'_1 j'_1 j'_2}^{\text{CC}} = \frac{\pi}{k_{n_1 j_1 j_2}^2 [j_1] [j_2]} \sum_{JLL} [J] |T_{n_1 j_1 j_2 j_2 L, n'_1 j'_1 j'_2 j'_2 L'}^J|^2, \quad (6)$$

where $k_{n_1 j_1 j_2}^2$ is the wave vector of the initial state, $[X] \equiv (2X + 1)$ and $T_{n_1 j_1 j_2 j_2 L, n'_1 j'_1 j'_2 j'_2 L'}^J$ are the T -matrix elements (i.e., the solutions of the CC equations). The rate coefficient from an initial state ($n_1 j_1 j_2$) to a final state ($n'_1 j'_1 j'_2$) can be obtained by integrating the CC cross section in Eq. (6) over a Maxwell-Boltzmann distribution of the collisional energy E_c :

$$\begin{aligned} k_{n_1 j_1 j_2 \rightarrow n'_1 j'_1 j'_2}^{\text{CC}}(T) &= \left(\frac{8}{\pi \mu (k_B T)^3} \right)^{1/2} \\ &\times \int_0^\infty \sigma_{n_1 j_1 j_2 \rightarrow n'_1 j'_1 j'_2}^{\text{CC}}(E_c) E_c e^{-E_c/k_B T} dE_c \end{aligned} \quad (7)$$

with μ the reduced mass of the collisional system and k_B the Boltzmann constant.

Details of the scattering calculations can be found in Appendix A. The spectroscopic parameters used in fine-structure calculations for NH and ND are summarized in Table 1. The scattering calculations were done using the HIBRIDON package of programs (Alexander et al. 2023).

3.2. Results

Figures 3 and 4 illustrate the temperature dependence of the fine-structure resolved rate coefficients for NH and ND in collision with ortho- and para-H₂. The magnitude of the rate coefficients

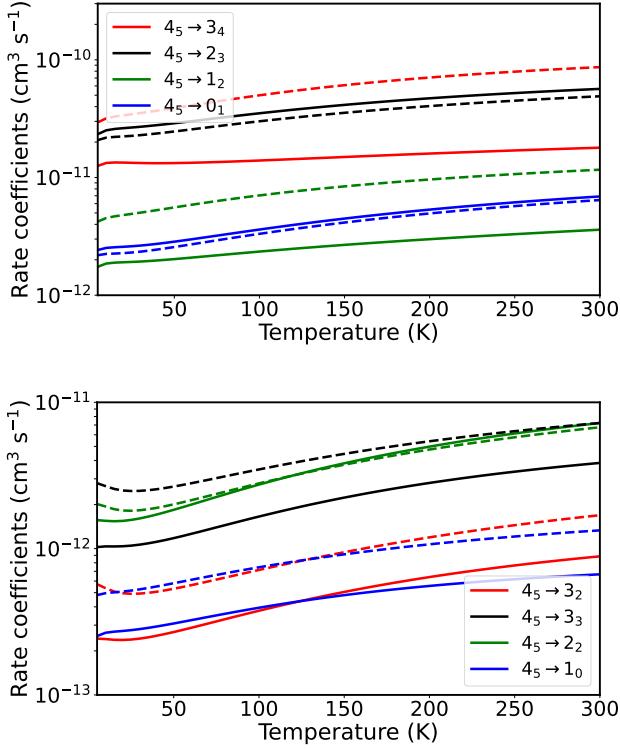


Fig. 3. Temperature dependence of fine-structure resolved de-excitation rate coefficients for NH in collision with para-H₂ (solid) and ortho-H₂ (dashed). The fine-structure conserving transitions ($\Delta n_1 = \Delta j_1$) are presented in the top panel; the fine-structure changing transitions ($\Delta n_1 \neq \Delta j_1$) are shown in the bottom panel.

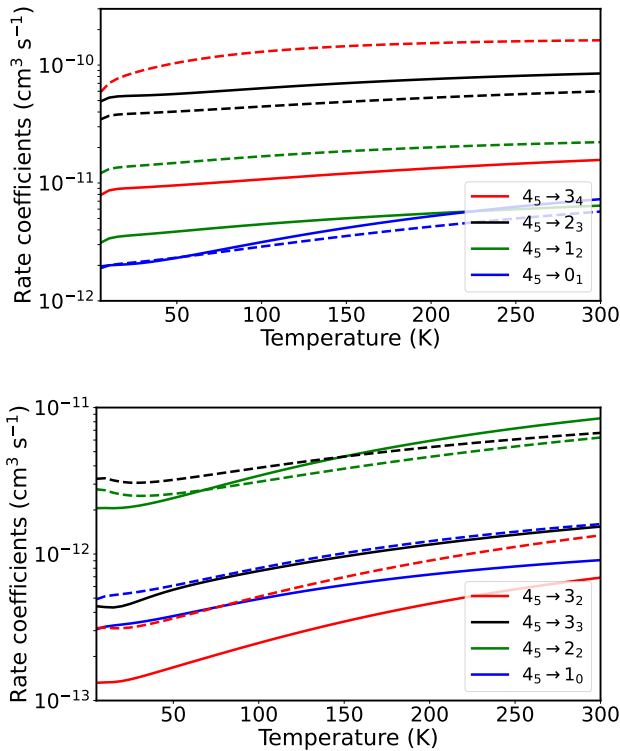


Fig. 4. Temperature dependence of fine-structure resolved de-excitation rate coefficients for ND in collision with para-H₂ (solid) and ortho-H₂ (dashed). The fine-structure conserving transitions ($\Delta n_1 = \Delta j_1$) are presented in the top panel; the fine-structure changing transitions ($\Delta n_1 \neq \Delta j_1$) are shown in the bottom panel.

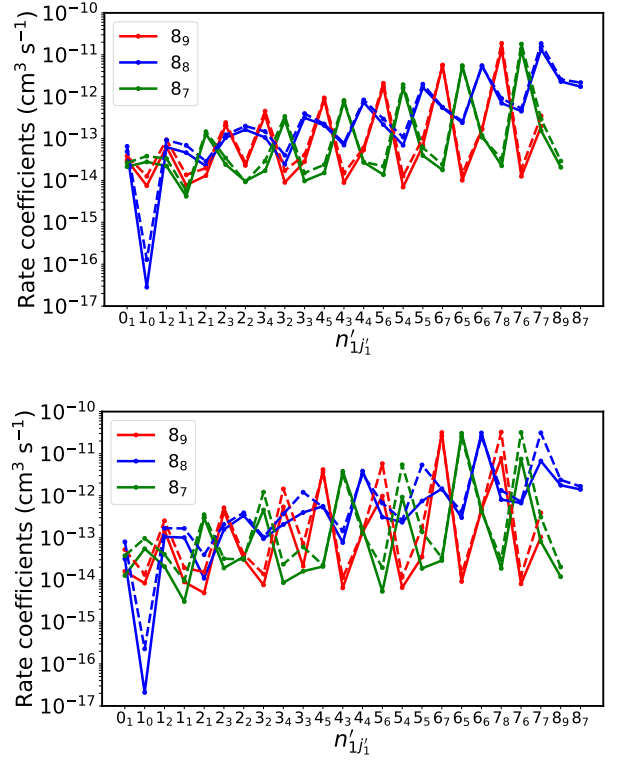


Fig. 5. Fine-structure resolved rate coefficients at 50 K for NH (top) and ND (bottom) de-excitations out of the $n_{1,j_1} = 8_{j_1}$ rotational level.

can vary up to a factor of 3 between low and high temperatures. In addition, most of the rate coefficients for transitions induced by ortho-H₂ are larger than those induced by para-H₂ by a factor of 3–10. This behavior arises due to the contributions of radial coefficients $v_{l_1 l_2 l}$ to the coupling between energy levels in scattering calculations. Specifically, ortho-H₂ collisions involve coefficients with $l_2 = 0, 2$, whereas para-H₂ collisions only consider coefficients with $l_2 = 0$. The ortho-H₂ collisions are then characterized by enhanced anisotropy for $j_2 > 0$ in the PES and tend to yield larger rate coefficients than for para-H₂ collisions, a well-known trend in neutral collisional systems involving H₂ (Kalugina & Lique 2015; Desrousseau et al. 2021; Demes et al. 2023).

As previously reported in Paper I, NH–ortho-H₂ collisions exhibit larger rate coefficients for odd Δn_1 transitions compared to NH–para-H₂ collisions. This is related to the magnitude of the v_{121} radial coefficient, which has a greater intensity compared to those with $l_2 = 0$ and provides a larger contribution in the coupling terms of the CC equations. A similar behavior is also observed for collisions involving ND.

Furthermore, Figs. 3 and 4 display that fine-structure conserving transitions ($\Delta n_1 = \Delta j_1$) dominate over fine-structure changing transitions ($\Delta n_1 \neq \Delta j_1$). Alexander & Dagdigan (1983) already investigated this propensity rule. This rule implies that the electronic spin acts as a spectator during collisions, conserving its projection, due to the absence of electronic spin dependence in the potential energy surface. The rule can be seen clearly in Fig. 5.

It is interesting to have a look at the impact of the isotopic substitution on the rate coefficients. Figure 6 compares rate coefficients for NH and ND in collisions with ortho- and para-H₂. The ND transitions exhibit rate coefficients that are nearly three

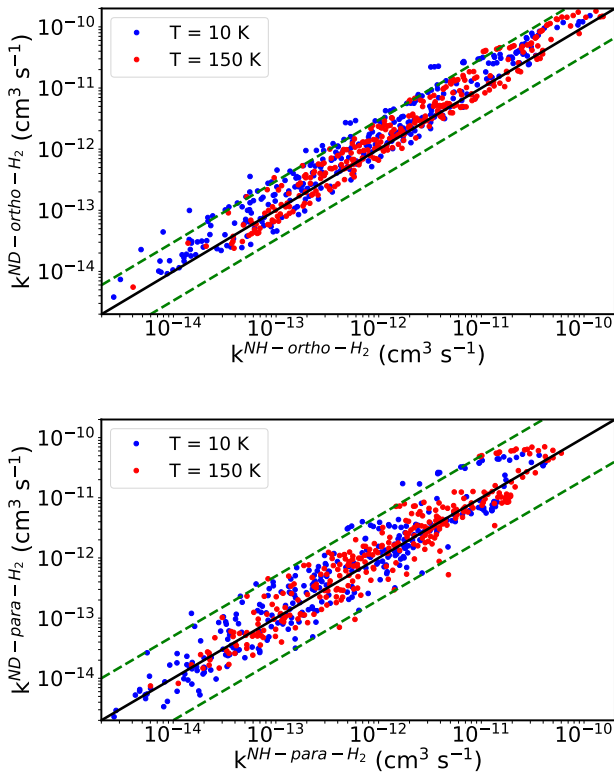


Fig. 6. Systematic comparison between NH and ND rate coefficients at 10 and 150 K. The top panel shows ortho-H₂ collisions, where the green dashed lines quantify deviations by a factor of 3. The bottom panel is related to para-H₂ collisions and the green dashed lines present differences of a factor of 5.

times larger than NH transitions for ortho-H₂ collisions, a disparity that jumps to a factor of 5 for para-H₂ collisions. This discrepancy arises from the displacement of the center of mass between NH-H₂ and ND-H₂ PESs and differences in NH and ND spectroscopic parameters (see Table 1). Similar isotopic differences have been observed in various collisional systems, particularly with light molecules such as NH/ND-He (Dumouchel et al. 2012) and OH/OD-H₂ (Dagdigian 2021). These differences become less pronounced for heavier molecules, as seen in HCO⁺/DCO⁺-H₂ (Denis-Alpizar et al. 2020).

When collisional data involving H₂ are not available, it is customary to use He as a proxy to estimate rate coefficients for the para-H₂(*j*₂ = 0) collider, based on the assumption that their cross sections are similar. Both He and para-H₂(*j*₂ = 0) possess two valence electrons and have a spherical shape. For NH or ND collisions, a mass-scaling relation can be used to model para-H₂ with He

$$k_{X\text{-para-H}_2}(T) \sim \left(\frac{\mu_{X\text{-He}}}{\mu_{X\text{-para-H}_2}} \right)^{1/2} k_{X\text{-He}}(T), \quad (8)$$

where X is either NH or ND.

Figure 7 displays the discrepancies between fine-structure rate coefficients computed in this work with those available from Dumouchel et al. (2012).¹ Specifically, we compare NH and ND

¹ Ramachandran et al. (2018) published more recent data about the NH-He complex that are consistent with those of Dumouchel et al. (2012), but did not provide fine-structure rate coefficients for the ND-He complex.

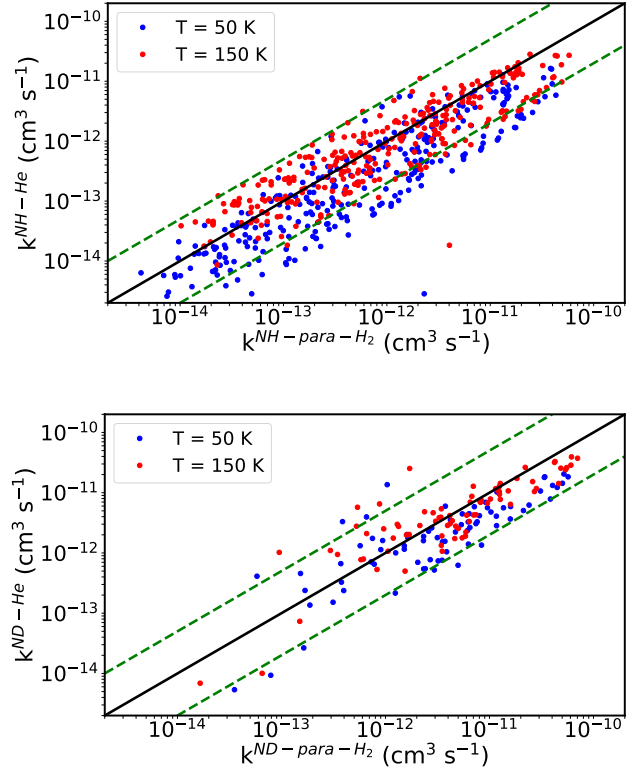


Fig. 7. Comparison between the present fine-structure resolved rate coefficients for NH and ND in collision with para-H₂ and those in collision with He done by Dumouchel et al. (2012). The dashed lines represent deviations of the data of a factor of 5.

in collision with para-H₂ and scaled-He. In the case of NH, substantial differences are observed. The para-H₂ rate coefficients are larger than those of He by more than a factor of 5, particularly at low temperatures (*T* ≤ 50 K). Some transitions can exhibit larger deviations even at higher temperatures, showing a strong temperature-dependence between the datasets. A similar behavior is observed in the case of ND. This could be explained by the contrasts in the interaction potentials. The PES calculated for NH-He by Cybulski et al. (2005) presents a well depth smaller by a factor ~7 compared to the NH-H₂ PES computed in Paper I. This difference leads to larger cross sections for para-H₂ collisions. As a conclusion, He is an unsuitable template for para-H₂(*j*₂ = 0) collisions, necessitating the explicit computation of these rate coefficients.

3.3. Hyperfine-structure excitation

Additional energy splittings occur for NH and ND due to the presence of the nuclear spins of the hydrogen, deuterium, and nitrogen atoms, *I*_H = 1/2, *I*_D = 1, and *I*_N = 1, respectively. These spins couple to the rotational quantum number, as

$$\mathbf{F}_1 = \mathbf{j}_1 + \mathbf{I}_{\text{H/D}} \quad \mathbf{F} = \mathbf{F}_1 + \mathbf{I}_{\text{N}}$$

with *F*₁ and *F* being the rotational quantum numbers including nuclear spins of the targeted isotopolog. Such splittings are generally small (10⁻³-10⁻⁴ cm⁻¹) due to the magnitude of the possible electric quadrupole and magnetic moments. In the case of NH, each rotational level (*n*₁ > 2) possesses 18 hyperfine components except for *n*₁ = 0,1,2, which have respectively 5, 13, and 17 hyperfine energy levels. For ND these splittings lead to 27 levels for *n*₁ > 2 and 7, 19, and 26 levels for *n*₁ = 0,1,2.

Collisional excitation between two molecules is a computational challenge, particularly in calculations involving open-shell molecules with two nonzero nuclear spins. The computational cost of scattering calculations becomes prohibitive with our current computational resources, due to the extensive number of channels that must be considered. For NH and ND, our objective is to provide hyperfine rate coefficients up to 200 K, taking into account energy levels up to 326 cm^{-1} for NH and up to 100 K with energy levels up to 176 cm^{-1} for ND. Achieving this goal entails accounting for 71 energy levels in the case of NH and 105 for ND. To account both the nuclear spins of the target and the internal structure of the collider, the IOS limit is tested and used.

3.3.1. Infinite-order sudden limit approach

It is possible to estimate state-to-state hyperfine resolved rate coefficients only by considering the fine-structure rate coefficient ($k_{n_1 j_1 j_2 \rightarrow n'_1 j'_1 j'_2}^{\text{CC}}$) out of the fundamental energy level. Based on several works (Alexander 1982; Orlikowski 1985; Lanza & Lique 2014), the hyperfine resolved rate coefficient for a $^3\Sigma$ electronic state molecule in collision with ortho- and para- H_2 can be written for an initial state $i = (n_1 j_1 F_1 F_j)$ to a final one $f = (n'_1 j'_1 F'_1 F'_j)$ as (see details in Appendix B)

$$k_{i \rightarrow f}^{\text{IOS-p}}(T) = [n_1 n'_1 j_1 j'_1 F_1 F'_1 F_j F'_j] \sum_{\lambda_1, \lambda_2} \frac{[\lambda_1]}{\lambda_1 + 1} \begin{pmatrix} n'_1 & \lambda_1 & n_1 \\ 0 & 0 & 0 \end{pmatrix}^2 \times \begin{pmatrix} j'_2 & \lambda_2 & j_2 \\ 0 & 0 & 0 \end{pmatrix}^2 \left\{ \begin{matrix} n'_1 & n_1 & \lambda_1 \\ j_1 & j'_1 & S \end{matrix} \right\}^2 \times \left\{ \begin{matrix} j_1 & j'_1 & \lambda_1 \\ F'_1 & F_1 & I_X \end{matrix} \right\}^2 \left\{ \begin{matrix} F_1 & F'_1 & \lambda_1 \\ F' & F & I_N \end{matrix} \right\}^2 \times k_{100 \rightarrow \lambda_1 + 1, \lambda_1, \lambda_2}^{\text{CC}}(T) \quad (9)$$

$$k_{i \rightarrow f}^{\text{IOS-o}}(T) = [n_1 n'_1 j_1 j'_1 F_1 F'_1 F_j F'_j] \sum_{\lambda_1, \lambda_2} \frac{[\lambda_1]}{\lambda_1 + 1} \frac{[\lambda_2]}{\lambda_2 + 1} \times \begin{pmatrix} n'_1 & \lambda_1 & n_1 \\ 0 & 0 & 0 \end{pmatrix}^2 \begin{pmatrix} j'_2 & \lambda_2 & j_2 \\ 0 & 0 & 0 \end{pmatrix}^2 \left\{ \begin{matrix} n'_1 & n_1 & \lambda_1 \\ j_1 & j'_1 & S \end{matrix} \right\}^2 \times \left\{ \begin{matrix} j_1 & j'_1 & \lambda_1 \\ F'_1 & F_1 & I_X \end{matrix} \right\}^2 \left\{ \begin{matrix} F_1 & F'_1 & \lambda_1 \\ F' & F & I_N \end{matrix} \right\}^2 \times k_{101 \rightarrow \lambda_1 + 1, \lambda_1, \lambda_2 + 1}^{\text{CC}}(T), \quad (10)$$

where $[abc \dots] \equiv (2a+1)(2b+1)(2c+1) \dots$, λ_1, λ_2 are chosen so that $|j_1 - j'_1| \leq \lambda_1 \leq j_1 + j'_1$ and $|j_2 - j'_2| \leq \lambda_2 \leq j_2 + j'_2$, $X \equiv \text{H}$ or D . Moreover, IOS-p stands for collisions with para- H_2 , whereas IOS-o stands for ortho- H_2 collisions. Equations (9) and (10) are used considering NH and ND in a pure Hund's case (b) limit. It should be noted that the rate coefficient can be replaced by the cross section for IOS calculations. Equations (9) and (10) can also be used by considering de-excitations rate coefficients through the detailed balance:

$$k_{100 \rightarrow \lambda_1 + 1, \lambda_1, \lambda_2}^{\text{CC}}(T) = [\lambda_1][\lambda_2] k_{\lambda_1 + 1, \lambda_1, \lambda_2 \rightarrow 100}^{\text{CC}}(T), \quad (11)$$

$$k_{101 \rightarrow \lambda_1 + 1, \lambda_1, \lambda_2 + 1}^{\text{CC}}(T) = \frac{[\lambda_1][\lambda_2 + 1]}{3} k_{\lambda_1 + 1, \lambda_1, \lambda_2 + 1 \rightarrow 101}^{\text{CC}}(T). \quad (12)$$

It is worth noting that the gap between hyperfine energy levels remains relatively small compared to the collisional energies involved. Consequently, it is reasonable to anticipate that the

IOS limit can provide reliable predictions for hyperfine resolved transitions. Then, the scaling relation can be used, first introduced by Neufeld & Green (1994, hereafter NG) as

$$k_{n_1 j_1 F_1 F_j \rightarrow n'_1 j'_1 F'_1 F'_j}^{\text{NG}}(T) = \frac{k_{n_1 j_1 F_1 F_j \rightarrow n'_1 j'_1 F'_1 F'_j}^{\text{IOS}}(T)}{k_{n_1 j_1 j_2 \rightarrow n'_1 j'_1 j'_2}^{\text{IOS}}(T)} k_{n_1 j_1 j_2 \rightarrow n'_1 j'_1 j'_2}^{\text{CC}}(T). \quad (13)$$

This relation is constructed so that the summation of the rate coefficients over the final hyperfine labels for a given transition gives the CC fine-structure rate coefficient:

$$\sum_{F'_1 F'_j} k_{n_1 j_1 F_1 F_j \rightarrow n'_1 j'_1 F'_1 F'_j}^{\text{NG}}(T) = k_{n_1 j_1 j_2 \rightarrow n'_1 j'_1 j'_2}^{\text{CC}}(T). \quad (14)$$

One can see that using Eq. (13) implies that the calculation of quasi-elastic transitions (i.e., $n_1 = n'_1$, $j_1 = j'_1$ and with $F_1 \neq F'_1$ and $F \neq F'$) requires the determination of fine-structure elastic transitions. However, these transitions are usually difficult to converge. In the following we provide quasi-elastic transitions without the NG correction and only using the IOS limit through Eqs. (9) and (10). In addition, the presence of 3j and 6j Wigner coefficients involves strict propensity rules. In particular, the 3j coefficient sets all hyperfine rate coefficients to zero for the case where $n_1 = n'_1 = 0$. The corresponding rate coefficients are only nonvanishing for hyperfine elastic transitions, which are beyond the scope of this work.

3.3.2. Validation of the IOS approach

The IOS approximation described previously can be tested and compared with the recoupling approach. This reference method, for hyperfine treatment can be found in detail in Alexander & Dagdigian (1985), among others. This comparison is applied to the NH- H_2 and ND- H_2 collisional systems, but taking into account only the nuclear spin of the hydrogen (or the deuterium). The IOS approach was tested for several cross sections at two different collisional energies.

Figure 8 displays a comparison of cross sections computed using the NG correction and the recoupling approach for NH and ND in collision with both ortho- and para- H_2 . Quasi-elastic transitions, calculated with the IOS approximation, are also included in these plots. Of all the tested collisional systems, the figure shows that most of the largest transitions match almost perfectly those obtained with the recoupling approach. It is possible to quantify the discrepancies between methods by introducing the weighted mean error factor (WMEF; Loreau et al. 2018),

$$\text{WMEF} = \frac{\sum_{i \rightarrow f} \sigma_{i \rightarrow f}^{\text{rec}} r_i}{\sum_i \sigma_{i \rightarrow f}^{\text{rec}}}, \quad (15)$$

with $\sigma_{i \rightarrow f}^{\text{rec}}$ being the hyperfine cross section obtained with the recoupling approach, $r_i = \max(\sigma_{i \rightarrow f}^{\text{rec}} / \sigma_{i \rightarrow f}^{\text{NG}}, \sigma_{i \rightarrow f}^{\text{NG}} / \sigma_{i \rightarrow f}^{\text{rec}})$. Larger discrepancies are observed for low collisional energies, while most transitions exhibit better agreement at higher energies. For para- H_2 collisions, the WMEFs remain of the same order of magnitude for NH and ND, regardless of the energy. The inclusion of quasi-elastic transitions has minimal impact in this case. Among all the tested collisional systems, ortho- H_2 collisions display the most noticeable deviations, mostly due to the inclusion of quasi-elastic transitions, which are among the most divergent transitions in terms of intensity. However, it is interesting to note that, with the exception of these transitions, the NG correction performs surprisingly well in the case of ortho- H_2 collisions.

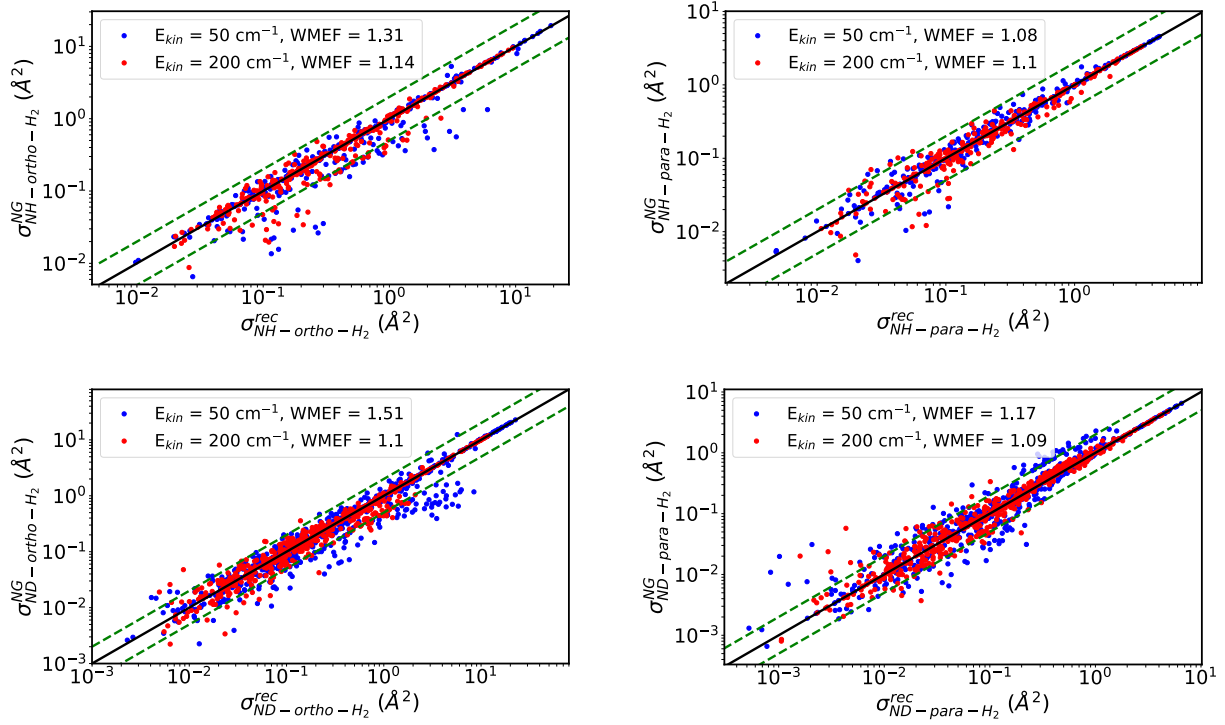


Fig. 8. Comparison between the NG correction and the recoupling approach for NH (top) and ND (bottom) cross sections for collisions with ortho- (left) and para-H₂ (right). Cross sections are displayed for collisional energies of 50 and 200 cm⁻¹. Quasi-elastic transitions computed in the IOS limit are also present. The dashed lines represent deviations of the data of a factor of 2.

3.3.3. NH–H₂ and ND–H₂ rate coefficients

Figure 9 displays the propensity rules discussed in Sect. 3.1 and applied here to the hyperfine rate coefficients computed through the IOS approach using Eqs. (9), (10), and (13). Among all collisional systems, the strong propensity rule governing $\Delta n_1 = \Delta j_1 = \Delta F_1 = \Delta F$ transitions is found. This rule can be explained by vector coupling arguments. Given the independence of nuclear spins from the potential, they remain spectators during the collision, and they cannot be reoriented. As in Sect. 3.1, ortho-H₂ collisions are governed by the odd Δn_1 propensity rule, except for NH for $\Delta F_1 \neq \Delta F$ transitions, where this rule stands for para-H₂ collisions. These trends are well known for various types of systems having one or two nuclear spins (Daniel et al. 2004; Dumouchel et al. 2012; Kalugina & Lique 2015; Lique et al. 2016; Klos et al. 2020; Lara-Moreno et al. 2021; Ndaw et al. 2021; Godard Palluet & Lique 2024).

4. Rotational excitation of NH in the ISM

Detections of several NH fine-structure lines in the ejecta of the massive binary star η Carinae have been reported by Gull et al. (2020). Additionally, Goicoechea & Roncero (2022) detected the submillimeter $1_2 \rightarrow 0_1$ fine-structure line in the Orion Bar PDR. To our knowledge, these are the only two sources where NH rotational lines are observed in emission, while all other previous detections report absorption lines. In both studies, modeling based on accurate NH–H₂ collisional data was not possible because of the lack of these data. In the absence of rate coefficients for NH–H₂ collisions, astrophysical modeling relied on He collisional data using the scaling relation given by Eq. (8) or based on crude estimation when even these data are missing.

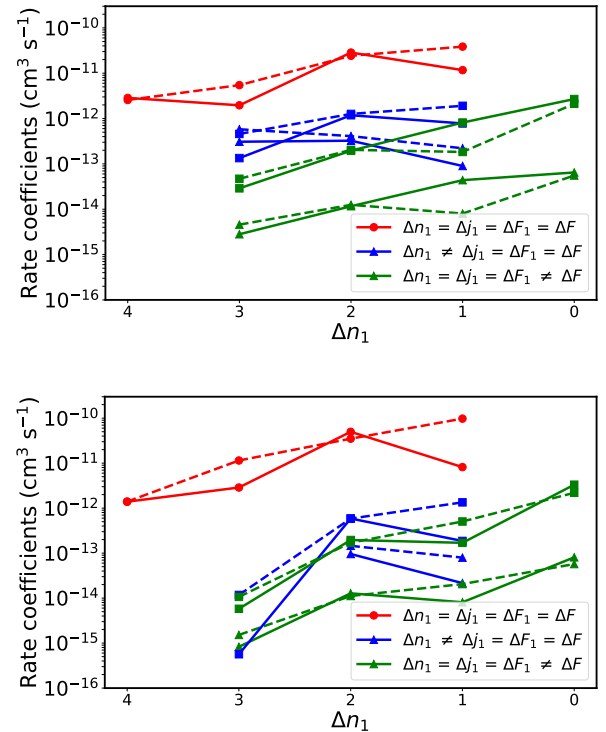


Fig. 9. Hyperfine rate coefficients of NH (top) out of the ($n_1 = 4, j_1 = 5, F_1 = 5.5, F = 6.5$) level and ND (bottom) out of the ($n_1 = 4, j_1 = 5, F_1 = 5, F = 6$) level at 50 K as a function of the variation in the rotational angular momentum n_1 . The solid lines stand for para-H₂ collisions and the dashed lines for ortho-H₂ collisions. The $\Delta F_1 = \Delta F - 2$ and $\Delta n_1 = \Delta j_1 - 2$ transitions are represented by triangles, whereas the $\Delta F_1 = \Delta F - 1$ and $\Delta n_1 = \Delta j_1 - 1$ transitions are represented by squares.

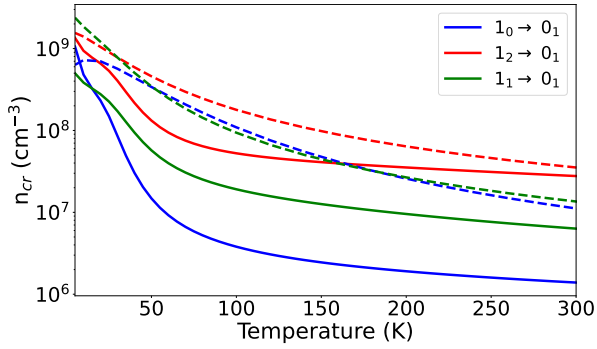


Fig. 10. Evolution of the critical density of NH with the temperature for the fine-structure components of the $1 \rightarrow 0$ line. The solid lines stand for NH–H₂ rate coefficients, whereas the dashed lines stand for NH–He coefficients.

In the following discussions, we focus on the three fine-structure lines $1_0 \rightarrow 0_1$ (946 GHz), $1_2 \rightarrow 0_1$ (974 GHz) and $1_1 \rightarrow 0_1$ (1000 GHz) detected by the *Herschel*/SPIRE survey in the study of Gull et al. (2020) and later toward the Orion Bar PDR with the *Herschel*/HIFI spectrometer by Goicoechea & Roncero (2022). We carried out simple radiative transfer modeling to assess the impact of the new NH–H₂ rate coefficients in comparison to scaled NH–He data. We explored the impact of the new NH–H₂ rate coefficients in modeling for typical conditions of these two environments with the RADEX non-LTE radiative transfer model using the escape probability approximation (Van der Tak et al. 2007).

4.1. General features: Critical densities and background continuum

A useful parameter for qualitatively understanding the excitation behavior of molecular lines is the critical density $n_{\text{cr}}^{ul}(T)$ from an upper level u to a lower one l , describing the gas density where radiative and collisional processes are in competition. Using the new fine-structure NH–H₂ rate coefficients, we estimated these critical densities to be

$$n_{\text{cr}}^{ul}(T) = \frac{\sum_{i < u} A_{ui}}{\sum_{u \neq i} k_{ui}(T)} = \frac{\sum_{i < u} A_{ui}}{\sum_{u \neq i} \left[\frac{\text{OPR}}{1 + \text{OPR}} k_{ui}^{\text{ortho-H}_2}(T) + \frac{1}{1 + \text{OPR}} k_{ui}^{\text{para-H}_2}(T) \right]}, \quad (16)$$

where OPR is the ortho-to-para-H₂ ratio assuming a thermalized distribution of the rotational population of H₂. We note, however, that the OPR can be out of equilibrium in various astrophysical environments, and can reach $\sim 10^{-3}$ at low temperatures (Faure et al. 2019). The A_{ul} are the fine-structure computed Einstein coefficients for NH radiative transitions (see Appendix C). These critical densities are compared to those computed with NH–He rate coefficients, also using Eq. (16), excluding the ortho-H₂ term and the OPR.

Figure 10 displays the critical density n_{cr} for each fine-structure component of the $1 \rightarrow 0$ rotational line. Due to the high rotational constant of NH, Einstein coefficients corresponding to these lines are large, of the order of $A_{ul} \sim 10^{-3} - 10^{-2} \text{ s}^{-1}$. This is why the computed critical densities are high compared to the density of molecular clouds ($n(\text{H}_2) \sim 10^3 - 10^6 \text{ cm}^{-3}$). At very low temperature, a very high gas density is needed to reach the LTE regime. In this case, most of the excitation is due to

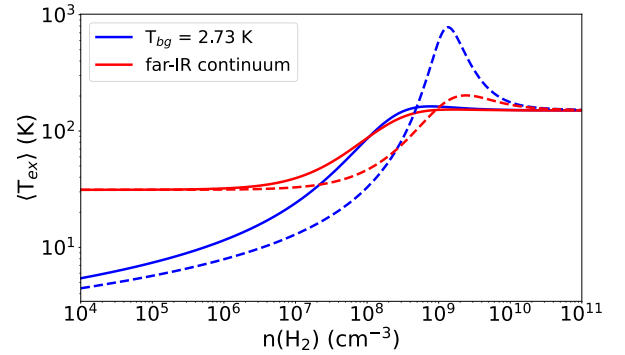


Fig. 11. Dependence of the excitation temperature of the $1 \rightarrow 0$ rotational line on the gas density. The solid lines stand for NH–H₂ rate coefficients, whereas the dashed lines stand for NH–He coefficients.

radiative processes (i.e., when inelastic collisions do not dominate) and NH can be easily detected in absorption toward strong submillimeter continuum sources. It can be seen from Eq. (16) that the evolution of the critical density strongly depends on the OPR, reflecting the importance of collisions induced by ortho-H₂ at high temperatures because of their different excitation efficiency. Discrepancies between H₂ and He critical densities are significant, exceeding an order of magnitude especially for the $1_0 \rightarrow 0_1$ line. These variations persist, even at low temperatures when para-H₂ collisions are dominant, reflecting the previously discussed differences between para-H₂ and He rate coefficients shown in Fig. 7.

It is interesting to assess the impact of rate coefficients on non-LTE modeling using He or H₂ sets of collisional data, particularly in environments influenced by a strong far-IR and submillimeter continuum. As an illustrative example, in these first models we adopt the physical parameters of Gull et al. (2020) for η Carinae; that is, we include a fixed column density $N(\text{NH}) = 5 \times 10^{15} \text{ cm}^{-2}$. We adopt a line width of 188 km/s in the ejecta (see Gull et al. 2020). These broad line widths ensure NH optically thin line emission. The kinetic temperature was chosen to be $T_{\text{k}} = 150 \text{ K}$.

Figure 11 presents the variations in the excitation temperatures derived from models using NH–H₂ and NH–He rate coefficients. We considered two distinct continua: the cosmic microwave background (CMB) described by a single blackbody at $T_{\text{bg}} = 2.73 \text{ K}$ and the modified source continuum that Gull et al. (2020) adopted. We found that excitation temperatures for individual fine-structure lines did not exhibit significant relative differences. Then we computed an average excitation temperature $\langle T_{\text{ex}} \rangle (n_1 = 1 \rightarrow n'_1 = 0)$ over these lines. Radiative processes dominate for very low gas densities, with $\langle T_{\text{ex}} \rangle \approx T_{\text{bg}}$ (i.e., radiative thermalization). Conversely, $\langle T_{\text{ex}} \rangle$ thermalizes to T_{k} when collisional processes are dominant for high densities. Given the typical conditions in η Carinae, a non-LTE behavior is obvious for both continua and sets of collisional data. The influence of the background continuum on excitation temperature is especially pronounced for low densities. When we adopt the specific source continuum, the averaged excitation temperature computed with NH–H₂ rate coefficients depart from a radiative regime at $n(\text{H}_2) \sim 10^7 \text{ cm}^{-3}$, whereas when the continuum is only the CMB, the NH excitation is in the non-LTE regime for a gas density of $\sim 10^4 - 10^5 \text{ cm}^{-3}$. However, the impact of the continuum on the excitation temperature using H₂ rate coefficients is negligible for $n(\text{H}_2) \geq 10^8 \text{ cm}^{-3}$ and excitation temperatures become identical between the two continua. On the other hand,

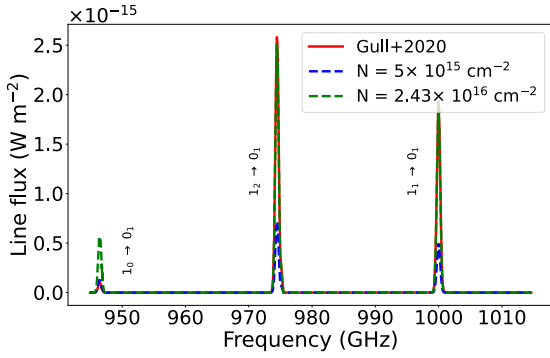


Fig. 12. Models of the NH $1 \rightarrow 0$ rotational line toward η Carinae. The solid curve represents the observations of Gull et al. (2020), while the dashed curves refer to modeling using fine-structure NH–H₂ rate coefficients.

for $n(\text{H}_2) \sim 4 \times 10^8 - 10^{10} \text{ cm}^{-3}$, models computed using the CMB and NH–He rate coefficients predict a supra-thermal excitation ($\langle T_{\text{ex}} \rangle > T_{\text{k}}$) which becomes moderate when we adopt the source continuum. This difference in behavior with the H₂ collisional data is related to the lower magnitude of He rate coefficients. Consequently, excitation temperatures computed from He rate coefficients are more influenced by the strength of the source continuum than those computed using H₂ rate coefficients.

Since the same excitation trends apply for both NH and ND, these results imply that the ND column densities inferred by Bacmann et al. (2016) in the prestellar core 16293E may be revised. Since ND is observed there in emission, a decrease in its calculated abundance can be anticipated. In addition, due to the larger values of the NH–H₂ rate coefficients compared to the NH–He values used in their work, models using the new collisional data may not be as sensitive to the modification of the background source continuum as they suggested.

4.2. Applications to the binary star η Carinae and the Orion Bar PDR

An essential parameter is the column density of the molecules, which allows us to infer the fractional abundance of a given molecule. For the η Carinae ejecta, Gull et al. (2020) determined a column density of $N(\text{NH}) = 5 \times 10^{15} \text{ cm}^{-2}$ for a gas density of $n(\text{H}_2) = 10^8 \text{ cm}^{-3}$ and a kinetic temperature $T_{\text{k}} = 200 \text{ K}$. Using the new set of fine-structure rate coefficients, we investigate the differences between the column density determined in their work and the value estimated in this study.

Figure 12 displays a simple model of the $1 \rightarrow 0$ rotational line compared to the model determined by Gull et al. (2020). Line fluxes computed using the previously determined column density and the new set of fine-structure rate coefficients show a significant deviation from the observations. These differences are likely to be produced by an overestimation of the inelastic rate coefficients by these authors. By fixing the kinetic temperature to $T_{\text{k}} = 200 \text{ K}$ and a gas density to $n(\text{H}_2) = 10^8 \text{ cm}^{-3}$, it is possible to set the column density by minimizing the χ^2 parameter. Based on our new collisional data, the minimization of this parameter must give an estimation of the integrated lines that best reproduce the observations. We found a column density of $N(\text{NH}) = 2.43 \times 10^{16} \text{ cm}^{-2}$, increasing the previous estimation by a factor of ~ 5 . It looks like the two most intense lines are actually able to reproduce much better the observations than the $1_0 \rightarrow 0_1$ line. This may be due to the larger intensity uncertainty of this

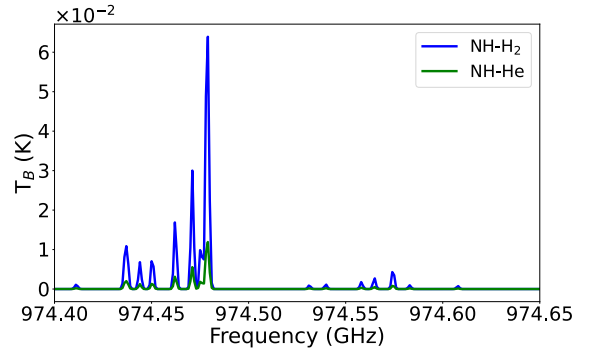


Fig. 13. Model of the NH hyperfine components of the $1_2 \rightarrow 0_1$ line. A line width value of $\Delta v = 0.5 \text{ km s}^{-1}$ is used to avoid overlap of the hyperfine lines displayed in the spectrum. The column density is set to $N(\text{NH}) = 10^{13} \text{ cm}^{-2}$.

weak line or due to anomalous hyperfine emission produced by hyperfine-structure line overlap effects not treated by RADEX.

A 3σ detection of the $1_2 \rightarrow 0_1$ (974 GHz) line in emission toward the Orion Bar was recently reported by Goicoechea & Roncero (2022). These authors estimated the NH excitation conditions and NH column density using a Monte Carlo non-LTE radiative transfer model. For these calculations, the authors used the available fine-structure NH–He collisional data from Toboła et al. (2011) to estimate the NH–H₂ rate coefficients through Eq. (8). These rate coefficients were also extrapolated to high temperatures. They estimated an excitation temperature of 10–15 K for the 974 GHz line and a column density of $1.3 \times 10^{13} \text{ cm}^{-2}$.

Figure 13 shows an illustration of the brightness temperatures for hyperfine transitions corresponding to the $1_2 \rightarrow 0_1$ line. These models were carried out using the new sets of hyperfine resolved rate coefficients, assuming a kinetic temperature of $T_{\text{k}} = 150 \text{ K}$, a gas density $n(\text{H}_2) = 10^5 \text{ cm}^{-3}$, and a typical column density of $N(\text{NH}) = 10^{13} \text{ cm}^{-2}$. The CMB was used as the background continuum and the hyperfine Einstein coefficients were extracted from the CDMS database (Endres et al. 2016). For the different sets of rate coefficients, we found quite important disparities in brightness temperatures. In particular, all the hyperfine-structure line peaks are brighter by a factor of 5 when using H₂ collisional data compared to those obtained with He rate coefficients. It was found that matching brightness temperatures for all components between the two sets of collisional data implied a decrease in the column density by a factor of ~ 5 when using NH–H₂ rate coefficients, leading to $N(\text{NH}) \sim 2 \times 10^{12} \text{ cm}^{-2}$. This discrepancy in column densities is due to the high contribution of ortho-H₂ rate coefficients. At $T_{\text{k}} = 150 \text{ K}$, the thermalized OPR is ~ 2.51 . Then each rate coefficient contributes $0.71 \times k_{ul}^{\text{ortho-H}_2} + 0.29 \times k_{ul}^{\text{para-H}_2}$ to the radiative transfer. As mentioned in the previous sections, the NH–ortho-H₂ rate coefficients are larger than those for NH–para-H₂ by a factor of more than 3, while the NH–para-H₂ rates, being larger than NH–scaled-He rates, are larger by up to a factor of 5.

5. Conclusion

We computed the first fine and hyperfine resolved rate coefficients for NH and ND in collision with both ortho- and para-H₂. These data are based on the 4D PES reported in Paper I. Fine-structure rate coefficients were determined with the CC method up to 300 K, taking into account NH and ND energy levels up to $n_1 = 8$. Both NH and ND displayed significantly larger fine-structure transitions when interacting with ortho-H₂ than with

para-H₂. This trend is standard for light neutral collisional systems. Moreover, these transitions display the usual properties of ³Σ systems where the magnitude of the transitions varies with the transferred angular momentum as ($\Delta n_1 = \Delta j_1$) > ($\Delta n_1 \neq \Delta j_1$).

ND collisions with H₂ yield rate coefficients that differ by a factor of 3–5 with respect to those of NH. These large differences could have been anticipated for such light collisional systems due to the large differences in spectroscopic parameters and the large displacement of the center of mass. Consequently, these findings highlight the importance of computing rate coefficients explicitly for deuterated isotopologs. Additionally, a comparison between H₂ and scaled-He colliders has shown deviations of a factor >5, emphasizing the inadvisability of using of He as a proxy for rate coefficients involving H₂.

The treatment of the hyperfine structure was done using the IOS approach (Faure & Lique 2012) with the NG correction (Neufeld & Green 1994), adapted for the first time to collisions between an open-shell target in a ³Σ electronic state and a linear molecule. This allowed us to provide hyperfine collisional data up to 200 K for NH collisions and 100 K for ND collisions, including energy levels up to $n_1 = 4$. The computed hyperfine rate coefficients follow a strong propensity for $\Delta n_1 = \Delta j_1 = \Delta F_1 = \Delta F$ transitions. A larger gap is observed between $\Delta n_1 \neq \Delta j_1 = \Delta F_1 = \Delta F$ and $\Delta n_1 = \Delta j_1 = \Delta F_1 \neq \Delta F$ transitions in the case of NH as opposed to ND collisions.

The new sets of NH–H₂ fine and hyperfine resolved rate coefficients were included in a radiative transfer modeling for typical conditions of the ejecta of the η Carinae binary star and the Orion Bar PDR where NH submillimeter lines have been detected in emission. We found important differences between the present column densities and those derived in the literature (up to a factor of ~5). These differences are mainly due to the use of the new NH–H₂ rate coefficients. These results suggest a downward revision of the calculation of the abundance of NH (and possibly ND) in these environments using more robust radiative transfer models. These data are expected to be useful for interpreting observations of these species detected in both cold and warm environments where both ortho- and para-H₂ coexist.

The computed collisional data for the fine and hyperfine structure of NH and ND in collision with both ortho- and para-H₂ will be available on the following data bases: EMAA², BASECOL (Dubernet et al. 2024), and LAMDA (Van der Tak et al. 2020).

Acknowledgements. We acknowledge financial support from the European Research Council (Consolidator Grant COLLEXISM, Grant Agreement No. 811363). We wish to acknowledge the support from the CEA/GENCI (Grand Equipement National de Calcul Intensif) for awarding us access to the TGCC (Très Grand Centre de Calcul) Joliot Curie/IRENE supercomputer within the A0110413001 project. J.R.G. thanks the Spanish MICINN for funding support under grant PID2019-106110GB-I00.

References

- Alexander, M. H. 1982, *J. Chem. Phys.*, **76**, 429
 Alexander, M. H., & Dagdigian, P. J. 1983, *J. Chem. Phys.*, **79**
 Alexander, M. H., & Dagdigian, P. J. 1985, *J. Chem. Phys.*, **83**, 2191
 Alexander, M. H., Dagdigian, P. J., Werner, H. J., et al. 2023, *Comp. Phys. Commun.*, **289**, 108761
 Axner, O., Gustafsson, J., Omenetto, N., & Winefordner, J. D. 2004, *Spectrochim. Acta*, **59**, 1
 Bacmann, A., Lefloch, B., Ceccarelli, C., et al. 2003, *ApJ*, **585**, L55
 Bacmann, A., Caux, E., Hily-Blant, P., Parise, B., & Pagani, L. 2010, *A&A*, **521**, L42
 Bacmann, A., Daniel, F., Ceccarelli, C., et al. 2016, *A&A*, **587**, A26
 Boys, S. F., & Bernardi, S. 1970, *Mol. Phys.*, **19**, 553

² <https://dx.doi.org/10.17178/EMAA>

- Caselli, P., Van der Tak, F. F. S., Ceccarelli, C., & Bacmann, A. 2003, *A&A*, **403**, L37
 Ceccarelli, C., Castets, A., Loinard, L., Caux, E., & Tielens, A. G. G. M. 1998, *A&A*, **338**, L43
 Cernicharo, J., Goicoechea, J. R., & Caux, E. 2000, *ApJ*, **534**, L199
 Corey, G. C., & McCourt, F. R. 1983, *J. Chem. Phys.*, **87**, 2723
 Cybulski, H., Krems, R. V., Sadeghpour, H. R., et al. 2005, *J. Chem. Phys.*, **122**
 Dagdigian, P. J. 2021, *MNRAS*, **505**, 1987
 Daniel, F., Dubernet, M. L., & Meuwly, M. 2004, *J. Chem. Phys.*, **121**, 4540
 Daniel, F., Dubernet, M. L., Meuwly, M., Cernicharo, J., & Pagani, L. 2005, *MNRAS*, **363**, 1083
 Demes, S., Lique, F., Loreau, J., & Faure, A. 2023, *MNRAS*, **524**, 2368
 Denis-Alpizar, O., Stoecklin, T., Dutrey, A., & Guilloteau, S. 2020, *MNRAS*, **497**, 4276
 Desrousseaux, B., Quintas-Sánchez, E. L., Dawes, R., Marinakis, S., & Lique, F. 2021, *J. Chem. Phys.*, **154**, 034304
 Dislaire, V., Hily-Blant, P., Faure, A., et al. 2012, *A&A*, **537**, A20
 Dubernet, M. L., Boursier, C., Denis-Alpizar, O., et al. 2024, *A&A*, **683**, A40
 Dumouchel, F., Klos, J., Tobiła, R., et al. 2012, *J. Chem. Phys.*, **137**, 114306
 Dunning, T. H. 1989, *J. Chem. Phys.*, **90**, 1007
 Endres, C. P., Schlemmer, S., Schilke, P., Stutzki, J., & Müller, H. S. P. 2016, *J. Mol. Spectrosc.*, **327**, 95
 Faure, A., & Lique, F. 2012, *MNRAS*, **425**, 740
 Faure, A., Hily-Blant, P., Rist, C., et al. 2019, *MNRAS*, **487**, 3392
 Fawzy, W. M., Kerenskaya, G., & Heaven, M. C. 2005, *J. Chem. Phys.*, **122**, 144318
 Flores-Mijangos, J., Brown, J. M., Matsushima, F., et al. 2004, *J. Mol. Spectrosc.*, **225**, 189
 Gerin, M., Neufeld, D. A., & Goicoechea, J. R. 2016, *ARA&A*, **54**, 181
 Godard Palluet, A., & Lique, F. 2024, *MNRAS*, **527**, 6702
 Goicoechea, J. R., & Roncero, O. 2022, *A&A*, **664**, A190
 Goicoechea, J. R., Rodríguez-Fernández, N. J., & Cernicharo, J. 2004, *ApJ*, **600**, 214
 Goicoechea, J. R., Lique, F., & Santa-Maria, M. G. 2022, *A&A*, **658**, A28
 Gordy, W., & Cook, R. L. 1984, *Microwave Molecular Spectra* (New Jersey: John Wiley & Sons, Inc)
 Gull, T. R., Morris, P. W., Black, J. H., et al. 2020, *MNRAS*, **499**, 5269
 Hily-Blant, P., Maret, S., Bacmann, A., et al. 2010, *A&A*, **521**, L52
 Huber, K. P., & Herzberg, G. 1979, *Molecular Spectra And Molecular Structure, IV. Constants Of Diatomic Molecules* (New York: Van Nostrand Reinhold)
 Kalugina, Y., & Lique, F. 2015, *MNRAS*, **446**, 21
 Keun Park, J., & Sun, H. 1993, *Chem. Phys. Lett.*, **211**, 6
 Klos, J., Dagdigian, P. J., Alexander, M. H., Faure, A., & Lique, F. 2020, *MNRAS*, **493**, 3491
 Knizia, G., Adler, T. B., & Werner, H. J. 2009, *J. Chem. Phys.*, **130**, 054104
 Lambert, D. L., & Beer, R. 1972, *ApJ*, **177**, 514
 Lanza, M., & Lique, F. 2014, *J. Chem. Phys.*, **141**, 164321
 Lara-Moreno, M., Stoecklin, T., & Halvick, P. 2021, *MNRAS*, **507**, 4086
 Le Gal, R., Hily-Blant, P., Faure, A., et al. 2014, *A&A*, **562**, A83
 Linsky, J. L., Drainie, B. T., Moos, H. W., et al. 2006, *ApJ*, **647**, 1106
 Lique, F., Bulut, N., & Roncero, O. 2016, *MNRAS*, **461**, 4477
 Loreau, J., Lique, F., & Faure, A. 2018, *ApJ*, **853**, L5
 Meyer, D. M., & Roth, K. C. 1991, *ApJ*, **376**, L49
 Ndaw, D., Bop, C. T., Dieye, G., Boye Faye, N. A., & Lique, F. 2021, *MNRAS*, **503**, 5976
 Neufeld, D. A., & Green, S. 1994, *ApJ*, **432**, 158
 Orlikowski, T. 1985, *Mol. Phys.*, **56**, 35
 Persson, C. M., De Luca, M., Mookerjee, B., Olofsson, A. O. H., & Black, J. H. 2012, *A&A*, **543**, A145
 Pirlot Jankowiak, P., Kalugina, Y., Ramachandran, R., et al. 2021, *J. Chem. Phys.*, **155**, 134303
 Pirlot Jankowiak, P., Lique, F., & Dagdigian, P. J. 2023, *MNRAS*, **523**, 3732
 Ramachandran, R., Klos, J., & Lique, F. 2018, *J. Chem. Phys.*, **148**, 084311
 Schmitt, J. L. 1969, *PASP*, **81**, 657
 Sobelman, I. I. 1979, *Atomic Spectra and Radiative Transitions* (New York: Springer-Verlag Berlin Heidelberg New York), 1
 Swings, P., Elvey, C. T., & Babcock, H. W. 1941, *ApJ*, **94**, 320
 Takano, S., Klaus, T., & Winnewisser, G. 1998, *J. Mol. Spectrosc.*, **192**, 309
 Tobiła, R., Dumouchel, F., Klos, J., & Lique, F. 2011, *J. Chem. Phys.*, **134**, 024305
 Van der Tak, F. F. S., Black, J. H., Schöier, F. L., Jansen, D. J., & van Dishoeck, E. F. 2007, *MNRAS*, **468**, 627
 Van der Tak, F. F. S., Lique, F., Faure, A., Black, J. H., & van Dishoeck, E. F. 2020, *Atoms*, **8**, 15
 Wagenblast, R., Williams, D. A., Millar, T. J., & Nejad, L. A. M. 1993, *MNRAS*, **260**, 420
 Werner, H. J., Knowles, P. J., Manby, F. R., et al., F. R. M. 2020, *J. Chem. Phys.*, **152**, 144107

Appendix A: Scattering parameters used for dynamical calculations

The resolution of the CC equations requires optimizing several parameters in order to converge fine-structure cross sections for different total energies E_{tot} . For NH and ND in collision with ortho- and para- H_2 , the total energy grid is chosen with an increasing step ΔE with the energy. The step is small at low energies to be able to describe resonances and becomes larger at higher energies to save computational time since the energy variation of the cross sections become smoother. The converged rotational basis n_{max} of the target considered and the total angular momentum J_{tot} are presented in the Tables A.1–A.2. These parameters were chosen in order to converge integral cross sections to 1% accuracy per parameter. The wavefunctions were propagated for all collisional systems from $3.75a_0$ to $60a_0$. The inclusion of the rotational basis $j_2^{\text{max}} = 0, 2$ for para- H_2 and $j_2^{\text{max}} = 1$ for ortho- H_2 were found to be enough for converged scattering calculations. As reported in Paper I, the impact of higher basis for both colliders on cross sections is less than 5% around $E_{\text{tot}} = 500 \text{ cm}^{-1}$ and can be neglected. The reduced mass used for the NH- H_2 and ND- H_2 collisional systems are respectively 1.777 and 1.790 amu.

Appendix B: Details about IOS scaling relations

We describe here a more detailed derivation of the IOS scaling relations. From Eq. (6), it is possible to use angular momentum algebra in order to write the collisional integral cross section between a $^3\Sigma$ target and a linear collider so that

$$\begin{aligned} \sigma_{n_1 j_1 j_2 \rightarrow n'_1 j'_1 j'_2} &= [n_1 n'_1 j'_1 j'_2] \sum_{\lambda_1 \lambda_2 \lambda} \begin{pmatrix} n'_1 & \lambda_1 & n_1 \\ 0 & 0 & 0 \end{pmatrix}^2 \\ &\times \begin{pmatrix} j'_2 & \lambda_2 & j_2 \\ 0 & 0 & 0 \end{pmatrix}^2 \left\{ \begin{matrix} j_1 & n_1 & S \\ n'_1 & j'_1 & \lambda_1 \end{matrix} \right\}^2 \\ &\times \sigma_{\lambda_1 \lambda_2 \lambda}, \end{aligned} \quad (\text{B.1})$$

where $\sigma_{\lambda_1 \lambda_2 \lambda}$ is a quantity defined as

$$\sigma_{\lambda_1 \lambda_2 \lambda} = \frac{\pi}{k^2} \sum_{LL'} (4\pi)^{-3} [\lambda LL'] \begin{pmatrix} L' & \lambda & L \\ 0 & 0 & 0 \end{pmatrix}^2 T_{\lambda_1 \lambda_2 \lambda}^2 \quad (\text{B.2})$$

and $T_{\lambda_1 \lambda_2 \lambda}$ represents the IOS T -matrix coefficients excluding the angular dependence, similar to the coefficients defined by Corey & McCourt (1983) applied for atom-molecule collisions.

Table A.1. Converged parameters used in close-coupling calculations for the NH- H_2 collisional system.

NH-ortho- H_2				NH-para- H_2			
E_{tot} (cm $^{-1}$)	ΔE (cm $^{-1}$)	n_{max}	J_{tot}	E_{tot} (cm $^{-1}$)	ΔE (cm $^{-1}$)	n_{max}	J_{tot}
150.3–153.7	0.1	7	8	31.6–35.0	0.1	7	15
153.8–168.7	0.1	7	13	35.1–50.0	0.1	7	20
168.8–218.7	0.1	7	20	50.1–100.0	0.1	7	23
218.8–318.7	0.1	10	40	100.1–200.0	0.1	8	28
318.9–418.7	0.2	10	60	200.2–300.0	0.2	10	50
419.2–618.7	0.5	10	70	300.5–500.0	0.5	10	60
619.2–818.7	0.5	10	85	500.5–700.0	0.5	10	65
819.7–1118.7	1	11	90	701–1000	1	12	80
1123.7–1318.7	5	12	95	1005–1200	5	12	85
1323.7–1618.7	5	12	100	1205–1500	5	13	115
1623.7–2118.7	5	14	125	1505–2000	5	13	120
2168.7–2568.7	50	15	140	2050–2450	50	14	125

Table A.2. Converged parameters used in close-coupling calculations for the ND- H_2 collisional system.

ND-ortho- H_2				ND-para- H_2			
E_{tot} (cm $^{-1}$)	ΔE (cm $^{-1}$)	n_{max}	J_{tot}	E_{tot} (cm $^{-1}$)	ΔE (cm $^{-1}$)	n_{max}	J_{tot}
135.2–153.7	0.1	6	15	16.5–35.0	0.1	6	15
153.8–168.7	0.1	6	18	35.1–50.0	0.1	7	17
168.8–218.7	0.1	8	24	50.1–100.0	0.1	8	21
218.8–318.7	0.1	8	33	100.1–200.0	0.1	8	27
318.9–418.7	0.2	10	36	200.2–300.0	0.2	10	27
419.2–618.7	0.5	12	45	300.5–500.0	0.5	10	30
619.2–818.7	0.5	12	51	500.5–700.0	0.5	12	39
819.7–1118.7	1	14	57	701–1000	1	14	45
1123.7–1318.7	5	14	60	1005–1200	5	14	51
1323.7–1618.7	5	14	66	1205–1500	5	14	54
1623.7–2118.7	5	16	75	1505–2000	5	16	63
2168.7–2568.7	50	18	81	2050–2450	50	18	69

Within the IOS approximation, we can express the integral cross section for a transition $n_1 j_1 j_2 \rightarrow n'_1 j'_1 j'_2$ out of the $n_{1,j_1} = 1_0$ fine-structure level. For collisions induced by H_2 , we detail two cases. These are treated in a pure Hund's case (b) even if the intermediate coupling is used for the calculations of the CC cross sections.

B.1. para- H_2

Setting $n_1 = 1$, $j_1 = 0$ and $j_2 = 0$ in (B.1) gives

$$\sigma_{100 \rightarrow n'_1 j'_1 j'_2} = 3[n'_1 j'_1 j'_2] \sum_{\lambda_1 \lambda_2 \lambda} \begin{pmatrix} n'_1 & \lambda_1 & 1 \\ 0 & 0 & 0 \end{pmatrix}^2 \times \begin{pmatrix} j'_2 & \lambda_2 & 0 \\ 0 & 0 & 0 \end{pmatrix}^2 \left\{ \begin{matrix} 0 & 1 & S \\ n'_1 & j'_1 & \lambda_1 \end{matrix} \right\}^2 \sigma_{\lambda_1 \lambda_2 \lambda}. \quad (\text{B.3})$$

It is possible to see that by setting $n'_1 = \lambda_1 + 1$, the 3j and 6j coefficients are nonzero for $j'_1 = \lambda_1$ and $j'_2 = \lambda_2$ so that

$$\sigma_{100 \rightarrow \lambda_1 + 1, \lambda_1, \lambda_2} = 3[\lambda_1 + 1][\lambda_1 \lambda_2] \begin{pmatrix} \lambda_1 + 1 & \lambda_1 & 1 \\ 0 & 0 & 0 \end{pmatrix}^2 \times \begin{pmatrix} \lambda_2 & \lambda_2 & 0 \\ 0 & 0 & 0 \end{pmatrix}^2 \left\{ \begin{matrix} 0 & 1 & S \\ \lambda_1 + 1 & \lambda_1 & \lambda_1 \end{matrix} \right\}^2 \times \sigma_{\lambda_1 \lambda_2 \lambda}. \quad (\text{B.4})$$

It should be noted that an equivalent set of equations like (B.4) can be found for $n'_1 = \lambda_1 - 1$. In the following and for the determination of the hyperfine rate coefficients, we chose to use the case where $n'_1 = \lambda_1 + 1$. The evaluation of the 3j and 6j coefficients in (B.4) leads to the expression for $\sigma_{\lambda_1 \lambda_2 \lambda}$:

$$\sigma_{\lambda_1 \lambda_2 \lambda} = \frac{[\lambda_1]}{\lambda_1 + 1} \sigma_{100 \rightarrow \lambda_1 + 1, \lambda_1, \lambda_2}. \quad (\text{B.5})$$

This relation stands for $S = 1$. By reintroducing (B.5) into (B.1), we obtain the IOS cross section scaling relation out of the $n_{1,j_1} = 1_0$ in the case of a collision with para- H_2 :

$$\sigma_{n_1 j_1 j_2 \rightarrow n'_1 j'_1 j'_2}^{\text{IOS-p}} = [n_1 n'_1 j'_1 j'_2] \sum_{\lambda_1 \lambda_2} \frac{[\lambda_1]}{\lambda_1 + 1} \begin{pmatrix} n'_1 & \lambda_1 & n_1 \\ 0 & 0 & 0 \end{pmatrix}^2 \times \begin{pmatrix} j'_2 & \lambda_2 & j_2 \\ 0 & 0 & 0 \end{pmatrix}^2 \left\{ \begin{matrix} n'_1 & n_1 & \lambda_1 \\ j'_1 & j_1 & S \end{matrix} \right\}^2 \times \sigma_{100 \rightarrow \lambda_1 + 1, \lambda_1, \lambda_2}^{\text{CC}}, \quad (\text{B.6})$$

where the IOS cross section is replaced by the CC cross section. It is also possible to replace the cross section by the rate coefficient. The extension to hyperfine scattering calculation gives directly Eq. (9).

B.2. ortho- H_2

Similarly, by applying $n_1 = 1$, $j_1 = 0$ and $j_2 = 1$ in (B.1), we find

$$\sigma_{101 \rightarrow n'_1 j'_1 j'_2} = 3[n'_1 j'_1 j'_2] \sum_{\lambda_1 \lambda_2 \lambda} \begin{pmatrix} n'_1 & \lambda_1 & 1 \\ 0 & 0 & 0 \end{pmatrix}^2 \times \begin{pmatrix} j'_2 & \lambda_2 & 1 \\ 0 & 0 & 0 \end{pmatrix}^2 \left\{ \begin{matrix} 0 & 1 & S \\ n'_1 & j'_1 & \lambda_1 \end{matrix} \right\}^2 \sigma_{\lambda_1 \lambda_2 \lambda}. \quad (\text{B.7})$$

In this case, for $n'_1 = \lambda_1 + 1$, the 3j and 6j coefficients give a contribution for $j'_1 = \lambda_1$ and $j'_2 = \lambda_2 + 1$. Replacing in (B.7), we find

$$\sigma_{101 \rightarrow \lambda_1 + 1, \lambda_1, \lambda_2 + 1} = 3[\lambda_1 + 1, \lambda_1, \lambda_2 + 1] \begin{pmatrix} \lambda_1 + 1 & \lambda_1 & 1 \\ 0 & 0 & 0 \end{pmatrix}^2 \times \begin{pmatrix} \lambda_2 + 1 & \lambda_2 & 1 \\ 0 & 0 & 0 \end{pmatrix}^2 \left\{ \begin{matrix} 0 & 1 & S \\ \lambda_1 + 1 & \lambda_1 & \lambda_1 \end{matrix} \right\}^2 \times \sigma_{\lambda_1 \lambda_2 \lambda}. \quad (\text{B.8})$$

The 3j and 6j coefficients in (B.8) are analyzed so that the expression for $\sigma_{\lambda_1 \lambda_2 \lambda}$ becomes

$$\sigma_{\lambda_1 \lambda_2 \lambda} = \frac{[\lambda_1]}{\lambda_1 + 1} \frac{[\lambda_2]}{\lambda_2 + 1} \sigma_{101 \rightarrow \lambda_1 + 1, \lambda_1, \lambda_2 + 1}. \quad (\text{B.9})$$

We can reintroduce (B.9) into (B.1) and obtain the IOS cross section scaling relation out of the $n_{1,j_1} = 1_0$ in the case of a collision with ortho- H_2 :

$$\sigma_{n_1 j_1 j_2 \rightarrow n'_1 j'_1 j'_2}^{\text{IOS-o}} = [n_1 n'_1 j'_1 j'_2] \sum_{\lambda_1 \lambda_2} \frac{[\lambda_1]}{\lambda_1 + 1} \frac{[\lambda_2]}{\lambda_2 + 1} \begin{pmatrix} n'_1 & \lambda_1 & n_1 \\ 0 & 0 & 0 \end{pmatrix}^2 \times \begin{pmatrix} j'_2 & \lambda_2 & j_2 \\ 0 & 0 & 0 \end{pmatrix}^2 \left\{ \begin{matrix} n'_1 & n_1 & \lambda_1 \\ j'_1 & j_1 & S \end{matrix} \right\}^2 \times \sigma_{101 \rightarrow \lambda_1 + 1, \lambda_1, \lambda_2 + 1}^{\text{CC}}. \quad (\text{B.10})$$

Similarly to the case of para- H_2 the extension to hyperfine scattering calculation is given by Eq. (10).

Appendix C: Details about fine-structure Einstein coefficients

For an open-shell molecule following the coupling scheme given in Sect. 3.1, the general form of the Einstein coefficient is given by (see, e.g., Sobelman 1979)

$$A_{n_1 j_1 \rightarrow n'_1 j'_1} = \frac{64\pi^4 \nu^3}{3hc^3} \frac{S'_{n_1 j_1 \rightarrow n'_1 j'_1}}{[j_1]}, \quad (\text{C.1})$$

$$S'_{n_1 j_1 \rightarrow n'_1 j'_1} = [j_1 j'_1] \left\{ \begin{matrix} n_1 & j_1 & S \\ j'_1 & n'_1 & 1 \end{matrix} \right\}^2 S'_{n_1 \rightarrow n'_1},$$

where ν is the frequency of the transition, h is the Planck constant, c is the speed of light, and $S'_{n_1 j_1 \rightarrow n'_1 j'_1}$ and $S'_{n_1 \rightarrow n'_1}$ are the line strength factors for a fine-structure and a rotational transition, respectively. The $S'_{n_1 \rightarrow n'_1}$ term depends on the electric dipole moment matrix elements, which allow transitions for $\Delta n_1 = \pm 1$ (Axner et al. 2004). It turns out that

$$S'_{n_1 \rightarrow n'_1} = \mu_D^2 \max(n_1, n'_1) = \mu_D^2 n_1. \quad (\text{C.2})$$

Reintroduce (C.2) into (C.1) simplifies to

$$A_{n_1 j_1 \rightarrow n'_1 j'_1} = \frac{64\pi^4 \nu^3}{3hc^3} \mu_D^2 n_1 [j_1] \left\{ \begin{matrix} n_1 & j_1 & S \\ j'_1 & n'_1 & 1 \end{matrix} \right\}^2. \quad (\text{C.3})$$

In the case of NH and ND, $S = 1$ and $\mu_D = 1.39$ D (Keun Park & Sun 1993).

BIBLIOGRAPHY

- [1] B. T. Draine, *Physics of the Interstellar and Intergalactic Medium* (Princeton Series in Astrophysics). Princeton University Press, 2011.
- [2] M. Asplund, N. Grevesse, A. Jacques Sauval, *et al.*, *ARA&A*, vol. 47, pp. 481–522, 2009.
- [3] M. F. Nieva and N. Przybilla, *A&A*, vol. 539, no. A143, 2012.
- [4] B. T. Draine, *ARA&A*, vol. 41, pp. 241–289, 2003.
- [5] A. Acker, *Astronomie Astrophysique*, 5e edition. Dunod, 2017.
- [6] R. J. Trumpler, *PASP*, vol. 42, p. 214, 1930.
- [7] J. S. Mathis, W. Rumpl, and K. H. Nordsieck, *ApJ*, vol. 217, pp. 425–433, 1977.
- [8] R. F. Knacke and R. K. Thomson, *PASP*, vol. 85, p. 341, 1973.
- [9] C. F. McKee and J. P. Ostriker, *ApJ*, vol. 218, pp. 148–169, 1977.
- [10] T. P. Snow and B. J. McCall, *Annu. Rev. Astron. Astrophys.*, vol. 44, pp. 367–414, 2006.
- [11] E. B. Jenkins and D. A. Meloy, *ApJL*, vol. 193, pp. 121–125, 1974.
- [12] P. C. Myers, R. A. Linke, and P. J. Benson, *ApJ*, vol. 264, pp. 517–537, 1983.
- [13] N. Sakai and S. Yamamoto, *Chem. Rev.*, vol. 113, pp. 8981–9015, 2013.
- [14] C. F. McKee and E. C. Ostriker, *Annu. Rev. Astron. Astrophys.*, vol. 45, pp. 565–687, 2007.
- [15] J. Lequeux, E. Falgarone, and C. Ryter, *Le Milieu Interstellaire*, CNRS Editions. Savoirs actuels, 2002.
- [16] S. Lizano and F. H. Shu, *ApJ*, vol. 342, pp. 834–854, 1989.
- [17] M. M. Dunham, A. M. Stutz, L. E. Allen, *et al.*, *The Evolution of Protostars: Insights from Ten Years of Infrared Surveys with Spitzer and Herschel*. University of Arizona Press, 2014.
- [18] P. André, D. Ward-Thompson, and M. Barsony, *ApJ*, vol. 406, pp. 122–141, 1993.
- [19] P. Caselli and C. Ceccarelli, *Astron. Astrophys. Rev.*, vol. 20, 2012.
- [20] J. Hartmann, *ApJ*, vol. 19, pp. 268–286, 1904.

-
- [21] P Swings and L. Rosenfeld, *ApJ*, vol. 86, pp. 483–486, 1937.
- [22] A. McKellar, *PASP*, vol. 52, p. 187, 1940.
- [23] A. S. Eddington, *Proc. R. Soc. Lond. A*, vol. 111, pp. 424–456, 1926.
- [24] B. A. McGuire, *ApJS*, vol. 259, p. 30, 2022.
- [25] S. Weinreb, A. H. Barrett, M. L. Meeks, *et al.*, *Nature*, vol. 200, no. 4909, pp. 829–831, 1963.
- [26] A. C. Cheung, D. M. Rank, C. H. Townes, *et al.*, *Phys. Rev. Lett.*, vol. 21, no. 25, pp. 1701–1705, 1968.
- [27] A. C. Cheung, D. M. Rank, C. H. Townes, *et al.*, *Nature*, vol. 221, no. 5181, pp. 626–628, 1969.
- [28] G. L. Pilbratt, J. R. Riedinger, T. Passvogel, *et al.*, *A&A*, vol. 518, no. L1, 2010.
- [29] R. Bustos, M. Rubio, A. Otárola, *et al.*, *PASP*, vol. 126, pp. 1126–1132, 2014.
- [30] F. Tercero, J. A. López-Pérez, and J. D. Gallego, *A&A*, vol. 645, p. 37, 2021.
- [31] J. P. Gardner, J. C. Mather, and M. Clampin, *Space Sci. Rev.*, vol. 123, no. 4, pp. 485–606, 2006.
- [32] M. Gerin, D. A. Neufeld, and J. R. Goicoechea, *Interstellar Hydrides*. Annu. Rev. Astron. Astrophys, 2016, vol. 54.
- [33] P. Friberg, S. C. Madden, A. Hjalmarsen, *et al.*, *A&A*, vol. 195, pp. 281–289, 1988.
- [34] H. W. Kroto, C. Kirby, and D. R. M. Walton, *ApJ*, vol. 219, pp. 133–137, 1978.
- [35] N. W. Broten, T. Oka, L. W. Avery, *et al.*, *ApJ*, vol. 223, pp. 105–107, 1978.
- [36] S. Cazaux, A. G. G. M. Tielens, C. Ceccarelli, *et al.*, *The Astrophysical Journal*, vol. 593, no. 1, p. L51, Jul. 2003, ISSN: 0004-637X.
- [37] C. P. Endres, S. Schlemmer, P. Schilke, *et al.*, *Journal of Molecular Spectroscopy*, vol. 327, pp. 95–104, 2016.
- [38] B. Rowe, A. Canosa, and D. E. Heard, *Uniform Supersonic Flows in Chemical Physics: Chemistry Close to Absolute Zero Studied Using the CRESU Method*. World Scientific Publishing Europe, 2022.
- [39] F. Lique and A. Faure, *Gas-Phase Chemistry in Space: From Elementary Particles to Complex Organic Molecules*. IOP Publishing, 2019.
- [40] Z. Herman and J. H. Futrell, *IJMSP*, vol. 377, pp. 84–92, 2015.
- [41] B. Rowe and J. B. Marquette, *IJMSP*, vol. 80, pp. 239–254, 1987.
- [42] S. Soorkia, C. Liu, and J. D. Savee, *Sci. Instrum.*, vol. 82, p. 124 102, 2011.

-
- [43] G. Brown, B. C. Dian, K. O. Douglass, *et al.*, *Rev. Sci. Instrum.*, vol. 79, no. 5, p. 053 103, 2008.
- [44] M. Kirste, L. Scharfenberg, J. Kłos, *et al.*, *PhysRev*, vol. 82, no. 042717, 2010.
- [45] V. Plomp, J. Onvlee, F. Lique, *et al.*, *J. Phys. Chem. A.*, vol. 127, pp. 2306–2313, 2023.
- [46] S. D. Hogan, M. Motsch, and F. Merkt, *Phys. Chem. Chem. Phys.*, vol. 13, pp. 18 705–18 723, 2011.
- [47] E. Roueff and F. Lique, *Chem. Rev.*, vol. 113, 2013.
- [48] A. Faure, F. Lique, and A. J. Remijan, *J. Phys. Chem. Lett.*, vol. 9, pp. 3199–3204, 2018.
- [49] F. F. S. Van der Tak, F. Lique, A. Faure, *et al.*, *Atoms*, vol. 8, no. 2, p. 15, 2020.
- [50] M. L. Dubernet *et al.*, *A&A*, 2023.
- [51] R. J. Gould and E. E. Salpeter, *ApJ*, vol. 138, p. 393, 1963.
- [52] T. Millar, E. Roueff, S. Charnley, *et al.*, *International Journal of Mass Spectrometry and Ion Processes*, vol. 149–150, pp. 389–402, Nov. 1995, ISSN: 0168-1176.
- [53] V. Wakelam, *ApJS*, vol. 217, no. 20, 2015.
- [54] T. J. Millar, C. Walsh, M. Van de Sande, *et al.*, *A&A*, 2023.
- [55] M. Agúndez and V. Wakelam, *Chem. Rev.*, vol. 113, no. 12, pp. 8710–8737, Dec. 2013, ISSN: 0009-2665.
- [56] A. Arthurs and A. Dalgarno, *Proc. R. Soc. Lond. A*, vol. 256, pp. 540–551, 1960.
- [57] M. Born and R. Oppenheimer, *adp*, vol. 389, 1927.
- [58] S. Chefdeville, T. Stoecklin, C. Naulin, *et al.*, *ApJL*, vol. 799, p. 4, 2015.
- [59] S. Green, *J. Chem. Phys.*, vol. 62, p. 2271, 1975.
- [60] S. Lepp, V. Buch, and A. Dalgarno, *ApJS*, vol. 98, p. 345, 1995.
- [61] G. Danby, D. R. Flower, P. Valiron, *et al.*, *Mon. Not. R. Astronom. Soc.*, vol. 235, no. 1, pp. 229–238, 1988.
- [62] S. Green, S. Maluendes, and A. D. McLean, *ApJS*, vol. 85, p. 181, 1993.
- [63] S. Chu and A. Dalgarno, *Proc. R. Soc. Lond. A.*, vol. 342, no. 1629, pp. 191–207, 1975.
- [64] M. Wernli, L. Wiesenfeld, A. Faure, *et al.*, *A&A*, vol. 464, pp. 1147–1154, 2007.
- [65] T. G. Phillips, S. Maluendes, and S. Green, *ApJS*, vol. 107, pp. 467–474, 1996.

-
- [66] L. Wiesenfeld and A. Faure, *Mon. Not. R. Astronom. Soc.*, vol. 432, pp. 2573–2578, 2013.
- [67] M. Wernli, P. Valiron, A. Faure, *et al.*, *A&A*, vol. 446, pp. 367–372, 2006.
- [68] Y. Kalugina, F. Lique, and J. Kłos, *Mon. Not. R. Astronom. Soc.*, vol. 422, pp. 812–818, 2012.
- [69] M. Hernández Vera, F. Lique, F. Dumouchel, *et al.*, *Mon. Not. R. Astronom. Soc.*, vol. 468, pp. 1084–1091, 2017.
- [70] C. T. Bop and F. Lique, *J. Chem. Phys.*, vol. 158, no. 074304, 2023.
- [71] F. Tonolo, L. Bizzocchi, V. M. Rivilla, *et al.*, *Monthly Notices of the Royal Astronomical Society*, vol. 527, no. 2, pp. 2279–2287, Jan. 2024, ISSN: 0035-8711. (visited on 11/20/2024).
- [72] O. Yazidi, D. Ben Abdallah, and F. Lique, *Mon. Not. R. Astronom. Soc.*, vol. 441, pp. 664–670, 2014.
- [73] O. Denis-Alpizar and J. Rubayo-Soneira, *Mon. Not. R. Astronom. Soc.*, vol. 486, no. 1, pp. 1255–1259, 2019.
- [74] M. Ben Khalifa, P. J. Dagdigian, and J. Loreau, *Mon. Not. R. Astronom. Soc.*, vol. 523, pp. 2577–2586, 2023.
- [75] S. Green, *J. Chem. Phys.*, vol. 64, pp. 3463–3473, 1976.
- [76] S. Green, *J. Chem. Phys.*, vol. 70, pp. 816–829, 1979.
- [77] F. Lique and J. Kłos, *J. Chem. Phys.*, vol. 128, no. 034306, 2008.
- [78] M. Żóltowski, F. Lique, A. Karska, *et al.*, *Mon. Not. R. Astronom. Soc.*, vol. 502, pp. 5356–5361, 2021.
- [79] J. M. Hutson and C. R. Le Sueur, *Computer Physics Communications*, vol. 241, pp. 9–18, 2019.
- [80] M. H. Alexander, P. J. Dagdigian, H. J. Werner, *et al.*, *Computer Physics Communications*, vol. 289, p. 108761, 2023.
- [81] G. C. Corey and F. R. McCourt, *J. Chem. Phys.*, vol. 87, pp. 2723–2730, 1983.
- [82] M. H. Alexander and P. J. Dagdigian, *J. Chem. Phys.*, vol. 83, p. 2191, 1985.
- [83] A. Faure and F. Lique, *Mon. Not. R. Astronom. Soc.*, vol. 425, pp. 740–748, 2012.
- [84] D. Galli and F. Palla, *A&A*, vol. 335, pp. 403–420, 1998.
- [85] C. D. Gay, P. C. Stancil, S. Lepp, *et al.*, *ApJ*, vol. 737, no. 44, 2011.
- [86] G. C. Schatz and A. Kuppermann, *J. Chem. Phys.*, vol. 65, pp. 4642–4667, 1976.

-
- [87] D. Skouteris, J. F. Castillo, and D. E. Manolopoulos, *Computer Physics Communications*, vol. 133, no. 1, pp. 128–135, 2000.
- [88] B. Desrousseaux, C. M. Coppola, M. V. Kazandjian, *et al.*, *J. Phys. Chem. A.*, vol. 122, pp. 8390–8396, 2018.
- [89] B. Desrousseaux, C. M. Coppola, and F. Lique, *Mon. Not. R. Astronom. Soc.*, vol. 513, pp. 900–905, 2022.
- [90] B. Desrousseaux and F. Lique, *J. Chem. Phys.*, vol. 152, no. 074303, 2020.
- [91] Y. Sun, R. C. Mowrey, and D. J. Kouri, *J. Chem. Phys.*, vol. 87, pp. 339–349, 1987.
- [92] S. Y. Lin and H. Guo, *Phys. Rev. A*, vol. 74, no. 022703, 2006.
- [93] O. Martinez Jr., S. G. Ard, A. Li, *et al.*, *J. Chem. Phys.*, vol. 143, no. 114310, 2015.
- [94] D. J. Hollenbach and A. G. G. M. Tielens, *Rev. Mod. Phys.*, vol. 71, no. 1, pp. 173–230, Jan. 1999.
- [95] B. Godard, E. Falgarone, M. Gerin, *et al.*, *A&A*, vol. 540, Apr. 2012.
- [96] N. Indriolo, D. A. Neufeld, M. Gerin, *et al.*, *ApJ*, vol. 800, no. 40, 2015.
- [97] J. Loreau, F. Lique, and A. Faure, *ApJL*, vol. 853, p. 5, 2018.
- [98] M. Konings, B. Desrousseaux, F. Lique, *et al.*, *J. Chem. Phys.*, vol. 155, no. 104302, 2021.
- [99] A. Szabo and N. S. Ostlund, *Modern Quantum Chemistry: Introduction to Advanced Electronic Structure Theory*, Dover Publications, Inc. General Publishing Company, 1996.
- [100] R. S. Mulliken, *Science*, vol. 157, no. 3784, pp. 13–24, 1967. JSTOR: [1721629](#).
- [101] J. C. Slater, *PhysRev*, vol. 34, no. 10, 1929.
- [102] C. Cohen-Tannoudji, B. Diu, and F. Laloë, *Mécanique Quantique - Tome II*, CNRS Editions. EDP Sciences, 2018.
- [103] F. Jensen, *Introduction to Computational Chemistry*, John Wiley & Sons, Ltd. Wiley, 2007.
- [104] M. W. Schmidt and K. Ruedenberg, *J. Chem. Phys.*, vol. 71, pp. 3951–3962, 1979.
- [105] T. H. Dunning, *J. Chem. Phys.*, vol. 90, pp. 1007–1023, 1989.
- [106] S. F. Boys and S. Bernardi, *Mol. Phys.*, vol. 19, pp. 553–556, 1970.
- [107] D. R. Hartree, *Proc. Camb. Phil. Soc.*, vol. 24, 89, 1928.

-
- [108] V. Fock, *Zeitschrift für Physik*, vol. 61, no. 1-2, pp. 126–148, 1930.
- [109] J. Čížek, *J. Chem. Phys.*, vol. 45, p. 4256, 1966.
- [110] J. A. Pople, M. Head-Gordon, and K. Raghavachari, *J. Chem. Phys.*, vol. 87, pp. 5968–5975, 1987.
- [111] P. J. Knowles, C. Hampel, and H. J. Werner, *J. Chem. Phys.*, vol. 99, p. 5219, 1993.
- [112] H. J. Werner, P. J. Knowles, and F. R. M. et al., *J. Chem. Phys.*, vol. 152, 2020.
- [113] T. Hollebeek, T.-S. Ho, and H. Rabitz, *Annu. Rev. Phys. Chem.*, vol. 50, pp. 537–570, 1999.
- [114] R. Dawes, A. F. Wagner, and D. L. Thompson, *J. Phys. Chem. A.*, vol. 113, pp. 4709–4721, 2009.
- [115] B. Jiang and H. Guo, *J. Chem. Phys.*, vol. 139, no. 054112, 2013.
- [116] W. Gordy and R. L. Cook, *Microwave Molecular Spectra*. John Wiley & Sons, Inc, 1984.
- [117] J. Brown and A. Carrington, *Rotational Spectroscopy of Diatomic Molecules*, Cambridge Molecular Science Series. Cambridge University Press, 2003.
- [118] F. Hund, *Allgemeine Quantenmechanik Des Atom- Und Molekelbaues*. Handbuch der Physik, 1933.
- [119] J. M. Launay, *Étude Théorique de Collisions Atomiques et Moléculaires d'intérêt Astrophysique*. 1978.
- [120] D. R. Flower, *Molecular Collisions in the Interstellar Medium*, Second edition. Cambridge astrophysics series, 2007.
- [121] R. T. Pack, *J. Chem. Phys.*, vol. 60, pp. 633–639, 1974.
- [122] P. McGuire, *J. Chem. Phys.*, vol. 62, pp. 525–534, 1975.
- [123] D. Secrest, *J. Chem. Phys.*, vol. 62, p. 710, 1975.
- [124] M. Lanza and F. Lique, *J. Chem. Phys.*, vol. 141, p. 164321, 2014.
- [125] R. B. Bernstein, A. Dalgarno, H. S. W. Massey, et al., *Proc. Roy. Soc.*, vol. 274, no. 1359, 1963.
- [126] P. Pechukas and J. C. Light, vol. 42, pp. 3281–3291, 1965.
- [127] W. H. Miller, *J. Chem. Phys.*, vol. 52, pp. 543–551, 1970.
- [128] M. Quack and J. Troe, *Berichte der Bunsengesellschaft für physikalische Chemie*, vol. 79, no. 2, 1975.

-
- [129] D. E. Manolopoulos, *J. Chem. Phys.*, vol. 85, no. 6425, 1986.
- [130] M. H. Alexander and D. E. Manolopoulos, *J. Chem. Phys.*, vol. 86, pp. 2044–2050, 1987.
- [131] R. G. Gordon, *J. Chem. Phys.*, vol. 51, pp. 14–25, 1969.
- [132] M. Abramowitz and I. A. Stegun, *Handbook of Mathematical Functions With Formulas, Graphs, and Mathematical Tables*, National Bureau of Standards. Dover Publications, 1964.
- [133] R. T. Rutten, *Radiative Transfer in Stellar Atmospheres*, ESMN. 1995.
- [134] V. V. Sobolev, *Moving Envelopes of Stars* (Harvard Books on Astronomy). Harvard University Press, 1960, vol. 10.
- [135] K. D. Tucker, M. L. Kutner, and P. Thaddeus, *ApJ*, vol. 193, pp. 115–119, 1974.
- [136] A. Wootten, E. P. Bozyan, D. B. Garrett, *et al.*, *ApJ*, vol. 239, pp. 844–854, 1980.
- [137] N. Sakai, O. Saruwatari, T. Sakai, *et al.*, *A&A*, vol. 512, 2010.
- [138] H. Beuther, D. Semenov, Th. Henning, *et al.*, *ApJ*, vol. 675, pp. 33–36, 2008.
- [139] S. P. Treviño-Morales, P. Pilleri, A. Fuente, *et al.*, *A&A*, vol. 569, 2014.
- [140] K. Yoshida, N. Sakai, Y. Nishimura, *et al.*, *Publ. Astron. Soc. Japan*, vol. 71, 2019.
- [141] M. Padovani, C. M. Walmsley, M. Tafalla, *et al.*, *A&A*, vol. 505, pp. 1199–1211, 2009.
- [142] A. Dutrey, S. Guilloteau, and M. Guélin, *Chemistry of Protosolar-like nebulae: The molecular content of the DM Tau and GG Tau disks*, 1996.
- [143] L. M. Ziurys, R. J. Saykally, R. L. Plambeck, *et al.*, *ApJ*, vol. 254, pp. 94–99, 1982.
- [144] D. Teyssier, D. Fossé, M. Gerin, *et al.*, *A&A*, vol. 417, pp. 135–149, Dec. 2003.
- [145] S. Cuadrado, J. R. Goicoechea, P. Pilleri, *et al.*, *A&A*, vol. 575, 2015.
- [146] Z. Nagy, V. Ossenkopf, F. F. S. Van der Tak, *et al.*, *A&A*, vol. 578, A124, 2015.
- [147] B. E. Turner, E. Herbst, and R. Terzieva, *ApJS*, vol. 126, p. 427, 2000.
- [148] D. L. Baulch, C. J. Cobos, R. A. Cox, *et al.*, *J. Phys. Chem. Ref. Data*, vol. 21, p. 411, 1992.
- [149] E. Herbst, *Chemical Physics Letter*, vol. 222, pp. 297–301, 1994.
- [150] A. Spielfiedel, N. Feautrier, F. Najar, *et al.*, *Mon. Not. R. Astronom. Soc.*, vol. 421, pp. 1891–1896, 2012.
- [151] F. Najar, D. Ben Abdallah, A. Spielfiedel, *et al.*, *Chemical Physics Letter*, vol. 614, pp. 251–257, 2014.

-
- [152] F. Dumouchel, F. Lique, A. Spieldiedel, *et al.*, *Mon. Not. R. Astronom. Soc.*, vol. 471, pp. 1849–1855, 2017.
- [153] P. J. Dagdigian, *Mon. Not. R. Astronom. Soc.*, vol. 479, pp. 3227–3231, 2018.
- [154] P. J. Dagdigian, *J. Chem. Phys.*, vol. 148, 2018.
- [155] S. Maret, A. Faure, E. Scifoni, *et al.*, *Mon. Not. R. Astronom. Soc.*, vol. 399, no. 1, pp. 425–431, 2009.
- [156] E. Herbst and E. F. van Dishoeck, *Annu. Rev. Astron. Astrophys.*, vol. 47, pp. 427–480, 2009.
- [157] A. Bacmann, F. Daniel, C. Ceccarelli, *et al.*, *A&A*, vol. 587, A26, 2016.
- [158] D. M. Meyer and K. C. Roth, *ApJ*, vol. 376, pp. L49–L52, 1991.
- [159] J. Cernicharo, J. R. Goicoechea, and E. Caux, *ApJ*, vol. 534, pp. L199–L202, 2000.
- [160] J. R. Goicoechea, N. J. Rodriguez-Fernandez, and J. Cernicharo, *ApJ*, vol. 600, pp. 214–233, 2004.
- [161] A. Bacmann, E. Caux, P. Hily-Blant, *et al.*, *A&A*, vol. 521, p. L42, 2010.
- [162] P. Hily-Blant, S. Maret, A. Bacmann, *et al.*, *A&A*, vol. 521, p. L52, 2010.
- [163] C. M. Persson, M. De Luca, B. Mookerjee, *et al.*, *A&A*, vol. 543, A145, 2012.
- [164] T. R. Gull, P. W. Morris, J. H. Black, *et al.*, *Mon. Not. R. Astronom. Soc.*, vol. 499, pp. 5269–5301, 2020.
- [165] J. R. Goicoechea and O. Roncero, *A&A*, vol. 664, A190, 2022.
- [166] R. Wagenblast, D. A. Williams, T. J. Millar, *et al.*, *Mon. Not. R. Astronom. Soc.*, vol. 260, pp. 420–424, 1993.
- [167] R. Le Gal, P. Hily-Blant, A. Faure, *et al.*, *A&A*, vol. 562, A83, 2014.
- [168] V. Dislaire, P. Hily-Blant, A. Faure, *et al.*, *A&A*, vol. 537, A20, 2012.
- [169] E. Vigren, V. Zhaunerchyk, M. Hamberg, *et al.*, *ApJ*, vol. 757, p. 34, 2012.
- [170] D. P. Linder and M. Page, *J. Phys. Chem.*, vol. 99, pp. 11 458–11 463, 1995.
- [171] R. Tobiła, F. Dumouchel, J. Kłos, *et al.*, *J. Chem. Phys.*, vol. 134, p. 024 305, 2011.
- [172] H. Cybulski, R. V. Krems, H. R. Sadeghpour, *et al.*, *J. Chem. Phys.*, vol. 122, 2005.
- [173] F. Dumouchel, J. Kłos, R. Tobiła, *et al.*, *J. Chem. Phys.*, vol. 137, p. 114 306, 2012.

-
- [174] R. Ramachandran, J. Kłos, and F. Lique, *J. Chem. Phys.*, vol. 148, p. 084311, 2018.
- [175] J. L. Linsky, B. T. Draine, H. W. Moos, *et al.*, *ApJ*, vol. 647, pp. 1106–1124, 2006.
- [176] C. Ceccarelli, A. Castets, L. Loinard, *et al.*, *A&A*, vol. 338, pp. L43–L46, 1998.
- [177] P. Caselli, F. F. S. Van der Tak, C. Ceccarelli, *et al.*, *A&A*, vol. 403, pp. L37–L41, 2003.
- [178] A. Bacmann, B. Lefloch, C. Ceccarelli, *et al.*, *ApJ*, vol. 585, pp. L55–L58, 2003.
- [179] R. Lucas and H. Liszt, *A&A*, vol. 337, pp. 246–252, 1998.
- [180] A. H. Salek, R. Simon, G. Winnewisser, *et al.*, *Can. J. Phys.*, vol. 72, 1994.
- [181] K. Taniguchi, E. Herbst, H. Ozeki, *et al.*, *ApJ*, vol. 884, 2019.
- [182] K. Giers, S. Spezzano, and P. Caselli, *A&A*, vol. 676, A78, 2023.
- [183] K. Furuya, Y. Aikawa, N. Sakai, *et al.*, *ApJ*, vol. 731, 2011.
- [184] C. A. Gottlieb, E. W. Gottlieb, and P. Thaddeus, *ApJ*, vol. 264, pp. 740–745, 1983.
- [185] J. M. Vrtilek, C. A. Gottlieb, W. D. Langer, *et al.*, *A&A*, vol. 296, pp. 35–38, 1985.
- [186] M. C. McCarthy, C. A. Gottlieb, and P. Thaddeus, *Journal of Molecular Spectroscopy*, vol. 173, pp. 303–307, 1995.
- [187] J. Flores-Mijangos, J. M. Brown, F. Matsushima, *et al.*, *Journal of Molecular Spectroscopy*, vol. 225, pp. 189–195, 2004.
- [188] S. Takano, T. Klaus, and G. Winnewisser, *Journal of Molecular Spectroscopy*, vol. 192, pp. 309–319, 1998.
- [189] P. Pirlot Jankowiak, Y. Kalugina, R. Ramachandran, *et al.*, *J. Chem. Phys.*, vol. 155, 2021.
- [190] K. P. Huber and G. Herzberg, *Molecular Spectra And Molecular Structure, IV. Constants Of Diatomic Molecules*. New York: Van Nostrand Reinhold, 1979.
- [191] W. M. Fawzy, G. Kerenskaya, and M. C. Heaven, *J. Chem. Phys.*, vol. 122, 2005.
- [192] M. Bogey, C. Demuynck, and J. L. Destombes, *Molecular Physics*, vol. 66, pp. 955–960, 1989.
- [193] P. Pirlot Jankowiak, F. Lique, and P. J. Dagdigian, *Mon. Not. R. Astronom. Soc.*, vol. 523, pp. 3732–3740, 2023.
- [194] P. Pirlot Jankowiak, F. Lique, and P. J. Dagdigian, *Mon. Not. R. Astronom. Soc.*, vol. 526, pp. 885–894, 2023.

-
- [195] P. Pirlo Jankowiak, F. Lique, and J. R. Goicoechea, *A&A*, vol. forthcoming article, 2024.
- [196] M. Costes and C. Naulin, *Chem. Sci.*, vol. 7, pp. 2462–2469, 2016.
- [197] M. H. Alexander and P. J. Dagdigian, *J. Chem. Phys.*, vol. 79, 1983.
- [198] G. C. Corey, M. H. Alexander, and J. Schaefer, *J. Chem. Phys.*, vol. 85, p. 2726, 1986.
- [199] Y. Kalugina and F. Lique, *Mon. Not. R. Astronom. Soc.*, vol. 446, pp. 21–25, 2015.
- [200] S. Demes, F. Lique, J. Loreau, *et al.*, *Mon. Not. R. Astronom. Soc.*, vol. 524, pp. 2368–2378, 2023.
- [201] A. R. Offer, M. C. van Hemert, and E. W. van Dishoeck, *J. Chem. Phys.*, vol. 100, 1993.
- [202] L. D. Landau and E. M. Lifshitz, *Quantum Mechanics, Non-relativistic Theory*, Third edition. Pergamon Press, 1977, vol. 3.
- [203] R. Goldflam, D. J. Kouri, and S. Green, *J. Chem. Phys.*, vol. 67, p. 5661, 1977.
- [204] F. Daniel, M. L. Dubernet, and M. Meuwly, *J. Chem. Phys.*, vol. 121, p. 4540, 2004.
- [205] M. H. Alexander, *J. Chem. Phys.*, vol. 76, 1982.
- [206] D. A. Neufeld and S. Green, *ApJ*, vol. 432, pp. 158–166, 1994.
- [207] M. Lara-Moreno, T. Stoecklin, and P. Halvick, *Mon. Not. R. Astronom. Soc.*, vol. 507, pp. 4086–4094, 2021.
- [208] A. Godard Palluet and M. Gueguen, *Philosophy of Science*, vol. 0, pp. 1–11, 2024.
- [209] F. F. S. Van der Tak, J. H. Black, F. L. Schöier, *et al.*, *Mon. Not. R. Astronom. Soc.*, vol. 468, pp. 627–635, 2007.
- [210] M. Lampton, B. Margon, and S. Bowyer, *ApJ*, vol. 208, pp. 177–190, 1976.
- [211] D. Hollenbach, M. J. Kaufman, D. A. Neufeld, *et al.*, *ApJ*, vol. 754, no. 105, 2012.
- [212] C. R. Markus, J. N. Hodges, A. J. Perry, *et al.*, *ApJ*, vol. 817, no. 138, 2016.
- [213] F. Wyrowski, K. M. Menten, R. Güsten, *et al.*, *A&A*, vol. 518, no. A26, 2010.
- [214] R. Güsten, L. A. Nyman, P. Schilke, *et al.*, *A&A*, vol. 454, pp. L13–L16, 2006.
- [215] P. P. van der Werf, K. G. Isaak, and R. Meijerink, *A&A*, vol. 518, no. L42, 2010.
- [216] M. J. Griffin, A. Abergel, and A. Abreu, *A&A*, vol. 518, no. L3, 2010.
- [217] Th. de Graauw, F. P. Helmich, and T. G. Phillips, *A&A*, vol. 518, no. L6, 2010.

-
- [218] S. Muller, H. S. P. Müller, J. H. Black, *et al.*, *A&A*, vol. 595, no. 128, 2016.
- [219] F. F. S. Van der Tak, Z. Nagy, V. Ossenkopf, *et al.*, *A&A*, vol. 560, no. A95, 2013.
- [220] I. Aleman, T. Ueta, D. Ladjal, *et al.*, *A&A*, vol. 566, no. A79, 2014.
- [221] A. Poglitsch, C. Waelkens, and N. Geis, *A&A*, vol. 518, no. L2, 2010.
- [222] M. Pereira-Santaella, L. Spinoglio, G. Busquet, *et al.*, *ApJ*, vol. 768, no. 55, 2013.
- [223] L. Spinoglio, M. Pereira-Santaella, and G. Busquet, *ApJ*, vol. 758, no. 108, 2012.
- [224] J. Li, R. Wang, and D. Riechers, *ApJ*, vol. 889, no. 162, 2020.
- [225] F. Stanley, K. K. Knudsen, S. Aalto, *et al.*, *A&A*, vol. 646, no. A178, 2021.
- [226] A. Kovalenko, T. D. Tran, and S. Rednyk, *ApJ*, vol. 856, no. 100, 2018.
- [227] D. Gerlich, P. Jusko, Š. Roučka, *et al.*, *ApJ*, vol. 749, no. 22, 2012.
- [228] N. Bulut, F. Lique, and O. Roncero, *J. Phys. Chem. A.*, vol. 119, pp. 12 082–12 089, 2015.
- [229] P. M. Hillenbrand, N. de Ruette, X. Urbain, *et al.*, *ApJ*, vol. 927, no. 47, 2022.
- [230] S. Gomez-Carrasco, B. Godard, and F. Lique, *ApJ*, vol. 794, no. 33, 2014.
- [231] J. D. Burley, K. M. Ervin, and P. B. Armentrout, *International Journal of Mass Spectrometry and Ion Processes*, vol. 80, pp. 153–175, 1987.
- [232] X. Li, Y. L. Huang, G. D. Flesch, *et al.*, *J. Chem. Phys.*, vol. 106, pp. 564–571, 1997.
- [233] F. Le Petit, C. Nehmé, J. Le Bourlot, *et al.*, *ApJS*, vol. 164, no. 506, 2006.
- [234] T. Stoecklin, M. A. Gannouni, N. E. Jaidane, *et al.*, *J. Phys. Chem. A.*, vol. 119, pp. 12 599–12 606, 2015.
- [235] F. Lique, N. Bulut, and O. Roncero, *Mon. Not. R. Astronom. Soc.*, vol. 461, pp. 4477–4481, 2016.
- [236] T. D. Tran, S. Rednyk, and A. Kovalenko, *ApJ*, vol. 854, no. 25, 2018.
- [237] S. S. Kumar, F. Grussie, Y. V. Suleimanov, *et al.*, *Sci. Adv.*, vol. 4, no. 6, 2018.
- [238] H. Song, A. Li, and H. Guo, *J. Phys. Chem. A.*, vol. 120, pp. 4742–4748, 2016.
- [239] A. J. Merer, D. N. Malm, R. W. Martin, *et al.*, *Can. J. Phys.*, vol. 53, pp. 251–283, 1975.
- [240] R. Martinez, J. Millan, and M. Gonzalez, *J. Chem. Phys.*, vol. 120, no. 10, 2004.
- [241] M. Paniagua, R. Martinez, P. Gamallo, *et al.*, *Phys. Chem. Chem. Phys.*, vol. 16, no. 23594, 2014.

-
- [242] A. Li and H. Guo, *J. Phys. Chem. A.*, vol. 118, pp. 11 168–11 176, 2014.
- [243] T. R. Huet, C. J. Pursell, W. C. Ho, *et al.*, *J. Chem. Phys.*, vol. 9, pp. 5977–5987, 1992.
- [244] K. Irikura, *J. Phys. Chem. Ref. Data*, vol. 36, pp. 389–397, 2007.
- [245] J. D. C. Jones, K. Birkinshaw, and N. D. Twiddy, *Chemical Physics Letter*, vol. 77, no. 3, pp. 484–488, 1981.
- [246] J. M. Shul, R. Passarella, L. T. DiFazio Jr., *et al.*, *J. Phys. Chem.*, vol. 92, no. 17, pp. 4947–4951, 1988.
- [247] S. E. Strahan, R. P. Mueller, and R. J. Saykally, *J. Chem. Phys.*, vol. 85, pp. 1252–1260, 1986.
- [248] D. Forney, M. E. Jacox, and W. E. Thompson, *J. Chem. Phys.*, vol. 98, pp. 841–849, 1993.
- [249] F. Lique, N. Bulut, and O. Roncero, *Mon. Not. R. Astronom. Soc.*, vol. 461, pp. 4477–4481, 2016.
- [250] M. E. Rose, *Elementary Theory of Angular Momentum*. John Wiley & Sons, Inc, 1957.
- [251] A. Messiah, *Quantum Mechanics*. Amsterdam: North Holland Publishing Company, 1962, vol. 2.
- [252] I. I Sobelman, *Atomic Spectra and Radiative Transitions*. Springer-Verlag Berlin Heidelberg New York, 1979, vol. 1.

Titre : Excitation collisionnelle de radicaux d'intérêt astrophysique

Mot clés : Dynamique quantique, excitation collisionnelle

Résumé : La modélisation des spectres moléculaires interstellaires nécessite la compréhension des processus radiatifs et collisionnels de transferts d'énergie entre espèces chimiques. Des taux de collisions d'état à état précis pour les molécules interstellaires, en collision avec H_2 , H et He, sont alors essentiels.

Ces données peuvent être obtenues via la résolution des équations close-coupling indépendantes du temps, étant la méthode la plus précise pour les calculs à basse températures. Cependant, certaines molécules comme les radicaux présentent des structures énergétiques complexes en raison de leurs spins

électroniques et nucléaires, rendant la description précise des transitions fines et hyperfines théoriquement coûteuse en ressources numériques. D'importants systèmes collisionnels souffrent donc d'un manque de données pour les interprétations astrophysiques.

Ce travail de thèse vise à quantifier l'excitation collisionnelle de radicaux d'intérêt astrophysique en développant des outils méthodologiques et numériques pour surmonter ces défis. De nouveaux taux de collision fins et hyperfins ont été calculés pour les systèmes suivants : $NH-H_2$, $ND-H_2$, C_2H-H_2 , C_2D-H_2 , $^{13}CCH-H_2$, et $C^{13}CH-H_2$.

Title: Collisional excitation of radicals of astrophysical interest

Keywords: Quantum dynamics, molecular scattering, astrophysical modeling

Abstract: Modeling molecular spectra from interstellar environments requires understanding radiative and collisional energy transfer processes. Accurate state-to-state collisional rate coefficients for interstellar molecules in collision with H_2 , H, and He are then necessary.

These collisional data can be obtained via quantum time-independent scattering calculations using the close-coupling approach, being the most accurate approach for low temperatures. However, molecules like radicals have complex energy structures due to electronic and nuclear spins, making the pre-

cise description of fine and hyperfine transitions challenging and computationally intensive. Then, important collisional systems suffer from lack of data for interpreting astrophysical observations.

This thesis quantifies the collisional excitation of astrophysically relevant radicals by developing methodological and numerical tools to address these challenges. New fine and hyperfine resolved rate coefficients have been computed for the following systems: $NH-H_2$, $ND-H_2$, C_2H-H_2 , C_2D-H_2 , $^{13}CCH-H_2$, and $C^{13}CH-H_2$.